CASTING ALUMINUM ALLOYS

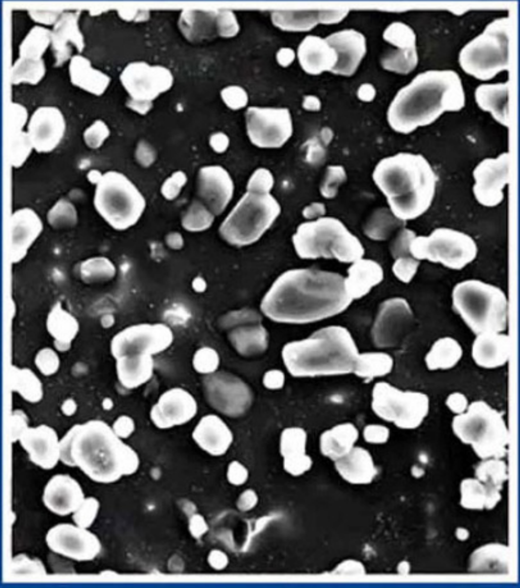

VADIM S. ZOLOTOREVSKY
NIKOLAI A. BELOV
MICHAEL V. GLAZOFF

CASTING ALUMINUM ALLOYS

This page intentionally left blank

CASTING ALUMINUM ALLOYS

VADIM S. ZOLOTOREVSKY and NIKOLAI A. BELOV
Moscow Institute of Steel and Alloys – State Technical University, 119049, Moscow, 4 Leninsky Pr., Russian Federation

MICHAEL V. GLAZOFF
Alcoa Technical Center, Alcoa Center, PA 15069, USA

ELSEVIER

Amsterdam • Boston • Heidelberg • London • New York • Oxford
Paris • San Diego • San Francisco • Singapore • Sydney • Tokyo

Elsevier
Linacre House, Jordan Hill, Oxford OX2 8DP, UK
Radarweg 29, PO Box 211, 1000 AE Amsterdam, The Netherlands

First edition 2007

Copyright © 2007 Elsevier Ltd. All rights reserved

Notice
No responsibility is assumed by the publisher for any injury and/or damage to persons or property as a matter of products liability, negligence or otherwise, or from any use or operation of any methods, products, instructions or ideas contained in the material herein. Because of rapid advances in the medical sciences, in particular, independent verification of diagnoses and drug dosages should be made

British Library Cataloguing in Publication Data
A catalogue record for this book is available from the British Library

Library of Congress Cataloging-in-Publication Data
A catalog record for this book is available from the Library of Congress

ISBN: 978-0-08-045370-5

Printed and bound in Great Britain
07 08 09 10 10 9 8 7 6 5 4 3 2 1

Working together to grow
libraries in developing countries

ELSEVIER BOOK AID International Sabre Foundation

CONTENTS

Preface ix
Notations xiii

1. Alloying Elements and Dopants: Phase Diagrams **1**

1.1 The Role of Alloying Elements and Dopants: Basic Alloy Systems 1
1.2 Phase Diagrams of Ternary Systems 14
  1.2.1 The Al–Be–Fe system 14
  1.2.2 The Al–Be–Si system 15
  1.2.3 The Al–Ce–Cu system 16
  1.2.4 The Al–Ce–Fe system 18
  1.2.5 The Al–Ce–Ni system 20
  1.2.6 The Al–Ce–Si system 21
  1.2.7 The Al–Cr–Fe system 22
  1.2.8 The Al–Cr–Mg system 23
  1.2.9 The Al–Cr–Mn system 24
  1.2.10 The Al–Cr–Si system 26
  1.2.11 The Al–Cu–Fe system 26
  1.2.12 The Al–Cu–Mg system 29
  1.2.13 The Al–Cu–Mn system 32
  1.2.14 The Al–Cu–Ni system 34
  1.2.15 The Al–Cu–Si system 36
  1.2.16 The Al–Cu–Zn system 36
  1.2.17 The Al–Fe–Mg system 38
  1.2.18 The Al–Fe–Mn system 39
  1.2.19 The Al–Fe–Ni system 41
  1.2.20 The Al–Fe–Si system 42
  1.2.21 The Al–Mg–Mn system 45
  1.2.22 The Al–Mg–Si system 45
  1.2.23 The Al–Mg–Zn system 47
  1.2.24 The Al–Mn–Ni system 49
  1.2.25 The Al–Mn–Si system 53
  1.2.26 The Al–Ni–Si system 54
1.3 Phase Diagrams of Four-Component Systems 55
  1.3.1 The Al–Be–Fe–Si phase diagram 56
  1.3.2 The Al–Cu–Fe–Mg system 58
  1.3.3 The Al–Cu–Fe–Mn system 58
  1.3.4 The Al–Cu–Fe–Ni system 60
  1.3.5 The Al–Cu–Fe–Si system 62
  1.3.6 The Al–Cu–Mg–Mn system 64

1.3.7 The Al–Cu–Mg–Si system 64
1.3.8 The Al–Cu–Mg–Zn system 66
1.3.9 The Al–Fe–Mg–Mn system 68
1.3.10 The Al–Fe–Mg–Si system 70
1.3.11 The Al–Fe–Mn–Si system 74
1.3.12 The Al–Fe–Ni–Si system 77
1.3.13 The Al–Mg–Mn–Si system 79
1.3.14 The Al–Mg–Ni–Si system 79
1.4 Five-Component Phase Diagrams 81
1.4.1 The Al–Fe–Cu–Mg–Si system 85
1.4.2 Five-component Systems with manganese 91

2. Structure and Microstructure of Aluminum Alloys in As-Cast State 95

2.1 Phase Diagrams, Thermodynamics, and Alloy Microstructure 95
2.2 Equilibrium Thermodynamics and Its Development 97
2.2.1 Classical equilibrium thermodynamics 97
2.2.2 Equilibrium thermodynamics of concentrationally non-uniform systems 98
2.3 Brief Description of Solidification Microstructure Evolution in Casting Aluminum Alloys via the “Phase-Field” Approach 101
2.3.1 Phase-field approach applied to solidification 102
2.3.2 Dendritic solidification of pure metals 102
2.3.3 Phase-field model for solidification of eutectic alloys[11] 104
2.3.4 Solidification microstructure calculations: perspectives and future work 106
2.4 Quantitative Characteristics of Alloy Structure and Methods of its Evaluation 107
2.5 Non-Equilibrium Solidification of Binary Alloys 114
2.5.1 Microsegregation 115
2.5.2 Influence of cooling rate upon solidification and formation of constituent particles of secondary (excessive) phases 128
2.6 Non-Equilibrium Solidification of Multi-Component Alloys 134
2.6.1 Non-equilibrium phase diagrams of multicomponent systems 134
2.6.2 Microsegregation in three-component and industrial aluminum alloys 145
2.7 Microstructure of Cast Aluminum Alloys 154
2.8 Substructure of Casting Aluminum Alloys 162
2.8.1 Types of dislocation structures in as-cast aluminum alloys of different systems 162
2.8.2 The influence of solidification conditions upon dislocation microstructure 166
2.8.3 The mechanisms of formation of dislocation microstructures in cast aluminum alloys 171
2.8.4 Decomposition of aluminum solid solution in the process of alloy cooling after the completion of solidification 177

3. Influence of Heat Treatment Upon Microstructure of Casting Aluminum Alloys 183

3.1 Homogenizing Heat Treatment 184
  3.1.1 Dissolution of non-equilibrium constituent particles in the course of homogenization 184
  3.1.2 Elimination of microsegregation during homogenization 200
  3.1.3 Fragmentation and spheroidization of constituent particles 213
  3.1.4 Changes of grain and dislocation microstructure of aluminum solid solution in the course of homogenization 222
  3.1.5 Decomposition of aluminum solid solution in the process of isothermal heat treatment before quenching 230
  3.1.6 Development of porosity during homogenization 240
3.2 Aging After Casting and Quenching 240

4. Dependence of Castability and Mechanical Properties on Composition and Microstructure of Aluminum Alloys 247

4.1 Castability 247
  4.1.1 General characterization of castability 247
  4.1.2 Concentration dependence of casting properties 258
4.2 Mechanical Properties 262
  4.2.1 Geometry of elongation diagrams for as-cast and quenched aluminum alloys, and its connection to the structural transformations accompanying deformation 266
  4.2.2 Quantitative analysis of relations between tensile mechanical properties and structural characteristics of castings 280
  4.2.3 Calculations of mechanical properties of castings using the totality of microstructural characteristics 295
  4.2.4 The influence of casting microstructure upon fracture toughness and fatigue properties 302
  4.2.5 Some regularities in changes of mechanical properties with alloy chemical composition 311

5. Industrial Casting Aluminum Alloys 327

5.1 Al–Si Alloys 327
  5.1.1 General characterization of Al–Si alloys 327
  5.1.2 Industrial 4xx and 3xx casting alloys without copper and zinc (“copper-less” alloys) 336
  5.1.3 Industrial Al–Si alloys with copper and zinc 351
  5.1.4 Engine piston Al–Si alloys 367
5.2 Alloys on the Basis of the Al–Cu System 376
5.3 Al–Mg and Al–Mg–Zn Alloys 386
  5.3.1 General characteristic of Al–Mg alloys 386
  5.3.2 Industrial Al–Mg and Al–Mg–Zn alloys 390

6. New Alloys **397**
6.1 Alloys with Small Amounts of Eutectic 397
6.2 General Principles of Alloying for Eutectic Materials 405
6.3 High-Strength Alloy AZ6N4 and ATs7Mg3N4 (734) 418
6.4 Alloys Doped with Transition Metals for Improved Thermal Stability 425
6.5 Alloys with Small Amounts of Silicon (<4%Si) 441

Literature *449*

Appendix 1 Compositions of Standard Casting Aluminum Alloys 461
Appendix 2 Principal Characteristics of Binary Phase Diagrams Closer to Aluminum Side 487
Appendix 3 Guaranteed Mechanical Properties of Standard Russian Aluminum Alloys 491
Appendix 4 Recommended Heat Treatments of Standard Russian Casting Aluminum Alloys 499
Appendix 5 Data on Fracture Toughness and Shock Toughness, Fatigue Life, Characteristics of Thermal Stability, Corrosion Resistance, and Castability of Standard Al–Si Alloys 507
Appendix 6 Derivation of Equations Describing Uniaxial Tensile Testing in Finite Deformations 511
A.6.1 The Case of Infinitesimally Small Deformations 513
A.6.2 The Case of Finite Deformations 515

Index *523*

PREFACE

By definition, casting alloys are materials used for the production of shape castings, that is aluminum alloy products with complex geometrical shape(s). Casting aluminum alloys are quite widespread and find more and more applications in modern industry.

According to different estimates, up to 20–30% of all aluminum products manufactured worldwide are used for shape castings. Suffice it to say that in addition to such giants as Alcoa Inc. and Alcan, there are literally hundreds of cast houses in North America. Aluminum castings are also manufactured by different companies that specialize in end materials/products other than aluminum (e.g., General Motors, Ford, etc.)

Aluminum castings can be and indeed are produced with very substantial amounts of recycled aluminum scrap. For example, in the USA, Western Europe, and Japan up to 75–80% of the overall alloy mass comes from recycled aluminum/scrap. This is several times higher than the corresponding numbers for wrought aluminum alloys. Earlier it was hypothesized that the general level of properties required of cast aluminum products was lower, and they were used mostly for the production of non-critical (e.g., not heavily loaded) parts. Indeed, for such parts the application of recycled aluminum with elevated levels of impurities was quite acceptable.

However, during the last 10 or 15 years this situation has started to change. Due to considerable improvements in casting technologies, now it is possible to produce high-quality castings with properties that are comparable to those of similar wrought products. Moreover, this can be done not only for high-quality alloys, but also for those manufactured with substantial amounts of aluminum scrap. In the latter case the advantage, of course, is in lower production costs.

Significant improvements in the quality of shape castings were achieved due to improved production processes. Today it is possible to employ modern methods of molten metal handling, which result in dramatic reduction of harmful nonmetallic impurities. Hot isostatic pressing is used to reduce shrinkage porosity. All these, and many other, innovations result in significant improvement of aluminum shape casting quality.

There are several important requirements to casting aluminum alloys: good corrosion resistance, high level of mechanical properties (such as ultimate tensile strength (UTS), yield strength (YS), and elongation (El.)) and, finally, good castability. This last property is particularly important; it implies that solidifying metal is not prone to hot cracking, possesses excellent fluidity in molten state, and minimal shrinkage porosity. It is because of excellent castability that Al–Si casting alloys (containing more than 4%Si) have retained their leading role among all other casting alloy compositions during the last 60 years, even though the general level of all other properties is quite average. Indeed, as far as low temperature strength is concerned, Al–Cu and Al–Zn–Mg–Cu alloys are considerably better than Al–Si. Creep resistance is the best for Al–Cu–Mn alloys, corrosion resistance is better for Al–Mg and Al–Zn–Mg alloys. However, mostly due to excellent castability, more than 90% (!) of all shape castings today are manufactured from Al–Si alloys.

Obviously, this situation is not normal as it seriously impedes further development of aluminum alloy shape castings. Evidently, there are two principal ways to approach this important and old problem:

1. Casting technology improvement and development of principally new technological processes that would ensure a high quality of castings made from alloys with low castability.
2. Development of new casting alloy compositions that would combine excellent level of properties with good castability using traditional approaches (e.g., sand casting, permanent mold casting, etc.).

Today there is no doubt that the automotive industry is the most important consumer of aluminum alloy shape castings. Each year the overall volume of cast aluminum in automotive technologies grows steadily. This is especially true during the last 10 years, when the production of "aluminum" cars started and the number of aluminum-intensive vehicles grew rapidly. Such details as cylinder blocks, pistons, other engine parts, frames, and covers of different devices "under the hood" are traditionally cast from aluminum now.

All these complex details and products are manufactured using different casting techniques and amount to many millions of parts per year.

Due to their excellent specific strength, corrosion resistance, and relatively low labor intensity of production, cast aluminum alloys are also widely used in other transportation sectors of the economy such as aerospace, marine, and railroad transportation.

It was mentioned above that in the automotive industry Al–Si alloys find the most widespread application. However, in the aerospace industry a substantial number of all castings are made of high-strength Al–Cu alloys of the 2xx series, while in shipbuilding the corrosion-resistant Al–Mg alloys of the 5xx series[1] are ubiquitous. Alloys of the Al–Mg and Al–Si types are also used in railroad car construction (e.g., massive brake gear).

Large amounts of aluminum alloy castings are consumed by the defense industry, electronics, nuclear industry, etc. Examples of large cast aluminum parts include gaskets of electric motors, wheels of armored vehicles, and tank turrets.

It is obvious that further successes in perfection of already existing and development of novel casting aluminum alloys will be defined by our understanding of their metals science and metals physics, that is our capability to relate alloy properties to their composition and microstructure. In the second half of the 20th century this level was significantly raised; however, there are still many questions and problems that remain unsolved. To a significant degree, such a situation arises because only a limited (and decreasing) number of specialists in several countries were involved in aluminum research. For example, in major American universities this area of research is no longer "fashionable". Consequently, the actual aluminum research is conducted mostly in technical centers of large industrial companies, such as Alcoa Inc.

---

[1] Here and below the classification of cast alloys adopted by the Aluminum Association will be used.

The present monograph mostly summarizes research conducted at the Moscow Institute of Steel and Alloys over many decades (Chair of Non-Ferrous Metals), in part together with Alcoa Inc. (especially during the last 5–7 years). This research was initiated by such talented scientists as A.A. Bochvar between 1930 and 1940, I.I. Novikov between 1950 and 1960, and continued by the authors of the present work. Many dozens of professors, research scientists, graduate and undergraduate students took part in it. The authors would like to express their gratitude to all these numerous researchers. One of the authors (M.V. Glazoff) expresses his sincere gratitude to the Technical Director of the Alcoa Technical Center, Dr. William A. Cassada, III, and to the Division Managers, Dr. Jonell M. Kerkhoff and Dr. Ralph R. Sawtell, for permission to publish this monograph and for continuous support of our research efforts.

Finally, it was decided to retain the original nomenclature for most Russian casting alloys and references used in this monograph. This was done to facilitate direct discussions between the interested researchers without causing otherwise inevitable spelling or translation problems. The authors would like to hope that it will not cause confusion in understanding the corresponding parts of this book.

Moscow, Pittsburgh 2007

This page intentionally left blank

NOTATIONS

(Al), (Si)	Solid solutions on the basis of aluminum, silicon (and other elements)
D	Grain size of primary dendrites of (Al): D_{min}, D_{max} – minimal and maximal sizes
d	Dendritic parameter of (Al) primary crystals
d'	Subgrain size
D_e	Average size of eutectic colonies
d_e	Dendrite arms spacing
V_c	Cooling rate upon solidification
S	Specific surface of inclusions (grain boundaries)
C_x	Concentration of a given component in alloy: C_1, C_2, C_{Cu}, C_{Fe}
C_{x-y}	Concentration of a component in a phase: C_{1-2}, C_{2-2}, C_{Cu-Al}
C_e, C_a	Concentration of component in eutectic and limit solubility in (Al)
ΔC, C_{min}, C_{max}	Concentration difference, minimal and maximal concentration
K	Distribution coefficient for an element
Q_V	Volume fraction of phases, pores, and eutectic
Q_M	Mass fraction of a phase or eutectic
m	Thickness of the second phase inclusions
I	Distance among inclusions
γ	Specific weight (density)
ρ	Density of dislocations
ρ_1, ρ_2	Density of dislocations outside and inside planar subgrain boundaries
b	Dislocation Burgers vector
a	Lattice spacing
θ	Angle of disorientation between subgrains
D_V	Coefficient of volume diffusion
T	Temperature
τ	Time

This page intentionally left blank

CHAPTER ONE

ALLOYING ELEMENTS AND DOPANTS: PHASE DIAGRAMS

1.1 THE ROLE OF ALLOYING ELEMENTS AND DOPANTS: BASIC ALLOY SYSTEMS

Today more than several dozens of aluminum alloys are used in different areas of manufacturing and technology (e.g., automotive, aerospace, etc.) [1–13]. Patents have been issued for thousands of alloy compositions. However, most of them contain a relatively limited number of alloying elements. This is illustrated by Appendix 1, which provides information on the most widely used US casting aluminum alloys.

All alloying elements that are used for aluminum alloy design can be classified into three principal groups: basic alloying elements, ancillary additions (or dopants), and impurities. Depending upon the nature of an alloy, the same elements could play different roles.

In the overwhelming majority of all cases only four alloying elements are used: metals magnesium, zinc, and copper; and semiconductor silicon. We call these chemical elements "basic", or "principal", because they are introduced into aluminum alloys in (relatively) large amounts and define their microstructure and properties. For example, the Mg content in Al–Si casting alloys with 7%Si or 9%Si is only ~0.3%, but it is this small amount that defines the alloy's strength. In this sense, Mg is the principal alloying element in these alloys. On the other hand, Mn in similar alloys can be present in the amounts 0.5% and even more, but should be considered a small addition since its principal role is auxiliary, to neutralize the harmful influence of iron. Another example: in alloys on the basis of the Al–Cu system containing less than 1%Mn, the latter should be considered the key element because it significantly increases the alloy's thermal stability.

The introduction of relatively large amounts of principal alloying elements is possible because they are characterized by considerable solubility in (Al) (as follows from the respective binary phase diagrams [14, 15]). It is known that maximum solubility in (Al) exceeds 1% only for the following seven elements: magnesium, copper, silicon, lithium, manganese, germanium, and silver. However, not a single one of these chemical elements can form continuous solid solutions, that is, at some critical concentration none enters an intermediate compound or

Casting Aluminum Alloys
ISBN-13: 978-0-08-045370-5

© 2007 Elsevier Ltd.
All rights reserved.

forms its own solid solution (see Appendix 2). All other chemical elements possess much lower solubility in (Al), that is, of the order of 0.1–0.01%.

Of these seven elements two can hardly be used as principal alloying elements in aluminum alloys, mostly because of economic considerations. Silver is a precious and expensive metal, while germanium is also an expensive material widely used in the semiconductor industry. Additionally, these two elements do not render any new or interesting properties to aluminum alloys; their influence is not more significant than that of the other five easily available elements. One should mention, however, that silver is used as an ancillary addition in some casting alloys, such as AA201.0 (Appendix 1). Lithium has found widespread applications in wrought aluminum alloys, but not in castings, mostly because of technological problems. Moreover, in Al–Si casting alloys, in spite of the significant strengthening effect [16], it is considered to be one of the most harmful additions, along with other alkaline metals [17].

All of the principal alloying elements form eutectic phase diagrams with aluminum (see Figure 1.1). The corresponding parameters of these binary eutectics are given in Table 1.1. All industrial alloys (see Appendix 1) may be classified, in as-cast condition, into the following four groups:

1. Alloys of the "solid solution type" (e.g., some Al–Cu and Al–Mg alloys); these alloys are characterized by the presence of a non-equilibrium degenerate eutectic reaction, which disappears upon T6 heat treatment (Figure 1.2a).
2. Hypo-eutectic alloys in which, as a rule, the eutectic component has two-phase structure (e.g., Al–Si alloys with 7%Si) (Figure 1.2b).
3. Eutectic alloys in which eutectic is the principal microstructural component (e.g., Al–Si alloys with 12%Si) (Figure 1.2c).
4. Alloys with primary crystals of excessive phases (constituent particles) (e.g., hyper-eutectic Al–Si alloys) (Figure 1.2d).

This classification is quite well applicable to those alloys of which the structure can be roughly described by the corresponding binary phase diagram (Figure 1.1). However, the numerous experimental data existing for a number of alloys should be approached with caution. For example, if the Fe concentration for alloys belonging to the 1st, 2nd, and 3rd groups is high, then crystals of Fe-bearing constituent phases could be formed, and such alloys should be classified as belonging to the 4th group.

The first and foremost function of the alloying elements is to increase alloy strength (pure aluminum has very low strength, $\sigma_{0.2} < 60$ MPa). A strengthening effect is achieved via solid solution formation and, in some cases, via dispersion hardening. On the other hand, the presence of alloying elements also affects castability very strongly. This latter property, to a very significant extent, will define whether a given casting alloy could be used in industry or not.

Solid solution strengthening is defined by a number of factors, including atomic size mismatch. The relative difference of the Al atomic radius and that of an alloying element $((R_{\text{Al}} - R_2)/R_{\text{Al}}) \times 100\%$ attains the maximal value for

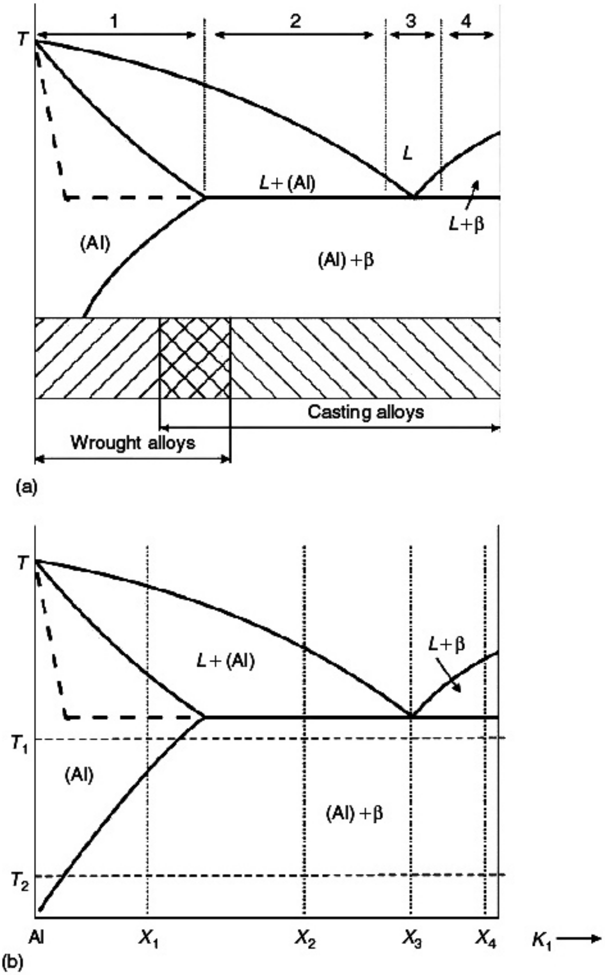
T
1
2
3
4
L
L + (Al)
L+β
(Al)
(Al) +β
Casting alloys
Wrought alloys
(a)
T
L+β
L + (Al)
T_1
(Al)
(Al) +β
T_2
Al
X_1
X_2
X_3
X_4
K_1 ⟶
(b)

Figure 1.1 Schematic of a binary phase diagram Al–B (2nd component) of the eutectic type: (a) domains of wrought and casting alloys; (b) typical alloys.

magnesium (11.7%) and *copper* (10.5%). These two alloying additions ensure the maximal solid solution strengthening effect ($\Delta\sigma_b/1\text{at.\%} = 30$–$40$ MPa). Alloys of the Al–Mg system are non-heat treatable and possess low thermal stability. In principle, they could be subjected to quenching and aging (as follows from Figure 1.3), but the strength increase will be insignificant because of the small number density of precipitates – products of aging. However, magnesium increases corrosion resistance of aluminum, only insignificantly decreases its formability and

Table 1.1 Characteristics of eutectic phase diagrams (Figure 1.1) of Al with principal alloying elements [14]

No.	Alloying elements	C_a[a]		C_e[b]		T_e[c] (°C)	Phases in equilibrium with (Al) (contents of the 2nd component, mass%)
		Mass%	At.%	Mass%	At.%		
1	Cu	5.7	2.5	33.2	17.5	547	$CuAl_2$ (52%Cu)
2	Mg	17.4	18.5	35	36	450	Mg_5Al_8 (35%Mg)
3	Zn	82	49.3	94.9	75	382	(Zn) (99%Zn)
4	Si	1.65	1.59	12	12	577	(Si) (99.5%Si)

[a] Limit solubility at eutectic temperature.
[b] Concentration at eutectic point.
[c] Solidification temperature of binary eutectic.

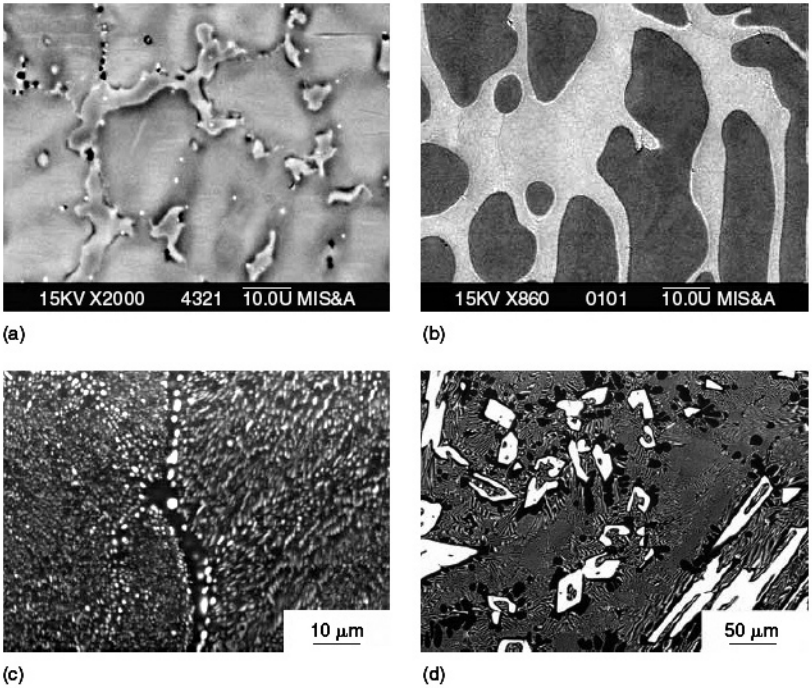

Figure 1.2 Typical microstructures of binary aluminum alloys in as-cast condition (see Figure 1.1b: (a) X_1, (b) X_2, (c) X_3, (d) X_4); (a) Light microscopy and (b–d) SEM.

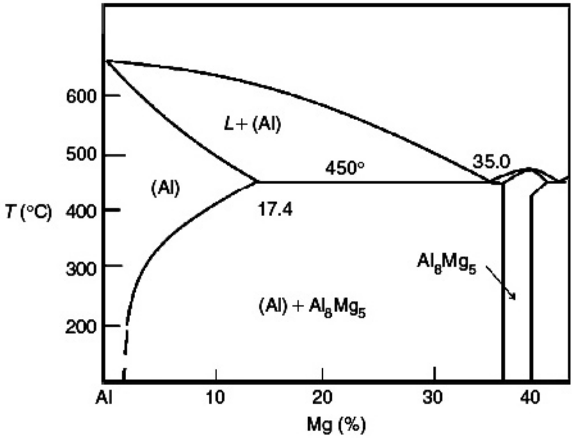

Figure 1.3 Phase diagram Al–Mg.

results in a complex of properties that make the Al–Mg family of wrought alloys (5xxx series) one of the most widespread aluminum alloys. Al–Mg can be used as casting alloys, but their castability is low.

Additions of copper can result not only in a solid solution strengthening effect, but also in substantial dispersion hardening after solid solution heat treatment (SHT), quenching, and aging inasmuch as its solubility in (Al) dramatically decreases with temperature (see Figure 1.4). For this reason, Al–Cu alloys generally have higher yield strength and ultimate tensile strength (UTS) in a broader temperature range, compared to Al–Mg alloys. Unfortunately, copper reduces corrosion resistance of aluminum and any of its alloys. In this sense it is a harmful additive, and its concentration needs to be limited. Similar to Mg, the phase diagram of the Al–Cu system is characterized by large ($T_{\mathrm{liq}} - T_{\mathrm{sol}}$) ranges, which makes castability of Al–Cu-based alloys very low.

Additions of *zinc* exert a very minor solid solution strengthening effect because of a small atomic radii mismatch factor, and do not represent any interest when zinc is the only alloying element. However, when it is introduced together with other additives, especially with Mg and Cu, it exerts a profound effect on alloy properties (see Sections 5.3 and 6.1).

Binary Al–Si alloys are non-heat treatable, in spite of some changes of Si solubility in (Al) with temperature (Figure 1.5). Additional alloying with magnesium and copper makes these alloys susceptible to quenching and aging. For this reason, only multicomponent alloys are used (e.g., Al–Si–Mg, Al–Si–Cu, and Al–Si–Cu–Mg) (see Section 5.1). It should be noted that *silicon* is introduced into aluminum alloys not only because of its solubility in (Al), but also due to the formation of the (Al) + (Si) eutectic, which defines many of the Al–Si alloys' properties (such as castability). For this reason the total Si concentration should be subdivided into two components: the first (<1.65%) represents Si in the aluminum matrix

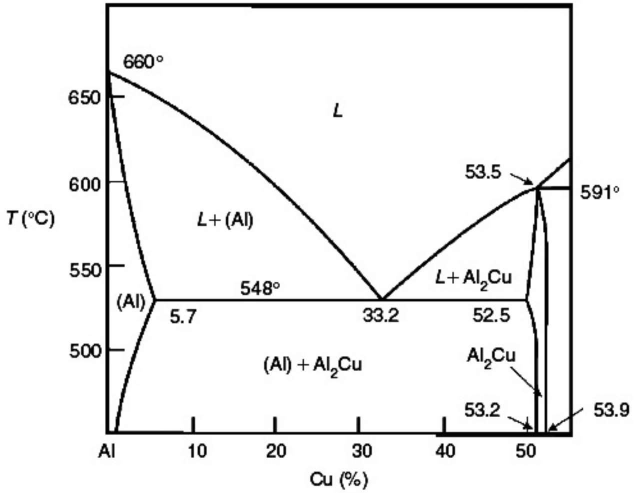

Figure 1.4 Phase diagram Al–Cu.

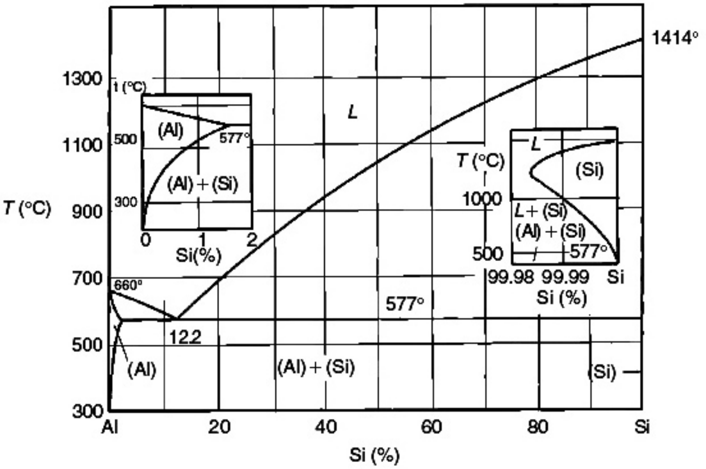

Figure 1.5 Phase diagram Al–Si.

(either in solid solution or as precipitates); the second component (20% and more) represents Si in constituent particles/phases, mostly in the form of (Si).

In addition to the principal alloying elements (usually >1%), most industrial alloys contain one or more alloying elements that are usually called "ancillary

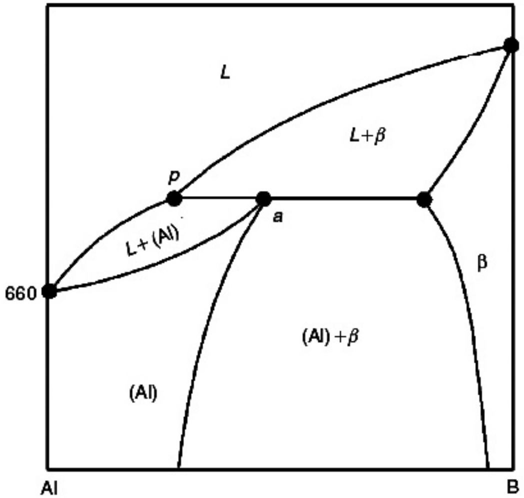

Figure 1.6 Schematic of the Al–B (2nd component) phase diagram of the peritectic type.

additions", since their concentration typically is of the order of 10^{-2}–10^{-1}%. In many cases these are transition and rare earth metals such as manganese, titanium, chromium, vanadium, nickel, iron, cerium, scandium, and also beryllium, cadmium, boron, and others. With Al these chemical elements can form phase diagrams of eutectic (Figure 1.1) and peritectic (Figure 1.6) types. In the first case their solubility in (Al) is very low (with the exception of Mn and Sc) and in the second case this can be ~0.1% and higher. It is important that under the conditions of non-equilibrium solidification the solubility of the latter can be increased substantially. This phenomenon is explained in terms of transformation of the aluminum corner of the phase diagram from the peritectic type to the "cigar-shaped" continuous solid solutions (dotted line in Figure 1.6) [18]. For transition and rare earth metals, which are often used as alloying additions in aluminum alloys, the key parameters of the corresponding phase diagrams are presented in Table 1.2.

Analysis of Appendix 1 (compositions of industrial aluminum alloys) immediately reveals that the most widespread ancillary addition is *manganese*, which is added to most alloys in the amounts from 0.1% to 1%. The principal goal of the introduction of Mn and such transition metals as Ti, Zr, Cr, and V is in achieving an additional strengthening effect. This additional strengthening takes place due to the formation of anomalously supersaturated solid solutions under the conditions of non-equilibrium solidification (Figure 1.6). These supersaturated solid solutions decompose after subsequent heat treatment operations, while the dispersoids of aluminides themselves enhance strengthening somewhat, especially at elevated temperatures.

Table 1.2 Characteristics of binary phase diagrams of Al with transition metals used in aluminum alloys either as alloying elements or ancillary additions

No.	Alloying elements (type of phase diagram)[d]	C_{a}[a]		$C_{\mathrm{e,p}}$[b]		$T_{\mathrm{e,p}}$[c] (°C)	Phase in equilibrium with (Al) (contents of the 2nd component, mass%)
		Mass%	At.%	Mass%	At.%		
1	Fe (e)	0.05	0.03	1.8	0.9	655	$FeAl_3$ (40%Fe)
2	Ni (e)	0.04	0.02	6.0	2.8	640	$NiAl_3$ (42%Ni)
3	Ce (e)	0.05	0.01	12	2.6	650	$CeAl_4$ (57%Ce)
4	Mn (e)	1.8	0.89	1.9	0.91	658	$MnAl_6$ (25%Mn)
5	Sc (e)	0.3	0.2	0.6	0.4	655	$ScAl_3$ (36%Sc)
6	Ti (p)	1.3	0.8	0.12	0.08	661	$TiAl_3$ (37%Ti)
7	Zr (p)	0.28	0.1	0.11	0.04	661	$ZrAl_3$ (53%Zr)
8	Cr (p)	0.8	0.4	0.4	0.2	661	$CrAl_7$ (22%Cr)

[a] Limit solubility at eutectic (e) or peritectic (p) temperature.
[b] Concentration in eutectic or peritectic point.
[c] Temperature of eutectic or peritectic solidification.
[d] e: Eutectic, and p: peritectic.

In addition to the strengthening effect, transition metals in aluminum alloys often improve their formability due to grain refinement. *Titanium* (together with boron and independently) and *zirconium* are particularly effective for this purpose. Additions of Zr, Cr, Mn, and V improve resistance to different forms of corrosion [9, 12]. However, it is critical to emphasize that the positive effect of these additions can be achieved only if all of the standard procedures of technological process are strictly obeyed. Otherwise their presence in aluminum alloys may be neutral, if not detrimental. For example, if the temperature of molten metal containing these additives was too low, then the microstructure of castings might be negatively affected by coarse primary aluminide crystals. In turn, this results in deterioration of the alloy mechanical properties.

Nickel, *iron*, *cerium*, and most of the other eutectic-forming transition metals are characterized by low solubility in (Al) (maximum ∼0.01–0.03%) and do not form supersaturated solid solutions even after relatively rapid solidification. Their introduction into aluminum alloys always causes the formation of excessive phases (constituent particles) that often reduce formability and corrosion resistance. For this reason, in many cases these elements are undesirable as alloying elements (as it was pointed out above, iron and silicon are the two most widespread impurities in technical aluminum). However, the refractory aluminides of nickel, iron, and cerium are very beneficial for improving the alloy thermal stability, so when this property is the most important, Ni, Fe, and Ce can be used as alloying elements [10]. Using high-temperature heat treatments it is possible to spheroidize these eutectic particles (similar to silicon), in which case their negative influence upon formability and elongation is practically neutralized [6, 18]. One should also mention that these additives, even in small amounts, increase the eutectic volume fraction and, consequently, improve alloy's castability [6, 19].

Beryllium is also an interesting additive in aluminum alloys. It creates on the surface of molten and even solid aluminum a strong oxide film, which protects the alloy surface from further oxidation. This is particularly important for Al–Mg alloys. In addition, beryllium is the most effective morphology modifying agent for iron-bearing constituent particles [6, 12, 20–22]. The reason is that beryllium can form compact particles of complex phases with Al and Fe and to a significant extent neutralize the harmful effects of iron upon formability and fracture toughness. There is also substantial information about the influence of Be upon processes at elevated temperatures, but their interpretation is inconclusive. Unfortunately, beryllium and its compounds are highly toxic, so their application in industry is quite limited.

Cadmium is the most effective ancillary addition capable of significantly increasing the strength of aluminum alloys (mostly for materials on the basis of the Al–Cu and Al–Si–Mg–Cu systems) after aging. The introduction of 0.2–0.3% of Cd into the alloy composition results in different phases – products of aging – and also in their higher dispersion. That increases strength of Al–Cu alloys after T6 heat treatment by 100–150 MPa [9, 12]. This idea was realized in the case of high-strength Russian casting alloy Al–4.5%Cu with Cd additions.

Recently the aluminum industry began to use *scandium* as a strengthening addition, mostly for Al–Mg alloys [23–25]. Similar to other transition metals, Sc can form supersaturated solid solution (Al) upon solidification. After its decomposition during aging above 300°C, highly dispersed coherent precipitates of Al_3Sc will be formed (in this sense it is very different from Mn-bearing supersaturated aluminum alloys). In spite of small amounts of Sc in aluminum alloys (not more than 0.2–0.3%) we believe it is appropriate to call it a "principal" alloying element, since it can make a very significant contribution to strengthening processes comparable, for example, with several percentage of Mg.

Among other ancillary additions one should mention *sodium* and *strontium*, which are used in small quantities (~0.01%) as Al–Si eutectic modifiers in casting alloys of the 3xx series [3, 4, 11, 26]. Refinement of the Si primary crystals in hyper-eutectic 3xx alloys can be achieved using *phosphorus*.

The last group of chemical elements that may enter aluminum alloy compositions is called *impurities*. These can be introduced into aluminum alloys in the process of melting (from casting molds, used instruments, etc.). Of these, *iron* and *silicon* are particularly detrimental (in those cases where these elements are not used intentionally as alloying additions). This is mostly because of "sharp" Fe- and Si-bearing constituent particles that negatively affect the mechanical properties

Table 1.3 Chemical composition of several grades of primary aluminum manufactured in Russia (GOST 11069–2001)

Grade	Fe (%)	Si (%)	Cu (%)	Zn (%)	Ti (%)	Bal. (%)	Impurities (Total %)	Al (%), not less than
High purity								
A995	0.0015	0.0015	0.001	0.001	0.001	0.001	0.005	99.995
A99	0.003	0.003	0.002	0.003	0.002	0.001	0.01	99.99
A98	0.006	0.006	0.002	0.003	0.002	0.001	0.01	99.98
A97	0.015	0.015	0.005	0.003	0.002	0.002	0.03	99.97
A95	0.03	0.03	0.015	0.005	0.002	0.005	0.05	99.95
Technical purity								
A85	0.08	0.06	0.01	0.02	0.01	0.02	0.15	99.85
A8	0.12	0.10	0.01	0.04	0.02	0.02	0.20	99.80
A7	0.16	0.15	0.01	0.04	0.02	0.02	0.30	99.70
A7E	0.2	0.08	0.01	0.04	0.02	0.02	0.30	99.70
A7∋	0.2	0.1	0.01	0.03	0.02	0.03	0.30	99.70
A6	0.25	0.18	0.01	0.06	0.03	0.03	0.30	99.60
A5E	0.35	0.1	0.02	0.05	0.01	0.02	0.20	99.50
A5	0.30	0.25	0.02	0.06	0.03	0.03	0.30	99.50
A35	0.65 (Fe + Si)		0.05	0.1	0.02	0.03	1.00	99.35
A0	0.95 (Fe + Si)		0.05	0.1	0.02	0.03	1.00	99.00

of alloys, especially elongation, fracture toughness, and fatigue properties. For this reason, in the most complex cases, in particular for the aerospace industry and in military applications, it becomes imperative that materials of extremely high purity be used (see, e.g., Table 1.3) [27].

In other specific alloys impurities other than Fe and Si could be most detrimental. This might be true even for principal alloying elements. For example, in many Al–Mg alloys the amounts of Cu must be controlled very rigorously. On the other hand, in Al–Cu alloys with high thermal stability the amount of Mg must not exceed 0.05%.

In casting aluminum alloys it is often critical to control the amount of alkaline metals (Li, Na, and K), alkaline earths (Ca and Sr), and heavy metals with low melting point (Pb, Sn, Bi, and Sb). Sometimes these chemical elements can be used as additives (see Appendix 1).

In spite of many years of intensive research, both in the aluminum industry and in academia, the physico-chemical mechanisms and roles of alloying elements and additives are far from being completely understood. This prevents "the first-principles" approach to alloy development, at least for now. The development of novel aluminum alloys is still a tedious and lengthy experimental process. The fundamental goal of accelerated casting aluminum alloy design can be achieved only if all of the microstructure peculiarities and properties are well understood for all stages of the technological process, from casting to final heat treatment(s). Good understanding of phase diagrams, both equilibrium and non-equilibrium, is absolutely critical for these purposes. Information on binary systems of Al with all of the chemical elements mentioned above is presented in Appendix 2.

Summing up, the principal alloying elements for the absolute majority of aluminum alloys are copper, magnesium, silicon, and zinc. Appendix 1 clearly indicates that these elements are used in different combinations and concentrations in industrial alloys; this gives the possibility to conveniently classify them into several groups, or "series" (Table 1.4).

Speaking about casting aluminum alloys, the most important system is *Al–Si*. It is characterized by the absence of intermediate phases and the relatively small limit solubility of Si. The presence of silicon, either in the form of an eutectic or as primary crystals, is the key feature of this group of alloys. This is illustrated in Figure 1.1 (groups 2, 3, and 4 belong to this class of casting aluminum alloys).

In the *Al–Cu* and *Al–Mg* systems (Al) will be in equilibrium with the Al_2Cu and Al_5Mg_8 phases, which are always present in cast structure. The compositions of these casting alloys are selected to make sure that at homogenization temperature they will be in the one-phase field of the diagram (1st group in Figure 1.1). This gives a possibility to obtain, after heat treatment, an alloy microstructure that is completely free of any constituent particles (provided non-soluble impurities are removed).

Most industrial alloys contain many components, so to analyze their phase composition with a reasonable degree of accuracy one needs to understand at least the corresponding three-component phase diagrams. Often an analysis of quaternary and even five-component phase diagrams is required for a good understanding of the alloy behavior and properties (see Sections 1.3–1.5).

In the first approximation, multicomponent alloys, similar to binary alloys, may be classified using Figure 1.1. In particular, for Al–Si alloys with additions of Mg and Cu, the basic alloy systems are *Al–Mg–Si*, *Al–Si–Cu*, and *Al–Si–Cu–Mg* [3, 13]. However, since the concentrations of these additives are, as a rule, within the limits of solubility in (Al), a good assessment of the alloy structure (Figure 1.2) can be made using the binary Al–Si phase diagram.

Table 1.4 Chemical and phase composition of industrial casting alloys (without ancillary additions and impurities)

No.	Basic system	Si (mass%)	Mg (mass%)	Cu (mass%)	Zn (mass%)	Phase composition of eutectics	Strengthening phases[a]	T_e (°C)
1	Al–Si	4, 5–13	–	–	–	(Al) + (Si)	–	577
2	Al–Si–Mg	6–11	0.1–0.6	–	–	(Al) + (Si) + Mg_2Si (β)	β', β''	555
3	Al–Si–Cu	7–13	–	1.5–5	–	(Al) + (Si) + Al_2Cu (θ)	θ', θ''	525
4	Al–Si–Cu–Mg	4–23	0.2–1.1	0.5–8	–	(Al) + (Si) + Al_2Cu + $Al_5Cu_2Mg_8Si_6$ (W)	$\theta', \theta'', \beta', \beta''$, S ($Al_2CuMg$)	505
5	Al–Si–Cu–Mg–Zn	6–10	0.1–0.5	0.3–1.5	5–12	(Al) + (Si) + Al_2Cu + $Al_5Cu_2Mg_8Si_6$ (W)	$\theta', \theta'', \beta', \beta''$, S ($Al_2CuMg$)	505
6	Al–Cu	–	–	3.5–11	–	(Al) + Al_2Cu	θ', θ''	548
7	Al–Mg	–	2.5–12	–	–	(Al) + Al_8Mg_5	–	450
8	Al–Mg–Zn	–	0.5–2.4	–	2.5–6.5	(Al) + $MgZn_2$ (η) + Al_3Mg_2Zn (T)	η, η', T'	475
9	Al–Zn–Mg–Cu	–	1.5–2.5	0.4–1.5	5–8	(Al) + M + T (Al, Cu, Mg, Zn)	η, η'	470–475

[a] Formed after SHT, quenching, and aging.

On the other hand, copper and magnesium will exert significant influence upon solidification of these alloys (e.g., upon the temperature of the lowest-melting eutectic). The composition of the products of heat treatment will also be affected (see Table 1.4). We want to emphasize that when using only binary phase diagrams it is impossible to get the required information.

A number of perspective casting alloys belong to the *Al–Mg–Zn* and *Al–Zn–Mg–Cu* groups [9, 12], but so far they have not found widespread application. These alloys contain alloying elements that can be completely dissolved in (Al) (i.e., belong to the first structural group). These alloys can be dispersion hardened with the products of decomposition of supersaturated solid solution (Al), with subsequent aging. As a result, their strength is higher than that of casting alloys from different groups.

An important characteristic of all basic alloy systems is the temperature of the low-melting eutectic (T_E), which, for most alloys, is typically non-equilibrium (Figure 1.1). This temperature corresponds to the solidus line (either equilibrium or non-equilibrium), which, in turn, defines such an important characteristic as the temperature of SHT (before quenching, see Section 3.1), and also affects castability (Section 4.1). The T_E values for all basic aluminum alloy systems are presented in Table 1.4.

Some qualitative characteristics of basic aluminum alloy groups can be found in Table 1.5. Depending upon a required set of properties, an alloy developer or a product designer will select the alloy system which is the most perspective. Of course, Table 1.5 is somewhat idealized; it gives a possibility of only a general qualitative comparison of alloys belonging to different alloy systems, and only for the alloy concentration range, which is known and used today. For example, alloys of the Al–Mg system are characterized by average values of strength, but higher concentrations of magnesium and zinc could achieve record high strength levels. However, because of the strong tendency of these alloys to stress corrosion cracking, they cannot find applications in real life. On the other hand, alloys that contain relatively small amounts of magnesium and zinc (not more than 6% total) have quite mediocre levels of strength ($\sigma_b < 350$ MPa).

Another important drawback of Table 1.5 is that it reflects the level of alloy properties achieved today, with modern technological processes. It cannot be excluded, though, that the application of more advanced processes may result in different (elevated) values of properties. Subsequent heat treatments are also extremely important. For example, Al–Si alloys with additions of Mg have higher UTS values (compared to binary Al–Si) only after heat treatment, while in the F-temper their properties are quite similar.

As can be seen from Table 1.5, industrial alloys with magnesium, copper, and zinc in any combinations possess low castability. Of the basic alloying elements, only silicon can ensure good castability, which is needed for shaped castings. This is attained due to the relatively narrow solidification range and the formation of a large amount of eutectic component in the microstructure (see Section 4.1). Of course, in alloys of the Al–Cu and Al–Mg systems it is also possible to get a high

Table 1.5 Qualitative comparison of the level of key aluminum alloy properties[a] belonging to different basic systems

System	Strength	Formability	Thermal stability	Corrosion resistance	Casting properties	Weldability
Al–Si	1	2	1	2	3	3
Al–Si–Mg	2	1–2	1	2	3	3
Al–Si–Cu	2	1–2	2	1	2–3	3
Al–Si–Cu–Mg	2–3	1	2	1	2–3	3
Al–Cu	3	3	3	1	1	1–2
Al–Mg	1–2	3	1	3	1–2	3
Al–Mg–Zn	2–3	2	1	3	1	2
Al–Zn–Mg–Cu	3	2	1	1	1	1

[a] 1: Low level, 2: average level, and 3: high level.

eutectic volume fraction (see Table 1.1), but at such high concentrations of Cu and/or Mg that alloys lose strength and become brittle.

Aluminum cerium alloys possess excellent castability [10]. Unfortunately, because of the relatively high cost of cerium they have not found widespread application.

An alloying addition with much perspective is nickel and Al–Ni alloys. They possess excellent castability and can compete with such mainstream casting materials as Al–Si alloys. They will be discussed in greater detail in Chapter 6 of the present monograph.

1.2 PHASE DIAGRAMS OF TERNARY SYSTEMS

1.2.1 The Al–Be–Fe system

Since beryllium is the most effective morphology modifier of iron-bearing constituent particles, its optimal concentration can be determined from the analysis of the Al–Fe–Be ternary phase diagram. As of now, this diagram was not studied in its entirety. In particular, data on the temperatures of multi-phase transformations and the character of solidification process are practically absent.

At 600°C in aluminum-rich alloys, equilibrium will be established among (Al), (Be), Al_3Fe, and $Al_4Fe_2Be_5$. This last phase can be also described by the formula

$Al_2FeBe_{2.3}$ [28] or $Al_7Fe_3Be_7$ [15]. According to Ref. [28], there are two ternary eutectics in this system:

$L \Rightarrow (Al) + (Be) + Al_3Fe$
$L \Rightarrow (Al) + (Be) + Al_4Fe_2Be_5$

According to Ref. [29], in which the authors studied microstructure and phase composition of the Al–Mg–Zn–Fe–Be alloys within concentration limits up to 1.5% Fe and 1%Be, the first variant is hardly feasible as the (Be) and Al_3Fe phases are not in equilibrium with each other.

The (Be) phase represents a low-temperature modification (<1227°C) of aluminum solid solution in Be. This phase has an hexagonal crystalline lattice (space group P6₃/mmc, 2 atoms per unit cell) with parameters $a = 0.2286$ nm and $c = 0.3584$ nm [14]. The $AlFeBe_4$ (40–42%Fe, 32–36% Be) has fcc lattice of the Cu_2Mg type (space group Fd3m, 24 atoms per unit cell) with the lattice parameter $a = 0.606$ nm [28]. The $Al_4Fe_2Be_5$ phase (40–42%Fe, 17–20%Be) belongs to the Laves-type phase similar to Cu_2Mg. The atoms of Be and Fe are located in the positions of the copper atoms in such a way that the lattice symmetry changes from cubic to monoclinic [14]. This phase belongs to the C2/m space group with a defective elementary cell, in which 12 crystallographic positions in the lattice are occupied by 11 atoms. The parameters of the lattice are $a = 0.7718$ nm, $b = 0.44554$ nm, $c = 0.4542$ nm, $\beta = 124.53°$. The density of this phase is 3.470 g/cm^3.

The phase, which is usually denoted as Al_3Fe (this corresponds to Fe concentration 40.7%), has a broad homogeneity range spanning from 37.3 to 41.1%Fe and can be described by different formulae: Al_7Fe_2, $Al_{13}Fe_4$, $Al_{19}Fe_6$, and Al_3Fe. This phase has monoclinic lattice, space symmetry group C2/m with 100 atoms per unit cell, and lattice parameters $a = 1.549$ nm, $b = 0.808$ nm, $c = 1.248$ nm, $\beta = 107.72°$ at 33.5 at.%Fe [6]. The Al_3Fe phase can dissolve up to 1.4%Be [14].

Figure 1.7 represents the distribution of phase fields in the solid state (430°C) in aluminum alloys containing Fe and Be.

1.2.2 The Al–Be–Si system

Beryllium is not used as an addition to binary Al–Si alloys. However, it is important to understand this phase diagram in order to conduct further analysis of the quaternary Al–Be–Fe–Si quaternary system (Section 1.3.1), which explains the modifying effect of this element upon the morphology of the Fe-bearing phase.

This is a simple eutectic system (Figure 1.8) without any binary or ternary intermediate compounds [14]. The ternary eutectic forms according to the phase reaction $L \Rightarrow (Al) + (Si) + (Be)$ at 572°C, 12–13%Si, and 1–1.5%Be. This eutectic has an anomalous structure with particles of Si- and Be-bearing phases distributed in (Al). The limit joint solubility of Si and Be in (Al) at 572°C is equal to 1.5% and 0.05%, respectively.

The (Si) phase represents almost pure silicon and has cubic crystalline lattice of the diamond type (space symmetry group Fd3m, 8 atoms per unit cell) with lattice

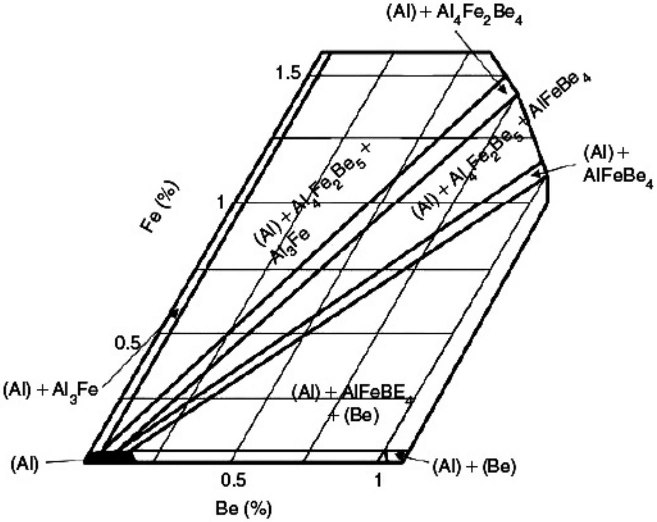
(Al) + Al$_4$Fe$_2$Be$_4$
1.5
(Al) + Al$_4$Fe$_2$Be$_5$ + AlFeBe$_4$
(Al) + AlFeBe$_4$
(Al) + Al$_4$Fe$_2$Be$_5$ + Al$_3$Fe
(Al) + Al$_4$Fe$_2$Be$_5$
Fe (%)
1
0.5
(Al) + Al$_3$Fe
(Al) + AlFeBE$_4$ + (Be)
(Al)
0.5
1
(Al) + (Be)
Be (%)

Figure 1.7 Phase diagram Al–Be–Fe (distribution of phase domains in solid state).

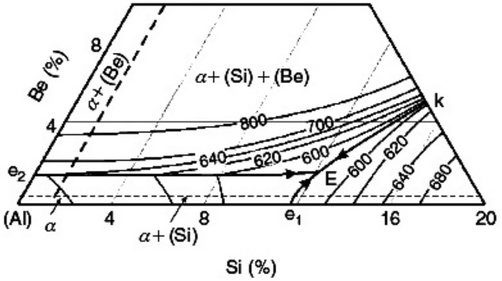
8
Be (%)
α + (Be)
α + (Si) + (Be)
k
4
800
700
640
620
600
e$_2$
E
600
620
640
680
(Al)
α
4
8
e$_1$
16
20
α + (Si)
Si (%)

Figure 1.8 Phase diagram Al–Be–Si (liquidus projection).

parameter $a = 0.54285$ nm and density 2.33 g/cm^3 [5]. The Vickers hardness of (Si) is 8.7–13.5 GPa in the 27–327°C range and drops to 3 GPa at 627°C. Silicon has microhardness 12.3 GPa at 20°C and 1-hour microhardness 8 GPa at 300°C.

1.2.3 The Al–Ce–Cu system

This system, as well as others with cerium, is of interest in the development of casting aluminum alloys of the new generation, in which the application of Ce is economically feasible (Section 6.5).

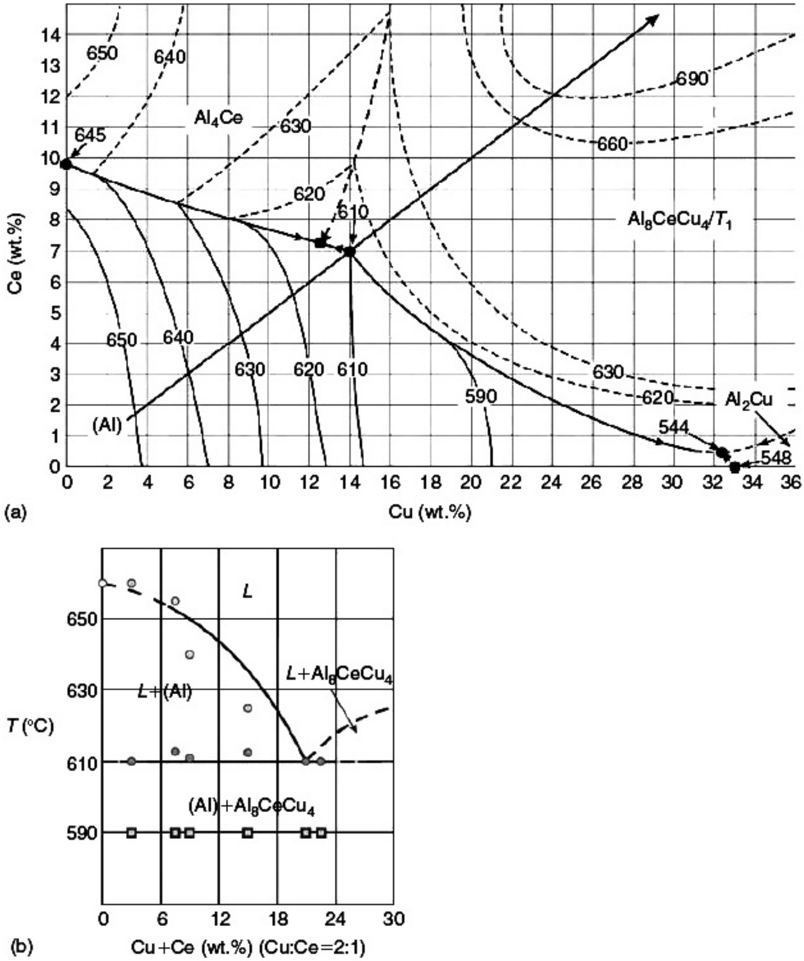

Figure 1.9 Phase diagram Al–Ce–Cu: (a) liquidus projection and (b) same for the Cu/Ce = 2:1 ratio.

Literature data on the Al–Cu–Ce phase diagram are not abundant. It follows that, in addition to the binary aluminides Al_2Cu and Al_4Ce, two ternary compounds can participate in equilibrium with (Al), that is, Al_8CeCu_4 (19.2%Ce and 42.5%Cu) and Al_4CeCu (45.1%Ce and 20.2%Cu) [14]. The liquidus surface (Figure 1.9) and non-variant reactions of solidification are described in the only available work [30]. The authors conclude [30] that both ternary compounds result in the formation of quasi-binary cross-sections and, correspondingly, divide

Table 1.6 Non-variant reactions in the aluminum corner of the Al–Cu–Ce system [30]

Point in Figure 1.9	Reaction	*T* (°C)	Composition *L*	
			Cu (%)	Ce (%)
E_1	$L \Rightarrow (Al) + CeCu_4Al_8 + Al_2Cu$	541	28.42	4.57
E_2	$L \Rightarrow (Al) + CeCu_4Al_8 + Al_4CeCu$	550	11.89	9.33
E_3	$L \Rightarrow (Al) + Al_4CeCu + Al_4Ce$	550	3.01	15.93
E_4	$L \Rightarrow (Al) + CeCu_4Al_8$	585	16.91	7.72
E_5	$L \Rightarrow (Al) + Al_4CeCu$	595	4.37	8.64

the Al–Cu–Ce phase diagram into three simple diagrams with ternary eutectics:

1. $(Al) + Al_2Cu + Al_8CeCu_4$
2. $(Al) + Al_8CeCu_4 + Al_4CeCu$
3. $(Al) + Al_4CeCu + Al_4Ce$

The parameters of non-variant reactions given in Table 1.6 indicate that the temperatures of all eutectics are not higher than 595°C. However, our experiments indicated that if alloys of this system containing significant amounts of eutectic are annealed at 600°C, this does not result in burn out. Consequently, at least some of the eutectic temperatures given in Ref. [30] are too low. Thermal analysis also indicates that eutectic temperatures corresponding to quasi-binary cross-sections are higher than 600°C.

According to Ref. [14], the Al_4Ce (56.5%Ce) phase possesses either body-centered tetragonal lattice (space group I4/mmm and 10 atoms per unit cell) with lattice parameters $a = 0.437$ nm, $c = 1.003$–1.012 nm; or orthorhombic structure (space group Immm or Imma) with parameters $a = 0.4395$ nm, $b = 1.3025$ nm, $c = 1.0092$ nm. The density of Al_4Ce phase is equal to 4.05 g/cm^3. Both ternary phases possess a tetragonal crystalline lattice: Al_8CeCu_4 (I4/mmm, 26 atoms/cell, $a = 0.884$ nm, $c = 0.517$ nm) and Al_4CeCu ($a = 0.896$–0.898 nm, $c = 1.304$–1.307 nm) [30]. According to Ref. [30] the Al_4CeCu phase has a broad homogeneity range, which corresponds to formula $Al_{3\text{-}3.25}CeCu_{1\text{-}0.75}$. Solubility of cerium in the Al_2Cu phase is negligibly small, while $CeAl_4$ at 527°C can dissolve up to 2%Cu [14].

1.2.4 The Al–Ce–Fe system

The Al–Ce–Fe phase diagram is studied in the concentration range up to 72%Ce and 100%Fe. However, understanding of solidification processes in the aluminum corner is somewhat limited. There is ample information on the phase composition of ternary alloys at 500°C [31] and 550°C [32]. It was discovered that the following compounds may be in equilibrium with (Al): Al_3Fe, Al_4Ce,

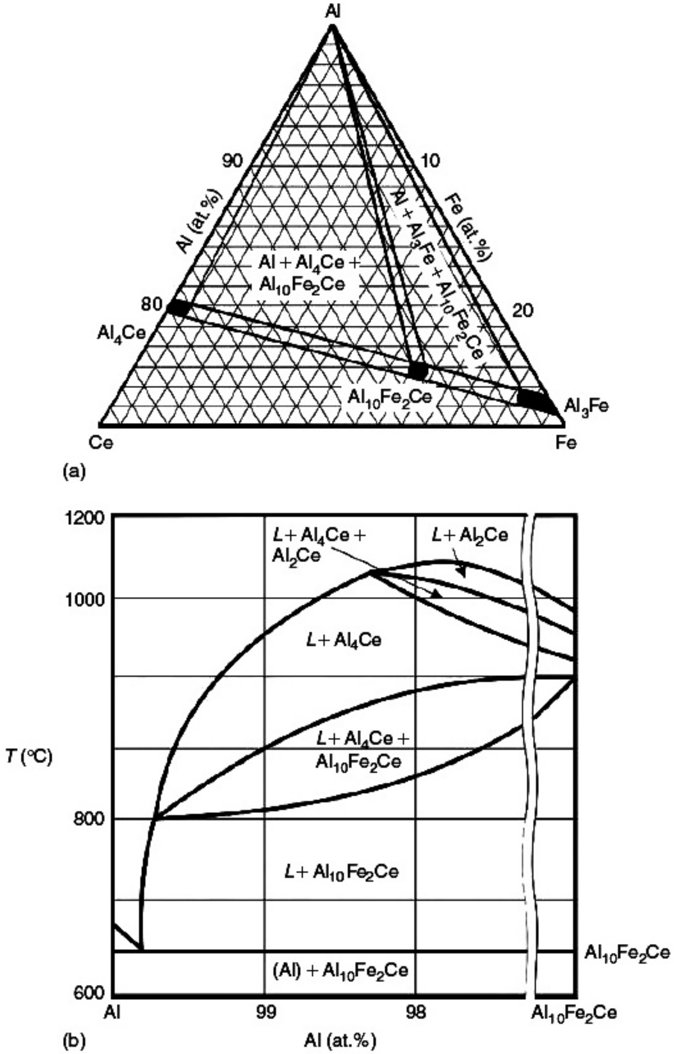

Figure 1.10 Phase diagram Al–Ce–Fe: (a) distribution of phase domains in the solid state, (b) quasi-binary cross-section Al–$Al_{10}Fe_2Ce$ and (c) liquidus projection.

and $Al_{10}Fe_2Ce$ (ψ'). Solidification results in the formation of the following phase fields: (Al) + Al_3Fe, (Al) + Al_4Ce, (Al) + $Al_{10}Fe_2Ce$, (Al) + Al_3Fe + $Al_{10}Fe_2Ce$, and (Al) + Al_4Ce + Al_{10} Fe_2Ce (Figure 1.10a). Figure 1.10b illustrates partially quasi-binary cross-section between (Al) and the ternary phase.

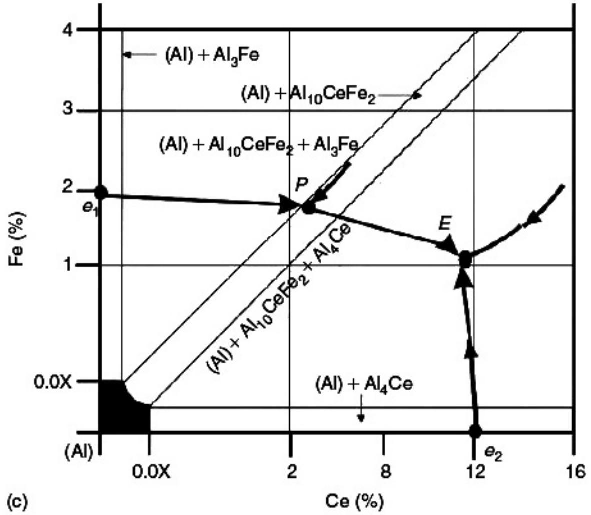

Figure 1.10 (Continued)

Recent work [33] was carried out with the goal of understanding the most probable variant of the liquidus surface in the aluminum corner (Figure 1.10c). Two non-variant reactions with the participation of (Al) are possible:

$$L \Rightarrow (\mathrm{Al}) + \mathrm{Al_4Ce} + \mathrm{Al_{10}Fe_2Ce} \quad \text{at } 640^\circ\mathrm{C}, 10\%\mathrm{Ce}, 1\%\mathrm{Fe}$$

$$L + \mathrm{Al_3Fe} \Rightarrow (\mathrm{Al}) + \mathrm{Al_{10}Fe_2Ce} \quad \text{at } 650^\circ\mathrm{C}, 2.5\%\mathrm{Ce}, 2\%\mathrm{Fe}$$

The ternary compound $Al_{10}Fe_2Ce$ (26.7%Ce, 21.6%Fe) has either a body-centered tetragonal lattice (space group I4/mmm), which is isomorphic to $Al_{10}Fe_2Nd$ [14], or an orthorhombic lattice with parameters $a = 0.894$ nm, $b = 1.022$ nm, $c = 0.906$ nm [34].

1.2.5 The Al–Ce–Ni system

The authors of Refs. [35, 36] provide the most detailed analysis of this phase diagram up to 20%Ce and 10%Ni. It was demonstrated that in addition to (Al) containing less than 0.05%Ce and Ni, only equilibrium phases Al_4Ce and Al_3Ni are present in all conditions. This agrees well with the data from Ref. [37], in which six ternary compounds were described, and none of them can be in equilibrium with (Al). The solubility of a third element in binary aluminides is generally low [35]. In the aluminum corner of the Al–Ce–Ni system, a ternary eutectic reaction takes place according to the following equation (Figure 1.11):

$$L \rightarrow (\mathrm{Al}) + \mathrm{CeAl_4} + \mathrm{NiAl_3} \quad \text{at } 12\%\mathrm{Ce}, 5\%\mathrm{Ni}, \text{and } T = 628^\circ\mathrm{C}$$

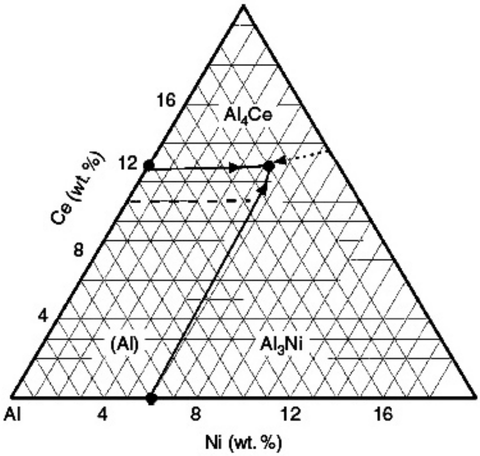

Figure 1.11 Phase diagram Al–Ce–Ni (liquidus projection).

The overall volume fraction of aluminides in this ternary eutectic is about 25 volume%, which is much more than in binary eutectics.

The Al_3Ni phase (42%Ni) has an orthorhombic structure (space group Pnma, 16 atoms/cell) with parameters $a = 0.6611$ nm, $b = 0.73662$ nm, and $c = 0.4812$ nm. The density of this phase in a binary Al–Ni system is 3.95–3.96 g/cm^3. The Vickers hardness is 7–7.7 GPa at 27°C, and it changes insignificantly upon heating up to 327°C, then decreases linearly to 2 GPa at 577°C. Microhardness of this phase at 20°C is 5.95 GPa, while 1-hour microhardness at 300°C is 3.54 GPa. Consequently, Ni_3Al can be classified as a thermally stable compound (i.e., superalloys).

1.2.6 The Al–Ce–Si system

According to the existing literature data [14, 15], (Al) can be in equilibrium with (Si), Al_4Ce, ternary compound Ce_2SiAl_3, and solid solution of Al in the $CeSi_2$ phase. The distribution of phase regions in the solid state is presented in Figure 1.12. There is no information on the liquidus surface or on solidification paths in this system.

The ternary compound has the chemical formula best described as Ce_2SiAl_3 (67.15%Ce and 13.43%Si) with lattice parameters $a = 0.624$ nm and $c = 0.730$ nm, its density is 5.62 g/cm^3. The homogeneity range of the $CeSi_2$ phase (containing 71.4%Ce) in the ternary system broadens up to 22%Al, 7%Si, 72%Ce; this corresponds to the formula Ce_2SiAl_3. The $CeSi_2$ phase has a body-centered tetragonal lattice with parameters $a = 0.417$ nm, $c = 1.385$ nm in the binary system, and $a = 0.431$ nm, $c = 1.51$ nm, when Al enters the phase composition.

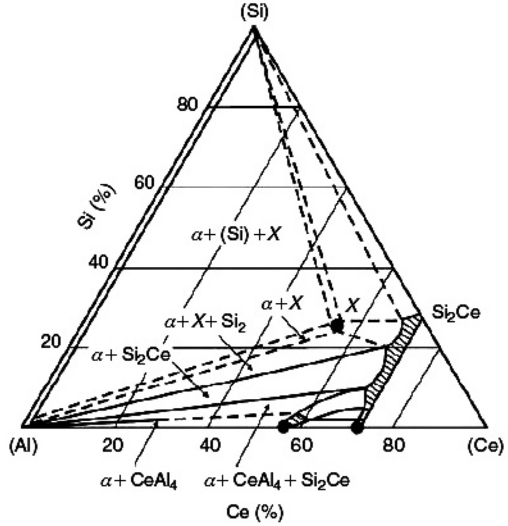

Figure 1.12 Phase diagram Al–Ce–Si (distribution of phase fields in the solid state).

1.2.7 The Al–Cr–Fe system

This phase diagram is considered because the ancillary additions of chromium can form different phases with principal alloying elements and impurities in a number of industrial alloys, which may affect their properties quite significantly (see Appendices 1 and 2).

In aluminum-rich alloys of the Al–Cr–Fe system, ternary compounds were not discovered. Equilibrium exists among (Al) and phases Al_3Fe and Al_7Cr (Figure 1.13).

The solidification surface has two non-variant points corresponding to the following quaternary phase reactions [14, 15, 28]:

$$L + Al_5Cr \Rightarrow Al_7Cr + Al_3Fe\ (709°C,\ 4.2\%Fe,\ 2.1\%Cr)$$

$$L \Rightarrow (Al) + Al_3Fe + Al_7Cr\ (640°C;\ 1.7\%Fe,\ 0.3\%Cr)$$

Thermodynamic calculations in the aluminum corner of the Al–Fe–Cr phase diagram show that the peritectic reaction occurs at 709°C and concentrations 3.09%Fe and 0.61%Cr. Eutectic equilibrium takes place at 2.02%Fe, 0.19%Cr, and $T = 654.5°C$ [38].

The Al_7Cr phase (21.6%Cr) is also denoted as Al_6Cr, $Al_{45}Cr_7$, and $Al_{13}Cr_2$, which correspond to different chemical compositions of crystals extracted from the solidifying melt [14]. A number of crystalline structures are attributed to this compound. Most often the following data is cited: orthorhombic lattice with parameters $a = 2.48$ nm, $b = 2.47$ nm, and $c = 3.02$ nm (1160 atoms/unit cell). Another possibility is the monoclinic cell of the $Al_{45}V_7$ type with parameters

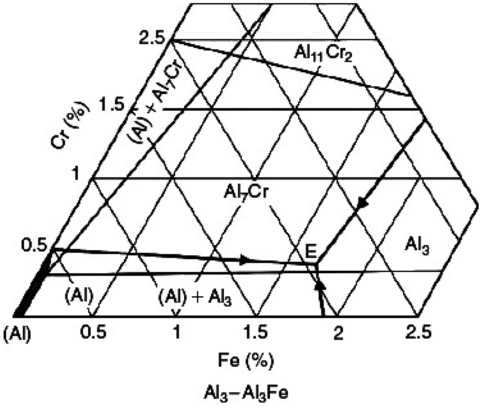

Figure 1.13 Phase diagram Al–Cr–Fe (liquidus projection and distribution of phase fields in the solid state).

$a = 2.5196$ nm, $b = 0.7574$ nm, $c = 1.0949$ nm, and $\beta = 128.7°$ [5, 6, 14]. This phase in binary alloys has density 3.14 g/cm^3 andVickers hardness 5–7 GPa (25°C) and 4 GPa (527°C). Microhardness of this phase at 20°C is 5.2 GPa; 1-hour hardness at 300°C is 3.72 GPa (i.e., it is a thermally stable phase) [10]. In ternary alloys Al_7Cr can dissolve up to 4–6%Fe and contains up to 20%Cr. Al_3Fe can dissolve up to 4%Cr.

1.2.8 The Al–Cr–Mg system

According to Ref. [14], (Al) can be in equilibrium with the following phases: Al_7Cr and Al_8Mg_5. In addition to that, a ternary compound, $Al_{18}Cr_2Mg_3$ (15.7%Cr, 11.1%Mg), may participate in the following reactions:

$$L \Rightarrow (\mathrm{Al}) + \mathrm{Al_{18}Cr_2Mg_3} + \mathrm{Al_8Mg}\ (1.7\%\mathrm{Cr}, 31.1\%\mathrm{Mg}, 437.4°\mathrm{C})$$

$$L + \mathrm{Al_7Cr} \Rightarrow (\mathrm{Al}) + \mathrm{Al_{18}Cr_2Mg_3}\ (1.7\%\mathrm{Cr}, 12.8\%\mathrm{Mg}, 633°\mathrm{C})$$

$$L + \mathrm{Al_{17}Cr_2} \Rightarrow \mathrm{Al_7Cr} + \mathrm{Al_{18}Cr_2Mg_3}\ (2.3\%\mathrm{Cr}, 12\%\mathrm{Mg})$$

Figure 1.14a illustrates the liquidus projection in the aluminum corner of this phase diagram. It indicates that the concentration boundary corresponding to the formation of the primary aluminide crystals shifts toward higher Cr concentrations as the Mg content increases. In our opinion, this is hardly possible since it contradicts the existing experimental data on the structure of Al–Mg alloys.

The Al_8Mg_5 phase has complex face-centered cubic lattice (space group Fd3m, 1166 atoms/unit cell) with parameter $a = 2.82$ nm (on the aluminum side) and 2.86 nm (on the magnesium side) [14]. Its density is 2.23 g/cm^3. The Vickers

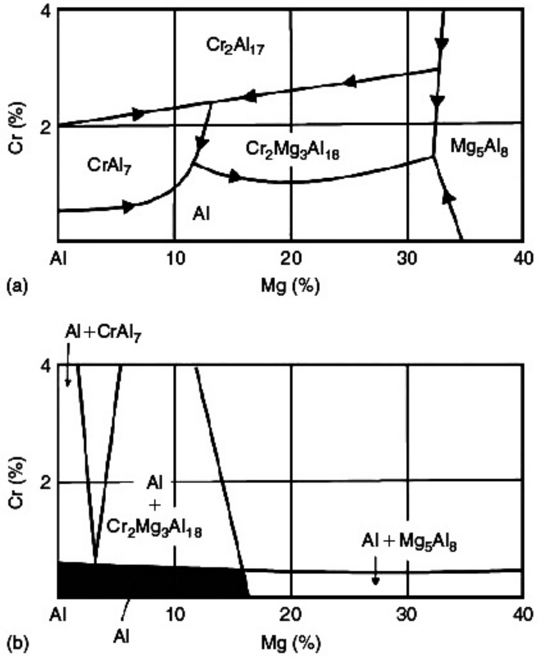

Figure 1.14 Phase diagram Al–Cr–Mg: (a) liquidus projection and (b) distribution of phase fields in the solid state.

hardness is 2–3.4 GPa at 27°C, 1.6 GPa at 327°C, and ~0 at 450°C. Its microhardness is equal to 2.8 GPa at 20°C, 1-hour microhardness at 300°C is 0.65 GPa. Consequently, this compound is not thermally stable [10].

The $Al_{18}Cr_2Mg_3$ phase has a cubic lattice Fd3m, 184 atoms/unit cell, the lattice parameter $a = 1.453–1.468$ nm with density 2.87 g/cm^3. When the temperature goes down, the whole phase field consisting of (Al) and $Al_{18}Cr_2Mg_3$ becomes much narrower. In particular, in point B, shown on the isothermal cross-section in Figure 1.14b at 207°C, the concentrations of Cr and Mg are less than 0.03% and 2%, respectively.

1.2.9 The Al–Cr–Mn system

There is one ternary phase in this system; however, only binary compounds are formed upon solidification [14]. The four-phase eutectic reaction takes place at 657°C:

$$L \Rightarrow \mathrm{Al} + \mathrm{CrAl_7} + \mathrm{MnAl_6}$$

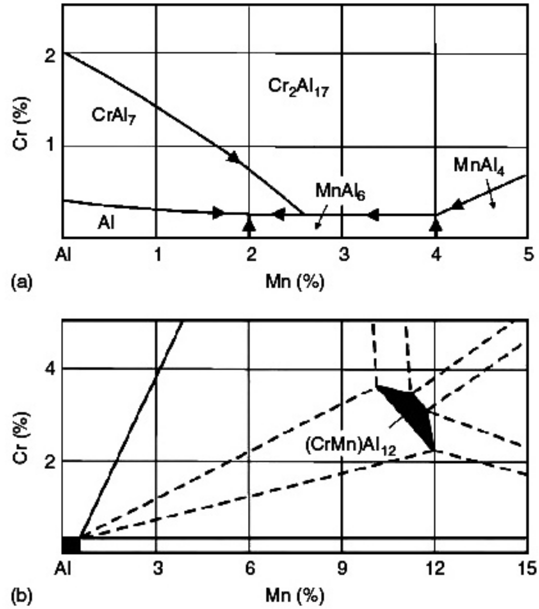

Figure 1.15 Phase diagram Al–Cr–Mn: (a) liquidus projection and (b) distribution of phase fields in the solid state.

Eutectic contains 0.3%Cr and 2%Mn. The introduction of Mn results in smaller phase field corresponding to the primary solidification of $CrAl_7$. When the concentration of Mn is ~2.5%, the formation of the Cr_2Al_{11} phase takes place instead (Figure 1.15). The solidification range of (Al) also becomes smaller. The solubility of Cr in liquid aluminum decreases to ~0.15% at 0.5%Mn. There is a ternary phase in solid alloys, which forms according to the peritectoid reaction at 587°C:

$$Al + CrAl_7 + MnAl_6 \rightarrow (CrMn)Al_{12}$$

Another peritectoid reaction takes place in the temperature range 587–547° C; it can be best described by the following relation:

$$CrAl_7 + MnAl_6 \rightarrow Cr_2Al_{11} + (CrMn)Al_{12}$$

The Al_6Mn phase has orthorhombic lattice (space group Ccmm, 28 atoms/unit cell) with the parameters $a = 0.6498$ nm, $b = 0.7540$ nm, $c = 0.8858$ nm, and the density 3.09–3.27 g/cm^3. The Vickers hardness is 5.4–5.6 GPa at room temperature and it practically does not change up to 427°C. After that it decreases sharply. Microhardness at 20°C is 6.9 GPa and 1-hour microhardness is 4.13 GPa. This is a thermally stable compound [10].

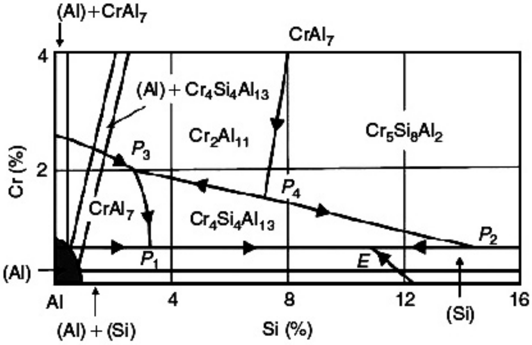

Figure 1.16 Phase diagram Al–Cr–Si (liquidus projection and distribution of phase fields in the solid state).

$(CrMn)Al_{12}$ is a metastable phase corresponding to the thermodynamically stable $MnAl_{12}$; it is stabilized via substitution of Mn with chromium atoms. It exists in the concentration range from 2 to 4%Cr and from 12 to 10%Mn. This phase has bcc lattice (space group Im3, 26 atoms/unit cell) with the lattice parameter $a = 0.7507$–0.7509 nm and density 2.92 g/cm^3. Another possibility described in the literature is a cubic lattice (space group Fm3m, 180 atoms/unit cell) with the parameter $a = 1.465$ nm and formula $CrMn_4Al_{65}$ (2.5%Cr and 10.5%Mn).

In the compounds $CrAl_7$ and Cr_2Al_{11}, chromium may be substituted with manganese. $CrAl_7$ may contain up to 13.55%Cr and 11.55%Mn, and Cr_2Al_{11} may contain up to 2.99%Cr and 26.61%Mn. The solubility of Cr in $MnAl_6$ and $MnAl_4$ is quite limited (not more than 1%) at all temperatures.

1.2.10 The Al–Cr–Si system

There are two ternary phases forming directly from the melt in this system: α ($Cr_4Si_4Al_{13}$) and β ($Cr_5Si_8Al_2$). However, only the first phase can be in equilibrium with solid (Al) in the solid state [14, 15]. According to Figure 1.16, several non-variant phase reactions can take place in the Al-rich corner of the phase diagram. These reactions are presented in Table 1.7.

$Cr_4Si_4Al_{13}$ (31%Cr and 16.7%Si) contains, according to the data of chemical analyses, 30.5%Cr and 17.5%Si [14]. It has cubic lattice (space group F43m, 84 atoms/unit cell) with lattice parameter $a = 1.0917$ nm and density 3.4 g/cm^3. The $CrAl_7$ phase can dissolve only about 0.3%Si.

1.2.11 The Al–Cu–Fe system

The analysis of this phase diagram is very educational since it gives a possibility to trace the role and influence of iron impurities upon the phase composition

Table 1.7 Non-variant phase reactions in the aluminum corner of the Al–Cr–Si system [14, 39]

Reaction	T (°C)	Composition of the melt (%)	
		Cr	Si
$L \rightarrow Al + Si + Cr_4Si_4Al_{13}$	577	0.5	11
$L + CrAl_7 \rightarrow Al + Cr_4Si_4Al_{13}$	627	0.5	2.9
$L + Cr_5Si_8Al_2 \rightarrow Si + Cr_4Si_4Al_{13}$	587	0.5	13
$L + Cr_2Al_{11} \rightarrow CrAl_7 + Cr_4Si_4Al_{13}$	677	2	2.5
$L + Cr_2Al_{11} + Cr_5Si_8Al_2 \rightarrow Cr_4Si_4Al_{13}$	707	1.5	7.5

of industrial Al–Cu alloys. It is also necessary for subsequent analyses of more complex Cu- and Fe-bearing phase diagrams (see Sections 1.3–1.5).

The aluminum corner of this phase diagram was studied in the concentration range up to 40%Cu and 3.5%Fe. The following phases can be in equilibrium with (Al): binary Al_3Fe, Al_2Cu, and ternary Al_7FeCu_2 and $Al_6(FeCu)$ [14, 15, 39]. The Al_3Fe phase can dissolve up to 0.5% Cu. Depending on the alloy composition these ternary phases can precipitate either as constituent particles, or via peritectic reactions. The projections of solidification surfaces and an isothermal cross-section at 500°C are presented in Figure 1.17. Non-variant reactions in the Al–Fe–Cu system and the limit concentration of saturated (Al) are given in Tables 1.8 and 1.9.

Copper and iron do not influence their mutual solubility in aluminum. However, since copper reduces the temperatures of Fe-bearing eutectic phase reactions, the maximal amount of iron in solid solution decreases.

The Al_2Cu phase has tetragonal structure (space group I4/mmm, 12 atoms/unit cell) with parameters $a = 0.6063$ nm and $c = 0.4872$ nm. The solubility range for this phase is from 52.5%Cu to 53.9%Cu, which is below the stoichiometric copper concentration of 4.34 g/cm^3. The Vickers hardness is 4–6 GPa at room temperature. It gradually decreases with temperature increase up to 327°C, and then hardness drops rapidly [5, 6, 14]. The microhardness of this phase at 20°C is 5.3 GPa, 1-hour hardness at 300°C is 2 GPa [10]. This is a moderately creep resistant (thermally stable) compound.

The $Al_6(FeCu)$ phase (7%Cu, 24.6%Fe) is also known as $Al_{23}Fe_4Cu$ or α(FeCu). It is a metastable modification of the Al_6Fe phase, which becomes stable when the content of Cu reaches 7–8% and iron 22–25%. According to Ref. [39], this compound has orthorhombic lattice of the Al_6Mn type with the space group $Ccm2_1$ and 28 atoms/unit cell, with parameters $a = 0.64343$ nm, $b = 0.74604$ nm, $c = 0.87769$ nm. The density of this phase is 3.45 g/cm^3.

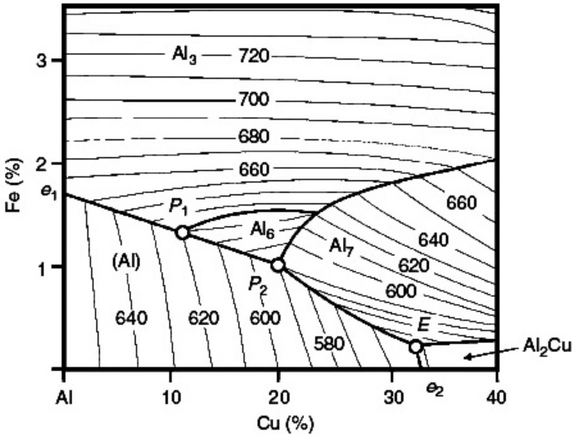
Al$_3$
720
700
680
660
660
640
620
600
P$_1$
Al$_6$
Al$_7$
(Al)
P$_2$
640
620
600
580
E
Al$_2$Cu
e$_1$
e$_2$
Fe (%)
1
2
3
Al
10
20
30
40
Cu (%)

(a) $Al_3–Al_3Fe$, $Al_6–Al_6CuFe$, $Al_7–Al_7Cu_2Fe$

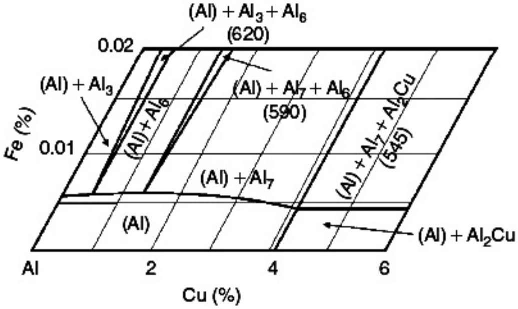
(Al) + Al$_3$ + Al$_6$
(620)
0.02
(Al) + Al$_3$
(Al)+Al$_6$
(Al) + Al$_7$ + Al$_6$
(590)
Fe (%)
0.01
(Al) + Al$_7$
(Al)+Al$_7$+Al$_2$Cu
(545)
(Al)
(Al) + Al$_2$Cu
Al
2
4
6
Cu (%)

(b) $Al_3–Al_3Fe$, $Al_6–Al_6CuFe$, $Al_7–Al_7Cu_2Fe$

Figure 1.17 Phase diagram Al–Cu–Fe: (a) liquidus projection and (b) distribution of phase fields in the solid state.

Table 1.8 Non-variant reactions in the aluminum corner of the Al–Fe–Cu system [14]

Reaction	T (°C)	Composition of the melt (%)		(Al) composition (%)	
		Cu	Fe	Cu	Fe
$L + Al_3Fe \Rightarrow (Al) + Al_6(FeCu)$	620	10.8	1.4	1.5	0.03
$L + Al_6(FeCu) \Rightarrow (Al) + Al_7FeCu_2$	590	20.0	1.0	3.0	0.02
$L + Al_3Fe \Rightarrow Al_6(FeCu) + Al_7FeCu_2$	622	23.6	1.5	–	–
$L \Rightarrow (Al) + Al_2Cu + Al_7FeCu_2$	542	32.5	0.3	5.3	0.03

Table 1.9 Solubility of copper and iron in solid aluminum in the vertices of three-phase domains [14]

T (°C)	(Al) + Al_2Cu + Al_7FeCu_2		(Al) + $Al_6(FeCu)$ + Al_7FeCu_2		(Al) + Al_3Fe + $Al_6(FeCu)$	
	Cu (%)	Fe (%)	Cu (%)	Fe (%)	Cu (%)	Fe (%)
552	5.65	0.018	2.00	0.015	0.60	0.013
527	5.00	0.012	1.75	0.010	0.50	0.009
502	4.00	0.005	1.50	0.005	0.40	0.006
477	3.30	0.003	1.00	0.003	0.30	0.003
452	2.56	0.002	0.80	0.002	0.23	0.002
427	1.50	0.001	0.58	0.001	0.19	0.001

The Al_7FeCu_2 (36.9%Cu, 16.2%Fe), also denoted as β(FeCu) or N-phase, has a broad homogeneity range from 29 to 39%Cu and from 12 to 20%Fe [14]. The structure of this phase belongs to the tetragonal type (space group P4/mnc, 40 atoms per unit cell) with parameters $a = 0.6336$ nm, $c = 1.4879$ nm [39]. The density of this phase is 4.3 g/cm^3. Its microhardness at 20°C is 5.95 GPa, 1-hour hardness at 300°C is 2.6 GPa, which indicates that this compound is thermally stable.

At sufficiently high solidification rate a different phase, Al_6FeCu_2 (16.2%Fe, 36.9%Cu), may be formed [14].

1.2.12 The Al–Cu–Mg system

This system is the key for a large class of aluminum alloys, which are mostly used as wrought materials. However, there is also a number of casting alloys described by the Aluminum Association (e.g., AA206.0) (see Appendix 1). Because of its importance, the Al–Cu–Mg system and its phase diagram are well studied, especially in the Al corner. The most detailed experimental data were reported in Ref. [40]; these data are usually presented in reference books [14, 15, 41]. Moreover, a thermodynamic model of this system constructed using the ThermoCalc is available that displays good agreement with experiment [42]. The widely accepted variant of this phase diagram is presented in Figure 1.18. The nonvariant phase reactions with (Al) taking place in this system are described in Table 1.10.

Aluminum solid solution can be in equilibrium with binary phases Al_2Cu and Al_8Mg_5, and also ternary phases Al_2CuMg (S) and Al_6CuMg_4 (T). Table 1.11

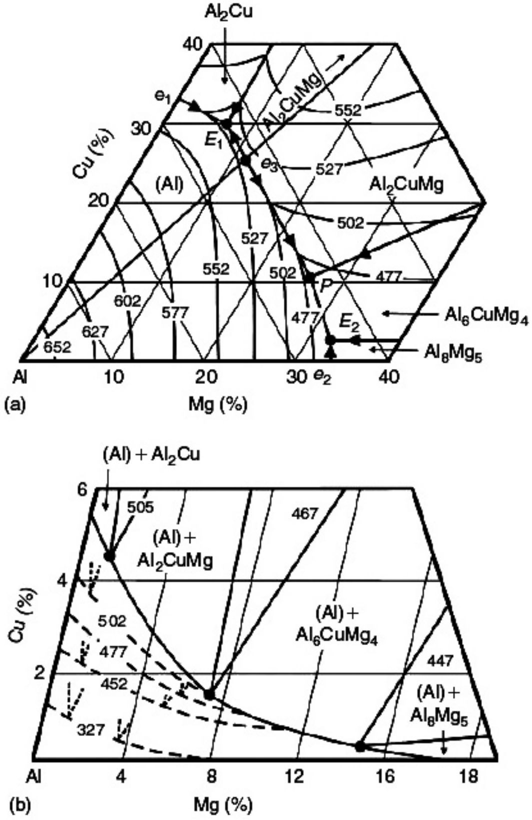
Al2Cu
40
e1
30
E1
Al2CuMg
552
e3
527
Cu (%)
(Al)
Al2CuMg
20
502
527
552
502
P
477
10
602
577
477
E2
Al6CuMg4
627
652
Al8Mg5
Al
10
20
30 e2
40
(a)
Mg (%)
(Al) + Al2Cu
6
505
467
(Al)+
Al2CuMg
4
Cu (%)
502
(Al)+
Al6CuMg4
477
2
452
447
(Al)+
Al8Mg5
327
Al
4
8
12
16
18
(b)
Mg (%)

Figure 1.18 Phase diagram Al–Cu–Mg: (a) liquidus projection and (b) distribution of phase fields in the solid state.

provides the values of limit solubility of copper and magnesium in (Al) in the vertices of the three-phase domains [15]:

$$(Al) + Al_2Cu + Al_2CuMg$$

$$(Al) + Al_2CuMg + Al_6CuMg_4$$

$$(Al) + Al_8Mg_5 + Al_6CuMg_4$$

The presence of a partially quasi-binary cross-section Al–S gives a possibility to divide the aluminum corner of this phase diagram into two domains. The metastable modifications of the Al_2Cu phases (i.e., θ' and θ'') and also Al_2CuMg (S') ensure a substantial effect of dispersion hardening in the course of decomposition of supersaturated solid solutions.

Table 1.10 Non-variant reactions in the Al–Cu–Mg system [14]

Reaction	T (°C)	Composition of molten metal	
		Cu (%)	Mg (%)
$L \Rightarrow (Al) + Al_2Cu$	549	33	–
$L \Rightarrow (Al) + Al_2Cu + Al_2CuMg$ (S)	507	30	6
$L \Rightarrow (Al) + Al_2CuMg$ (quasi-binary eutectic)	518	24.5	10.1
$L + Al_2CuMg \Rightarrow (Al) + Al_6CuMg_4$ (T)	467	10	26
$L \Rightarrow (Al) + Al_8Mg_5 + Al_6CuMg_4$	449	2.7	32
$L \Rightarrow (Al) + Al_8Mg_5$	450	–	34

Table 1.11 Mutual solubility of copper and magnesium in aluminum [14]

T (°C)	$(Al) + Al_2Cu + Al_2CuMg$		$(Al) + Al_2CuMg + Al_6CuMg_4$		$(Al) + Al_8Mg_5 + Al_6CuMg_4$	
	Cu (%)	Mg (%)	Cu (%)	Mg (%)	Cu (%)	Mg (%)
450	2.0–2.6	0.6–1.1	0.3–0.35	8.5	0.3	10.5
400	1.4–1.8	0.4–0.8	0.2–0.3	7.4	0.2	9.2–9.5
350	0.9	0.5	0.1	6.2	0.1	7.6
300	0.6	0.2	0.1	5.0	0.1	5.6

The Al_2CuMg (S) (46%Cu, 17%Mg) compound is characterized by a narrow homogeneity range. It has orthorhombic lattice (space group Cmcm, 16 atoms/unit cell) with parameters $a = 0.401$ nm, $b = 0.925$ nm, and $c = 0.715$ nm. The calculated density of this phase is 3.55 g/cm^3 [5]. Microhardness at 20°C is 4.44 GPa, 1-hour microhardness at 300°C is 2.22 GPa [15].

The Al_6CuMg_4 compound (22–27%Cu, 27.5–30%Mg) has defect bcc lattice (space group Im3, 162 atoms/unit cell) with parameter $a = 1.428$–1.431 nm [14]. The density of this phase is 4.14 GPa [5]. Its microhardness at room temperature is 4.14 GPa, 1-hour hardness at 300°C is 1.46 GPa [10]. This compound is usually denoted as the T-phase, and it is isomorphic to the $Al_2Mg_3Zn_3$ phase of the Al–Mg–Zn system.

The other two phases, AlCuMg and $Al_5Cu_6Mg_2$, are not in equilibrium with (Al), but these phases can form (similar to Al_6CuMg_4) continuous solid solutions with $MgZn_2$ and Mg_2Zn_{11} phases from the Al–Mg–Zn system (see

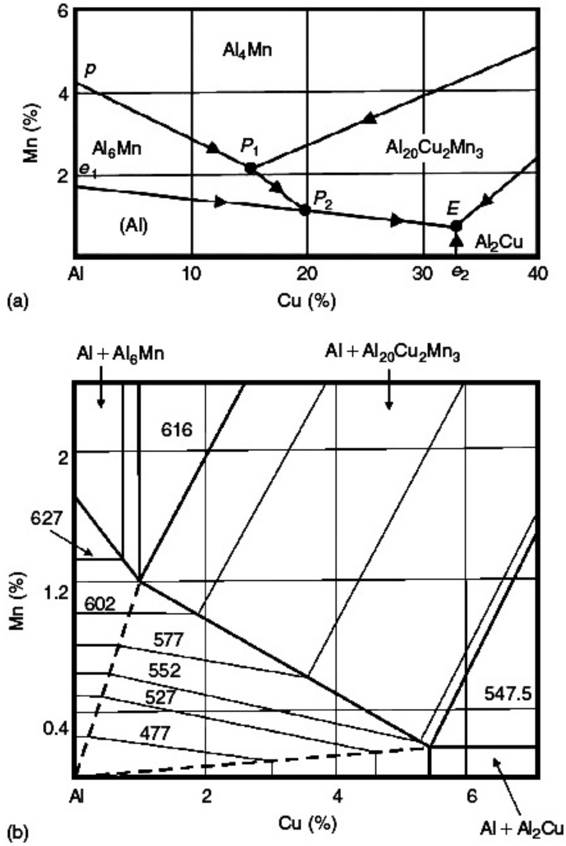
Al4Mn
p
P1
P2
E
e1
e2
Al6Mn
Al20Cu2Mn3
(Al)
Al2Cu
Mn (%)
Cu (%)
Al
(a)
Al + Al6Mn
Al + Al20Cu2Mn3
616
627
602
577
552
527
477
547.5
Al + Al2Cu
(b)

Figure 1.19 Phase diagram Al–Cu–Mn: (a) liquidus projection and (b) distribution of phase fields in the solid state.

Section 1.2.3). This fact needs to be taken into account when analyzing different phase compositions belonging to the quaternary system Al–Cu–Mg–Zn (Section 1.3.8).

1.2.13 The Al–Cu–Mn system

Understanding the Al–Cu–Mn phase diagram gives a possibility to correctly analyze phase compositions of a number of thermally stable alloys, similar to Russian alloy AM5 (Appendix 5). Inasmuch as the Mn influence is quite substantial, it is not sufficient to just understand the binary Al–Cu phase diagram.

In the aluminum corner of the Al–Cu–Mn system (Figure 1.19), (Al) can be in equilibrium with Al_2Cu, Al_6Mn, and ternary compound T ($Al_{20}Cu_2Mn_3$ or

Table 1.12 Non-variant phase reactions in ternary alloys of the Al–Cu–Mn system [14]

Reaction	T (°C)	Composition of the melt	
		Cu (%)	Mn (%)
$L + Al_4Mn \Rightarrow Al_6Mn + 4Al_{12}CuMn_2$	625	15.6	2.1
$L + Al_6Mn \Rightarrow (Al) + Al_{12}CuMn_2$	616	14.8	0.9
$L \Rightarrow (Al) + Al_2Cu + Al_{12}CuMn_2$	547.5	32.5	0.6

Table 1.13 Mutual solubility of copper and manganese in solid Al at different temperatures [15]

T (°C)	$(Al) + Al_6Mn + Al_{12}CuMn_2$		$(Al) + Al_2Cu + Al_{12}CuMn_2$	
	Cu (%)	Mn (%)	Cu (%)	Mn (%)
623.5	1.4	1.17	–	–
616	1.3	1.0	–	–
610	1.3	1.0	–	–
600	1.1	0.9	–	–
550	0.85	0.6	–	–
547.5	–	–	5.5	0.2
525	0.95	0.44	4.95	0.2
500	0.65	0.4	4.05	0.2
450	0.5	0.2	2.55	0.15
400	0.4	0.1	1.5	0.1

$Al_{12}CuMn_2$) [14]. The non-variant phase reactions in this system in the Al-rich domain are presented in Table 1.12.

The ternary T-phase has homogeneity range 12.8–19%Cu and 19.8–24%Mn. This allows for two possible interpretations of this phase's chemical formula: $Al_{20}Cu_2Mn_3$ (15.3%Cu, 19.8%Mn) or $Al_{12}CuMn_2$ (12.8%Cu, 22.1%Mn). The latter formula seems to be correct [14].

The Al_2Cu phase can dissolve up to 0.1%Mn, while the Al_6Mn up to 0.2%Cu. The mutual solubility of copper and manganese in solid aluminum is presented in Table 1.13.

The $Al_{12}CuMn_2$ compound has orthorhombic structure with parameters $a = 2.411$ nm, $b = 1.251$ nm, and $c = 7.71$ nm [5]. Its density is equal to 3.59 g/cm^3.

1.2.14 The Al–Cu–Ni system

This phase diagram is important for understanding the phase composition and properties of a thermally stable alloy (Russian AL33). Besides copper, they contain nickel and, quite often, other chemical elements. In the aluminum corner of the Al–Cu–Ni system (Figure 1.20), there is a ternary phase Al_7Cu_4Ni. In addition

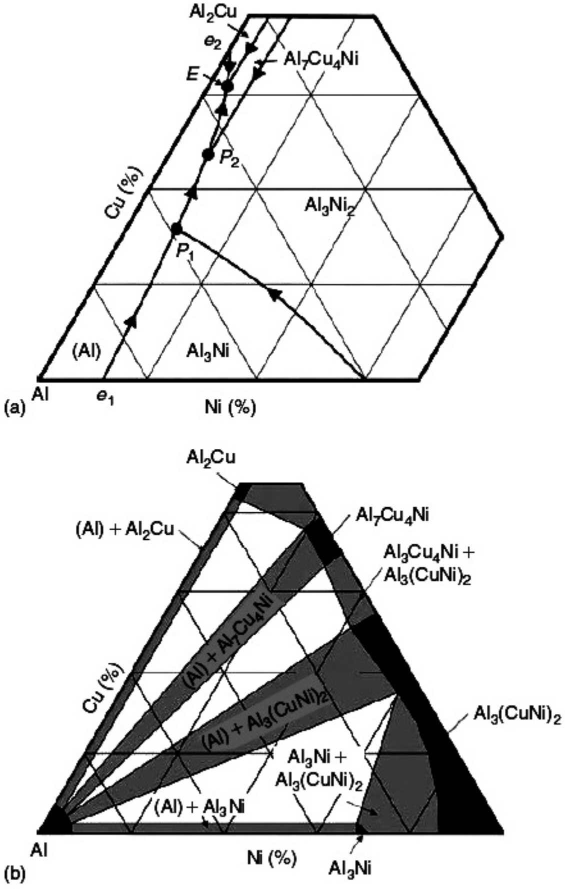
Al_2Cu
e_2
E
Al_7Cu_4Ni
P_2
Cu (%)
Al_3Ni_2
P_1
(Al)
Al_3Ni
(a)
Al
e_1
Ni (%)
Al_2Cu
(Al) + Al_2Cu
Al_7Cu_4Ni
Al_3Cu_4Ni +
$Al_3(CuNi)_2$
(Al) + Al_7Cu_4Ni
Cu (%)
(Al) + $Al_3(CuNi)_2$
$Al_3(CuNi)_2$
Al_3Ni +
$Al_3(CuNi)_2$
(Al) + Al_3Ni
Al
Ni (%)
Al_3Ni
(b)

Figure 1.20 Phase diagram Al–Cu–Ni: (a) liquidus projection and (b) distribution of phase fields in the solid state.

to that, Al_2Cu, Al_3Ni, and Al_3Ni_2 can also be in equilibrium with (Al). Table 1.14 presents non-variant phase reactions in this ternary system [14, 15].

The solubility of nickel in aluminum is very small, while the data on the solubility of copper in ternary alloys is presented in Table 1.15 [14]. The ternary phase (Al_7Cu_4Ni) has a homogeneity range 38.7–50.7%Cu and 11.8–22.2%Ni. Al_3Ni_2, which in binary Al–Ni system cannot be in equilibrium with (Al), also has a broad homogeneity range, which in ternary system spreads the range up to 31.2%Cu, 29.9%Ni, or up to the composition Al_3CuNi (Figure 1.20).

The Al_7Cu_4Ni phase is also known as Al_6Cu_3Ni, Al_7CuNi, Al_3Cu_2Ni, or Al_9Cu_3Ni. It has ordered rhombohedral lattice with parameters $a = 1.35$ nm, $\alpha = 17°27'$. Alternatively, it may have hexagonal lattice with parameters $a = 0.4101$–0.4119 nm, $c = 0.497$–0.5025 nm [14], or bcc lattice with parameter $a = 1.46$ nm [5]. The phase density is 5.48 g/cm^3. The Vickers hardness is 9.87–10 GPa, 1-hour hardness at 300°C is 5.8 GPa. This phase is thermally stable [10, 15].

The Al_3Ni_2 phase has hexagonal lattice (space group P3m1; 5 atoms/unit cell) with parameters in the binary system $a = 0.4036$ nm, $c = 0.490$ nm. The phase density is 4.76 g/cm^3 [5]. The Vickers hardness exceeds 11 GPa at 27°C and 5 GPa at 577°C [14]. This phase is also thermally stable.

Table 1.14 Non-variant phase reactions in the Al-rich alloys of the Al–Cu–Ni system [14]

Reaction	T (°C)	Composition of the melt	
		Cu (%)	Ni (%)
$L + Al_3Ni \Rightarrow (Al) + Al_3Ni_2\ (Al_3CuNi)$	630	16	4
$L + Al_3Ni_2 \Rightarrow (Al) + Al_7Cu_4Ni$	590	22	2
$L \Rightarrow (Al) + Al_2Cu + Al_7Cu_4Ni$	546	32.5	0.9

Table 1.15 Limit solubility of copper (%) in (Al) in three-phase domains of the Al–Cu–Ni phase diagram [14]

T (°C)	$(Al) + Al_3Ni + Al_3Ni_2$	$(Al) + Al_3Ni_2 + Al_7Cu_4Ni$	$(Al) + Al_2Cu + Al_7Cu_4Ni$
561	–	4.35	–
554	1.7	–	–
547	–	–	5.3
527	1.5	3.3	3.8
427	1.2	1.5	1.9

1.2.15 The Al–Cu–Si system

Using the Al–Cu–Si phase diagram, one can reliably analyze phase compositions of the Cu-bearing Al–Si alloys with low content of iron and magnesium. This diagram is also helpful in analysis of other more complex systems with the participation of Cu and Si as alloying elements (Sections 1.3–1.5).

There are no any ternary compounds in the Al–Cu–Si system. Saturated Al-base solid solution can be in equilibrium only with Al_2Cu and (Si). The liquidus and the solidus of the aluminum corner of the Al–Cu–Si phase diagram are given in Figure 1.21. The ternary eutectic (Al) + Al_2Cu + (Si) is formed at 520–525°C and contains 26–31%Cu and 5–6.5%Si [14].

The solubility of copper in (Si) and silicon in Al_2Cu is negligibly small. The maximal mutual solubility of copper and silicon in solid aluminum at the eutectic temperature (525°C) is 4.5%Cu and 1.1%Si, respectively. As temperature goes down, the solubility of copper and silicon in aluminum also decreases [15]:

T (°C)	500	460	400	300
Cu (%)	4.1	3.6	1.5	0.4
Si (%)	0.85	0.6	0.25	0.1

1.2.16 The Al–Cu–Zn system

Although industrial alloys on the basis of the Al–Cu–Zn system are practically absent (see Appendix 1) this ternary diagram is important for understanding more complex systems containing copper and zinc. First and foremost, this is true with respect to the Al–Cu–Mg–Zn system which lays at the foundation of high-strength aluminum alloys.

The most probable variant of this diagram is given in Ref. [15]. According to this work, in addition to Al_2Cu and (Zn), two more phases can be in equilibrium with (Al), namely $Cu_5Zn_2Al_3(\tau)$ and $CuZn_5$. The field of primary solidification of (Al) lies in a broad concentration range of this system (Figure 1.22). The non-variant phase reactions with the participation of (Al) are presented in Table 1.16.

The zinc-based solid solution has hcp lattice (space group P63/mmc, 2 atoms/unit cell) with parameters $a = 0.26584$ nm, $c = 0.49387$ nm (99.95%Zn). Its density is 6.49 g/cm^3. Microhardness of zinc at 20°C is 0.6 GPa, 1-hour microhardness at 300°C is 33 MPa, which is a clear indication of its low thermal stability [10].

The ternary τ-phase has homogeneity range from 56 to 58%Cu and from 10 to 30%Zn. There is data on the two different structures of this phase (i.e., τ and τ'), but the corresponding two phase area was not found. The structure of this phase at relatively high concentrations of aluminum is close to that of compound Cu_4NiAl_7. Alloys with concentrations closer to the Cu–Zn side of this ternary diagram also have the structure of τ-phase. Its composition is close to the formula $Cu_5Zn_2Al_3$ (60.1%Cu and 24.7%Zn). This phase has cubic lattice (space group Pm3m, 2 atoms/unit cell) with weakly expressed ordering of the CsCl type. The

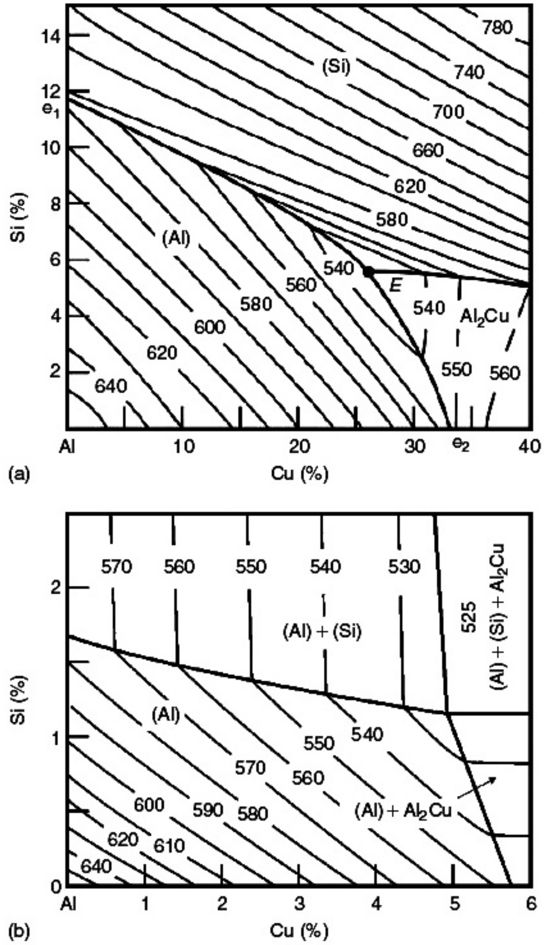

Figure 1.21 Phase diagram Al–Cu–Si (a) liquidus projection and (b) distribution of phase fields in the solid state.

lattice parameter of the elementary cell changes from $a = 0.291$ nm at 57%Cu and 10%Zn to $a = 0.294$ nm at 57%Cu and 25%Zn. The lattice is distorted bcc; XRD data indicates that there are strong super structural peaks of the CsCl-type lattice. The $CuZn_5$ compound can dissolve up to 5%Al. If this phase does not contain Al and the Zn concentration is 82%, then it has hcp lattice (space group $P6_6/mmc$) with parameters $a = 0.274$ nm and $c = 0.429$ nm. The $CuAl_2$ phase can dissolve up to 2–3%Zn; its properties and the lattice parameter do not change

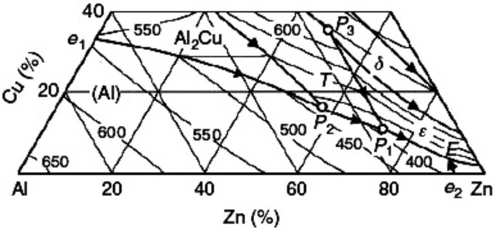

Figure 1.22 Phase diagram Al–Cu–Zn (liquidus projection).

Table 1.16 Non-variant reactions in the Al–Cu–Zn system with the participation of (Al) [14]

Phase reaction	Concentration of different elements								T (°C)
	I		II		III		IV		
	Cu	Zn	Cu	Zn	Cu	Zn	Cu	Zn	
$L + \tau \rightarrow Al + CuZn_5$	10.5	74	55.5	14	1.8	72	23	72	396
$L + (Al) \rightarrow CuZn_5 + (Zn)$	6	84	–	–	–	–	–	–	–
$L \rightarrow CuZn_5 + (Al) + (Zn)$	3.71	89.3	1.5	78.1	15.5	83.3	2.75	96	379.5

significantly. At the eutectic melting temperature (379°C), the Zn-based solid solution can contain up to 1.25%Al and 2.75%Cu.

1.2.17 The Al–Fe–Mg system

The analysis of this phase diagram gives a possibility to trace the role and influence of iron additions and impurities upon the phase composition of Al–Mg casting alloys containing small amounts of silicon, manganese, and other possible elements. It is also necessary for understanding more complex diagrams with the participation of Mg and Fe (see Sections 1.3–1.5).

There are no any ternary compounds in the Al–Fe–Mg system [14, 15, 40]. (Al) can be in equilibrium with binary phases Al_3Fe and Al_8Mg_5.

There is only one non-variant eutectic transformation in the aluminum corner of this system:

$$L \Rightarrow (Al) + Al_3Fe + Al_8Mg_5 \quad \text{at } 451°\text{C [43], or at } 445°\text{C [15]}$$

The resulting eutectic has completely degenerate microstructure.

The solubility of Mg in Al_3Fe and Fe in Al_8Mg_5 is negligibly small. The solubility of iron in solid aluminum decreases somewhat with the introduction of

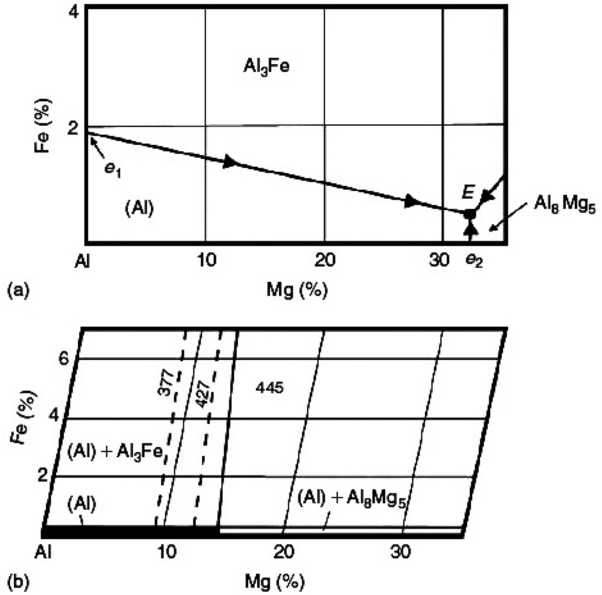

Figure 1.23 Phase diagram Al–Fe–Mg: (a) liquidus projection and (b) aluminum corner.

magnesium. On the contrary, Fe substantially decreases the solubility of magnesium in aluminum, which comprises 14.1%Mg at the temperature of the ternary eutectic [14]. The distribution of different phase fields at 452°C, 427°C, and 377°C is presented in Figure 1.23.

According to Ref. [14], the tendency to degenerate ternary eutectic formation increases with higher solidification rate. This process is accompanied by the formation of large needle-like crystals of Al_3Fe even at low Fe concentrations, while the Al_8Mg_5 compound forms at 2–3%Mg.

1.2.18 The Al–Fe–Mn system

This phase diagram is important because Fe and Mn enter the alloy compositions of many industrial alloys, forming different phases (mostly constituent particles). Without this analysis it is practically impossible to understand four- and five-component phase diagrams, which, as a rule, have very complex topology (see Sections 1.3 and 1.4).

Several binary phases can be formed in the aluminum corner of the Al–Fe–Mn phase diagram [6, 14, 15]. However, only Al_3Fe and $Al_6(FeMn)$ can be in equilibrium with (Al). Iron substitutes Mn in the Al_6Mn phase, resulting in the formation of $Al_{12}FeMn$ (12.85%Fe; 12.64%Mn).

The limit solubility of manganese in Al_3Fe corresponds is of the order of 4–5%, which corresponds to the formula $Mn_{0.12}Fe_{0.88}Al_3$. Additionally, manganese may stabilize the metastable Al_6Fe phase, which in the corresponding ternary system forms continuous solid solutions with the Al_6Mn phase.

In the aluminum-rich alloys, two non-variant transformations can take place [14, 44]:

$$L + Al_3Fe + Al_4Mn \Rightarrow Al_6(FeMn)(727{-}730°C;\ 2.5\%Fe,\ 3.45\%Mn)$$
$$L \Rightarrow (Al) + Al_3Fe + Al_6(FeMn)(654°C;\ 0.75\%Mn,\ 1.75\%Fe).$$

However, the authors of Ref. [45] believe that the ternary eutectic contains smaller amounts of manganese and iron: ~0.43%Mn and ~1.7%Fe. The vertices of the eutectic triangle correspond to the following compounds: Al_3Fe (36.9%Fe, 4.6%Mn), Al_6(FeMn) (19.6%Fe, 7.1%Mn), and (Al) (0.044%Fe, 0.23%Mn). This implies that the Al_6(FeMn) phase composition is different from the one given in Refs. [14, 44].

The Al_6(FeMn) phase has orthorhombic lattice isomorphic to the phases Al_6Fe and Al_6Mn with parameters $a = 0.75518$ nm, $b = 0.64978$ nm, and $c = 0.88703$ nm [44]. According to Ref. [14], this phase's lattice parameters are $a = 0.7498$ nm, $b = 0.6495$ nm, and $c = 0.8837$ nm. The projection of the solidification surfaces is presented in Figure 1.24a; the isothermal cross-section at 627°C is given in Figure 1.24b.

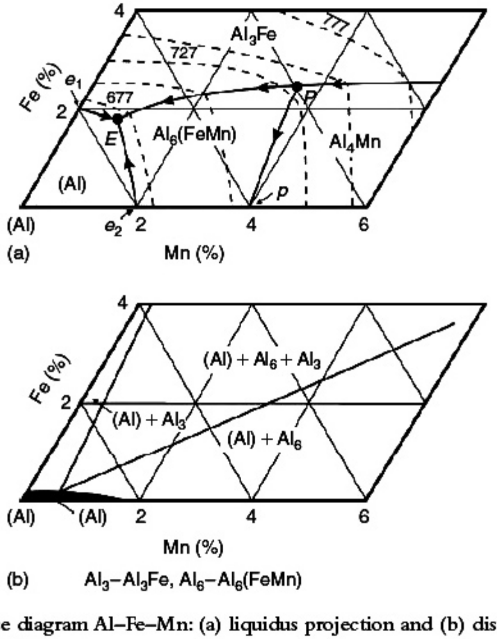

Figure 1.24 Phase diagram Al–Fe–Mn: (a) liquidus projection and (b) distribution of phase fields in the solid state.

1.2.19 The Al–Fe–Ni system

The following phases can be in equilibrium with (Al) in the Al–Fe–Ni ternary system: Al_3Fe, Al_3Ni and Al_9FeNi. However, it is the latter phase that defines the importance of this whole diagram for alloy design. The reason is that this phase possesses a unique combination of favorable morphology, properties, and economical alloying. This fact lies in the foundation of successful development of such alloys as wrought alloy AA8001 and casting alloy AA393.0. Without the analysis of this phase diagram (Al–Fe–Ni) it is impossible to understand more complex alloys with participation of Fe and Ni. Such systems are not well studied up until the present time.

Figure 1.25 represents the solidification surface projection and the distribution of phase domains in solid state in the Al corner of this phase diagram.

The Al_9FeNi phase is formed according to the following peritectic reaction:

$$L + Al_3Fe + Al_3Ni \Rightarrow Al_9FeNi\ (809^\circ C;\ 3.8\%Fe,\ 20.5\%Ni)$$

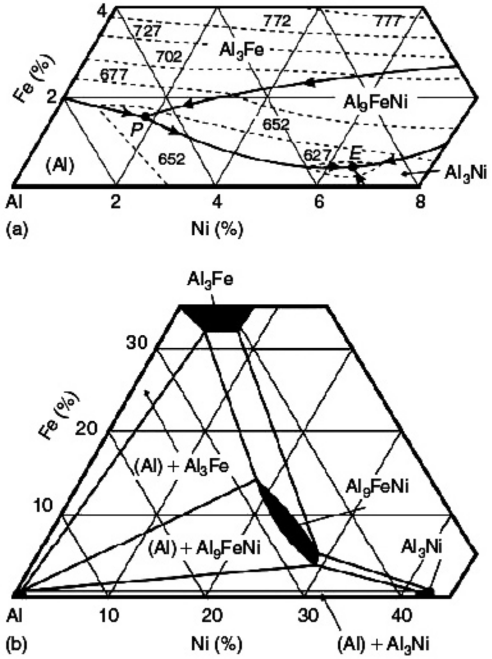
4
727
772
777
702
Al3Fe
677
Fe (%)
2
Al9FeNi
P
652
652
627
E
(Al)
Al3Ni
Al
2
4
6
8
(a)
Ni (%)
Al3Fe
30
Fe (%)
20
(Al) + Al3Fe
Al9FeNi
10
(Al) + Al9FeNi
Al3Ni
Al
10
20
30
40
(b)
Ni (%)
(Al) + Al3Ni

Figure 1.25 Phase diagram Al–Fe–Ni: (a) liquidus projection and (b) distribution of phase fields in the solid state.

Table 1.17 Non-variant reactions in the Al corner of the Al–Fe–Si system [40]

Phase reaction	Concentration of element, in phases (%)								T (°C)
	I		II		III		IV		
	Fe	Si	Fe	Si	Fe	Si	Fe	Si	
$L \Rightarrow (\mathrm{Al}) + \mathrm{Al_5FeSi} + (\mathrm{Si})$	0.7	12	0.01	1.6	25	15	0	99.8	576
$L + \mathrm{Al_8Fe_2Si} \Rightarrow (\mathrm{Al}) + \mathrm{Al_5FeSi}$	1.7	6.5	33	7	0.04	1.1	25	13	629
$L + \mathrm{Al_3Fe} \Rightarrow (\mathrm{Al}) + \alpha\mathrm{Al_8Fe_2Si}$	2	4	36	0.01	0.05	0.6	33	7	611

In Al-rich alloys two non-variant phase reactions take place [14, 46]:

$$L + \mathrm{Al_3Fe} \Rightarrow (\mathrm{Al}) + \mathrm{Al_9FeNi}\ (649-650.2^\circ\mathrm{C};\ 1.7\%\mathrm{Fe},\ 1.7\%\mathrm{Ni})$$

$$L \Rightarrow (\mathrm{Al}) + \mathrm{Al_3Ni} + \mathrm{Al_9FeNi}\ (638-640^\circ\mathrm{C};\ 0.2-0.3\%\mathrm{Fe}, 6.5\%\mathrm{Ni})$$

The Al_3Fe phase dissolves up to 3–4% (1.4–1.9 at.%) of nickel, while the Al_3Ni phase can dissolve not more than 1% (0.5 at.%) of iron. The homogeneity range of the Al_9FeNi phase extends from 4.5%Fe to 14% Fe and from 28%Ni to 18%Ni [14, 46]. This phase contains 15.6%Fe and 16.4%Ni; it has monoclinic lattice of the Al_9Co_2 type (space group $P2_1/c$, 22 atoms/unit cell) with parameters $a = 0.8598$ nm, $b = 0.6271$ nm, $c = 0.6207$ nm, $\beta = 94.66°$ [46].

1.2.20 The Al–Fe–Si system

The Al–Fe–Si system is the key for analysis of 1xxx alloys, pure commercially aluminum with minor Fe and Si impurities, and binary Al–Si casting alloys (which, as a rule, contain certain amounts of Fe impurities). Detailed studies of the Al–Fe–Si phase diagram were conducted in Ref. [40], where the interested reader can find detailed figures of the liquidus, solidus, and solvus isotherms, as well as intermediate phase reactions. The numerous subsequent studies of this system did not bring any substantial changes in our understanding of the Al corner of this phase diagram; usually these results are presented in different reference texts (see Refs. [14, 15, 57]). It is generally accepted today that (Al) can be in equilibrium with (Si), Al_3Fe, Al_8Fe_2Si, and Al_5FeSi, which may participate in different non-variant reactions (Table 1.17, also see Figure 1.26). The solubility of iron and silicon in (Al) at different temperatures are presented in Table 1.18.

The solubility of silicon in Al_3Fe is in the range from 0.2% to 6%, as there is a considerable scatter in the reported experimental results. The dependence of

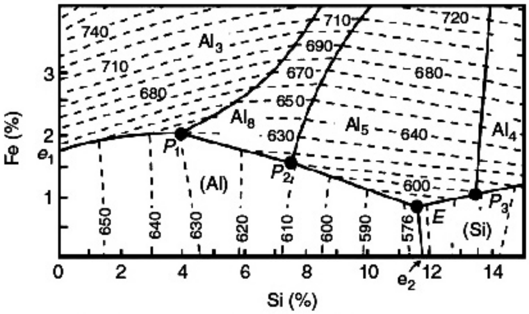

(a) Al_3-Al_3Fe, Al_5-Al_5FeSi, $Al_8-Al_8Fe_2Si$, $Al_4-Al_4FeSi_2$

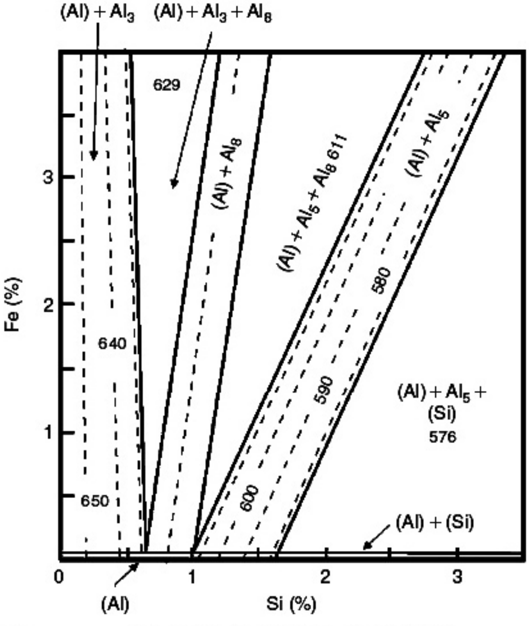

(b) Al_3-Al_3Fe, Al_5-Al_5FeSi, $Al_8-Al_8Fe_2Si$

Figure 1.26 Phase diagram Al–Fe–Si: (a) liquidus projection and (b) solidus projection.

the lattice parameter upon phase composition can be described by the following equations:

$$a = 1.505 + 1.14 \times 10^{-3}\,[\mathrm{Fe}] - 0.41 \times 10^{-3}\,[\mathrm{Si}]$$

$$b = 0.8628 - 1.14 \times 10^{-3}\,[\mathrm{Fe}] - 1.3 \times 10^{-3}\,[\mathrm{Si}]$$

In these equations, the concentrations of [Fe] and [Si] are given in mass% [47].

Table 1.18 Solubility of iron and silicon in solid aluminum [40]

T (°C)	(Al) + Al_3Fe + α(AlFeSi)		(Al) + α(AlFeSi) + β(AlFeSi)		(Al) + β(AlFeSi) + (Si)	
	Fe (%)	Si (%)	Fe (%)	Si (%)	Fe (%)	Si (%)
629	0.052	0.64	–	–	–	–
611	–	–	0.04	0.82	–	–
600	0.033	0.4	0.033	0.82	–	–
578	–	–	–	–	0.01	1.65
550	0.016	0.2	0.016	0.42	0.008	1.3
500	0.009	0.11	0.008	0.22	0.005	0.8
450	0.004	0.06	0.004	0.11	0.003	0.44
400	0.002	0.03	0.002	0.06	0.002	0.30

The solubility of iron in silicon is negligibly small [14]. The Al_8Fe_2Si compound (31.6%Fe, 7.8%Si) is also denoted as $Al_{12}Fe_3Si_2$ (30.7%Fe, 10.2%Si), $Al_{7.4}Fe_2Si$, α(AlFeSi), or c(AlFeSi). It exists in the homogeneity range 30–33%Fe, 6–12%Si and possesses hexagonal lattice (space group P6$_3$/mmc) with lattice parameters $a = 1.23$–1.24 nm, $c = 2.62$–2.63 nm. The density of this phase is 3.58 g/cm^3 [14, 47].

The Al_5FeSi phase (25.6%Fe, 12.8%Si) is also denoted as $Al_9Fe_2Si_2$, β(AlFeSi), and m(AlFeSi); it exists in the homogeneity range 25–30%Fe, 12–15%Si. This phase has monoclinic lattice with parameters $a = b = 0.612$ nm, $c = 4.148$–4.150 nm, $\beta = 91°$. Its density is 3.3–3.6 g/cm^3, the Vickers hardness is equal to 5.8 GPa [14, 47, 48]. Microhardness of β(AlFeSi) at 20°C is 11.47 GPa, while the 1-hour microhardness at 300°C is 7.85 GPa (i.e., this is a phase with exceptional thermal stability) [10].

The Al_4FeSi_2 compound (25.4%Fe, 25.5%Si) is also denoted as Al_3FeSi_3, δ(AlFeSi), or t(AlFeSi). It has a homogeneity range that is narrower than that of α(AlFeSi) or β(AlFeSi). This phase possesses tetragonal lattice of the $PdGa_5$ type with the following parameters: $a = 0.607$–0.63 nm, $c = 0.941$–0.953 nm. The density of this phase is 3.3–3.36 g/cm^3 [14, 48]. Microhardness at 20°C is equal to 10.97 GPa, 1-hour microhardness at 300°C is 5.18 [10].

The Al_3FeSi phase (33.9%Fe, 16.9%Si), sometimes also denoted as γ(AlFeSi), has monoclinic structure with parameters $a = 1.78$ nm, $b = 1.025$ nm, $c = 0.890$ nm, and $\beta = 132°$ [14].

The Al–Fe–Si phase diagram is very complex. There is still ongoing debate about the existence of certain ternary phases, or temperatures, and compositions of non-variant phase reactions. The domains of existence of these ternary phases are in many cases beyond their respective field of primary solidification, and for this reason to achieve equilibrium, cascades of peritectic reactions have to be completed. As a result of this complexity, real industrial alloys may contain coexisting phases such as Al_3Fe, Al_6Fe, α(AlFeSi), β(AlFeSi), and δ(AlFeSi). The identification of these phases is often a very difficult problem because the same phase(s) may have very different morphologies as a function of their origin: either primary crystals (constituent particles) or the products of peritectic and eutectic phase reactions. Besides silicon, stable, metastable, and non-equilibrium phases may precipitate out of supersaturated solid solutions or in the process of ingot or casting cooling, and also undergo different transformations during heat treatment.

1.2.21 The Al–Mg–Mn system

This phase diagram gives a possibility to correctly analyze the phase composition of many Al–Mg casting alloys (which often contain manganese) in the case of high purity with respect to Fe and Si. It is also necessary for analysis of more complex diagrams with participation of Mg and Mn (Sections 1.3–1.5).

Figure 1.27 illustrates the aluminum corner of the Al–Mg–Mn system. (Al) can be in equilibrium with Al_6Mn, Al_8Mg_5, and ternary compound $Al_{10}(MgMn)_3$ (13.7%Mg, 13.5%Mn) or $Al_{10}Mg_2Mn$ (12.8–13.03%Mg, 14.72–14.8%Mn) [14]. Ternary compound is formed according to the following peritectic reactions:

$$L + Al_4Mn \Rightarrow Al_6Mn + Al_{10}(MgMn)_3 \ (18\%Mg, 2\text{–}3\%Mn)$$

$$L + Al_6Mn \Rightarrow (Al) + Al_{10}(MgMn)_3 \ (22\%Mg, <0.5\%Mn)$$

At $T = 437°C$, most probably, an eutectic phase reaction takes place [14]:

$$L \Rightarrow (Al) + Al_8Mg_5 + Al_{10}(MgMn)_3 \ ({\sim}33\%Mg, 0.1\text{–}0.2\%Mn).$$

The $Al_{10}(MgMn)_3$ ($Al_{18}Mg_3Mn_2$) phase has cubic lattice of the $Al_{18}Cr_2Mg_3$ and $Al_{12}Mn$ (space group Fd3m, 184 atoms/unit cell) with lattice parameter $a = 1.453$ nm [49].

The solubility of manganese in aluminum decreases with additions of magnesium. For example, at 597°C the introduction of 2%Mg decreases Mn solubility in aluminum from 0.96% to 0.8%. The maximal Mg solubility in aluminum also decreases in the presence of manganese: the maximal solubility in the ternary system is 14%Mg, while in the corresponding binary system 17.4%Mg.

The solubility of Mg in Al_6Mn and Mn in Al_8Mg_5 is very low [14].

1.2.22 The Al–Mg–Si system

The Al–Mg–Si phase diagram is very important for understand such alloys as AA356.0 and also of Al–Mg casting alloys. If the Fe content is low, then this

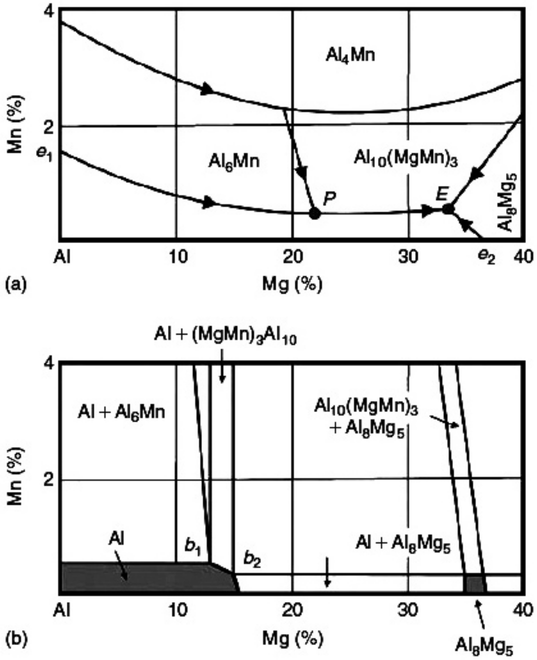

Figure 1.27 Phase diagram Al–Mg–Mn: (a) liquidus projection and (b) distribution of phase fields in the solid state.

diagram gives a possibility to make many quantitative estimates, because it has been studied in great detail in Refs. [3, 6, 14, 15, 40]. It is also necessary for analysis of more complex diagrams with the participation of Mg and Si (e.g., Al–Cu–Mg–Si).

The aluminum corner of the Al–Mg–Si phase diagram is presented in Figure 1.28. (Al) can be in equilibrium with Mg_2Si, Al_8Mg_5, and (Si) [14, 15, 40]. The quasi-binary cross-section between (Al) and Mg_2Si corresponds to the concentration ratio Mg:Si = 1.73. This cross-section divides the phase diagram into two simple eutectic diagrams: Al–Mg–Mg_2Si and Al–Si–Mg_2Si. The non-variant phase reactions taking place in this system are presented in Table 1.19.

The solubility of Mg_2Si in aluminum decreases somewhat in the presence of excess amounts of Si, and decreases dramatically when Mg is present in excess of the stoichiometric Mg:Si ratio. The joint solubility of Mg and Si in solid aluminum is presented in Table 1.20 [14].

The Mg_2Si (63.2%Mg, 36.8%Si) compound has cubic lattice (Fm3m, 12 atoms/unit cell) with lattice parameter $a = 0.635–0.640$ nm. Its melting temperature is 1087°C, density 1.88 g/cm^3, Vickers hardness is 4.5 GPa [14]. Microhardness of this compound at room temperature is 5.36 GPa, while

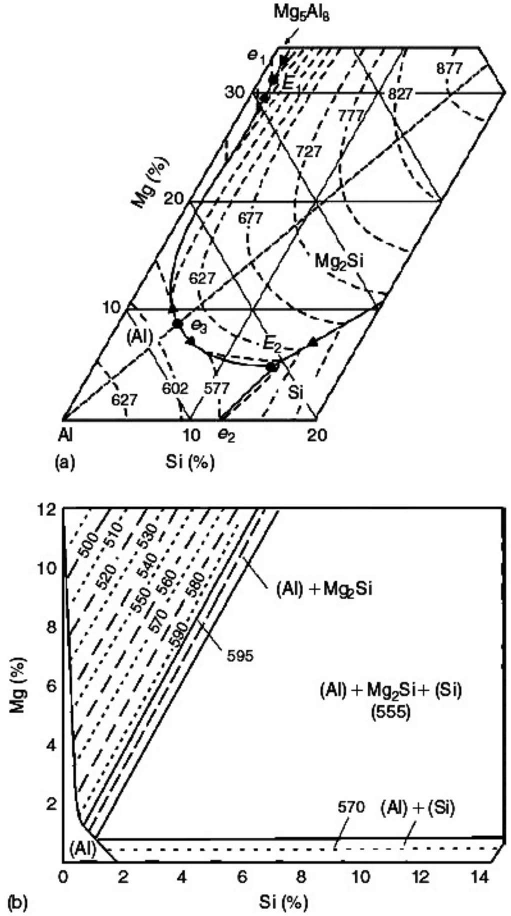

Figure 1.28 Phase diagram Al–Mg–Si: (a) liquidus projection, (b) solidus projection, and (c) aluminum corner.

1-hour microhardness at 300°C is 1.77 GPa. This is an indication of low thermal stability of this phase [10]. The metastable coherent modifications of Mg_2Si (β'- and β''-phases) can be very effective strengthening phases in many heat treatable aluminum alloys.

1.2.23 The Al–Mg–Zn system

This phase diagram is the key for understanding the behavior and properties of a number of industrial aluminum alloys. With some restrictions it could be used

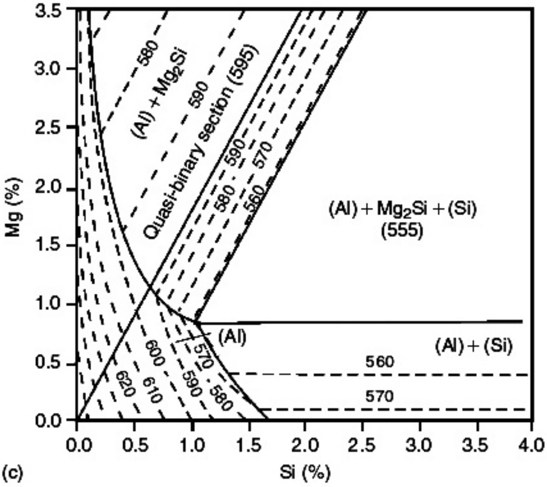

Figure 1.28 (Continued)

Table 1.19 Non-variant phase reactions in the ternary system Al–Mg–Si [14]

Phase reaction	*T* (°C)	Composition of liquid	
		Mg (%)	Si (%)
$L \Rightarrow (Al) + Mg_2Si$ (quasi-binary cross-section)	595	8.15	7.75
$L \Rightarrow (Al) + (Si) + Mg_2Si$	555	4.96	12.95
$L \Rightarrow (Al) + Mg_2Si + Al_8Mg_5$	449	32.2	0.37

for analysis of high-strength Al–Zn–Mg–Cu alloys containing less than 1–2%Cu. Since this phase diagram is quite well understood [14, 40, 50] it could be used for quantitative predictions.

The most probable variant of this phase diagram is presented in Ref. [14], reflecting the absence of a hypothetical AlZn compound. According to Ref. [14], (Al) can be in equilibrium with such phases as Al_8Mg_5, $Al_2Mg_3Zn_3$, $MgZn_2$, Mg_2Al_{11}, and (Zn). Figure 1.29 gives a general view of the Al–Mg–Zn phase diagram, including the liquidus, solidus, and solvus isotherms (in the Al corner). The non-variant reactions with (Al) are given in Table 1.21. Two quasi-binary cross-sections can be considered in the Al–Mg–Zn system: the Al–$Al_2Mg_3Zn_3$ (489°C) and the Al–$MgZn_2$ (475°C). In the latter case, the three-phase non-variant phase

Table 1.20 Joint solubility of magnesium and silicon in solid aluminum at the maximal solubility points [40]

T (°C)	(Al) + Mg_2Si + Al_8Mg_5		(Al) + Mg_2Si		(Al) + (Si) + Mg_2Si	
	Mg (%)	Si (%)	Mg (%)	Si (%)	Mg (%)	Si (%)
595	–	–	1.17	0.68	–	–
577	–	–	1.10	0.63	–	–
552	–	–	1.00	0.57	0.83	1.06
527	–	–	0.83	0.47	0.6	0.8
502	–	–	0.70	0.40	0.5	0.65
452	15.3	0.1	0.48	0.27	0.3	0.45
402	11	<0.01	0.33	0.19	0.22	0.3
302	5	<0.01	0.19	0.11	0.1	0.15

transformation coincides with the four-phase reaction. The solubility of magnesium and zinc in (Al) significantly decrease at lower temperatures (Table 1.22). This results in a significant effect of dispersion hardening related to the precipitation of metastable phases $Al_2Mg_3Zn_3$ (T') and $MgZn_2$(η'').

The Mg_5Al_8 can dissolve up to 10%Zn, but (Zn) dissolves not more than 0.1%Mg. The $MgZn_2$ compound is the prototype of so-called "hexagonal Laves phase". It belongs to the P6$_3$/mmc space group (12 atoms/unit cell) with parameters $a = 0.516$–0.522 nm and $c = 0.849$–0.856 nm. This compound forms continuous solid solutions with the AlCuMg phase of the Al–Cu–Mg system. This phase can also dissolve up to 3%Al. The Mg_2Zn_{11} (6.33%Mg) has cubic lattice (space group Im3 and 39 atoms/unit cell) with lattice parameter $a = 0.855$ nm. Both phases can dissolve not more than 1%Al. Mg_2Zn_{11} and $Al_5Cu_6Mg_2$ can form continuous solid solutions. The chemical composition of the ternary phase varies in the range from 20 to 35%Mg, and from 22 to 65%Zn. This corresponds to chemical formula $Al_2Mg_3Zn_3$ or $(AlZn)_{49}Mg_{32}$. It has cubic lattice (space group Im3 with 162 atoms/unit cell). The lattice parameter "a" varies from 1.429 to 1.471 nm as the concentration of zinc grows. Usually this phase is denoted as T and it is isomorphic to a similar phase from the Al–Cu–Mg system.

1.2.24 The Al–Mn–Ni system

The authors of the present monograph demonstrated (see Section 6) that the Al–Ni–Mn system can serve as the basis for development of a number of

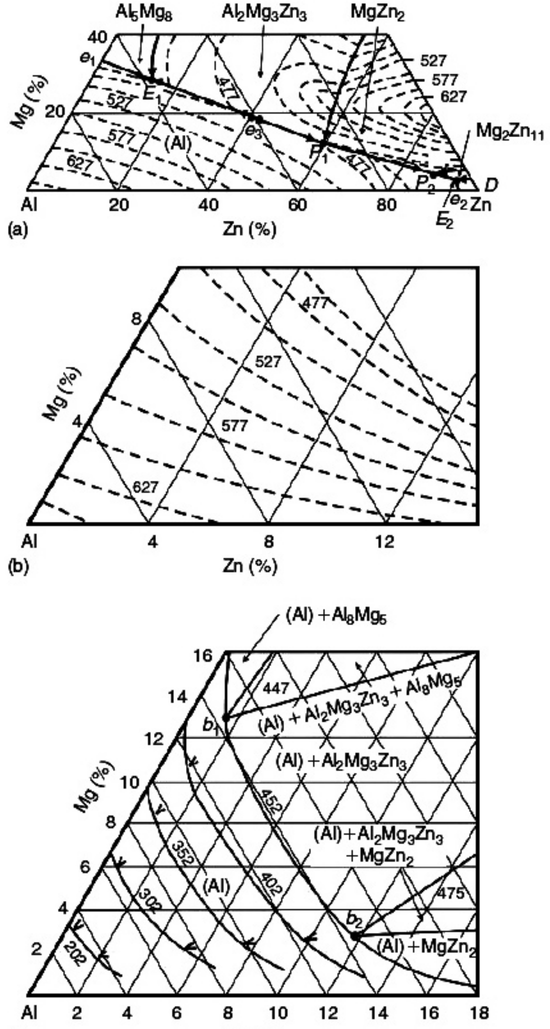
Al$_5$Mg$_8$
Al$_2$Mg$_3$Zn$_3$
MgZn$_2$
40
e_1
E_1
527
577
627
Mg (%)
20
(Al)
477
e_3
P_1
P_2
Mg$_2$Zn$_{11}$
D
e_2
E_2
Al
20
40
60
80
Zn
Zn (%)
(a)
477
527
577
627
8
4
Mg (%)
Al
4
8
12
Zn (%)
(b)
(Al) + Al$_8$Mg$_5$
16
14
12
10
8
6
4
2
Mg (%)
447
b_1
(Al) + Al$_2$Mg$_3$Zn$_3$ + Al$_8$Mg$_5$
(Al) + Al$_2$Mg$_3$Zn$_3$
452
(Al)+Al$_2$Mg$_3$Zn$_3$ +MgZn$_2$
352
402
302
202
(Al)
475
b_2
(Al) + MgZn$_2$
Al
2
4
6
8
10
12
14
16
18
Zn (%)
(c)

Figure 1.29 Phase diagram Al–Mg–Zn: (a) liquidus projection and (b) distribution of phase fields in the solid state.

perspective casting alloys with an interesting combination of properties and excellent castability.

The literature data on the Al–Ni–Mn system is scarce. It follows that (Al) can be in equilibrium with two binary compounds (Al_3Ni and Al_6Mn) and a

Table 1.21 Non-variant phase reactions in ternary alloys of the Al–Mg–Zn system [14]

Phase reaction	T (°C)	Chemical composition, in phases[a] (%)							
		I		II		III		IV	
		Mg	Zn	Mg	Zn	Mg	Zn	Mg	Zn
$L \rightarrow Al + Mg_5Al_8 + Al_2Mg_3Zn_3$	447	30	12	13	2	34	10	30	26
$L \rightarrow Al + Al_2Mg_3Zn_3$	489	18	45	5	12	21	54	–	–
$L \rightarrow Al + MgZn_2$ $L \rightarrow Al + MgZn_2 + Mg_3Zn_3Al_2$	475	11.3	60.4	3	14	16	83	20	64
$L + MgZn_2 \rightarrow Mg_2Zn_{11} + (Al)$	368	3.5	92	15	85	7	92	1	78
$L \rightarrow Mg_2Zn_{11} + (Al) + (Zn)$	343	3	93	1	80	7	92	0.5	99

[a] I–IV: phases participating in reactions.

Table 1.22 Mutual solubility of magnesium and zinc in solid aluminum at the points of maximal solubility [15]

Phase domain	T (°C)	475	460	447	440	400	350	300	200
$Al + Mg_5Al_8$	Mg (%)	–	–	12.5	12.3	10.5	8.4	6.0	2.8
$+ Al_2Mg_3Zn_3$	Zn (%)	–	–	1.8	1.6	1.1	0.6	0.4	0.2
$Al + MgZn_2$	Mg (%)	2.8	2.6	–	2.3	1.7	1.1	0.7	0.2
$Al + MgZn_2$	Zn (%)	14.3	12.5	–	11.4	8.6	6.0	3.7	1.0

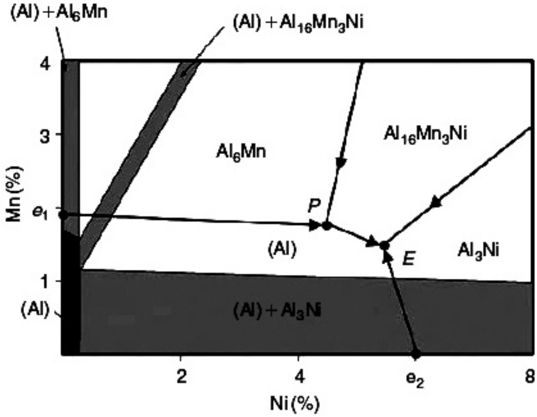

Figure 1.30 Phase diagram Al–Mn–Ni (liquidus projection and distribution of phase fields in the solid state).

ternary compound often described as Mn_3NiAl_{16} [14]. The liquidus surface and isothermal cross-section at 627°C are presented in Figure 1.30. There are two non-variant reactions that can take place in alloys rich in aluminum:

$L + MnAl_6 \rightarrow Al + T$ at 645°C, 1.7%Mn and 4.5%Ni

$L \rightarrow Al + NiAl_3 + T$ at 637°C (eutectic contains 1.3%Mn and 5.3%Ni)

The T-phase contains 23–26%Mn and 5.6–9.5%Ni. The Mn_3NiAl_{16} phase has orthorhombic lattice (space group Bbmm, Bbm2, and Bb2m, ~160 atoms/unit cell) with parameters $a = 2.38$ nm, $b = 1.25$ nm, $c = 0.755$ nm and density $3.62\,\Gamma/\mathrm{cm}^3$. The solubility of nickel in solid aluminum is very low. The solubility of manganese at 627°C decreases in the presence of nickel and comprises 1%Mn in binary alloys and 0.8% in alloys with Ni. The $MnAl_6$ dissolves less than 0.05%Ni. The maximal solubility of manganese in Al_3Ni is 0.26% [14].

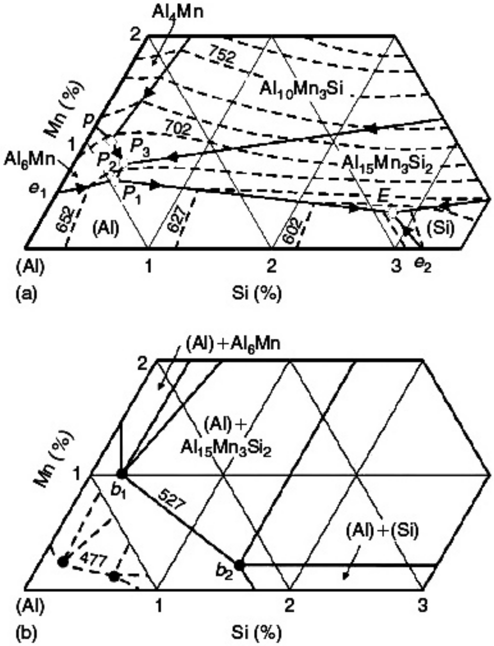

Figure 1.31 Phase diagram Al–Mn–Si: (a) liquidus projection and (b) distribution of phase fields in the solid state.

1.2.25 The Al–Mn–Si system

Al–Si alloys without magnesium, copper, iron, but with the addition of manganese are practically not used. Despite that, the analysis of this ternary diagram is important to understand the behavior of quaternary alloys Al–Fe–Mn–Si as it helps explain the modifying effect of Mn upon the morphology of iron-bearing phases.

The aluminum corner of this phase diagram is rather complex (Figure 1.31). (Al) can be in equilibrium with Al_6Mn, (Si), and ternary phase $Al_{15}Mn_3Si_2$[13–15, 50, 51]. However, in non-equilibrium solidification conditions, Al_4Mn and $Al_{10}Mn_3Si$ can also be formed. The non-variant four-phase reactions in the Al-rich corner of this phase diagram are described in Table 1.23. Mutual solubility of manganese and silicon in (Al) is tabulated in Table 1.24.

The $Al_{15}Mn_3Si_2$ phase (26.3%Mn, 8.9%Si) is also denoted as $Al_{10}Mn_2Si$, $Al_{12}Mn_3Si$, $Al_9Mn_2Si_{1.8}$, or α(MnSi). It exists in the homogeneity range from 25 to 29%Mn and from 8 to 13%Si. This phase has cubic lattice (space group Pm3 with 138 atoms/unit cell) with lattice parameter $a = 1.265$–1.268 nm [14] or 1.260 nm [50]. Its density is 3.55 g/cm^3, microhardness at room temperature is 8.8 GPa, while 1-hour microhardness at 300°C is 4.65 GPa [10]. The solubility

Table 1.23 Non-variant four-phase reactions in the Al–Mn–Si system [15]

Reaction	T (°C)	Composition of liquid	
		Mn (%)	Si (%)
$L + Al_4Mn \Rightarrow Al_6Mn + Al_{10}Mn_3Si$	690	3.4–3.8	0.5–0.7
$L + Al_{10}Mn_3Si \Rightarrow Al_6Mn + Al_{15}Mn_3Si_2$	655–657	2.7–2.8	1.3–1.6
$L + Al_6Mn \Rightarrow (Al) + Al_{15}Mn_3Si_2$	648–649	2.5–2.8	1.5–1.7
$L \Rightarrow (Al) + (Si) + Al_{15}Mn_3Si_2$	573–574	1.0–1.2	≈12

Table 1.24 Maximum solubility of manganese and silicon in aluminum [15]

T (°C)	$(Al) + Al_6Mn + Al_{15}Mn_3Si_2$		$(Al) + (Si) + Al_{15}Mn_3Si_2$	
	Mn (%)	Si (%)	Mn (%)	Si (%)
649	1.3	0.1	–	–
600	0.73	0.09	–	–
573	–	–	0.08	1.66
550	0.44	0.08	0.07	1.36
500	0.25	0.08	0.06	0.85
450	0.15	0.08	0.05	0.45
400	0.06	0.08	0.04	0.25

of silicon in Al_6Mn is insignificant. The solubility of manganese in (AlMnSi) is ~0.7–0.8%.

1.2.26 The Al–Ni–Si system

The Al–Si–Ni system is important for understanding the behavior of more complex four- or five-component alloys.

There are no ternary compounds in this system, and only three phases are present in the solid state: (Al), Al_3Ni, and (Si). Ternary eutectic transformation $L \rightarrow Al + NiAl_3 + (Si)$ takes place at 557°C, 5%Ni, and 11–12%Si. The aluminum corner of the Al–Ni–Si phase diagram is given in Figure 1.32. The solubility of Si in Al_3Ni is approximately 0.4–0.5%; the solubility of nickel in solid aluminum is only 0.04%, corresponding to the melting temperature of the binary eutectic. In the presence of nickel the Si solubility in (Al) decreases [14].

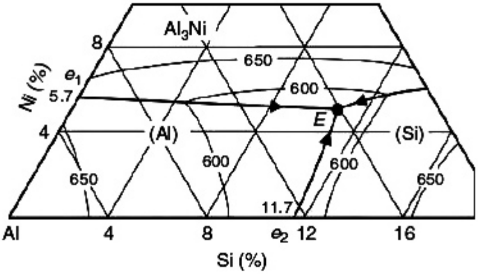

Figure 1.32 Phase diagram Al–Ni–Si (liquidus projection).

1.3 PHASE DIAGRAMS OF FOUR-COMPONENT SYSTEMS

It is not possible to develop a spatial representation for four-component phase diagrams in a way similar to binary and ternary diagrams. One of the ways around this difficulty is the construction of a tetrahedron in the concentration space at constant temperature. To construct a planar projection (representation), different techniques can also be used.

The first method is projecting the aluminum corner of isothermal tetrahedron upon the concentrational basal plane [14]. With this technique, each value of temperature corresponds to one triangular projection. The compositions of binary alloys correspond to the triangle vertices, ternary alloys are located on its sides, and quaternary alloys on the plane inside the triangle. It is important to mention that such technique gives only approximate representation of experimental data on phase equilibria. The concentrations of components are expressed not in absolute values (%), but rather, in the relative amounts of the three components (i.e., ratios). Another conjecture is that the solubility of alloying elements in aluminum is taken equal to zero. Consequently, this method gives a possibility to assess the phase composition of alloys in the Al corner of the phase diagram, only if the concentrations of alloying elements exceed their maximal (limit) solubility in Al-based solid solution.

The second method involves the construction of isothermal cross-sections at constant concentration of a given alloying element, or polythermal cross-sections at constant concentration of the two selected components [52, 53]. This latter technique is more illustrative and yields some semi-quantitative estimates. However, in many cases its use is complicated by the absence of the necessary cross-sections.

Thermodynamic and other computational approaches are the most perspective for obtaining quantitative estimates. However, today only a small number of all relevant multi-component Al-based phase diagrams have been computed using the CALPHAD approach. Mostly these are ternary systems (e.g., Al–Cu–Mg) [42]. At least in part this is related to the lack of reliable thermodynamic parameters. From the practical perspective an approach which is completely based on the

Table 1.25 Composition of Fe-bearing phases in the Al corner in the Al–Be–Fe–Si system [20, 21]

Phase	Notation (see Figure 1.23)	Composition (%)		
		Fe	Si	Be
Al_5FeSi	Al_5	24–28	12–15	–
Al_8Fe_2Si	Al_8	30–33	6–10	–
Al_3Fe	Al_3	37–38	–	–
$Al_4Fe_2Be_5$	Al_4	38–40	<1	~15–22
$AlFeBe_4$	Al_1	~32–42	<0.5	~30–35
$Al_{16}Fe_4Be_3Si_2$	Al_{16}	~25–33	6–10	~4–5

analysis of experimental data and general properties of phase diagrams could be equally attractive. This approach is considered in Refs. [6, 54, 55].

1.3.1 The Al–Be–Fe–Si phase diagram

This phase diagram is important as it helps explain the modifying effect that Be exerts upon Fe-bearing constituent particles in Al–Si casting alloys. There is not much experimental data described in the literature. The most complete studies of the Al corner of the Al–Fe–Be–Si phase diagram (in the concentration range up to 12%Si, 3%Fe, 1.5%Br) were presented in Refs. [20, 21]. The authors of Refs. [20, 21] established the chemical compositions of a number of Fe-bearing phases (see Table 1.25). In addition to the phases described in this table (Al) can be in equilibrium with (Si) and (Be).

In the case of alloys without Be the principal iron-bearing phase is β(AlFeSi). It is of eutectic origin and solidifies in the form of long plates (looking like needles under the microscope). When the concentration of iron is around 3%, constitutive phases will be mostly represented by α(AlFeSi) and Al_3Fe having relatively compact shapes (in alloys with 5%Si) or very large plates of the β(AlFeSi) phase (in alloys containing 8%Si). Small additions of beryllium (0.1–0.2%) will result in the formation of the Fe-bearing phase with “Chinese script” skeletal morphology rather than β(AlFeSi). The assumption about the existence of this fourth Fe-bearing phase called φ was made on the basis of chemical composition studies for particles with typical morphology. Besides, it is hardly feasible that Be could be dissolved in existing Fe-bearing phases in appreciable amounts.

The authors of Ref. [22] note that the Al_8Fe_2BeSi phase forms according to a peritectic phase reaction. However, we believe this is hardly possible because at large Fe concentrations (2–3%) the colonies will be formed consisting of (Al) and this a fourth phase, a clear indication of an eutectic phase reaction.

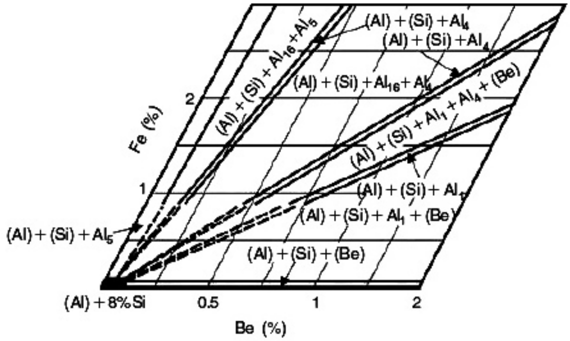
(Al) + (Si) + Al4
(Al) + (Si) + Al4
(Al) + (Si) + Al16 + Al5
(Al) + (Si) + Al16 + Al4
(Al) + (Si) + Al1 + Al4 + (Be)
(Al) + (Si) + Al1
(Al) + (Si) + Al1 + (Be)
(Al) + (Si) + Al5
(Al) + (Si) + (Be)
Fe (%)
2
1
(Al) + 8%Si
0.5
1
2
Be (%)

(a) Al_1–$AlFeBe_4$, Al_3–Al_3Fe, Al_4–$Al_4Fe_2Be_5$

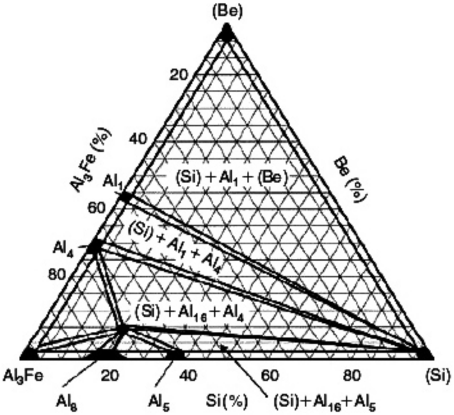
(Be)
20
40
60
80
Al_3Fe (%)
Be (%)
Al_1
Al_4
(Si) + Al1 + (Be)
(Si) + Al1 + Al4
(Si) + Al16 + Al4
Al_3Fe
20
40
60
80
(Si)
Al_8
Al_5
Si(%)
(Si)+Al16+Al5

(b) Al_5–Al_5FeSi, Al_8–Al_8Fe_2Si, Al_{16}–$Al_{16}Fe_4Si_2Be_3$

Figure 1.33 Phase diagram Al–Be–Fe–Si: (a) cross-section at 8%Si and 500 °C and (b) distribution of phase fields in the solid state in the aluminum corner.

The cross-sections of this phase diagram were studied in Ref. [6] at room temperature and Si concentrations of 5–8% (Figure 1.33). The projection of the phase domains of the concentration tetrahedron which are in equilibrium with (Al) on the opposite plane is presented in Figure 1.33b. According to the constructed fragment of this phase diagram, the additions of Be- to Fe-bearing Al–Si alloys will result in sequential replacement of Fe-bearing phases according to the following schematic:

$$\beta(\mathrm{AlFeSi}) \Rightarrow \mathrm{Al}_{16}(\mathrm{AlFeBeSi}) \Rightarrow \mathrm{Al}_4(\mathrm{AlFeBe}) \Rightarrow \mathrm{Al}_1(\mathrm{AlFeBe})$$

Iron will be bound completely into the Al_4(AlFeBe) phase when the ratio Be/Fe is equal to 0.6. If Be/Fe > 0.9, alloy will contain the Be-based saturated solid solutions, or (Be).

Studies of the 7%Si–0.3%Mg–0.64%Fe–0.26%Be alloys [22] confirmed the existence of the 4th phase. According to X-ray spectroscopy data, it has the following chemical composition: 56.4%Al, 9.3%Si, 31.8%Fe, 2.4%Be, which corresponds to stoichiometric compound Al_8Fe_2BeSi. It has orthorhombic lattice with parameters $a = 0.6571$ nm, $b = 0.433$ nm, $c = 1.9236$ nm, and its density is equal to 3.5 g/cm^3.

1.3.2 The Al–Cu–Fe–Mg system

This phase diagram is useful for analysis of the influence of iron impurities upon the phase composition of such alloys as AA206.0 when the concentration of silicon is low. Moreover, without understanding this quaternary phase diagram, it is virtually impossible to understand more complex quinary diagrams (e.g., Al–Cu–Fe–Mg–Si), which is most important for most of the existing casting aluminum alloys.

There are no any quaternary phases in the Al–Fe–Cu–Mg system. (Al) can be in equilibrium with such phases as Al_2Cu, Al_3Fe, Al_8Mg_5, Al_7FeCu_2, Al_2CuMg, and Al_6CuMg_4 [15]. According to Ref. [14], in addition to these phases, a ternary compound $Al_6(FeCu)$ can also be in equilibrium with (Al). The projection of the liquidus surface and the distribution of phase domains in the solid state are presented in Figure 1.34. Possible non-variant five-phase reactions are given in Table 1.26.

All monovariant lines of this phase diagram are close to the Al–Cu–Mg side of the concentration tetrahedron, while the corresponding non-variant reaction points are close to those of the ternary Al–Cu–Mg system (Figure 1.34a).

1.3.3 The Al–Cu–Fe–Mn system

This phase diagram helps analyze the influence of iron impurities upon the phase composition of such alloys as Al-5%Cu at low silicon impurity concentrations. It is also the key for analysis of all important Mn-bearing quinary phase diagrams.

There are no true quaternary phases in the Al corner of the Al–Fe–Cu–Mn phase diagram. However, because the Al_6Mn and $Al_6(FeCu)$ phases are isomorphic, they can form continuous solid solutions denoted as $(AlCu)_6(FeCuMn)$ [14].

Figure 1.35 provides data on the solidification surfaces (a) and distribution of phase domains in solid state (b) in the Al corner of the Al–Fe–Cu–Mn phase diagram.

In addition to the three- and four-phase reactions in this quaternary system, there are also two non-variant five-phase reactions

$$L \Rightarrow (Al) + Al_2Cu + Al_7FeCu_2 + Al_{12}CuMn_2$$

$$(T > 537^\circ C, 31\text{–}33\%Cu,\ <0.5\%Fe,\ <0.5\%Mn,\ \text{see J in Figure 1.35a})$$

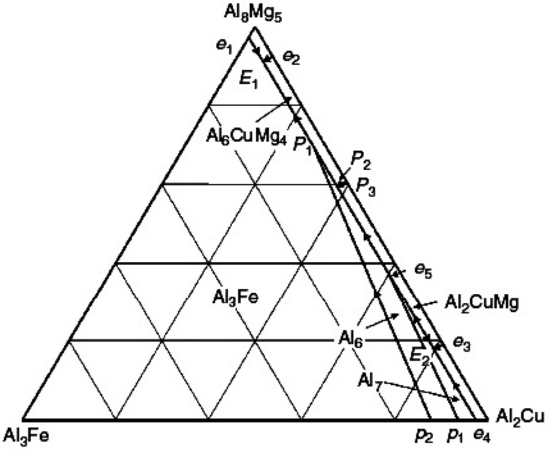
Al_8Mg_5
e_1
e_2
E_1
Al_6CuMg_4
P_1
P_2
P_3
e_5
Al_3Fe
Al_2CuMg
Al_6
e_3
E_2
Al_7
Al_2Cu
Al_3Fe
p_2
p_1
e_4

(a) $Al_6-Al_6(FeCu)$, $Al_7-Al_7FeCu_2$

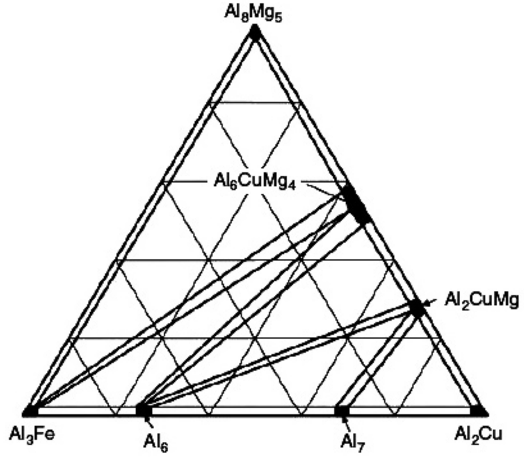
Al_8Mg_5
Al_6CuMg_4
Al_2CuMg
Al_3Fe
Al_6
Al_7
Al_2Cu

(b) $Al_6-Al_6(FeCu)$, $Al_7-Al_7FeCu_2$

Figure 1.34 Phase diagram Al–Cu–Fe–Mg: (a) polythermal diagram and (b) distribution of phase fields in the solid state in the aluminum corner.

$$L + (AlCu)_6(FeCuMn) \Rightarrow (Al) + Al_7FeCu_2 + Al_{12}CuMn_2$$
$$(T < 587^\circ C, 15\text{–}20\%Cu, <1\%Fe, <1\%Mn, \text{see Figure 1.35a})$$

One should also mention that the monovariant line FD (see Figure 1.35a) changes its character from eutectic in point F: ($L \Rightarrow (Al) + Al_3Fe + Al_6Mn$) to

Table 1.26 Non-variant phase reactions in quaternary alloys of the Al–Cu–Fe–Mg system [14, 15]

Phase reaction	Notation in Figure 1.34a	*T* (°C)	Concentration in liquid (%)		
			Cu	Fe	Mg
$L + Al_7FeCu_2 \Rightarrow (Al) + Al_6(FeCu) + Al_2CuMg$	*M*	<587	25	<1	<5
$L + Al_3Fe \Rightarrow (Al) + Al_7FeCu_2 + Al_2CuMg$		510			
$L \Rightarrow (Al) + Al_2Cu + Al_7FeCu_2 + Al_2CuMg$	*L*	500–505	33	0.3	5
$L + Al_2CuMg \Rightarrow (Al) + Al_6(FeCu) + Al_6CuMg_4$	*N*	465	10	<1	20–25
$L + Al_6(FeCu) \Rightarrow (Al) + Al_3Fe + Al_6CuMg_4$	*O*	450	5	<1	25–30
$L \Rightarrow (Al) + Al_3Fe + Al_8Mg_5 + Al_6CuMg_4$	*P*	445	2	0.1	33

peritectic in point *D*: ($L + Al_3Fe \Rightarrow (Al) + Al_6(FeCu)$). The $(AlCu)_6(FeCuMn)$ constituents have chemical composition 7.76%Cu, 0.75%Mn and 1.5%Fe. Its crystalline lattice has the following parameters: $a = 0.7473$ nm, $b = 0.6452$ nm, $c = 0.8794$ nm [14]. These values agree well with the crystalline lattice parameters of the Al_6Mn and $Al_6(FeCu)$ compounds.

1.3.4 The Al–Cu–Fe–Ni system

This phase diagram is useful for analysis of the phase composition of some Ni-bearing industrial alloys (AA203.0, AA242.0). Unfortunately, the experimental data on this system is very scarce.

According to Refs. [14, 15], in the Al–Fe–Cu–Ni system (Al) can be in equilibrium with binary phases and also with Al_7FeCu_2, Al_7Cu_4Ni, Al_9FeNi, $Al_6(FeCu)$, and $Al_3(CuNi)_2$. However, this system is explored only in the domain where (Al) is in equilibrium with Al_2Cu, Al_7FeCu_2, and Al_7Cu_4Ni [15]. At temperature 537°C and 32–33%Cu, <1%Fe, and <1%Ni, the following non-variant eutectic transformation takes place [14]:

$$L \Rightarrow (Al) + Al_2Cu + Al_7FeCu_2 + Al_7Cu_4Ni$$

When the Cu concentration is less than 3%, the solidification surface of the Al–Fe–Cu–Ni system practically coincides with that of the ternary system

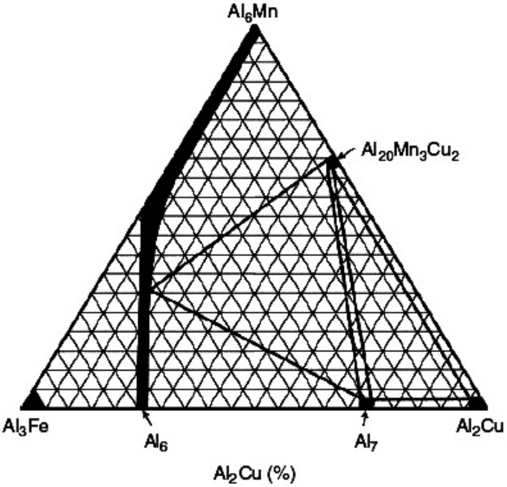
Al6Mn
Al20Mn3Cu2
Al3Fe
Al6
Al7
Al2Cu
Al2Cu (%)

(a) Al_6–Al_6(FeCu), Al_7–Al_7Fe_2Cu

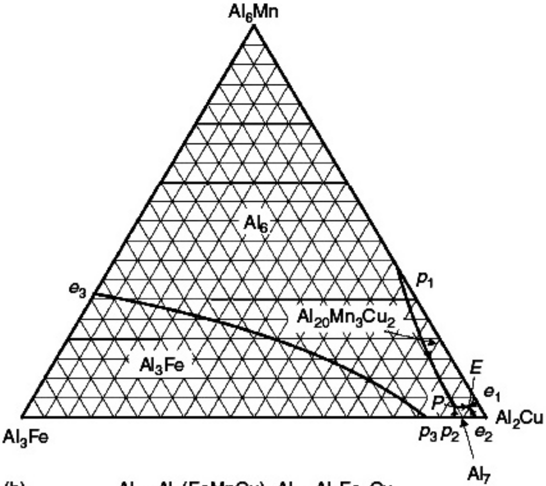
Al6Mn
Al6
p1
e3
Al20Mn3Cu2
Al3Fe
E
e1
P
Al2Cu
Al3Fe
p3 p2
e2
Al7

(b) Al_6–Al_6(FeMnCu), Al_7–Al_7Fe_2Cu

Figure 1.35 Phase diagram Al–Cu–Fe–Mn: (a) polythermal diagram and (b) distribution of phase fields in the solid state in the aluminum corner.

Al–Fe–Ni (Figure 1.25). At higher concentrations of copper the domain of primary solidification of Al_3Fe/Al_9FeNi shifts toward the Al–Cu–Ni side of the concentration tetrahedron. The general tendency is that the Al_9FeNi primary solidification range becomes narrower with the increased Cu content [15].

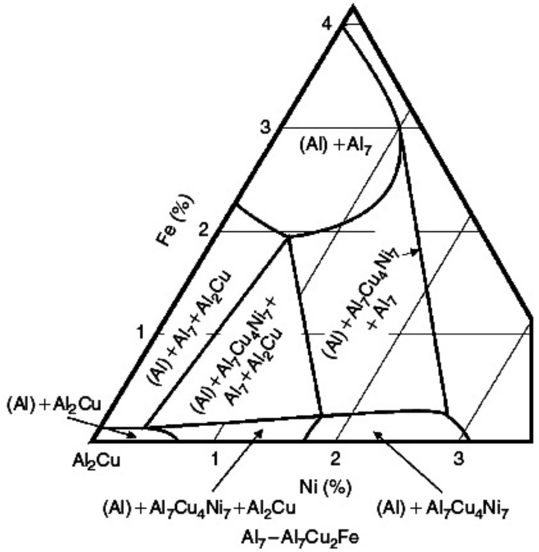

Figure 1.36 Phase diagram Al–Cu–Fe–Ni (distribution of phase fields in the solid state in the aluminum corner at 530°C).

Ni can substitute for up to 6.5–6.8%Fe in the Al_7FeCu_2 phase. The solubility of iron in Al_7Cu_4Ni does not exceed 1% and the solubility of copper in the Al_9FeNi phase does not exceed 2.5%. Some literature data indicates that substantial amounts of iron, up to 4–5%, can be dissolved in $Al_3(CuNi)_2$. Nickel has appreciable solubility in $Al_6(FeCu)$ [14].

Figure 1.36 represents the distribution of phase domains at 530°C in the comparatively well-known part of the Al–Fe–Cu–Ni phase diagram. One needs to note, however, that the diagram variant proposed in Ref. [14] causes some misgivings. First, the Al_2Cu phase should be in equilibrium with Al_9FeNi, which is conformed by the numerous studies of wrought aluminum alloys of the AA2618 type. Secondly, the homogeneity domain of the Al_9FeNi phase on the Al_3Fe–Al_3Ni side of the diagram must be substantially broader.

1.3.5 The Al–Cu–Fe–Si system

This diagram gives an opportunity to correctly analyze the phase composition of Al–Si alloys with Mg when the concentration of Mg is low. Unlike many other quaternary phase diagrams, the Al–Fe–Cu–Si system has been studied in detail, and this helps to make some important quantitative assessments. Alloys of this system do not contain four-component phases. (Al) can be in equilibrium with such phases as Al_2Cu, Al_3Fe, Al_7FeCu_2, $Al_6(FeCu)$, Al_8Fe_2Si, Al_5FeSi, and (Si) [14]. Figure 1.37 represents the distribution of phase domains

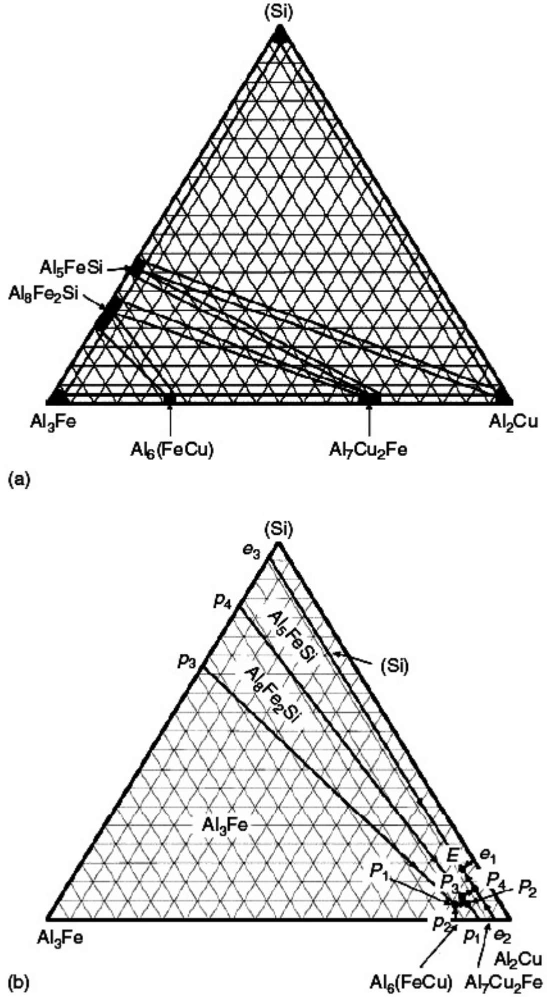
(Si)
Al5FeSi
Al8Fe2Si
Al3Fe
Al6(FeCu)
Al7Cu2Fe
Al2Cu
(a)
(Si)
e3
p4
p3
Al5FeSi
Al8Fe2Si
(Si)
Al3Fe
E
e1
P1
P3
P4
P2
p2
p1
e2
Al3Fe
Al2Cu
Al6(FeCu)
Al7Cu2Fe
(b)

Figure 1.37 Phase diagram Al–Cu–Fe–Si: (a) polythermal diagram and (b) distribution of phase fields in the solid state in the aluminum corner.

in the solid state (a), and also the liquidus surface projection (b). Five-phase nonvariant reactions, which may occur in the Al–Fe–Cu–Si system, are described in Table 1.27 [14].

We believe that the variant of this phase diagram provided in Ref. [14] is the most reliable one. Nevertheless, a different point of view exists [56], according to

Table 1.27 Five-phase non-variant reactions in the Al–Fe–Cu–Si system [14]

Phase reaction	T (°C)	Concentration in liquid (%)		
		Cu	Fe	Si
$L+Al_3Fe \Rightarrow (Al)+Al_6(FeCu)+Al_8Fe_2Si$	612	13.7	1.4	0.65
$L+Al_6(FeCu) \Rightarrow (Al)+Al_8Fe_2Si+Al_7FeCu_2$	607	15.2	1.3	0.7
$L+Al_8Fe_2Si \Rightarrow (Al)+Al_5FeSi+Al_7FeCu_2$	579	16.7	0.8	3.2
$L+Al_7FeCu_2 \Rightarrow (Al)+Al_2Cu+Al_5FeSi$[b] $L+Al_5FeSi \Rightarrow (Al)+(Si)+Al_7FeCu_2$[b]	534	27.5	0.35	4.1
$L \Rightarrow (Al)+(Si)+Al_2Cu+Al_5FeSi$[a] $L \Rightarrow (Al)+(Si)+Al_2Cu+Al_7FeCu_2$[a]	525 520	26.2 26.0	0.4 0.5	5.5 6.5

Note: Both variants of this reaction can be found in the literature. It depends in a complex way on the mutual positions of the quaternary eutectic point[a], five-phase peritectic transformation[b] and also on the nature of phase forming according to the eutectic reaction[a] – Al_5FeSi or Al_7FeCu_2. We believe that the variant presented in Table 1.27 is correct.

which the following non-variant five-phase reactions can take place:

$$L+Al_3FeSi \Rightarrow (Si)+Al_7FeCu_2+Al_8Fe_2Si\ (620°C)$$

$$L+Al_4FeSi_2 \Rightarrow (Si)+Al_2Cu+Al_7FeCu_2\ (567°C)$$

$$L \Rightarrow (Al)+(Si)+Al_2Cu+Al_7FeCu_2\ (520°C)$$

According to Ref. [14], the solubility of copper in (AlFeSi) and of silicon in (AlFeCu) does not exceed 1%. However, according to Ref. [56], the composition of constituent particles formed in alloys Al (0–10%)Fe (25%)Cu (0–11%)Si is a clear indication of substantial solubility of copper in the Al_8Fe_2Si phase. The parameters of the crystalline lattice attain the following values: $a = 1.245$ nm, and $c = 2.459$ nm.

1.3.6 The Al–Cu–Mg–Mn system

Despite the importance of understanding of this system for a large number of commercial aluminum alloys, it is still practically not understood. Some ideas put forward in Ref. [14] related to the position of the liquidus projections (Figure 1.38a) still need to be proven. This is also true with respect to the distribution of phases in the solid state (Figure 1.38b) and the non-variant reactions of solidification (Table 1.28).

1.3.7 The Al–Cu–Mg–Si system

This system is very important for all Cu-bearing Al–Si casting alloys, including the ones that possess the highest strength, AA354.0. This alloy cannot be analyzed

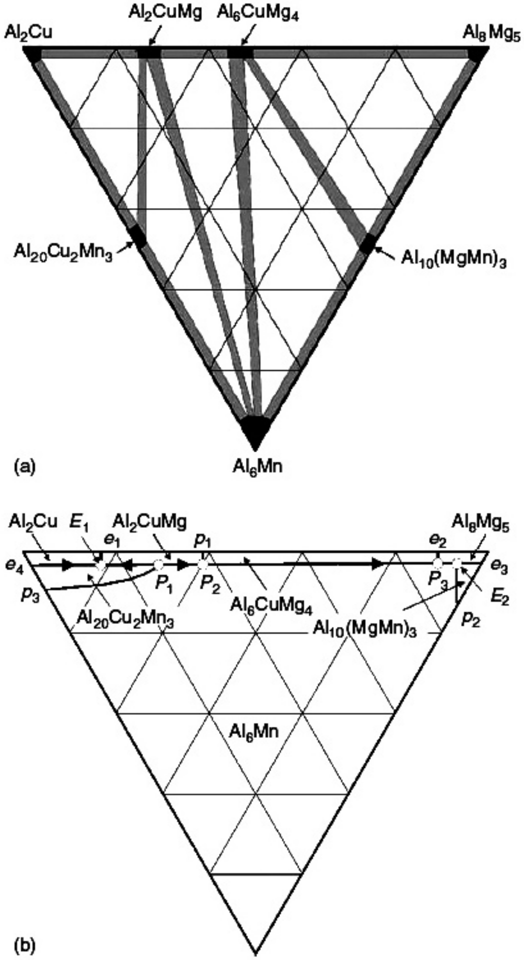
Al2CuMg
Al6CuMg4
Al2Cu
Al8Mg5
Al20Cu2Mn3
Al10(MgMn)3
(a)
Al6Mn
Al2Cu
E1
Al2CuMg
e1
p1
Al8Mg5
e2
e4
e3
p3
P1
P2
P3
E2
Al20Cu2Mn3
Al6CuMg4
Al10(MgMn)3
p2
Al6Mn
(b)

Figure 1.38 Phase diagram Al–Cu–Mg–Mn: (a) polythermal diagram and (b) distribution of phase fields in the solid state in the aluminum corner.

satisfactorily using ternary phase diagrams because of the formation of a quaternary compound $Cu_4Mg_5Si_4Al_x$. It is usually denoted as Q or W. This compound can appear only in alloys with high silicon content.

According to the most reliable variant of the Al–Cu–Mg–Si phase diagram [14] (Figure 1.39) the field of "primary" solidification of the Mg_2Si phase occupies a significant part of the whole concentration domain. The non-variant phase reactions in quaternary alloys of this system with the participation of (Al) are presented

Table 1.28 Non-variant reactions in quaternary alloys of the Al–Cu–Mg–Mn system [14]

Reaction	Concentration in liquid (%)			T (°C)
	Cu	Mg	Mn	
$L \rightarrow Al + CuAl_2 + CuMgAl_2 + Cu_2Mn_3Al_{20}$	–	26.4	0.15	437
$L + Cu_2Mn_3Al_{20} \rightarrow Al + CuMgAl_2 + MnAl_6$	~32	~6	~0.5	>497
$L + Cu_2Mn_3Al_{20} \rightarrow Al + CuMgAl_2 + MnAl_6$	–	–	–	–
$L + CuMgAl_2 \rightarrow Al + CuMg_4Al_6 + MnAl_6$	~10	~25	~0.3	~467
$L \rightarrow Al + CuMg_4Al_6 + (MgMn)_3Al_{10} + Mg_5Al_8$	~2.5	~30	~0.2	~447
$L + MnAl_6 \rightarrow Al + Mg_5Al_8 + (MgMn)_3Al_{10}$	<2.5	<32	<0.2	–

in Table 1.29. Given that Si, Cu, and Mg possess relatively high solubility in (Al) (see Table 1.1) their mutual influence is extremely important for selection of the optimal concentrations of alloying elements and temperatures of heat treatment(s). This influence may be illustrated by the total volume of single-phase domain [15] and the corresponding values of maximal solubility (Table 1.30).

The analysis of "primary" constituents indicates that these crystals contain 14–17%Cu, 28–30%Mg, and 27–29%Si. This chemical composition corresponds to chemical formulae $CuMg_4Si_4Al_4$ and $CuMg_5Si_4Al_4$. Compounds containing 19.2%Cu, 33%Mg, 32.1%Si and 20.6%Cu, 31.8%Mg, 31.4%Si can be adequately described by the formula $Cu_2Mg_8Si_6Al_5$ (20.3%Cu, 31.1%Mg, 27%Si). The fourth phase has hexagonal lattice with parameters $a = 1.032$ nm, $c = 0.405$ nm [14], and density 2.79 g/cm^3 [5].

1.3.8 The Al–Cu–Mg–Zn system

Although this system serves as the key for development of high-strength aluminum alloys (both casting and wrought) it is still studied insufficiently even in the domains corresponding to well-known industrial alloys. Substantial amount of experimental data is described and generalized in Refs. [13–15]. However, the fundamental understanding of the (Al) corner of this diagram, in particular, the liquidus projections and solidification surface are absent. For this reason, Figure 1.40 represents the results obtained by the authors based on many years of joint work upon this subject. Table 1.31 provides the corresponding non-variant phase reactions. One should mention that the latter take place at concentrations, which are quite different from those corresponding to known industrial alloys. For this reason the most valuable information is contained in the isothermal cross-sections described in detail in Ref. [57] and also provided in Figure 1.40.

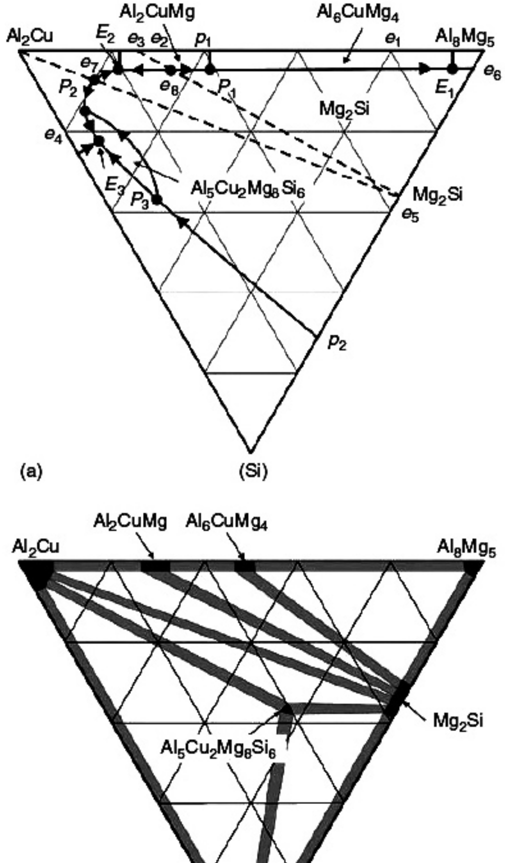
Al2CuMg
Al6CuMg4
Al2Cu
E2
e3
e2
p1
e1
Al8Mg5
e7
e6
P2
e8
P1
E1
Mg2Si
e4
E3
P3
Al5Cu2Mg8Si6
Mg2Si
e5
p2
(a)
(Si)
Al2CuMg
Al6CuMg4
Al2Cu
Al8Mg5
Mg2Si
Al5Cu2Mg8Si6
(b)
(Si)

Figure 1.39 Phase diagram Al–Cu–Mg–Si: (a) polythermal diagram and (b) distribution of phase fields in the solid state in the aluminum corner.

An important peculiarity of this phase diagram is that the three phases of the Al–Mg–Zn system and the three phases of the Al–Cu–Mg system form continuous solid solutions. It is important that in the Al–Cu–Mg system, the CuMgAl and $Cu_6Mg_2Al_7$ compounds are not in equilibrium with (Al) and additions of zinc are required so that these equilibria could take place. There are three domains corresponding to continuous solid solutions formed by the phases $CuMg_4Al_6$ and $Mg_3Zn_3Al_2$, $MgZn_2$ and CuMgAl, and $Cu_6Mg_2Al_5$ and Mg_2Zn_{11}.

Table 1.29 Non-variant reactions in quaternary alloys of the Al–Cu–Mg–Si system [14]

Phase reaction	Content of alloying elements (%)			*T* (°C)
	Cu	Mg	Si	
$L \rightarrow Al + Mg_5Al_8 + Mg_2Si + CuMg_4Al_6$	1.5	32.9–33	0.3	444–448
$L + CuMgAl_2 \rightarrow Al + Mg_2Si + CuMg_4Al_6$	10	25.5	0.3	467
$L \rightarrow Al + Mg_2Si + CuMgAl_2$	23	10.5	0.3	516
$L \rightarrow Al + CuAl_2 + CuMgAl_2 + Mg_2Si$	30–33	6.1–7.1	0.3–0.4	500
$L \rightarrow Al + CuAl_2 + Mg_2Si$	31.5	3.9	2.3	515
$L + Mg_2Si \rightarrow Al + CuAl_2 + Cu_2Mg_8Si_6Al_5$	31	3.3	3.3	512
$L \rightarrow Al + CuAl_2 + Si + Cu_2Mg_8Si_6Al_5$	28	2.2	6	507
$L + Mg_2Si + Si \rightarrow Al + Cu_2Mg_8Si_6Al_5$	13.8	3.3	9.6	529

The $CuMg_4Al_6$ and $Mg_3Zn_3Al_2$ phases in ternary systems exist in a broad range of concentrations. In the quaternary system the phase domain occupied by the quaternary solid solution (the *T*-phase) is also quite broad (Figure 1.40a). The *T*-phase has cubic lattice (space group Im3, 162 atoms/unit cell) with lattice parameter "*a*" that varies from 1.415 to 1.471 nm. The quaternary solid solution between compounds CuMgAl and $MgZn_2$ (the so-called *M*-phase) is characterized by hexagonal structure (space group P6$_2$/mmc, 12 atoms/unit cell) with lattice parameters $a = 0.518$ nm and $c = 0.852$ nm. The solid solution formed by $Cu_6Mg_2Al_5$ and Mg_2Zn_{11} compounds (the *Z*-phase) has cubic lattice (space group Im3, 39 atoms/unit cell) with lattice parameter $a = 0.831–0.855$ nm. The $CuAl_2$ phase practically does not dissolve magnesium and dissolves not more than 2%Zn. The $CuMgAl_2$ phase also has very limited solubility range, and can dissolve less than 1%Zn. In alloys containing 4–8%Zn and 0.5–1.0%Cu, the lattice parameter increases with Mg content in solid solution, reaching values of $a = 0.407–0.408$ nm at 6–7%Mg.

1.3.9 The Al–Fe–Mg–Mn system

This phase diagram is particularly important for understanding the influence of iron impurities on the phase composition of Al–Mg casting alloys with additions of Mn at loss concentrations of Si impurity. Experimental data on this system is

Table 1.30 The maximal solubility of copper, magnesium, and silicon in (Al) for different phase domains at 500°C [15]

Point on Figure 1.39c	Concentration (%)			Boundary of phase domain[a]
	Cu	Mg	Si	
A	–	–	0.80	(Si)
B	–	0.55	0.80	(Si), Mg_2Si, (Si) + Mg_2Si
D	4.00	–	–	Al_2Cu
E	4.00	–	0.80	(Si), Al_2Cu, (Si) + Al_2Cu
F	4.00	0.30	0.77	(Si), Al_2Cu, $Cu_2Mg_8Si_6Al_5$, (Si) + Al_2Cu, (Si) + $Cu_2Mg_8Si_6Al_5$, Al_2Cu + $Cu_2Mg_8Si_6Al_5$, (Si) + Al_2Cu + $Cu_2Mg_8Si_6Al_5$
G	3.85	0.60	0.35	Mg_2Si, Al_2Cu, $Cu_2Mg_8Si_6Al_5$, Mg_2Si + Al_2Cu, Mg_2Si + $Cu_2Mg_8Si_6Al_5$, Al_2Cu + $Cu_2Mg_8Si_6Al_5$, Mg_2Si + Al_2Cu + $Cu_2Mg_8Si_6Al_5$
H	3.70	1.40	0.05	Mg_2Si, Al_2Cu, $CuMgAl_2$, Mg_2Si + Al_2Cu, Mg_2Si + $CuMgAl_2$, Al_2Cu + $CuMgAl_2$, Mg_2Si + Al_2Cu + $CuMgAl_2$
K	3.90	1.50	–	$CuMgAl_2$, Al_2Cu, $CuMgAl_2$ + Al_2Cu
L	1.05	0.40	0.77	Mg_2Si, (Si), $Cu_2Mg_8Si_6Al_5$, Mg_2Si + (Si), Mg_2Si + $Cu_2Mg_8Si_6Al_5$, (Si) + $Cu_2Mg_8Si_6Al_5$, Mg_2Si + (Si) + $Cu_2Mg_8Si_6Al_5$

[a] +(Al)

scarce. According to Refs. [14, 15], quaternary phase are absent in the Al–Fe–Mg–Mn system. (Al) can be in equilibrium with such phases as Al_3Fe, Al_8Mg_5, $Al_6(FeMn)$, and $Al_{10}(MgMn)_3$. Figure 1.41 represents a projection of the Al corner of the Al–Fe–Mg–Mn phase diagram. Two non-variant phase reactions can take place in the domain close to the Al–Mg side of the concentration tetrahedron:

$$L + Al_6(FeMn) \Rightarrow (Al) + Al_3Fe + Al_{10}(MgMn)_3$$

$$L \Rightarrow (Al) + Al_3Fe + Al_8Mg_5 + Al_{10}(MgMn)_3$$

Both transformations occur at temperatures and concentrations that are close to the point of binary eutectic in the Al–Mg system: 450°C and 35%Mg [14]. Chemical composition of crystals precipitating from the quaternary alloy matrix comprised of 10–12%Mg, 14–18%Mn, and less than 1%Fe [14].

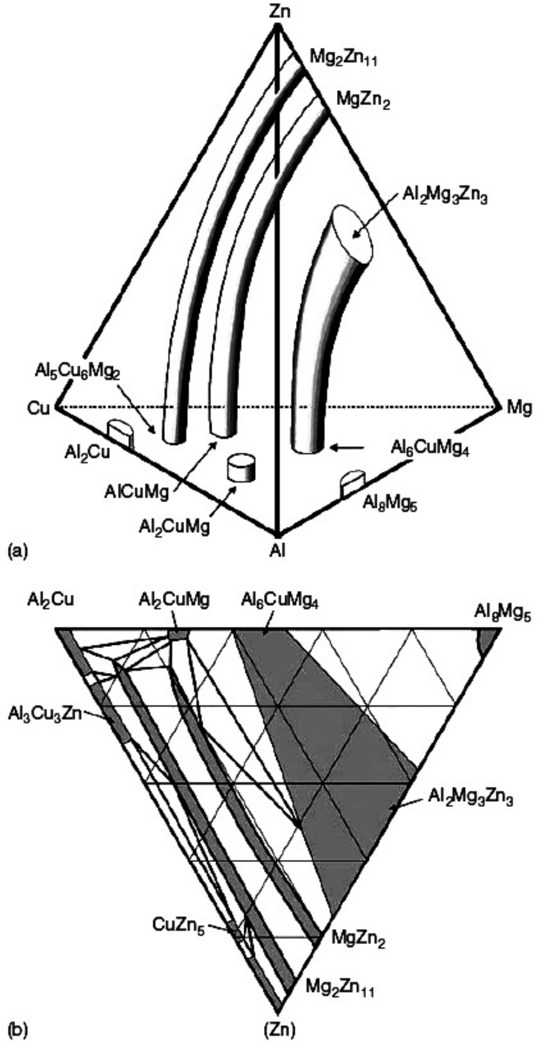
Zn
Mg2Zn11
MgZn2
Al2Mg3Zn3
Al5Cu6Mg2
Cu
Mg
Al2Cu
Al6CuMg4
AlCuMg
Al8Mg5
Al2CuMg
(a)
Al
Al2Cu
Al2CuMg
Al6CuMg4
Al8Mg5
Al3Cu3Zn
Al2Mg3Zn3
CuZn5
MgZn2
Mg2Zn11
(b)
(Zn)

Figure 1.40 Phase diagram Al–Cu–Mg–Zn: (a) polythermal diagram, (b) distribution of phase fields in the solid state in the aluminum corner, and (c) single-phase domains.

1.3.10 The Al–Fe–Mg–Si system

This system is important for many industrial casting alloys, in particular, Al–Si and Al–Mg. This is, first and foremost, related to the existence of quaternary

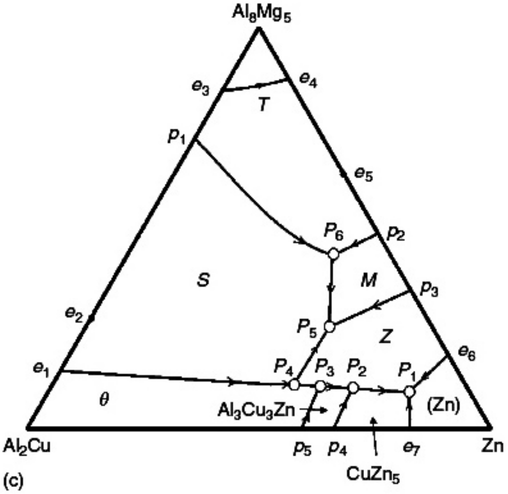

Figure 1.40 (Continued)

Table 1.31 Non-variant reactions in quaternary alloys of the Al–Cu–Mg–Zn system

Point in Figure 1.40a	Phase reaction	Composition of liquid (%)			T (°C)
		Zn	Mg	Cu	
P_1	$L + CuZn_5 \Rightarrow (Al) + (Zn) + Z$	91.1	2.2	3.4	350
P_2	$L + Cu_3ZnAl_3 \Rightarrow (Al) + CuZn_5 + Z$	82.6	2.4	10.1	363
P_3	$L + Al_2Cu \Rightarrow (Al) + Cu_3ZnAl_3 + Z$	77.2	3.0	9.8	377
P_4	$L + Al_2CuMg + Al_2Cu \Rightarrow (Al) + Z$	6.5	6.5	38.9	482
P_5	$L + Al_2CuMg \Rightarrow (Al) + Z + M$	–	–	–	<467
P_6	$L + T \Rightarrow (Al) + Al_2CuMg + M$	–	–	–	<467

compound, which makes analysis of ternary phase diagrams to determine alloy phase composition impossible.

The quaternary compound, often denoted as the π-phase, has narrow homogeneity range around composition corresponding to chemical formula $Al_8FeMg_3Si_6$ (10.9%Fe, 14.1%Mg, 32.9%Si). In addition to this quaternary phase,

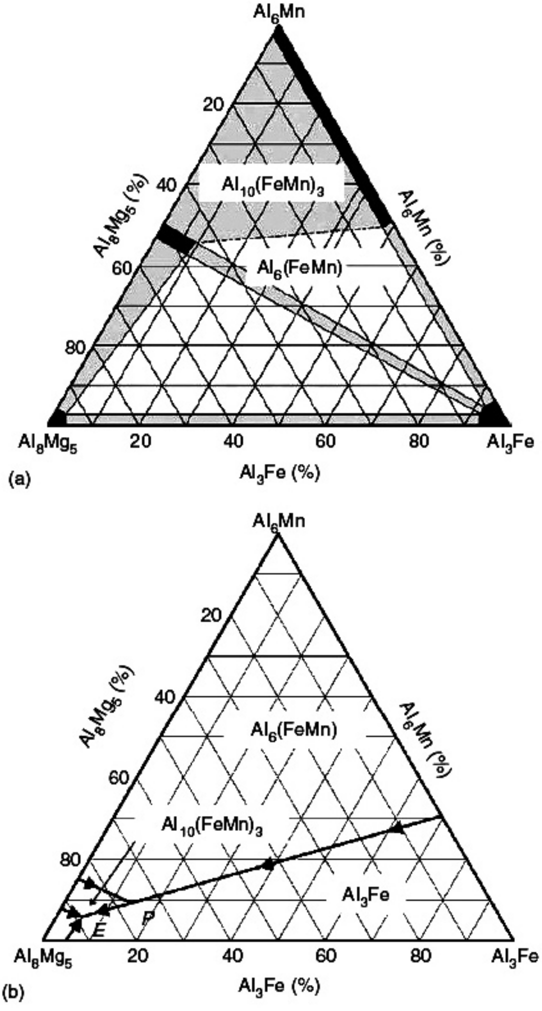
Al6Mn
20
40
60
80
Al10(FeMn)3
Al6(FeMn)
Al8Mg5 (%)
Al6Mn (%)
Al8Mg5
20
40
60
80
Al3Fe
Al3Fe (%)
(a)
Al6Mn
20
40
60
80
Al8Mg5 (%)
Al6Mn (%)
Al6(FeMn)
Al10(FeMn)3
Al3Fe
E
P
Al8Mg5
20
40
60
80
Al3Fe
Al3Fe (%)
(b)

Figure 1.41 Phase diagram Al–Fe–Mg–Mn: (a) polythermal diagram and (b) distribution of phase fields in the solid state in the aluminum corner.

(Al) can be in equilibrium with Al_3Fe, Al_8Mg_5, Mg_2Si, Al_8Fe_2Si, Al_5FeSi, and (Si) [14]. Figure 1.42 illustrates the projection of liquidus surface (a) and the distribution of phase domains in the solid state (b) for alloys of the Al–Fe–Mg–Si system. Non-variant five-phase reactions in this system are documented in Table 1.32 [14]. There is a quasi-binary cross-section (Al)–Mg_2Si in the Al–Mg–Si system. For this reason one can define quasi-ternary cross-section

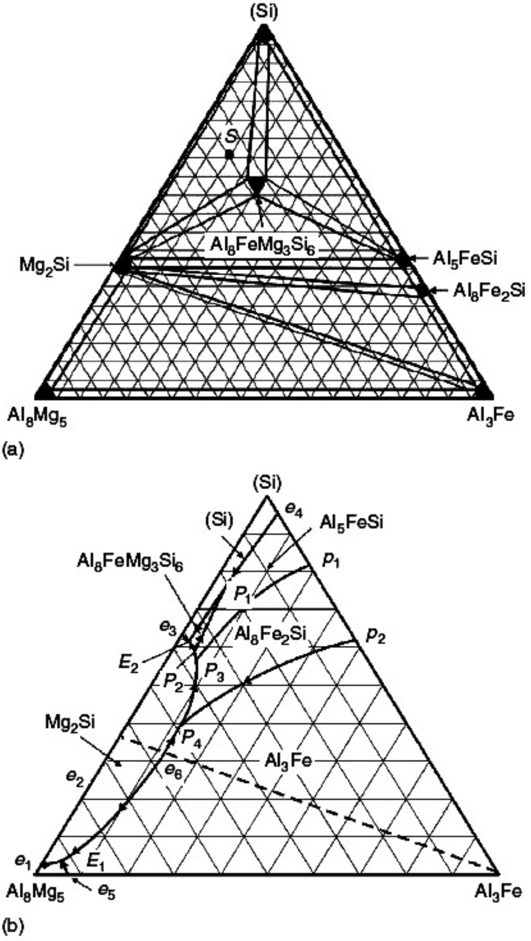
(Si)
S
$Al_8FeMg_3Si_6$
Mg_2Si
Al_5FeSi
Al_8Fe_2Si
Al_8Mg_5
Al_3Fe
(a)
(Si)
e_4
(Si)
Al_5FeSi
$Al_8FeMg_3Si_6$
p_1
P_1
e_3
Al_8Fe_2Si
p_2
E_2
P_3
P_2
Mg_2Si
P_4
Al_3Fe
e_6
e_2
e_1
E_1
Al_8Mg_5
e_5
Al_3Fe
(b)

Figure 1.42 Phase diagram Al–Fe–Mg–Si: (a) polythermal diagram and (b) distribution of phase fields in the solid state in the aluminum corner.

(Al)–Mg_2Si–Al_3Fe, which will divide the Al–Fe–Mg–Si phase diagram into two parts (Figure 1.42).

The $Al_8FeMg_3Si_6$ phase (also denoted as π or *h*(AlFeMgSi)) has hexagonal lattice (space group P62 m, 18 atoms/unit cell) with parameters $a = 0.663$ nm, $c = 0.794$ nm. The density of this phase is 2.82 g/cm^3 [14]. Its microhardness at room temperature is equal to 5.85 GPa, while the 1-hour microhardness at 300°C is 3.76 GPa [10]. This phase has a good level of thermal stability.

Table 1.32 Non-variant five-phase reactions in the Al-corner of the Al–Fe–Mg–Si system

Phase reaction	Symbol[a]	*T* (°C)	Composition of liquid (%)		
			Fe	Mg	Si
$L \Rightarrow \text{(Al)} + Al_3Fe + Mg_2Si$	O	>587	~1.0	~10.0	~7.0
$L + Al_3Fe \Rightarrow \text{(Al)} + Mg_2Si + Al_8Fe_2Si$	N	586	1.35	7.25	7.05
$L + Al_8Fe_2Si \Rightarrow \text{(Al)} + Mg_2Si + Al_5FeSi$	M	576	0.82	6.45	9.50
$L + Al_5FeSi \Rightarrow \text{(Al)} + Mg_2Si + Al_8FeMg_3Si_6$	L	568	0.55	6.0	11.4
$L + Al_5FeSi \Rightarrow \text{(Al)} + \text{(Si)} + Al_8FeMg_3Si_6$	K	567	0.52	2.9	12.15
$L \Rightarrow \text{(Al)} + \text{(Si)} + Mg_2Si + Al_8FeMg_3Si_6$	J	554	0.15	4.9	12.9
$L \Rightarrow \text{(Al)} + Al_3Fe + Al_8Mg_5 + Mg_2Si$	P	448	0.11	33.3	0.35

[a] See Figure 1.42.

It is clear that the solidification field of the quaternary phase is relatively small and is located somewhat apart from the homogeneity domain of this compound in the solid phase. One should also mention that the Mg_2Si phase is in equilibrium with all other phases and can be present in most alloys in the solid state.

In non-equilibrium solidification conditions most of the peritectic reactions will not be completed (i.e., suppressed), and alloys will contain larger number of phases than could be predicted according to the corresponding equilibrium phase diagram.

1.3.11 The Al–Fe–Mn–Si system

This phase diagram is important for understanding the modifying effect of Mn upon the morphology of Fe-bearing particles in 3xx series casting alloys, mostly the Al_5FeSi phase. The general topology of the Al–Fe–Mn–Si phase diagram is still a subject of discussions. The disagreements are mostly around the existence (or absence) of a quaternary phase. An assumption was made early on that the Al_8Fe_2Si and $Al_{15}Mn_3Si_2$ compounds can form continuous solid solutions. However, later it was abandoned because they have different crystalline lattices hexagonal and cubic, respectively.

Today it is accepted that a broad homogeneity range exists on the basis of the $Al_{15}Mn_3Si_2$ compound, which is extended in the direction of the Al–Fe–Si side of

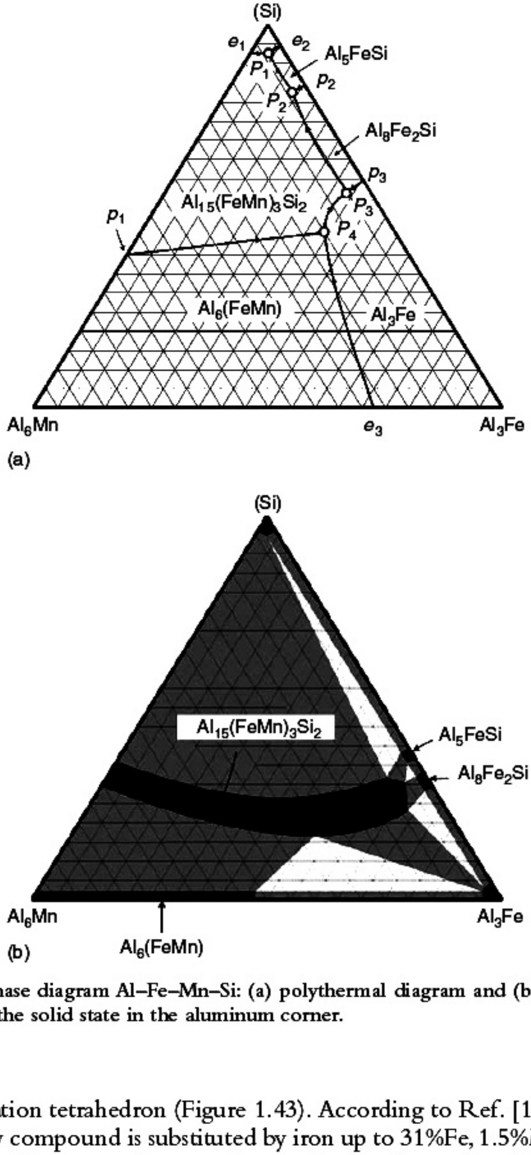
(Si)
e1
e2
Al5FeSi
P1
p2
P2
Al8Fe2Si
p3
Al15(FeMn)3Si2
P3
p1
P4
Al6(FeMn)
Al3Fe
Al6Mn
e3
Al3Fe
(a)
(Si)
Al15(FeMn)3Si2
Al5FeSi
Al8Fe2Si
Al6Mn
Al3Fe
(b)
Al6(FeMn)

Figure 1.43 Phase diagram Al–Fe–Mn–Si: (a) polythermal diagram and (b) distribution of phase fields in the solid state in the aluminum corner.

the concentration tetrahedron (Figure 1.43). According to Ref. [14], manganese in this ternary compound is substituted by iron up to 31%Fe, 1.5%Mn, and 8%Si, while the broad homogeneity range is treated as the formation of the quaternary phase $Al_{15}(FeMn)_3Si_2$. Table 1.33 represents the non-variant phase reactions that can take place in the Al–Fe–Mn–Si system for this distribution of the phase fields and at concentrations up to 12%Si, 1%Fe, 2%Mn [14].

Table 1.33 Non-variant five-phase reactions in the Al–Fe–Mn–Si system [14]

Phase reaction	Symbol[a]	T (°C)	Composition of liquid (%)		
			Si	Fe	Mn
$L + Al_3Fe + Al_6(FeMn) \Rightarrow (Al) + Al_{15}(FeMn)_3Si_2$	J	648	1.75	2.0	0.35
$L + Al_3Fe \Rightarrow (Al) + Al_8Fe_2Si + Al_{15}(FeMn)_3Si_2$	K	627–632	3–5	2–0.5	<0.2
$L + Al_8Fe_2Si \Rightarrow (Al) + Al_5FeSi + Al_{15}(FeMn)_3Si_2$	L	597–607	5–10	1–2	0.1–0.5
$L + Al_5FeSi \Rightarrow (Al) + (Si) + Al_{15}(FeMn)_3Si_2$	M	575	11.7	0.6	0.2

[a] See Figure 1.43.

Table 1.34 Non-variant reactions in the Al–Fe–Mn–Si system

Phase reaction	T (°C)	Composition of liquid (%)		
		Si	Fe	Mn
$L + Al_4FeSi_2 \Rightarrow (Si) + Al_5FeSi + Al_{16}(FeMn)_4Si_3$	596	–	–	–
$L \Rightarrow (Al) + (Si) + Al_{16}(FeMn)_4Si_3$	576	12.4	0.36	0.40
$L \Rightarrow (Al) + (Si) + Al_5FeSi + Al_{16}(FeMn)_4Si_3$	574	12.3	0.65	0.29
$L \Rightarrow (Al) + (Si) + Al_{15}Mn_3Si_2 + Al_{16}(FeMn)_4Si_3$	575	12.4	0.17	0.52

On the other hand, the authors of Refs. [51, 56, 58] claim that in alloys containing 10–14%Si, 0–3%Fe, and 0–4%Mn, another quaternary compound may exist, which has chemical formula $Al_{16}(FeMn)_4Si_3$. In turn, it gives rise to the formation of a quasi-ternary cross-section $Al–Al_{16}(FeMn)_4Si_3–Si$. On both sides of this cross-section two derivative systems can be formed: $Al–Al_{16}(FeMn)_4Si_3–Al_5FeSi–Si$ (adjacent to the Al–Fe–Si side) and $Al–Al_{16}(FeMn)_4Si_3–Al_{12}Mn_3Si_2–Si$ (adjacent to the Al–Mn–Si side). Additionally, one more derivative system could be considered, $Al_5FeSi–Al_4FeSi_2–Al_{16}(FeMn)_4Si_3–Si$, which exists below 596°C.

According to Refs. [51, 56, 58] the following non-variant phase reactions take place in alloys containing 10–14%Si (Table 1.34).

If the Mn to Fe ratio is equal to 1.1, then solidification will be completed at 576°C, and the system will contain in the solid state such phases as (Al),

Table 1.35 Chemical composition of intermediate phases in the Al–Fe–Mn–Si system [58]

Phase	Composition		
	Si (%)	Fe (%)	Mn (%)
Al_5FeSi	12.8–13.3	25.5–26.5	≤ 0.8
Al_4FeSi_2	25.3–26.4	25.9–27.8	≤0.8
$Al_{15}Mn_3Si_2$	10.2–10.7	≤1.8	27.7–29.5
$Al_{16}(FeMn)_4Si_3$	10.4–12.0	10.4–15.3	14.6–19.7

$Al_{16}(FeMn)_4Si_3$, and (Si). For alloys with Mn/Fe < 1.1, solidification will be completed at 575°C, with (Al), $Al_{16}(FeMn)_4Si_3$, $Al_{15}Mn_3Si_2$, and (Si) forming in the solid state.

The data on chemical compositions of intermediate phases that can be formed in the Al–Fe–Mn–Si system is presented in Table 1.35. One should note the insignificant solubility of Mn in (AlFeSi) phase and iron in the (AlMnSi).

According to Ref. [14], solid solution of iron in $Al_{15}Mn_3Si_2$ has cubic lattice with parameter "*a*" decreasing with growing Fe content from 1.265 nm (0%Fe) to 1.25 nm (31.1%Fe). The quaternary phase discovered in Ref. [58] has face-centered cubic lattice with parameter $a = 1.252 \pm 0.04$ nm. The close proximity of the phase lattice parameters discovered in Refs. [14] and [58] does not give a possibility to make unambiguous conclusions about the correct variant of the Al–Fe–Mn–Si phase diagram.

Recently 24 alloys belonging to the Al–Fe–Mn–Si system were studied within the framework of European Research Program Al–Fe–Mn–Si. These alloys were annealed at 550°C for 12 weeks. The results obtained in this study confirmed the phase diagram variant described in Ref. [14], according to which any quaternary compounds are absent, but a broad homogeneity range on the basis of the $Al_{15}(FeMn)_3Si_2$ exists instead (Figure 1.43).

1.3.12 The Al–Fe–Ni–Si system

This diagram is useful for analysis of some commercial Ni-bearing casting alloys, mostly of the 3xx series. The most complete data on the structure of Al corner of this diagram is presented in Refs. [5, 21]. According to these studies, there are no quaternary compounds in the Al–Fe–Ni–Si system. (Al) can be in equilibrium with Al_3Fe, Al_3Ni, Al_9FeNi, Al_8Fe_2Si, Al_5FeSi, and (Si).

On the basis of existing experimental data we propose the most probable variant for the Al corner of this phase diagram (projections of the liquidus surface (Figure 1.44a), diagrams of the distribution of phase domains in the solid state (Figure 1.44b)).

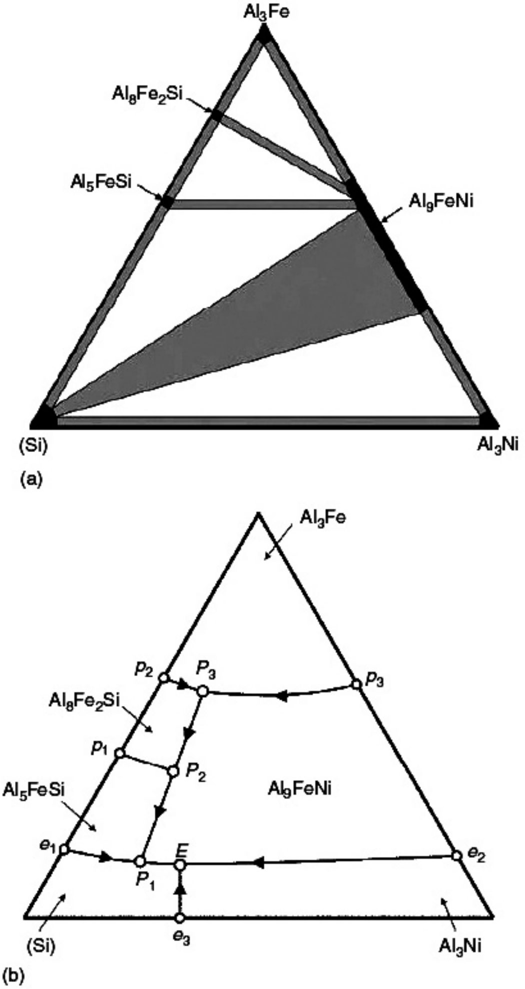
Al_3Fe
Al_8Fe_2Si
Al_5FeSi
Al_9FeNi
(Si)
Al_3Ni
(a)
Al_3Fe
p_2
P_3
p_3
Al_8Fe_2Si
p_1
P_2
Al_5FeSi
Al_9FeNi
e_1
E
e_2
P_1
(Si)
e_3
Al_3Ni
(b)

Figure 1.44 Phase diagram Al–Fe–Ni–Si: (a) polythermal diagram and (b) distribution of phase fields in the solid state in the aluminum corner.

Four non-variant phase reactions can take place in the aluminum corner of the Al–Fe–Ni–Si system: three peritectic reactions (P_1, P_2, P_3) and one eutectic (E). The corresponding temperatures and component concentrations for the liquid phase are provided in Table 1.36.

When the concentration of silicon decreases from 8% to 5%, a substantial broadening of the primary solidification of (Al) takes place up to 1.7%Fe and

Table 1.36 Non-variant phase reactions in the Al–Fe–Ni–Si system

Figurative point[a]	Phase reaction	Concentration in liquid phase (%)			T (°C)
		Fe	Ni	Si	
E	$L \Rightarrow (Al)+(Si)+Al_3Ni+Al_9FeNi$	0.2–0.4	4–5	12–14	562–565
P_1	$L+Al_8Fe_2Si \Rightarrow (Al)+Al_5FeSi+Al_9FeNi$	3–4	1–2	6–8	600–610
P_2	$L+Al_5FeSi \Rightarrow (Al)+(Si)+Al_9FeNi$	0.6–1	2.5–3	13–14	573–576
P_3	$L+Al_3Fe \Rightarrow (Al)+Al_9FeNi+Al_8Fe_2Si$	3–5	1–1.5	4–6	620–628

[a] See Figure 1.44a.

1.7%Ni [21]. When the concentration of silicon is higher than 8%, the crystals of the *β*- or *T*-phases can be found only at relatively low concentrations of Fe and Ni (0.6–0.8%). This may result in detrimental effect of Ni additions for modifying the morphology of the iron-bearing phases.

The solubility of nickel in Al_5FeSi is insignificant (<1%). The solubility of silicon in Al_9FeNi is up to 4%. As the amount of silicon in a given alloy composition grows, the ratio Ni/Fe also has a tendency to increase in the Al_9FeNi phase [21].

1.3.13 The Al–Mg–Mn–Si system

This phase diagram is useful for analysis of the phase composition of Al–Mg casting alloys, which often contain manganese as an alloying addition and silicon as impurity. However, because of the scarcity of available experimental data we believe that the variant of the phase diagram built under the assumption of absence of any quaternary phases provided in Figure 1.45 should be considered the most probable. According to this variant [14], (Al) can be in equilibrium with only binary and ternary phases: (Si), Mg_5Al_8, $MnAl_6$, $(MgMn)_3Al_{10}$, and $Mg_3Si_2Al_{15}$. The non-variant reactions presented in Ref. [14] that also reflect our point of view are provided in Table 1.37.

1.3.14 The Al–Mg–Ni–Si system

This system is studied extensively in the general domain of the Al–Mg_2Si–Si–Al_3Ni tetrahedron. According to Ref. [60], there are no any new phases in this domain compared to binary or ternary systems. This diagram has a very simple

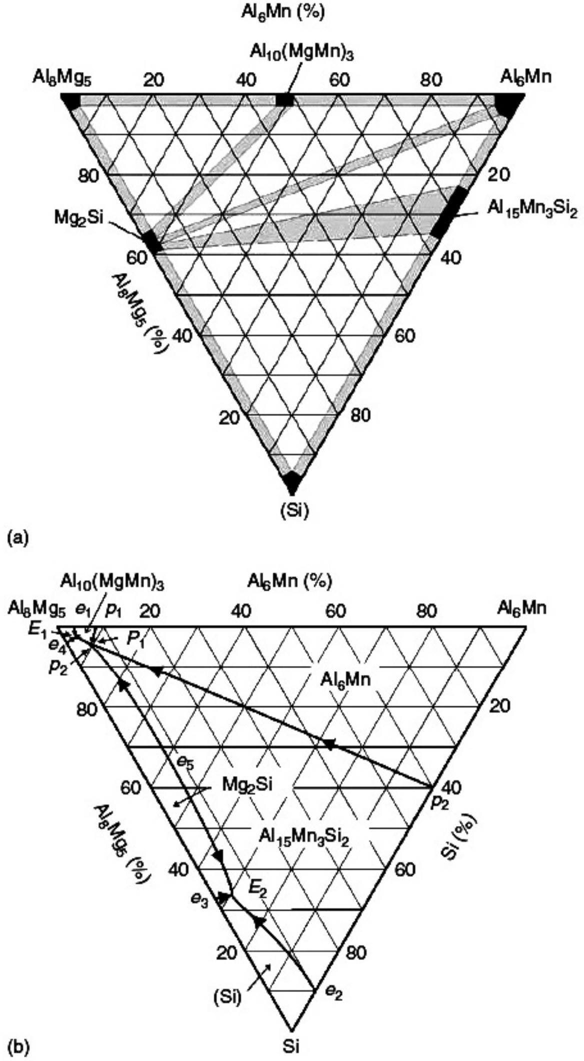
Al$_6$Mn (%)
Al$_{10}$(MgMn)$_3$
Al$_8$Mg$_5$
20
40
60
80
Al$_6$Mn
80
Mg$_2$Si
60
Al$_8$Mg$_5$ (%)
40
20
20
Al$_{15}$Mn$_3$Si$_2$
40
60
80
(Si)
(a)
Al$_{10}$(MgMn)$_3$
Al$_6$Mn (%)
Al$_8$Mg$_5$
e_1
p_1
20
40
60
80
Al$_6$Mn
E_1
P_1
e_4
p_2
Al$_6$Mn
80
20
e_5
60
Mg$_2$Si
40
p_2
Si (%)
Al$_8$Mg$_5$ (%)
Al$_{15}$Mn$_3$Si$_2$
40
E_2
60
e_3
20
80
(Si)
e_2
Si
(b)

Figure 1.45 Phase diagram Al–Mg–Mn–Si: (a) Polythermal diagram and (b) distribution of phase fields in the solid state in the aluminum corner.

structure (Figure 1.46), which makes it convenient for teaching the concept of multi-phase eutectics to students and engineers. Inasmuch as all these phases have practically constant composition, the calculation of their respective mass and volume fractions becomes an easy task.

Table 1.37 Non-variant reactions in the Al–Mg–Mn–Si system [14]

Figurative point (Figure 1.45a)	Phase reactions	Concentration in liquid (%)			
		Mg	Mn	Si	*T* (°C)
J	$L \rightarrow Al + Mg_5Al_8 + (MgMn)_3Al_{10} + Mg_2Si$	~30	~0.1	~0.2	~435
K	$L + Mg_3Si_2Al_{15} \rightarrow Al + MnAl_6 + Mg_2Si$	~30	~0.3	~0.5	<527
L	$L \rightarrow Al + Mg_2Si + Si + Mg_3Si_2Al_{15}$	<5	<1	~12	<557
M	$L + MnAl_6 \rightarrow Al + (MgMn)_3Al_{10} + Mg_3Si_2Al_{15}$	<30	~0.1	<0.2	?

In quaternary alloys two eutectic reactions can take place:

$$L \rightarrow (Al) + Mg_2Si + (Si) + Al_3Ni \text{ at } 550°C, 13\%Si, 3.5\%Mg, \approx 2\%Ni$$

$$L \rightarrow (Al) + Mg_2Si + Al_3Ni(\text{quasi-ternary}) \text{ at } 590°C, 4.8\%Si, 7.4\%Mg, \approx 3\%Ni$$

1.4 FIVE-COMPONENT PHASE DIAGRAMS

The existing experimental data on Al-based five-component phase diagrams are very scarce; this information is mostly related to commercial aluminum alloys. As a rule, it is limited to the discovered phases and speculations about possible non-variant phase reactions. In most cases the identification of such phase reactions is based on one or two experimental papers and has hypothetical character. Since the proposed equilibria in quinary systems often contradict to ternary and quaternary phase diagrams, it was our aim to identify all these contradictions and to come up with a more suitable variant of a corresponding phase diagram. In so doing, we employed an original technique of forecasting and construction of five-component phase diagrams, which was approbated for a number of the most important groups of commercial aluminum alloys [5, 54, 55]. The principal idea of that method is briefly described below.

Many commercial aluminum alloys typically contain some basic elements in such quantities that irrespective of the concentrations of other components, (Al) will be in equilibrium with a certain key phase. For example, in Al–Si casting alloys this phase is (Si), and in Al–Mg alloys Al_8Mg_5. This observation helps simplify all calculations quite substantially using the technique illustrated below for alloys of the 3xx series in which the second basic component, together with aluminum, is silicon.

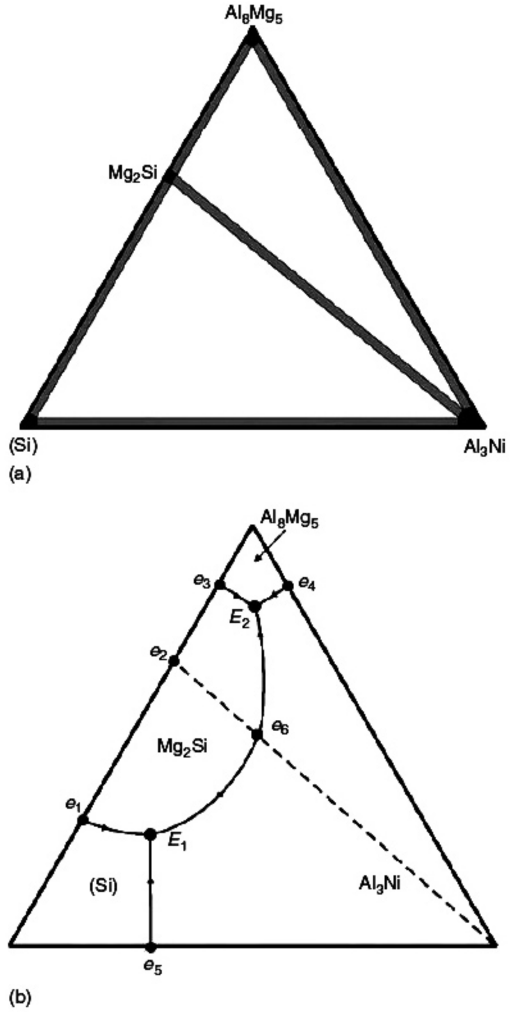
Al_8Mg_5
Mg_2Si
(Si)
Al_3Ni
(a)
Al_8Mg_5
e_3
e_4
E_2
e_2
e_6
Mg_2Si
e_1
E_1
(Si)
Al_3Ni
e_5
(b)

Figure 1.46 Phase diagram Al–Mg–Ni–Si: (a) polythermal diagram and (b) distribution of phase fields in the solid state in the aluminum corner.

The Al–Fe–Cu–Mg–Si system represents the most interesting case because many casting aluminum alloys contain magnesium, copper, and silicon as alloying elements and silicon as impurity (see Appendix 1). These elements, as a function of their concentrations, may enter into the composition of many different phases.

For this reason prediction of a given alloy's phase composition using ternary and/or quaternary phase diagrams is hardly feasible.

Generalizing the available data on 3xx series casting alloys, one can confidently state that all phases discovered therein contain not more than four components. This fact was used in the proposed method of forecasting the five-component phase diagrams, because the absence of five-component phases substantially simplifies their understanding and construction.

It is well known that in quaternary Al-based systems one can conduct qualitative phase analysis on the plane using the concentration triangle for all the alloy components. For this reason it was proposed to generalize this technique to the case of five-component systems, using the most obvious topological analogies. Below we discuss the main features of this approach as applied to the phase composition analysis of five-component alloys using the concentration triangle.

When analyzing phase composition of any 3xx alloy, it is natural to take into account the presence of not only (Al), but also of (Si) (i.e., silicon-based solid solution). This gives a possibility to consider the influence of the remaining three elements using the concentration triangle, since the maximal number of the remaining equilibrium phases is equal to just three. Thus, the constriction of a five-component phase diagram is reduced to its "triangulation", that is, there is a clear analogy with the technique of describing phase domains of quaternary systems (see Section 1.3). The difference, however, is that we have to consider not the projection of the Al corner, but rather of the alloy Al–X%Si, the composition of which lies at the foundation of the concentration triangle with the vertices:

$$\text{Al–X\%Si–Y}_1\text{\%K}_1$$

$$\text{Al–X\%Si–Y}_2\text{\%K}_2$$

$$\text{Al–X\%Si–Y}_3\text{\%K}_3$$

where K_i represent the remaining components of the five-component system under consideration, and Y_i represent their concentrations. In this case the triangle vertices represent the projects of the phase domains (Al)–(Si)–F_i of the corresponding ternary systems Al–Si–K_i, the sides the projection of the (Al)–(Si)–F_i–F_j phase domains of the respective quaternary systems Al–Si–K_i–K_j (F_i, F_j stand for the phases of ternary and quaternary systems that are in equilibrium with (Al) and (Si)). Obviously, the concentrations Y_i for all element ratios must be lower than the values at which (Si) could disappear from the phase composition. In this case the phase boundaries of the concentration triangle will be constant at different amounts of Si. For further analysis, it is necessary to identify the five-phase ("quasi-three-phase") domains. At least partly this could be done *a priori*, using the well-known triangulation rules [53] and partly using experimental data on 3xx casting alloys available from the literature. Only after this preliminary work it does makes sense to plan additional experiments.

To analyze eutectic and peritetic phase reactions in five-component alloys it is proposed to introduce an additional constraint: to consider alloys in which (Al) solidifies first, and then the formation of the (Al) + (Si) eutectic takes place. The

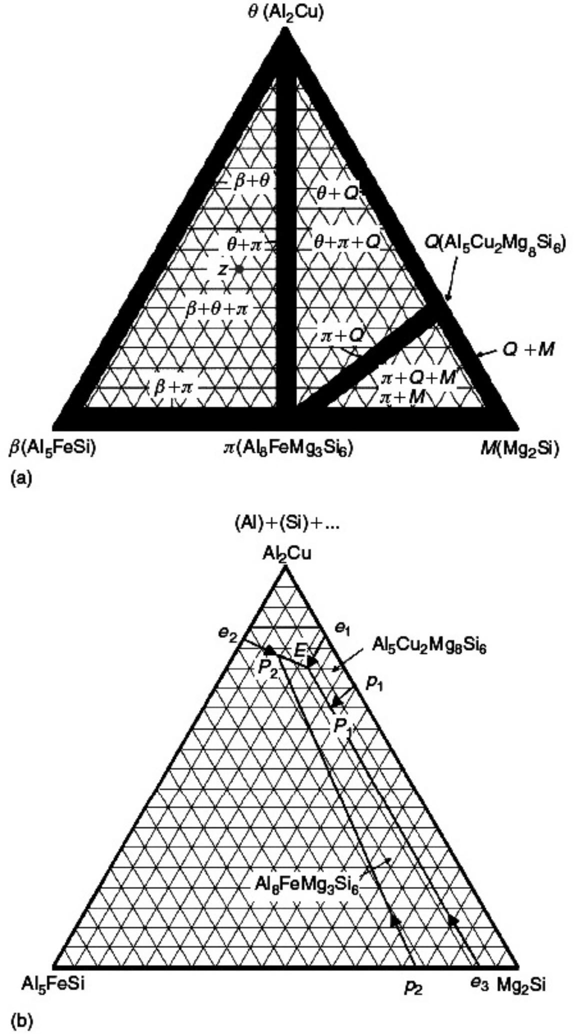
θ (Al2Cu)
β+θ
θ+Q
θ+π
θ+π+Q
Q(Al5Cu2Mg8Si6)
z
β+θ+π
π+Q
Q +M
π+Q+M
β+π
π+M
β(Al5FeSi)
π(Al8FeMg3Si6)
M(Mg2Si)
(a)
(Al)+(Si)+...
Al2Cu
e2
e1
E
Al5Cu2Mg8Si6
P2
p1
P1
Al8FeMg3Si6
Al5FeSi
p2
e3 Mg2Si
(b)

Figure 1.47 Phase diagram Al–Cu–Fe–Mg–Si in the domain of Al–Si alloys: (a) distribution of phase fields in the solid state and (b) polythermal diagram.

idea is clear: with this constraint only four-, five-, and six-phase reactions with mandatory participation of (Al) and (Si) will take place.

It is these reactions that are supposed to be represented on the concentration triangle. When such an approach is adopted, two-dimensional phase fields

Table 1.38 Bivariant reactions in the Al–Fe–Cu–Mg–Si system with participation of Al- and Si-based solid solutions

Phase reaction	Domain in Figure 1.47b
$L \Rightarrow (Al) + (Si) + Al_5FeSi$	$\beta – e_2 – P_2 – p_2 – \beta$
$L \Rightarrow (Al) + (Si) + Al_8FeMg_3Si_6$	$p_2 – P_2 – E – P_1 – e_3 – p_2$
$L \Rightarrow (Al) + (Si) + Mg_2Si$	$M – e_3 – P_1 – p_1 – M$
$L \Rightarrow (Al) + (Si) + Al_5Cu_2Mg_8Si_6$	$P_1 – P_1 – E – e_1 – p_1$
$L \Rightarrow (Al) + (Si) + Al_2Cu$	$\theta – e_1 – E – P_2 – e_2 – \theta$

will correspond to bivariant eutectic reactions of the $L \Rightarrow (Al) + (Si) + F_i$ type; lines will correspond to monovariant tarnsformations, and points to non-variant transformations. This requirement can certainly be satisfied for 3xx series casting alloys containing 9–11%Si and up to 0.6%Fe, that is, below the line connecting the compositions of (Al) and eutectic alloy Al–11%Si–0.8%Fe on the Al–Fe–Si phase diagram (Figure 1.26). In principle, this technique can be applied for analysis of solidification processes of Al–Si alloys with different compositions on the stage when all reactions without (Si) are already considered.

Obviously, this technique can also be applied not only to Al–Si alloys, but also to alloys on the basis of other binary systems, for example, Al–Cu and Al–Mg, in which the basic phases are Al_2Cu and Al_8Mg_5, respectively (their presence is mandatory at all concentration ratios of the remaining three alloying elements). We will consider such systems below.

1.4.1 The Al–Fe–Cu–Mg–Si system

1.4.1.1 Alloys with high content of silicon

In alloys of the Al–Fe–Cu–Mg–Si system that contain high concentrations of silicon, the following phases can be present: (Al), (Si), $\vartheta(Al_2Cu)$, $M(Mg_2Si)$, $\beta(Al_5FeSi)$, $W(Al_5Cu_2Mg_8Si_6)$, and $\pi(Al_8FeMg_3Si_6)$. This is confirmed by the results of structural studies presented in Refs. [5, 54, 55].

On the basis of our method described above, utilizing *a priori* information and experimental data available in the literature, we have constructed the Al–Fe–Cu–Mg–Si phase diagram at 10%Si. Figure 1.47a represents the distribution of phase fields in the solid state, which clearly indicates that the β- and W-phases cannot be in equilibrium. Knowing the distribution of the phase fields one can make an attempt to construct the corresponding isothermal cross-sections, some of which are given in [6]. In particular, analysis of the (Al–10%Si–0.3%Mg)–Fe–Cu cross-section indicates that impurities or ancillary additions of copper and iron may result not only in the formation of the additional phases W, β, π, and ϑ, but also in the disappearance of the M-phase which is the key for Al–Mg–Si alloys.

Table 1.39 Monovariant reactions in the Al–Fe–Cu–Mg–Si system with participation of (Al) and (Si)

Phase reaction	Line in Figure 1.47b
$L + \mathrm{FeSiAl_5} \Rightarrow \mathrm{(Al)} + \mathrm{(Si)} + \mathrm{Al_8FeMg_3Si_6}$	p_2–P_2
$L \Rightarrow \mathrm{(Al)} + \mathrm{(Si)} + \mathrm{Mg_2Si} + \mathrm{Al_8FeMg_3Si_6}$	e_3–P_1
$L + \mathrm{Mg_2Si} \Rightarrow \mathrm{(Al)} + \mathrm{(Si)} + \mathrm{Al_5Cu_2Mg_8Si_6}$	p_1–P_1
$L \Rightarrow \mathrm{(Al)} + \mathrm{(Si)} + \mathrm{Al_2Cu} + \mathrm{Al_5FeSi}$	e_2–P_2
$L \Rightarrow \mathrm{(Al)} + \mathrm{(Si)} + \mathrm{Al_5Cu_2Mg_8Si_6} + \mathrm{Al_8FeMg_3Si_6}$	P_1–E
$L \Rightarrow \mathrm{(Al)} + \mathrm{(Si)} + \mathrm{Al_2Cu} + \mathrm{Al_5Cu_2Mg_8Si_6}$	e_1–E
$L \Rightarrow \mathrm{(Al)} + \mathrm{(Si)} + \mathrm{Al_2Cu} + \mathrm{Al_8FeMg_3Si_6}$	P_2–E

Table 1.40 Non-variant reactions in the Al–Fe–Cu–Mg–Si system with participation of Al- and Si-based solid solutions

Phase reaction	Point in Figure 1.47b	Concentration of components (%)				T (°C)
		Si	Fe	Cu	Mg	
$L \Rightarrow \mathrm{(Al)} + \mathrm{(Si)} + \mathrm{Al_2Cu} + \mathrm{Al_5Cu_2Mg_8Si_6} + \mathrm{Al_8FeMg_3Si_6}$	E	5–6	0.1–0.2	26–28	2–3	503–507
$L + \mathrm{Mg_2Si} \Rightarrow \mathrm{(Al)} + \mathrm{(Si)} + \mathrm{Al_5Cu_2Mg_8Si_6} + \mathrm{Al_8FeMg_3Si_6}$	P_1	7–10	0.1–0.2	14–17	3–6	516–520
$L + \mathrm{Al_5FeSi} \Rightarrow \mathrm{(Al)} + \mathrm{(Si)} + \mathrm{Al_2Cu} + \mathrm{Al_8FeMg_3Si_6}$	P_2	5–6	0.2–0.4	26–28	1–2	550–554

On the contrary, the (Al–10%Si–4%Cu)–Fe–Mg cross-section dictates that the additions of sufficiently large amounts of magnesium and iron to the base alloy ensure that the original ϑ-phase, will be retained.

Since all of the considered phases have narrow homogeneity ranges, one can calculate the relative weight and volume fractions of different phases using the technique described in Refs. [5, 54, 55].

All bi-, mono- and non-variant phase reactions, and also the corresponding lines and points in Figure 1.47b are presented in Tables 1.38–1.40.

One should mention that the proposed variant of this phase diagram differs from that presented in Ref. [14]. The principal difference is that according to Ref. [14], (Al) and (Si) can be in equilibrium with the Al_7FeCu_2 phase, but not Al_5FeSi, and this corresponds to the non-variant phase reaction:

$$L + Al_5FeSi \Rightarrow (Al) + (Si) + Al_7FeCu_2 + Al_5Cu_2Mg_8Si_6$$

As it was argued above, this contradicts to experimental data and the most reliable variant of the quaternary phase diagram Al–Fe–Cu–Si (see Section 1.3.5).

1.4.1.2 Alloys with high content of copper

According to the quaternary phase diagrams Al–Fe–Cu–Si, Al–Fe–Cu–Mg, and Al–Cu–Mg–Si, (Al) and Al_2Cu can be in equilibrium with the following phases: Al_7FeCu_2, Al_2CuMg, Al_5FeSi, Mg_2Si, $Al_5Cu_2Mg_8Si_6$, and (Si). The principal difficulty with the construction of this five-component phase diagram is in the presence of the $Al_8FeMg_3Si_6$ compound, which must be in equilibrium with the four phases described above. The analysis of alloys with high content of silicon indicates that Al_5FeSi and $Al_5Cu_2Mg_8Si_6$cannot be in equilibrium with each other. This gives us a possibility to propose the following variant of phase distribution with the participation of the Al_2Cu phase (Figure 1.48a, Table 1.41).

The triangle vertices (Figure 1.48) correspond to the three-phase domains $(Al) + \theta + Y_i$ and are denoted with phase Y_i from the corresponding ternary system: S(Al_2CuMg), (Si), and N(Al_7FeCu). All ternary alloys, in which (Al) and the θ-phase will be present, correspond to these vertices. The sides characterize phase compositions of quaternary alloys, while all compositions corresponding to five-component alloys will be located inside the triangle. Since these phases have relatively narrow homogeneity ranges, the corresponding domains were marked with points.

There are no other phases on the S–N side, which stems directly from the analysis of the Al–Cu–Mg–Fe phase diagram. At the same time, such phases as $M(Mg_2Si)$, $W(Al_5Cu_2Mg_8Si_6)$, and $\beta(Al_5FeSi)$ will appear on the S–(Si) and (Si)–N sides of the triangle (Figure 1.48). The corresponding points on the triangle sides, as well as the triangle vertices, correspond to three-phase domains. Besides, there will be an additional three-phase domain inside the triangle $(Al) + \theta + \pi$. This is because the quaternary compound $\pi(Al_8FeMg_3Si_6)$ can be in equilibrium with the (Al) and θ-phases (direct conclusion based on analysis of the Al–Cu–Fe–Mg–Si phase diagram, constructed for the Al–Si domain of different alloys) [6].

The location of these phases assumes that several variants of triangulation could be proposed for the five-phase domains $(Al) + \theta + Y_1 + Y_2 + Y_3$, where Y_i stands for phases denoted in the concentration triangle. Figure 1.48 illustrates a case of equilibrium between the M- and N-phases, which results in the decomposition of the whole triangle into two large domains: simple one with the only five-phase $(Al) + \theta + S + N + M$, and complex, which requires additional "triangulation"

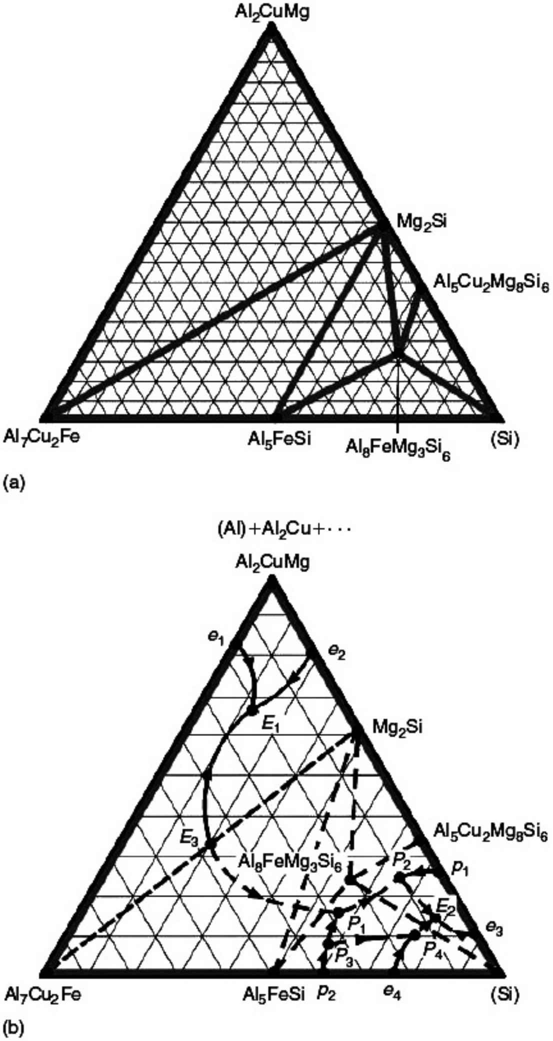
Al$_2$CuMg
Mg$_2$Si
Al$_5$Cu$_2$Mg$_8$Si$_6$
Al$_7$Cu$_2$Fe
Al$_5$FeSi
Al$_8$FeMg$_3$Si$_6$
(Si)
(a)
(Al)+Al$_2$Cu+· · ·
Al$_2$CuMg
e_1
e_2
E_1
Mg$_2$Si
Al$_5$Cu$_2$Mg$_8$Si$_6$
E_3
Al$_8$FeMg$_3$Si$_6$
P_2
p_1
E_2
P_1
e_3
P_4
P_3
Al$_7$Cu$_2$Fe
Al$_5$FeSi
p_2
e_4
(Si)
(b)

Figure 1.48 Phase diagram Al–Cu–Fe–Mg–Si in the Al–Cu alloy domain: (a) distribution of phase fields in the solid state and (b) polythermal diagram.

itself. The Al–Cu–Fe–Mg–Si phase diagram constructed mostly for analyses of 3xx casting alloys shows that $\beta(\mathrm{Al_5FeSi})$ can be in equilibrium with $M(\mathrm{Mg_2Si})$, while its equilibrium with $W(\mathrm{Al_5Cu_2Mg_8Si_6})$ is excluded (Figure 1.47a). This fact helps complete the analysis of this phase diagram in the solid state.

Table 1.41 Non-variant phase reactions of solidification in alloys of the Al–Cu–Fe–Mg–Si system with participation of (Al) and Al_2Cu

Point[a]	Phase reaction	Composition of liquid (%)				
		Cu	Fe	Mg	Si	*T* (°C)
E_1	$L \Rightarrow (Al) + Al_2Cu + Mg_2Si + Al_7FeCu_2 + Al_2CuMg$	≈33	<0.3	≈5	<0.3	≈500
E_2	$L \Rightarrow (Al) + Al_2Cu + (Si) + Al_8FeMg_3Si_6 + Al_5Cu_2Mg_8Si_6$	≈28	<0.2	≈2	≈6	≈505
E_3	$L \Rightarrow (Al) + Al_2Cu + Mg_2Si + Al_7FeCu_2$ (quasi-quaternary)	~23	<0.3	~10	~2	~515
P_1	$L + Al_7FeCu_2 \Rightarrow (Al) + CuAl_2 + Mg_2Si + Al_8FeMg_3Si_6$	–	–	–	–	–
P_3	$L + Al_7FeCu_2 \Rightarrow (Al) + CuAl_2 + Al_5FeSi + Al_8FeMg_3Si_6$	~27	<0.3	<1	~4	~530
P_2	$L + Mg_2Si \Rightarrow (Al) + Al_2Cu + Al_8FeMg_3Si_6 + Al_5Cu_2Mg_8Si_6$	≈30	<0.3	≈3	≈3	≈510
P_4	$L + Al_5FeSi \Rightarrow (Al) + CuAl_2 + (Si) + Al_8FeMg_3Si_6$	~27	<0.3	<2	<5	~520

[a] See Figure 1.48b.

To identify multi-phase eutectic and peritectic reactions we have modeled the solidification sequence for the system under consideration. Our scheme assumes that (Al) solidifies first, followed by the eutectic $L \Rightarrow (Al) + Al_2Cu$. In alloys containing more than 0.1–0.2% Fe, the second stage of solidification might be the formation of eutectics such as:

$$L \Rightarrow (Al) + N(Al_7FeCu) \quad \text{or} \quad L \Rightarrow (Al) + \beta(Al_5FeSi)$$

However, this is not important for analysis of subsequent phase reactions, which are denoted by points, lines, and areas on the concentration triangle.

It was assumed that seven non-variant reactions could take place in the studied phase domain: three eutectic and four peritectic reactions (Table 1.41). Identification of the first eutectic reaction (point E_1 in Figure 1.48b) seems to be the most obvious:

$$L \Rightarrow (Al) + Al_2Cu + Mg_2Si + Al_7FeCu_2 + Al_2CuMg$$

The temperature and liquid composition for this reaction must be close to the corresponding quaternary eutectic reaction in the Al–Cu–Mg–Si system (point e_3 in Figure 1.39 and in Table 1.29). Location of points E_2 and P_4 becomes clear

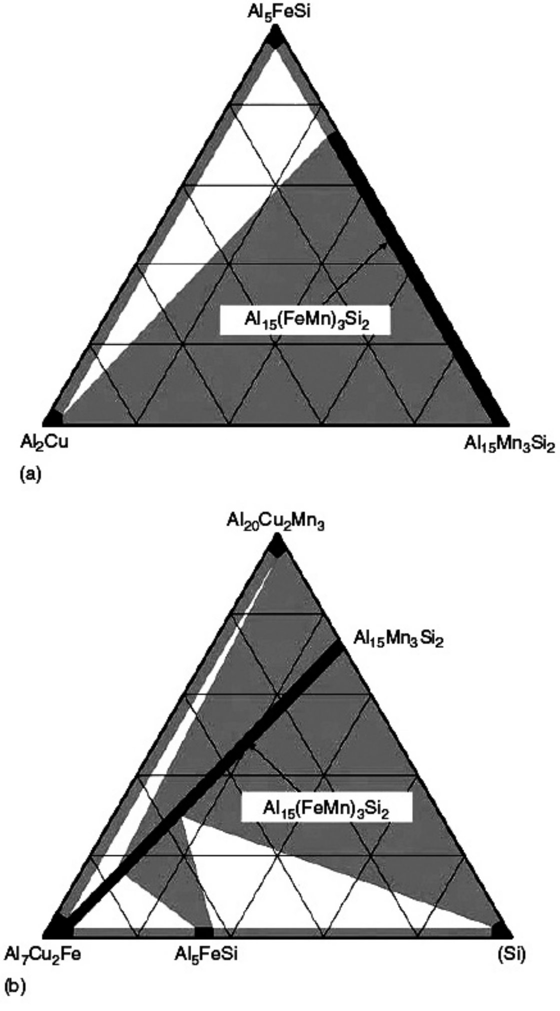
Al5FeSi
Al15(FeMn)3Si2
Al2Cu
Al15Mn3Si2
(a)
Al20Cu2Mn3
Al15Mn3Si2
Al15(FeMn)3Si2
Al7Cu2Fe
Al5FeSi
(Si)
(b)

Figure 1.49 Phase diagram Al–Fe–Cu–Mn–Si (distribution of phase fields in the solid state): (a) in the domain of Al–Si alloys and (b) in the domain of Al–Cu alloys.

from analysis of Figure 1.47b. The point E_3 was placed into the phase diagram under the assumption that there is a quasi-quaternary cross-section in the system (Al)–Al_2Cu–Mg_2Si–Al_7FeCu_2. The location of other figurative points (P_1, P_2, and P_3) is a direct consequence of the proposed variant of "triangulation".

We should mention that our variant is in disagreement with that proposed in Ref. [14]. According to Ref. [14], the following eutectic reaction should take place:

$$L \Rightarrow (\mathrm{Al}) + (\mathrm{Si}) + \mathrm{Al_2Cu} + \mathrm{Al_7FeCu_2} + \mathrm{Al_2CuMg}$$

However, this reaction may become possible only when using dubious experimental data on the quaternary diagram Al–Fe–Cu–Si (Section 1.3.5).

1.4.1.3 Alloys rich in magnesium

According to the quaternary phase diagrams Al–Fe–Cu–Mg (Figure 1.34), Al–Fe–Mg–Si (Figure 1.42), and Al–Cu–Mg–Si (Figure 1.39), (Al) and Al_8Mg_5 can be in equilibrium with only three phases: Al_3Fe, Mg_2Si, and Al_6CuMg_4. This corresponds to the non-variant eutectic $L \Rightarrow (\mathrm{Al}) + \mathrm{Al_8Mg_5} + \mathrm{Al_3Fe} + \mathrm{Mg_2Si} + \mathrm{Al_6CuMg_4}$ and extremely simple distribution of phase domains [6].

1.4.2 Five-component systems with manganese

These five-component systems also represent a considerable practical interest, because manganese enters into chemical composition of many industrial aluminum alloys and forms different phases with Fe, Si, Cu, and Mg (Appendix 1). However, information on these systems is too scarce in order to conduct our analyses discussed above. For this reason we only provide a forecast of the phase composition in the solid state.

1.4.2.1 The Al–Fe–Cu–Mg–Mn system

In quaternary systems Al–Fe–Cu–Mg, Al–Fe–Cu–Mn, and Al–Cu–Mg–Mn, (Al) and Al_2Cu can be in equilibrium with only three phases: Al_7FeCu_2, $Al_{20}Cu_3Mn_2$, and Al_2CuMg. This corresponds to the non-variant eutectic $L \Rightarrow (\mathrm{Al}) + \mathrm{Al_2Cu} + \mathrm{Al_7FeCu_2} + \mathrm{Al_2CuMg} + \mathrm{Al_{20}Cu_3Mn_2}$ and simple distribution of phase domains in the area of Al–Cu alloys of this diagram [6].

According to the quaternary phase diagrams Al–Fe–Cu–Mg, Al–Fe–Mg–Mn, and Al–Cu–Mg–Mn, (Al) and Al_8Mg_5 can be in equilibrium with three phases: Al_3Fe, $Al_{10}(MgMn)_3$, and Al_6CuMg_4. This corresponds to the non-variant reaction $L \Rightarrow (\mathrm{Al}) + \mathrm{Al_3Fe} + \mathrm{Al_8Mg_5} + \mathrm{Al_6CuMg_4} + \mathrm{Al_{10}(MgMn)_3}$ and very simple distribution of the phase domains [6]. One should mention that this reaction is different from the one described in Ref. [14]; according to the authors of Ref. [14], (Al), Al_3Fe, Al_6CuMg_4, and Al_8Mg_5 must be in equilibrium with $Al_6(FeCuMn)$, which solidifies according to the eutectic reaction:

$$L \Rightarrow (\mathrm{Al}) + \mathrm{Al_3Fe} + \mathrm{Al_8Mg_5} + \mathrm{Al_6CuMg_4} + \mathrm{Al_6(FeCuMn)}$$

However, this contradicts to the existing quaternary phase diagram Al–Cu–Mg–Mn (Section 1.36). Following the latter, it is logical to hypothesize that $Al_6(FeCuMn)$ disappears according to the peritectic reaction:

$$L + \mathrm{Al_6(Fe, Cu, Mn)} \Rightarrow (\mathrm{Al}) + \mathrm{Al_3Fe} + \mathrm{Al_{10}(MgMn)_3} + \mathrm{Al_8Mg_5}$$

1.4.2.2 The Al–Fe–Cu–Mn–Si system

According to quaternary phase diagrams Al–Fe–Mn–Si, Al–Fe–Cu–Si, and Al–Cu–Mn–Si, (Al) and (Si) can be in equilibrium with only three phases: Al_2Cu, Al_5FeSi, and $Al_{15}Mn_3Si_2$ corresponding to one of the two non-variant reactions:

$$L + Al_5FeSi \Rightarrow (Al) + (Si) + Al_2Cu + Al_{15}(FeMn)_3Si_2$$

$$L \Rightarrow (Al) + (Si) + Al_2Cu + Al_5FeSi + Al_{15}(FeMn)_3Si_2$$

The distribution of phase domains in the general area of commercial 3xx casting alloys is characterized by a very broad homogeneity range $Al_{15}(FeMn)_3Si_2$ (Figure 1.49a). One should mention that the proposed variant differs from the one discussed in Ref. [14], according to which (Al) and (Si) must be in equilibrium with the Al_7FeCu_2 phase instead of Al_5FeSi, which corresponds to the tentative eutectic:

$$L \Rightarrow (Al) + (Si) + Al_2Cu + Al_7FeCu_2 + Al_{15}(FeMn)_3Si_2$$

In quaternary systems Al–Fe–Cu–Mn, Al–Fe–Cu–Si, and Al–Cu–Mn–Si, (Al) and Al_2Cu can be in equilibrium with the following phases: (Si), Al_7FeCu_2, $Al_{20}Cu_3Mn_2$, Al_5FeSi, and $Al_{15}Mn_3Si_2$, which implies the existence of the following three 6-phase reactions in the domain of the Al–Cu alloys:

$$L \Rightarrow (Al) + Al_2Cu + Al_7FeCu_2 + Al_{20}Cu_2Mn_3 + Al_{15}(FeMn)_3Si_2$$

$$L + Al_7FeCu_2 \Rightarrow (Al) + Al_2Cu + Al_5FeSi + Al_{15}(FeMn)_3Si_2$$

$$L + Al_5FeSi \Rightarrow (Al) + (Si) + Al_2Cu + Al_{15}(FeMn)_3Si_2$$

These non-variant reactions differ from the variant proposed in Ref. [14], where the following phase reaction was proposed:

$$L \Rightarrow (Al) + (Si) + Al_2Cu + Al_7FeCu_2 + Al_{15}(FeMn)_3Si_2$$

We constructed this phase diagram (Figure 1.49b) under the assumption of equilibrium between Al_7FeCu_2 and $Al_{15}(FeMn)_3Si_2$.

1.4.2.3 The Al–Fe–Mg–Mn–Si system

According to quaternary phase diagrams Al–Fe–Mg–Si, Al–Fe–Mn–Si, and Al–Mg–Mn–Si, (Al) and (Si) can be in equilibrium with the following four phases: Mg_2Si, Al_5FeSi, $Al_{15}Mn_3Si_2$, and $Al_8FeMg_3Si_6$. As a result, two 5-phase domains can be identified in the solid state for alloy compositions close to 3xx commercial alloys (Figure 1.50) and two non-variant reactions are proposed:

$$L \Rightarrow (Al) + (Si) + Mg_2Si + Al_{15}(FeMn)_3Si_2 + Al_8FeMg_3Si_6$$

$$L + Al_5FeSi \Rightarrow (Al) + (Si) + Al_{15}(FeMn)_3Si_2 + Al_8FeMg_3Si_6$$

This corresponds well to the results presented in Ref. [14].

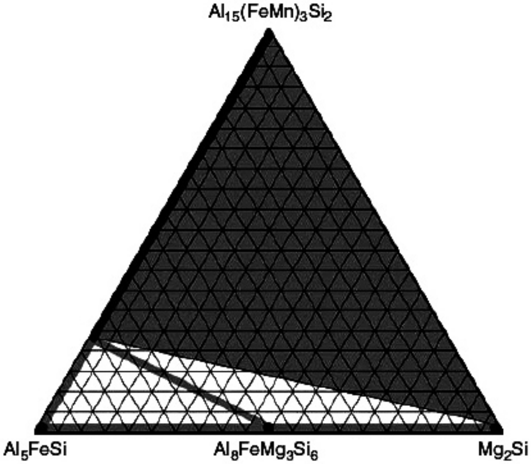

Figure 1.50 Phase diagram Al–Fe–Mg–Mn–Si (distribution of phase fields in the solid state B in the domain of Al–Si alloys).

In alloys of the Al–Fe–Mg–Mn, Al–Fe–Mg–Si, and Al–Mg–Mn–Si systems, (Al) and Al_8Mg_5 may be in equilibrium only with three phases: Al_3Fe, Mg_2Si, and $Al_{10}(MgMn)_3$, which corresponds to non-variant eutectic reaction:

$$L \Rightarrow (\mathrm{Al}) + \mathrm{Al_3Fe} + \mathrm{Mg_2Si} + \mathrm{Al_8Mg_5} + \mathrm{Al_{10}(MgMn)_3}$$

The corresponding distribution of the phase fields is extremely simple [6].

We can conclude that even today our level of knowledge and understanding of multi-component Al-based phase diagrams is still very low. For this reason the analyses of compositions of real aluminum alloys with Fe and Si impurities that often contain more than five elements, one has to construct the phase diagram fragments (both isothermal and polythermal cross-sections), taking into account as much data about simpler phase diagrams as possible.

This page intentionally left blank

CHAPTER TWO

STRUCTURE AND MICROSTRUCTURE OF ALUMINUM ALLOYS IN AS-CAST STATE

2.1 PHASE DIAGRAMS, THERMODYNAMICS, AND ALLOY MICROSTRUCTURE

The concept of "structure" comprises all elements of crystalline and interdendritic ingot features. Usually the term "*macrostructure*" is used for crystalline (grain) structure that can be seen with the unarmed eye if grain size is greater than 0.5 mm. If average grain size falls below this value, one has to apply more sophisticated techniques (e.g., microscopy).

Intergranular structure is usually called "*microstructure*". It is always analyzed with the help of microscopes – optical and electronic. The term "microstructure" is typically used only in those cases when an alloy intergranular structure is studied at optical microscope magnifications not exceeding X-1000–2000. However, if structure is analyzed using electron microscopy with high magnifications that help image dislocations and the products of decomposition of supersaturated solid solution(s), then one should use the term "substructure".

Microstructure is, undoubtedly, one of the most important features of casting aluminum alloys. Their *physical* properties are strongly influenced by the chemical and phase composition. Dislocations and grain boundaries to a significant extent affect, and consequently control, alloys' *mechanical* properties.

Following the classification proposed by Staley,[1] one could describe the relevant metallurgical features and the processing steps leading to their formation as follows: constituent particles (solidification), dispersoids (ingot thermal treatment), grain structure (bulk deformation) and its evolution, dislocations (cold work after quenching), low-temperature clustering reactions, coherent, semi-coherent, and non-coherent precipitates (including Guinier–Preston zones), both metastable and thermodynamically stable (final heat treatment). Additionally there are such features as twins, stacking faults, and different kinds of phase interfaces (both diffuse and sharp).

In Russian scientific literature a somewhat different classification is widely adopted. According to this classification, "primary crystals" are those that are

---

[1] Staley, J.T., Metallurgical aspects affecting strength of heat-treatable alloy products used in the aerospace industry. *Proc. 3rd International Conference on Aluminum Alloys*, 1992, pp. 107–143.

Casting Aluminum Alloys
ISBN-13: 978-0-08-045370-5

© 2007 Elsevier Ltd.
All rights reserved.

formed directly in the course of aluminum alloy solidification (in most cases, crystals of saturated aluminum solid solution) when the temperature is below liquidus. It is important to note that crystals/particles that are formed according to a phase reaction with participation of a liquid phase (e.g., in eutectic or peritectic reactions) *are not called primary anymore*. "Secondary crystals" are formed in the solid state, typically as a result of the decomposition of aluminum solid solution during homogenizing or aging heat treatments. In castings, such crystals may form at any temperature below solidus.

The relationship between these two classifications is quite transparent. "Primary" phases could be associated with "constituent particles", while "secondary" with dispersoids and precipitates. Both classifications will be used extensively in this work.

In Chapter 1, a detailed review of aluminum-based phase diagrams was conducted. Understanding these phase diagrams, both equilibrium and non-equilibrium, is of paramount importance for casting aluminum alloy design and the development of their novel heat treatments. While it is clear that equilibrium (or metastable) phase diagrams could be computed in a self-consistent way using the data on thermodynamic properties of alloys, the relationship between microstructure of alloys, phase diagrams, and thermodynamic properties is considerably less obvious. It is these relationships existing among alloy microstructure (solidification, heat, and deformation treatments), equilibrium and non-equilibrium phase diagrams, and alloy thermodynamic properties that are going to become the next research frontier in developing a much deeper understanding of modern casting alloys.

The underlying mechanisms of solidification microstructure formation can be both kinetically and thermodynamically driven, and thus mathematics – somewhat different in these two cases: in the first case one needs to analyze dissipative nonlinear systems of partial differential equations and to associate symmetry-breaking transitions and spatio-temporal patterning with the corresponding bifurcation points (nonlinear, non-equilibrium thermodynamics); while in the latter case one typically deals with variational problems of minimization of a certain free energy functional, which depends on "order parameters" (the phase-field approach, Section 2.3.1).

This section deals with the phenomenological continuum approach to modeling aluminum alloy systems with microstructure called "phase-field theory".[2] It does not cover the vast area of Gibbsian phenomenological thermodynamics[3]; For example, the development of self-consistent models of phase equilibria and thermodynamic properties of aluminum alloys, although it is clear that such models and databases must be seamlessly integrated into the framework of microstructure calculations.

---

[2] Cahn, J.W., Adapting thermodynamics to materials science problems, *Journal of Phase Equilibria*, vol. 15, No. 4, 1994. pp. 373–379.

[3] Gibbs, J.W., The Collected Works in Two Volumes, Yale University Press, New Haven, 1906.

In Section 2.2, a relationship between thermodynamics, diffusion, phase equilibria, and the problem of microstructure is briefly discussed. Without such an overview it is difficult to understand the principles of the phase-field approach to solidification. Several important examples of microstructure formation and evolution are discussed in Section 2.3, including solidification of pure aluminum, its binary and ternary alloys. Finally, Section 2.4 gives an outlook of possible future work.

2.2 EQUILIBRIUM THERMODYNAMICS AND ITS DEVELOPMENT

2.2.1 Classical equilibrium thermodynamics

The main breakthrough achieved by Gibbs some 130 years ago was the understanding that at equilibrium a system of coexisting phases can always be characterized by some appropriate potential functions that achieve minimum (maximum – for entropy), and the derivation of many powerful laws (e.g., the Phase Rule, the Gibbs–Duhem equation, etc.) that could be applied to understanding the behavior of heterogeneous mixtures.[4] However, neither the classical Gibbsian thermodynamics nor phase diagram research do not pursue the goal of incorporating *microstructure* of heterogeneous systems into its formalism; that is, the spatial distribution of phases and their temporal evolution toward equilibrium. While the theory can predict the concentrations of components and the relative amounts of the competing phases (using the common tangent construction and the Lever Rule) in a heterogeneous mixture at equilibrium, it cannot predict how coexisting phases will be distributed in space. The main reason is that *Gibbsian formalism does not contain intrinsic length scales*, and considers all interfaces as mathematical surfaces that are infinitely thin (or "sharp"). Of course, the classical Gibbsian thermodynamics is internally consistent, it is just that Gibbs purposefully chose not to deal with interfaces of a certain finite width (e.g., in his theory of absorption), neither can it predict their characteristic length scale(s).

---

[4] The importance of the Phase Rule for metallurgy, materials science, mineralogy, physics, and chemistry is very difficult to overestimate, and more than 50 years after the publication of the Gibbs' famous treatise "On the Equilibrium of Heterogeneous Substances", Gibbs 1876–1878, have been dedicated almost completely to this exciting area of materials research. This period was summarized and evaluated in the issue of the Dutch journal "Chemisch Weekblad 1926, published in 1926 which contained the papers of W.P. Jorissen, H. Le Chatelier, W. Ostwald, J.D. Van der Vaals, L. in English, French, German, and Dutch languages. A very good description of the "heroic époque" in metallurgy that followed after this discovery was given by Duhem in his excellent review of Gibbs' scientific heritage (Duhem, P., Josiah Willard Gibbs. A propos de la publication de ses "Memoirs Scientifiques." In: *Bull. Sci. Math.*, 31 1907):

"Van der Vaals and Bakhuis Roozeboom were able to exhume, from the algebraic equations of Gibbs, the Phase Rule. Immediately after that, with extreme activity, Rooseboom started demonstrating in his numerous works, what order this Rule brought to Chemical Statics, in particular, to his own works and to those of Mr. J.-H. Van't Hoff. They found for this Rule new and remarkable applications; around them, the young chemists of the University of Leiden – Stortenbeker, Schreinemakers, guided by the conductor's button that the Rule gave to them – braved the most complicated labyrinths of Chemical Statics. Later on, the same spirit of bravery characterized the atmosphere in the Amsterdam laboratory after Roozeboom had replaced Van't Hoff there; the latter, in his turn, brought the Phase Rule to a triumph in Berlin, with his admirable works on the Stassfurt saline depots (Van't Hoff was able to understand, using the Phase Rule, the mechanisms of formation and decomposition of some double salts in the oceanic salt deposits of the Stassfurt potash basin in Germany, thus having established the scientific foundations of modern mineralogy – M.V.G.). In less than twenty years, the ideas contained in the algebraic equations of the professor from New Haven have dramatically transformed the knowledge that chemists had about alloys and isomorphous mixtures; in its turn, this has revolutionized the theoretic foundations of Metallurgy and Mineralogy" (our translation from French – M.V.G.).

In the asymptotic limit both the sharp interface and the diffuse-interface formalisms coalesce (see below), and that has lead many researchers to believe that there is no any fundamental difference between the two. However, in the models with sharp interfaces it is impossible to observe the nucleation of a new phase, or its complete disappearance (e.g., the Stefan problem in solidification with different front-tracking techniques). Thus, the Gibbsian approach, supplemented with databases on chemical element mobility data, is restricted to studies of systems with sharp interfaces and does not exhibit intrinsic length scales.

In its classical form it is hardly applicable to the description of solids. It is instructive to observe the conceptual difficulties arising when one tries to transfer this formalism developed for fluids to solid systems. Some difficulties arising from consideration of thought experiments with adding atoms to different crystallographic planes of aluminum and other metals were described by Cahn (1994).[2]

These difficulties of adjusting thermodynamics for the description of systems with microstructure resulted in attempts to introduce some modifications into its formalism and culminated in the development of equilibrium thermodynamics of concentrationally non-uniform systems in the fundamental works of Cahn and Hilliard (1958) and Hilliard (1970).[5]

2.2.2 Equilibrium thermodynamics of concentrationally non-uniform systems

Approximately in the mid-1950s Hillert[6] at MIT worked on understanding the thermodynamics and kinetics of nucleation in some metallic systems. He realized that in order to describe the problem adequately, the thermodynamic formalism should incorporate characteristic length scale(s). However, instead of a rigorous continuum approach, Hillert chose to solve systems of coupled difference equations in order to obtain equilibrium interface width – a cumbersome procedure which does not allow one to write out a close-form solution of the problem. As a result, his formalism did not properly reveal the general underlying problem (Cahn and Hilliard, 1958).[5]

Some time later the fundamental papers on equilibrium thermodynamics of concentrationally non-uniform system were published by Cahn and Hilliard.[5]

---

[5] Cahn J.W., and Hilliard, J.E., Free Energy of a Non-uniform System: I. Interfacial free energy, *J. Chem. Phys.*, vol. 28, 1958, p. 258; Cahn J.W., and Hilliard, J.E., Free energy of a Non-uniform system, III. Nucleation in a two-component incompressible fluid. In: *J. Chem. Phys.*, vol. 31, 1959, p. 688; Hilliard, J.E. Spinodal decomposition, Phase Transformations, Chapter 12, American Society for Metals, Metals Park, OH, 1970.

[6] Hillert, M. 1956, A theory of nucleation for solid metallic solutions, D.Sc. Thesis, Massachusetts Institute of Technology, Cambridge, MA.

These workers' main idea was that of a "diffuse interface", that is in order to understand systems with interfaces of some finite width (and all real interfaces are usually diffuse, rather than sharp), it is necessary to employ the concentration gradient (or, more, broadly, the gradient of an order parameter), ∇c, as an *independent variable*. Below a brief derivation of the key expression for free energy functional will be given, which later became the basis of "phase-field" theory.

For concentrationally non-uniform systems the local free energy of a particle should depend not only on concentration itself, but also on its gradient(s). In order to work in the continuum approximation, it is necessary to assume that the composition gradient is small compared to the reciprocal distance between the particles. Following Cahn and Hilliard (1958),[5] one can write down:

$$\begin{aligned} f(c, \nabla c, \nabla^2 c, \ldots) = f_0(c) &+ \sum_i L_i \left(\frac{\partial c}{\partial x_i}\right) + \sum_{i,j} k_{ij}^{(1)} \left(\frac{\partial^2 c}{\partial x_i \partial x_j}\right) \\ &+ \left(\frac{1}{2}\right) \sum_{i,j} k_{ij}^{(2)} \left(\frac{\partial c}{\partial x_i}\right)\left(\frac{\partial c}{\partial x_j}\right) + \cdots \end{aligned} \tag{2.1}$$

For the phenomenological coefficients one gets, Cahn and Hilliard (1958)[5]:

$$\begin{aligned} L_i &= [\partial f/\partial(\partial c/\partial x)]_0 \\ k_{ij}^{(1)} &= [\partial f/\partial(\partial^2 c/\partial x_i \partial x_j)]_0 \\ k_{ij}^{(2)} &= [\partial^2 f/\partial(\partial c/\partial x_i)\partial(\partial c/\partial x_j)]_0 \end{aligned} \tag{2.2}$$

These phenomenological coefficients are components of a polarization vector in a polar crystal (L_i), and tensors reflecting the crystal symmetry ($k_{ij}^{(1)}$ and $k_{ij}^{(2)}$). In the case of a cubic crystal or an isotropic medium there are certain symmetry operations which can be imposed to obtain the correct form of the free energy functional: it must be invariant with respect to the symmetry operations of reflection ($x_i \rightarrow -x_i$) and of rotation around a fourfold axis ($x_i \rightarrow x_j$). As a result of the application of these requirements it becomes possible to write down for a cubic lattice (Cahn and Hilliard)[5]:

$$f(c, \nabla c, \nabla^2 c, \ldots) = f_0(c) + k_1 \nabla^2 c + k_2 (\nabla c)^2 + \cdots \tag{2.3}$$

Integrating over the volume V and using the divergence theorem for the second term of decomposition (2.3), one can get the key expression for the free energy functional of a concentrationally non-homogeneous system:

$$F = N_V \int_V [f_0 + k(\nabla c)^2 + \cdots] \mathrm{d}V \tag{2.4}$$

In equation (2.4), $k = -\mathrm{d}k_1/\mathrm{d}c + k_2 = -[\partial^2 f/\partial c \partial \nabla^2 c]_0 + [\partial^2 f/\partial(\nabla c)^2]_0$. The resulting expression for the free energy (i.e., the free energy functional) in the simplest variant of phase-field approach this expression looks as follows:

$$F[c] = \int_V \{f_0 + k(\nabla c)^2\} \mathrm{d}V \tag{2.5}$$

In equation (2.5) f_0 is the free energy density for a concentrationally *uniform* system. The coefficient "k" is necessary on the dimensional grounds, *and it is via this coefficient that a length scale comes into the constitutive equation(s) naturally.*

This is the key expression because it provides one with an ability to create equilibrium systems with microstructure. Originally, this approach was used to describe microstructure arising as a result of spinodal decomposition. Specifically, the dynamics of spinodal decomposition could be considered within the framework of partial differential equations that describe such gradient systems with the potential function $F[c]$ as a Lyapunov functional. Thus, in a sense, although the problem is dynamical, the final (steady-state) solution will minimize F.

The most impressive demonstration of this statement was the successful modeling of kinetics of spinodal decomposition by Cahn and Hilliard described in detail by Hilliard (1970).[5] For a "traditional" flux problem the potential for diffusion is determined by the derivative $\mathrm{d}f/\mathrm{d}c$; in the case when the free energy of the system is defined, one needs to solve a variational problem of minimization of the functional (2.5) subject to condition that the average composition of the system as a whole remains constant, that is $\int (c - c_0)\mathrm{d}x = 0$. This results in the following modified diffusion equation (Hilliard, 1970)[5]:

$$\frac{\partial c}{\partial t} = -(1/N_V)\frac{\partial J}{\partial x} = (1/N_V)\left[k_1 \cdot f''\left(\frac{\partial^2 c}{\partial x^2} - k_2\frac{\partial^4 c}{\partial x^4}\right)\right] \tag{2.6}$$

If $k_1 f''$ and k_2 are constants, expression (2.6) represents the linearized Cahn–Hilliard equation. Microstructure, or "phase patterning", arises as a result of competition of the second and the fourth gradient terms, and the resulting pattern undoubtedly minimizes the free energy functional (Hilliard, 1970).[5] The only order parameter in this case is concentration, a conserved value. Experimental data indicates that microstructure morphology typical of spinodal decomposition is highly nontrivial, its most important feature being the periodic modulation of composition inside the miscibility gap (Hilliard, 1970).[5]

Summing up, it is useful to outline the main steps in the description of phase microstructures with phase-field approach as given by Chen.[7] Microstructures are described by a set of space- and time-dependent variables ("fields"). These variables are called "order parameters". The latter can be "conserved" and "non-conserved". An example of a conserved order parameter is concentration in the problem of solidification of a two-component alloy. The word "conserved" used in the description of such parameters implies that a conservation law must be obeyed, that is: $\partial c/\partial t = -\nabla J$. The flux J can be determined as a gradient of chemical potential, a variational derivative of the Landau free energy functional.

---

[7] Chen, L.-Q., Phase-Field Models of Microstructure Evolution, *Annual Rev. Mate. Res.*, vol. 32, 2002, p.113.

If a field variable η is not conserved, as in the case of solidification of one- and multicomponent alloys (Chen and Wang, 1996; Boettinger *et al.*, 2002),[8] then its evolution can be described by a relaxation-type time-dependent Ginzburg–Landau equation, sometimes also called the “Allen–Cahn equations”:

$$\frac{\partial \eta}{\partial t} = -L \frac{\delta F}{\delta \eta(r, t)} \tag{2.7}$$

For example, in the case of a two-component heterogeneous system one has to solve a set of equations:

$$\begin{aligned} d\eta_i^{\alpha}(r, t)/dt &= -L_i^{\alpha}(\delta F/\delta \eta_i^{\alpha}(r, t)), \quad i = 1, 2, \ldots, p \\ dC(r, t)/dt &= \nabla\{L_C \nabla[\delta F/\delta c(r, t)]\} \end{aligned} \tag{2.8}$$

In this equations F stands for the Lyapounov functional, α denotes a particular phase, and L is the “relaxation” constant. For a two-component system, the maximum number of coexisting phases is equal to 3. The derivatives in the right-hand side of expressions (2.7) and (2.8) should be understood as “variational”.[9]

2.3 Brief Description of Solidification Microstructure Evolution in Casting Aluminum Alloys via the “Phase-Field” Approach

With the approach outlined above it becomes possible to treat on a common methodological basis different phenomena in materials science systems associated with symmetry-breaking transitions (patterning) and the evolution of emerging microstructure: solidification, spinodal decomposition, martensitic transformations, grain growth, precipitation in the presence of dislocations, etc.

In this work emphasis is made on the applications of phase-field methodology to understanding the evolution of microstructure of solidifying aluminum casting alloys, following the framework outlined in equations (2.8).

---

[8] Chen L.-Q., and Wang, Y., The continuum field approach to modeling micro-structural evolution. In: *J. of Metals*, vol. 48, No. 12, 1996, pp. 13–18; Boettinger, W.J., Warren, J.A., Beckermann C., and Karma, A., Phase-Field Simulation of Solidification, *Annual Rev. Mater. Sci.*, vol. 32, 2002, pp. 163–194. Also see: Lewis, D., Pusztai, T., Gránásy, L., Warren J., and Boettinger, W., Phase-Field Models for Eutectic Solidification, *JOM*, 2004, pp. 34–39

[9] Let us remind the reader the definition of “variational” (or functional) derivative:

$$\frac{\delta F[u]}{\delta u(r_1)} = \lim_{\int \delta u \delta r \to 0} \frac{F[u + \delta u] - F[u]}{\int \delta u(r) dr}$$

where the variation δu is localized in the area of point $r = r_1$.

2.3.1 Phase-field approach applied to solidification

A well-written review on the applications of phase-field models to solidification (including dendritic single-phase, eutectic two-phase solidification, and particle spheroidization upon reheating) was given by Boettinger *et al.*[8] Following this review, for a simple two-component system one needs to introduce just two-order parameters – conserved representing concentration and a non-conserved representing the phase composition of a given alloy at prescribed temperature.

In this case, the equation for the non-conserved order parameter ϕ can be written as follows (Boettinger *et al.*):[8]

$$\frac{\partial \phi}{\partial t} = -M_\phi \left[\frac{\partial f}{\partial \phi} - \varepsilon_\phi^2 \nabla^2 \phi \right] \tag{2.9}$$

For the conserved order parameter, concentration c, we will have an equation of the Cahn–Hilliard type:

$$\frac{\partial c}{\partial t} = \nabla \left[M_c c(1-c) \left(\frac{\partial f}{\partial c} - \varepsilon_c^2 \nabla^2 c \right) \right] \tag{2.10}$$

Solving equations (2.9) and (2.10) using a suitable finite difference or finite element technique, it becomes possible to obtain solutions for the solidification field and resulting microstructure, both for isothermal solidification and rapid quenching. Note that expression in square brackets in equation (2.9) stands for the variational derivative of the free energy with respect to the non-conserved order parameter, $\delta F/\delta\phi$, in agreement with equation (2.10). Coefficient M_ϕ plays the role of L in equation (2.7); it represents the relaxation parameter necessary for the description of the interface kinetics; while $f = f(c, T, \phi)$ stands for the free energy density.

Equation (2.10) is equivalent in its structure to equation (2.6), originally used for the description of spinodal decomposition in a binary system. As before, $\frac{\delta F}{\delta c}$ stands for the variational derivative of the free energy with respect to time- and coordinate-dependent concentration $\frac{\delta F}{\delta c} = \frac{\partial f}{\partial c} - \varepsilon_c^2 \nabla^2 c$. M_c represents the solute diffusion coefficient and f stands for the free energy density. Below several important examples are discussed.

2.3.2 Dendritic solidification of pure metals

In design of casting aluminum alloys researchers have to deal with multi-component alloys, in many cases with eutectic microstructure that is required for good castability. However, from the methodological standpoint it is more convenient to begin with a one-component system.

Figure 2.1 illustrates growth of dendrites from a pure one-component molten state.[8] These results were obtained for the low supercooling conditions. Today, such calculations were conducted, for example for pure nickel, Hoyt *et al.*

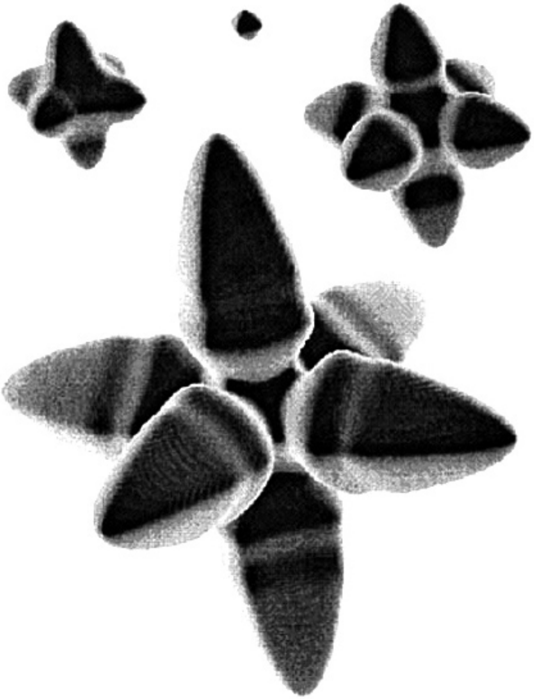

Figure 2.1 3D Phase-field modeling of dendritic solidification, after Boettinger *et al.*[8] (see text).

(1999),[10] and also for rapid solidification of pure aluminum melt containing just 0.02 at.% Cu (Kim *et al.*, 2003).[10] The effects of convection and 3D simulations of free dendritic solidification with fluid flow are also underway. In particular, it was demonstrated that the addition of fluid flow may result in significant distortion of the crystal shape and elimination of the symmetries pertaining to the solidification of free dendrites (Lu *et al.* unpublished research, cited after).[8] For the most recent update on the general field of phase-field modeling, the interested reader is referred to the recent monographs by Emmerich and Nastac.[10]

---

[10] Hoyt, J.J., Sadigh, B., Asta, M., and Foiles, S.M., *Acta Mater*, vol. 47, 1999, pp. 3181–3187. For solidification of pure Al, see Kim, S.G.; Kim, W.T.; Suzuki, T., Phase-field modeling of rapid solidification in small alloy droplets, *ISIJ International*, vol. 43, no. 11, 2003, pp. 1758–1766. Lewis, D., Pusztai, T., Gránásy, L., Warren, J., and Boettinger, W., Phase-Field Models for Eutectic Solidification, *JOM*, 2004, pp. 34–39. Recent monographs on phase-field approach to solidification include: Emmerich, H., The Diffuse Interface Approach in Materials Science: Thermodynamic Concepts and Applications of Phase-Field Models (Lecture Notes in Physics), Springer (2003); Nastac, L., Modeling and Simulation of Microstructure Evolution in Solidifying Alloys, Kluwer Academic Publishers, 2004.

2.3.3 Phase-field model for solidification of eutectic alloys[11]

This model was proposed by Wheeler *et al.*[11]. The principal complication in this case, compared to pure metals, is that solidification of a eutectic alloy from the melt or liquid phase produces two solid phases, rather than one. As it was discussed above (see Section 2.2.1) the morphology of the resulting two-phase system could be quite different. Since many casting aluminum alloys possess eutectic microstructure (e.g., AL–Si, Al–Mg, etc.), it is important to understand the relationship between thermodynamics, phase diagrams, and processing conditions as they will all affect the emerging microstructure and its morphology.

Phase-field approaches for the solidification of pure one-component materials were developed in the early 1980s. However, models for the solidification of two-component systems having simple phase diagrams were developed only in the last 10 years by Wheeler and other researchers.[10,11] Typically, such models feature a free energy that depends on the solute concentration in addition to the temperature and the phase field. It is very important to emphasize that the corresponding free energy functional is constructed in such a way that the appropriate phase diagrams for the system are recovered. In the case of eutectic solidification the most general model includes two non-conserved order parameters, rather than a single one. The first one, often denoted as ϕ, is used to indicate whether the system is in a solid or in a liquid phase, while the other order parameter, ψ, and indicates which of the two possible solid phases is present. With this free energy it is possible to recover the appropriate eutectic phase diagram.

The resulting phase-field model, Wheeler,[11] was used to study the formation of tri-junctions in which both solid phases are in equilibrium with the liquid phase. The angles formed by the interphase boundaries should meet must satisfy Young's law. An example is shown in Figure 2.2 (I)[11] (temperature gradient was imposed in the vertical direction). The top figure shows the tri-junction region, consisting of the liquid phase above the two solid phases, α and β. Contour lines are shown for the solute field. The middle figure shows contour lines for the phase field ϕ, which defines the solid–solid interface. The lower figure shows contour lines for the phase field ϕ, which determines the solid–liquid interfaces.[11] Another example of eutectic solidification was discussed by Boettinger *et al.*,[8] the results of 3D-phase-field simulations of these authors are presented below in Figure 2.2 (II).

A very interesting phase-field simulation of eutectic solidification in a binary Al–Si system can be found online at the website (http://www.msm.cam.ac.uk/phase-trans/phase.field.models/NESTLER.AVI). The interphase boundary was treated as a continuous transition between adjacent grains across a thin layer of finite thickness. The value of a phase-field variable identifies the location of the boundary and all grains. The movie allows observing how the eutectic spacing changes as solidification proceeds, and the nature of the solute diffusion field at the solidification front. The diffusion distance is approximately equal to the spacing of the lamellae.

---

[11] Wheeler, A.A., McFadden G.B., and Boettinger, W.J., Phase-field model for solidification of a eutectic alloy, Proc. of the Royal Soc. of London, Series A – Mathematical, physical, and engineering sciences, vol. 452, 1996, pp. 495–525.

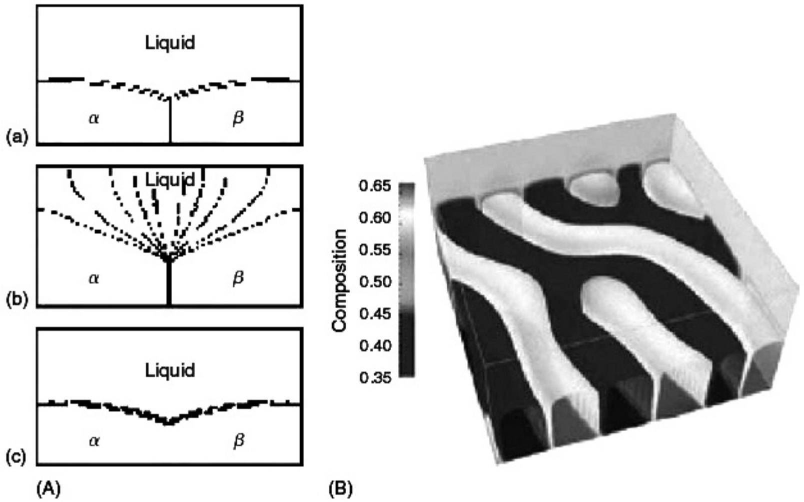

Figure 2.2 (A) Phase-field computation for a eutectic tri-junction situated in a temperature gradient, showing contours of (a) the concentration field; (b) the phase field ψ; and (c) the phase field ϕ after Wheeler *et al.*[11]; (B) Phase-field modeling of eutectic solidification in 3D, after Wheeler *et al.*[11]

Macrosegregation of ternary aluminum Al–Cu–Si alloys was studied by Ferreira *et al.*[12] both experimentally and from the modeling standpoint. Suzuki *et al.*[12] have also introduced the phase-field models for a number of binary and ternary alloys. These authors conducted computer simulations of isothermal dendrite growth for such alloys as Al–Cu, for Fe–C, Fe–P, and Fe–C–P.[12] It was demonstrated that calculations of the secondary arm spacing in Al–Cu numerically predicted using the phase-field model agreed well with the experimental data. These authors have also conducted simulations of rapid quenching of the corresponding melts. It was concluded that the models of this class were potentially applicable to commercially important Al and Fe alloys.[12]

Kim *et al.*[12] reported that they have been successful in the development of a new phase-field model describing rapid directional solidification with constant cooling rate. The banded structures in an Al–Cu eutectic alloy were successfully reproduced. These authors noted that concentration fluctuations played a crucial role in transition of the cell/dendrite growth mode into the plane-front mode, and in the pattern formation of microstructure with bands.

An interesting modified phase-field approach was proposed recently by Emmerich and Hubert.[13] The goal of this innovative work was to quantitatively describe the morphological evolution of intermetallic particles in aluminum casting alloys. The authors noted that recycling of aluminum alloys becomes progressively more and more difficult because of the increasing concentration of Fe and Mn in the aluminum alloy scrap. In turn, these chemical elements can readily form intermetallic compounds during processing and serve as nucleation sites for cracks or induce the formation of increased porosity. Consequently, an effort was made to simulate the behavior of intermetallic particles in the presence of forced flow (due to electromagnetic stirring). The results indicated that particle shapes were substantially different from the case of growth in a free-standing supercooled aluminum alloy melt.[13]

---

[12] Ferreira, I.L., Garcia A., and Nestler, B., On macrosegregation in ternary Al-Cu-Si alloys: Numerical and experimental analysis, *Scripta Materialia*, vol. 50/4, 2003, pp. 407–411; Suzuki, T., Ode, M., Kim, S.-G., Kim, W.-T., *ICCG International Conference on Crystal Growth, No. 13*, Kyoto, Japan, 2001.

[13] Emmerich H., and Hubert, J., A Phase-Field Model for the Morphological Evolution of Intermetallic Phases in Al Cast Alloys, International Aluminum Congress, Essen, Germany 2006.

2.3.4 Solidification microstructure calculations: perspectives and future work

A very significant progress has been achieved in understanding the fundamentals of solidification microstructure formation during the last 10–15 years. The group of methods generally called "phase-field models" holds a special place in this development. The advantages of such an approach are obvious: it contains intrinsic length scales necessary on the dimensional grounds (chemical species mobility, relaxation parameters) and gives a possibility to avoid computationally expensive complex techniques of front tracking in problems of the Stefan type.[14] It can naturally account for emerging phases or their dissolution. Furthermore, it could be seamlessly integrated with other continuum models such as convection and electromagnetic stirring, thus giving a possibility to achieve conditions very close to reality.

In its structure the phase-field method is similar to strain-gradient plasticity, where it becomes possible to describe plastic instabilities of finite size using the length scale(s) that naturally come with this formalism. Indeed, in the Cahn–Hilliard equation the distinctive microstructure formation accompanying spinodal decomposition is achieved via competition of the length scales that are intrinsically present in the diffusion coefficient and the second mobility coefficient. This analogy has been explored in detail by Glazoff *et al.*[15]

Sometimes an opinion is expressed in the literature that diffuse interface approach to solidification problems is just "regularization" of the mathematical "sharp interface" Stefan problem, which makes it easier to solve such problems. However, within the limits of a sharp interface approach it is difficult to observe the nucleation of new phases, or complete dissolution of the existing ones. In phase-field approach this is achieved "naturally"; it is also easily integrated with the existing thermodynamic/phase equilibria databases such as ThermoCalc. Indeed, a phase-field software package called "Micress" exists today that allows the user to calculate microstructure of sufficiently complex aluminum alloys, including ternary and quaternary compositions. Furthermore, while our principal goal was aimed at understanding the formation and evolution of solidification microstructure, the phase-field approach is easily applicable to modeling different heat treatment operations in the solid phase (e.g., coarsening of precipitates, such as $Al_3(Zr; Sc)$ after solution heat treatment and quench)[16].

---

[14] Indeed, diffusion coefficient D is scaled as $D \propto l^2/\tau$, where l stands for the characteristic diffusion path (a "natural" length scale of a given diffusion problem) and τ stands for the corresponding diffusion time scale. It is the competition of these length and time scales in real-life problems (along with expressions for the interface energies) that defines the characteristic length scales of a given microstructure.

[15] M.V. Glazoff *et al.*, Continuum physics of phase and defect microstructures: bridging the gap between physical and mechanical metallurgy of aluminum alloys, ***Int. J. of Plasticity***, vol. 20, 2004, p. 346–402.

Among the shortcomings of this approach one should mention the need for significant computer power and lengthy computation times required today to achieve the representation of cooling conditions typical of a casting shop (from 0.1 K/s (for investment castings) to ~200 K/s (die casting) even for binary or ternary aluminum alloys. Realistic treatment of the simplest industrial casting aluminum alloys often requires that at least four or five components be taken into consideration. However, with the current advancements both in computing power and in algorithm development (e.g., finite element techniques with adjustable mesh size) one could express hope that these obstacles will be removed soon.

2.4 QUANTITATIVE CHARACTERISTICS OF ALLOY STRUCTURE AND METHODS OF ITS EVALUATION

As it was pointed out earlier, today the methods of quantitative modeling and prediction of microstructure still have not attained the level when it becomes possible to predict, using just aluminum alloy composition and the conditions of its thermomechanical or solidification processing, its equilibrium or non-equilibrium microstructure. As a result, it is still necessary to employ simpler techniques based on some fundamental materials science relations (e.g., the Hall–Petch equation), stereological analysis, regression modeling, and similar methods. Their application is justified because they provide a plant engineer with the information necessary to cast a high-quality aluminum alloy casting. For this reason below we will be mostly concerned with these semi-quantitative and phenomenological methods.

The principal phase of every aluminum alloy in any structural state is Al-based solid solution or (Al). It may enter into the compositions of different structural entities. In most cases this solid solution forms from the melt, which is sufficiently supersaturated. The volume and mass % of such primary crystals can vary in a broad range from almost 100% to 0%.

Alloys which contain more than 90–95 vol.% of (Al) primary crystals are called "alloys of the solid solution type" (it is the first structural group in Section 1.1). Typically, such alloys contain in as-cast condition relatively insignificant volume

---

[16] N. Lecoq, N., Zapolsky, H., Patte, R., Phase Field Simulations of Coarsening Kinetics of Gamma' Particles in Ternary Al–Zr–Sc Alloys, International Aluminum Congress, Essen, Germany 2006.

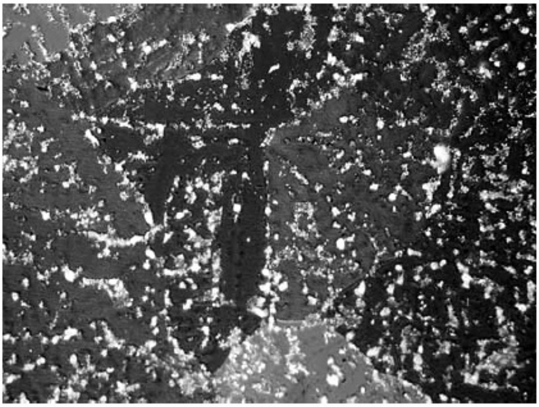

Figure 2.3 Grain microstructure of cast aluminum alloy (polarized light); light microscopy.

fraction of eutectic or peritectic phases (up to 10 vol.%) (Figure 1.1a). On the contrary, alloys of the eutectic type contain less than 90% (Al), especially if large amounts of eutectic phases are formed.

Alloys with large amounts of eutectic phases can be hyper-eutectic, eutectic, and hypo-eutectic – see structural groups 2–4 in Section 1.1 (Figure 1.1a). In the alloys belonging to these two latter groups, the primary crystals of (Al) are practically absent, but the (Al) phase will nevertheless be present as it enters into eutectic compositions.

Rigorously speaking, alloys of the solid solution type can be considered as hypo-eutectic (e.g., alloy X_2 in Figure 2.4). However, small amounts of eutectic in such alloys are typically comprised of the β-phase, and alloy X_2 does not differ in terms of its microstructure from alloy X_1, in which eutectic can be formed only as a result of non-equilibrium solidification (Figure 2.4).

Casting alloys of the solid solution type are undoubtedly quite widespread. Moreover, this is true also with respect to wrought aluminum alloys. However, among industrial casting alloys most possess either hypo-eutectic or eutectic microstructure.

It is well known Refs. [61–63] that macrostructure (i.e., grain structure) of cast aluminum alloys may consist of the three zones: (1) narrow peripheral zone consisting of small equiaxed crystallites, (2) zone of columnar crystals, and (3) the central zone of equiaxed crystals. Modern casting technologies in most cases ensure uniform equiaxed grain structure along the whole ingot cross-section. For this reason we will use the *average lineal grain size*, *D*, as the principal quantitative characteristic of structure.

The value of D, as well as a number of other important metallographic parameters, can be assessed using the approaches of quantitative stereology [64]:

$$D = \frac{L}{n}\ (\text{mm}) \tag{2.11}$$

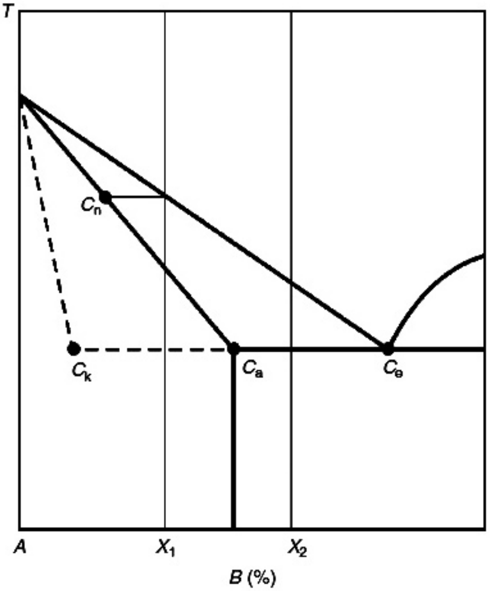

Figure 2.4 Schematic of a eutectic binary diagram with non-equilibrium solidus (dashed line).

In this equation L stands for the overall number of secant lines (in mm) and n is the number of grains that are crossed by these secant lines.

The reliability of determining the average grain size in cast alloys to a significant extent depends upon the accuracy of determining the positions of grain boundaries. The best results can be obtained via preparation of oxidized sample surfaces and their observation in polarized light (Figure 2.3). Oxidation of electropolished samples is usually conducted in a 2–10% solution of borohydrofluoric acid in water with voltage 25–30 V applied for ~2 minutes [65]. Electrolytic polishing is typically performed in a solution comprised of 61.7 ml H_3PO_4, 134 ml H_2SO_4, 240 ml H_2O, 156 g Cr_2O_3 at temperature 70° C and voltage 9–12 V.

In those cases when directional heat release results in the formation of columnar ingot structure, in addition to average lineal grain size D, it is also useful to assess the minimal (D_{min}), maximal (D_{max}) sizes, and the so-called shape coefficient:

$$k = \frac{D_{min}}{D_{max}} \tag{2.12}$$

Inside the grains of aluminum solid solution in cast aluminum alloys (solid solution or hypo-eutectic) one can observe, using an optical microscope, *dendritic cells*, that represent the cross-sections of dendrites (Figure 1.2a). It is generally accepted

Refs. [63, 66, 67] that the dendritic cell size is one of the most important parameters characterizing alloy microstructure. Quantitatively, it is easy to assess the average lineal size of dendritic cells, d. In principle, it is done in a way similar to the determination of D, only applying higher magnifications.

If the boundaries of dendritic cells contain grain boundary precipitates or eutectic colonies, then it is not important which particular technique of sample preparation is employed (as long as the eutectic component is clearly visible). However, if the overall volume of the eutectic is small, then samples should be prepared using etching and electro-polishing, using the recipes described above. This will ensure either the formation of a surface relief (depressions and elevations) or etching of the zones adjacent to the boundaries of dendritic cells due to the differences in chemical composition between the center and periphery of the cells.

The principal quantitative characteristics of different phases forming in the process of solidification of aluminum alloys are the volume fraction Q_V, the specific surface of this inclusion, S, and the average lineal size (thickness) of inclusions, m, and [65]:

$$Q_V = 100 \cdot \frac{1}{L} \text{ (vol.\%)} \tag{2.13}$$

$$S = \frac{4n^1}{L} \text{ (mm}^2\text{/mm}^3\text{)} \tag{2.14}$$

$$m = 1000 \cdot \frac{l^1}{n} \text{ (}\mu\text{m)} \tag{2.15}$$

In these equations l^1 stands for the portion of the total secant crossing phase inclusions other than (Al), in mm; n^1 is the total number of points in which a secant crosses the inclusions. In a number of cases one can also define the average distance between inclusions:

$$I = \frac{L}{n^1} \tag{2.16}$$

It can be easily seen that the values Q_V, S, and m are determined from the same data and are related by the following expression:

$$Q_V = \frac{S \cdot m}{40} \tag{2.17}$$

In eutectic, hypo- and hyper-eutectic alloys that comprise large volume of the eutectic phases, microstructure is best characterized by the average size of dendritic colonies, D_e, determined using equation (2.11). Microstructure is characterized by the volume fraction Q_v of the eutectic and primary crystals of (Al) (in eutectic alloys), their lineal size m, and also by the average lineal size of cross-sections of different phases comprising a given eutectic:

$$m^{e}_{\beta} = l^1_{\beta}/n^1_{\beta} \text{ (}\mu\text{m)} \tag{2.18}$$

where l_β^1 is the overall length of the secant for a given phase (in this case β-phase) comprising a eutectic colony; n_β^1 is the total number of points in which secants cross the body of a given phase.

Another microstructural feature often associated with dendritic cell and grains of Al-based solid solution is micropores, mostly of solidification shrinkage origin Refs. [62, 63]. Density γ is an integral function of porosity, which can be defined using the technique of hydrostatic weighing [68]. If the pores are revealed metallographically (e.g., in aluminum–magnesium alloys) then using equations (2.13–2.15) one can define their volume fraction Q_p, specific surface S_n, and average lineal size m_n of the pores. The cumulative volume fraction of the pores (Q_{V_p}) in a binary alloy can be easily calculated if densities and partial volume fractions are known:

$$Q_V = \frac{(Q_V \cdot \gamma_\beta + Q_\alpha \cdot \gamma_\alpha) - \gamma}{Q_V \cdot \gamma_\beta + Q_\alpha \cdot \gamma_\alpha} \tag{2.19}$$

In equation (2.19) $Q_\alpha = (1 - Q_V)$ is the volume fraction of (Al), while γ_α and γ_β stand for the densities of (Al) and additional phases (or eutectic).

Since the shape and/or size of the pores can be distorted in the process of metallographic sample preparation, one can also use the technique of X-ray microscopy that can provide volume picture of porosity [67].

Non-equilibrium solidification of (Al) is always accompanied by concentration micro-inhomogeneity (microsegregation). In order to get a measure of this phenomenon, researchers typically use the average concentrations of alloying elements in the center of dendritic cells C_1 and on the boundary C_2, and also the degree of microsegregation, which can be calculated for systems with the distribution coefficient $K < 1$ simply as $\Delta C = C_2 - C_1$. In these systems we have $C_1 \cong C_{\min}$, and $C_2 \cong C_{\max}$. If, on the other hand, $K > 1$, then $C_1 \cong C_{\max}$ and $C_2 \cong C_{\min}$; and then $\Delta C = C_1 - C_2$.

Experimentally microsegregation can be explored using different modifications of electron probe microanalysis [69–71]. The technique use most often is usually micro X-ray probe, which gives a possibility to determine concentrations in micro volumes with diameter 1–2 μm with high precision (absolute errors are the order of fraction of a percent, relative errors – up to 1.5%). Specimens can be prepared from massive samples and thin foils as well.

The same materials can also be studied using the method of X-ray energy-dispersive spectroscopy, where a solid X-ray detector is used, instead of a crystalline diffraction spectrometer. This latter technique is particularly convenient, especially if used in conjunction with transmission electron microscopy (TEM).

In addition to TEM, analyses of thin films can be conducted using the so-called EELS (electron energy-loss spectroscopy) method. Its advantage, in comparison to the other two techniques, is in ability to estimate concentrations of light elements (with $Z < 11$).

While the errors in concentration assessment are approximately the same for the last two techniques, their spatial resolution is much higher: the average diameter of the point in which concentrations can be measured, comprises from 10 to 30 nm. In order to reduce the determination errors, standard samples with well-defined concentrations of components should be used in all cases.

In addition to the characteristics of microsegregation, sometimes it is important to estimate the average concentration of the ith alloying element in solid solution, $C_{i\text{-(Al)}}$. This property can be calculated using data on the average concentration of a given element in alloy C_i, volume fraction Q_{Vi} of the corresponding phase (or phases), and its concentration in this phase $C_{i\text{-}j}$. Then for a two-phase alloy one can write down the following expression:

$$C_B = \frac{Q_\alpha \cdot C_B^\alpha \gamma_\alpha + Q_\beta \cdot C_B^\beta \cdot \gamma_\beta}{Q_\alpha \cdot \gamma_\alpha + Q_\beta \cdot \gamma_\beta} \tag{2.20}$$

The properties of casting aluminum alloys can depend not only upon the concentration inhomogeneities of the (Al) dendritic cells, but also on their internal substructure. The key characteristics of substructure are the density of dislocations ρ, the average lineal size of subgrains d' or dislocation cells d'', and the average disorientation angle θ. Inside dendritic cells additional secondary phases could be formed after cooling the system below the solidus temperature and subsequent homogenizing heat treatment. These phases could be well characterized by the average lineal particle size m, inter particle spacing l , and the number density distribution Δ_{BT}.

TEM still remains the most important tool for substructure studies. It is informative, gives a possibility to assess the properties of even finest particles as well as dislocation structures. The method of foil preparation out of cast aluminum alloys (as it is used now) has been refined, which in itself represented a very difficult task, mostly because of their structural and chemical inhomogeneity.

In most cases, the following recipe is used for the preparation of foils and their subsequent TEM analysis [72, 73]. Using mechanical sawing, one can prepare thin plates with the width of 0.8–1.5 mm. These samples are further polished to the width of 0.2–0.3 mm, and the disks with diameter 3 mm are cut. These disks are further subjected to electro-polishing in 25% HNO_3, which results in the formation of tiny cones on their surfaces. The final stage of the whole process is their electrolytic thinning in a special solution containing 23% $HClO_4$ with the density of 1.54 g/cm^3 and 77% ice acetic acid, or a mixture of $HClO_4$ and C_2H_5OH with the ratio 1:6. The voltage maintained in the bath during electro-polishing should be from 9 to 12 V.

Measurements are conducted using negatives obtained in the course of TEM work with foils. Alternatively, modern equipment allows monitoring data using a computer display. The average lineal size of subgrains surrounded by 3D dislocation networks is determined using the methods of stereometry (see equation (2.11) for D).

The density of dislocations ρ_1 that do not enter into planar sub-boundaries is determined using the technique described in [74, 75]:

$$\rho_1 = \frac{2 \cdot N}{t \cdot L}\ (\mathrm{cm}^{-2}) \tag{2.21}$$

where ρ_1 is the ratio of the total length of all dislocation lines to the foil volume; N is the number of crossings of dislocation lines with square grid; t is the foil thickness (which is determined experimentally) [75] or is taken equal to 200 nm. This latter number corresponds to the average thickness of transparent foil at accelerating voltage of 100 keV. Finally, L stands for the overall length of all secants.

The density of dislocations accumulated in grain boundaries and sub-boundaries (immobile dislocations) ρ_2 is usually assessed using equation (2.22) [77]:

$$\rho_2 = \frac{\theta}{d^1 \cdot b} \tag{2.22}$$

In equation (2.22) b is the Burgers vector of dislocations forming sub-boundaries.

This approach is based on the assumption that small-angle grain boundaries are mostly formed along the planes. However, if one takes into account that any such boundary typically surrounds a certain volume, for example, of cubic shape, then the equation needs to be modified. Indeed, if the number of dislocations n per boundary unit length is equal to $n = \theta/b$, then dislocations belonging to one cubic subgrain with the surface area $6(d')^2$ will be located upon the surface $3 \cdot (d')^2$, since each side of the cube belongs simultaneously to the two adjacent subgrains. Then the overall length of dislocations in the boundaries is equal to $3 \cdot (d')^2 \cdot \theta/b$. After dividing this value by the subgrain volume $(d')^3$, we obtain:

$$\rho_2 = \frac{3\theta}{d^1 \cdot b} \tag{2.23}$$

For aluminum and its alloys the Burgers vector $b = a/2<110>$, where a is the lattice period.[17] For this reason $b \cong 0{,}233$ nm; the formula for the calculation of ρ_2 could be written in the following way:

$$\rho_2 = 1.29 \times 10^9 \cdot (d^1)^{-1} \cdot \theta \tag{2.24}$$

In equation (2.23) d^1 is measured in cm, while angle θ in radians.

Both equations for ρ_2 (i.e. (2.23) and (2.24)) are derived under the assumption about a symmetric tilt boundary. In the general case the value of ρ_2 needs to be somewhat reduced because the subgrain disorientation is defined by the excess of dislocations of a particular sign in that boundary, not all dislocations. For this reason when an asymmetric tilt boundary is formed the total number of dislocations in it will be higher than according to predictions with (2.22)–(2.24).

To calculate the value of ρ_2 one needs to know the average disorientation angle θ for the subgrains. It can be defined using the method of Kikuchi patterns [78] with the accuracy of ±0.5°.

The total number of dislocations in alloys with subgrain microstructure is determined as the sum:

$$\rho = \rho_1 + \rho_2 \tag{2.25}$$

---

[17] The principal slip system for aluminum at room temperatures is $\{111\}<110>$.

The value of ρ in the general case will be some 10–50% lower because of the dislocation "exit" in the process of foil refinement [75], and also because of the lower value of ρ_2 discussed above [75].

The structural characteristics of precipitates, dispersoids, and constituent particles can be determined using the standard methods described in Refs. [75, 78]. Typically, measurements are conducted in such areas where overlap of the explored microstructural features can be safely ignored. As a result, their lineal size m_{BT} can be assessed using an equation, similar to (2.14), for the thickness of constituent particles in polished samples. The density of distribution of particles in the foil (number of particles per unit volume) is defined as:

$$A_1 = \frac{N}{t} \tag{2.26}$$

In equation (2.26) N is the total number of particles per unit of the foil surface.

Standard statistical techniques for assessment of errors include calculations of mean quadratic error, variance, and errors corresponding to a certain probability (usually 0.95) [64].

For all quantitative estimates the overall number of experimental points must be such that the data variance coefficient does not exceed 10–20%.

We have considered a significant number of different structural characteristics. However, this list is not complete and could be continued. For example, sometimes it may be necessary to estimate the average size and volume of non-metallic inclusions, because these values can exert significant influence upon the properties of cast aluminum alloys [79].

2.5 NON-EQUILIBRIUM SOLIDIFICATION OF BINARY ALLOYS

Solidification processes taking place in shape castings, ingots, or welding joints are always non-equilibrium. An important consequence of this fact is dendritic liquation (microsegregation) – a direct result of the suppression of diffusion processes in liquid and in solid phases.

Microsegregation develops in alloys that solidify in a certain temperature range. It results in the formation of concentration micro-inhomogeneity and non-uniform distribution of alloying elements and impurities across the volume of solid solution crystallites. Additionally, under certain conditions it may also result in the precipitation of excessive phases and/or structural features (in aluminum alloys – typically of eutectic or peritectic origin).

Today we have a significant number of studies on different aspects of non-equilibrium solidification (see e.g., [71, 80–82]). In particular, Pikunov [82] consider the whole solidification process as "decomposition" of liquid phase and "interaction" of precipitating crystals with the liquid that surrounds them. "Decomposition" takes place due to mass transfer between liquid and crystals, and also inside crystals. Under the conditions of non-equilibrium solidification this latter process is suppressed, which, in turn, results in the suppression of mass transfer between liquid and crystals.

We will adopt a somewhat different approach described below. To analyze the nature and extent of microsegregation we will consider three types of diffusion processes [83]. Firstly, the formation of crystals of equilibrium composition from the melt requires that atomic redistribution processes on the solidification front take place. This results in the equilibrium concentration difference, which can be determined as the distance between the lines of liquidus and solidus (in horizontal direction). We will call such a process "separating diffusion".

Secondly, the layer of molten metal adjacent to the surface of a growing crystal becomes enriched with one of the components. In molten metal this concentration difference needs to be smoothed out between this layer and part of the melt located at a distance from the front. This process goes via diffusion and convective mixing.

Thirdly, we need to consider the homogenizing diffusion in the solid phase, which removes the concentration gradients inside the crystals.

If at least one of these three processes is suppressed, then solidification will take place under non-equilibrium conditions, and microsegregation will develop.

2.5.1 Microsegregation

2.5.1.1 Theoretical analysis of microsegregation in two-component aluminum alloys

Most of the theoretical work on non-equilibrium solidification was performed for two-component systems. This analysis teaches us that the distribution of an alloying element across the crystallite volume (and its maximal and minimal concentrations in particular) and the degree of microsegregation ΔC – all these parameters depend upon the separation coefficient, diffusion coefficient in the solid and the liquid phases, and the solidification rate. It becomes quite clear that in an alloy of a given concentration the key variable factor defining the onset and development of microsegregation is solidification rate (or closely associated cooling rate), and its changes will exert a strong influence on all diffusion processes in the system.

As demonstrated in Chapter 1, aluminum forms diagrams of the eutectic type with all principal alloying components (copper, magnesium, zinc, silicon). For this reason we provide below analysis of the cooling rate upon the degree of microsegregation for these systems.

First, let us consider alloy X_1, the composition of which lies in the narrow homogeneity range (Figures 2.4 and 2.5). If solidification rate is very low, all diffusion processes take the system to equilibrium, $\Delta C = 0$, and chemical composition in the center of a grain, C_1 corresponds to the point X_1 through the whole volume of homogeneous solid solution (Figure 2.3). However, beginning with a certain solidification (cooling) rate, V_{c1}, the slowest diffusion rate will be suppressed, and upon completion of solidification the figurative point C_1 will be in between the points X_1 and C_n. If the solidification rate is higher but still within the range from V_{c1} to V_{c2} , then the chemical composition of the first crystallites will be closer and closer to C_n. Beginning with solidification rate V_{c2}, homogenizing diffusion in the central areas of growing crystals will be suppressed almost completely and in a broad solidification rate range C_1 will be determined by the point C_n of equilibrium solidus at the temperature of the solidification onset (ignoring concentration supercooling) (see Figure 2.4).

Once another critical value V_c is attained supercooling may develop such that thermodynamic potentials of solid and liquid solutions become equal, giving rise to diffusion-less solidification [84, 85]. As a result of such process the solid solution composition will be the same in every figurative point corresponding to solid solution and will attain the value X_1. In principle, there are two scenarios according to which C_1 may change when solidification rate approaches V_{c6}: jump-like rise from C_n to X_1 at V_{cb} or gradual change from C_n to X_1 in a certain range $V_{c4}-V_{c6}$ (Figure 2.5).

Judging by experimental data provided by Miroshnichenko [86], the second scenario will take place. Transition to X_1 will occur in a narrow range of solidification rates -10^7 to 10^8 K/s.

Transition from C_n to X_1 in the solidification rate range $V_{c4}-V_{c6}$ can be interpreted without the notion of diffusionless solidification. It may well be that homogenizing diffusion does not come to complete equilibrium and on the boundary of the solid and first liquid phases concentration difference will be established, which may be smaller than that defined by the equilibrium separation coefficient K (in other words, the effective separation coefficient attains value close to 1). As the solidification rate grows within the range $V_{c4}-V_{c6}$ progressive suppression of homogenizing diffusion takes place, and C_1 approaches X_1. Finally, when the critical solidification rate value, V_{c6} , is attained, then homogenizing diffusion is suppressed completely, and diffusionless solidification will commence.

Now let us explore how solidification rate affects the concentration C_2 of alloying element(s) on the boundaries of dendritic cells and grains of solid solution. This concentration, beginning with Vc_1 will deviate from X_1 toward the point of maximal solubility, C_a (because of suppression of homogenizing diffusion). When at rate Vc_2 the composition in the crystallite center(s) becomes practically constant, in the surface layers homogenizing diffusion will still take place because of high value of concentration gradient at the boundary [80]. As a result, concentration at the boundary will become equal to C_a, but only beginning with velocity V_{c3}. Non-equilibrium eutectic will be formed at the same solidification rate (Figure 2.5).

In a certain solidification rate interval, when diffusion processes are still not suppressed and diffusion in the solid phase is suppressed completely, solidification ends up with precipitation of non-equilibrium component [80], and concentration C_2 is constant and equal to C_a. If concentration of alloying element rises at the solidification front, (Figure 2.6), then concentration B in liquid phase at the front C_L^1 will exceed equilibrium value C_L at a given temperature. On the other hand, if diffusion takes place then solid solution enriched with component B will

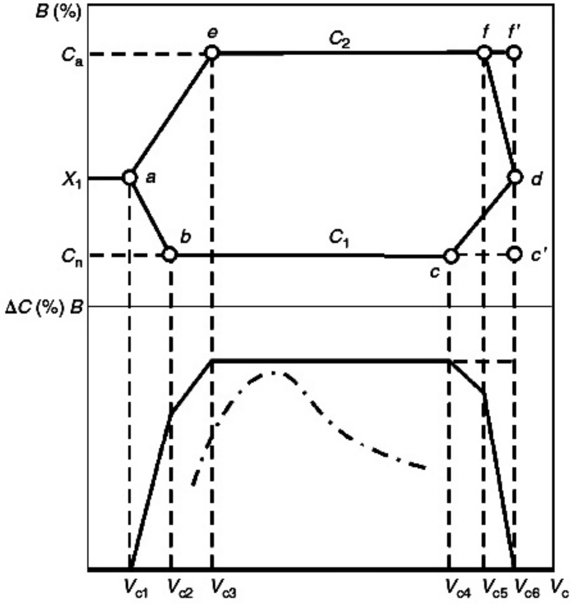

Figure 2.5 Schematic of the influence of solidification rate V_c upon composition of central areas C_1, boundaries C_2 of crystallites and the extent of microsegregation ΔC in alloy X_1.

be forming out of liquid C_L^1 as compared to equilibrium concentration at this temperature (C_s).

If eutectic solidifies without significant supercooling out of liquid with equilibrium eutectic composition, then the last layers of solid solution will not be supersaturated with respect to C_a. Indeed, in aluminum alloys with the key alloying elements such supersaturations were not found at least up to $5 \cdot 10^6$ K/s [87]. Consequently, one may assume that if diffusion processes take place, $C_2 \cong C_a$.

Further increases in solidification speed may result in two different processes: concentration jump C_2 when $V_c = V_{c6}$ (dashed line $f^1 d$ in Figure 2.5) or gradual decrease of C_2 from C_a down to X_1 in the range $V_{c5}- V_{c6}$ (domain "*fd*"). This jump-like change on the alloying element concentration at the crystallite boundary may take place when the solidification process is diffusionless, and C_a also changes in a jump (section $f^1 d$ corresponds to the domain $c^1 d$). Besides, constant concentration at the boundary also may be observed when concentration C_1 along *cd* changes continuously due to increased supersaturations. If diffusion processes are suppressed only partially, then beginning with a certain speed V_{c5}–V_{c6}, concentration at the boundary will be changing from C_a to X_1 (domain *fd*).

If we know the dependence of composition in the center and at the boundary as a function of solidification rate, then it becomes possible to plot the degree

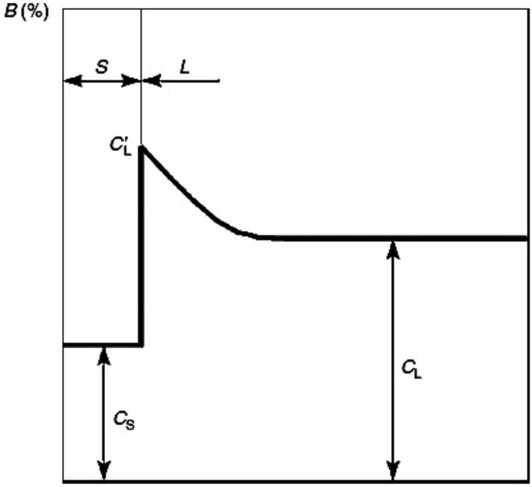

Figure 2.6 Distribution of alloying element close to solidification front (after Wagner).

of microsegregation ΔC as a function of solidification rate (see Figure 2.5). In the V_{c4}–V_{c6} solidification range three scenarios of microsegregation change are feasible, which would correspond to different variants of changes C_2 and C_1.

This implies that microsegregation in a given aluminum alloy must grow gradually as the solidification rate grows, then remain constant in a certain range, and then drop down to zero. Figure 2.7 represents similar dependencies of C_1, C_2, and ΔC from solidification rate for alloy X_2 (see Figure 2.4), and its solidification in equilibrium conditions must end via eutectic phase reaction. The principal difference from the case presented in Figure 2.5 is that at equilibrium solidification of similar alloys (in the range from V_{c0} to V_{c1}) both composition in the center and at periphery of crystals will be defined by concentration C_a, but not X_2. When at rate V_{c1} homogenizing diffusion in the solid phase becomes suppressed, that is the composition in the center changes from C_2 to C_n, then the degree of microsegregation as a function of solidification rate will be changing as shown in Figure 2.5.

The schemes considered above are of quite general nature and may be used for analysis of binary alloys of the peritectic type, and also non-equilibrium solidification of multicomponent alloys. Of course, these general schemes cannot describe all of the peculiarities of microsegregation, in particular the distribution of alloying element in the cross-sections of dendritic cells. However, giving the correct values for concentrations of the very first and last layers of solidifying liquid, they help analyze experimental data correctly. Using such schemes, it becomes possible to represent important characteristics of microsegregation as functions of alloy composition and non-equilibrium solidification.

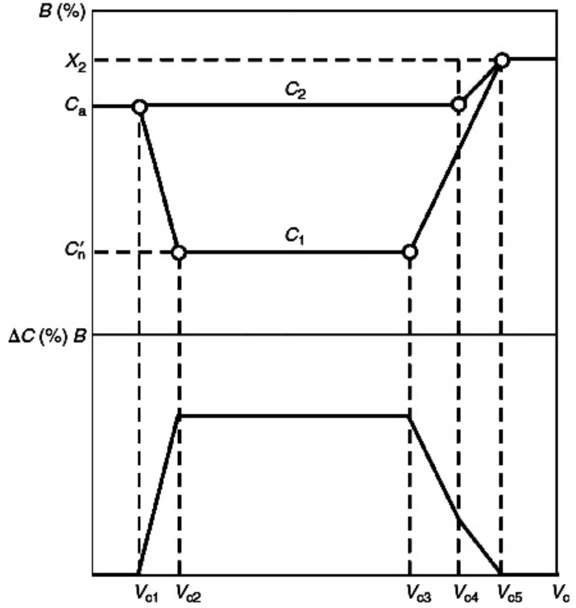

Figure 2.7 Schematic of the influence of solidification rate upon C_1, C_2, and ΔC in alloy X_2.

2.5.1.2 Experimental studies of microsegregation in binary aluminum alloys

Experimental data (see e.g., [63, 88]) indicate that for different ingot and shape casting techniques in industrial conditions solidification rate will vary from 10^{-1} to $\sim 10^2$ K/s. For powder metallurgy alloys and for solidifying welding joints this rate increases by one or two orders of magnitude. It is in this solidification range from 10^{-1} to 10^4 K/s that microsegregation of numerous aluminum alloys has been studied in great detail.

Using alloys Al–Cu and Al–Mg it was established [65] that the composition C_1 of central areas of dendritic cells for all solidification rates described above is approximately constant and close to the concentration of equilibrium solidus C_n at the temperature of the onset of solidification. Figure 2.8 represents the corresponding dependence for Al–2%Cu.

The composition of solid solution in the center of different dendritic cells is not the same. Alloying element concentration in the proximity of the dendrite center ("trunk") that forms at temperatures close to liquidus practically coincides with C_n. In the center of large dendritic branches the composition of aluminum solid solution lies in between the points C_n and X_1 (see Figure 2.4). For example, in alloy Al–5%Cu, where $C_n = 0.75$%Cu, for solidification rate ~3 K/s experimentally determined concentration in the center of dendrite trunks was

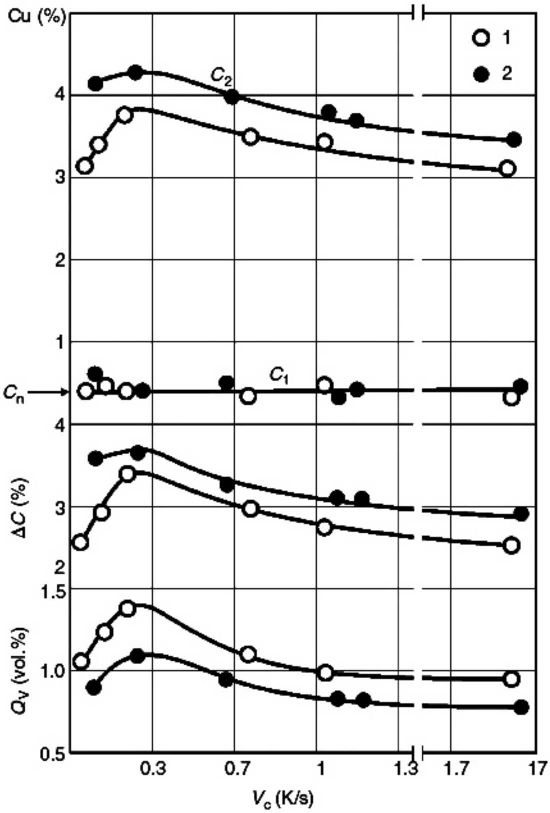

Figure 2.8 Dependencies C_1, C_2, and ΔC and volume fraction Q_V of eutectic component in alloy Al–2%Cu upon solidification rate in the course of solidification. Molten metal was overheated up to: 1 – 680°C; 2 – 900°C.

~0.7%Cu, while statistically determined average in the center of dendritic cells was ~1.2%Cu. Practical coincidence of this concentration with concentration C_n indicates that in the conditions of non-equilibrium solidification diffusion in the solid phase is almost suppressed, while separating diffusion in the liquid phase is practically completed.

Different branches of the same dendrite can be formed at different temperatures, and for this reason the concentration of alloying element (defined by the points of equilibrium solidus at the corresponding temperatures) should also differ in these branches. The lower the temperature of the dendrite branch formation is, the higher the concentration of alloying element in the center will be. In turn, this results in the local reduction of the solidus temperature.

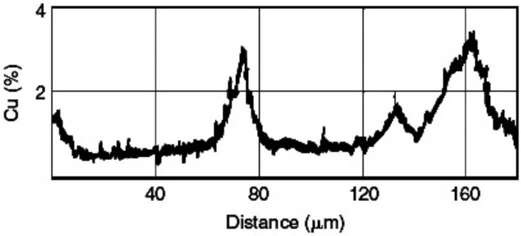

Figure 2.9 Typical Cu distribution curves for cross-sections of dendritic cells for alloy Al–4.5%Cu with $K < 1$.

In most aluminum alloys the concentration of alloying element varies insignificantly in the average part of dendritic cells and increases sharply (if $K < 1$) only at cell boundaries (Figure 2.9). Because of the large concentration gradient and insufficient "locality" of the existing techniques of measuring concentrations in micro volumes, it is difficult to obtain reliable quantitative data on composition exactly at grain boundaries and at boundaries of dendritic cells.

If diffusion is completely suppressed in the solid solution and separating diffusion proceeds freely, then the composition of last layers of solid solution must correspond to the maximal concentration of alloying element C_a (Figure 2.4). Experimentally composition can be determined not precisely at the boundary, but in the adjacent layer of a certain finite thickness (usually 1–6 μm). There are certain peculiarities of alloying element distribution along the boundaries of dendritic cells at different solidification rates. For this reason the concentration of alloying element in the peripheral dendrite layers at first increases, attains maximum value in the range of relatively small solidification rates (10^0-10^1 K/s), and then decreases (see Figure 2.5, dashed line; and also Figure 2.8). However, the "true" concentration on the boundary with eutectic inclusions must remain constant and equal to C_a practically in all range of solidification rates, until separating diffusion becomes suppressed. In Ref. [89] it was demonstrated that this conclusion holds at least until rates of the order of $5 \cdot 10^6$ K/s.

Thus, in a broad range of solidification rates non-equilibrium solidification of binary aluminum alloys takes place in conditions of unlimited separating diffusion and suppression, to a certain extent, of the homogenizing diffusion in the solid solution. For this reason experimental curves C_1, C_2 and ΔC, assessed in the solidification rate interval, usually lie between the values of Vc_2 and Vc_4 (see Figure 2.5).

In aluminum alloys with principal alloying elements – magnesium, copper, silicon, and zinc – supersaturated (with respect to C_a) solid solutions will not be formed in real-life conditions, and for this reason experimental values of C_1 are always less than C_a. However, in many aluminum alloys with refractory transition metals of the IV–VIII groups of the Mendeleyev Periodic Table of elements (Mn, Cr, Ti, Zr, Sc, and others) even at low solidification rates their concentration on the periphery (for systems with $K < 1$) or in the center (if $K > 1$) of dendritic

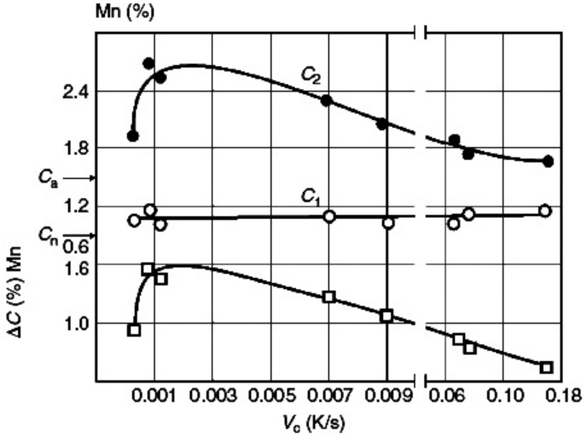

Figure 2.10 Dependence of the concentration Mn in the center and on periphery of dendritic cells and its ΔC in alloy Al–1.5%Mn, upon cooling rate during solidification.

cells will be significantly higher than their equilibrium solubility in aluminum at eutectic or peritectic temperatures.

Figure 2.10 illustrates the dependence of the Mn concentration in the center and on the periphery of dendritic cells and the degree of microsegregation in binary alloy Al–1.5%Mn, as a function of its solidification rate. It is clear that C_1, as usual, is close to the point C_n, while all experimental values of C_2 exceed C_a. It should be emphasized that "true" values of C_2 should be even higher.

It is well known that in alloys of aluminum with manganese and several other transition metals anomalously supersaturated solid solutions can be easily obtained (see e.g., [90–95]). Usually their formation is proved via the results of determination of the lattice constant of (Al) [86]. Typically average value of the lattice constant is taken into account and possible microsegregation is ignored.

Experimental data [89, 96, 97] indicate that the formation of Mn supersaturated (Al) in the peripheral zones of dendritic cells may take place in the whole range of practically realized solidification speeds, including slow cooling (e.g., sand casting or similar techniques). The average composition of solid solution may be lower than equilibrium solubility of Mn in (Al), because the central zones of dendrite cells that occupy a large portion of alloy volume are depleted with manganese. Additionally, in alloys containing more than 0.3–0.5% Mn a manganese-rich eutectic can be formed.

It is possible that solidification of Al–Mn alloys under industrial solidification conditions proceeds in a conventional diffusional way, but corresponding to the metastable diagram of state [86, 91]. According to this diagram, metastable equilibrium will correspond to the eutectic reaction with (Al) and Al_4Mn phase, instead of Al_6Mn in equilibrium phase diagram (Figure 2.11, dashed lines).

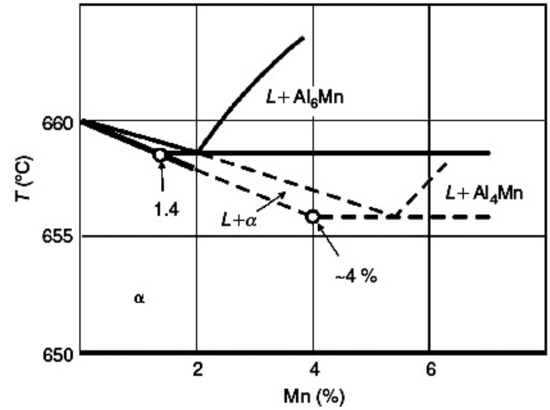

Figure 2.11 Stable (solid lines) and metastable (dashed lines) lines of liquidus and solidus for the Al–Mn system.

The limit solubility of Mn at eutectic temperature in metastable system is close to 4% [93]. Comparing Figures 2.10 and 2.11 one can see that the composition of the central area of dendritic cells is close to the point defined by equilibrium solidus at the temperature of solidification onset, while C_{Mn} on the periphery is lower than C_a (4%) because of insufficient spatial resolution of the used technique.

In alloys of other systems with very narrow solidification range and the presence of intermediate phases (e.g., Al–Ti, Al–Cr, Al–V) we will observe a picture of microsegregation that is quite opposite to the one described for Al–Mn alloys: the maximal concentration in alloys with peritectic systems with $K > 1$ will be observed in the center of dendritic cells, minimal – on the periphery [65].

Above we considered the influence of solidification rate upon such parameters as C_1, C_2, and ΔC in different alloys. The authors of Ref. [98] also studied the influence of molten metal superheating upon the same characteristics using alloys of the Al–Cu and Al–Mg systems. It was established that raising the temperature of molten metal before solidification does not exert any influence upon the composition in the center of dendritic cells at all solidification rates, but results in a significant increase of the experimentally determined values of C_2 and, respectively, ΔC (Figure 2.10). This is related to widening of the peripheral zone of dendritic cells enriched with alloying element as temperature of the melt goes up [65].

In addition to minimal and maximal concentrations of the alloying element and the degree of microsegregation, another important factor is average composition of aluminum-based solid solution C_{B}^{α}. The following expression can be derived for the case of non-equilibrium solidification described above [80]:

$$C_{\mathrm{B}}^{\alpha} = C_{\mathrm{B}} - \frac{C_{\mathrm{L}} - C_{\mathrm{B}}}{\left[\left(\dfrac{C_{\mathrm{L}} - 1}{C_{\mathrm{B}} - 1}\right) \cdot \dfrac{C_{\mathrm{B}}}{C_{\mathrm{L}}}\right]^{\frac{1}{1-K}} - 1}. \tag{2.27}$$

In equation (2.27) C_B and C_L stand for the concentrations of alloying element in the alloy and in liquid state at a given temperature; K is the coefficient of distribution that relates C_L to the alloying element concentration in the solid phase:

$$C_s = \frac{K \cdot C_L}{1 + (K - 1) \cdot C_L}.$$

Equation (2.27) is obtained under the assumption that K is constant in the whole solidification range, and that solidification front is a planar wave for alloy with unlimited mutual solubility of components in liquid and in solid states.

Rozin demonstrated [99] that the introduction of effective distribution coefficient gives a possibility to account for partial diffusion in the liquid state, and can change the average solid solution composition and its temperature dependence quite substantially (Figure 2.12). If K is constant:

$$C_B^{\alpha} = \frac{C_B - C_L \cdot \left(\frac{C_B}{C_L}\right)^{\frac{1}{1-K}}}{1 - \left(\frac{C_B}{C_L}\right)^{\frac{1}{1-K}}} \tag{2.28}$$

It can be seen from Figure 2.12 that as a result of concentration increase close to the solidification front the layers of solid solution will be formed that are enriched with the B component to a higher extent that it is predicted by the system solidus.

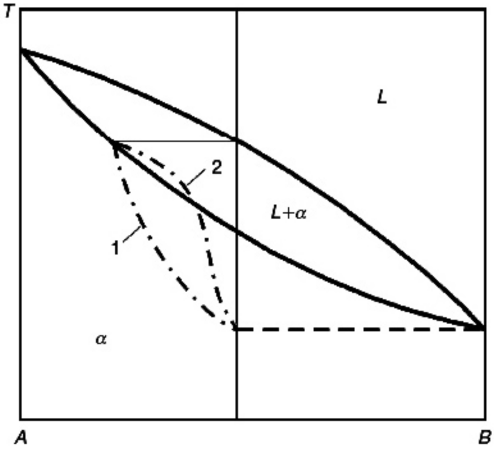

Figure 2.12 Schematic changes of the average concentration of solid solution during non-equilibrium solidification in the conditions of unrestricted homogenizing diffusion (curve 1 according to Ref. [80]) and partial diffusion in liquid phase (curve 2, according to Ref. [99]) with simultaneous suppression of diffusion in solid solution.

The average composition of solid solution in eutectic (or peritectic) systems after solidification can be calculated accurately using expression (2.20), if the volume fraction of non-equilibrium eutectic (or peritectic) can be determined experimentally.

2.5.1.3 Concentration threshold for appearance of non-equilibrium constituent particles (phases)

When diffusion is suppressed in solid solution and allowed near the solidification front (i.e., separating diffusion takes place), non-equilibrium solidification in eutectic and peritectic systems must end with appearance of the corresponding excessive phases even when the concentration of alloying element is vanishingly small. This effect was studied in detail in Refs. [65, 71, 80]. These predictions were confirmed experimentally for aluminum alloys with small amounts of alloying elements, which should be single-phase solid solutions according to the predictions based on equilibrium phase diagrams. A review of these results was published in Ref. [65].

In Table 2.1, we present experimental data [65] on the location of the concentration threshold for the formation of non-equilibrium eutectic in binary systems formed by Al and principal alloying elements at different solidification rates. For all studied systems, even at very low cooling rates, a significant shift of the eutectic appearance threshold takes place toward smaller concentrations of alloying element. In the Al–Cu and Al–Si systems the appearance of the second phase was documented even for minimal additions of copper and silicon (~0.1%). These results for alloys of any concentration imply that diffusion in the solid phase is practically suppressed for very low cooling rates. Increase in cooling rate does change the value of C_K substantially. At the same time, for Al–Zn and Al–Mg systems at very low cooling rates the point C_K is still pretty far from pure aluminum; if the cooling rate is increased to 1.33–1.67 K/s a more significant shift in the eutectic concentration threshold takes place toward smaller concentrations of Zn and Mg.

Table 2.1 Concentration threshold (C_K) of appearance of eutectic in binary systems with aluminum [65]

System	C^a (%)	$C_{K(min)}$ of alloying element corresponding to appearance of second phase* (%) for V_c (K/s)		
		0.01–0.33	1.33–1.67	16.7
Al–Zn	82.2	20	2	3
Al–Cu	5.7	0.1	0.1	0.3
Al–Mg	15.35	4.5	0.5	1.0
Al–Si	1.65	0.1	0.1	0.2

* All concentrations are determined by chemical or spectral analysis.

Most probably, these results can be explained by at least partial diffusion in solid solution for the systems with very low concentrations of alloying element. Moreover, this homogenizing diffusion takes place only in dendrite cell boundaries, where the concentration gradients are maximal. Experiments confirm that in dendrite cell centers this concentration is close to C_n (Figure 2.13) for any alloying element concentration. It is necessary to understand why homogenizing diffusion occurs in weakly alloyed systems, while in more concentrated alloys it is practically suppressed.

The maximal concentration jump inside dendrite cell is defined by the difference between concentration in the point of maximal solubility C_a and concentration C_n (Figure 2.13). At non-equilibrium solidification of alloy C_1 (system A–B in Figure 2.13a) the maximal $\Delta C = C_a - C_n^1$ will be significantly higher than that for a more concentrated alloy C_2 of the same system, and in the alloy C_1 with the same concentration of the second component in the system A–D (Figure 2.13b). For this latter system the concentration threshold for appearance of eutectic can be characterized by the value $(1 - C_K/C_a)$, and it will be located closer to pure component A, than in system A–B. The reason is that insignificant concentration gradient within a single dendritic cell even for weakly alloyed systems will not be sufficient for the homogenizing diffusion to occur, and solidification ends up with eutectic or peritectic transformation. In alloy C_2 of the system A–B eutectic will appear for the same reason – here ΔC is lower, since $C_n'' > C_n'$ at constant C_a (Figure 2.13a).

Another important factor is the temperature range of solidification ΔT. Let us compare systems A–B and A–C (Figure 2.13a) with the same concentration C_p, but different eutectic temperatures. In alloy C_1 the maximal concentration jump is about the $(C_a - C_n^1 \cong C_a - C_n''')$. However, in an A–C system with narrow solidification range this jump appears at higher temperatures, when diffusion processes proceed faster. For this reason the value of relative shift, $(1 - C_K/C_a)$, in the systems with narrow solidification range must be smaller than in the case of a broad solidification range. Indeed, in the latter even a big concentration jump may not result in significant homogenizing of solid solution as the temperature of the process is low.

Finally, there is the third principal parameter, which must affect non-equilibrium eutectics; it is the distribution coefficient K. Its value determines the character of distribution of alloying element across the crystallites, in particular, in the proximity to the boundaries [100]. The higher K, the steeper the concentration increase on the periphery of the dendrite cells will be. For the systems with K close to 1, the relative shift $(1 - C_K/C_a)$ at the same values of C_a and ΔT must be smaller compared to systems with broad solidification range (small K). Table 2.2 represents data on the maximal value of $(1 - C_K/C_a)$[18] in comparison to the values of C_a, ΔT, and K. This data indicates that the maximal shift $(1 - C_K/C_a)$ in all studied systems was more or less similar and close to unity. This happens for a number of reasons. In the case of Al–Cu and Al–Si systems

---

[18] Maximal shift for all cooling rates.

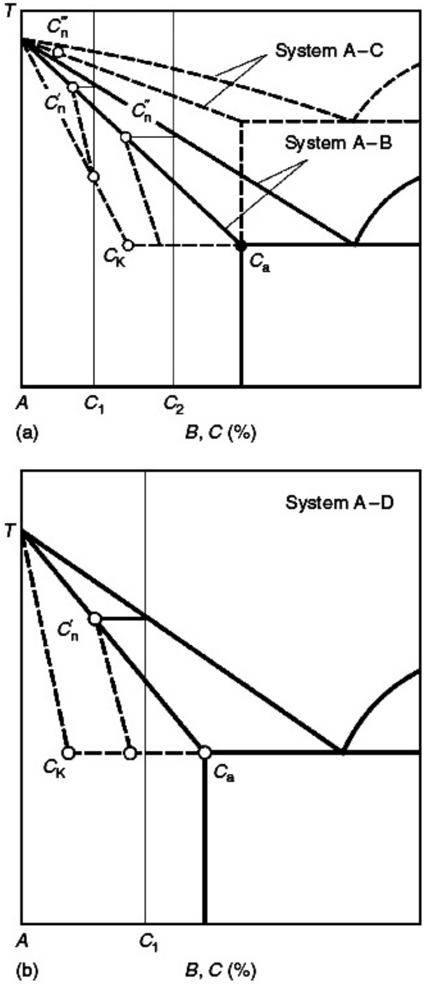

Figure 2.13 Illustration of the influence of phase diagram geometry upon concentration shift accompanying the appearance of non-equilibrium eutectic.

this is a considerable divergence of liquidus and solidus temperatures as functions of concentration; for Al–Zn and Al–Mg there is a broad solidification range; for Al–Si and Al–Cu there is also small limit solubility of alloying elements. In particular, the Al–Zn system demonstrates the need to account for all of these three parameters (C_a, ΔT, and K), when assessing the value of $(1 - C_K/C_a)$. When solidification rate is 1.67 K/s this shift attains maximal value, even in spite of the

Table 2.2 Relation between the concentration threshold of eutectic appearance in alloy microstructure and parameters of phase diagrams

System	$C_K{}^a$ (at.%)	$C_a{}^a$ (at.%)	ΔT^b (°C)	K^c	$1 - C_K/C_a$
Al–Zn	0.9	66.5	278	0.45	0.98
Al–Cu	0.04	2.5	112	0.17	0.98
Al–Mg	0.6	16.9	210	0.34	0.96
Al–Si	0.1	1.59	83	0.15	0.94

[a] Cooling rate 1.33-1.67 K/s.

[b] Difference between temperatures of eutectic and melting of aluminum.

[c] Distribution coefficients.

large values of C_a (66.5 at.%Zn) and of the distribution coefficient (0.45). However, the topology of the Al–Zn phase diagram is such that large concentration gradients in solid solution appear only in the lower part of the non-equilibrium solidification range, when diffusivities are low and homogenizing does not occur in dendritic cells at significant cooling rates. However, if the cooling rate is lower (e.g., 0.02–0.33 K/s), then non-equilibrium eutectic will be appearing only in alloys containing >20%Zn, while at cooling rate 1.67 K/s it appeared at 2%Zn (Table 2.1).

As can be seen from Table 2.1, the concentration threshold of non-equilibrium eutectic appearance goes in the "opposite direction" when cooling rate is increased to 16.7 K/s. However, this effect is insignificant and may be caused by disperse particles of the second phase which are difficult to distinguish from the defects of the polished surface itself at large magnifications of light microscope. By a similar token, this effect is difficult to measure using TEM or SEM because these particles are very scarce, located at large distance from each other and yet sufficiently massive to be transparent for electrons.

2.5.2 Influence of cooling rate upon solidification and formation of constituent particles of secondary (excessive) phases

2.5.2.1 Constituent particles

As it was demonstrated above, even weakly alloyed cast aluminum alloys may contain non-equilibrium phases – excessive constituent particles of eutectic or peritectic origin. These inclusions consist of very brittle particles, typically – of intermetallic compounds. Their volume fraction and average sizes exert strong influence upon the properties of alloys.

Principal alloying elements form such phases as β (Al_3Mg_2) in Al–Mg casting alloys; θ-phase ($CuAl_2$) in Al–Cu; θ and S (Al_2CuMg) in Al–Cu–Mg alloys; η ($MgZn_2$) and T (Al, Mg, Zn) in Al–Mg–Zn; Mg_2Si in Al–Mg–Si system, and so on. Practically all industrial aluminum alloys will contain iron-bearing

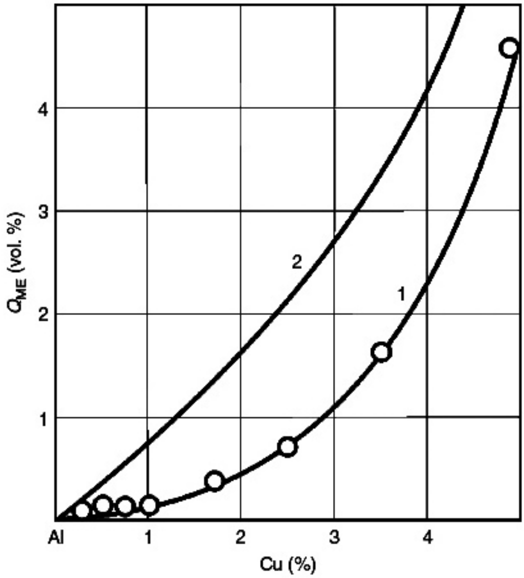

Figure 2.14 Dependence of the volume fraction of eutectic upon Cu concentration in Al–Cu alloys: 1 – experimental data for $Vc = 350°C/min$, 2 – calculation using formula (2.18).

constituents, often containing manganese and silicon. Constituent particles will also be formed if aluminum is alloyed with titanium, zirconium, chromium, etc. Detailed information about these phases can be found in Ref. [14].

For industrial range of cooling rates, when diffusion in (Al) is suppressed, the mass fraction of non-equilibrium eutectic (Q_{ME}) in a binary alloy with composition C_B is defined by the following equation:

$$Q_{ME} = \left(\frac{C_B}{C_E}\right)^{\frac{1}{1-K}} \tag{2.29}$$

In (2.29) C_E stands for the value of eutectic concentration [101]. Figure 2.14 illustrates the experimentally determined dependence of the volume fraction of non-equilibrium eutectic upon the concentration of Cu in aluminum for $V_c = 5.9\,K/s$. It can be seen that this value is close (in order of magnitude) to Q_{ME}. However, experimental points lie considerably lower than calculated according to formula (2.29), especially for small Cu concentrations.

Traditionally, it was believed [65] that the amount of non-equilibrium eutectic in a given alloy must increase if cooling rate is increased; it could become smaller only as a result of diffusionless solidification [85]. However, for a number of binary and multicomponent alloys it was demonstrated experimentally that this dependence is actually represented by curves with maximum (for the range of

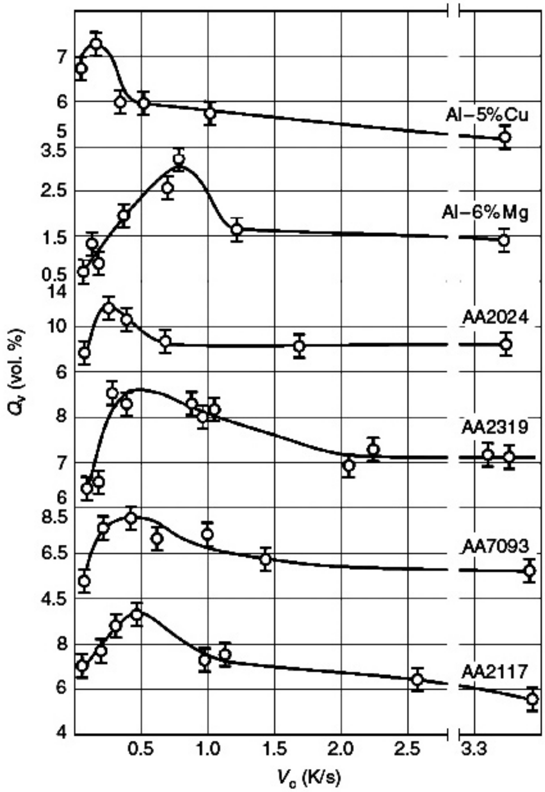

Figure 2.15 Dependence of the volume fraction of excessive microstructural components upon cooling rate during solidification in binary and ternary industrial aluminum alloys.

small cooling rates – 0.15–1 K/s). It is clear (see Figure 2.15) that diffusionless solidification is impossible under such conditions. It is important to emphasize that for cooling rates typically observed in industrial conditions the overall amount of excessive constituents either somewhat decreases or practically does not change.

If cooling rate grows the distribution of alloying elements in dendrite cells changes as well as the size of the cells themselves. At first the overall concentration of alloying elements in solid solution decreases, attains a minimum, then starts growing. Correspondingly, the amount of eutectic forming as a function of cooling rate yields a curve with a maximum. In industrial range of cooling rates the decrease of Q_{ME} is defined by the progressive suppression of homogenizing diffusion in the liquid phase. The concentration gradient that forms in the melt in the vicinity of solidification front (see Figure 2.6) results in the formation of layers

Table 2.3 Volume fraction (q_V) of non-equilibrium phases in commercial alloys

Alloy	Ingot D (mm)	V_c[a] (mm/min)	Analyzed area[b]	Concentration of alloying element (%)						Q_V (vol. %)
				Cu	Mg	Zn	Mn	Fe	Si	
~2017	410	44	C	4.06	0.69	0.14	0.70	0.31	–	5.3
			$\frac{1}{2}R$	4.36	0.68	0.14	0.67	0.32	–	5.9
			P	4.37	0.71	0.15	0.67	0.34	–	4.5
~2031	380	57	C	2.15	0.60	0.20	0.51	0.32	0.89	3.6
			$\frac{1}{2}R$	2.18	0.64	0.15	0.54	0.36	0.62	3.6
			P	2.22	0.64	0.19	0.54	0.35	0.95	3.4
~5556	520	22	C	0.04	6.20	–	0.56	0.17	0.13	3.5
			$\frac{1}{2}R$	0.04	6.60	–	0.55	0.19	0.15	3.9
			P	0.04	6.60	–	0.55	0.19	0.17	2.9
~7075	230	60	C	1.60	2.4	6.0	0.21	0.26	0.18	6.0
			$\frac{1}{2}R$	1.72	2.4	6.27	0.22	0.30	0.20	7.0
			P	1.75	2.4	6.25	0.19	0.25	0.21	5.4

[a] Casting rate.

[b] C: ingot center; P: periphery (close to surface).

of solid solution progressively more and more enriched with alloying element in amounts exceeding predictions according to equilibrium phase diagram(s). As a result of this process with growing solidification rate C'_{L} (see Figure 2.6) alloying of solid solution increases, while the volume fraction of eutectic decreases.

The initial growth Q_{ME} at low solidification rates (Figure 2.15) in most cases is defined by the progressing suppression of diffusion in the solid phase. It should be emphasized that in casting slowly cooled down below the solidus temperature the volume fraction of non-equilibrium phases may be somewhat lower than predicted by Figure 2.15, because in most experiments [65] the slowly cooled castings were quenched into water immediately after solidification in order to prevent homogenization. In industrial castings and especially in the case of semi-continuous casting the rate of solidification is different across the cross-section of castings. For this reason in the central parts of wrought alloy ingots the overall amount of non-equilibrium microstructure components is appreciably higher than on the periphery (Table 2.3), where solidification proceeds faster. It is interesting that the maximal solidification rates both in the center and on periphery lie to the right from the maximum in Figure 2.15. As can be seen from Figure 2.15, this effect is not related to microsegregation. Similar results are obtained for large shape castings made of Al–Si and Al–Si–Mg alloys.

At a first glance it is difficult to understand why for some alloys at $\frac{1}{2}R$ the overall amount of non-equilibrium phases attains maximum (see Table 2.3). So far we always assumed that cooling rate is directly proportional to the solidification rate. This assumption seems to be quite reasonable for small laboratory castings, but when applied to large cross-section ingots it may result in large mistakes. When directional solidification experiments are conducted, the minimal solidification speed is observed not in the ingot center, but somewhere in between the center and the surface [102, 103]. Since microsegregation is defined, rigorously speaking, not by the cooling rate, but by the solidification speed, it becomes understandable why the overall amount of non-equilibrium phases may grow at distance $R/2$.

Volume fraction of such phases also depends not only upon solidification speed, but also on the molten metal superheating. In aluminum alloys such superheating increases solubility of alloying elements in solid solution and, respectively, reduces the amount of non-equilibrium eutectic, (see Figure 2.8).

2.5.2.2 Suppression of peritectic reactions

Studies of the structure of aluminum castings in which peritectic phase reactions are supposed to take place indicate that the traces of these transformations can be detected at low solidification rates (as a rule, in the form of thin layers of the "new" phase on the surface of the "old" one). An interesting feature of such structures is related to the low cooling rate (V_c): the morphology of most particles of the "old" phases practically does not change. In the case of casting into metallic molds, when V_c is significantly higher, peritectic reactions will be almost completely suppressed. Assuming the absence of metastable phases one could come up with the following scenario for non-equilibrium solidification with peritectic transformations for relatively low cooling rates (10–100 K/s):

1. All peritectic reactions are completely suppressed.
2. All eutectic reactions proceed according to the equilibrium phase diagrams.

Using these assumptions, one can consider a principal scheme for non-equilibrium solidification of binary alloys with one eutectic and two peritectic reactions (Figure 2.16a). This will help illustrate the basic principles of the proposed analysis technique.

If alloy compositions lie to the left of the point P_1 (Figure 2.16) any "excessive" phases will be absent because there are no peritectic reactions. In between the points P_1 and P_2 an "extra" phase Y will appear because of the suppression of peritectic reaction $L + Y \Rightarrow X$. Similarly, to the right from point P an "extra" phase Z will appear as a result of peritectic reaction $L + Z \Rightarrow Y$. To denote the boundaries between different phase domains it is necessary to plot vertical lines. Non-equilibrium solidification diagram (Figure 2.16) indicates that only for alloy #1 its phase composition will correspond to equilibrium $(A + X)$; in alloys 2 and 3

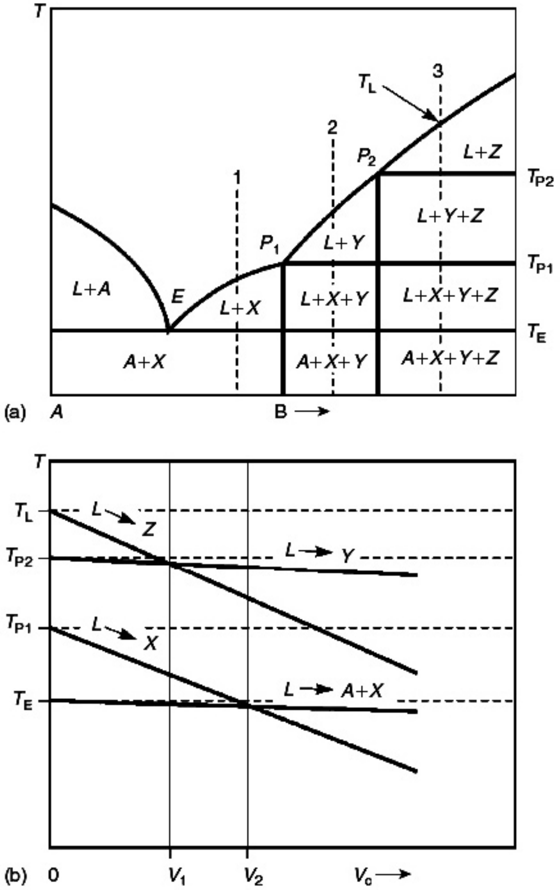

Figure 2.16 Schematic explaining (a) the formation of non-equilibrium phases during solidification of binary alloys and (b) Influence of cooling rate upon temperature of the formation of phases during non-equilibrium solidification.

there will be more phases than allowed by the equilibrium phase diagram – three $(A+X+Y)$ and four $(A+X+Y+Z)$, respectively.

It is known that as V_c is increased supercooling (ΔT) required for initiation of a given solidification phase reaction also grows. For this reason, it is justified to use non-equilibrium phase diagrams (Figure 2.16a) only for sufficiently small values of ΔT. Inasmuch as the increase of V_c with ΔT for different reactions will be non-uniform, a possibility exists that the solidification sequence will be changed as well as cast-alloy's microstructure.

Figure 2.16b illustrates the tentative influence of V_c upon the temperature of onset of the corresponding solidification reactions as applied to alloy 3. It follows from Figure 2.16a that the sequence of phase reactions will not be changed only if $V_c < V_{c1}$. Such alloys will contain three types of phases X, Y, Z and eutectic $A+X$. In the range $V_{c1} < V_c < V_{c2}$ precipitation of the Y phase will commence earlier than Z, while at $V_c > V_{c2}$ eutectic reaction $L \Rightarrow A + X$ will be preceded by the solidification of crystals of the X phase. Furthermore, it may be hypothesized that solidification of low-temperature phase may suppress the formation of equilibrium higher-temperature phase, for example, due to a higher value of ΔT required for its nucleation as the volume fraction of the low-temperature phase grows. This explains why in as-cast microstructure sometimes only one or two types of primary aluminum crystals can be found, not three. If phases X, Y, and Z have different morphologies, then by changing the V_c at least in principle, it becomes possible to significantly influence microstructure and, consequently, alloy properties.

2.6 NON-EQUILIBRIUM SOLIDIFICATION OF MULTI-COMPONENT ALLOYS

Analysis of non-equilibrium solidification in ternary and other multicomponent alloys is much more difficult than for binary alloys. Depending upon solidification conditions (first of all, solidification rate) different types of deviations from equilibrium conditions can develop. Let us consider several specific examples of deviation from equilibrium for solidification processes occurring in real three- and four-component systems.

2.6.1 Non-equilibrium phase diagrams of multicomponent systems

Assuming that the relations and rules described above will also hold for multicomponent systems, we have conducted analyses of non-equilibrium solidification for aluminum alloys of some three- and four-component systems containing iron. These results are mostly related to alloys containing (Al) formed directly after solidification; however, the same methods could be applied with equal success to different alloy systems.

2.6.1.1 System Al–Fe–Si

Inasmuch as this system is key for understanding the behavior and properties of so-called "technical' aluminum, there are many studies exploring non-equilibrium phase compositions and diagrams. In particular, the distribution of phase domains in as-cast condition was conducted by Philips [40]. It follows from his study that a significant part of the concentration field is occupied by four- and five-phase alloys (Figure 2.17a) – the most obvious proof of non-equilibrium nature of the corresponding alloys. The concentration fields of primary solidification of Al_3Fe,

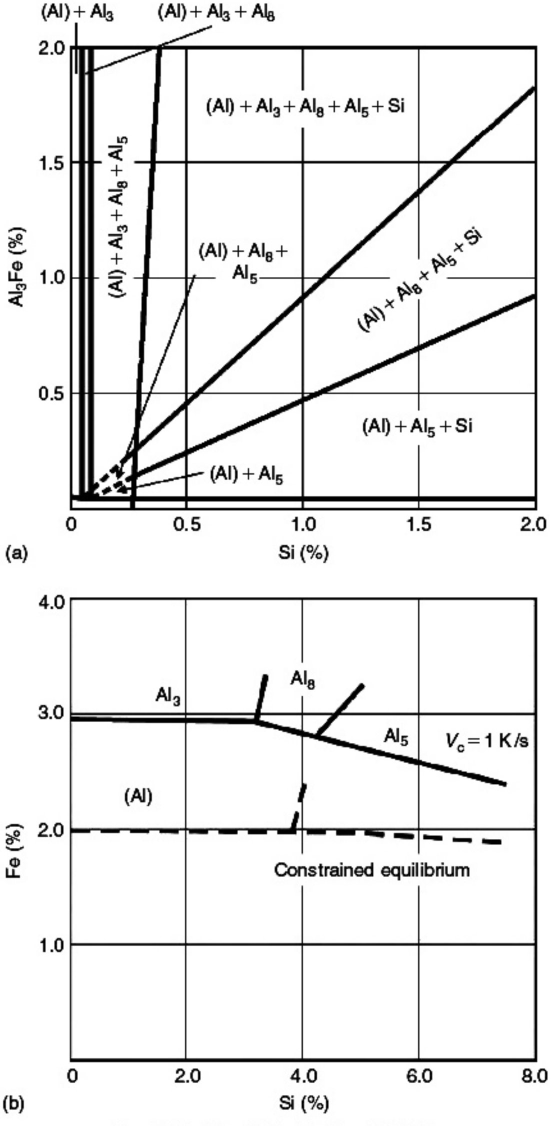

Al_3–Al_3Fe, Al_8–Al_8Fe_2Si, Al_5–Al_5FeSi

Figure 2.17 (a) Non-equilibrium distribution of the phase domains in the Al–Fe–Si system [40] and (b) Schematic illustrating the influence of solidification rate upon location of the domains of primary solidification in the same system [104].

Al_8Fe_2Si, and Al_5FeSi undergo shifts toward lower concentrations of Si (Figure 2.17b) as a function of the solidification rate V_c [104]. As a consequence, the probability of the Al_3Fe phase formation at elevated solidification rates becomes smaller even for alloys containing 2–3%Fe.

At relatively low values of V_c ($V_1 = 10^{-2}$–10^{-1} K/s) the onset of solidification can be analyzed correctly using equilibrium phase diagrams. However, the formation of primary (Al) crystals must be followed by binary eutectic reactions. In some alloys, because of the suppression of peritectic phase reactions, all three Fe-bearing binary eutectics can be formed. Non-equilibrium solidus temperature for most such alloys is equal to 576°C and corresponds to solidification according to this ternary eutectic reaction: $L \Rightarrow (Al) + (Si) + Al_5FeSi$. Consequently, only those alloys the chemical compositions of which lie in a narrow range along binary systems could solidify with the formation of binary eutectics.

In slowly solidified alloys containing Fe (>0.5%), the suppression of peritectic transformations $L + Al_8Fe_2Si \Rightarrow (Al) + Al_5FeSi$ and $L + Al_3Fe \Rightarrow (Al) + Al_8Fe_2Si)$ results in the following sequence of phase fields with growing silicon concentration (not counting (Al)): Al_3Fe; $Al_3Fe + Al_8Fe_2Si$; $Al_3Fe + Al_8Fe_2Si + Al_5FeSi$; $Al_3Fe + Al_8Fe_2Si + Al_5FeSi + (Si)$; $Al_8Fe_2Si + Al_5FeSi + (Si)$; $Al_5FeSi + (Si)$. This is in good agreement with the distribution of phases proposed in Ref. [40] (see Figure 2.17a). This can be traced in greater detail upon the polythermal cross-section (Al–1.7%Fe)–Si at different cooling rates (Figures 2.18a–c), and also gives a possibility to determine the critical temperatures as a function of silicon concentration.

When the solidification rate becomes higher ($V_2 = 10^0$–10^2 K/s) an appreciable shift in the position of the liquidus surface boundaries will take place (Figure 2.17b). In turn, this causes shifts in the boundaries corresponding to intermediate reactions (Figure 2.17b) and phase fields in as-cast state compared to the state obtained when the solidification rate is lower, V_1. In addition to these changes, at certain concentrations of Fe and Si eutectic reactions $L \Rightarrow (Al) + Al_5FeSi$ and $L \Rightarrow (Al) + (Si) + AlFeSi_5$ will also be suppressed. As a consequence, in as-cast state the Al_5FeSi phase will be absent, and phases Al_8Fe_2Si and (Si) will be present instead. In order to explain this experimental fact we propose to use a hypothesis already discussed in Section 2.2.2 for the case of a binary system, namely: rapid solidification results in significant supercooling ΔT, which is different for different eutectics. As far as the Al–Fe–Si system is concerned, the absence of Al_3Fe and Al_5FeSi at 2–3%Si and 2–3%Fe could be explained by the following reasons:

1. Eutectic reaction $L \Rightarrow (Al) + Al_3Fe$ is characterized by a significantly higher value of ΔT in comparison to eutectic reaction $L \Rightarrow (Al) + Al_8Fe_2Si$, and for this reason the formation of Al_3Fe constituent particles is suppressed.
2. Additionally, the formation of Al_5FeSi could be impeded due to the presence of substantial amounts of the Al_8Fe_2Si phase formed earlier – this might increase the supercooling threshold ΔT, required for the formation of Al_5FeSi phase.

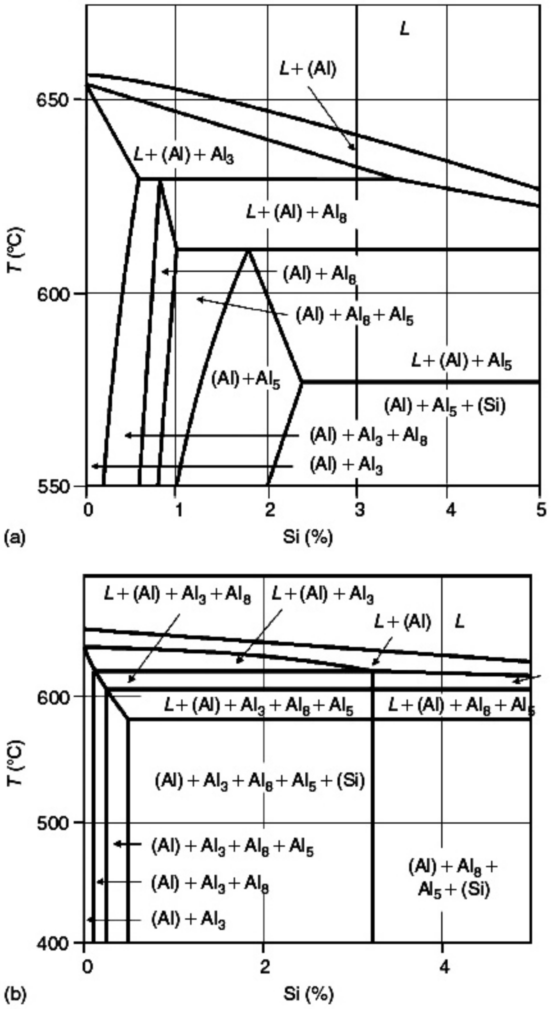

Figure 2.18 Influence of cooling rate upon the nature of polythermal cross-section (Al–1.7%Fe)–Si: (a) equilibrium conditions, (b) $V_c = 10^{-2}$ K/s, and (c) $V_c = 10$ K/s.

As a result of the suppression of eutectic reaction $L \Rightarrow (\mathrm{Al}) + \mathrm{Al_5FeSi}$ solidification will proceed according to the scheme $L \Rightarrow (\mathrm{Al}) + \mathrm{Al_8Fe_2Si}$. Moreover, ternary eutectic reaction $L \Rightarrow (\mathrm{Al}) + (\mathrm{Si}) + \mathrm{Al_5FeSi}$ could even be replaced by a hypothetical reaction $L \Rightarrow (\mathrm{Al}) + (\mathrm{Si}) + \mathrm{Al_8Fe_2Si}$. Because of the low concentration of iron in ternary eutectic its structure becomes "degenerate": colonies of

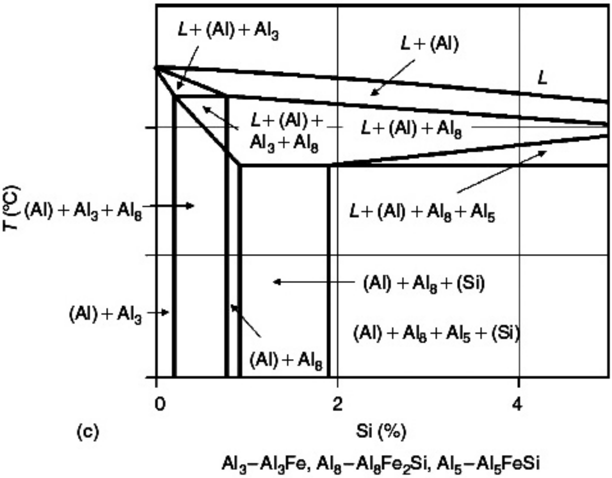

Figure 2.18 (*Continued*)

(Al) + (Si) or small amounts of (Si) decorating the boundaries of dendritic cells of (Al) solid solution.

Utilizing the results of analysis conducted above and experimental data on phase composition of cast alloys, it becomes possible to obtain the phase-field distribution in as-cast state corresponding to casting into metallic molds (V_c about 10 K/s, see Figures 2.19 and 2.20). It is very different from the non-equilibrium solidification diagram constructed for slower solidification (Figure 2.17a). Polythermal cross-section (Al–1.7%Fe)–Si for solidification rate V_2 (Figure 2.18) illustrates the influence of V_c very clearly. Rapid solidification results in a different set of phase fields in comparison to V_1: Al_3Fe; $Al_3Fe + Al_8Fe_2Si$; $(Si) + Al_3Fe + Al_8Fe_2Si$; $(Si) + Al_8Fe_2Si$; $(Si) + Al_8Fe_2Si + Al_5FeSi$; $(Si) + Al_5FeSi$. This fact has fundamental importance for low-silicon Al–Si alloys containing increased amounts of Fe because the morphology of the Al_8Fe_2Si phase is much better for alloy mechanical properties compared to all other Fe-bearing phases.

Literature data presented in Ref. [105] indicate that in pure aluminum ("technical" purity) and in alloys with small amounts of alloying elements containing up to 0.5%Fe and 0.5%Si different stable and metastable phases will be formed, which are close in chemical composition but possess different crystalline lattices. These phases can also be formed out of solid solution in the course of homogenization heat treatment. Among these phases one should mention the metastable modifications of Al_8Fe_2Si [6]. If the homogenization temperature is sufficiently high, these metastable phases, as a rule, will be transformed into the corresponding equilibrium phases.

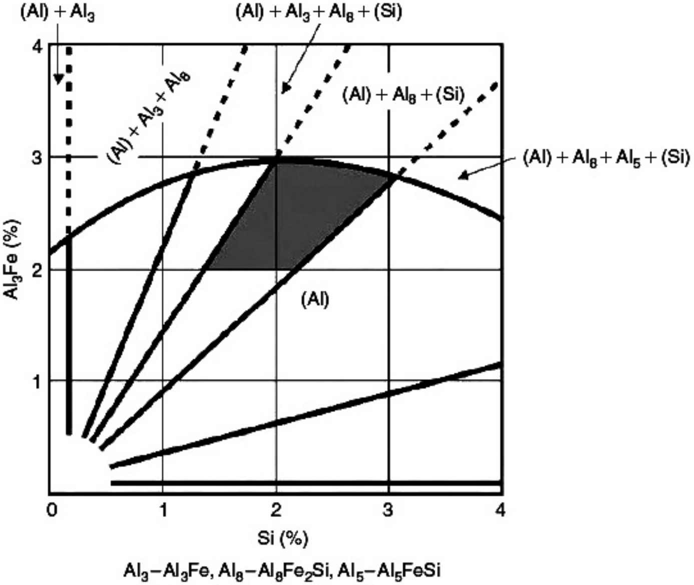

Figure 2.19 Distribution of phase domains in as-cast condition ($V_c = 10$ K/s) in the Al–Fe–Si system.

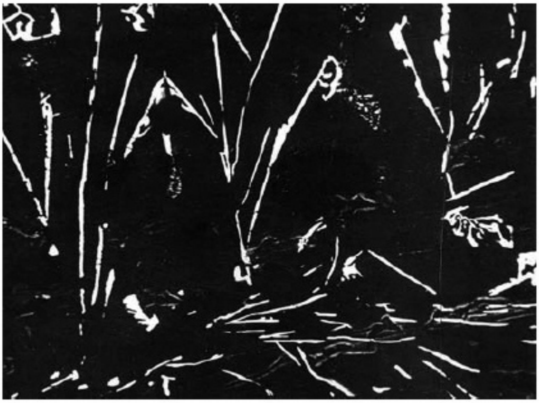

Figure 2.20 Microstructure of as-cast alloy Al–2.3%Fe–2.3%Si: (a) $V_c = 10^{-2}$ K/s and (b) $V_c = 10$ K/s.

2.6.1.2 System Al–Cu–Fe–Si

Using the most probable variant of this phase diagram (see Section 1.3.8) one can see that in most industrial Al–Si alloys (5–12%Si, up to 6%Cu, up to 1%Fe) iron is present in the form of the Al_5FeSi phase, which does not enter any peritectic reactions. For this reason phase composition of Cu-bearing alloys in solid state will correspond to equilibrium (Al) + (Si) + Al_2Cu + Al_5FeSi.

At lower concentration of Si and higher concentration of Cu the following two peritectic reactions may occur:

$$L + Al_8Fe_2Si \Rightarrow (Al) + Al_5FeSi + Al_7FeCu_2;$$

$$L + Al_7FeCu_2 \Rightarrow (Al) + (Si) + Al_5FeSi$$

These reactions, if incomplete, may result in the appearance of "excess" phases Al_8Fe_2Si and Al_7FeCu_2. The sequences of phase reactions corresponding to equilibrium and non-equilibrium solidification of alloy Al–2.5%Fe–5%Cu–2.5%Si are presented in Figure 2.21.

As concentration of Fe grows and concentration of Si decreases, the possibility of suppressing the peritectic reactions $L + Al_3Fe \Rightarrow (Al) + Al_8Fe_2Si + Al_6(FeCu)$; $L + Al_6(FeCu) \Rightarrow (Al) + Al_8Fe_2Si + Al_7FeCu_2$ becomes higher, which may result in the formation of such phases as $Al_6(FeCu)$ and Al_3Fe.

Faster solidification (in metallic molds) of ternary Al–Fe–Si alloys and quaternary alloys containing 2–3%Fe and 2–3%Si, suppresses the formation of equilibrium phase Al_5FeSi. These results in non-equilibrium phase composition of cast alloys: (Al) + (Si) + Al_2Cu + Al_8Fe_2Si. This exerts positive influence upon mechanical properties because the Al_8Fe_2Si morphology (Figure 2.20a) is more favorable than that of Al_5FeSi.

2.6.1.3 System Al–Fe–Mg–Si

As follows from the equilibrium phase diagram (Section 2.1) there are four Fe-bearing phases in the Al corner of phase diagram: Al_3Fe, Al_8Fe_2Si, Al_5FeSi, and $Al_8FeMg_3Si_6$. These phases may form as primary crystals or as a result of different eutectic and peritectic reactions (Table 1.32). Primary crystals of the first phase usually can be detected only when $C_{Si} < 3\%$ and $C_{Fe} > 2\%$. The last phase will be formed only when $C_{Si} > 7\%$, $C_{Mg} > 1\%$, and $C_{Fe} < 0.5\%$.

Similar to ternary system Al–Fe–Si, increased cooling rate will result in decreased phase domain corresponding to solidification of Al_3Fe. In alloys with increased Mg content, as it follows from equilibrium phase diagram Al–Fe–Mg–Si, in the presence of iron and irrespective of the silicon concentration, only one iron-bearing phase can be formed – Al_3Fe.

However, in industrial Al–Mg alloys with additions of Fe and Si, which contain less than 6%Mg obtained by casting into metallic molds, another Fe-bearing phase can be often formed (i.e., Al_8Fe_2Si). As in the case of ternary system Al–Fe–Si it can be explained by the influence of solidification rate. The higher the V_c, the higher the probability of the Al_8Fe_2Si phase formation. This can be illustrated using the liquidus projection of quaternary phase diagram (Figure 2.22). Dashed line in this figure illustrates the shift of the binary eutectic reaction boundary: $L \Rightarrow (Al) + Al_3Fe$ toward the Al–Mg side of the diagram as V_c increases (from line $D–N–O–P–I$ to line $D'–N'–I'$).

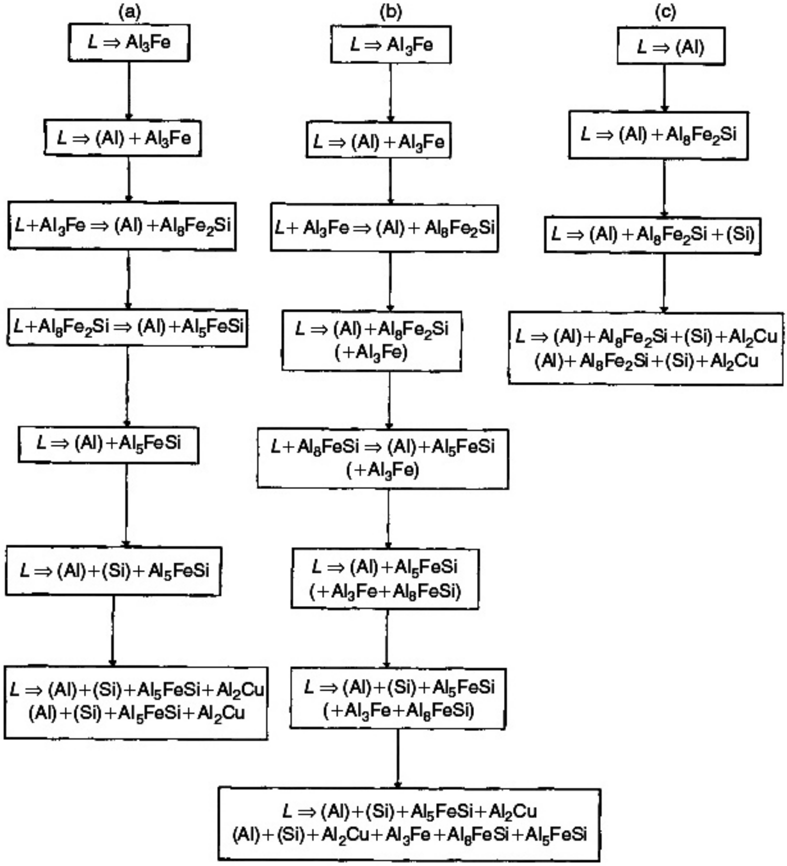
(a)
L ⇒ Al3Fe
L ⇒ (Al) + Al3Fe
L+Al3Fe ⇒ (Al) +Al8Fe2Si
L+Al8Fe2Si ⇒ (Al) +Al5FeSi
L ⇒ (Al) +Al5FeSi
L ⇒ (Al)+(Si)+ Al5FeSi
L ⇒ (Al)+(Si)+Al5FeSi+ Al2Cu
(Al) +(Si) +Al5FeSi+ Al2Cu
(b)
L ⇒ Al3Fe
L ⇒ (Al) +Al3Fe
L+ Al3Fe ⇒ (Al)+ Al8Fe2Si
L ⇒ (Al) +Al8Fe2Si
(+Al3Fe)
L+ Al8FeSi ⇒ (Al)+Al5FeSi
(+Al3Fe)
L ⇒ (Al) +Al5FeSi
(+Al3Fe+ Al8FeSi)
L ⇒ (Al)+(Si)+Al5FeSi
(+Al3Fe+Al8FeSi)
L ⇒ (Al)+(Si)+Al5FeSi+Al2Cu
(Al)+ (Si)+Al2Cu+ Al3Fe +Al8FeSi +Al5FeSi
(c)
L ⇒ (Al)
L ⇒ (Al) +Al8Fe2Si
L ⇒ (Al) +Al8Fe2Si + (Si)
L ⇒ (Al)+ Al8Fe2Si+(Si)+Al2Cu
(Al)+ Al8Fe2Si+(Si)+Al2Cu

Figure 2.21 Phase reactions taking place during (a) equilibrium and (b, c) non-equilibrium solidification. Solidification of alloy Al–2.5%Fe–5%Cu–2.5%Si, (b) $V_c = 10^{-2}$ K/s, and (c) $V_c = 10$ K/s.

Correspondingly, the eutectic domain $L \Rightarrow (Al) + Al_8Fe_2Si$ should broaden. As a result, the influence of the Fe concentration upon the phase composition of cast Al–Mg alloys also changes, see line S_0–S_3. This implies that in alloys belonging to the S_0–S_2 domain, after the completion of solidification of (Al) and binary eutectic reactions $(Al) + Mg_2Si$ or $(Al) + Al_8Fe_2Si$, a quaternary eutectic reaction $L \Rightarrow (Al) + Mg_2Si + Al_8Fe_2Si$ will occur. At large concentrations of magnesium, this reaction could degenerate into non-variant eutectic reaction $L \Rightarrow (Al) + Mg_2Si + Al_8Mg_5 + Al_8Fe_2Si$ (see point N'). Solidification of binary eutectic $(Al) + Al_3Fe$ is possible only in the S_2–S_1 domain. This

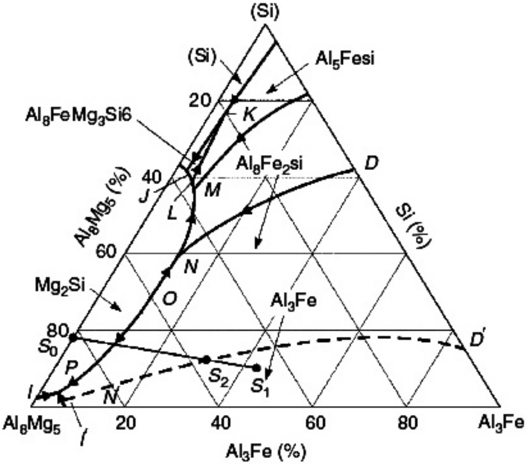

Figure 2.22 Influence of cooling rate upon the position of the onset of solidification domains for binary eutectics in the Al–Fe–Mg–Si system (solid lines, equilibrium variant; dashed line, $V_c = 10$ K/s).

idea is illustrated by non-equilibrium variants of the polythermal cross-section (Al–6%Mg–0.5%Si)–Fe for two different solidification rates (see Figure 2.22).

As far as Si-bearing casting alloys are concerned, the principal difficulty of their microstructure analysis is related to the peritectic reaction: $L + Al_5FeSi \Rightarrow (Al) + (Si) + Al_8FeMg_3Si_6$ (Table 1.32). For this reason below we consider solidification of alloys containing 10%Si, 0–2%Mg, and 0–0.5%Fe, in which the influence of the degree of completion of this phase reaction upon microstructure is maximally expressed. Since the solidification of these alloys involves the formation of (Al) and binary eutectic $L \Rightarrow (Al) + (Si)$, the analysis of multi-phase transformations becomes much easier.

More specifically, in the considered domain the following three eutectic reactions may take place (Table 1.32):

$$L \Rightarrow (Al) + (Si) + Al_5FeSi$$

$$L \Rightarrow (Al) + (Si) + Al_8FeMg_3Si_6$$

$$L \Rightarrow (Al) + (Si) + Mg_2Si$$

Solidus temperature for most alloys is equal to 554°C, which corresponds to the temperature of formation of the quaternary eutectic: $L \Rightarrow (Al) + (Si) + Mg_2Si + Al_8FeMg_3Si_6$. Consequently, only a fraction of all alloys solidifies according to the four-phase eutectic reactions. Using the calculated values for five-phase transformation boundaries, one could propose the following phase distribution for as-cast alloys belonging to the Al–10%Si–Fe–Mg cross-section (Figure 2.23a). Dashed curve corresponds to the appearance of the

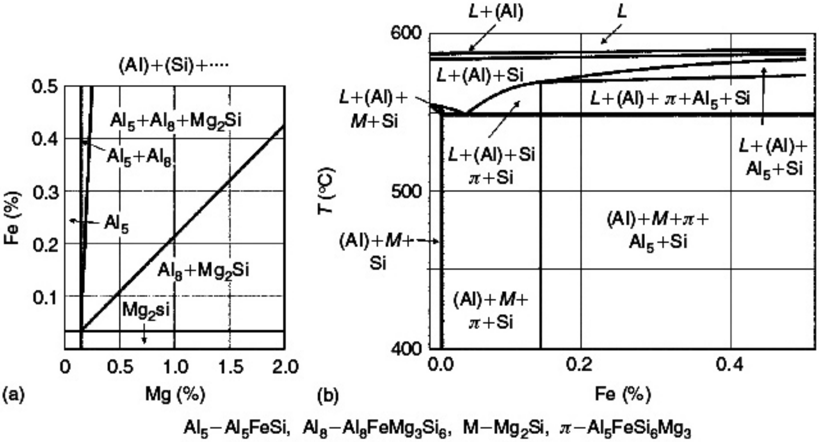

Figure 2.23 Distribution of phase domains for alloys of the (a) Al–Fe–Mg–Si system and (b) polythermal cross-section (Al–10% Si–1% Mg)–Fe, for non-equilibrium solidification conditions ($V_c = 10^{-2}$ K/s).

Al_5FeSi phase, which for the larger fraction of the considered domain should be considered "excessive". The influence of iron concentration upon phase composition can be traced using the polythermal cross-section (Al)–10%Si–1%Mg–Fe (Figure 2.23b). This figure illustrates the following sequence of phase formation (all alloys contain (Al) and (Si)): Mg_2Si; $Mg_2Si + Al_8FeMg_3Si_6$; and $Mg_2Si + Al_5FeSi + Al_8FeMg_3Si_6$. It immediately becomes clear from the analysis of this cross-section why an "extra" phase Al_5FeSi appears in microstructure of as-cast alloys even at small Fe concentrations, at which it should be entering completely into the composition of quaternary compound $Al_8FeMg_3Si_6$. The Fe–5% Cu–2.5%Si cross-section is illustrated by Figure 2.21.

2.6.1.4 Al–Fe–Ni–Si system

Analysis of non-equilibrium solidification in this system has practical significance. This is becasue nickel enters into chemical compositions of a number of important alloys (such as engine piston alloys); additionally, several peritectic reactions exert strong influence upon alloy microstructure.

As a rule, nickel is introduced into alloy compositions in order to induce the formation of a ternary compound, Al_9FeNi, which exerts positive influence upon such alloy characteristics as thermal stability. To minimize the negative impact of this phase upon formability and plasticity, the inclusions of Al_9FeNi must have favorable morphology – globular or "skeletal" (sometimes called "Chinese script" in the literature). Such morphology could be realized if this phase is formed according to a eutectic phase reaction.

On the other hand, iron should not form phases with needle-like morphology, in particular, Al_3Fe and Al_5FeSi. It should be noted that the ratio Fe:Ni = 1:1 is

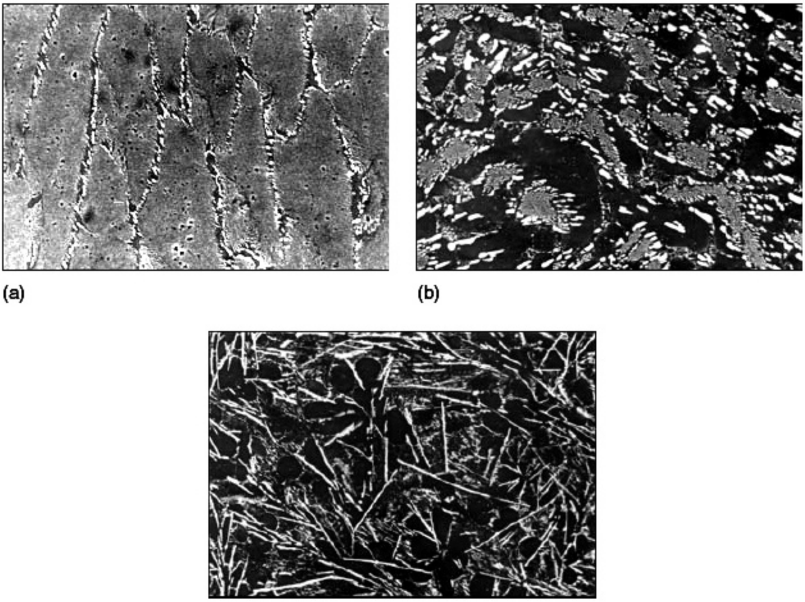

(a) (b)

(c)

Figure 2.24 Influence of the Si concentration upon morphology of iron-bearing phases in alloy Al–1.7% Fe–1.7%Ni: (a) 0%Si, phase Al_9FeNi; (b) 5% Si, phase Al_9FeNi; and (c) 12%Si, phases Al_5FeSi and Al_9FeNi.

sufficient only for alloys containing less than 5–6%Si. When the Si concentration is higher, there is always the danger of forming the needles of the Al_5FeSi phase – either as constituent particles forming directly from liquid phase or as a result of eutectic reactions. The microstructure of three alloys containing 1.7%Fe and 1.7%Ni each demonstrates strong influence of Si upon morphology of Fe-bearing phases (Figures 2.24a–c). To account for this influence, it is proposed to employ the variant of the Al–Fe–Ni–Si phase diagram (see Section 1.3.12) in which peritectic phase transformations are suppressed.

Out of three non-variant transformations taking place in this system (Table 1.36), for Si-bearing casting alloys the most important reaction is $L + Al_5FeSi \Rightarrow (Al) + (Si) + Al_9FeNi$. If it is not completed, an "excessive" Al_5FeSi phase may appear in alloy microstructure. Polythermal cross-sections Al–5%Si–1%Fe–Ni and Al–8%Si–1%Fe–Ni (Figures 2.25a and b) allow determining the minimal concentration of nickel (C_1) at which all iron will be tied up by the T phase (Al_9FeNi).

At 5%Si the value of C_1 is equal to 1%, that is the Fe:Ni = 1:1 ratio ensures solidification of only one Fe-bearing phase – Al_9FeNi (T). On the other hand, at 8%Si peritectic reactions $L + Al_5FeSi \Rightarrow (Al) + Al_9FeNi$ and

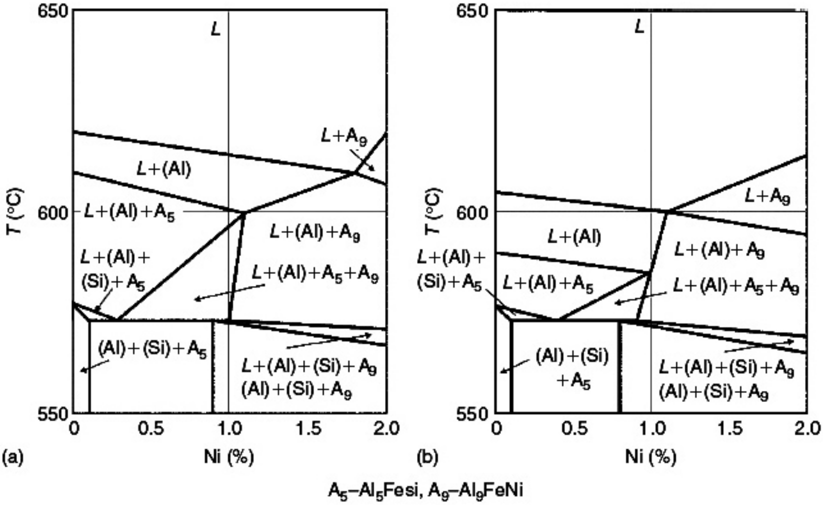

Figure 2.25 Non-equilibrium polythermal cross-sections of the Al–Fe–Ni–Si phase diagram at $V_c = 10^{-2}$ K/s: (a) 5%Si and 1%Fe; and (b) 8%Si and 1%Fe.

$L + Al_5FeSi \Rightarrow (Al) + (Si) + Al_9FeNi$ are suppressed. This implies that to ensure complete binding of Fe into the T phase C_1 must be greater than 1%. At 8%Si and 0.4%Fe the optimal range of Ni concentrations must be within the limits from 0.6 to 1%. At higher Ni concentrations the formation of Al_9FeNi constituent particles becomes possible. When the Fe concentration is raised to 0.8%, this range becomes even narrower. At even higher concentrations of iron and silicon alloying with nickel is no longer feasible because it is impossible to avoid the formation of sharp needle-like crystals of Al_5FeSi or coarse constituent particles of Al_9FeNi [106].

Polythermal cross-section at 5%Si indicates (Figure 2.25a) that in alloys with small amounts of silicon nickel can be used more effectively as an alloying addition compared to alloys containing more than 8%Si. When Ni and Fe concentrations fall in the range from 1% to 1.7%, a eutectic will be formed, $(Al) + Al_9FeNi$, which has more disperse and refined microstructure than at lower concentrations of the same elements (Figure 2.24) [107]. As a result the particles of the T-phase can be more easily broken and fragmented when heated for SHT and quench (also see Section 3.1.3).

2.6.2 Microsegregation in three-component and industrial aluminum alloys

2.6.2.1 Microsegregation of the key alloying elements

Experimental data is available in the literature on the distributions of different alloying elements across the metallic grains and the degree of microsegregation in multi-component alloys, including aluminum [89, 108–111]. In particular it was demonstrated [89], that the severity of microsegregation of each component is determined by its equilibrium distribution coefficient in binary alloys with aluminum. However, according to Refs. [112–114], the mutual influence of components upon their distribution coefficients should become pronounced already in ternary systems. In any case, to predict correctly the minimal and the maximal concentrations of alloying elements in solid solution, it is important to know and understand the corresponding phase diagram and to be able to determine the positions of tie-lines under different conditions of non-equilibrium solidification.

These problems were extensively explored in the computational and experimental works of Kuznetsov *et al.* [94, 95, 115] on non-equilibrium solidification of ternary and more complex (up to 11-component) alloys. In thermodynamic calculations some experimental data was usually used, in particular, the minimal and the maximal concentrations of alloying elements in (Al) obtained from X-ray spectrometry data. In this case the calculated concentration profiles, phase composition, and the results of other computations were quite close to experimental data. Calculations have been conducted for such conditions of non-equilibrium solidification when diffusion in the solid phase was completely suppressed, while separating diffusion was either complete or partial, close to complete.[19]

In particular, experiments with three-component alloys have been conducted. All alloys were prepared out of high-purity components; solidification rate was maintained at 0.16, 1, and ~16 K/s [116]. Alloy compositions are presented in Table 2.4.

Figure 2.26 represents isotherms of mutual solubility of magnesium and zinc in the Al–Mg–Zn system. The figurative points corresponding to alloys of five different compositions are presented in the same figure. As can be seen, they are located in the one-phase domain after the completion of equilibrium solidification. At room temperature all alloys with the exception of the first one, must comprise excessive phases precipitating out of Al-based solid solution (Al). After solidification constituent particles of non-equilibrium solidification origin were formed in all alloys, with a single exception of the first one. Table 2.4 provides data on the minimal ($C_{\min}$), the maximal ($C_{\max}$) concentrations of magnesium and zinc in dendritic cells of aluminum solid solution, as well as the concentration difference ΔC for all studied casting alloys (all values determined using X-ray spectrometry).

Analysis of data presented in Table 2.4 indicates that the concentrations of magnesium and zinc in the center and on periphery of dendritic cells are practically constant in all the range of the studied solidification rates. Consequently, the degree of microsegregation also does not depend upon the solidification rate. Similar conclusions were made by the authors of Ref. [89], which had conducted experiments with ternary Al–Cu–Mg alloys, and also in Ref. [138].

In order to understand the diffusion conditions corresponding to non-equilibrium solidification it was important to establish how close the alloying

---

[19] Similar calculations were conducted by Scheil and are called "the Scheil model" in the literature.

Table 2.4 Some characteristics of microsegregation in Al–Mg–Zn alloys [119]

Concentration in alloy (%)		V_c (K/s)	Zinc (%)			Magnesium (%)		
Zn	Mg		C_{min}	C_{max}	ΔC	C_{min}	C_{max}	ΔC
0.65	0.62	0.16	0.4	0.7	0.3	0.3	0.6	0.3
		1	0.6	0.9	0.3	0.4	0.6	0.2
		16	0.4	0.9	0.5	0.3	0.7	0.4
4.0	0.85	0.16	2.3	7.7	5.4	0.5	2.2	1.7
		1	2.8	8.0	5.2	0.5	2.2	1.7
		16	2.4	7.8	5.3	0.6	2.0	1.4
4.6	1.6	0.16	2.1	8.0	5.9	0.8	4.0	3.2
		1	2.1	7.8	5.7	0.8	3.7	2.9
		16	2.8	8.5	5.7	0.9	3.9	3.0
3.6	4.3	0.16	1.5	6.1	4.6	2.6	8.6	6.0
		1	1.5	6.2	4.7	2.6	8.6	4.2
		16	1.3	5.5	4.2	2.6	8.8	6.2
6.0	2.8	0.16	3.7	10.3	6.6	1.4	5.6	4.2
		1	3.8	10.2	6.4	1.5	5.5	4.0
		16	3.1	9.5	6.4	1.2	5.3	4.1

element concentrations in the dendrite cell center, C_1, are to their respective equilibrium values in aluminum solid solution, C_n, at the temperature of the onset of solidification. To determine C_n, one needs to know the position of the liquidus and solidus isotherms in the corresponding system, as well as the positions of the tie-lines. In the Al–Mg–Zn and Al–Cu–Mg systems such polytherms are constructed experimentally [116, 117]. The direction of tie-lines can be established using the method described in Ref. [118]. The authors of Ref. [118] obtained results close to the corresponding experimental values.

Table 2.5 calculated and experimental values of the concentrations of alloying elements at the temperatures of the onset of solidification are compared for some Al–Mg–Zn alloys. All calculations were conducted using the equilibrium values of the distribution coefficients for alloying elements. The values for C_1 presented in Table 2.5 are related only to one solidification rate. However, as it follows from

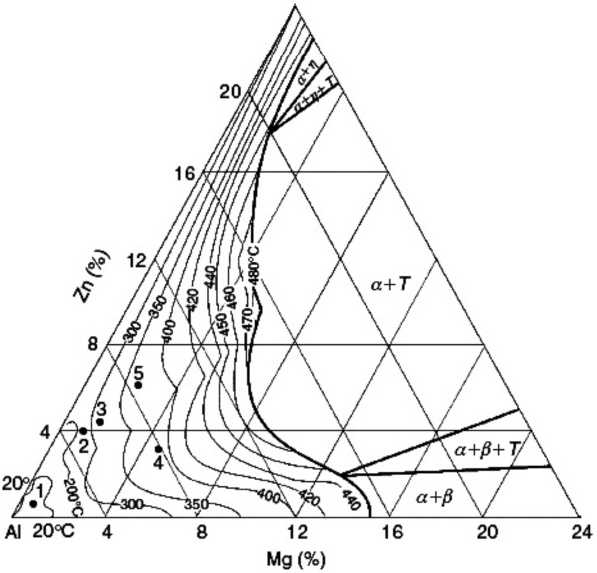
20
16
12
8
4
20%
Zn (%)
α+η
α+η+T
α+T
α+β+T
α+β
300
350
400
420
440
450
460
470
480°C
200°C
1
2
3
4
5
Al 20°C
4
8
12
16
20
24
Mg (%)

Figure 2.26 Isotherms of mutual solubility of Zn and Mg in aluminum solid solution [55].

Table 2.5 Concentration of alloying elements in the center of dendritic cells, C_1, and at the temperature of the onset of equilibrium solidification C_n [119]

Concentration in alloy (%)		C_1* (%)		C_n (%)	
Mg	Zn	Mg	Zn	Mg	Zn
0.62	0.65	0.3	0.4	0.2	0.2
0.85	4.0	0.6	2.4	0.5	2.2
1.6	4.6	0.3	2.1	0.6	1.9
4.3	3.6	2.6	1.3	1.4	1.2
2.8	6.0	1.5	3.1	1.5	1.4

* Solidification rate ~10K/s.

Table 2.4, at different solidification rates the minimal concentrations of alloying elements are practically the same.

The data presented in Table 2.5 clearly demonstrate the proximity of equilibrium calculated values C_n and the experimental values for the minimal concentration C_1 of alloying elements in aluminum solid solution. This represents direct evidence that in ternary (as well in binary) alloys solidification takes place under the conditions of almost complete suppression of diffusion in (Al) solid solution and unimpeded diffusion in the liquid phase.

The authors of Ref. [119] compared the experimental distribution coefficient curves for magnesium and zinc calculated using Ref. [118] for alloys, the composition of which was provided above. Non-equilibrium solidification was considered as the sequence of the initial moments of the onset of solidification for alloys the composition of which corresponded to the composition of the liquid phase that remained after each stage of this complex process. It was additionally assumed that diffusion is unimpeded at the solidification front and, consequently, the compositions of solid solution crystals should correspond to the equilibrium phase diagram.

All calculations were conducted for the following two cases:

1. Diffusion in the solid phase is suppressed, and in the liquid phases – comes to completion.
2. Diffusion in the solid phase is suppressed, while in the liquid phase is only partially unimpeded; in this latter case the layer of liquid phase before the solidification front is enriched with alloying additions.

In Ref. [120] it was demonstrated that the behavior of liquid and solid solutions in aluminum alloys could be described by the model of quasi-ideal diluted solutions. For this reason, in the first case one could use the distribution coefficients determined from equilibrium phase diagrams. In the second case effective distribution coefficients were used that were determined using the Pfann equation [121].

The calculated curves of the magnesium and zinc distribution across the dendritic cells were compared to the experimental values obtained for samples cut out of small ingots cast into graphite molds (mass 300 g; cooling rate $\sim 10^{-1}$ K/s). The averaged set of zinc and magnesium concentrations, in atomic percent, was related to the normalized distance R/R_0, where R_0 is the average radius of dendritic cells, R is the distance from the center of the cell to the point where measurements were taken.

As an illustration, Figure 2.27 represents calculated and experimental curves of the distribution of alloying elements in as-cast alloy Al + 4%Zn + 1.6%Mg. It is clear that the calculated and experimental values are quite close in most cases, especially for the case of only partial completion of diffusion processes in the liquid phase. The discrepancy does not exceed the accuracy of the experimental and computational procedures up to the values of normalized distances 0.8–0.9.

Several important conclusions can be made now. Non-equilibrium solidification of ternary aluminum alloys for the 10^0–10^2 K/s solidification rates proceeds under the conditions of practically complete suppression of diffusion in the solid phase, and only partial completion of diffusion in the liquid phase. In order to use equilibrium phase diagrams for calculation of the three principal characteristics of microsegregation – C_1, C_2, and ΔC – one needs to know the position of the liquidus and solidus isotherms, and also the direction of the tie-lines in the two-phase areas. If the corresponding experimental data is unavailable, one could use the methods developed, for example in Ref. [118].

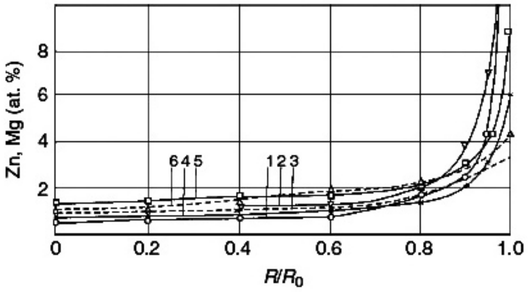

Figure 2.27 Calculated (1–5) and experimental (3, 6) curves of Mg (1–3) and Zn (4–6) distribution across dendritic cell cross-sections in as-cast alloy Al–4.6%Zn – 1.6%Mg; R stands for distance from cell center, R_0 is the average cell radius.

Table 2.6 Concentration of some alloying elements in the center and on periphery of dendrite cell for ingots and castings prepared out of industrial aluminum alloys

Alloy	V_c (K/s)	Ingot diameter (Mm)	Concentration (%)					
			Mg			Cu		
			C_1	C_2	ΔC	C_1	C_2	ΔC
Al–6%Mg	7	20	3.0	10.3	7.3	–	–	–
Al–10%Mg	2	50	6.2	14.0	7.8	–	–	–
2017[a]	10^1	270	0.2	0.8	0.6	0.2	3.9	3.7
2024[b]	10^1	270	0.9	1.7	0.8	1.1	3.8	2.7
7050[b]	10^1	370	0.8	2.3	1.5	0.4	1.0	0.6
2219	10^1	270	–	–	–	1.5	5.0	3.4

[a] According to Ref. [122].

[b] Concentration of zinc $C_1 = 4.7\%$, $C_2 = 9.6\%$, and $\Delta C = 4.9\%$.

In more complex, multicomponent systems the *a priori* calculation of the microsegregation parameters becomes even more complicated. While the estimate of C_1 could be done according to the methods described in Ref. [120], it is virtually impossible to determine C_2. For this reason one has to employ mostly experimental data in such situation.

Table 2.6 represents data obtained using X-ray spectrometry for the values of C_1, C_2, and ΔC in several industrial aluminum alloys. The results on C_1, C_2, and ΔC presented in this table should not be particularly dependent on the cooling rate (or ingot diameter) for all solidification rates that are used in practice.

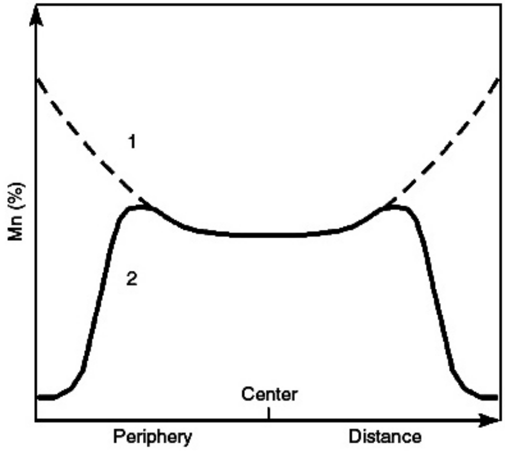

Figure 2.28 Schematic for the two types of Mn distribution across dendritic cells in aluminum alloys [65].

2.6.2.2 Microsegregation of manganese in multi-component aluminum alloys

Manganese is introduced into many commercial aluminum alloys in the amounts from 0.3% to 1.5%. Although manganese is not considered as one of the key alloying elements, it exerts a strong influence upon properties of aluminum alloys, especially in wrought condition [123]. The nature of this influence should be traced to its distribution in aluminum solid solution after casting [89, 124].

The authors of Refs. [125, 126] have made systematic efforts to study microsegregation of manganese in ternary, quaternary, and more complex alloys. All alloys were prepared using only 99.99% pure aluminum and a number of industrial alloys. Most experiments were conducted in laboratory conditions with cooling rates $\geq$0.16 K/s. Samples of industrial alloys were cut out of semi-continuously cast ingots with diameter 270–540 mm. The distribution of manganese was studied using the method of X-ray spectrometry.

It was established that the distribution of manganese in multicomponent alloys is different and usually more complex than in binary Al–Mn alloys. However, all this variety of experimental distributions could be reduced to two qualitatively different types (Figure 2.28). In the middle part of dendritic cells a “normal” increase of manganese concentration is observed from center to periphery (because the distribution coefficient of Mn in Al is less than one). However, in some cells this effect is only slightly visible and could be within the limits of experimental error of X-ray spectrometry method.

The principal difference between the curves of two types can be observed only on the periphery of dendritic cells. In some cases, as for binary alloys Al–Mn, the Mn concentration grows up to and including the cell boundary [123]

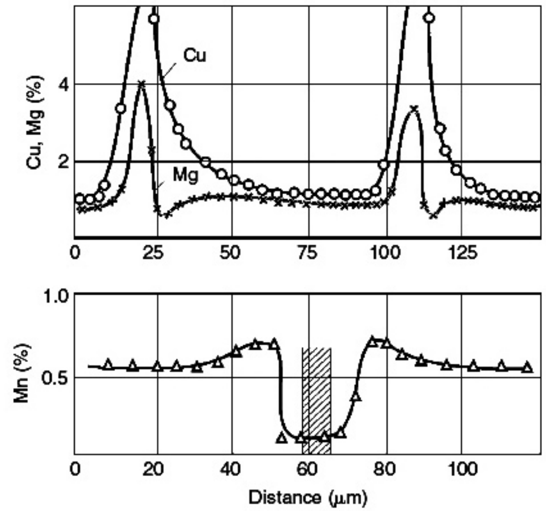

Figure 2.29 Distribution of Cu, Mg, and Mn in dendritic cells of Russian casting alloy D16. Dashed area corresponds to eutectic inclusions on the boundary.

(Figure 2.28, curve 1). The difference between the maximal and the minimal Mn concentrations for this distribution type is always small, from 0.1% to 0.2–0.3%.

Distribution curves of the second type (Figure 2.28, curve 2) are encountered more often; this case is characterized by the sharp depletion of the cell boundary with manganese. Figure 2.18 demonstrates the experimental curves of distribution for magnesium, copper, and manganese across the dendritic cells of wrought aluminum alloy 2024. It shows the Mn-depleted zones adjacent to the cell boundaries.

The minimal Mn concentration at the dendrite cell boundaries is much lower than its concentration in the middle of the cells and often reaches 0.1–0.2% (while in the cell center it can be up to 1%). The width of depleted zones at solidification rates ≥0.16 K/s varies from 10 to 50 μm. In industrial alloys it is directly proportional to the ingot diameter. For example, in alloy ~2017 ingots with diameter 540 mm it varies from 20 to 30 μm. This value is quite substantial and eliminates any possibility of experimental error. The reliability of this data is also supported by the presence of Mn-depleted zones in the areas of direct vicinity to Mn-bearing particles, where the concentration of manganese is significantly higher than in aluminum solid solution. It is also important to mention that Mn-depleted zones were observed not only close to "clean" dendritic cell boundaries, but also around inclusions that did not contain manganese (in particular, around some eutectic inclusions) (Figure 2.29).

The formation of Mn-depleted zones in relatively slowly solidified aluminum alloys was discovered experimentally by Setjukov [125, 126]. However, some

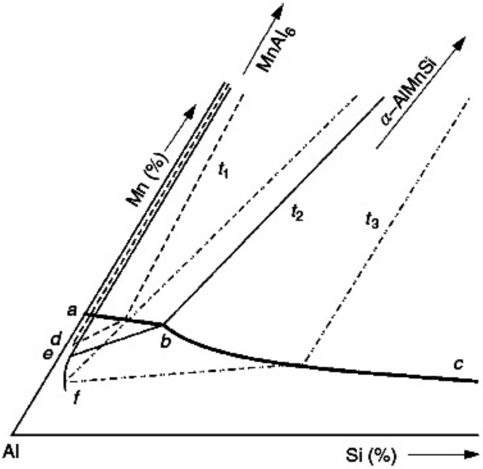

Figure 2.30 Schematic of solidification for an alloy of the Al–Mn–Si system, [67] ($t_1 > t_2 > t_3$). Line abc characterizes the composition of liquid in equilibrium with aluminum solid solution (its composition changes along the line def) and Al_6Mn (α-Al,Mn,Si).

notions about existence of such zones around Fe- and Mn-bearing particles were put on record earlier in Refs. [124, 127–128] – these works have been conducted in parallel to Refs. [125, 126]. These zones were retained even after heat treatment and deformation; in homogenized ingot and deformed semi-fabricated wrought products that could be observed easily using metallography. However, the nature of such zones was not completely understood.

Two explanations could be given as far as the formation of the Mn-depleted zones is concerned. Firstly, it is defined by the phase diagram of the corresponding multicomponent system, according to which in range of temperatures and as a result of primary, eutectic, and peritectic phase reactions aluminum solid solution at first gets enriched, then depleted with manganese. For example, in the ternary system Al–Mn–Si [127] upon cooling of alloy in the three-phase area $L + (Al) + Al_6Mn$, or α-(Al,Mn,Si), the vertices of the tie-line triangle characterizing the chemical composition of (Al), could shift toward lower manganese concentration (Figure 2.30).

Secondly, in the course of non-equilibrium solidification the primary aluminum solid solution can become supersaturated with manganese. However, when Mn-enriched phases solidify, the liquid phase becomes Mn-depleted, and at the same time solidification of (Al) continues. As a result, on the periphery of dendrite cells the formation of Mn-depleted zones may take place.

Whatever the mechanism of formation, the appearance of such zones must result in the increased volume fraction of Mn-bearing phases. Consequently, the volume fraction of Mn-depleted zones must also increase. This was confirmed experimentally in Ref. [126]. The average zone width decreases as the solidification rate increases; this seems to be a natural result of the refinement of dendritic cells and constituent particles. In this case, smaller zone width is compensated by the increased surface of the boundaries among dendritic cells. As a result, the volume fraction of Mn-depleted zones weakly depends upon solidification rate.

2.7 MICROSTRUCTURE OF CAST ALUMINUM ALLOYS

The most important qualitative characteristics of structure of cast aluminum alloys, which could be determined using just an optical microscope, were discussed in Section 2.1. For alloys of the X_1 type (Figure 1.1a) these are the lineal grain size, D, and the lineal size of dendritic cells, d, of the aluminum solid solution; the volume fraction, Q_V, average width, m, and the specific surface, S, of inclusions of different constituent phases. Finally, characteristics of porosity, which is always present in castings, are also very important. In all subsequent discussion we will call such parameters metallographically determined properties of a given microstructure or microstructure characteristics.

The general rules establishing the influence of chemical composition and conditions of solidification upon these properties of microstructure are well known [63, 67, 108, 124, 129–135]. However, this knowledge exists mostly on the qualitative level. For this reason in the following text we make an attempt to formalize some of these concepts in order to develop capabilities of *a priori* calculations of microstructure characteristics determined from metallographic analysis.

The most detailed data exists so far on the influence of composition and solidification rate (cooling) upon the dendrite cell average size. Both qualitatively and quantitatively [63, 132] it was demonstrated that significant refinement of dendritic cells takes place as solidification rate grows. It was established [109, 135–137] that d depends upon cooling rate (V_c) as follows:

$$d = B \cdot V_c^{-n} \tag{2.30}$$

In equation (2.30) the coefficient B is considered to be dependent upon the diffusion coefficient of alloying element in the liquid phase. This latter parameter defines the extent of completion of homogenizing diffusion and, consequently, the formation of a layer enriched with alloying element of a certain thickness (see Figure 2.6) around the growing dendrite arm.

In Ref. [135] it was demonstrated that linear dependence (on logarithmic scale) exists between d and V_c, which holds up to very high cooling rates (10^8–10^9 K/s) (see Figure 2.31). Moreover, this dependence is quite general for aluminum alloys of different systems, including Al–Si casting alloys with Si concentration up to 5–7%.

The authors of Refs. [138–140] have established the influence of alloy composition upon the functional dependence of d on V_c. According to Ref. [138] for binary alloys:

$$d = A \cdot e^{\mathrm{B} \cdot \ln V_c} + K' \cdot C_{\mathrm{B}} \tag{2.31}$$

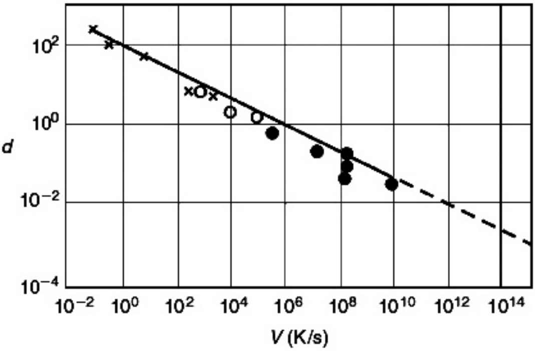

Figure 2.31 Dependence of dendritic cell size upon cooling rate during solidification [88].

In equation (2.31) the constants A, B, and K' are characteristic of a particular aluminum alloy while C_B stands for the alloying element concentration.

Increased solidification rate also affects the average size of constituent particles [63, 129, 141], and the coefficients d and m vary in parallel.

Thus, we can conclude that accelerated solidification results in refinement of grain microstructure that can be observed using a conventional light microscope. However, such a clear and direct relation between the grain size and the cooling rate simply does not exist. More specifically, the value of D is defined to a greater extent by the molten metal temperature right before casting [63, 133, 142]. It is also known that, unlike the coefficient d, grain size can vary very significantly due to the presence of modifying additions [143] and mixing of molten metal using different techniques.

All these functional dependencies were studied in great detail in Ref. [144] using laboratory castings made of binary alloys of aluminum with copper (up to 5%) and magnesium (up to 11%), as well as some industrial alloys like AA203.0, AlMg10, and others, and also alloys belonging to the Al–Zn–Mg and Al–Zn–Mg–Cu systems. All studied alloys represent typical compositions with average to high content of the key alloying elements (from 4% to 11% total). After solidification with different cooling rates samples obtained out of these castings were tested extensively, and statistical analysis was used to establish correlations among different alloy properties.

Figure 2.32 illustrates how the average dendrite cell size, thickness, and specific surface of eutectic inclusions depend upon cooling rate for alloys with different contents of magnesium. It is clear that the nature of dependence of d and m upon V_c is qualitatively similar. However, the straight lines "$\lg(m) - \lg(V_c)$" are unique for each alloy, while the average dendrite cell size is connected with cooling rate via the same scaling relation for all binary and industrial alloys described above:

$$\lg d = 2.6 - 0.4 \cdot \lg V_c \quad \text{or} \quad d = 380 \cdot V_c^{-0{,}4} \tag{2.32}$$

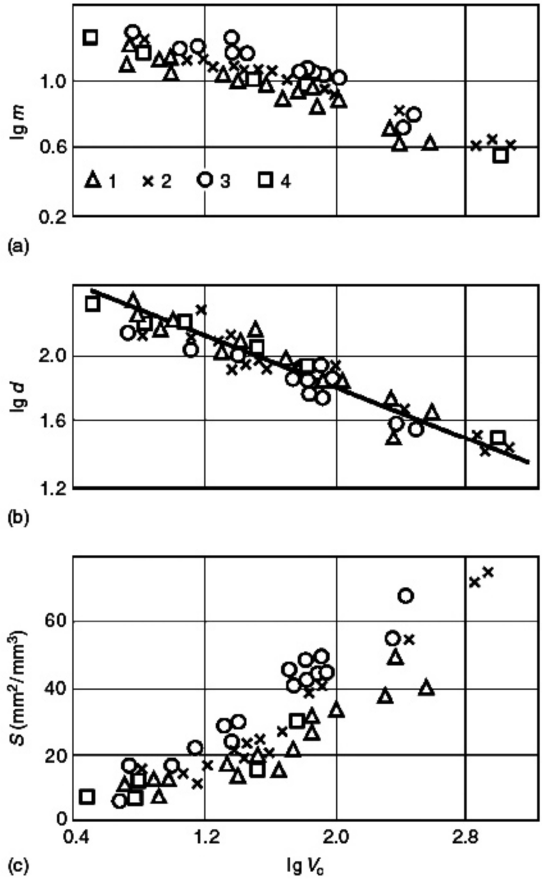

Figure 2.32 Dependence of the average thickness m of the eutectic β-phase inclusions upon: (a) average size of dendritic cell; (b) specific surface S of the β-phase and (c) upon cooling rate during solidification of alloy AMg10 containing 9.5 (1) 10.2, (2) 11.6%Mg and (3) binary alloy Al–10%Mg (4).

This expression agrees well with equation (2.31) and experimental data in the literature [134, 139]. Equation (2.32) can be used to get an estimate of the cooling rate using experimental data on the average dendrite cell size. Similar functional dependence can be established for the average thickness of constituent particles; however, its coefficients will be different for alloys with different chemical compositions.

The general character of the scaling equation (2.32) for alloys with medium-to-high content of alloying additions is determined by the peculiar features of dendritic solidification. Each dendrite arm is surrounded by a diffusion layer during its growth (see Figure 2.6). Its width is determined by the coefficients of distribution and diffusion of alloying elements in molten metal and solidification rate [100]. One could assume that nucleation and growth of new dendritic arms takes place on a length scale(s) correlated to the average thickness of diffusion zone. Since the diffusion and distribution coefficients of the basic alloying elements in aluminum at temperatures above solidus are of the same order, one could expect that the diffusion zone width (and, consequently, average dendrite cell sizes) are defined mostly by the applied cooling rate.

The value of the specific surface for inclusions of constituent particles grows with the applied cooling rate (Figure 2.32c). In particular, for aluminum–magnesium alloys containing 9.5–11.6% Mg, this dependence is adequately described by the following equation:

$$S = 18 \cdot \lg V_c \tag{2.33}$$

However, this equation is not general for different aluminum alloys. In fact, "separation" of experimental points corresponding to different magnesium content is evident even in Figure 2.32c. The value of S, according to equation (2.33), is determined by the spatial frequency (number density) of constituent particles. Since we discuss here only phases of eutectic or peritectic origin, which are mostly located along the dendritic cell boundaries, this value will depend on their average size and linear density of constituent particles along cell boundaries. As V_c grows, the number density of constituent particles along the dendritic cell boundaries changes insignificantly, while d decreases quite substantially. As a result, S grows.

As far as shrinkage and hydrogen porosity are concerned, only the average linear size of pores, m_p, is related to solidification rate. The nature of dependence of m_p upon V_c is qualitatively the same as for m and d. The volume fraction (Q_{Vp}) and specific surface area (S_p) depend not only upon V_c but also on the thermal treatment of molten metal directly before solidification. It is this thermal history that defines the overall amount of dissolved gases, as well as alloy composition and solidification technique. If all conditions of casting/solidification are the same, one could expect lower values for Q_{Vp} and higher – for S_p as solidification rate is increased.

Summing up, the average dendritic cell size for (Al) is quantitatively dependent upon cooling rate for casting aluminum alloys and can be calculated if V_c is known. The value of d defines some other characteristics of microstructure – shrinkage porosity and the degree of refinement of constituent particles. Below these characteristics will be discussed in greater detail.

In the course of alloy solidification the growing dendrite arms will repel the liquid phase enriched with alloying element(s) toward the place of contact of several arms (branches). It is in these places that eutectic will be formed; its inclusions could be observed along dendrite cell boundaries using metallography. In the same places micropores will be formed (because of solidification of the last isolated portions of the melt). From stereometry it is known that the radius r of smaller spheres located in contact with larger spheres of radius R are related via a linear equation. The same result must be true for the case of linear sizes of dendritic cells and pores or constituent particles:

$$m(m_n) = K_1 \cdot d \tag{2.34}$$

Similar dependence between d and the diameter of inclusions of lead in Cu–34%Pb alloy was already discovered in Ref. [145].

To determine the specific surface area of inclusions one could use the following formula: $S = 4 \cdot n'/L$. In this equation n′ stands for the total number of crossings for a straight line (lineal analysis) with inclusions at the cell boundaries. In addition to that, the secant line will cross n'' of cell boundaries that are free from inclusions ($n' + n'' = n$). Then for the overall value we get $L = nd$, and

$$S = \frac{4 \cdot n'}{n \cdot d} \tag{2.35}$$

This equation demonstrates that the specific surface area of constituent particles is inversely proportional to the average size of dendritic cells. The proportionality coefficient, $C = n'/n$, characterizes the lineal density of inclusions along the dendritic cell boundaries. The relation between S and thickness m can be established if one assumes that the volume fraction of such particles, Q_V, is constant for an alloy of a given composition. In this case, according to equation (2.16), $S = A/m$, where A is a constant defined by the averaged value of Q_V.

These relations among different elements of microstructure can be expressed by the following equations:

$$m(m_n) = K_1 d \quad \lg S = K_2 - \lg d \quad \lg S = K_3 - \lg m$$

where

$$K_2 = \lg(4C) \quad K_3 = \lg(40Q)$$

From equations (2.34) and (2.35) it follows that $S = 4C/d = 40Q_V/m$, whence $m = (10Q/C)d$, where $10Q/C = K_1$. Thus, coefficient K_1 in equation (2.34) will be defined by the ratio of the volume fraction of constituent particles, to their lineal number density along dendritic cell boundaries.

Experimental verification of the obtained relations is provided in Figure 2.33. It turned out that the dependencies $d - m$, $\lg S - \lg d$ and $\lg S - \lg \mathrm{m}$ are linear for different alloys. It should be noted that for very coarse dendritic cells ($d > 100$–$150\,\mu\mathrm{m}$) the direct proportionality between m and d breaks down somewhat. Equation most general for all alloys,

$$m = 2.3 + 0.05 \cdot d \tag{2.36}$$

is characterized by mean square error for m within the limits of $\pm 1.8\,\mu\mathrm{m}$.

Figure 2.33 clearly demonstrates some discrepancy of experimental data points related to alloys of different compositions. This is related to different values of

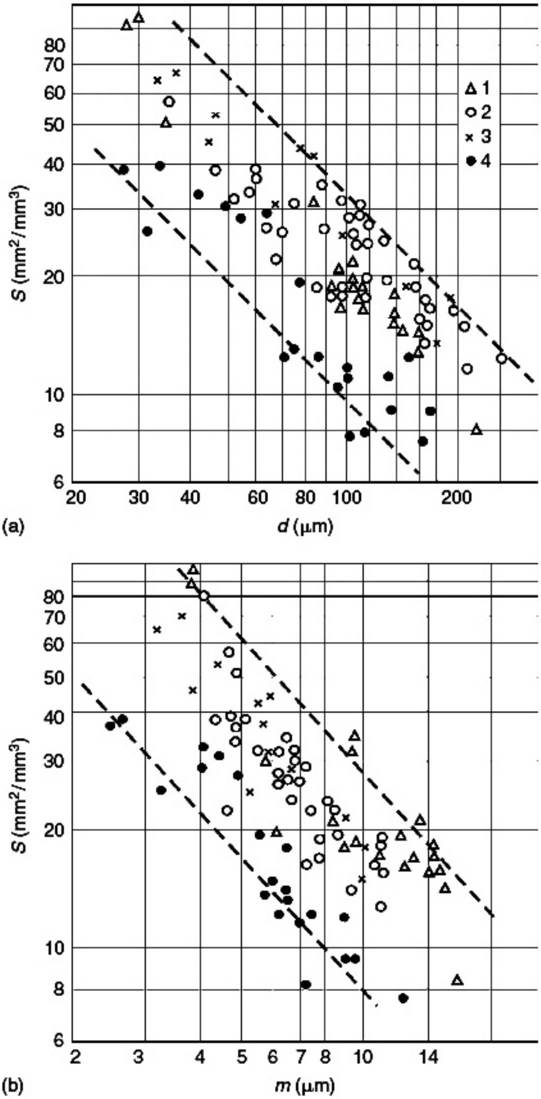

Figure 2.33 (a) Connection between the specific surface S of constituent particles and the average dendritic cell sized (b) connection between S and average thickness of inclusions m and (c) connection between d and m; the following alloys were considered: Al + 10%Mg (1), Al + 4.5%Cu (2), AM5 (3), and Al–Zn–Mg–Cu with $C_{Zn}/C_{Mg} = 2$ (4).

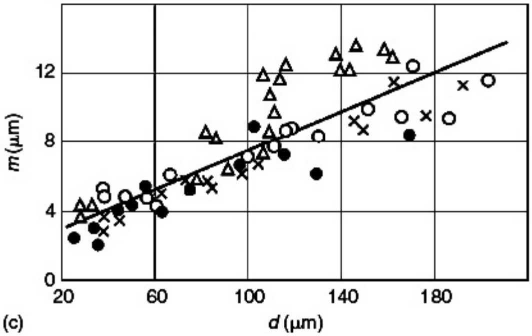

Figure 2.33 (*Continued*)

volume fractions of constituent particles in different alloys. The higher the value of Q is, the higher the value of S will be for a given set of d or m.

Another parameter influencing the general character of such dependencies is the cooling rate upon solidification because it affects Q_v of constituent particles. This effect is particularly pronounced for lower cooling rates, where smaller value of V_c results in reduction of Q_v (see Figure 2.15). As a result, coefficients K_1 and K_3 attain smaller values for minimal d and m which, in turn, results in some deviations of predicted dependencies from observed experimentally.

The average size of equiaxial grains, D, for most castings is linearly related to the dendritic cell size. For example, in cast alloys Al with 3–9%Mg the coefficient of pair correlation between D and d was 0.656. However, such direct proportionality between grain size and dendritic cell size is not general even for alloys of the same chemical composition. If chemical composition is varied, it exerts very strong influence upon the value of D, while at the same time dendritic cell size does not change appreciably. It is well known that the average grain size in ingots and castings depends strongly upon the degree of molten metal supercooling – the higher the value of supercooling, the larger average grain size [62, 103, 146, 147]. At the same time studies conducted for laboratory alloys Al–Cu demonstrated that the degree of molten metal superheating does not change dendritic cell size provided the cooling rate is maintained the same. In alloys of the second and third groups (see Section 1.1) for which eutectic component may attain 100% and is almost completely equilibrium, the most important structural parameter is the morphology of eutectic colonies (Figure 1.26a and b). Typical representatives of this group are hypo-eutectic and eutectic 3xx series alloys, for which the key microstructural components are (Al) and eutectic colonies, (Al + Si). According to modern concepts, eutectic colonies can be best represented as bi-crystals formed for a single center of origin. Such colonies can be characterized by their size (in analogy to grain size) and a parameter d_c characterizing its refinement. This parameter could be determined, for example, using the distance between the branches (arms) of the second phase, or their average cross-section diameter.

Similar to d, the value of d_e decreases with increased cooling rate, but it is also very sensitive to alloy chemical composition. In particular, small additions of sodium and strontium (~0.01% or so) into Al–Si casting alloys enhance the formation of refined eutectic colonies even for sand casting.

The influence of composition can be explored if microstructure of a multicomponent alloy contains different eutectic colonies. In particular, one could see that ternary eutectics are more disperse than binary, quaternary more disperse than ternary, and so on. For example, in Al–Si casting alloys containing copper and magnesium, eutectic $(Al + Si) + Al_2Cu + Al_5Cu_2Mg_8Si_6$ formed during the final stage of solidification process, possesses the most disperse structure.

Another type of intermediate morphology of constituent particles is "skeletal", which is also referred to as "Chinese script". This type of morphology is essentially a eutectic with insufficiently disperse microstructure (the value of d_e is relatively large). As a rule, it does not characterize uniquely a particular phase. For example, magnesium silicide, which is present in microstructure of many aluminum alloys, can be found in all three morphological types: elongated particles (Al–Si alloys), Chinese script (Al–Mg), and finely dispersed particles in alloys close to eutectic on quasi-binary cross-section $Al–Mg_2Si$. Other phases (e.g., Fe bearing), which in industrial conditions possess skeletal morphology could, under certain laboratory (composition, cooling rate) enter finely dispersed eutectics.

The peculiarities of microsegregation inside eutectic colonies are still poorly understood. As-cast microstructure of hypo-eutectic alloys should be considered both in terms of Al-based solid solution microstructure and constituent particles.

Very important microstructural parameters for alloys of the fourth group (e.g., hyper-eutectic Al–Si alloys) are the size of constituent particles, their morphology and distribution. If morphology is defined mostly by the nature of a given phase (e.g., primary crystals of (Si) have polyhedral shapes) such parameters as size and distribution depend very strongly upon solidification conditions (cooling rate, mixing, application of powerful ultrasound, etc.).

Constituent particles are generally located in the middle part of dendritic cell of (Al). If the density of a phase is significantly different from that of liquid aluminum, these crystals may settle or, on the contrary, float, which will result in their non-uniform distribution in as-cast microstructure. The latter, as a rule, is undesirable, both in laboratory and in commercial alloys. For example, this could happen due to elevated concentration of iron or "hyper-alloying" with such transition metals as titanium, chromium, or manganese.

It is also necessary to include into consideration non-metallic inclusions, first of all oxides (alpha- and gamma-Al_2O_3, magnesium spinels), which are always present in industrial alloys and at least partially (after refining and molten metal filtering) are transferred into an ingot or shape casting. Overall as-cast microstructure of hyper-eutectic Al–Si casting alloys must be analyzed taking into account the fundamentals of microstructure formation considered above for alloys of the first two groups.

2.8 SUBSTRUCTURE OF CASTING ALUMINUM ALLOYS

By the term substructure we will understand, as it was pointed out in Section 2.1, the internal structure of dendritic cells of (Al) solid solution. For casting aluminum alloys it is studied insufficiently. A significant part of the experimental studies in this field is related to single crystals, most often of pure metals with small amounts of admixtures and/or alloying elements (see, e.g., [148–155]). At the same time, conditions of solidification of polycrystalline industrial alloys differ significantly from those in which single crystals are grown. Correspondingly, the substructure of such alloys also must be different.

Fine structure of metals and alloys exerts a very strong influence upon their properties. By the same token it may be stated that the properties of casting aluminum alloys also should depend, to a certain degree, upon their substructure.

In 1940s Bochvar formulated an important hypothesis, according to which even crystals of Al-based solid solution that look completely homogeneous under a microscope, in reality possess a certain substructure forming due to the dendritic nature of their growth [156]. At the same time Bochvar clearly identified the need for direct studies of dendrite microstructure using electron microscopes [156, 157]. In this section we describe the results of systematic XRD and electron microscopy studies of the role and influence of alloying and solidification conditions upon the dislocation structure inside dendritic cells of aluminum solid solution and also its decomposition after cooling and solidification (see mostly [122, 158–161]).

2.8.1 Types of dislocation structures in as-cast aluminum alloys of different systems

The first task was to establish which type(s) of dislocation structure(s) can be formed in different aluminum alloys under the same solidification conditions. For that goal aluminum of different purity and its alloys with different concentrations of alloying elements (copper, magnesium, zinc) as well as manganese, beryllium, and germanium, was selected in order to create different levels of internal stresses. All materials were prepared out of 99.99% pure aluminum and alloying elements containing not more than 0.1% impurities. Solidification was conducted in a copper mold with inner volume 20 mm × 40 mm × 90 mm. Solidification rate was ~15 K/s, which approximately corresponds to cooling rates for semi-continuous casting and shape casting processes in metallic molds.

The compositions of all studied alloys are given in Table 2.7. All selected alloying elements form eutectic phase diagrams with aluminum, and their concentrations were lower than the maximum solubility in aluminum at eutectic temperature. In order to obtain comparable data for chemical elements with higher solubility (Mg, Si, Cu, Zn, Ge) their concentrations were selected to be the same – 0.6% and 2.2% (at.). The maximal concentrations of alloying additions were: for magnesium – 14 at.% or ~12.7 wt.%; for copper – 2.2 at.%, or ~5 wt.%.

Table 2.7 Different types of dislocation structures in cast aluminum alloys [158]

Alloy*	Cells			Subgrains			Cells and subgrains			
Al–0.6Si	–	0/+	0/+	–	–	–	–	–	–	–
Al–0.6Mg	+	–	+	–	–	–	–	0	–	–
Al–2.2Mg	–	–	–	+	–	–	0	–	0	–
Al–14Mg	–	–	–	0/+	–	–	–	–	–	–
Al–0.6Ge	–	0	–	–	–	–	–	–	–	–
Al–0.6Zn	0	–	0	–	–	–	–	–	–	–
Al–2.2Zn	0	–	0	–	–	–	–	–	–	–
Al–0.17Be	+	–	0	–	0	–	–	0	–	–
Al–0.6Mn	0	–	0	–	+	+	–	–	–	–
Al–0.6Cu	0	+	0/+	–	–	–	–	–	–	–
Al–2.2Cu	–	–	0/+	–	–	0/+	–	–	–	0

Note: symbol "0" denotes as-cast state; symbol "+" denotes homogenized state.
* All concentrations are given in % (at.).

This corresponds approximately to the highest content of Mg and Cu in industrial aluminum alloys. All studied alloys immediately after solidification must possess in equilibrium state single-phase structure of aluminum solid solution. However, because of the microsegregation phenomena most of these alloys contained a certain amount of non-equilibrium eutectics.

TEM analysis confirmed that dislocation structures depended upon alloy composition. The observed dislocation structures can be subdivided into four major classes: cell, subgrain, mixed, and irregular dislocation structures. The latter was observed only in single crystals of aluminum and was characterized by the absence of voluminous dislocation networks and planar small-angle boundaries (Figure 2.34a). The boundaries of very large subgrains (which, possibly, were present in single crystals) were not found in our TEM analyses.

In as-cast state for most aluminum alloys and in pure polycrystalline aluminum cell dislocation structures were revealed, with more or less formed dislocation cell walls (Figure 2.34b). Pure subgrain structure was observed only in alloy with 14 at.% Mg (Figure 2.34c), while in materials less alloyed with Mg, as well as in alloys with Be and 2.2 at.% Cu, mixed dislocation structures were observed (Figure 2.34d). As the concentration of magnesium was raised, the overall volume of planar subgrain boundaries also increased.

Table 2.7 presents data on different types of dislocation structures for several aluminum casting alloys. For example, in alloy with 2.2 at.%Cu one could observe

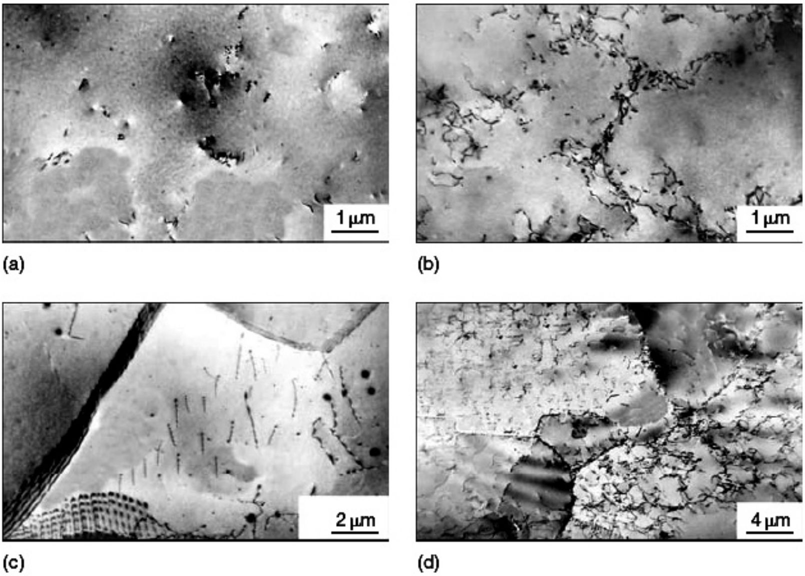

Figure 2.34 Typical dislocation microstructures in as-cast condition: (a) Al single crystal; (b) binary alloy Al + 0.6 at.Cu; (c) Al + 14%Mg, and (d) Al + 2.2%Mg; $V_{\text{cooling}} = 15$ K/s (TEM).

both subgrain and cell dislocation microstructures (it should be noted that inside cells and subgrains individual dislocations can be observed sometimes; that us, there is some irregularity of the dislocation structures that were not mentioned in Table 2.7. In alloy with 2.2 at.%Mg dislocation cells are often immobilized inside subgrains (Figure 2.34d.).

In addition to qualitative characteristics of dislocation structures in cast aluminum alloys, some quantitative parameters were also determined. Using TEM data for thin foils, average linear dimensions of dislocation cells d'', subgrains d', as well as the dislocation density ρ were also determined (Table 2.8). In alloys Al–Cu and Al–Zn, in addition to average dislocation density, the values for the dendritic cell center and periphery were also measured (in zones adjacent to the boundaries, with width $1/4d$). When computing dislocation density for alloys with subgrain and mixed dislocation structures not only dislocations inside subgrains were taken into account, but also those dislocations that formed planar boundaries between subgrains (using data on average subgrain size d' and their disorientation angle θ).

From Table 2.8 it follows that in alloys with cell dislocation structure average cell size(s) are pretty close (within the limits of experimental error). As the concentration of alloying element in (Al) grows, there is a tendency toward smaller values of d''. This tendency becomes even more pronounced for subgrains in Al–Mg alloys.

Table 2.8 Quantitative characteristics of dislocation structures in cast aluminum alloys

Alloy[a]	d'' (μm)	d' (μm)	$\rho \cdot 10^{-9}$ (cm^{-2})			ΔC (at.%)	$\rho'_T \cdot 10^{-7}$ (cm^{-2})
			Average	Center[b]	Periphery[b]		
Al + 0.6Mg	1.7 ± 0.4	–	–	–	–	0.4	2.7
Al + 2.2Mg	–	5.5 ± 0.9	2.4 ± 0.2	–	–	1.4	2.5
Al + 14Mg	–	1.2 ± 0.2	–	8.2 ± 2.9	–	8.5	–
Al + 0.6Ge	2.4 ± 0.3	–	–	–	–	0.45	2.4
Al + 2.2Ge	–	–	2.2 ± 0.3	–	–	2.3	14
Al + 0.6Cu	2.4 ± 0.3	–	3 ± 0.4	2.4 ± 0.5	3.5 ± 1.1	0.5	2.9
Al + 2.2Cu	1.7 ± 0.5	4.7 ± 1.3	2.9 ± 0.4	2 ± 0.3	3.8 ± 0.8	2.1	37
Al + 0.6Zn	2.9 ± 0.5	–	2 ± 0.2	1.8 ± 0.5	2.2 ± 0.2	0.4	0.6
Al + 0.17Be	1.8 ± 0.1	–	2.8 ± 0.4	–	–	–	–
Al + 0.6Mn	1.9 ± 0.2	–	2.4 ± 0.5	–	–	–	–

Note: Average density of dislocations ρ in single crystals of aluminum and in polycrystalline aluminum (99% pure) is $(0.03 \pm 0.011)10^9$ and $(0.05 \pm 0.01)10^9$ cm^{-2}, respectively; ρ'_T – stands for calculated dislocation density using Tiller's formula.

[a] Concentration of alloying element (at.%).

[b] Dendritic cells.

The average density of dislocations in all alloys (except Al–14 at.%Mg) does not depend much upon the nature of a given alloy and concentration of alloying elements; it is approximately equal to $(2/3)10^9$ cm^{-2} (Table 2.8). In castings of polycrystalline aluminum it is smaller almost by one order of magnitude, while for aluminum single crystals – by two orders of magnitude. Inside dendritic cells there is always a tendency to higher values of dislocation density at the cells periphery. This is qualitatively illustrated by the data presented in Table 2.8. In aluminum alloys with subgrain structure this effect manifests itself in the form of significantly smaller average subgrain size(s) at the periphery of dendritic cells. For example, in alloy Al–14 at.%Mg the subgrain size closer to the cell center is 1.7 ± 0.2 μm, while in the boundary region is 0.8 ± 0.1 μm.

Castings made of industrial multicomponent alloys on the basis of the binary systems discussed above (Al–Mg and Al–Cu) generally retain all of the peculiarities of their respective dislocation structures of these basic alloys. For example, when the solidification rates are of the order of 10^1–10^2 K/s, commercial Al–Mg alloys containing 6%Mg and 10%Mg possess subgrain dislocation structure, while for Al–Cu-based commercial alloys – distorted cell dislocation structure.

The total dislocation density in industrial alloys at such cooling rates is close to that observed in binary aluminum alloys. For example, in binary alloy Al–6.5%Mg, $\rho = (3.5 \pm 1.5)10\,\mathrm{cm}^9$, while in a similar commercial alloy containing 6%Mg, $\rho = (2.4 \pm 1.0)10^9\,\mathrm{cm}^{-2}$ (at cooling rate ~7 K/s). In alloy Al + 2.2 at.%Cu (5% mass) after solidification with cooling rate 7 K/s, $\rho = (1.0 \pm 0.2)$ $10^9\,\mathrm{cm}^{-2}$, in the corresponding commercial Cu-bearing alloy with 4.7%Cu, $\rho = (0.7 \pm 0.2)10^9\,\mathrm{cm}^{-2}$. In many commercial alloys, for example 356.0, 305.0, 359.0, one could expect the formation of cell dislocation structure with dislocation densities of the order of $10^9\,\mathrm{cm}^{-2}$ (similar to Figure 2.34b).

It needs to be emphasized that dislocation structure of industrial alloys was studied not only using lab castings, but also on samples cut out of commercial plant castings. No qualitative difference in their substructure was determined.

This data implies that the prevalent type of dislocation microstructure in multicomponent industrial alloys is determined, to a very significant extent, by the principal alloying elements, which enter Al-based solid solution in significant amounts. Other alloying elements and admixtures exert only weak influence upon the character of substructure and dislocation density.

In alloys on the basis of the Al–Zn–Mg and Al–Zn–Mg–Cu systems, which contain several principal alloying elements, the dislocation microstructure type is determined mostly by the concentration of magnesium. It was established that if its content exceeds 4–5%, then mixed subgrain/cell microstructure will be formed. However, if the concentration of magnesium is smaller, then irregular or cell structures will be formed instead. For example, in semi-continuous casting process for alloys 7016, 7019, 7028 of the Al–Zn–Mg system, in which Mg contents is ~2% (and Zn is ~4%) subgrains are not present inside dendritic cells. Most part of such cells will be populated with dislocations in the form of cell microstructure. In alloy of the same system with the concentration ratio $C_{Zn}/C_{Mg} \cong 0.5$ dislocation microstructure is qualitatively similar to that observed in Al–Mg casting alloys: a network of small-angle grain boundaries inside dendritic cells.

2.8.2 The influence of solidification conditions upon dislocation microstructure

Before we start discussing the influence of alloying upon dislocation microstructures, it is important to consider how it depends on solidification conditions.

These fundamental questions have been addressed in Refs. [158–160]. Given there are several distinctive dislocation microstructure types, experiments were conducted with alloys in which all of these microstructures were present. In particular, studies of subgrain microstructure were conducted for commercial alloys belonging to the Al–Mg system – first alloy contained 6%Mg, 0.66%Mn, 0.2%Fe, 0.13%Si, 0.05%Ti, and 0.025%Be; second alloy contained 10.4%Mg, 0.095%Ti, 0.075%Zr, 0.1%Be, and 0.044%Fe. Al–Cu alloys (both binary with 0.5–5.0%Cu) and commercial, represented materials with cell and mixed dislocation microstructures. In addition to that, alloy Al + 4%Cu was used to study the influence of overheating molten metal upon dislocation microstructure after

Table 2.9 Characteristics of dislocation microstructures in as-cast aluminum alloys Al–6%Mg and Al–10%Mg after solidification with different cooling rates (V_c)

V_c (K/s)	V^a (µm)	Subgrain size^b (µm)	Δl^c (µm)	θ^d (°)	$\rho\ 10^{-9}$ (cm^{-2}) Inside subgrains	$\rho\ 10^{-9}$ (cm^{-2}) General
Alloy Al–6%Mg						
1.25	97	–/–	–	10 ± 2	2.2 ± 0.1	–
1.7	82	>10/–	–	3.4 ± 0.7	2.7 ± 0.1	–
6.7	28	3.6 ± 1.1/–	7.5 ± 1.3	2.5 ± 0.5	2.4 ± 0.5	–
16.7	14	2.7 ± 0.5/–	–	6.1 ± 1.2	4.1 ± 0.5	–
38.3	8	1.6 ± 0.5/–	2.7 ± 0.9	2.4 ± 0.5	3.4 ± 0.5	–
10^3	1.7	–/–	–	0.5 ± 0.2	1 ± 0.1	–
Alloy Al–10%Mg						
1	93 ± 7	10 ± 3.65/–	–	1.5 ± 0.5	0.7 ± 0.1	4.0 ± 1.1
2.1	86 ± 7	$3.5 \pm 1.5/11 \pm 2.5$	7 ± 1.5	0.5 ± 0.2	0.7 ± 0.1	2.2 ± 1.0
2.8	37 ± 2	$2 \pm 1.2/4 \pm 2$	4 ± 1.5	1 ± 0.3	2.6 ± 0.2	13.9 ± 0.7
16.7	20 ± 1.5	$1.5 \pm 1/3 \pm 1$	3 ± 1	0.8 ± 0.2	2.9 ± 0.2	9.1 ± 1

[a] Average size of dendrite cells.

[b] Ratio of periphery concentration to dendritic cell center concentration.

[c] Width of the zone of fine subgrains.

[d] Average angle of disorientation on the boundaries of dendritic cells for alloy Al–6%Mg and on the boundaries of subgrains for alloy Al–10%Mg.

solidification with different cooling rates. The selected rate range was within the limits from 10^0 to 10^3 K/s. Experiments were conducted with laboratory and commercial castings; in all cases castings were cooled down to room temperature inside and together with the mold.

2.8.2.1 Alloys on the basis of the Al–Mg system

Dislocation microstructure of the two Al–Mg casting alloys (see above) in as-cast condition at all studied solidification rates is characterized by the presence of planar dislocation grid boundaries. However, their size and distribution across the dendrite cell cross-sections differ quite significantly as a function of the applied cooling rate.

Quantitative characteristics of dislocation microstructures are presented in Table 2.9. The maximal solidification rate – 1000 K/s – was achieved for alloy

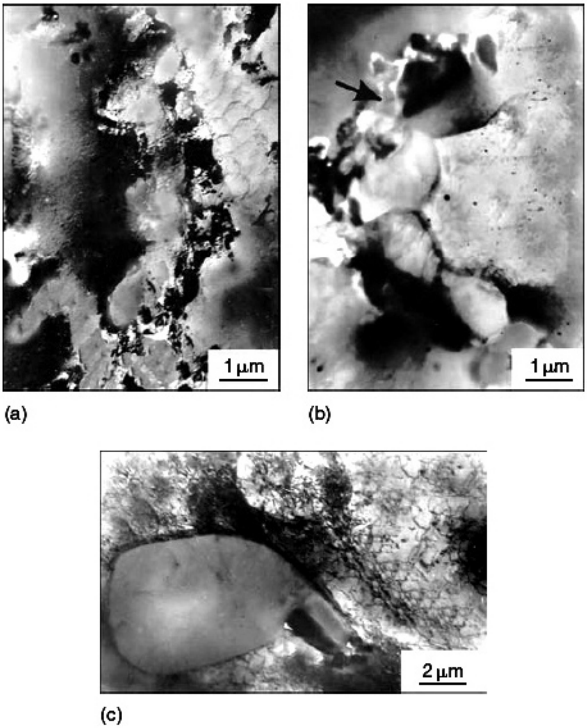

Figure 2.35 (a) Substructure of alloy AMr6 after solidification with cooling rate 10^3 K/s; (b, c) 40 K/s: arrows point to the inclusions of eutectic origin, TEM.

Al–6%Mg upon solidification of molten metal droplet in between two polished copper plates. In obtained thin aluminum films planar dislocation boundaries were observed very rarely. In most cases they coincided with the boundaries of dendritic cells surrounding constituent particles (Figure 2.35a). Due to the small grain size in thin films high-angle boundaries were observed quite often and also associated with constituent particles. Thus, TEM observations of thin films indicated that inside grains mixed (subgrain cell) dislocation microstructure was observed.

At smaller solidification rates – in the range from 40 to ~1.6 K/s – in both studied Al–Mg casting alloys well-developed subgrain dislocation microstructure was observed. In the first alloy at cooling rate 40 K/s along the boundaries of dendritic cells one row of fine subgrains with average lineal size ~1.6 μm (Table 2.9), while in the middle part of dendritic cell several relatively large subgrains are located (Figure 2.35b). The boundaries of dendritic cells are represented by the planar dislocation sub-boundaries. Sometimes it can be seen that these boundaries are shifted somewhat with respect to populations of constituent particles.

This implies that even at such relatively high solidification rates migration of the formed subgrains in the solid state remains possible.

In the same samples in proximity to dendrite cell boundaries subgrains of roughly round shape often were observed. Inside these subgrains the density of dislocations is appreciably smaller than in adjacent areas (Figure 2.35c). When the aluminum alloy foil was tilted in electron microscope such subgrains located within one grain are imaged similarly, indicating their similar crystallographic orientation. At least in visual appearance, it reminds the nuclei of recrystallization. However, the observed subgrains are surrounded by small-angle boundaries. It is quite feasible that upon subsequent heating these boundaries would be transformed into high angle, as it can be observed for weakly deformed metals [162].

When solidification rate was reduced from 16 to 7 K/s, in alloy Al+6%Mg small subgrains on the periphery of dendritic cells could be observed very rarely. At the lowest cooling rate of 1.2 K/s for alloy #1 and 1 K/s for alloy #2 these subgrains disappeared completely. The average size of subgrains was so large that their boundaries could hardly be seen in TEM. Their location with respect to dendritic cell boundaries was quite arbitrary. Most probably, at such low solidification rates the migration of subgrain boundaries may occur quite noticeably.

At those cooling rates of Al–Mg alloys when a zone of fine subgrains adjacent to the cell boundary is formed, its characteristic width is clearly correlated with the width of Mg-enriched zone on the periphery of dendritic cells. This was established using X-ray spectroscopy studies of Mg distribution across the dendritic cells at different cooling rates (Table 2.10). We have plotted the curves of Mg distribution similar to the ones shown in Figure 2.10. Using this data, the width of the enriched zone Δl was calculated. As it follows from Table 2.10, it decreases as the cooling rate increases, in parallel with decrease of the fine subgrains zone (Table 2.9). Comparison of Tables 2.9 and 2.10 indicates that in alloy Al–6%Mg (see above) this width is close in its absolute value to Δl.

Table 2.10 indicates that there exists a direct proportionality between the average dendrite cell and subgrain size in the center and on the periphery of dendritic cells. Similar relationship is observed for parameter d and average subgrain size d' (Figure 2.36). This fact has important implications since the value of d', as it is well known, exerts significant influence upon aluminum alloy properties.

The density of dislocations in all studied castings depends weakly on solidification rate (Table 2.9). Given the experimental error in determining ρ one could speak only about a tendency to growth of the number density of dislocations located inside subgrains. This tendency was established for aluminum alloy Al+10%Mg.

2.8.2.2 Alloys on the basis of the Al–Cu system

Using alloy Al + 4%Cu as an example it was demonstrated that any change in the supercooling of molten metal (in the range from 670°C to 850°C) practically does not affect the nature of dislocation microstructures and their number density after solidification with cooling rates from 7 to 25 K/s. In all cases, in spite of the substantial changes in the shape and size of grains and dendritic cells, slightly

Table 2.10 Characteristics of microsegregation in cast aluminum alloys #1 and #2 (Al–6%Mg, 0.66%Mn, 0.2%Fe, 0.13%Si, 0.05%Ti, 0.025%Be and 10.4%Mg, 0.095%Ti, 0.075%Zr, 0.1%Be, 0.044%Fe, respectively)

V_c (K/s)	Δl* (μm)	$(C_p - C_c)/\Delta l$ (%Mg/μm)
Alloy Al–6%Mg, 0.66%Mn, 0.2%Fe, 0.13%Si, 0.05%Ti, 0.025%Be		
1.25	32.5 ± 5	0.35 ± 0.1
6.7	10.3 ± 3	1.0 ± 0.25
16.7	5 ± 1,5	2.3 ± 0.5
38.3	2.3 ± 1	4.9 ± 0.9
Alloy Al–10.4%Mg, 0.095%Ti, 0.075%Zr, 0.1%Be, 0.044%Fe		
1	23 ± 4.5	0.16 ± 0.06
2.1	22 ± 4	0.27 ± 0.07
16.7	8 ± 2	1.2 ± 0.3

* Width of Mg-enriched zone.

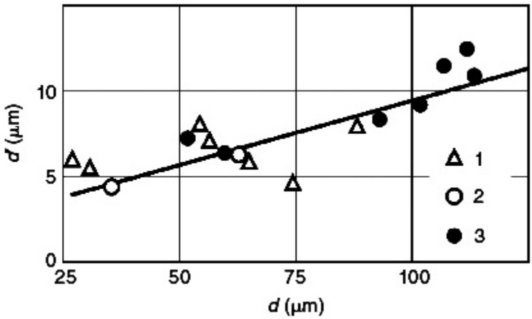

Figure 2.36 Connection between average size of dendritic cells, *d*, and sub-grains, *d*′, in casting alloys of Al with 3% (1), 6% (2), and 9%Mg (3).

deformed cell dislocation structure was formed inside the cells with the average dislocation density of $(1.5 \pm 0.7)10^9\,\mathrm{cm}^{-2}$.

Changes in the applied cooling rate also exert weak influence upon the total dislocation number density. However, it may change significantly the character of forming dislocation microstructures in binary Al–Cu alloys. At cooling rates from 7 to 19 K/s cell microstructure will be formed (which is similar to microstructure shown in Figure 2.34b). Another possibility is the formation of mixed cell/subgrain microstructure. Typically, several dislocation cells will be located inside each dendritic cell. At higher solidification rates, in particular, in welded joints where cooling rate may attain ~1000 K/s, the sizes of dendritic and dislocation cells coincide. Similarly to rapidly solidified thin films [163–165], dislocation "forests" will be observed only on the periphery of dendritic cells, along their boundaries.

If cooling rate for binary alloys is reduced to 0.65 K/s, the distributions of dislocations become more uniform, and cell dislocation microstructure less pronounced. In slowly cooled ($V_c = 0.2$ K/s) industrial castings made of copper-bearing aluminum alloy 203.0 with 0.2%Cd dislocations do not form cells at all, while dislocation density attains a value of $\sim 0.3 \cdot 10^9\,\text{cm}^{-2}$. This is half order of magnitude less than in binary alloys at cooling rates >0.7 K/s. In industrial castings made of alloy 203.0 with 0.2%Cd the total dislocation density turned out to be significantly lower even at relatively high solidification rates: $(0.5 \pm 0.1)10^9$ at $V_c = 0.7$ K/s and $(0.7 \pm 0.2)10^9\,\text{cm}^{-2}$ at $V_c = 7.5$ K/s. Additionally, systematic growth of ρ was observed as solidification rate increased.

Although in Al–Cu casting alloys dislocations mostly form bundles ("forest"), in certain conditions one may expect the formation of planar dislocation boundaries. This depends upon the concentration of copper in alloys and also on the applied cooling rate. In Al–Cu alloy containing 0.5%Cu subgrain boundaries are not formed at any solidification rates. On the other hand, in an alloy containing 4%Cu, planar dislocation boundaries are observed at rates <400°C/min, mostly on the periphery of dendritic cells. Finally, in an alloy containing 5%Cu subgrain boundaries will be observed in welded joints ($V_c = 10^3$ K/s).

2.8.3 The mechanisms of formation of dislocation microstructures in cast aluminum alloys

In order to discuss the empirical rules of formation of dislocation microstructures and the role of solidification conditions it is important to answer the fundamental question: Which mechanism(s) are responsible for the formation of these dislocations? This question becomes even more important if we take into account that their density in as-cast alloys is quite high ($\sim 10^9\,\text{cm}^{-2}$) and comparable to the density of dislocations in metal work hardened at elevated temperatures [166].

Possible mechanisms of dislocation nucleation upon molten metal solidification were analyzed in many works (see, e.g., [130, 167–169]). In our opinion, the following mechanisms of dislocation formation are operable for as-cast aluminum alloys:

1. Stress concentrations arising because of microsegregation processes of alloying elements.
2. Thermal and shrinkage stresses.
3. Collapse of dislocation disks.
4. Stresses at the interface between constituent particles and Al-based solid solution.

5. Merging of dendritic branches originally disoriented with respect to one another.

In most experimental works on dislocation microstructures of cast aluminum alloys [163–165, 170–172] the results are interpreted using the theory of concentration stresses. This theory was developed by Tiller [167, 173, 174] on the basis of a mechanism proposed by the authors of Ref. [175]. The principal idea is that in the presence of concentration gradients (inevitable due to non-aquarium nature of solidification process) in the continuously solidifying layers of (Al) solid solution will have different values of lattice parameters due to the difference in atomic radii of Al and principal alloying elements. As a result, these layers accommodate arising stresses due to the formation of interface dislocations [173].

The density of dislocations ρ_T forming under the influence of concentration stresses, should be equal, according to Tiller:

$$\rho_T = \frac{\Phi}{2 \cdot b}\left(\frac{\Delta C \cdot \Delta r}{r} - e_p\right) \tag{2.37}$$

In equation (2.37) r stands for the atomic radius of the matrix; Δr is the difference in atomic radii between the matrix and the alloying element; b is the Burgers vector of dislocations; Φ is the geometrical factor (for equiaxed cells $\sim 8/d$, where d – is the cell size); ΔC is the difference of concentrations for alloying element in the domain of a sharp concentration gradient; and e_p is the ultimate elastic deformation.

Experimental data [137, 151, 176–179] indicates that the mechanism of formation of dislocations in single crystals due to concentration-related stresses is responsible for a significant contribution to the overall density of dislocations. As far as the polycrystalline aluminum alloys are concerned, the Tiller theory was tested for these materials only on a qualitative level [163–165, 170–172].

Above we considered the results obtained in Ref. [180] related to comparative analyses of dislocation structures of different binary and multicomponent alloys after solidification in different conditions. These conditions were chosen in such a way that the levels of concentration stresses were very different. As it follows from Table 2.11 the difference in atomic radii of aluminum atoms and those of alloying elements, Δ, in selected systems varied from 0.005 to 0.031 nm, while the maximal difference in concentrations (for the case of complete suppression of diffusion in the solid phase, i.e., Scheil model) – from 0.15 to 65.5 at.%. As a result, the number density of dislocations, ρ_T, calculated according to equation (2.37), must vary within two orders of magnitude for different alloys. At the same time experimentally determined total dislocation density was about the same for all studied materials (see Table 2.9).

Additionally, for all alloys (with the exception of Al–Mg and Al–Zn) calculations using the values of ΔC_{max} yield the values of dislocation density one to orders of magnitude lower than in experiment (see Tables 2.11 and 2.8). If experimental values of ΔC are used for calculations (as it was done in Table 2.8) then the difference between calculated ρ'_T and experimentally determined ρ dislocation

Table 2.11 Characteristics of alloying elements and calculated density of dislocations ρ_T in aluminum alloys of different systems

Alloying element[a]	$\Delta r = r_{Al} - r_{all}$ (nm)	C_a (at.%)	$\Delta C_{max} = C_a - C_n$[b] (at.%)	$\rho_T \cdot 10^{-8}$ (cm^{-2})
Mg	+0.17	18.9	18.1	33
Mn	−0.13	0.7	0.37	0.38
Cu	−0.15	2.5	2.2	4
Zn	−0.05	66.5	65.5	28
Be	−0.31	0.19	0.15	0.48
Ge	−0.06	2.8	2.55	1.5

[a] For alloys with 2.2% at. addition (with the exception of alloys Al–Mn (0.6%) and Al–Be (0.17 %)).
[b] C_n is concentration of alloying element in solid solution formed at the onset of solidification.

densities will be practically for all alloys from one to two orders of magnitude. The corrected calculated values ρ'_T in Table 2.8 were significantly lower than ρ_T in Table 11. The values of ΔC in Table 2.8 were presented according to the data of micro-X-ray spectroscopy analysis for those samples that were used for preparing foils for TEM studies. ΔC values were calculated as the average difference of concentrations of the alloying element on the periphery and in the center of ~5–10 dendritic cells. The variability coefficient for ΔC was not higher than 20%.

Tiller's theory predicts that the overall dislocation density should increase when the concentration of alloying element soluble in (Al) goes higher. However, this is observed only for Al–Mg alloys, and even in this case deviations from the theory predictions are quite substantial.

Thus, we can conclude that in as-cast aluminum alloys concentration stresses are not the principal reason for the formation of dislocations. Obviously, some other mechanisms must be at work for polycrystalline aluminum alloys. However, it is necessary to emphasize that at least in principle, for single crystals the observed changes in the density of dislocations (10^6–10^8 cm^2) could be explained by the differences in concentration stresses.

A second possible mechanism of dislocation nucleation might be related to thermal and shrinkage stresses that inevitably arise in the course of solidification and subsequent cooling. It is clear that if their values exceed the alloy's elastic modulus (which is very low at high temperatures anyway) then plastic deformation will develop and new dislocations will nucleate. According to the existing data the density of dislocations having this origin does not exceed 10^5 cm^{-2} for single crystals [181–184]. In large ingots, where thermal stresses can be quite substantial, one should expect higher values of dislocation density (formed as a direct result of these stresses).

Stresses arising in the course of ingot solidification and cooling due to shrinkage often may result in the formation of ingot cracks, both hot and cold. This fracture could be preceded by plastic deformation of the relatively soft, especially at high temperatures, aluminum solid solution accompanied by the formation and multiplication of dislocations. The difference between thermal and shrinkage stresses in all studied castings made of different aluminum alloys solidified in similar conditions was insignificant – it could arise only due to the differences in alloy chemical compositions. When the conditions of solidification are changed, in particular, the cooling rate, this difference should become more pronounced. However, as it was demonstrated above, one should not expect significant differences in dislocation densities even in this case. It should be reminded that all laboratory castings were of small size and of a simple cylindrical shape; so even at relatively high solidification rates large shrinkage and thermal stresses should not be expected.

In order to see appreciable differences in the values of thermal and shrinkage stresses and to evaluate their respective contributions to the overall dislocation density, special studies were conducted [180]. Polycrystalline aluminum (99.99%) and alloy $Al + 2.2$ at.%Cu were cast into a special graphite mold with one movable head, in which it solidified in the conditions of stress free shrinkage, and also in conditions mimicking significant stresses – the latter was achieved by adding to the movable head of different weights. However, even in the conditions of maximal resistance to solidification (shrinkage stress ~1 MPa) the density of dislocations increased only very insignificantly. For example, in pure aluminum it increased from $(5.3 \pm 0.8)10^8$ up to $(7.3 \pm 0.5)10^8$ cm^{-2} at maximal resistance to shrinkage. For alloy $Al + 2.2$ at.% Cu solidified under the conditions of complicated shrinkage, the density of dislocations remained practically the same in the vicinity of the crack and far from it.

To obtain different levels of thermal stresses samples made out of alloys [$Al + 0.6$ at.%Mn] and [$Al + 0.6$ at.%Cu] were cooled after one hour of homogenization at temperature equal to $0.9\ T_m$ in the furnace. The density of dislocations in all alloys changed very insignificantly: for example in alloy $Al + 0.6\,Mn$ – from $(7.8 \pm 0.5)10^8$ for rapid cooling to $(4.4 \pm 0.3)10^8$ cm^{-2} in the case of slow cooling.

Additional experiments were conducted in such a way that after cooling with a predetermined rate ($V_c = 0.5$ K/s) in the solidification range, after the solidus temperature was achieved, subsequent cooling was conducted by quenching into water ($V_c \cong 16$ K/s). Alternatively, casting was cooled very slowly with the furnace. In the first case ρ was equal to $(1 \pm 0.5)10^9$, in the second case $-\rho = (0.2 \pm 0.02)10^9$ cm^{-2}. One should keep in mind that when the cooling rate (below the solidus temperature) was three orders of magnitude lower, this not only reduced the overall level of thermal stresses, but also ensured substantial perfection of the dislocation structure. As a result, dislocation density could have decreased somewhat.

Consequently, even very different solidification conditions (and subsequent cooling) do not exert appreciable influence upon dislocation density due to different thermal and shrinkage stresses. This conclusion is confirmed by the comparison of the dislocation density in different aluminum alloys obtained in laboratory and industrial conditions (in the form of ingots of different sizes, shape castings, welded joints). In all cases the dislocation density was equal to $\rho \cong 10^9\ \text{cm}^{-2}$.

It is also known that disk-shaped clusters of vacancies can "shut down" upon achieving a certain critical size; and dislocation loops are formed as a result [185–187]. Behind the solidification front there is always a certain vacancy supersaturation. These vacancies may form clusters, and in the case of sufficiently rapid cooling – dislocation loops.

Even if a tenfold supersaturation with vacancies is achieved, the maximal dislocation density (provided there are no vacancy sinks present in the system), does not exceed $10^6\ \text{cm}^{-2}$ [188]. Even in pure metals this mechanism can become operational only upon alloy quenching. However, in aluminum alloys dissolved atoms can bind vacancies into complexes and decrease the concentration of free vacancies. As a result, the density of dislocations formed from vacancies also decreases [189, 190]. For example, the data from [190] indicates that increased concentration of magnesium in aluminum solid solution from 1.12 to 8.2 at.% decreases the density of dislocation loops formed after quenching almost by three orders of magnitude. If the vacancy mechanism of dislocation formation is to be considered dominant, then the density of dislocations should decrease with heavier alloying, for example, in the Al–Mg system. However, as it was pointed above, dislocation density in cast aluminum alloys practically does not change, while in the Al–Mg based alloys it even becomes higher as the concentration of magnesium increases (see Table 2.8).

Experimental observations also demonstrated that the overall number of vacancy loops in studied castings is very low even after solidification with relatively high cooling rates (granules, welded joints). Besides, cooling rate affects the density of dislocations only very weakly, while the vacancy mechanism assumes that the number of dislocations will grow when the applied cooling rate becomes higher. This contradiction will not disappear if we use the notions about the nucleation of new dislocation loops at relatively low vacancy supersaturations proposed by Bardeen and Herring [191]. In this latter case the number of forming vacancies will also be ultimately determined by the excess amount of non-equilibrium vacancies. This, in turn, should also depend upon the applied cooling rate.

On the basis of these considerations we can make a conclusion that in the explored range of solidification rates the role of vacancy mechanism of dislocation formation is insignificant. The presence of different number of dislocations most probably influences the ease of double cross-slip in the process of restructuring of a given dislocation microstructure.

The presence of constituent particles may cause, in the process of solidification, the formation of elastic stresses at the interphase surfaces due to different thermal compression of the matrix and the particles, and also because of the difference in their elastic modules. These stresses can exceed the elastic modulus (limit) of the matrix and result in the generation of dislocation loops [188]. This mechanism was laid as the foundation of the technique of reduction of internal stresses using thermo-cycling stabilizing heat treatment proposed by Henkin [192].

However, this mechanism seems to be not very effective in the case of solidification and cooling. Otherwise we would have observed a difference in the density of dislocations in alloys with small and large amounts of constituent particles. In reality, such a difference is simply absent.

According to Prohazka [193], dislocations could nucleate due to the temperature gradient between the adjacent dendrite arms. When such arms coalesce, the arising "dilation" stresses may result, according to the author's calculations, in the formation of new dislocations. However, their density cannot exceed $10^6\,\text{cm}^{-2}$. The experimental verification of this hypothesis was not done; moreover, it is very difficult even to envision such an experiment.

The last of the considered dislocation nucleation mechanisms in the course of solidification is related to the coalescence of adjacent crystallites with different crystallographic orientation. According to Bochvar [168], the thoughts on a possibility of such a mechanism were expressed in 19th century by Cnernov.

In the course of dendrite formation upon solidification, the mutual pressure exerted by weak and plastic dendrite arms may cause their bending. When two arms coalesce, they become disoriented with respect to each other, and the nucleation of dislocations in the positions with the maximal disorientation becomes inevitable [168, 194, 195]. The quantitative estimate of the density of dislocations forming according to this mechanism was provided in Ref. [161].

In order to obtain such an estimate experiments with a number of binary alloys solidified in similar conditions were conducted. In as-cast samples the authors obtained a metallographic estimate of the average size of dendritic cells. Experiments with foils provided the average disorientation angle along the boundaries. Then the obtained results were used to calculate the density of dislocations ρ''_{T}, which would correspond to coalescence (merging) of the cells with diameter d oriented at angle θ with respect to each other:

$$\rho''_{\mathrm{T}} = 3d^{-1} \cdot \frac{\theta}{b}$$

The calculated ρ''_{T} density was compared to the experimentally determined dislocation density ρ (see Table 2.12).

As can be seen from Table 2.12, when the average size of dendritic cells is about the same, the disorientation angles are relatively small. As a result, the values of ρ''_{T} for all studied alloys are almost identical. Most importantly, they are very close in their absolute values to the experimentally determined value of ρ. This result is very important. It is a clear indication that the coalescence of dendritic arms may be the principal cause for the formation of dislocations in as-cast aluminum samples. However, this conclusion still requires some additional verification. The principal reason for that is because the measurements of d and θ were conducted in castings at room temperature, while their values, especially θ, could change in the process of cooling after solidification.

Table 2.12 Density of dislocations in as-cast alloys

Alloy composition	d, μm	θ, degrees (θ, radians)	$\rho''_T 10^{-9}$, cm^{-2} ($\rho \cdot 10^{-2}$, cm^{-2})
Al + 0.6 at.%Mn	32 ± 2	1° 50′ ± 40′ (0.032)	1.29 ± 0.6 (1.3 ± 0.2)
Al + 2.2 at.%Zn	51 ± 5	2° 30′ ± 60′ (0.044)	1.09 ± 0.5 (1.9 ± 0.15)
Al + 2.2 at.%Ge	25 ± 2	1° 13′ ± 30′ (0.019)	1.46 ± 0.6 (2.6 ± 0.2)
Al + 2.2 at.%Cu	22 ± 2,5	58′ ± 25′ (0.017)	0.8 ± 0.4 (1.2 ± 0.1)

Specially designed experiments demonstrated that θ remained practically the same both for samples quenched into water and cooled down slowly inside the furnace. However, even these results are not a direct indication that the disorientation angles measured at room temperature stayed the same in the course of dendritic arms coalescence, because polygonization processes still could, at least to some extent, proceed even in the course of rapid cooling. However, the available body of experimental work allows one to assume that most dislocations are formed according to this mechanism. Other mechanisms can also cause the formation of dislocations, but their overall number should be at least one to two orders of magnitude lower. When temperature falls below solidus line, the overall amount of dislocations varies very insignificantly.

The type of the formed dislocation microstructure, most probably, is defined by the dislocation behavior after the completion of solidification. In this sense it is easy to understand such processes as the perfection of the alloy substructure as the cooling rate after solidification decreases. However, the relationship between dislocation microstructures and alloy composition remains unexplained.

For example, the formation of subgrain microstructure in alloys with elevated magnesium concentration is an indication of the relative ease of polygonization processes in such alloys. However, it is still difficult to explain *why* this happens. Existing literature data on work-hardening (and partial softening) mechanisms accompanying deformation and post-deformation heat treatments are quite contradictory. According to Refs. [196–198], the additions of magnesium to aluminum increase the overall concentration of vacancies, which, in turn, may facilitate the formation of subgrain microstructure. However, according to Refs. [196, 198], at higher concentrations of magnesium the tendency to polygonization becomes less pronounced, while experiments clearly indicate that it grows as the concentration of Mg increases from 0.6 to 14 at.%.

2.8.4 Decomposition of aluminum solid solution in the process of alloy cooling after the completion of solidification

At temperatures below the line of non-equilibrium solidus technical aluminum and most aluminum alloys possess two and multi-phase microstructure. Due to

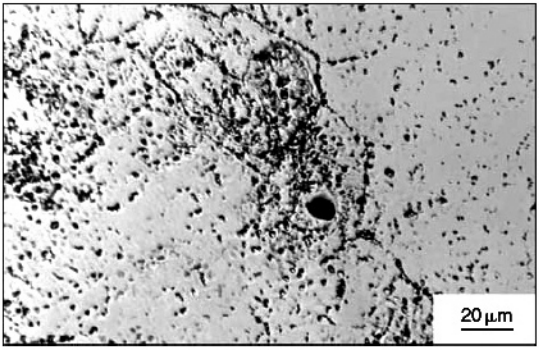

Figure 2.37 Secondary precipitates in microstructure of Russian casting alloy АЛ24М ($V_c = 0.13$ K/s); optical microscopy.

the decreased maximum solubility of alloying elements in aluminum with lower temperatures, aluminum solid solution will be supersaturated. This is particularly true with respect to peripheral layers of dendrites enriched with the basic alloying elements. As a result, in the process of cooling below the solidus temperature decomposition of this supersaturated solid solution may take place, accompanied by the formation of dispersoids or precipitates that represent an important part of alloy microstructure. This process is well known and was discussed in Refs. [129, 199, 200].

At low cooling rates ($<10^1$ K/s) the products of decomposition can be observed even using an optical microscope (Figure 2.37). This scenario is typically observed for massive castings and large diameter ingots (especially sand cast). At higher cooling rates dispersoids and precipitates cannot be observed in optical microscope, although it is natural to assume that decomposition takes place in a certain range of these higher cooling rates. Direct observation of dispersoids and precipitates is possible using SEM and/or TEM.

Below we provide the data on TEM studies (both in imaging and in diffraction mode) of dispersoids in cast aluminum alloys of different chemical composition after solidification and cooling with different cooling rates [180]. The principal goal of these studies was to assess the maximal cooling rates at which the formation of different dispersoids and precipitates for alloys of different chemical composition. Additionally, it was attempted to compare the degree of decomposition of aluminum solid solution in different alloys in similar cooling conditions, to the strength increase achieved after aging without quench (i.e., T5 heat treatment). These goals are important, in particular, for selection of the perspective systems and alloying additions for development of high-strength casting aluminum alloys.

The following alloys were studied: binary systems Al–Cu (4–5%), Al–Mg (6–10%), ternary systems Al–Mg–Zn (4%Zn + 2%Mg and 4%Mg + 3.5%Zn), and also industrial alloys on the basis of these systems–203.0 with 0.2%Cd, AlMg6, AlMg10, 7016, 7019, AlMg4Zn3, and Si-bearing alloys 356.0, A355.0, and

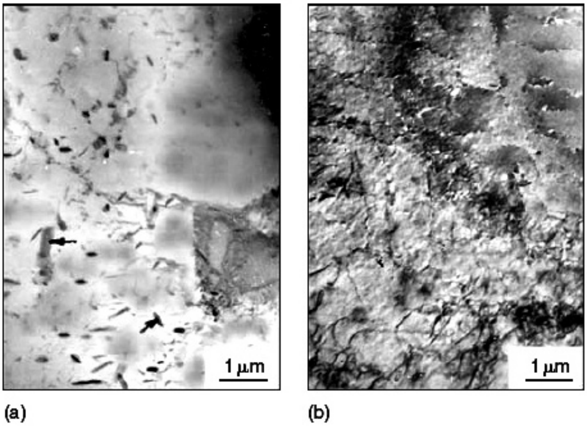

Figure 2.38 Secondary precipitates in microstructure of alloys (a) Al + 4.5Mg + 3.5Zn, $V_c = 10$ K/s TEM and (b) Al + 5%Cu, $V_c = 0.16$ K/s TEM.

AlSi5Cu7. In binary alloys of the Al–Cu and Al–Mg systems dispersoids with average size less than 0.1 μm can be observed in an electron microscope at cooling rates of the order of ~10 K/s. They are typically located on the periphery of dendritic cells (Figure 2.38). As the cooling rate becomes lower, natural coarsening of the dispersoids and the increase of their volume fraction were observed. For example, in alloy AlMg6 after cooling with the rate of 75° C/min the linear size of dispersoids was ~0.6 μm. These dispersoids were classified as the equilibrium β-phase. The cooling rate below the solidus line was somewhat lower, but it was not always determined. For this reason we provide data on the cooling rate inside the solidification range. It needs to be stressed that in all samples the products of decomposition of (Al) could not be revealed using an optical microscope.

As it is known from the literature, alloys of the Al–Mg–Zn system are considered to be self-quenching [123, 202]. This implies that their mechanical properties after quenching and aging are almost independent of the quench rate (i.e., exhibit no quench sensitivity), while the properties of welded joints after aging without preliminary quenching are close to the properties of selected material after full thermal treatment. For castings the property of self-quench is also very important because it allows, at least in principle, to obtain high alloy strength using only T5 heat treatment (i.e., aging without quench).

TEM studies demonstrated that the ability of Al–Mg–Zn alloys to self-quench in the course of cooling after solidification depends very strongly upon the content of principal alloying elements (magnesium and zinc) and also additions of transition metals that typically result in improved mechanical, technological, and corrosion properties of alloys.

In ternary alloy with 4%Zn and 2%Mg, and also in ingots of industrial alloys 7016 and 7028 with diameter 92 mm with the same amounts of zinc and magnesium at cooling rate 8 K/s decomposition of (Al) did not take place. However, in a more alloyed material containing 4%Mg and 3.5%Zn (and even more so in multi-component alloys on the basis of this composition) the first indications of (Al) decomposition appear at the same cooling rates as in binary systems Al–Cu and Al–Mg. Moreover, if one compares the degree of such decomposition (presence and number density of dispersoids and precipitates, their averages size and composition) after cooling with different rates, we arrive to a single overriding conclusion that it is more complete in Al–Mg–Zn alloys.

Special experiments were conducted with castings made of different alloys. Each alloy was cooled inside its solidification range with four different rates: 27, 95, 20, and 67 K/s. TEM analyses of as-cast ingots demonstrated that dispersoids in binary systems with 5%Cu and 10%Mg and in similar industrial alloys are formed only after cooling with the minimal rate of 2.7 K/s. In ternary alloy Al + 4%Zn + 2%Mg they could be found at higher cooling rate (9.5 K/s), while in alloy Al–4%Mg – 3.5%Zn and commercial alloys – at even higher rates (20 K/s, or even 67 K/s (e.g., in alloy AlMg4Zn3).

At first it looks like these results are in direct contradiction with the concept of self-quenching of alloys in the Al–Zn–Mg system. However, Table 2.13 illustrates that the increase of castings strength after aging without quenching, in spite of the lower stability of (Al), is much greater than for Al–Mg and Al–Cu alloys with approximately the same relative degree of alloying of the solid solution (the ratio of concentration of alloying elements to their maximal concentration at the temperature of quenching).

We can conclude that ability to self-quench for castings made of different alloys (assessed primarily as the effect of hardening after aging without quenching) may not necessarily be connected to the stability of aluminum-based solid solution. Most probably the principal factor defining hardening of casting alloys after aging is connected to the nature, quantity, and morphology of the products of (Al) decomposition, while the degree of its alloying plays a secondary role. It is for this reason that Al–Zn–Mg alloys can be hardened considerably to a greater extent than alloys of all other systems.

If alloys of the same alloying system but having different chemical compositions are compared, then a direct correlation can be established between (Al) stability and the effect of hardening without quench.

After etching of the Al–Zn–Mg alloy specimens in the Keller reactive, it becomes clearly visible in optical microscope that the zones on the periphery of dendritic cells are etched to a higher extent (see Figure 2.39). According to the TEM analysis these zones more or less rigorously correspond to micro volumes containing the products of (Al) decomposition with respect to either Mg or Zn. For this reason if we determine the volume fraction of the zones with enhanced degree of etching (Q_z), it becomes possible to make a judgment about the degree of (Al) decomposition at cooling below the solidus temperature. This can be easily done using conventional methods of metallographic analysis.

In Table 2.13, we compare a number of alloys on the basis of the Al + 4%Mg + 3.5%Zn composition with respect to such characteristics as Q_z

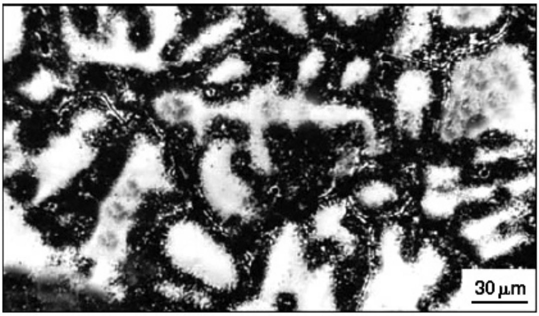

Figure 2.39 Zones highly susceptible to etching (dark areas) on the periphery of dendritic cells in Russian casting alloy "Aл24M" (light microscopy).

Table 2.13 Increase of the yield strength $\Delta\sigma_{0.2}$ and ultimate tensile strength $\Delta\sigma_B$ at room temperature after aging* without quenching of castings made of alloys of different (solidification into metallic mold with diameter 50 mm and ($V_c \cong 350$°C/min)

Concentration of alloying element (%)						Q_z (vol.%)	$\Delta\sigma_{0,2}$ (MPa)	$\Delta\sigma_B$ (MPa)
Mg	Zn	Ti	Fe	Si	Other			
–	–	–	<0.2	<0.2	Cu 5	–	11	8
–	–	0.25	<0.2	<0.2	Cu 5, Mn 0.6	–	11	3
10	–	–	<0.2	<0.2	–	–	8	6
10	–	0.1	<0.1	<0.1	Zr 0.1, Be 0.1	–	12	15
2	4	–	<0.1	<0.1	–		42	38
4	3.5	0.15	<0.1	<0.1	–	29 ± 5	120	60
4	3.5	–	<0.1	<0.1	–	33 ± 6	110	40
4	3.5	0.15	<0.1	<0.1	Ce 0.2	33 ± 6	120	70
4	3.5	0.15	<0.1	<0.1	Ce 0.2	32 ± 6	130	50
4	3.5	0.15	<0.1	<0.1	Ce 0.2, Mn 0.4, Cr 0.1	100	70	40
4	3.5	0.15	0.4	0.1	Zr 0.15, Be 0.1	100	50	40

* Aging was conducted in a way ensuring the maximal hardening effect: alloys of the Al–Cu system – at 150°C, 3–6 hours, alloys of the Al–Mg system – at 80°C, 20 hours, alloys of the Al–Zn–Mg system – at 110°C, 10 hours + 150°C, 16 hours.

and the degree of alloy hardening after aging without quenching. It is obvious that in alloys where decomposition achieved some 30–33% of the whole volume of dendritic cells, the degree of hardening (especially increase in YS) after aging is considerably higher than in multicomponent alloys (where after cooling of castings below the solidus temperature a more complete decomposition of solid solution took place). This higher degree of decomposition with respect to the principal alloying components is explained via lower stability of aluminum solid solution after the introduction of additions of transition metals [203]. It should be noted here that not in a single casting alloy did we discover aluminides of transition metals. Of course, it cannot be excluded that very fine dispersoids still are formed at low cooling rates. In any case, decomposition of (Al) with respect to transition metal additions is insignificant, and in the first approximation it can be omitted from consideration.

CHAPTER THREE

INFLUENCE OF HEAT TREATMENT UPON MICROSTRUCTURE OF CASTING ALUMINUM ALLOYS

Castings made of aluminum alloys can be subjected to different kinds of heat treatment (e.g., homogenizing to remove residual stresses, heterogenizing, solution heat treatment with subsequent quench). Sometimes aging of castings can be conducted without prior quench (e.g., T5 temper) using the effect of supersaturation of Al-based solid solution in the course of non-equilibrium solidification. In certain cases (particularly often after casting under pressure) aluminum alloys can be used without any heat treatment (i.e., in the F-temper). This is the foundation of the so-called CTS-production approach (Cast-Trim-Ship).

The standard types of heat treatments are described in Table 3.1. Such tempers as T4 (quenching without artificial aging) and T6 (aging for maximal strength) are used most often.

Table 3.1 Types of heat treatment for casting aluminum alloys

Heat treatment	Designation in Russia (GOST 1583–93)	Designation in the USA (Aluminum Association)
Without heat treatment	–	F
Artificial aging after casting	T1	T5
Annealing	T2	O
Quenching (plus natural aging)	T4	T4
Quenching and incomplete artificial aging	T5	(T6)
Quenching and artificial aging for maximal strength (complete aging)	T6	T6
Quenching and overaging	T7	T7
Quenching and significant overaging	T8	–

Casting Aluminum Alloys
ISBN-13: 978-0-08-045370-5

© 2007 Elsevier Ltd.
All rights reserved.

3.1 HOMOGENIZING HEAT TREATMENT

After casting most aluminum alloys are typically subjected to homogenizing heat treatment, which for casting alloys can be combined with isothermal tempering before quenching. Homogenizing heat treatment is the most widespread type of heat treatment for casting alloys. Its primary goal is to eliminate the consequences of microsegregation, as well as to raise the level of properties for shaped castings. In the case of wrought aluminum alloys, another advantage is in increased technological formability before subsequent thermo-mechanical treatments such as rolling, extruding, etc. [88, 123, 204].

In the course of homogenization of aluminum alloys the following processes take place:

1. Dissolution of non-equilibrium phases and corresponding constituent particles.
2. Elimination of concentration inhomogeneities for the alloying elements (micro segregation).
3. Changes in phase composition and constituent particle morphology.
4. Changes in grain and dislocation microstructures of aluminum solid solution.
5. Decomposition of aluminum solid solution in the course of isothermal heat treatment accompanied by the formation of dispersoids (in alloys containing additions of transition metals).
6. Development of secondary porosity.
7. Decomposition of solid solution with respect to the principal alloying elements upon cooling after isothermal heat treatment.

All of these processes are described in detail below.

3.1.1 Dissolution of non-equilibrium constituent particles in the course of homogenization

Dissolution of non-equilibrium excessive constituent particles is one of the most important goals of homogenization heat treatment. This was stressed by Voronov Ref. [205] who believed that improved mechanical properties of casting alloys after homogenization are directly related to the dissolution of excessive constituent particles.

Quantitative experimental and analytical studies of dissolution in the course of homogenization appeared only in the beginning of the sixties of the last century. Diffusion calculations were conducted for the process of dissolution for binary cast alloys. Since the process of dissolution is governed by the diffusion equations, its kinetics can be assessed using such calculations. It was established that in as-cast aluminum alloys typically only those excessive phases will be dissolved during homogenization that are formed by the principal alloying elements. With aluminum, these elements give phase diagrams of the eutectic type. Let us consider alloy X of such a system located in between the points of limit solubility, C_a, and

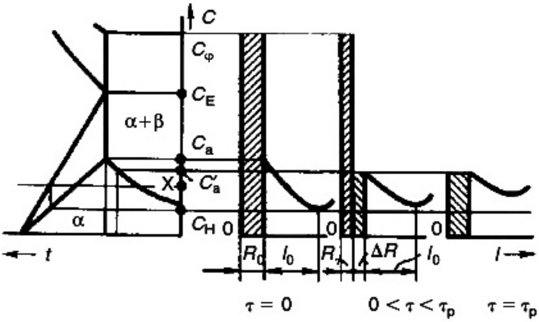

Figure 3.1 Schematic of alloying element concentration changes in the vicinity of dissolving inclusion during homogenization of casting alloy X.

the ordinate axis corresponding to pure aluminum (Figure 3.1). As a result of microsegregation, as it was discussed above, a non-equilibrium eutectic can be formed, which often degenerates into β-phase. In the course of homogenization at the corresponding temperature, the alloy figurative point is located in the single phase domain corresponding to the α-phase. Consequently, the β-phase must dissolve completely with time. In Ref. [144] an expression for the expected dissolution time was obtained based on the Fick's first law. Indeed, the mass of substance dm (grams) that diffuses during time dτ (sec) through a surface with the area dS (cm^2):

$$\mathrm{d}m = D_\mathrm{V} \cdot \frac{\mathrm{d}c}{\mathrm{d}l} \cdot \mathrm{d}S \cdot \mathrm{d}\tau \tag{3.1}$$

where dc/dl stands for the concentration gradient, and D is the diffusion coefficient.

Substituting differentials for finite differences, we get:

$$\Delta m = D_\mathrm{V} \cdot \frac{\Delta C}{\Delta l} \cdot \Delta S \cdot \Delta\tau \quad \text{or} \quad \Delta\tau = \frac{\Delta m \cdot \Delta l}{D_\mathrm{V} \cdot \Delta C \cdot \Delta S} \tag{3.2}$$

Now it is possible to express the coefficients of equation (3.2) via the structural characteristics and physical constants of a given alloy. If one assumes that the dissolution of the β-phase takes place as a result of diffusion of the alloying element B from this phase into solid solution α, then to achieve complete dissolution it is necessary to transfer into solid solution the amount of B equal to the difference between its concentration in the β-phase and limit solubility in α-solid solution at the temperature of homogenizing heat treatment (C'_a in Figure 3.1).

The relative amount of component B contained in the β-phase (in mass%) can be found using the equation below:

$$M'_\beta = \mathrm{Qv}_\beta \cdot \frac{\gamma_\beta}{\gamma_\mathrm{alloy}} \cdot \frac{C_\beta}{100}$$

In this equation Q_{V_β} is the volume fraction of the β-phase (vol%); γ_β, γ_{alloy} are the densities of β-phase and alloy, respectively (in g/cm^3); C_β is the concentration of component B in the β-phase.

If one assumes that after the dissolution of the β-phase the concentration of solid solution will correspond to the limit value at the temperature of annealing (C'_{a} in Figure 3.1), then the amount of component B, remaining at the site of the dissolved constituent particle of the β-phase, will be equal (in mass%) to:

$$M'_\alpha = Q_{V_\beta} \cdot \frac{\gamma_\alpha}{\gamma_{\text{alloy}}} \cdot \frac{C'_{\text{a}}}{100}$$

In this expression, γ_α is the density of (Al) with concentration C'_1.

The amount of component B (in mass%), that has diffused from the β-phase in the course of its dissolution is equal to:

$$\Delta m = M'_\beta - M'_\alpha \cdot \left[\left(\frac{Q_{V_\beta}}{100} \cdot \left(\frac{\gamma_\beta}{\gamma_{\text{alloy}}} \cdot C_\beta - \frac{\gamma_\alpha}{\gamma_{\text{alloy}}}\right) \cdot C'_{\text{a}}\right)\right] \qquad (3.3)$$

To calculate the value of the concentration gradient it is necessary to define a model for the process of dissolution of excessive constituent particles during homogenization. The following model was selected which allowed to obtain the best coincidence between calculated and experimental data.

In as-cast alloy after non-equilibrium solidification each constituent particle is surrounded by the Al-based solid solution of variable composition. In the process of annealing the elimination of microsegregation takes place. The concentration of B in (Al) in the vicinity of the β-phase particles goes down from the limit value C_{a} corresponding to the eutectic temperature, and must be lower than C'_{a} corresponding to the temperature of annealing (Figure 3.1). Only after that the process of dissolution of excess phases will commence; during that process the (Al) concentration will remain equal to C'_{a} near the interphase boundary.

The dissolution of the β-phase inclusions is controlled by diffusion processes in the α-solid solution beyond the limits of the original location of the interphase boundary. The transition of atoms across this boundary is a sufficiently rapid process ensuring that the concentration of solid solution remains constant as an inclusion gets dissolved at the homogenization temperature T. Within the framework of such a model where the β-phase is considered to be a source of the diffusing component, the concentration gradient can be determined as the ratio of the concentration difference (ΔC) of component B in (Al) near the inclusion of the β-phase and inside the cell, to the characteristic length scale of diffusion process. The concentration of component B near the inclusions will be constant and equal to C'_{a}, while its concentration inside the dendritic cells will be growing as the β-phase continues to dissolve. One can get an estimate for the average value for equation (3.2) as:

$$\Delta C_{\text{cp}} = \frac{\Delta C_0 + \Delta C_2}{2}$$

where ΔC_0 and ΔC_2 stand for the differences of concentrations in the initial moment and final moment of the dissolution process.

The content of B inside dendritic cells of (Al) before (C_n) and after dissolution (C_K) of the β-phase can be determined as the difference between its relative amount in the alloy and in the β-phase (or in (Al)), and concentration C'_a, at the site where that particle is dissolved. The values of C_n and C_K will be somewhat high because we did not take into account the concentration rise near inclusions.

For C_n and C_K, we get (in mass%):

$$C_n = X - M'_\beta = X - Q_{V_\beta} \cdot \frac{\gamma_\beta}{\gamma_{\text{alloy}}} \cdot \frac{C_\beta}{100}$$

$$C_K = X - M'_\alpha = X - Q_{V_\beta} \cdot \frac{\gamma_\alpha}{\gamma_{\text{alloy}}} \cdot \frac{C'_a}{100}$$

If calculations are made for 100 g of alloy, then we get for C_H and C_K (g/cm^3):

$$C_n = X \cdot \frac{\gamma_{\text{alloy}}}{100} - Q_{V_\beta} \cdot \gamma_\beta \cdot \frac{C_\beta}{10^4}$$

$$C_K = X \cdot \frac{\gamma_{\text{alloy}}}{100} - Q_{V_\beta} \cdot \gamma_\alpha \cdot \frac{C'_a}{10^4}$$

The difference of concentrations in the initial and final moments of dissolution (g/cm^3):

$$\Delta C_K = C'_a \cdot \frac{\gamma_\beta}{100} - X \cdot \frac{\gamma_{\text{alloy}}}{100} + Q_{V_\beta} \cdot \gamma_\alpha \cdot \frac{C'_a}{10^4}$$

The average concentration difference (g/cm^3):

$$\Delta C_{cp} = \frac{\Delta C_n + \Delta C_K}{2} = C'_a \cdot \frac{\gamma_\alpha}{100} - X \cdot \frac{\gamma_{\text{alloy}}}{100} + \frac{Q_{V_\beta}}{2 \times 10^4} \cdot (\gamma_\beta \cdot C_\beta + \gamma_\alpha \cdot C'_a) \tag{3.4}$$

In the initial approximation the concentration gradient can be calculated as:

$$\frac{\Delta C}{\Delta l} = \frac{\Delta C_{cp}}{\left(\frac{d}{2}\right)} \tag{3.5}$$

The value of $d/2$ stands for the radius of dendritic cells in equation (3.5). As it was demonstrated earlier, the concentration of allowing element changes most dramatically near the boundary of dendritic cells, at ~1/4–1/3 of its diameter. For this reason using the value of $\Delta l = d/2$ in equation (3.5) will give a somewhat low value of the concentration gradient.

The surface area ΔS through which diffusion takes place is taken to be equal to the overall surface S of all constituent particles of the β-phase in the alloy used in the present study. Taking into account that experimentally determined surface typically has the dimension of mm^2/mm^3, we get (in $cm^2/100\,g$):

$$\Delta S = \frac{S \cdot 10^3}{\gamma_{\text{alloy}}} \tag{3.6}$$

The diffusion coefficient D within the framework of our accepted model must be determined for the case of diffusion of alloying element from solid solution of the limit concentration C'_n into (Al) inside the dendritic cells. Substituting equations (3.3)–(3.6) into expression (3.2), we obtain the average time of complete dissolution of constituent particles β-phase (in sec):

$$\tau_{pacy} = \Delta\tau = \frac{Q_{V_\beta} \cdot \left(\frac{\gamma_\beta}{\gamma_{\text{alloy}}} \cdot \frac{Q_{V_\beta}}{100} - \frac{\gamma_\alpha}{\gamma_{\text{alloy}}} \cdot \frac{C'_a}{100}\right) \cdot \frac{d}{2} \cdot 10^{-4}}{D_V \cdot S\left(C'_a \cdot 10 \cdot \frac{\gamma_\alpha}{\gamma_{\text{alloy}}} - 10 \cdot X\right) + Q_{V_\beta} \cdot \frac{\gamma_\beta \cdot C_\beta + \gamma_\alpha \cdot C'_a}{2 \cdot \gamma_{\text{alloy}}}}$$

$$= \frac{Q_{V_\beta} \cdot A \cdot \frac{d'}{2} \cdot 10^{-4}}{D_V \cdot S \cdot (B + K \cdot Q_{V_\beta})} \tag{3.7}$$

In this last expression A, B, and K are the coefficients constant for an alloy of a given chemical composition and depending upon its physical constants (properties).

Coefficients A, B, and K can be determined from reference tables, while Q_β, d, and S need to be assessed experimentally.

Expression (3.7) can also be used for calculation of the dissolution time of non-equilibrium excessive eutectic phase in hypo-eutectic alloys with composition falling in between C_n and eutectic concentration. In this case the value Q_{V_β} will represent not the overall volume fraction of eutectic, but only its non-equilibrium (excessive) part. To calculate Q_{V_β} it is necessary to subtract from the experimentally determined eutectic volume fraction in as-cast alloy its equilibrium fraction, which can be assessed using the corresponding equilibrium phase diagram. To verify equation (3.7) experimentally the dissolution times for non-equilibrium eutectics ($\alpha + CuAl_2$) in alloy Al + 4.5%Cu, and that of β-phase in alloy Al + 10%Mg were determined metallographically. Different values of Q_{V_β}, d, and S were obtained for different solidification rates. Homogenizing heat treatment was conducted at temperature $(440 \pm 2)°C$ for Al–Mg alloys and $(535 \pm 2)°C$ for Al–Cu alloys. After every 30 min of heat treatment samples were quenched into water and analyzed metallographically. Thus, the maximal error in determination of the dissolution time did not exceed 30 min.

To determine $\tau_{\exp}$ we used the values of density provided in Ref. [206] and diffusion coefficients given in Refs. [207, 208].

Figure 3.2 provides experimental and modeling data for the dissolution time(s) of non-equilibrium eutectics in the studied alloys. For alloy with 4.5%Cu a good agreement between experimental and calculated values is observed until

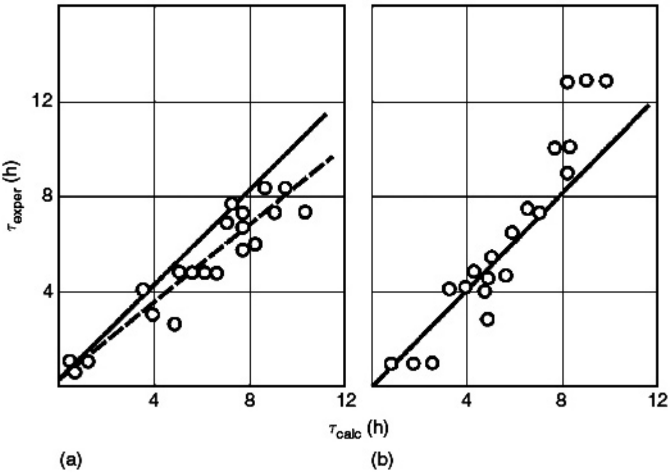

Figure 3.2 Comparison of calculated τ_{calc} (using equation (3.7)) and experimental τ_{exp}. times of non-equilibrium eutectic dissolution in alloys: (a) Al + 10%Mg and (b) Al + 4.5%Cu.

$\tau_{calc} \cong 7$ hours. For slowly solidified alloys calculation yields somewhat lower values. This could be explained by the presence of rough inclusions in microstructure, which require more time for complete dissolution. The mean square error in calculation of the dissolution time for this alloy was ~2 hours.

For alloy with 10%Mg calculations yield values that are some 20% higher than the actual dissolution times (Figure 3.2a). This could be explained due to the imperfections of the model. Another factor is that we used the diffusion coefficients from alloys with 5.5–11%Mg into pure aluminum [207], rather than into solid solution with magnesium concentration of ~5.5%.

After publication of Ref. [144] a number of articles appeared [209–216], in which dissolution times for different phases were studied. In particular, the authors of Ref. [213] compared different equations describing dissolution to each other and to available experimental data. As can be seen from Figure 3.3 [213], equation (3.7) gives the best prediction for the complete dissolution time of Al_2Cu phase of eutectic origin in alloy Al–4.5%Cu. For intermediate moments of time during the annealing process the predicted values are somewhat higher than the results obtained using other models (Figure 3.3). This is quite natural, because in equation (3.7) one uses an average value for the concentration gradient, while in the very first moments of annealing it should be much higher. The average gradient was used by the authors of Ref. [144] because they wanted to obtain an equation for the dissolution time, rather than the volume fractions in different intermediate moments. Based on the satisfactory agreement of data calculated using equation (3.7) and experimental data on dissolution times (Figures 3.2 and 3.3) this goal

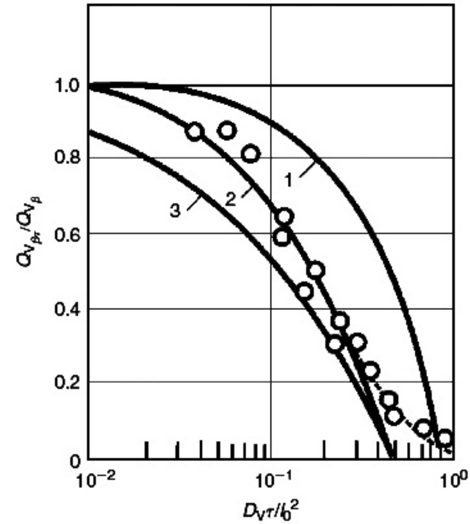

Figure 3.3 Experimental data (points and dashed line) and the results of calculations using different models for dissolution kinetics of the eutectic phase $CuAl_2$ at 545°C in as-cast alloy Al + 4.5%Cu [213]; D stands for the diffusion coefficient of Cu in Al and l_0 is the diffusion path length according to: (1) Ref. [205], (2) Ref. [213], and (3) Ref. [210].

was achieved. At the same time one could make a conclusion about the essential correctness of the dissolution model proposed in Ref. [144].

3.1.1.1 Experimental studies of kinetics of dissolution of non-equilibrium phase in the course of homogenizing heat treatment

As demonstrated in the previous section, for binary alloys it is possible to evaluate the overall dissolution time of non-equilibrium eutectics quite satisfactorily using equation (3.7). At the same time equation proposed in Ref. [213] gives a possibility to compute its volume fraction, but only during the initial stages of the dissolution process (Figure 3.3). For that goal equation (3.8) proposed in Ref. [211] should be used:

$$\frac{Q_{V_{\beta\tau}} + \alpha}{Q_{V_\beta} + a} = e^{-\left[\frac{D\cdot\tau}{\left(\frac{d}{2}\right)^2}\cdot\frac{\pi}{2}\right]} \tag{3.8}$$

where $Q_{V_{\beta\tau}}$ stands for the volume fraction at moment τ after the beginning of annealing; a is the constant defined from the corresponding phase diagram, and other symbols are the same as in equation (2.33).

To conduct such calculations it is necessary to determine experimentally a, d, and S, which makes such computations quite labor-intensive. As far as

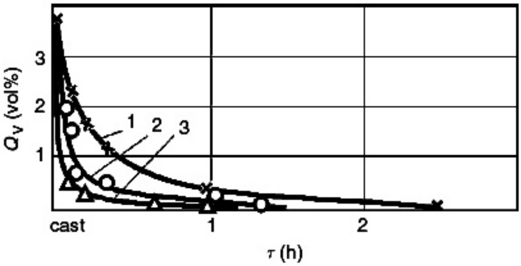

Figure 3.4 Dependence of the volume fraction Q_V of non-equilibrium eutectic ($\alpha + CuAl_2$) on homogenization time τ of alloy Al + 5%Cu at temperatures: (1) 535°C, (2) 555°C, and (3) 565°C.

multicomponent alloys are concerned, such methods are not developed at all. In principle, for ternary and quaternary alloys one could get equations similar to equation (3.8). However, their systematic application would be limited because of the lack of experimental data on diffusion coefficients in multicomponent systems. For this reason experimental studies on dissolution kinetics of non-equilibrium phases were conducted for the process of homogenizing heat treatment for binary and commercial alloys on the basis of the Al–Cu, Al–Mg, and Al–Mg–Zn systems [217–221]. The ultimate goal of these studies was to develop a fast and convenient technique for calculation of dissolution time using data on alloy microstructure.

Binary alloys of aluminum with 1.5–5%Cu, 6–10%Mg, and also industrial alloys on the base of systems Al–Cu, Àl–Mg, Al–Cu–Mg, Al–Zn–Mg, Al–Zn–Mg, and others were solidified with different cooling rates in the range from 10^{-2} to 10^{2} K/s, and then annealed at temperatures below and above the temperature of non-equilibrium solidus. For different times of heat treatment, the volume fraction of non-equilibrium Q_V or the specific surface of inclusions were quantitatively determined. Figures 3.4–3.6 illustrate the dependence of Q_V on the time of homogenizing heat treatment τ for a number of the studied samples. After each exposure samples were quenched into water. The diameter of all samples was less than 15–20 mm; the time of the complete and uniform heating did not exceed 2 minutes. This time was not taken into account when plotting curves in Figures 3.4–3.6.

As can be seen from the presented illustrations the larger fraction of non-equilibrium constituent particles gets dissolved immediately after the beginning of homogenizing treatment. Indeed, in all studied alloys after 1 hour of homogenization Q_V decreased by several times. With time the rate of dissolution becomes lower. This nature of dissolution kinetics is defined by smaller concentration gradient in aluminum solid solution in the course of annealing. This, in turn, as it was demonstrated above, defines the rate of diffusion of alloying element atoms from the dissolved inclusions (and, consequently, their dissolution rate). The general shape of the $Q_V - \tau$ curves in Figures 3.4–3.6 qualitatively

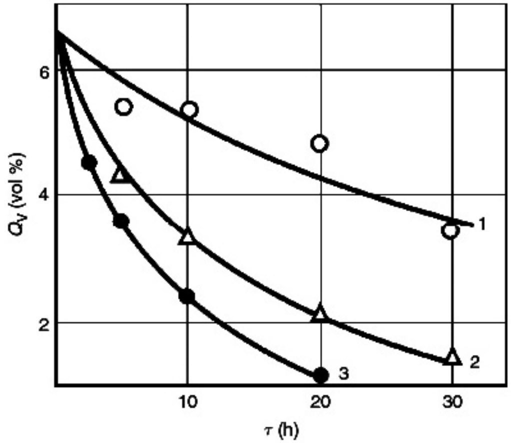

Figure 3.5 Dependence of the volume fraction Q_V of excessive phases in alloy Al19 upon homogenization time, τ, at temperatures: (1) 510°C, (2) 530°C, and (3) 540°C.

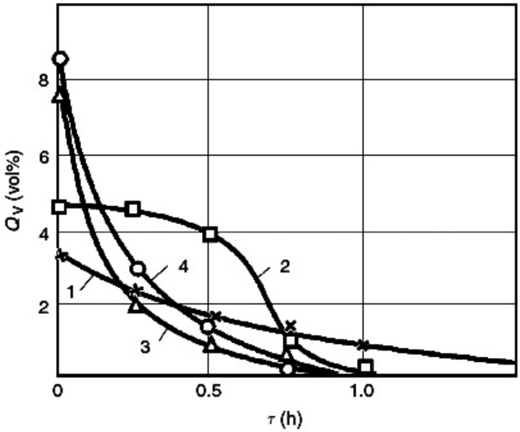

Figure 3.6 Dependence of the volume fraction Q_V of the eutectic β-phase upon time of heat-up before quench at 440°C for alloy Al + 10%Mg; alloys were solidified at different cooling rates (°C/min): (1) 2.9 K/s, (2) 19 K/s, (3) 150 K/s, and (4) 400 K/s.

corresponds to that predicted by equations (3.7) and (3.8). It can be describe by the following equation [219]:

$$Q_V = Q_{V_0} \cdot e^{(-a \cdot \tau^b)} \tag{3.9}$$

where Q_{V_0} stands for the volume fraction of non-equilibrium component in as-cast condition.

Figure 3.5 represents the dependence of the total volume fraction of excessive microstructural components as a function of the homogenization time. The $Q_V - \tau$ dependencies for individual microstructural components look similar. If a particular component is not completely dissolved at a given temperature, then the corresponding curve plateaus and the ordinate on the graph defines the volume fraction of that microstructural component remaining in the ingot after homogenizing heat treatment.

The time of complete dissolution of non-equilibrium constituent particles in most cases turned out to be significantly lower than one could expect based on the regimes used in industry. For example, in the case of shaped castings and ingots obtained via semi-continuous casting with diameter less than 500 mm, this time usually does not exceed 2 to 3 hours. For wrought alloys of the 5xxx and Al–Zn–Mg alloys it is less than 1–2 hours. For this reason dissolution in plant conditions must come to completion already in the process of ingot and casting heat-up to the temperature of isothermal heat treatment.

The kinetics of dissolution of excessive phases depends very strongly upon homogenization temperature. Due to the exponential temperature dependence of diffusion coefficients for alloying elements even minor elevation of the homogenizing heat treatment temperature (but 10–20°C) could appreciably reduce the total dissolution time. For example, in an alloy of the Al–Mg–Si system increasing homogenization temperature from 540°C to 560°C results in dissolution times that are 5 to 6 times shorter! [221].

In our opinion, the so-called "high-temperature homogenization" process is very perspective. It was proposed originally by Bochvar [223], and then further studied by Dobatkin and Livanov [224, 225]. It was conducted in between the temperatures of non-equilibrium and equilibrium solidus for a given system. According to Ref. [226], dramatic acceleration of homogenization process above the temperature of non-equilibrium solidus is connected to the appearance of liquid phase, with its rate of "dissolution" being much faster than that of the solid non-equilibrium phases. However, according to the model adopted here, it follows that the rate of dissolution is controlled by diffusion processes in the solid phase. In turn, their rates are defined by the concentration gradients and diffusion coefficients of the alloying elements. Consequently, according to this model changes of the aggregate state (e.g., solid–liquid) of the dissolved inclusions should not affect the kinetics of their dissolution. The increased rate of dissolution at temperatures above non-equilibrium solidus, within the framework of this model, must be defined mostly by the natural growth of diffusion mobility of atoms in the solid solution as temperature of the homogenizing treatment is raised.

To understand the true nature of this accelerated dissolution of excessive microstructure components above the non-equilibrium solidus temperature it is desirable to estimate the activation energy of the dissolution process. If at temperatures below and above non-equilibrium solidus this energy will remain the same, then acceleration is mostly determined by the growing rate of diffusion in the solid solution to increased temperature. If, however, these energies turn out to be different, this could direct toward possible influence of melting upon dissolution.

The value of activation energy E_ρ for the dissolution process was determined using experimental curves of the dependence of the volume fraction of excessive microstructural components upon annealing time at different temperatures (see Figures 3.4 and 3.5). Calculation of E_ρ was conducted according to the Arrhenius equation:

$$V_\rho = V_0 \cdot e^{\left(-\frac{E_\rho}{RT}\right)} \tag{3.10}$$

where V_ρ is the dissolution rate at any given moment of time; T is the temperature of heat treatment; and K, V_0 are the coefficients.

The rate of dissolution was determined according to equation (3.9) as follows:

$$V_\rho = \frac{\mathrm{d}Q_V}{\mathrm{d}\tau} = a \cdot b \cdot Q_{V_0} \cdot \tau^{b-1} \cdot e^{(-a \cdot \tau^b)} \tag{3.11}$$

Coefficients a and b can be determined from the experimental data on the $\lg(\lg Q_0 - \lg Q) - \lg \tau$ plots.

To obtain the value of the activation energy of the dissolution process E_ρ one also needs to calculate, using equation (3.11), the rate of dissolution at different temperatures in the moment of dissolution corresponding to the same volume fraction of excessive phases (e.g., 50% of the initial value).

Figure 3.7 represents the lg V_ρ–$1/T$ graphs for binary alloys Al + 3%Cu and Al + 10%Mg, where V_ρ stands for the dissolution rate at the moment when $Q = 0.5Q_{V_0}$. It is clear that all points corresponding to these alloys, including temperatures above non-equilibrium solidus, are well described by one straight line. Similar results were obtained for other alloys. This implies that the acceleration of dissolution of excessive constituent particles at temperatures above non-equilibrium solidus is related to the normal and expected increased values of diffusion coefficients of alloying elements in (Al) as temperatures goes up [207, 208].

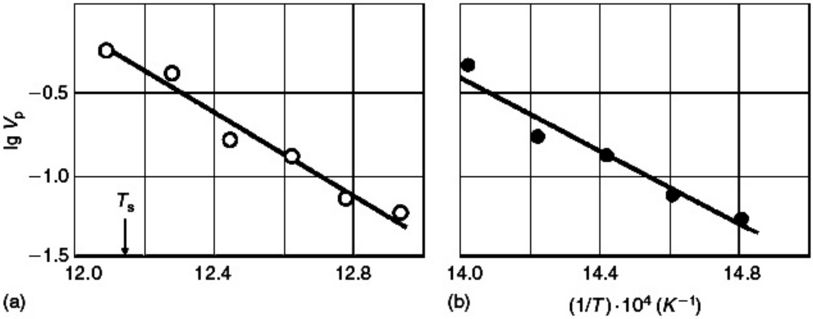

Figure 3.7 Dependence of the dissolution rate (V_p) 50% of non-equilibrium eutectics on the reciprocal temperature of homogenization for alloys: (a) Al + 3%Cu and (b) Al + 10%Mg. T_{sol} stands for non-equilibrium solidus temperature.

3.1.1.2 The influence of refinement of as-cast microstructure upon the time of excessive phase dissolution

The results of diffusion calculations and experimental data indicate (see Figure 3.6) that dissolution kinetics of constituent particles depends upon the original as-cast alloy microstructure. Qualitatively it is known that with increased refinement of microstructure homogenizing processes go faster (see e.g., [228–230]). Sometimes this effect is used in practical work when ingots and castings are divided into groups differing in thickness of casting walls, or cross-section diameter. Then lengthier homogenizing heat treatment is prescribed for thicker and larger castings and ingots [228–230].

For alloy of a given composition refinement of as-cast microstructure is defined mostly by the applied solidification rate, the higher the rate, the more refined microstructure will be obtained (smaller dendrite cell sizes and constituent particles). These parameters directly define the dissolution times via reduced diffusion paths and different values of concentration gradients. Consequently, it is quite natural that as solidification rate is increased, the overall dissolution time of excessive constituent particles decreases (Figure 3.8).

Inasmuch as the solidification rate affects the dissolution kinetics of constituents via microstructural characteristics of castings or ingots, it is important to obtain quantitative expressions directly relating the time of complete dissolution τ_ρ to several microstructure parameters, or their combinations. To solve this important problem a statistical approach was employed in Refs. [217, 218, 221, 231].

More specifically, four characteristics of as-cast microstructure were selected in which all could be defined from metallographic studies. These characteristics, as it was demonstrated above, define the kinetics of excessive phase dissolution: their volume fraction (Q_V), specific surface (S), thickness (m), and lineal size (d) of dendritic cells (Al). Several binary and industrial alloys were studied, which were solidified with different rates from 10^{-2} to 10^2 K/s (about 15–30 samples

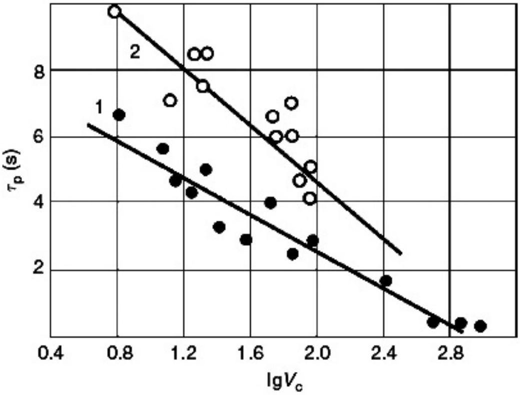

Figure 3.8 Dependence of the dissolution time, τ_p, of eutectic phase β on the cooling rate during solidification of alloy AMg10 (520.0) containing (1) 10.2% Mg and (2) 11.6%Mg.

Table 3.2 Coefficients of pair correlation between dissolution times of excessive phases and microstructure characteristics

Alloy	Mg (%)	Q_V (vol%)	S (mm²/mm³)	m (μm)	d (μm)
AlMg	10	−0.439	−0.786*	0.928*	0.863*
AlMg10	9.5	−0.329	−0.915*	0.978*	0.888*
AlMg10	10.2	−0.709*	−0.906*	0.977*	0.893*
AlMg10	11.6	−0.120	−0.821*	0.930*	0.721*

* Valid correlation coefficient. The validity of the pair correlation coefficients, that is, the presence of a non-random linear dependence among different factors was assessed using tables provided in Ref. [234] with 95% probability.

for each alloy). At first all of the microstructure characteristics mentioned above were measured, then dissolution times τ_ρ were determined using the methods described above.

Using obtained experimental data, the authors calculated the correlation coefficients [232, 233] between τ_ρ and the characteristics of microstructure. Table 3.2 summarizes these results in terms of correlation among the dissolution times of the β-phase and alloy microstructure parameters. Several Al–Mg alloys were studied: binary Al–10%Mg and industrial alloy AlMg10 with different magnesium content.

The analysis of the pair correlation coefficients demonstrated that time τ_ρ is most closely connected to the thickness of dissolved constituent particles. As can be seen from the given data, in alloys of the Al–Mg class this coefficient is very close to unity.

Similar situation is observed in the case of alloys belonging to other systems. Figure 3.9 illustrates the dependence of dissolution time of different constituent particles upon their thickness in castings. It is clear that any group of experimental points related to a particular alloy is approximated well either by a straight line or by an exponential curve. For all studied alloys, binary and multicomponent (casting and wrought), the method of the least squares yielded the following equations described in Table 3.3.

Table 3.3 demonstrates that for aluminum alloys belonging to different systems it is possible to obtain simple equations that could predict with sufficiently high accuracy (0.3–2 hours) the values of τ_ρ using just one microstructural parameter – thickness of dissolved constituents, m. Experimentally m can be easily determined and requires not more than 30–40 minutes of work either using the methods of lineal analysis for light microscopy data or using optical set-up of a microhardness measuring device. It is important to stress that when deriving equations in Table 3.3 the whole range of m's was used that corresponds to practically all methods of casting, since it was derived for the samples solidified in a very wide range of cooling rates.

Table 3.3 also indicates that for some alloys linear equations provide less accurate predictions for τ_ρ than exponents. However, the latter are more universal and more adequately reflect the physical nature of diffusion processes of dissolution.

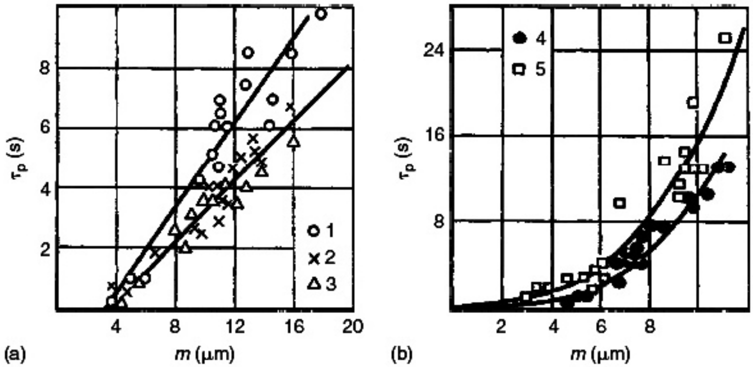

Figure 3.9 Dependence of the dissolution time τ_p of non-equilibrium eutectics upon the average thickness of their inclusions, m, in alloys AMg10 containing (1) 11.6%Mg, (2) 9.5%Mg, and (3) 10.2%Mg; data presented in (4) correspond to alloy Al + 4.5%Cu; data presented in (5) corresponds to alloy AM5.

Indeed, the fundamental laws of diffusion teach that the depth of penetration h of the diffusing substance during time τ is defined by the equation:

$$h = k \cdot \tau^f \tag{3.12}$$

where k and f represent coefficients [222].

In our case the process of dissolution must come to completion after the diffusing atoms pass an average distance of $(h - m/2)$ from solid solution inside an "inclusion". Then $m/2 = k \cdot \tau_\rho^f$, and we get:

$$\tau_p = \frac{1}{2(k)^{\frac{1}{f}}} \cdot m^{\frac{1}{f}} \tag{3.13}$$

Introducing new notation, we get a simple power law equation (3.14):

$$\tau_\rho = a \cdot m^b \tag{3.14}$$

Growing prediction error for τ_ρ for the linear equation (as compared to power law) most probably could be explained as follows. In the studied range of m values experimental points are located only on the ascending portion of the curve $\tau_\rho = a \cdot m^b$ (see Figure 3.9a). For this reason they could be better approximated by the straight line.

In the course of diffusion dissolution of non-equilibrium constituent particles the exponent b in equation (3.14) must be equal to 2 [222]. Table 3.3 shows that in reality it varies from 1.2 to 1.6. As it was explained in Ref. [235] the value of b for experimental dependencies of the $\tau_\rho = a \cdot m^b$ type is affected very strongly

Table 3.3 Equations relating dissolution times of excessive phases (τ_ρ) to the thickness of dissolved particles (m)

Alloy	Content of principal alloying element (%)	T_g (°C)	$\tau_\rho = b_o + b_1 m$				$\tau_\rho = am^b$			Dissolving phase
			b_o	b_1	Range (µm)	Mean quadratic error (in hours)	a	b	Mean quadratic error (in hours)	
Binary alloys										
Al + 10%Mg	10 Mg	440	−1.39	0.586	2.4–16	0.82	0.22	1.3	0.88	β (Al_3Mg_2)
Al + 4.5%Cu	4.5 Cu	540	−9.56	2.060	4.7–11	0.96	0.034	2.5	1.14	$CuAl_2$
Casting alloys										
AlMg10	9.5 Mg	440	−1.41	0.452	3.2–16	0.31	0.096	1,5	0.39	β (Al_3Mg_2)
	10.2 Mg	440	−1.77	0.507	3.5–17	0.37	0.62	1.7	0.39	
	11.6 Mg	440	−2.32	0.700	3.3–18	0.97	0.18	1.4	0.99	
	First two compositions	440	−1.63	0.484	3.2–18	0.36	–	–	–	
~203	4.6 Cu, 0.8 Mn, 0.22 Ti	535	−10.9	0.88	3.2–16	0.31	0.096	1.5	0.39	$CuAl_2$
Wrought alloys										
~7075	6.5 Zn, 2.5 Mg, 1.7 Cu, 0.4 Mn, 0.15 Cr	450	−0.80	1.215	2.5–11.7	1.25	0.74	1.2	1.41	M,T

~7449	6.6 Zn, 2.0 Mg, 0.9 Cu	460	−2.99	1.049	2.8–12.1	0.41	0.14	1.7	0.46	M,T
~2024	3.9 Cu, 1.3 Mg, 0.6 Mn	480	−0.64	1.64	2–7.1	0.56	1.11	1.2	0.52	S, $CuAl_2$
		515	0.23	0.86	2–7.1	0.18	0.69	1.2	0.53	
	4.5 Cu, 1.5 Mg, 0.6 Mn	480	−1.07	1.72	2.2–8	0.56	1.09	1.2	0.54	
		515	0.42	0.80	2.2–8	0.16	0.67	1.2	0.43	
	4.8 Cu, 1.75 Mg, 0.6 Mn	480	−0.78	1.64	2.3–8.8	0.48	1.07	1.2	0.49	
		515	0.67	0.73	2.3–8.8	0.19	0.63	1.2	0.50	
	For all three compositions	480	−0.79	1.66	2–8.8	0.54	1.09	1.2	0.52	
		515	0.50	0.78	2–8.8	0.20	0.66	1.2	0.49	

by how the distribution of particles with respect to their sizes changes as a function of the applied cooling rate. For this reason inequality $b \neq 2$ should not be considered a violation of validity of conventional diffusion process laws accompanying the dissolution of excessive phases. Of course, when annealing temperature changes, the coefficients of the corresponding equations also change (see Table 3.2)

For practical application of equations in Table 3.3 to industrial alloys it is important to understand how sensitive their coefficients are to variations in concentrations of the principal alloying elements within the limits of their allowable composition windows. From Table 3.3, we see that for most alloys with relatively low-level, medium-, and high-level concentrations the coefficients of the equations change rather weakly. It gives a possibility to use a single equation, with its coefficients, for many industrial alloys.

However, in some alloys raising the concentration of alloying elements (which define the volume fraction of inclusions and concentration gradient in the solid solution) results in substantial changes in the values of these coefficients. For example, in alloy AlMg10 with the maximal content of magnesium (11.6%) the dissolution time of the β-phase is significantly higher, at the same thickness of particles, when compared to alloys containing 9.5–10.2%Mg (see Figure 3.9a). Naturally, the coefficients describing these alloys also change (Table 3.3).

Let us now return to analysis of the influence of the applied cooling rate upon dissolution of excessive constituent particles. The conducted statistical analysis of binary correlations demonstrated that τ_ρ depends strongly upon thickness of particles, m, their specific surface area, S, and dendritic cell size, d (Table 3.2). All these microstructure characteristics are uniquely defined by the solidification rate, V_c. This is why there is direct correlation between τ_p and V_c (Figure 3.8):

$$\tau_p = K - B \cdot \lg V_c \tag{3.15}$$

For example, for alloy AlMg10 containing 10.2%Mg, $\tau_p = 7.74 - 2.25 \cdot \lg V_c$. This equation allows one to calculate τ_ρ using the known casting cooling rate, with mean quadratic error ±0.5 hours. Such equations, along with relations presented in Table 3.3, provide quantitative data for the optimal time of heat-up before quenching of shaped castings and homogenizing heat treatment of ingots for wrought aluminum alloys. Dissolution of non-equilibrium excessive phases leaves traces in microstructure: one can clearly see the areas where the dissolved particles were located immediately before the dissolution. This effect of microstructure heredity is especially pronounced for alloys of the Al–Mg system [219, 236].

3.1.2 Elimination of microsegregation during homogenization

Obtaining a more uniform distribution of alloying element concentrations in dendritic cells is analyzed theoretically much better than dissolution of excessive constituent particles. Analytical solutions for kinetics of elimination of concentration gradients inside dendrites were obtained for binary and even ternary alloys [81, 237–244]. A number of experimental studies also were conducted to understand how homogenizing heat treatment of casting aluminum alloys affects microsegregation [81, 125, 219, 245–250]. In the present section we analyze experimentally established relations between characteristics of microsegregation for binary, ternary, and industrial aluminum alloys and their as-cast microstructure. These results are compared to the existing theoretical concepts.

3.1.2.1 Binary alloys

First, let us consider the influence of applied homogenization time upon chemical composition of central, C_1, and peripheral, C_2, areas of dendritic cells, the extent of microsegregation ΔC, and the distribution of alloying elements with respect to cross-sections of these dendritic cells in binary alloys.

The authors of Refs. [219, 246] have studied alloys Al–Cu (1.5–6%) and Al + 10.6%Mg. All materials were prepared out of 99.99% pure aluminum and solidified with different rates from 0.03 to 16 K/s. Al–Cu alloys were homogenized at temperatures 500–540°C, Al + 10.6%Mg alloys at 400–440°C, with duration of heat treatment from 10 minutes to 60 hours. After prescribed annealing time all samples were quenched into water. Concentration was determined using the method of X-ray spectral analysis with homogenized master alloys of known concentrations.

Figure 3.10 illustrates the dependence of the average values of C_1, C_2, and ΔC upon annealing time at 540°C for Al–Cu alloys, all of which were solidified in the same conditions. Figure 3.11 represents distribution curves of copper across the dendritic cells in alloys containing 1.5 and 5%Cu after homogenization during different periods of time. Each point in Figure 3.11 corresponds to the average of 75–90 measurements of concentration of copper at a given distance from the boundary of dendritic cell.

Concentration of copper in the central areas of dendritic cells C_1 starts growing immediately after the onset of annealing treatment, approaching either the

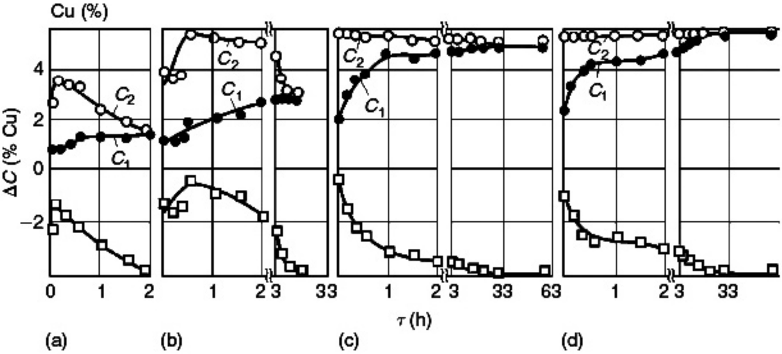

Figure 3.10 Dependence of Cu concentration in the center of dendritic cells, C_1, and on their periphery, C_2; also see data on the extent of microsegregation ΔC for alloys of Al with (a) 1.5%Cu, (b) 3%Cu and (c) 5%Cu, and (d) 6%Cu as functions of homogenization time τ at 540°C.

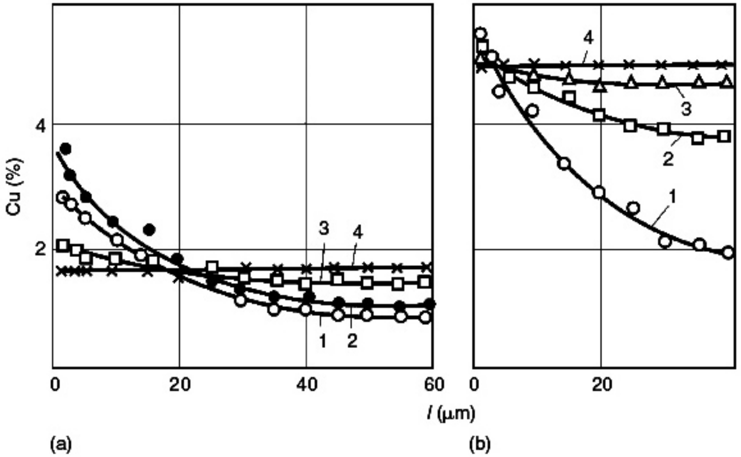

Figure 3.11 Cu distribution curves across the dendritic cells in alloys of Al with (a) 1.5%Cu, and (b) 5%Cu; *l* is the distance; 1: as-cast state; 2–4 corresponds to heat treatment at 540°C during 0.2, 1.5 and 2 hours, respectively.

average composition in alloys the ordinates of which do not cross the eutectic horizontal line of equilibrium phase diagram Al–Cu (1.5%Cu, 3%Cu, and 5%Cu, Figure 3.10a–c) or the limit concentration of (Al) at temperature of homogenization (in alloy with 6%Cu, Figure 3.10d). Particularly steep increase of C_1 was observed for alloys with 5 and 6%Cu during the initial stages of homogenization. The time when the maximal concentration of copper was achieved in the central areas of dendrites decreased with the concentration of copper in a given alloy (see Figure 3.10).

The concentration of copper C_2 on the periphery of dendritic cells varies as a function of homogenization time as a curve with a maximum corresponding to weakly alloyed materials (with 1.5 and 3%Cu, Figure 3.10a, b) and continuously decreases for alloy with 5%Cu (Figure 3.10c). The extent of microsegregation ΔC with homogenization time either smoothly decreases (alloys with 5 and 6%Cu, Figure 3.10c, d) or increases somewhat during the first minutes of heat treatment, then starts decreasing (alloys with 1.5 and 3%Cu, Figure 3.10a, b). The time required for complete eliminates of microsegregation grows with increased amount of alloying element in the alloy compositions. Similar results were obtained for the Al–Mg alloys.

Rising concentration of alloying element(s) in the middle of dendritic cells in the course of homogenization can be explained by the process of homogenizing diffusion in the solid solution. It is also natural to expect that this concentration will go up steeply in the initial stages of annealing, when the concentration gradient of copper and magnesium along the dendrites is the highest. Sharp increase of the magnesium and copper concentration in the center of dendritic cells at the initial stages of heat treatment for more heavily alloyed samples can be explained by the increased amounts of eutectic. Its rapid dissolution in the first minutes of heat treatment results in the significant enrichment of Al-based solid solution with alloying element(s).

Experimental curves illustrating variations of the copper concentration on the periphery of dendritic cells represent the most interest. Indeed, their general behavior defines how homogenization time will be affected by the degree of mcirosegregation in alloys. Let us analyze the distribution of copper across dendritic cells at different stages of homogenization (Figure 3.11). In as-cast samples the concentration of copper in aluminum solid solution at the boundary with eutectic must correspond to the point of maximum solubility at eutectic temperature. In the proximity of dendrite cell boundaries the concentration of copper goes down rapidly, while the middle part of the cell has approximately constant composition (Figure 3.11, curve 1). The concentration fall-off is so sharp that with limited spatial resolution of experimental techniques (in our case a circular area with diameter of $\sim 4\,\mu m$ was studied) the measured concentration will always be somewhat lower than the actual value. Of course, the sharper this fall-off, the lower concentrations will be measured [65]. For this reason in similar solidification conditions the discrepancy between the actual and experimentally determined concentration will be increasing with smaller copper concentrations in alloys (Figures 3.10 and 3.11).

During the initial stages of homogenization of weakly alloyed materials broadening of the peripheral layers enriched with copper takes place (as compared to the average alloy composition) (Figure 3.11, curve 2). This happens because eutectic dissolves and atoms of copper diffuse from the boundaries of the (Al) dendritic cells; hence the initial rise of C_2 (Figures 3.10 and 3.11a, b).

When the larger part of eutectic gets dissolved, the strongly enriched copper boundary layer starts shrinking (Figure 3.11a, curve 3), due to diffusion of copper inside the dendritic cells. Experimentally determined value of C_2 goes down until the average alloy composition value is achieved (Figure 3.10a, b).

In alloys with 5 and 6%Cu homogenization helps make the distribution of copper atoms across the dendritic cells more uniform (Figure 3.10b). However, it affects the near-boundary concentrations very weakly (Figure 3.10c, d). Some decrease in the copper level in alloy containing 5%Cu (Figure 3.10c) could be explained by the fact that during the initial stages of homogenization, until complete dissolution of non-equilibrium eutectic, the concentration of Cu at its boundary with Al-solid solution must correspond to the maximum value at the homogenization temperature (at 540°C it is equal to 5.3%), not maximal eutectic concentration (5.7%Cu [251]).

Consequently, experimental curves describing changes of concentration of alloying element(s) on the periphery of dendritic cells as a function of applied homogenization time may look differently. This is determined by the alloy concentration and the spatial resolution of the device for measuring concentration profiles.

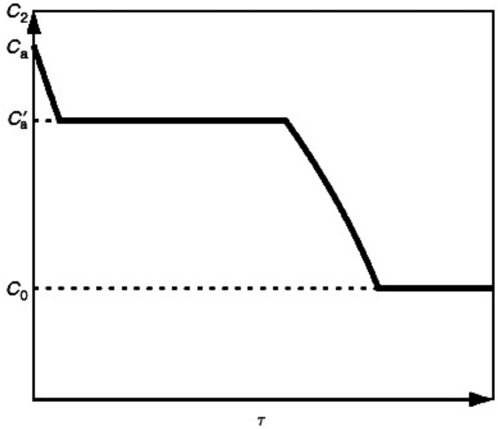

Figure 3.12 Schematic of the true alloying element concentration variation on the boundaries of dendritic cells, C_2, as a function of the homogenization time, τ.

Changes in the "true" concentration of alloying element on the boundaries of dendritic cells of (Al) during homogenization in eutectic alloys can be represented in the form of a simple schematic (Figure 3.12). Solid line describes alloys the concentrations of which are located in between the ordinate corresponding to pure aluminum, and maximal solubility at eutectic temperature (in our case alloys with 1.5, 3, and 5%Cu and with 10.6%Mg).

In these alloys during the first minutes of homogenization and until the beginning of non-equilibrium eutectic dissolution the boundary concentration C_2 must decrease from the solubility limit C_a to the concentration C_a' at the homogenization temperature. Until the complete eutectic dissolution $C_2 = C_a'$, because these concentrations cannot change in the presence of a non-equilibrium eutectic. After its complete dissolution, C_2 goes down and attains the value of C_0, the average concentration of alloying element in a given sample, and does not change anymore in the course of subsequent homogenization. It is obvious that for alloys the ordinates of which cross the eutectic horizontal (Al + 6%Cu), after initial concentration decrease from C_2 to C_a' no concentration changes on the crystal boundaries will take place (dashed line in Figure 3.12). The presented schematic demonstrates that the "true" degree of microsegregation must continuously decrease as homogenization progresses, taking into account the corresponding concentration increase in the center of dendritic cells (Figure 3.11).

The experimental results on the kinetics of microsegregation elimination in as-cast binary alloys were compared to the already mentioned theoretical models [81, 239–242]. It showed that the best agreement was obtained when using the results and models from Ref. [242]. In that work an assumption about the sinusoidal distribution of alloying elements in as-cast condition was made. The

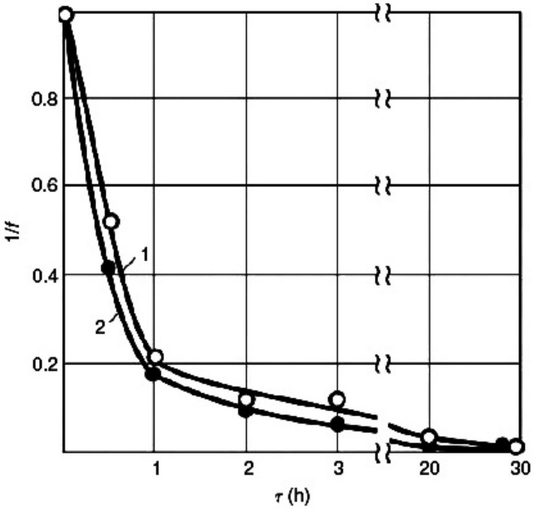

Figure 3.13 Dependence of the $1/f$ factor on alloy homogenization time, τ, for alloy Al + 5%Cu with the initial average dendritic cell size equal to 0.12 mm; 1: experiment, 2: calculation.

decrease in the extent of microsegregation as characterized by a factor f equal to the ratio of the initial amplitude to the amplitude achieved during annealing time, τ:

$$f = \frac{(H_\tau + 1) \cdot (H_0 - 1)}{(H_\tau - 1) \cdot (H_0 + 1)} \tag{3.16}$$

where $H_\tau = C_{\max}/C_{\min}$ is the ratio of concentrations after annealing during time τ and $H_0 = C_{\max}/C_{\min}$ is the ratio in as-cast state before annealing.

Factor f changes with annealing time according to equation [241]:

$$\frac{1}{f} = e^{\left(\frac{-\pi^2 \cdot D_V \cdot \tau}{l_0^2}\right)} \tag{3.17}$$

where l_0 is the radius of dendritic cells.

Figure 3.13 represents experimental values of $1/f$, determined using equation (3.16) and using the data in Figure 3.10c calculations were made for alloy Al + 5%Cu using equation (3.17) for the experimentally determined dendritic cell size of 120 μm. The correlation between theory and experiment is good.

Using equation (3.17) one could obtain the working formula for calculation of the microsegregation elimination time τ_B (i.e., taking into account the error of experimental measurements for $\Delta C \leq 0.2\%$). It turns out that $1/f = 0.03$ and

$$\tau_B = \frac{5.8 \cdot l_0^2}{\pi^2 \cdot D_V} \tag{3.18}$$

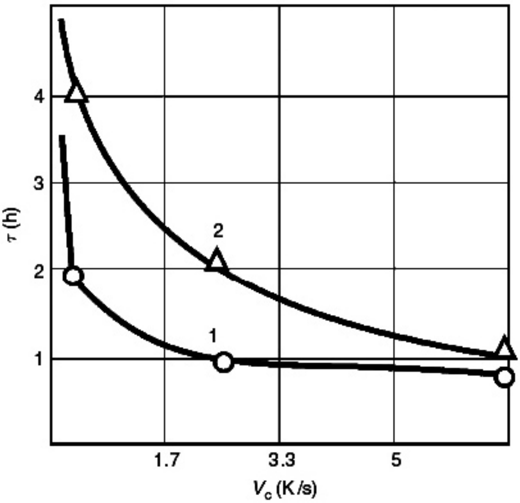

Figure 3.14 For alloy Al + 10.6%Mg: (1) dependence of the complete dissolution time τ for the eutectic β-phase; and (2) elimination of microsegregation after annealing at 440°C, as functions of the cooling rate during solidification.

Above we considered the kinetics of microsegregation elimination for binary alloys that were solidified in identical conditions. This kinetics, as in the case of the dissolution of excessive eutectic phases, will depend upon refinement of the original as-cast microstructure (i.e., the cooling rate upon solidification). Indeed as it can be seen from Figure 3.14, as the solidification rate grows, the time to achieve complete microsegregation elimination continuously decreases. For alloy of a given composition this is defined by the reduction in average diffusion path l_0 in equations (3.17) and (3.18) as a result of accelerated solidification.

The annealing time required to achieve $\Delta C = 0$ in aluminum solid solution is usually higher than the time of complete dissolution of non-equilibrium eutectic constituent particles (Figure 3.14). However, if one compares the curves in Figure 3.10c with the Q–τ curves for the same alloy Al + 5%Cu in Figure 3.4, then it is easy to see that at the moment of complete dissolution of excessive constituent particles ($Q = 0$ in Figure 3.4) the degree of microsegregation is already quite insignificant (less than 20% of the original value). This practical conclusion is valid for all studied binary aluminum alloys.

3.1.2.2 Multicomponent alloys

Now let us consider ternary alloys belonging to the Al–Cu–Mg and Al–Mg–Zn systems with contents of the principal alloying elements approaching well-known industrial alloys 2024 (Al + 4.5%Cu + 1.5%Mg), ~7004 (Al + 4.6%Zn + 1.6%Mg), $AlMg_4Zn_3$ (Al + 3.2%Zn + 4.3%Mg) and 7075 without

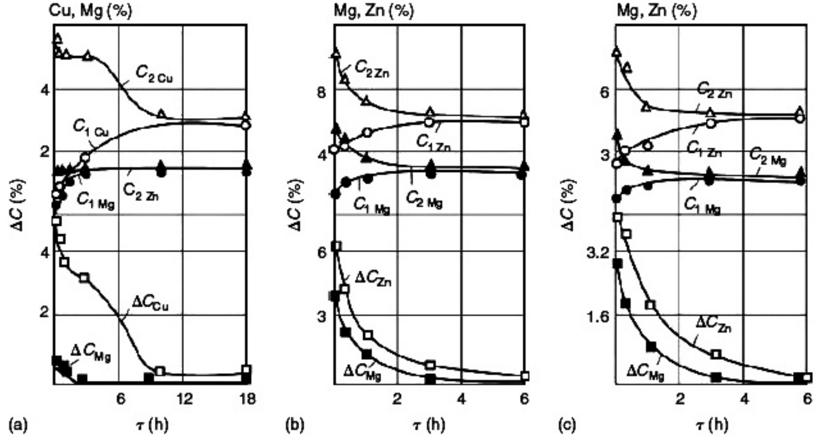

Figure 3.15 Dependence of $C_1 = C_{\min}$, $C_2 = C_{\max}$, and ΔC upon homogenization time τ for ternary alloys: (a) Al + 4.5%Cu + 1.5%Mg at 490°C, (b) Al + 6% Zn + 2.8% Mg, and (c) Al + 4.6%Zn + 1.6%Mg at 460°C.

copper (Al + 6%Zn + 2.8%Mg) [180]. All these ternary alloys in equilibrium state immediately after the completion of solidification must be single phase. In as-cast state, in addition to compositionally non-uniform aluminum solid solution, they should contain small amounts of excessive constituent particles of eutectic origin.

All alloys were prepared out of aluminum and zinc of 99.99% purity and magnesium 99.92% purity. They were cast into a copper mold with diameter 40 mm. Alloy Al + 4.5%Cu + 1.5%Mg was annealed at (490 ± 5)°C, while alloys Al–Zn–Mg at (460 ± 5)°C during a period of time from 15 min to 6 hours. Figure 3.15 illustrates how the concentration of alloying elements in the center of dendritic cells, on their periphery, and ΔC depend upon homogenization time for alloys Al + 4.5%Cu + 1.5%Mg, Al + 6%Zn + 2.8%Mg, and Al + 4.6%Zn + 1.6%Mg. It can be seen that the general character of behavior of C_1 and C_2 during homogenization of ternary alloys are similar to that of binary alloys (see Figure 3.10).

Models for binary [241] and ternary [242] alloys were used to test their validity for prediction of kinetics of microsegregation elimination. The results of these calculations according to equation (3.17) and Ref. [241] are compared to experimental data for alloys Al + 4.5%Cu + 1.5%Mg and Al + 6%Zn + 2.8%Mg, and presented in Figure 3.16. In all calculations diagonal diffusion coefficients for copper, magnesium, and zinc were used from the corresponding binary alloys (Al + 4.5%Cu, Al + 1.5%Mg, Al + 6%Zn, Al + 2.8 Mg) into pure aluminum, which were determined experimentally (see description below). As can be seen from Figure 3.16, the model proposed in Ref. [183] for binary alloys can be successfully used for ternary alloys as well.

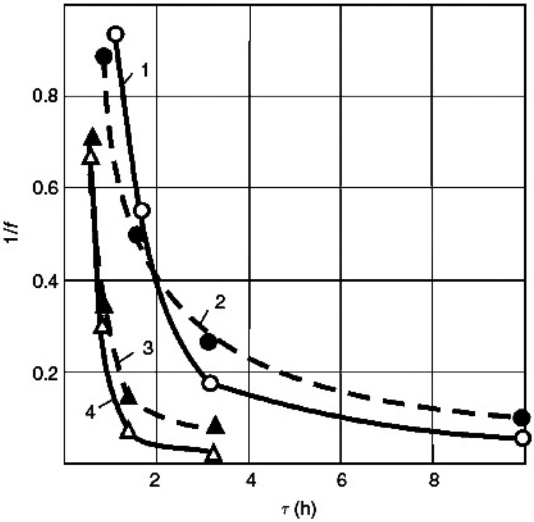

Figure 3.16 Changes in the experimentally determined and theoretically calculated factor $1/f$ for copper and zinc [241]: (1, 2) alloy Al + 4.5%Cu + 1.5%Mg; (3, 4) alloy Al + 6%Zn + 2.8Mg; (1, 4) calculations, (2, 3) experiment.

In Ref. [242] this problem was solved in application to ternary solid solution. The initial concentration distribution for alloying elements was supposed to be sinusoidal. The solution of the Fick's second law for a ternary system can be written as follows:

$$C_{m_1} = \sin\left(\frac{\pi \cdot x}{l_0} \cdot \left\{C_1^0 \cdot \cosh\left(\frac{\pi^2}{l_0^2}\right) \cdot \beta \cdot \tau + \left[\frac{C_1^0}{2} \cdot \frac{(D_{22} - D_{11}) - C_{m_2}^0 \cdot D_{12}}{B}\right] \cdot \sinh\left(\frac{\pi^2}{l_0^2}\right) \cdot B \cdot \tau\right\} \cdot e^{-\alpha \cdot \tau}\right) \tag{3.19}$$

where C_{m_1} and C_{m_2} stand for the changes in initial deviation from the average concentration of components C_1^0 and C_2^0 in any point at a distance x from the dendrite cell boundary, τ is the annealing time, and coefficients

$$\alpha = \left(\frac{\pi^2}{l_0^2}\right) \cdot \left(\frac{D_{11} - D_{22}}{2}\right); \quad B = \frac{D_{11} - D_{22}}{2} + (D_{12} \cdot D_{21})^{\frac{1}{2}} \tag{3.20}$$

where D_{11} and D_{22} stand for the diagonal diffusion coefficients of the first and second components in the ternary solid solution; D_{12}, D_{21} are the off-diagonal diffusion coefficients, which account for the mutual influence of alloying element atomic fluxes.

The values of D_{12} and D_{21} for many aluminum alloys are not known, while the values of D_{11} and D_{22} should be double-checked. This is desirable because the data on diffusion coefficients available from the literature [207, 208, 254] were obtained for diffusion couples with pure aluminum, not aluminum-based solid solution.

All four coefficients were determined using the method of Kirkaldi [255, 256]. For example, when studying alloys of the Al–Cu–Mg system the following diffusion couples were constructed (marked with arrows):

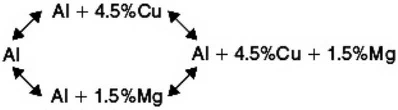

In the case of Al–Zn–Mg alloys the following diffusion couples were studied:

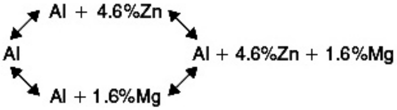

All binary and ternary alloys were homogenized, and then subjected to mechanical treatment, annealed, and quenched to obtain homogeneous solid solution. The choice of diffusion couples was conducted using the following criteria:

1. One of the independent concentrations must remain constant: (a) $C_1^0 \neq C_1'$, $C_2^0 = C_2'$, where indices 1 and 2 are related to alloying elements: (b) $C_1^0 = C_1'$, $C_2^0 \neq C_2'$.
2. In the course of annealing there should be no formation of an intermetallic layer in the contact zone (i.e., the content of alloying elements should not exceed their limits of mutual solubility in aluminum).

Using the technique of micro X-ray spectroscopy, the depth of mutual penetration of alloying elements was determined. The values of D_{11} and D_{22} were assessed using the method of Matano; D_{12} and D_{21} were calculated using the method described in Ref. [257]. It was established that $D_{\mathrm{Al}}^{\mathrm{Cu}} = 4.3 \times 10^{-10}\ \mathrm{cm}^2/\mathrm{s}$, $D_{\mathrm{Al}}^{\mathrm{Mg}} = 6.5 \times 10^{-10}\ \mathrm{cm}^2/\mathrm{s}$, $D_{\mathrm{MgCu}} = 0.12 \times 10^{-10}\ \mathrm{cm}^2/\mathrm{s}$, $D_{\mathrm{CuMg}} = 0$ at 490°C, $D_{\mathrm{Al}}^{\mathrm{Zn}} = 5.8 \times 10^{-10}\ \mathrm{cm}^2/\mathrm{s}$, $D_{\mathrm{Al}}^{\mathrm{Mg}} = 5.9 \times 10^{-10}\ \mathrm{cm}^2/\mathrm{s}$, $D_{\mathrm{MgZn}} = 0$, $D_{\mathrm{ZnMg}} = 0$ at 460°C.

Using the obtained values of diffusion coefficients, the values of $C_{\mathrm{m}1}$ and $C_{\mathrm{m}2}$ were calculated according to the equations given above. This was done for alloys Al + 4.5%Cu + 1.5%Mg and Al + 46%Zn + 1.6 Mg for different times of annealing heat treatment. The results of these calculations, compared to experimental data, are presented in Figure 3.17. It can be seen that for magnesium and zinc

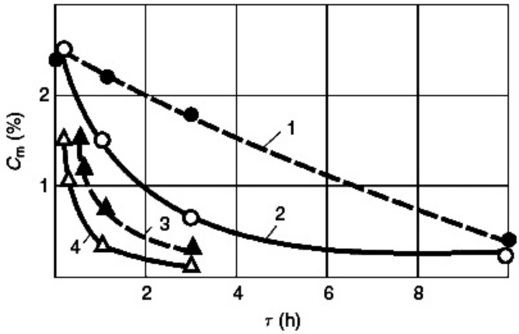

Figure 3.17 Changes in the copper concentration amplitude, C_m, calculated using the model described in Ref. [242]; (1, 2) alloy Al + 4.5%Cu + 1.5%Mg; (3, 4) alloy Al–4.6%Zn + 1.6%Mg, as function of the homogenization time, τ: (1, 3) experiment; (2, 4) calculation.

there is very good agreement between theory and experiment, while for copper there is a significant discrepancy. This could be explained by the fact that during homogenization of alloy Al + 4.5%Cu + 1.5%Mg an intensive dissolution of substantial amounts of eutectic takes place. Since the used model was derived only for solid solutions, theoretical calculations yield somewhat lower results compared to experiment.

Knowing the kinetics of dissolution of non-equilibrium eutectics, one could calculate the amount of copper that is continuously supplied into the solid solution. Taking this factor into account, the empirical equation for calculation of homogenization kinetics will be modified as follows:

$$C_{\mathrm{m}}^{\tau} = \Delta(\tau) + C_{\mathrm{m}}^{0} \cdot e^{\frac{-\pi^2 \cdot D_V \cdot \tau}{l_0^2}} \tag{3.21}$$

where $\Delta(\tau) = 0.4$ for $\tau = 1$–3 hours, and $\Delta(\tau) = 0.1$ for $\tau = 3$–10 hours.

Obviously, practical calculations using the model from Ref. [242] are much more cumbersome and their accuracy is worse compared to a much simpler model [241].

The kinetics of elimination of microsegregation during homogenizing heat treatment was studied for industrial aluminum alloys. Consider alloy 2024 as an example [245]. All studies were conducted on ingots with diameter 270 mm, obtained using the technique of semi-continuous casting and having the following composition (%): 4.3Cu, 1.6Mg, 0.75Mn, 0.18Fe, 0.16Si. Samples cut out of these ingots were annealed at 490°C and 515 ± 5°C from 10 minutes to 18 hours then quenched into water. As in all previous experiments with binary and ternary alloys, annealing was conducted in a molten salt bath.

Figure 3.18 illustrates the kinetics of elimination of microsegregation for principal alloying elements, copper and magnesium, in the process of homogenization. As can be seen, during the initial stages of heat treatment the

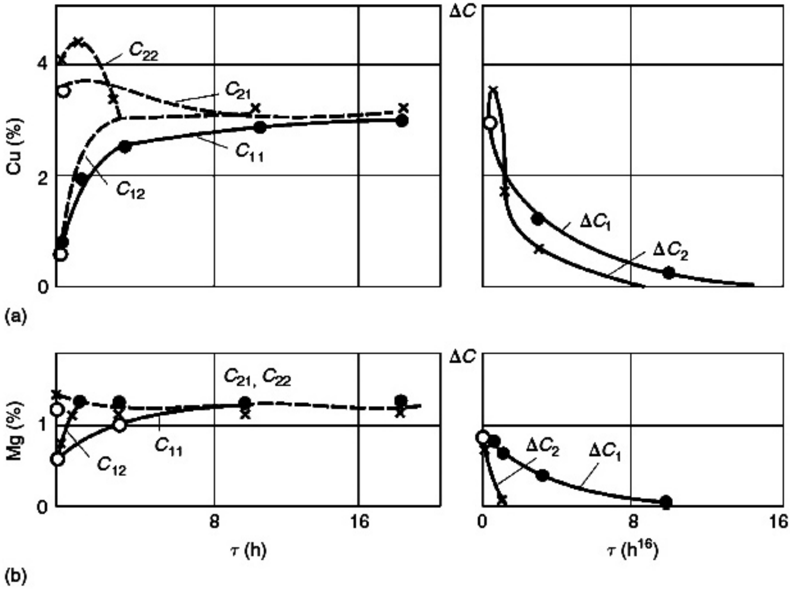

Figure 3.18 Dependence of the: (a) Cu concentration and (b) Mg concentration in the center and on the periphery of dendritic cells and ΔC for alloy D16 ingot, upon homogenization time τ at 490°C (index "1") and 515°C (index "2").

experimentally determined concentration of copper (both in binary and in ternary alloys) grows, and then starts decreasing. After high-temperature homogenization at 515°C (the solidus temperature for this alloy is 508°C) the initial growth of C_2^{Cu} is somewhat more pronounced. Magnesium concentration on the periphery of dendritic cells in the course of annealing practically does not change (Figure 3.18b). In the central parts of dendritic cells the copper content grows immediately after the onset of annealing (Figure 3.18a). During high-temperature homogenization the growth of alloying element concentrations (especially magnesium) in the center of dendritic cells becomes accelerated. Consequently, the time for elimination of microsegregation goes down. In particular, the concentration non-uniformity of copper distribution at 490°C disappears after ~18 hours, at 515°C – after ~10 hours. Magnesium diffuses faster than copper and is characterized by more pronounced temperature dependence of its diffusion coefficient [208]. For this reason its microsegregation at 490°C can be eliminated in about 10 hours, at 515°C – in just 1 hour.

Experimental data on the kinetics of microsegregation elimination of copper and magnesium in alloys close in composition to 2024 and 7449, similar to binary and ternary alloys, agree well with the results of calculation using the $1/f$ factor and model [241]. One comes to a conclusion that the latter is quite universal for binary and multicomponent alloys and could be used for practical calculations. The diffusion coefficient D in aluminum solid solution for the principal alloying elements in equation (3.21) could be taken equal, without much error, to the value of the diffusion coefficient into pure aluminum from its binary alloy of the same concentrations in the studied multicomponent alloy.

Using alloy 2024 as an example it was demonstrated that acceleration of homogenizing diffusion for all principal alloying elements is connected not to the appearance of the liquid phase, but only to the increased diffusivities of atoms in the solid state at elevated temperatures. This conclusion was obtained (similar to the results for dissolution of excessive constituent particles, Figure 3.19) using the Arrhenius plots in the lg $\tau_{1/4}$–$1/T$ coordinates, where $\tau_{1/4}$ is the time of 25% growth of copper concentration in the middle of dendritic cells. Points in Figure 3.19 related to the temperatures above and below non-equilibrium solidus, fit the linear dependence well. Similar results were obtained for binary Al–Cu alloys. These results as well as studies of microsegregation in homogenized ingots and quenched castings of different industrial alloys of the Al–Cu, Al–Mg, Al–Cu–Mg, Al–Mg–Zn, Al–Mg–Zn–Cu, and others clearly demonstrated that it can be completely eliminated using homogenization practices accepted in the plants for all principal alloying elements copper, magnesium, and zinc. At the same time microsegregation of manganese, chromium, and other transition metals is retained practically at the same level as for as-cast ingots. In particular, Mn-depleted zones survive near the boundaries of dendritic cells, and the concentration gradient in their middle part also cannot be eliminated completely (see Figure 2.27).

Weak changes in the concentration profiles for manganese and other transition metals during homogenization of as-cast aluminum alloys is related to relatively low values of their diffusion coefficients at the conventionally used annealing

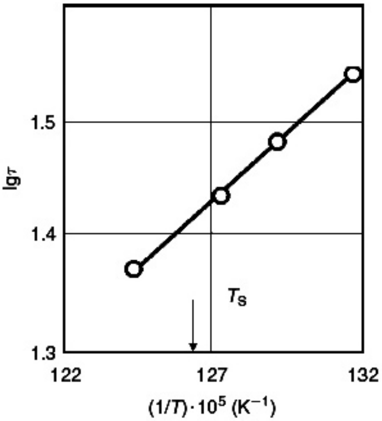

Figure 3.19 Dependence of the 25% Cu concentration change (τ) in the center of dendritic cells during homogenization, upon the reciprocal temperature of annealing for ingot made of alloy D16; T_{sol} is the temperature of non-equilibrium solidus.

temperatures. For example, at 500° C the diffusion coefficients, according to the literature [141,142, 198, 199], are equal to:

Metal	Mg	Cu	Zn	Mn	Cr	Fe
D (cm^2/s)	2×10^{-9}	2.8×10^{-10}	$\sim 10^{-9}$	10^{-11}	10^{-15}	10^{-17}

It is clear that the principal alloying elements possess diffusion coefficients which are several orders of magnitude higher. As a result, the annealing times used in current plant practices (hours, dozens of hours) are quite sufficient to eliminate microsegregation of copper, magnesium, and zinc, while for manganese, chromium, iron, and other transition metals this time is insufficient to achieve concentration uniformity.

3.1.3 Fragmentation and spheroidization of constituent particles

The process of dissolution of excessive constituent particles is accompanied not only by the reduced volume fraction in microstructure, but also by changes in the particle morphologies. Of particular importance is the change of shape of constituent particles, which can only partially be dissolved in (Al) during homogenization.

It is known that in as-cast 3xx-series alloys eutectic silicon inside each colony represents a single crystal of a complex shape [260] (see Figure 3.20a). In the process of isothermal heat treatment before quenching such a single crystal gets divided into multiple relatively small crystals, and each of these strives to attain spherical shape (Figure 3.20b). With increased time of heat treatment the degree of attainment of such spherical shape(s) grows; simultaneously the process of coagulation, or coarsening of silicon particles, is observed (Figure 3.20b).

The processes of fragmentation, coagulation, and spheroidization, similar to dissolution, are directly related to diffusion movements of atoms. For this

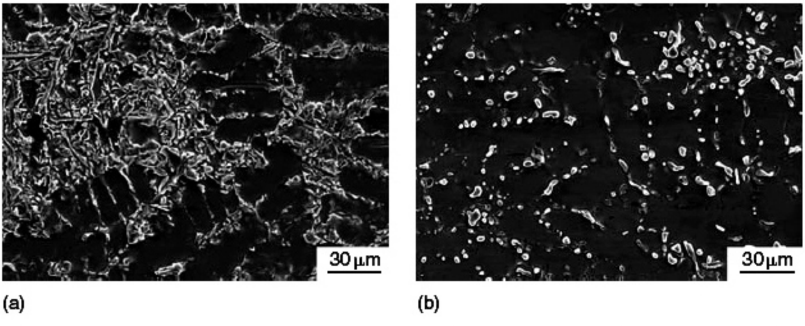

Figure 3.20 Microstructure of Al–Si alloy AK7$_{pch}$: (a) in as-cast condition and (b) after heat treatment before quenching (540°C, 10 hours).

reason such processes proceed faster in those cases when the solubility and mutual diffusivity of atoms forming excessive phases in (Al) grow. Metallographic analysis indicates that the tendency to significant changes in morphology at high-temperature heat treatment is the characteristics of many constituent particles of different phases (mostly of eutectic origin), forming in aluminum alloys Mg_2Si, Al_8Fe_2Si, Al_3Ni, and others.

For alloys with a large amount of eutectic (Figure 1.2b–d), and first of all 3xx-series alloys, spheroidization of the eutectic particles is the primary goal of the whole homogenization process. Practically all constituent particles in aluminum alloys are brittle. For this reason these particles reduce the characteristics of ductility and formability, fracture toughness, fatigue properties, and other structurally sensitive properties. The degree of their detrimental influence is to a significant extent dependent upon their morphology. The preferred particle shape for all properties is globular, but since it is very difficult to obtain this particle morphology directly after casting, spheroidizing heat treatment is used. In most cases it can be combined with homogenizing heat treatment. One has to keep in mind that to obtain the best results it is desirable to conduct spheroidizing heat treatment close to the temperature of equilibrium solidus, including the two-step heat-up procedure (*1st step*: below non-equilibrium solidus; *2nd step*: below equilibrium solidus). For most industrial alloys the temperature of equilibrium solidus is of the order of 500–550°C. Consequently, the temperature of the second step cannot exceed this temperature range.

The intensity of fragmentation and subsequent spheroidization processes depends upon the refinement of the as-cast microstructure. This makes perfect sense – the smaller the dendrite arms of excessive phase(s) inside the eutectic colonies, the faster these processes will proceed in the course of homogenization. In particular, for Al–Si casting alloys obtained via casting into metallic molds, one could obtain almost perfect spherical particles of the silicon phase particles (Figure 3.20b). However, in slowly cooled (sand) castings of the same alloys the morphology of the (Si) particles changes insignificantly.

In principle, it is possible to achieve spheroidization of practically all eutectic phases, including Fe-bearing ones (Figure 3.21), if upon solidification they form finely dispersed eutectic colonies. The particles of those phases that contain elements with insignificant solubility in (Al) and possessing needle-like morphology ($\sim 1\ \mu m$ in thickness), as a rule, retain their morphology even after lengthy heat treatments at temperatures near equilibrium solidus. For this reason the application of spheroidizing heat treatment does not give any positive results. As an example, consider particles of Al_5FeSi (Figure 3.22), the presence of which results in dramatic deterioration of mechanical properties of Al–Si alloys.

In massive castings, for which small cooling rates are typical ($V_c = 10^{-2}$–10^{-1} K/s), no significant changes in morphology of excessive phases, including eutectic and primary particles, are ever observed even after lengthy annealing near the solidus temperature. This is related to the relatively large size of such particles. For relatively thin-walled castings, obtained by casting into metallic molds ($V_c = 10^0$–10^2 K/s), the degree of microstructure modifications in constituent particles depends upon refinement of as-cast ingot and annealing temperature.

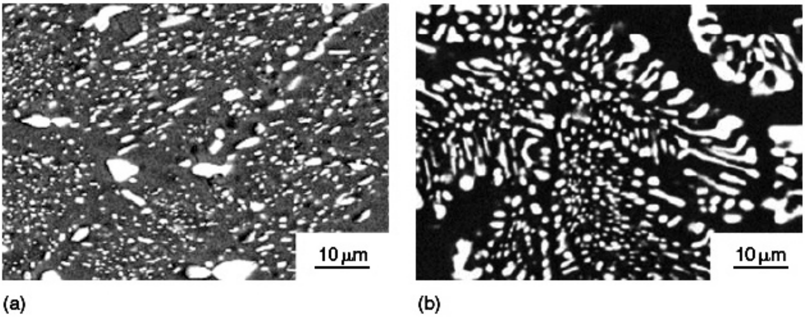

Figure 3.21 Spherical particles of the: (a) Al_3Ni phase and (b) Al_8Fe_2Si, in alloys Al–6%Ni and Al–2.3%Si–2.3%Fe after heat treatment: (a) 600°C, 3 hours; (b) 550°C, 3 hours.

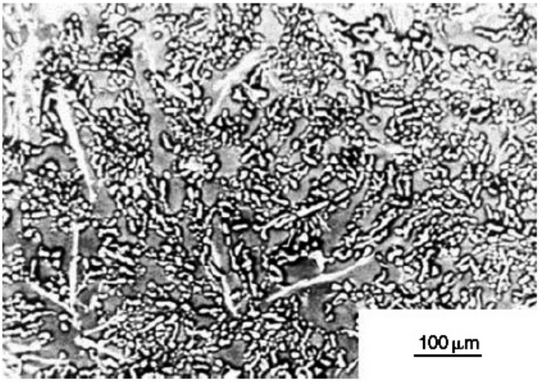

Figure 3.22 Needle-like particles of the Al_5FeSi phase in alloy Al–11%Si–1%Fe after heat treatment at 550°C for 10 hours (SEM).

It should be mentioned that plate-like particles (which look like needles in the planar metallographic samples) cannot be fragmentized and/or spheroidized during annealing because of their smooth planar surfaces. This conclusion is substantiated by data on the directionally solidified eutectic alloy Al–6%Ni, from which it follows that smooth planes of the Al_3Ni phase are stable to heat-ups up to 600°C. However, if some curvature is present, a dramatic reduction of thermal stability of microstructure is observed, resulting in the fragmentation of plate-like particles and the formation of globular inclusions [261]. In the case of refined eutectic colonies (e.g., (Al) + Al_3Ni) which could be obtained by casting into metallic molds, intensive fragmentation and spheroidization occur already at 450–500°C during 1–3 hours [262].

The thermodynamic driving force that causes changes in particle morphology is the tendency to minimize the overall Gibbs free energy of the system, which in the case of equilibrium phases consists of the three principal contributions: bulk or volume component, (G_v), surface (G_s), and elastic (G_e). Fine eutectics possess large interfacial free energy G_s. For this reason the processes of fragmentation and spheroidization, resulting in the formation of relatively large particles, are thermodynamically justified. In the case of smooth plates or needles the reduction of G_s into course of transition to globular particles must be smaller in value than the increase in elastic energy G_e, which, in turn, may hinder the processes of morphology changing. Additionally, the spheroidization of perfectly smooth platelets and needle-like particles may be more difficult because of the surface energy anisotropy, when the conjugation of an Fe-bearing phase and (Al) along certain crystallographic planes is energetically more favorable than the formation of compact particles in aluminum matrix. This is further confirmed by the data on the influence of heat treatment upon microstructure of Al–Fe–Si alloys with phases Al_5FeSi (thin platelets) and Al_8Fe_2Si ("Chinese script" in as-cast state) [263].

It is well known that the thermodynamic driving force alone is not a sufficient condition for the processes of particle shape changes to occur. These processes have diffusional mechanism and, consequently, depend upon the diffusion coefficient of iron in aluminum very substantially. To understand whether bulk diffusion can provide sufficient mass transfer for the processes of fragmentation and especially spheroidization during annealing heat treatment, simple calculations of diffusion paths λ were made for 1-hour thermal exposure. The coefficients of diffusion of iron in aluminum at different temperatures can be calculated using the Arrhenius equation and the known data on pre-exponential coefficients and diffusion activation energies (see Section 2.4.2). As can be seen from Table 3.4, at 400° C that value of λ is less than 1 μm, and the processes of shape changing ("patterning") for the Fe-bearing phases at this temperature could be observed only in rapidly solidified alloys. When $T > 500°$C, the value of λ exceeds 1 μm, which makes it possible to spheroidized iron-bearing constituents in castings and ingots provided the as-cast microstructure was sufficiently refined. This latter characteristic depends not only on the cooling rate but also on the alloy composition.

Table 3.4 Characteristic diffusion length (λ) for atoms of iron in aluminum at different temperatures during 1 hour

T (°C)	D_V (cm²/s)	λ (μm)
400	1.4×10^{-14}	0.1
450	1.1×10^{-13}	0.3
500	7.1×10^{-13}	0.7
550	3.6×10^{-12}	1.6
600	1.5×10^{-11}	3.3

For understanding the mechanism of the initial fragmentation stages it is particularly important to note the average size of dendrites of excessive phase(s) in as-cast condition. For example, if Fe-bearing phase in eutectic colonies is finely dispersed (<0.5 μm), in particular, in rapidly quenched alloys, then the formation of sufficiently large globular inclusions will take place (i.e., well-developed coalescence process).

Such microstructure impedes the observation of the initial fragmentation stages quite significantly since the size of the thinnest parts of dendritic arms (in which the process of fragmentation is supposed to commence) is close to the resolution of an optical microscope (≈0.2 μm). On the contrary, when microstructure is too coarse and the cross-section diameter exceeds 2 μm fragmentation proceeds very slowly. This is true, for example, for alloy Al–2.8%Fe–2.5%Si–1%Mn in which the formation of the $Al_{15}(FeMn)_3Si_2$ phase takes place (Table 3.5).

For these reasons to develop understanding of the fragmentation, spheroidization, and coalescence processes, alloys containing additions of iron, nickel, cerium, and manganese were studied. Their microstructure contains different phases with refined or skeletal morphologies (Table 3.5) [264].

Rectangular ingots ("book molds") with dimensions 160 × 20 × 10 mm were obtained by casting into graphite mold ($V_c = 10^1$ K/s), after which annealing was conducted in the temperature range from 400°C to 600°C. The choice of these alloys as models was dictated by the fact that all forming Fe-bearing phases are in equilibrium in the whole temperature range, which excludes the occurrence of phase reactions.

Microstructural aspects of the fragmentation and spheroidization in considered eutectic alloys were studied using the technique of precision photography of the sample surfaces after different annealing times when heating the samples in a conventional lab furnace. Microstructure was studied using scanning electron microscope (SEM) JSM-35CF at magnifications up to ×20,000 using the regime of back-scattered electrons. For uniform smooth surface the preliminary comparison of microstructural changes on the surface of the samples did not reveal any significant variations. All samples were prepared using mostly the technique of electro polishing, because this method gives a possibility to achieve a much better surface quality compared to conventional mechanical polishing. As a result, much finer microstructural features could be observed. In a number of cases the compositions of the studied alloys were chosen in such a way that microstructure contained only insignificant amount of the primary crystals of Fe-bearing phases. This selection facilitated further search of locations on the surface for taking micrographs.

To get a more detailed understanding of the spatial morphology of the crystals of Fe-bearing phases a transmission electron microscope (TEM) JEM-2000EX was used. This is illustrated in Figure 3.23 using alloy Al–6%Ni–0.5%Zr as an example.

The principal element of the cast microstructure of all studied alloys (Table 3.5) was the eutectic colonies comprised of (Al) and the corresponding Fe-bearing phases. TEM and SEM microstructure studies revealed continuity (single crystals within a given eutectic colony) of the Fe-bearing phases, in which all

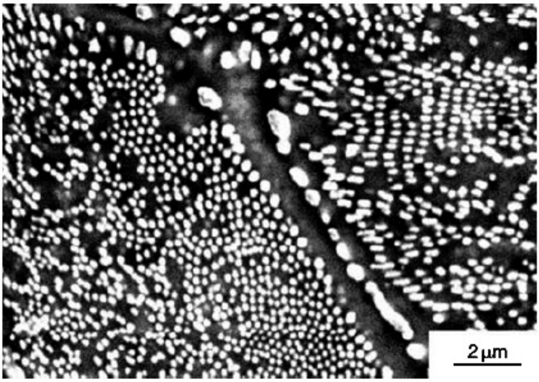

Figure 3.23 Globular inclusions of the Al_3Ni phase in alloy Al–6%Ni–0.5%Zr after heat treatment at 450°C for 10 hours.

Table 3.5 Compositions and characteristics of eutectic alloys selected for fragmentation, spheroidization, and coalescence studies[a]

Concentration of elements (%)					Eutectic phase, composition[a]	Q_M[b] (mass %)	Q_V[b] (vol%)	T_s[c] (°C)
Fe	Si	Mn	Ni	Ce				
1.7	–	–	1.7	–	Al_9FeNi 16%Fe, 16%Ni	9.9	7.9	649
2	–	–	–	2	$Al_{10}Fe_2Ce$ 22%Fe, 27%Ce	9.1	5.1	650
1.8	2.5	1	–	–	$Al_{13}(FeMn)_3Si_2$ 32%(Fe+Mn), 8%Si	8.8	6.9	577
2.8	2.5	–	–	–	Al_8Fe_2Si 32%Fe, 8%Si	8.8	6.9	577
2	–	–	–	–	Al_6Fe 25% Fe	8	6.8	655

[a] The balance is aluminum.

[b] Q_M and Q_V: mass and volume fractions of Fe-bearing phases, respectively.

[c] T_s: solidus temperature.

possessed typical dendritic microstructure with different degree of branching, (Figure 3.24a).

As far as morphology is concerned (from the mechanical properties point of view) the best eutectic phase amongst all studied was Al_8Fe_2Si with cross-section of dendritic branches from 0.5 to 2 μm. For this reason the Al–2.8%Fe–2.5%Si alloy was selected for studies of the fragmentation processes (Table 3.5).

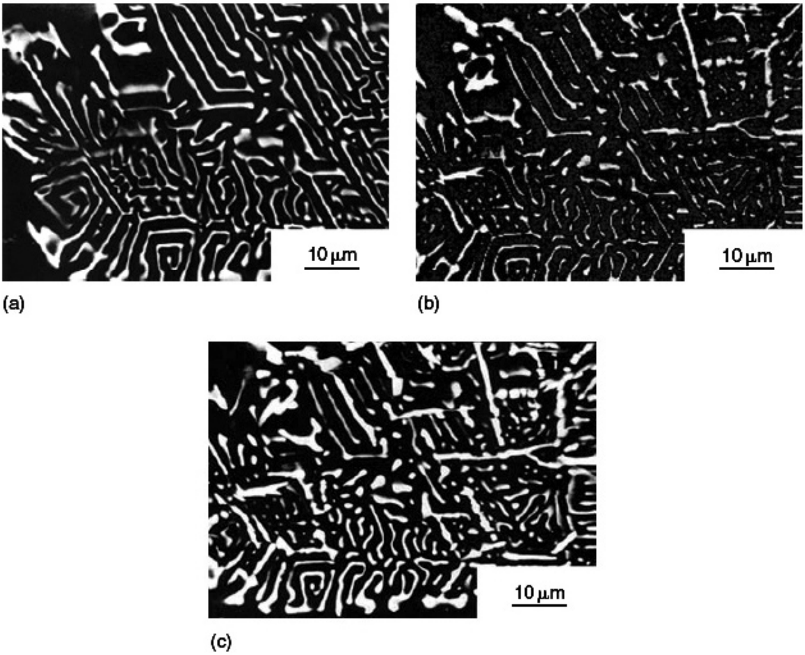

Figure 3.24 Initial fragmentation of the eutectic phase Al_8Fe_2Si particles at 550°C in alloy Al–2.5%Si–2.8%Fe (SEM, ×2000): (a) as-cast state, (b) 0.5 hours, and (c) 1 hour.

Micrographs of this alloy contain several areas in which the fragmentation of Al_8Fe_2Si begins (Figure 3.24). Division of the branches of this phase at 550°C commences already after minimal heat treatment (~0.5 hour). The morphology of the first fragments is still far from globular; in other words, one could conclude this is just the onset of the whole process. As one could expect, at first branches with increased curvature get affected by the subdivision process, these are usually located in the central parts of eutectic colonies. The peripheral and linear parts of the dendrite branches are the most stable (the former because of higher thickness, the latter due to smaller curvature).

If the heat treatment time increases, fragmentation spreads over a larger volume of the eutectic crystals of Fe-bearing phases. In parallel, spheroidization of the just formed smaller fragments takes place. This is followed by coalescence (i.e., growth of some particles at the expense of all others).

It needs to be noted that these processes proceed quite non-uniformly in different parts of different crystals. For this reason qualitative comparative assessment of the crystal shape changes as a function of the heat treatment time requires that a sufficiently big number of the areas of the sample be inspected. To obtain quantitative integral estimates one could use two parameters: specific interphase area (S) and the number of particles (particle cross-sections) per unit area (N). These parameters can be determined using microphotographs and lineal analysis (stereology). The application of the first parameter is recommended because the morphology of the Fe-bearing particles does not play any role in its determination. This is important during the initial stages of fragmentation, since it is very difficult to discern the cross-sections of globular particles from cross-sections of non-fragmented dendritic arms. With a high probability one can conclude that the morphology of phases inside the samples changes in a similar way to the changes observed on its surface. This is confirmed by the comparison of the S and N values determined with and without preliminary polishing.

Obviously, during spheroidization and subsequent coalescence the value of S must decrease. However, at the first stage of fragmentation the total surface area may grow. To obtain a preliminary assessment of this kinetics we used a simplified scheme (Figure 3.25) according to which a refined eutectic crystal of an iron-bearing phase could be present in the form of a group of rods with diameter d_0 and length L ($L \gg d_0$). Simple calculations demonstrate that the subdivision of such rods into n_0 cylinders with length $l_0 = d_0$ ($L = n_0 d_0$), which corresponds to ideal fragmentation without spheroidization, the value of S will increase by a factor of 1.5 compared to the initial state (S_0). On the other hand, the spheroidization of these fragments (i.e., ideal spheroidization without coalescence) results in the formation of small balls ($d = 1.14d_0$) and to the reduction of the S value, which, nevertheless, must exceed the initial value of S_0 by a factor of 1.3. At the next stage these balls will be coalescing, and in the theoretical limit there will be only one large ball left. Changes in d and S with decreasing n are defined by the following relations:

$$d = 1.14 \cdot \left(\frac{n_0}{n}\right)^{\frac{1}{3}} \tag{3.22a}$$

$$S = 1.3 \cdot S_0 \cdot \left(\frac{n_0}{n}\right)^{\frac{1}{3}} \tag{3.22b}$$

Defining different values of n_0 (which in real microstructure corresponds to different ratios of the total length of dendritic arms of Fe-bearing phases to their diameter) one could theoretically assess the maximal range for changes of the S value. Since in reality the processes of fragmentation and spheroidization happen concurrently (i.e., the formation of short cylinders is quite impossible) we should accept as the maximal value of specific interphase surface $1.3S_0$. The minimal value of S, as it follows from the above analysis, depends upon the refinement of the original microstructure: parameter S/S_0 decreases for finer microstructures.

Experimentally determined S for alloy Al–1.7%Fe–1.7%Ni displayed a clearly pronounced tendency: increasing the time of heat treatment at 600°C to 8 hours results in the decrease of S to the level of 0.7–$0.8S_0$ (Figure 3.26). During the first hour of heating intensive fragmentation of Fe-bearing phases takes place. Correspondingly, the S–t curve displays a maximum (approximately $1.2S_0$). With time the value of S decreases due to coalescence of the particles. The maximal changes

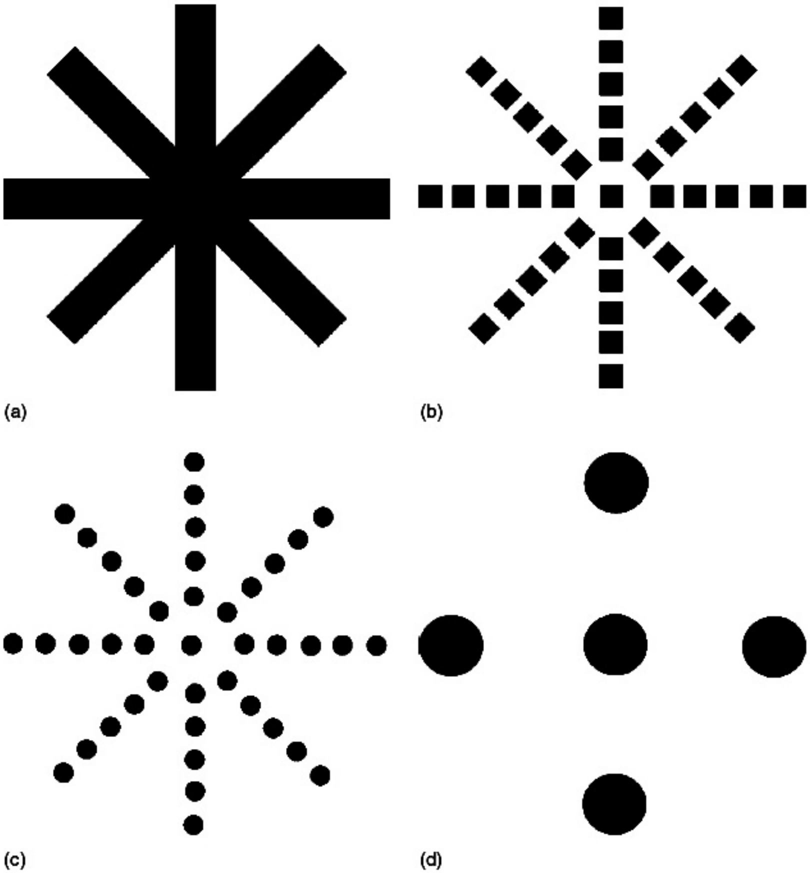

Figure 3.25 Schematic illustrating fragmentation, spheroidization, and coalescence of the Fe-bearing phase particles within the limits of one eutectic colony in the process of homogenizing heat treatment: (a) as-cast state illustrating continuous structure of dendritic crystal; (b) fragmentation of dendritic branches (arms); (c) spheroidization of fragments (particles); and (d) coalescence of globular particles.

take place during the second hour of heat treatment, after that the intensity of the process is quite negligible. This is easy to understand: as the average size of particles grows, their growth rate becomes smaller in complete accordance with the Ostwald equation [265]. Spheroidization of particles can be established already after minimal exposure (~30 minutes) to heat treatment. One could note that the value of diffusion path λ at temperatures 550–600°C (Table 3.4) is significantly higher than the average thickness of dendrite arms. This facilitates active processes of patterning and changes of crystal shapes. At 500°C the value of diffusion

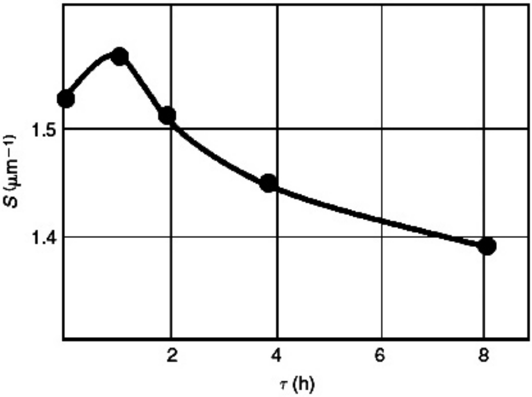

Figure 3.26 Dependence of specific interphase surface area (S) upon heat-up time at 600°C in alloy Al–1.7%Fe–1.7%Ni.

coefficient is comparatively small, and 8 hours of annealing at this temperature allow fragmentation processes to proceed only in relatively thin places.

3.1.4 Changes of grain and dislocation microstructure of aluminum solid solution in the course of homogenization

Until recently it was widely accepted that in the process of homogenization the average grain size in ingots and castings either does not change or grows in the process of recrystallization [62, 266, 267]. In Al–Si casting alloys, for example, the average grain size in aluminum solid solution practically does not change at any heating regimes and/or treatments. However, a high density of dislocations and particularly well-developed subgrain microstructure were discovered, especially in aluminum alloys with $C_{Mg} > 4\%$ (see Section 2.5). This resulted in a hypothesis that at least in some alloys for different annealing schedules the process of primary recrystallization may occur, resulting in grain refinement. These suggestions were based also on the data presented in Refs. [108, 130, 201] on recrystallization processes immediately after cooling following the completion of solidification for alloys with small amounts of excessive constituent particles.

In connection with these observations it was decided to study how grain and dislocation microstructures change upon annealing of binary alloys belonging to different systems with different types of dislocations microstructures in as-cast state. Additionally, industrial alloys on the basis of the Al–Mg, Al–Cu, and Al–Mg–Zn systems were studied (AlMg6, AlMg10, AM5, and 1915 with the ratio of concentrations $C_{Zn}/C_{Mg} \cong 0.5$). These data were presented in publications [159, 161, 270].

First, the role of equiaxed grain size changes in as-cast alloys was studied. All alloys were solidified with the same cooling rate (~14 K/s) and then annealed in similar conditions at homological temperature $0.9T_S$ (T_S is the temperature of non-equilibrium solidus) during 1 hour. After annealing samples were quenched into water, and some samples were slowly cooled with the furnace. Grain size D was determined using oxidized polished samples in polarized light. The results of measurements of D in as-cast and quenched samples are provided in Table 3.6.

As it follows from Table 3.6, in most binary weakly alloyed materials prepared out of pure aluminum (99.99%), 1-hour annealing results in a significant grain growth. In some alloys (Al + 0.6%Ge, AA224.0) the average grain size practically does not change, while in Mg-bearing aluminum alloys it declines quite substantially. This unusual effect of grain microstructure refinement upon annealing of Al–Mg alloys was studied in detail in Ref. [269] using several alloys as examples: AlMg6 (6.3%Mg, 0.6%Ti, 0.003%Be, 0.15%Fe, 0.15% Si), and AlMg10 (10%Mg, 0.1%Ti, 0.1%Zr, 0.1%Be, and 0.03% Fe and Si).

Figure 3.27 presents data on the dependence of the relative grain size changes on the time of alloy annealing at 435° C. All alloys were solidified with the cooling

Table 3.6 Changes of grain size for different casting alloys as a result of homogenization at $0.9T_S$ during 1 hour

Alloy* (at.%)	0.6 Cu	0.6 Mg	2.2 Mg	14 Mg	AlMg6
D (μm) as-cast state	168	265	268	110	257
D (μm) after homogenization for 1 hour at $0.9T_S$	1760	375	456	103	159
Alloy* (at.%)	AlMg10	0.6 Ge	0.6 Mn	2.2 Zn	224.0
D (μm) in as-cast state	123	306	536	842	165
D (μm) after homogenization for 1 hour at $0.9T_S$	92	320	530	1362	160

Note. The variation coefficient for grain size measurements was within the limits of 20%.
* Alloy designation or amount of alloying element in binary aluminum-based alloy.

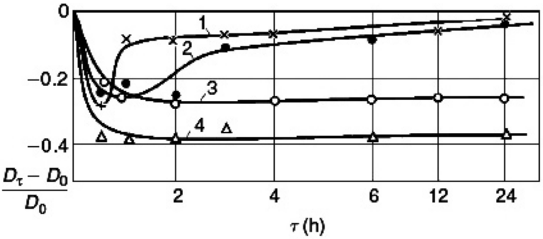

Figure 3.27 Dependence of the relative grain size change, $(D_\tau – D_0)/D_0$, upon homogenization time τ at 435°C for alloys: (1) Al + 10%Mg; (2) Al + 6%Mg; (3) AMg10; and (4) AMg6.

rate of ~14 K/s. It is clear that substantial grain size reduction (~24–50%) takes place during the first hour of heat treatment. Further increase of annealing time in industrial alloys practically does not affect D_τ, while in binary alloys grain size grows up to the values close to D_0. Similar data were obtained for the Al–Mg–Zn system alloys, where the relative grain refinement in a number of cases reached up to 300%.

In all studied alloys significant scatter of results on grain size was observed. For this reason the size distribution curves were constructed using 150–350 measurements.

A significant scatter in grain sizes was observed for the studied samples. To achieve even higher accuracy and reliability of data these measurements were conducted using one sample for each alloy, which was electrolytically re-polished after a certain heat treatment, and the top 0.3–0.5 mm of the surface were removed. The analysis of the obtained frequency curves indicated that the reduction of D_τ after annealing was related to the increased volume fraction of the relatively fine grains (Figure 3.28). In binary alloys after heat treatment bimodal distribution of grain sizes was observed. One of the maximums after 1-hour annealing was close to the average grain size in as-cast state, while the other corresponded to the average grain size twice as small (Figure 3.30a). Such distribution, as can be seen from the results of metallographic analysis (Figure 3.29), is directly related to the fact that after 1-hour heat treatment a fraction of the original grains remains practically unchanged, but at the same time new, finer grains nucleate. This process of nucleation is even more intensive in industrial aluminum alloys. For such materials unimodal distribution was observed after 1-hour annealing, the maximum of which was shifted toward smaller grain sizes (compared to the original average) (Figure 3.28). Unlike in the case of binary alloys, the "tail" of this distribution gets shortened, which is an indication of the suppression of grain growth due to the presence of alloying additions and admixtures.

Lengthy annealing (24 hour) of binary alloys results in the broadening and flattening of the distribution curves for D_τ, and also in their shift toward larger values of D_τ due to growth of "old" and "new" grains. As a result, the average size approaches D_0. In industrial alloys the main maximum after 24 hours of heat treatment is shifted toward even smaller values of D_τ, while the average size remains about the same due to the increased volume fraction of the relatively large grains (~100 μm) (Figure 3.28).

If the temperature of heat treatment for binary alloys containing 6 and 10%Mg is raised above non-equilibrium solidus (i.e., 560°C and 510°C, respectively), this results in substantial increase of D_τ after lengthy heat treatments, while the effect of grain refinement becomes completely eliminated. For example, after 24 hours of annealing in alloy with 6%Mg, $D_\tau/D_0 \cong 5$, while for alloy with 10%Mg, $D_\tau/D_0 \cong 10$. In industrial alloy AlMg6 high-temperature homogenization at 560°C, as well as at the temperature below solidus, causes grain refinement, although somewhat less pronounced. For alloy AlMg10, heat-up at 510°C before quenching results in some grain roughening at 510°C.

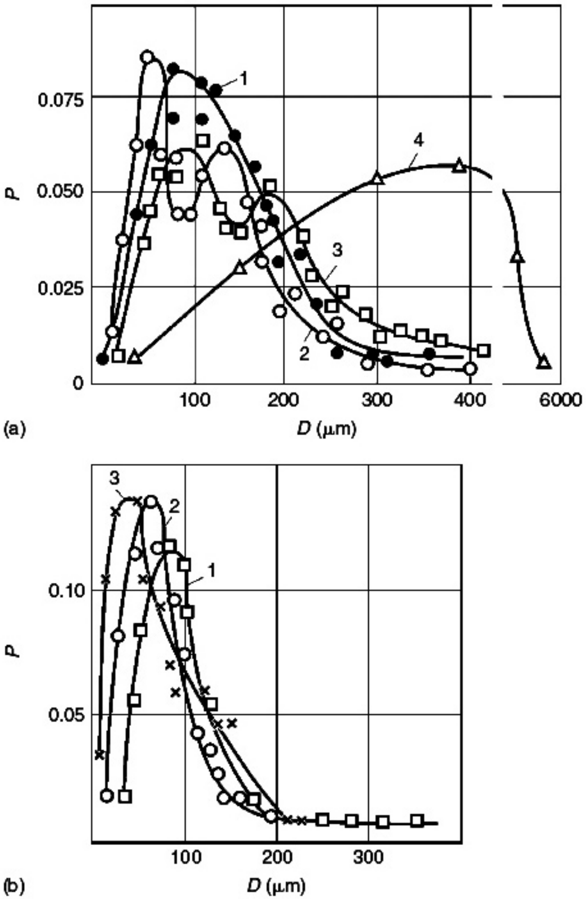

Figure 3.28 Frequency distribution curves for grain size, D, in alloys (a) Al + 10%Mg and (b) VAL10, in (1) as-cast and (2–4) homogenized states. The applied homogenization regimes were as follows: (2) −435°C, 1 hour; (3) −435°C, 24 hours; and (4) −510°C, 24 hours.

It is established that solidification rate exerts a strong influence upon the degree of grain refinement after homogenization. As it can be seen from Table 3.7 (data for alloy AlMg10), for slowly cooled castings that contained originally coarse grain microstructure, the effect of refinement after annealing was particularly well observed.

Analyses of grain size distribution curves and direct metallographic observations indicate that the smaller average grain size in homogenized alloys of the

Table 3.7 Influence of the cooling rate (V_c) upon grain size after homogenization (D_τ)

V_c (K/s)	D_o (μm)	D_τ* (μm)	$(D_o - D_\tau)/D_o$
1	314 ± 20	236 ± 20	0.25
3	238 ± 20	185 ± 20	0.22
4	208 ± 15	178 ± 15	0.14
17	204 ± 15	179 ± 15	0.14

* Grain size was determined in castings after heat-up before quenching for 24 hours at 435°C.

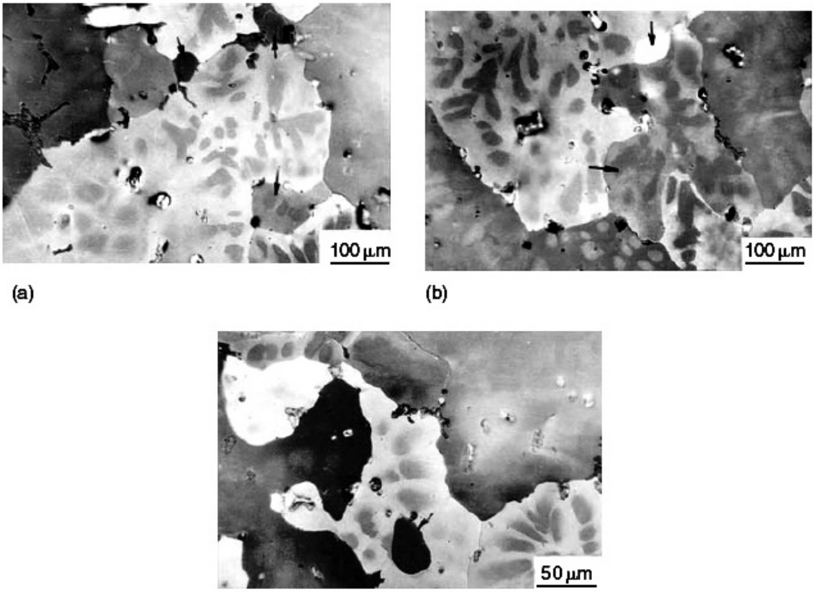

Figure 3.29 Formation of new grains (indicated by arrows) during homogenization of casting aluminum alloy AMg6 (polarized light).

Al–Mg and Al–Mg–Zn systems is related to the formation, in the process of heat treatment, of new high-angle grain boundaries inside the original crystals. Oxidized metallographic samples of alloys AlMg6 and AlMg10 containing titanium, after homogenization clearly reveal (in polarized light) typical dendritic microstructure inside the metallic grains (Figure 3.29). As it was demonstrated by X-ray micro spectroscopy analysis, dark axis of dendrites is revealed due to the elevated concentration of titanium. Its non-uniform distribution is not eliminated after annealing due to its low diffusion coefficient. The revealed dendritic "script" helps identify the sites where preferential formation of the new high-angle boundaries takes place during heat treatment.

The fact that new grains in Figure 3.29 are indeed surrounded by high-angle boundaries was proved by revealing the etching traces, which were oriented in arbitrary directions in all grains that differed by their coloration in polarized light. Inside the original crystallites the formation of high-angle boundaries occurs either inside a single dendritic cell (Figure 3.29a, b) or around several cells, when a new grain is formed out of a whole dendritic branch (Figure 3.29c). New grains form particularly often near the original grain boundaries (Figure 3.29a) and in the proximity of large inclusions of constituent particles (Figure 3.29c). A particular feature related to the new grains is their small size (relative to the original grains) and arbitrary crossings with dendritic script.

Before discussing the nature of grain morphology changes in the course of homogenizing heat treatment of different casting alloy compositions, let us consider changes in their dislocation microstructure incurred by homogenizing. Since this heat treatment is conducted at very high homological temperatures, it is natural that the processes of dynamic redistribution of dislocations and changes in dislocation structures take place. Dislocation microstructure that was formed in the course of solidification and cooling of casting becomes more ordered. This process manifests itself in the form of creating more stable dislocation configurations and the general reduction of dislocation density.

Electron microscopy observations partially summarized in Table 3.8 indicate that in some alloys with original or mixed dislocation microstructure

Table 3.8 Density of dislocations ρ and subgrain size d' in binary aluminum alloy castings after quenching and annealing at $0.9T_S$ during 1 hour

Alloying element contents (at.%)	Quenching		Annealing (cooling with furnace)	
	$\rho \times 10^{-9}$ (cm^{-2})	d' (μm)	$\rho \times 10^{-9}$ (cm^{-2})	d' (μm)
0.6Mg	7.6 ± 2.1	–	–	–
2.2Mg	–	–	–	–
14Mg	7.0 ± 2.5	6 ± 1.2	5 ± 2	11 ± 2.5
0.6Cu	4.7 ± 0.8	–	3.2 ± 0.8	–
2.2Cu	2.7 ± 0.8	–	3.5 ± 0.5	–
0.6Ge	6.2 ± 1.9	–	–	–
0.6Mn	5.4 ± 1.0	8 ± 1.5	3.1 ± 0.9	16 ± 3.5
0.2Zn	4.8 ± 0.7	–	–	–

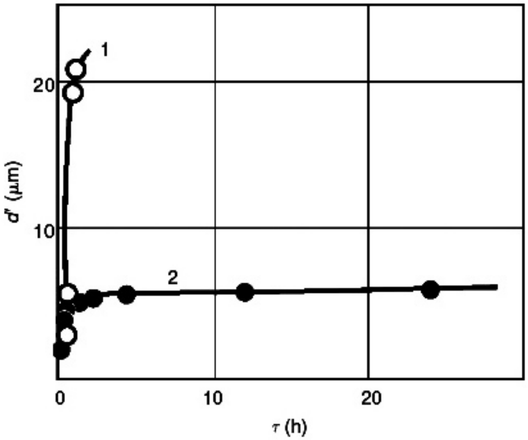

Figure 3.30 Dependence of the average subgrain size, d', in casting alloys (1) Al + 10%Mg and (2) AMr10ч upon homogenization time τ at 435°C.

homogenizing heat treatment results in polygonization process (alloys Al–Cu, Al–Mg–Zn, Al–0.6 at.%Mn). In other alloys with similar microstructure its character does not change and its perfection is manifested in the formation of a more regular cell microstructure (e.g., in alloys with 0.6 at.% of Ge and Mg). In aluminum–magnesium alloys with the original subgrain microstructure annealing results in the growth of subgrains (Table 3.8) and in the reduction of dislocation density inside the subgrains. For higher solidification rates and smaller subgrains in the original as-cast state, after homogenizing subgrains will also remain smaller.

The reduction (in comparison with as-cast state) of the general density of dislocations, even in the case of slow cooling from homogenization temperature, never exceeds one order of magnitude (compare data in Tables 3.8 and 2.7). This is related to both binary and multicomponent alloys. Lower dislocation density and large subgrains in annealed state in comparison to the quenched state can be explained, most probably, by the additional perfections of dislocation microstructure in the course of slow cooling ($C_{\text{cooling}} = 0.06\,\text{K/s}$).

The kinetics of subgrain growth during homogenization of alloys with original subgrain microstructure depends very strongly upon alloy composition, in particular, upon the presence of ancillary additions and admixtures of different elements. This was demonstrated for alloy Al + 10%Mg and industrial alloy AlMg10 with the same magnesium content (Figures 3.30 and 3.31). In binary alloy very rapid and intensive growth of subgrains (~ by 7 times!) takes place already during the very first minutes of annealing. Indeed, the zone of fine crystals on the periphery of dendritic cells disappears after 5 min of heating (see Figure 2.33). However, in industrial alloy AlMg10 changes of the average size of subgrains are much slower and come to completion after ~2 hours of heat treatment, after which the average subgrain size does not change anymore. Subgrains in this case become larger

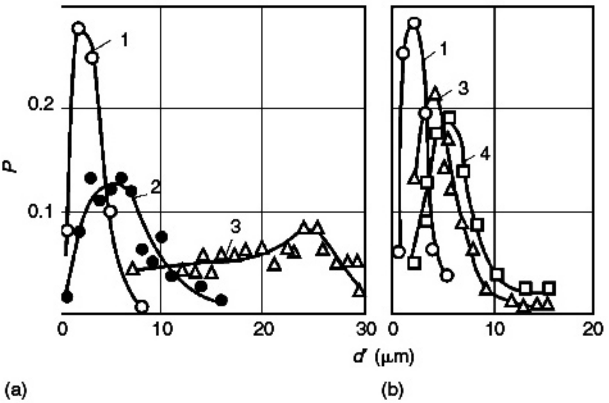

Figure 3.31 Frequency distribution curves for subgrain size, d, in alloy (a) Al + 10%Mg and (b) AL27-1; (1) illustrates distribution curves for alloys in as-cast condition while (2, 3, 4) provide results on these distributions after annealing at 435°C during 0.25, 0.5, and 24 hours, respectively.

only by a factor of 3. It is also important to stress that in both alloys the largest subgrains are close in their size to the new nucleated subgrains that are formed in the process of annealing (see Figures 3.28 and 3.31).

On the basis of the presented data one could conclude that in the course of homogenizing heat treatment of aluminum alloys the average grain size of equiaxed grains can increase, decrease, or stay the same. The direction of these changes is defined by the alloy's chemical composition, the nature of the original dislocation microstructure and its changes during annealing, and also the annealing temperature.

However, no matter what original dislocation microstructure or heat treatment, the average grain size remains the same for those alloys in which the larger part of the grain boundaries is occupied by eutectic phases or excessive constituents, which cannot be dissolved during homogenization.

In alloys with cell or cell-subgrain dislocation microstructure in as-cast state, which in the process of homogenization remain or become single-phase materials, grain size at any annealing temperatures grows. Examples include such binary alloys as Al + 0.6at.%Cu, and Al + 2.2at.%Zn. Grain growth occurs, in agreement with earlier ideas, via recrystallization and migration of the relatively mobile grain boundaries. In multicomponent industrial alloys with similar dislocation microstructures boundary migration is more difficult to achieve due to the presence of alloying elements, admixtures, and impurities in solid solution and in constituent particles and dispersoids. Consequently, the average grain size hardly changes after homogenization heat treatment. Constant grain size could also be observed for binary aluminum alloys prepared out of the purest aluminum, if during heat treatment a sufficient amount of excessive constituent particles are retained, or the formation of multi-phase microstructure takes place (e.g., as in Al–0.6 at.%Mn alloy; see below in Chapter 6).

In alloys of the Al–Mg and Al–Mg–Zn systems with subgrain or cell-subgrain microstructure in as-cast condition initial stages of homogenizing heat treatment are accompanied by grain refinement (due to primary recryallization processes). Its mechanism, based on the data presented above, is directly related to the coarsening of already existing or new nucleating subgrains in the process of heat treatment. Figures 3.30 and 3.33 provide direct evidence in support of this statement.

In industrial alloys on the basis of the Al–Mg and Al–Mg–Zn systems, the discovered effect of grain refinement in the beginning of isothermal heat treatment turned out to be quite robust and persevered even at the most lengthy annealing treatments. Grain refinement could be reliably established at any homogenization temperatures, up to and including temperatures above non-equilibrium solidus. This is related to the absence of migration of the newly formed and original high-angle boundaries due to the presence of impurities and alloying elements in industrial alloys. In binary Al–Mg alloys, where such additions and impurities are practically absent, the initial grain refinement is followed by the D_r growth as annealing time increases (Figure 3.27). The analysis of distribution curves (see Figure 3.28) indicates that growth of the average grain is defined by the simultaneous coarsening of the new and old crystallites due to the migration of their boundaries. When the temperature of homogenization is chosen above non-equilibrium solidus the effect of refinement cannot be persistent due to the high rate of the boundary migration causing substantial coarsening of grains (compared to the original, as-cast state).

3.1.5 Decomposition of aluminum solid solution in the process of isothermal heat treatment before quenching

After non-equilibrium solidification of any aluminum alloy the forming solid solution is supersaturated at the temperature of subsequent homogenization below non-equilibrium solidus. Indeed, if one takes, for example, Al–Mg alloy containing 10.6%Mg, then in the course of solidification at any practically applied cooling rate the periphery of its dendritic cells will be enriched with the layers of solid solution with the concentration up to C_a. At homogenization temperature equal to 400°C the boundary layers containing magnesium in higher concentrations than the corresponding solvus C'_a (~12%) will inevitably exceed this maximal solubility. This causes the decomposition of the α-solid solution. Such a decomposition can be observed metallographically during the first hour of annealing [180].

If further heat-up causes more uniform concentrations of alloying element(s) across the volume of dendritic cells, then the already formed excessive crystals will be dissolved. Precisely this situation is observed in binary and multicomponent aluminum alloys containing only principal alloying elements: magnesium, copper, zinc, and also silicon. For this reason decomposition with respect to these chemical elements in the process of homogenization does not have any practical significance and can be safely ignored for all practical purposes.

However, if aluminum alloy contains additions of such transition elements as manganese, titanium, zirconium etc., then the products of decomposition of the supersaturated solid solution will be retained in alloy's microstructure practically at any heat treatment regimes. This is due to the already mentioned slow diffusion rates of transition metal atoms in aluminum and their persistent microsegregation after homogenization using any practical heat treatment regime. Besides, as it was demonstrated in Section 2.2, transition metals can be dissolved in aluminum solid solution at the realistic rates of non-equilibrium solidification; their respective amounts will be substantially higher than the limit solubility at eutectic or peritectic temperature(s). This results in the increased volume fraction of the solid solution with concentrations corresponding to heterogeneous regions of the corresponding phase diagrams at homogenization temperature(s). As a result, homogenized ingots containing 0.1% and higher of the aforementioned transition elements will contain *dispersoids* in their microstructure. Of course, such alloys comprise the absolute majority of commercial alloys of this class.

Data on the decomposition of supersaturated solid solutions of transition metals in aluminum were initially generalized and presented by Elagin [123]. Decomposition was studied for many alloys containing different concentrations of transition elements; stability of solid solution during heat treatment was established. Finally, inhomogeneities in the distribution of the products of decomposition across dendritic cells were established related to the phenomenon of microsegregation of the corresponding transition elements.

In earlier studies the techniques of light microscopy and micro X-ray spectroscopy were employed most often. Using the latter method, it was possible to estimate the value of the lattice parameter, while optical microscopy helped observe the morphology of the decomposition products. However, in most aluminum alloys after homogenization it were difficult to see individual particles, only the zones with higher etching rate could be observed. Such zones, of course, contained higher amounts of the products of (Al) decomposition (Figure 3.32).

In Refs. [159, 245, 272–279] where TEM in the diffraction mode was used as the primary exploratory tool, composition and crystalline structure of the aluminides of transition metals was studied quantitatively, as well as the shapes, sizes, and distribution of such dispersoids at different stages of homogenization of alloys obtained using different solidification schemes. Typical dispersoids, which can be present in casting aluminum alloys, are shown in Figure 3.33.

The decomposition of (Al) supersaturated with respect to transition metals was studied using alloys of the Al–Mg system (AlMg6, AlMg10), Al–Mg–Zn system (1915, and also alloy with the concentration ratio $C_{\mathrm{Zn}}/C_{\mathrm{Mg}} \approx 0.5$), Al–Cu–Mg (2024), Al–Si–Mg–Cu, etc. These alloys contained such additions as manganese, titanium, zirconium, chromium, and scandium. Several generalities in morphology of the dispersoids were established, as well as the other products of decompositions of supersaturated solid solutions.

In alloys containing *manganese*, the corresponding aluminides forming during isothermal heat treatments at 350–560°C are concentrated mostly on the periphery of dendritic cells, where the Mn concentration is elevated as a result of non-equilibrium solidification. In the boundary regions depleted with manganese

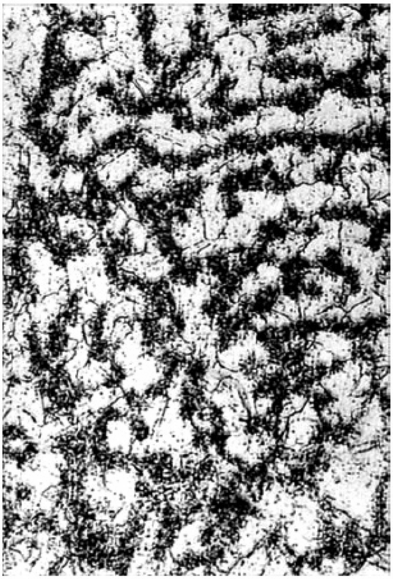

Figure 3.32 Non-uniform etching of a metallographic sample prepared out of alloy 1915 with additions of Ti; etching was conducted in Keller's reactive, alloy was homogenized for 24 hours at temperature 450°C.

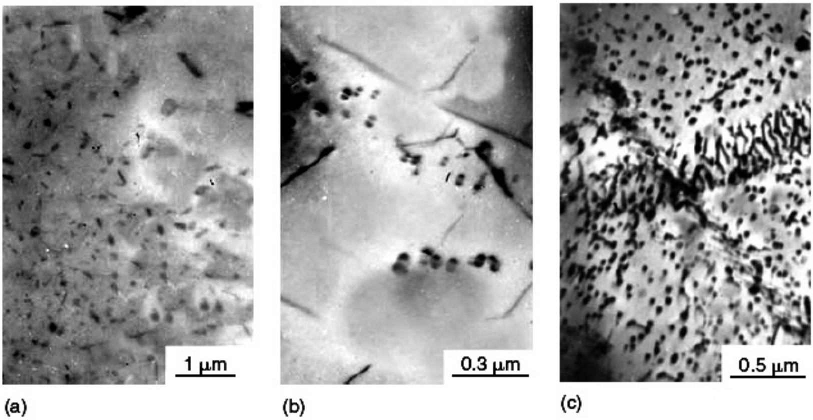

Figure 3.33 Secondary precipitates of (a) manganese aluminides; (b) zirconium aluminides; and (c) titanium aluminides in aluminum alloys of the Al–Mg, and Al–Mg–Zn systems; (a) alloy AMg6; (b) alloy 1915; (c) alloy AMg10ch.

these dispersoids are not formed. Quite often the amount of the (Al) decomposition products is relatively small, or they are completely absent in the centers of dendritic cells. Thus, the distribution of Mn-bearing particles exactly corresponds to the concentration profile of Mn distribution across dendritic cells of (Al) in as-cast condition (Figure 2.26). This latter, as it was already mentioned above, practically does not change after homogenization.

The difference in manganese concentrations in the centers of dendritic cells and in the point of its maximal concentration on the distribution curve along the cell cross-section (see Figure 2.26) is usually less than 0.2%. At the same time the difference in the number density of Mn-bearing particles in the center and on the periphery of dendritic cells is often quite significant. For this reason a question arises whether such a small concentration of inhomogeneities could serve the principal cause of the inhomogeneities of the solid solution decomposition. To address this important question, special measurements were conducted in Ref. [245] for castings (obtained using semi-continuous casting technique) of alloy ~2024 (4.3%Cu, 1.6%Mg, 0.75%Mn, 0.18%Fe, and 0.14%Si) with diameter 270 mm. After homogenization at 490°C for 18 hours the difference in Mn concentrations for those areas where decomposition has and has not taken place (excluding narrow zones adjacent to the boundaries) was ~0.1–0.2%Mn. Using SEM micrographs the average particle volume Mn-bearing particles on the periphery of dendritic cells was determined to be $8.9 \times 10^{-5} \mu m^3$. Their number per volume unit was 172 particles/μm^3, and volume fraction was equal to 1.5 vol%. The formation of such amount of dispersoids could be explained with the observed concentration difference of Mn (0.1–0.2%), if the precipitating phase contains considerable amount of aluminum and possesses chemical formula close to $Al_{12}Mn$. As it will be demonstrated below, this is quite possible and, consequently, one could state that even small manganese microsegregation should be sufficient to obtain non-uniform distribution of the products of its solution decomposition in aluminum across dendritic cells.

Manganese-bearing particles that are not connected to dislocations, subgrain, and grain boundaries typically possess regular geometrical shapes: in foils they look like quadrangles, triangles, rods, trapezoidal particles (Figure 3.33a), and often plates.

Precipitates that nucleate heterogeneously on linear or planar defects of the crystalline lattice, typically have irregular shapes, especially after annealing at relatively low temperatures. Linear sizes of such particles grow with increased distance from the boundaries of dendritic cells and, naturally, with increased temperature of annealing. In alloys on the basis of the Al–Mg and Al–Mg–Zn systems that are characterized by broad range of possible homogenization temperatures, one could control the size of and distance between particles of manganese aluminides in a very broad interval. For example, in alloy AlMg6 the average linear size of Mn-bearing precipitates after annealing at 380°C for 18 hours is approximately 0.1 μm, while after heat treatment at 510°C for the same 18 hours it is about 0.6 μm. The interparticle distance grows in concert with the particle size. However, at any realistic homogenization schedules the average size of Mn-bearing aluminum dispersoids and the distance between the particles are of the order of several tenth of a micrometer. In other words, it is considerably higher than the value typical of the conventional products of low-temperature aging of aluminum alloys (dozens of nanometers).

Diffraction mode TEM analyses indicate that the phase composition of Mn-bearing dispersoids is rather complex and depends upon concentration of the studied alloys. Thermodynamically stable binary phase Al_6Mn, contrary to earlier opinions expressed in the literature [280], is formed far from often. Of course, at high-temperature heating of 7019 and 7028 binary Al–Mn alloys the formation of metastable phases could take place as well [87, 281].

The most detailed description of Mn dispersoids was obtained for such alloys as AlMg6, AlMg10, ~7019, ~7028, and ~7075 [180]. The analysis of the numerous electron diffraction patterns proved that in Al–Zn–Mg ingots after homogenization at 450–550°C the formation of several phases takes place. These patterns were partially identified as corresponding to simple cubic lattice with the lattice period in the range 1.25–1.35 nm. Out of all phases that can possibly be formed in alloys, this lattice and close values of the lattice parameter correspond to the metastable phase $Al_{12}Mn$ with $a = 1.328$ nm, and ternary phase $Al_{12}Mn_2Si$ with $a = 1.265$ nm. The balance of diffraction patterns were not identified – they did not correspond to either of the well-known phases, the formation of which is at least in principle, possible in alloys of Al–Mg–Zn with Mn. Apparently, they correspond to the particles of multicomponent Mn-bearing phases.

Similar situation was observed for homogenized ingots of alloy AlMg6. Table 3.9 indicates that at least two phases with cubic symmetry could be formed with lattice parameters of 1.46 ± 0.02 and 1.07 ± 0.01 nm. Besides, another phase of non-cubic symmetry was discovered, with one of the interplanar spacing values ~2.12 nm. Electron diffraction patterns from this phase contained elongated reflections in one of the crystallographic directions. Typically this is an indication of the presence of defects in crystalline lattice [75]. None of the three phases had any analogs among the already known phases.

The authors of Ref. [252] have performed precision electron diffraction work of the Mn-bearing dispersoids in two alloys: AlMg10 and AlZn6Mg1.5Cu1 with addition of 0.4%Mn. Alloys were solidified with the rate of 100°C/min, then annealed during 10 minutes to 20 hours at 300–500°C. Taking into account the complex picture of diffraction patterns arising from the presence of several phases, the patterns were taken only for the most informative planes in the reciprocal space: $\{100\}$, $\{111\}$, $\{110\}$, $\{211\}$. For interpretation of the electron diffraction patterns the authors made computer simulations, then compared the results to the experiment. Theoretically the patterns were simulated on a computer using a special code that allowed the construction of any crystallographic plane in the reciprocal space. This analysis could be conducted both when the orientation relation "matrix/phase" was known and when this information was not *a priori* available.

As a result it was established that in alloy AlMg10Mn0.4, the Al_6Mn phase was formed with rhombohedral lattice and lattice periods $a = 0.65$ nm, $b = 0.75$ nm, and $c = 0.887$ nm and metastable phase $Al_{12}Mn$ with cubic lattice $a = 0.754$ nm. In the alloy AlZn6Mg1.5Cu1Mn0.4 mostly the particles of the $Al_{18}Mg_3Mn_2$ phase with cubic lattice were discovered (lattice parameter $a = 1.453$ nm), as well as the thermodynamically stable Al_6Mn phase.

As can be seen from Figure 3.34, the kinetics of decomposition and the aluminide phases forming in these two aluminum alloys are very different. In alloy AlMg10Mn0.4 binary aluminides are formed, while in AlZn6Mg1.5Cu1Mn0.4

Table 3.9 Experimental values of interplanar spacing values d_1, d_2, angles between planes θ, and lattice spacing values in Mn-bearing dispersoids with cubic symmetry in homogenized ingots of alloy AlMg6

d_1 [a] (nm)	d_2 [a] (nm)	θ[b] (degrees)	a (nm)
Rods			
0.236 (532)	0.198 (633)	87.5	1.46
0.743 (002)	0.514 (220)	90	1.48
0.216 (631)	0.248 (530)	36	1.46
0.216 (422)	0.198 (521)	13.5	1.08
0.353 (322)	0.617 (211)	43	1.46
Quadrangles			
0.825 (111)	0.512 (220)	90	1.44
0.617 (111)	0.532 (200)	52	1.06

[a] In brackets the Miller indices of the planes are given.

[b] Angle between planes.

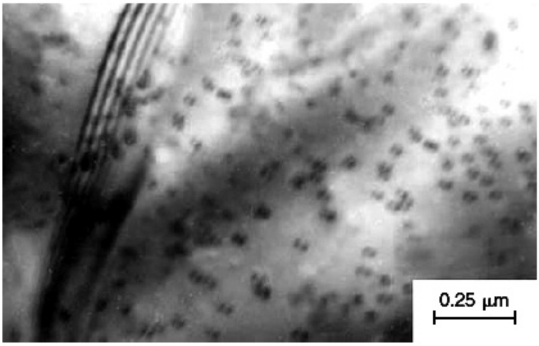

Figure 3.34 Secondary coherent precipitates of Al_3Sc in alloy Al–6%Mg–0.6Sc.

a ternary compound is formed at first. Besides, in AlMg10Mn0.4 the decomposition at temperatures higher than 400°C is significantly accelerated and accompanied by the formation of Al_6Mn. This result agrees well with the data presented in Ref. [67] on the decreased solubility of manganese in (Al) as the concentration of magnesium grows.

At temperatures of annealing below 400°C a quite opposite picture is observed: the decomposition with respect to Mn proceeds slower in the alloy AlMg10Mn0.4 than in AlZn6Mg1.5Cu1Mn0.4. This could be explained by the fact that in AlMg10Mn0.4 at lower temperatures the precipitation of Mn-bearing particles directly related to the Mg concentration in (Al), commences only after the dissolution of the significant part of non-equilibrium $\beta(Al_3Mg_2)$ phase; in other words, only after practically all magnesium goes into solid solution.

The results of described experiments demonstrate the relationship between the processes of homogenizing and heterogenizing heat treatments of as-cast aluminum alloys, linked via diffusion processes, and also the possibility of formation of numerous binary and multicomponent Mn-bearing dispersoids.

Everything is much simpler with the formation of *zirconium*-bearing dispersoids and precipitates. When its concentration in a given alloy is higher than 0.1%Zr, irrespective of the concentration of all other alloying elements, homogenization results in the formation of disperse spherical precipitates with diameter 10–15 nm (Figure 3.33b). Often these precipitates can be observed due to the deformation contrast in TEM micrographs, with a band of zero contrast in the middle. The morphology of these particles is dramatically different from that of Mn-bearing particles. Additionally, they are distributed relatively uniformly across the dendritic cells, again in full accordance with the Zr distribution profile after non-equilibrium solidification. In industrial alloys based on the Al–Mg and Al–Mg–Zn systems, Zr microsegregation is not observed, although the atoms of zirconium must, in accordance with its distribution coefficient $K > 1$, enrich the central areas of dendritic cells.

Dispersoids similar to the ones shown in Figure 3.33 were also observed in binary [272, 273] and commercial alloys with zirconium [274, 275]. These have been identified as particles of the metastable phase Al_3Zr with simple cubic lattice and the lattice parameter of 0.408 nm. The precipitates are coherent to the matrix, which is clear from observation of the nature of contrast in TEM micrographs. Moreover, this coherency is retained even after the lengthiest heat treatments at maximal temperatures. For example in alloy ~7019 this can be observed after 24 hours of heat treatment at 550°C.

In Ref. [253] the studies of perspective high-temperature casting alloys with increased amounts of Zr were conducted. Using the method of TEM the authors explored the peculiarities of solid solution decomposition with Zr concentration up to 1.5%Zr. It was demonstrated that when $C_{Zr} < 1\%$, zirconium can enter solid solution completely. At higher concentrations in the process of solidification of rough primary crystals of the $D0_{23}$ Al_3Zr thermodynamically stable phase are formed. The precipitation of metastable aluminide, which is a very good strengthening agent, can proceed via the mechanisms of single-phase and two-phase decomposition. It was shown that in the presence of other transition metals (manganese, chromium, nickel, etc.) the character of decomposition does not change significantly.

The decomposition of aluminum solid solutions containing *titanium* in the course of homogenization also proceeds in a similar way for different aluminum alloys. It can be easily observed using electron microscopy analysis if the titanium content in alloy exceeds 0.08–0.1% (Figure 3.33c). Unlike in the case of zirconium, the distribution of titanium across dendritic cells is quite non-uniform. If alloy AlMg10 contains 0.15%Ti, then its concentration along the dendrite axes is 0.2–0.3%, while in the areas in between the axes (only ~0.05%) (for titanium, as for zirconium, the distribution coefficient is higher than unity). In alloys of the 7075 type titanium microsegregation is manifested even stronger, from 0.02% on the periphery up to ~1% in the centers of dendritic cells. As a result, titanium aluminides (if they are formed at all) are distributed very non-uniformly and have a tendency to be located closer to the centers of dendritic cells. This helps to reveal the dendritic microstructure after homogenization.

The morphology of Ti-bearing dispersoids is close to that observed for the Al–Zr phase. Most dispersoids have spherical shape with diameter from 30 to 50 nm (Figure 3.33c). Although electron diffraction patterns were not obtained, they are most probably coherent to the aluminum matrix. Given that the crystalline lattices of the thermodynamically stable aluminides Al_3Zr and Al_3Ti are identical one could assume that in alloys with titanium the formation of metastable phase takes place. However, in principle one could not rule out the possibility of precipitation of the tetragonal Al_3Ti phase that lattice parameter "*a*" of which is closer to aluminum than that of Al_3Zr.

Decomposition of Ti-bearing solid solutions in the process of homogenization does not take place in all aluminum alloys. For example, in ingots on the basis of the Al–Zn–Mg–Cu and Al–Cu systems, Ti aluminides are not observed. It is difficult to observe these particle in Al–Si alloys as well.

Scandium is broadly used today for strengthening aluminum alloys: first of all, Al–Mg-based materials [201, 283–290]. Homogenization results in a picture of decomposition similar to that with zirconium. However, the peculiarity associated with scandium is that it can form anomalously supersaturated Al solid solution already at relatively low cooling rates in the process of solidification. At the cooling rate of ~2 K/s its maximum solubility in aluminum increases more than 1.5 times and attains ~0.6% [283–289]. The decomposition of these supersaturated solid solutions in the temperature ranges from 250° C to 400° C results in the formation of extremely fine, fully coherent Al_3Sc precipitates of spherical shape. Their size is of the order of several nanometers (see Figure 3.34). When annealing temperature equal to and above 400°C is used, the particle radii attain the value of ~20 nm, accompanied by the loss of coherent conjugation with the (Al) matrix and rapid coarsening of the Al_3Sc particles.

Similarity in the decomposition of aluminum solid solution with respect to zirconium and scandium is most probably related to the identical crystalline structures of Al_3Zr and Al_3Sc. For this reason, joint introduction of these chemical elements is accompanied during homogenization by the formation of ternary coherent particles $Al_3(Sc, Zr)$, which is more stable and less prone to coagulation and coarsening than the binary phase Al_3Sc.

As pointed out above, light microscopy often allows, directly or indirectly, revealing the particles of transition metal-bearing dispersoids in homogenized ingots and quenched castings. In most cases the size of these precipitates or dispersoids (particularly containing scandium, titanium, and zirconium) is so small that they cannot be observed in light microscope. However, the areas where such precipitates are located can be revealed due to the increased degree of their etching.

Good correspondence between linear sizes of the areas of increased etching on metallographic samples and the size of micro-volumes with increased density of the decomposition products (TEM) was proved by the special experiments conducted using different alloys of the Al–Mg–Zn system. This allowed employing much more productive technique of light microscopy for quantitative estimates of non-uniformity of the aluminum solid solution decomposition supersaturated with transition metals. In particular, such factors as conditions of solidification and the regimes of homogenizing heat treatments were studied in detail.

The hereditary influence of the cooling rate upon solidification manifests itself in the form of different general pictures of non-uniform decomposition of solid solution after homogenization using the same scheme. Specifically, the concentration profiles of distribution of transition metals across the dendritic cells may change quite substantially. As the solidification rate grows, the PFZs (precipitate-free zones) around the dendritic cell boundaries become more narrow, which is related to the refinement of dendritic cells. At high cooling rates metallographic examination does not reveal any distribution non-uniformities, and TEM studies are required to achieve this goal. On the contrary, after slow solidification PFZs can have linear sizes attaining dozens of micrometers. The volume fraction of PFZs, as well as the sizes and density of the products of decomposition change weakly. This is yet another demonstration of the fact that in a broad cooling rate range the formation of solid solution more or less similarly supersaturated with manganese and other transition metals takes place according to the metastable diagram of state.

Increased homogenization time causes natural decrease in the volume fraction of supersaturated solid solution in the centers of dendritic cells and, at the same time, results in the larger PFZ areas. This effect might be related to some broadening of the Mn concentration profile in the proximity of dendritic cells in the process of a higher-temperature or more lengthy heat treatment.

Table 3.10 represents the data illustrating the influence of the cooling rate and temperature of homogenizing heat treatment during 24 hours upon the volume fraction (Q) and average width (b) of the boundary zones free from Mn-bearing dispersoids in alloy $AlZn_6Mg_2Cu_2$ containing 0.4%Fe and 0.1%Si [126].

Non-uniformity of the (Al) decomposition, morphology, and phase composition of dispersoids depend very strongly upon the concentrations and the ratio of the key impurities (iron and silicon). In all alloys, irrespective of the concentrations of the primary alloying elements and additions of transition metals, the increased

Table 3.10 The influence of cooling rate (V_c) upon volume fraction (Q) and average width (b) of Mn-free PFZs

V_c (°C/min)	Q^* (vol%)	b^* (μm)
15	25/32	35/40
100	19/28	18/25
600	19/25	8/10

* The values of "*b*" obtained after annealing at 460°C and at 500°C, respectively.

concentration of impurities will result in a more uniform distribution of the dispersoids at homogenization across most of the dendritic cells.

Electron microscopy analysis indicates that in alloys with high concentration of impurities Mn-bearing dispersoids form not only on the periphery of dendritic cells but also in their central areas. As a result, the overall amount of dispersoids grows; they also become more refined and more equiaxed.

Increased concentration of the Fe-bearing impurities exerts influence upon the decomposition of aluminum solution with respect to zirconium and titanium. For example, in alloy AA7019 containing more than 0.5% of impurities the particles of metastable aluminide align themselves into chains or form rods elongated in the <100> direction of the (Al) matrix. It is possible that in the presence of impurities decomposition is accompanied by the precipitation of particles having intermediate structure between cubic metastable phase Al–Zr and tetragonal thermodynamically stable Al_3Zr precipitating in the form of rods.

Decomposition of supersaturated (Al) containing transition metals becomes easier in the areas with lower concentration as the concentration of impurities grows. This is mostly related to the increased supersaturations of solid solution. Besides, iron and silicon may enter the composition of the precipitating particles, and the increase in their concentrations must cause growth of such dispersoids.

In alloys containing manganese, the increase in concentration of impurities proceeds in parallel to the more uniform distribution of Mn-bearing aluminides in the central parts of dendritic cells. At the same time, broadening of the near-boundary zones free from Mn-containing dispersoids takes place. Consequently, in relatively slowly solidified ingots and castings where the width of Mn-depleted zones is significant, in general increased concentration of impurities even enhances the non-uniformity of metallographically observed picture of decomposition accompanying homogenizing.

As it was demonstrated in Refs. [125, 126, 291], broadening of the near-boundary PFZs and their increased volume fraction in the case of increased concentration of impurities is directly related to the growing sizes and volume fraction of Mn-containing constituent particles. Manganese from the near-boundary areas of the cells is expended for the formation and growth of such particles.

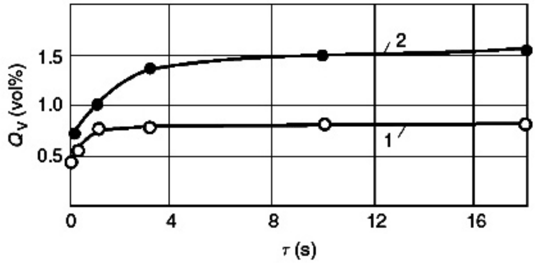

Figure 3.35 Dependence of the pore volume fraction Q_p in ingot of alloy D16 upon homogenization time at (1) 490°C and (2) 515°C.

3.1.6 Development of porosity during homogenization

One more important process that accompanies homogenizing (or heat up for quenching) of casting aluminum alloys is the formation and development of porosity. New pores are formed in lieu and next to the dissolving inclusions of excessive constituent phases because of the difference of their specific volume and also the Kirkendall effect. The growth of pores mostly proceeds because they serve as vacancies sink.

Porosity becomes particularly noticeable at high-temperature homogenization above the non-equilibrium solidus (Figure 3.35). It is assumed that as a result of non-equilibrium eutectic melting reactions hydrogen from supersaturated (Al) diffuses into these micro-volumes of molten metal. After their diffusional disappearance pores will be left after annealing that are filled with hydrogen under large pressure. Hence the well-known fear of high-temperature homogenization processes, which could be related to partial melting in the casting or ingot. Such melting could be forestalled if one uses slow or several-step heat-up, during which the most easily melting components have ample time to get dissolved in the aluminum matrix below non-equilibrium solidus.

The techniques for compete elimination of the development of secondary porosity during homogenization are not developed as yet. However, it could be almost completely eliminated if annealing is conducted in conditions under pressure that would ensure “welding-like curing” of pores due to the plastic deformation of micro-volumes surrounding discontinuous sites in the ingot. For aluminum alloys this expensive technique is used very rarely.

3.2 AGING AFTER CASTING AND QUENCHING

As it was demonstrated in Section 3.1, during isothermal exposure (homogenization) before quenching there are processes of decomposition that are taking place actively in (Al). These processes are accompanied by the formation of transition metal aluminide particles.

In ingots of wrought alloys, which are cooled slowly after homogenizing, partial decomposition of (Al) takes place accompanied by the precipitation of phases formed by the principal alloying elements, similar to the decomposition in ingots after the completion of solidification (Section 2.5.4).

However, in shaped castings, which are usually quenched after homogenization, this decomposition process usually does not occur. Most of the casting aluminum alloys are subjected to artificial aging immediately after quenching and sometimes even without it. In some alloys aging can proceed at room temperatures.

Aging of aluminum alloys belonging to the most important alloy systems was studied in great detail (see, e.g., reviews [190, 204, 292]). The established principles are common both to wrought and casting alloys. However, data on the influence of the original as-cast microstructure upon the decomposition of (Al) is very scarce.

Castings made of aluminum alloys are usually subjected to aging in some cases immediately after casting (T1–T3 tempers), but mostly after quenching (T6–T7 tempers). Consequently, the original (i.e., before aging) microstructure could be as-cast or obtained after homogenization and quenching.

The influence of as-cast structure upon the decomposition of (Al) accompanied by the formation of principal strengthening phases must be defined, first and foremost, by the characteristics of microsegregation and substructure of dendritic cells. In general, the amount of precipitates, their sizes, and interparticle spacing values depend upon the average composition C_B^α of (Al) before aging. As it was shown in Section 2, this average composition in a given alloy is a function of the volume fraction of non-equilibrium excessive constituent particles and dispersoids formed by the principal alloying elements. Consequently, C_B^α is defined in practice by the cooling rate upon solidification and below the solidus temperature. Besides, C_B^α depends upon the alloy composition. These issues have already been discussed in the previous sections.

As the concentration of alloying elements grows, the optimal aging schedule results in the formation of finer products of decomposition, their greater number density, and smaller interparticle distances. All these changes must enhance strength after aging. In the general case of non-optimal aging schedule (i.e., not ensuring the maximum strength) one could say only that the higher the value of C_B^α, the greater the extent of decomposition of (Al) and the volume fraction of its products. Overaging, for example, could result in coarser particles than in castings with smaller C_B^α.

Due to microsegregation of alloying elements the distribution of the decomposition products after aging of casting alloys is quite non-uniform across the dendritic cells: the extent of decomposition is always greater at the periphery enriched with the principal alloying elements (Cu, Mg, Zn, and Si). Different degree of alloying of aluminum solid solution in the middle and on the periphery

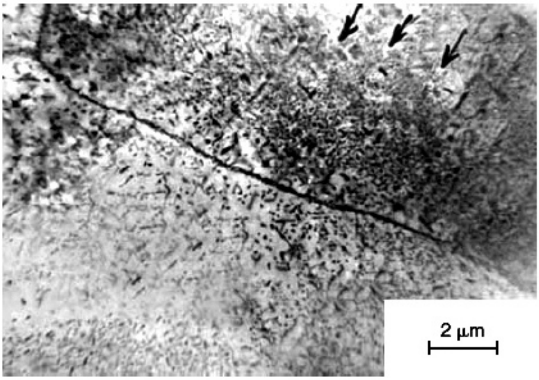

Figure 3.36 Microstructure of alloy AL24M after aging without quenching. Arrows indicate the boundaries of a dendritic cell (TEM).

of dendritic cells could, under certain aging conditions, result in the formation of structurally different products.

For example, during aging of casting Al–Zn–Mg alloys the GP zones could be formed in the center parts of the cells, while the particles of the T'-phase could be formed at the same time on the periphery (Figure 3.36).

Dislocation microstructure of casting aluminum alloys exerts relatively weak influence over the general picture of the (Al) decomposition practically at all aging regimes used today. This is explained by the homogeneity of particle nucleation at low-temperature aging, and also by the relatively small differences in the characteristics of dislocation microstructures in compositionally different casting alloys, and different castings of the same alloy. However, in a number of cases, when alloys are compared that possess different dislocation microstructures, the effect of strengthening after aging [166] is more pronounced in alloys with higher dislocation density and subgrain microstructure. Differences in microstructure of quenched castings after subsequent aging could be explained by the thermo-temporal regimes of isothermal heat treatment before quenching and differences in the original as-cast structures.

The applied homogenization schedule before quenching defines the degree of alloying of the (Al), via the extent of dissolution of non-equilibrium excessive constituent particles. Secondly, different temperatures and time of heat treatment before quenching may result in industrial alloys in the formation of different distributions of transition metal aluminides, which could serve, during cooling of homogenized ingots as the nucleation sites for the principal strengthening phases [203].

The influence of dispersoids of transition metal aluminides, their volume fraction and sizes, upon the kinetics of (Al) decomposition is analyzed in detail in Ref. [203]. It was demonstrated that the stability of solid solution can be reduced more effectively as the dispersoids become more refined. Transition metals in solid

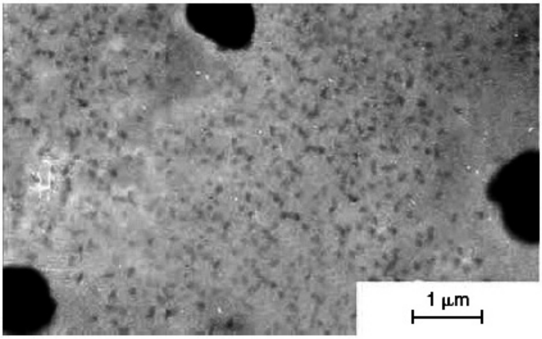

Figure 3.37 Microstructure of alloy 1925 after quenching and aging for 5 hours at 180°C (TEM).

solution also reduce the thermodynamics stability of solid solution. This needs to be taken into account when analyzing aging according to the T5–T7 tempers, and the T1–T2 tempers as well. (In as-cast state the formation of aluminides is usually not observed).

In addition to the conclusions made in Ref. [203] it is necessary to mention that, according to the results of TEM studies, the degree of refinement of the decomposition products depends rather weakly on the size and distribution of transition metal-bearing dispersoids. The formation of coarse products takes place directly on these particles; this is accompanied by the formation of PFZs around them (Figure 3.37).

As a result, in alloys with large number densities of relatively disperse aluminide particles the general amount of the principal strengthening phases could be reduced somewhat. However, this effect is not very significant because the increase of strength during aging after quench according to different regimes practically does not change, if the exposition time exceeds the average dissolution time for excessive constituent particles.

In Ref. [159] it was demonstrated that dispersoids could serve as nucleation sites for the products of (Al) decomposition not only during artificial but also during natural aging. This becomes particularly true when we have to deal with the early stages of decomposition accompanied by the redistribution of atoms in solid solution. For example, 1 year of natural aging of castings made of alloy AA520.0 type results in different shapes of Al_3Ti particles when observed in electron microscope. Instead of almost spherical shape in as-quenched state these particles attained the shapes of crosses, crossed bars that were located parallel to crystallographic directions <100> and <110> (Figure 3.38). It is interesting that these changes could be observed in electronic microscope even though no traces of (Al) decomposition were identified. The formation of the latter, obviously, is related to a certain orientation of elastic fields in the matrix in the direct vicinity of interphase boundaries during the initial stages (Figure 3.38).

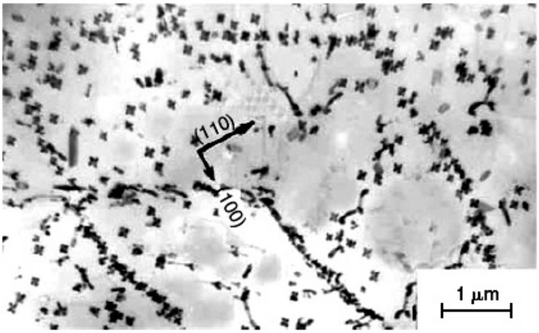

Figure 3.38 Microstructure of a quenched casting made of alloy AMg10ch after natural aging during 1 year (TEM).

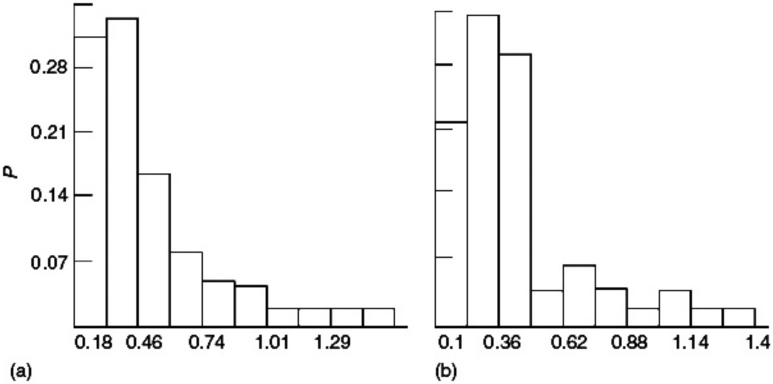

Figure 3.39 Histograms for particle size distribution; particles of Q-phase of average size m in alloy Al + 1.7%Cu solidified with cooling rate V_{cooling} = (a) 0.3 K/s and (b) 9 K/s, after quenching from 530°C and aging at 185°C for 10 days.

In Ref. [203] it was established that the initial microstructure of ingots of industrial alloys exerts hereditary influence upon the stability of aluminum solid solution during aging after homogenization, deformation, and quenching. This is explained via increased supersaturation of aluminum solid solution by transition metals as the rate of solidification increases and by the corresponding growth of the number of intermetallic dispersoid particles forming mostly during homogenization and retaining during subsequent treatment up to the final aging process. Thus, the change in solidification rate affects the stability of (Al) and, probably, the degree of refinement of the products of decomposition similar to the influence of homogenization regime before quenching.

In alloys which do not contain transition metals it was established [180] that the density of the decomposition products during aging of castings with different original microstructure remains practically constant after quenching using the same scheme. In Al + 5%Cu after solidification with the cooling rates of 0.3 and 9 K/s, quenching from 530°C after 7 hours of treatment and aging at 185°C during 10 days the histograms of particle size distributions were constructed for the θ'-phase. These data, obtained using electron microscopy, are presented in Figure 3.39. It is obvious that irrespective of the cooling rate during solidification particles of the same size 0.2–0.5 μm are formed. The density of the precipitate distributions in the studied castings also was practically identical: $(7.8 \pm 0.9) \times 10^{13}$ and $(8.2 \pm 0.5) \times 10^{13} \mathrm{cm}^{-3}$ for the cooling rates of 9 and 0.3 K/s, respectively.

This page intentionally left blank

CHAPTER FOUR

DEPENDENCE OF CASTABILITY AND MECHANICAL PROPERTIES ON COMPOSITION AND MICROSTRUCTURE OF ALUMINUM ALLOYS

4.1 CASTABILITY

4.1.1 General characterization of castability

In order to be able to make good shaped castings, aluminum alloys need to possess good castability. The term "good" can be elaborated as a homogeneous casting, uniform in its composition without pores and cracks and with the surfaces exactly reproducing the internal geometry of the mold used for the casting process.

The level of casting properties is determined by the alloy composition and the technological aspects of the process. Among the most important casting properties it is necessary to mention liquid fluidity, shrinkage, and associated with it are hot cracking and tendency to the formation of shrinkage porosity and macrosegregation.

Liquid fluidity could be characterized as alloy's ability to fill the mold. It is a typical technological property because it is affected very strongly by the conditions and methods of experimental work. First of all, this is related to the temperatures of casting and the used mold, metallostatic pressure, etc. [293]. All these factors affect molten metal fluidity via the physical properties of the melt (viscosity, surface tension), and also via alloy microstructure forming during solidification. Molten metal fluidity could be determined using the so-called "pencil probe" or "spiral probe" (Figure 4.1). In both cases, the measure of liquid metal fluidity is defined as the length (in mm) of the rod solidified either in sand or in metallic mold, with all other conditions being the same. The higher the length of the obtained rod (straight or spiral), the better molten metal fluidity will be.

In the course of molten metal cooling at temperatures above liquidus, during solidification (i.e., when temperature is in between the liquidus and the solidus surfaces) and subsequent cooling in the solid state the volume of metal decreases. As a result, the linear size(s) of castings also decrease. It is particularly important for obtaining quality castings how shrinkage develops during solidification. Indeed, shrinkage voids and stresses may result in the formation of extremely undesirable hot cracks [294].

© 2007 Elsevier Ltd.

ISBN-13: 978-0-08-045370-5

All rights reserved.

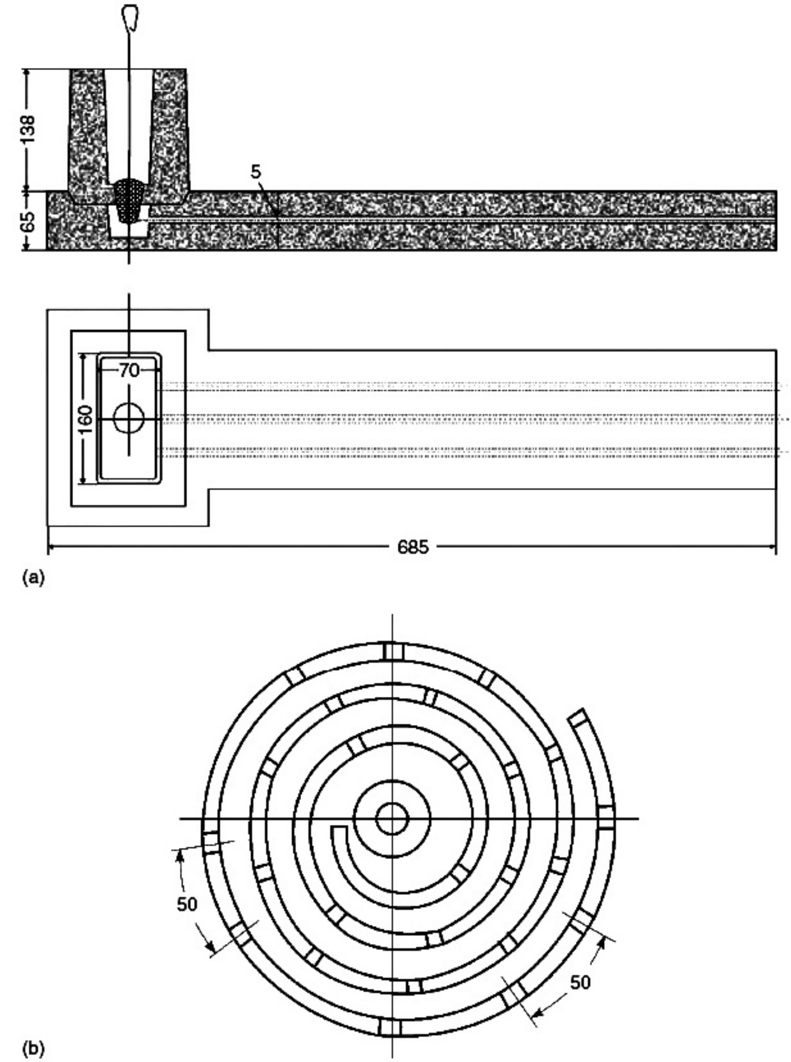

Figure 4.1 Schematics illustrating the so-called (a) "rod" and (b) spiral probes, respectively, for assessing molten metal fluidity.

The formation of shrinkage cavities is the direct consequence of the sample volume shrinkage in the solidification temperature range:

$$\varepsilon_{\text{vol}} = \frac{V_{\text{L}} - V_{\text{T}}}{V_{\text{L}}} \cdot 100\%$$

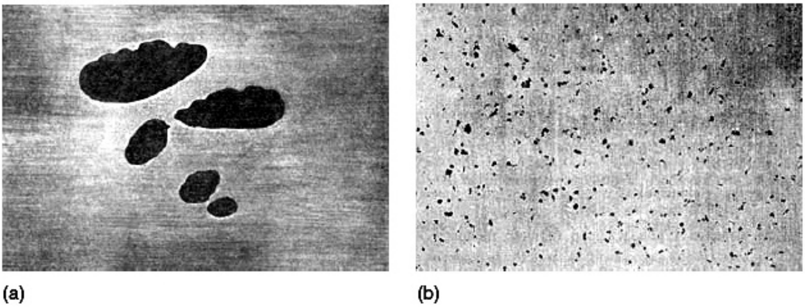

Figure 4.2 Casting containing (a) one large shrinkage cavity, and (b) scattered porosity.

In this expression V_L is the specific volume of liquid alloy at the liquidus temperature; V_T stands for the specific volume of the solidified alloy at the solidus temperature. It is very important that the overall casting quality will be defined not by the value of ε_{vol} but rather, by the morphology of the shrinkage cavities – whether it will appear in the form of a single large cavity or diffuse shrinkage porosity (Figure 4.2). The cavity volume is evaluated by filling it with sand or a liquid, while shrinkage porosity V_p (i.e., the overall volume of scattered pores) could be assessed via the relative difference in the casting density γ_o (usually determined using the method of hydrostatic weighing), and the theoretical alloy density or experimentally determined density of a poreless probe, γ_T:

$$V_n = \frac{\gamma_T - \gamma_o}{\gamma_T} \cdot 100\%$$

The appearance of scattered porosity results in the reduction of so-called "casting hermeticity". By this term we will define ability of the casting to sustain a certain pressure of a liquid or a gas without leaking [293]. This characteristic is also often used for assessment of casting properties. More specifically, hermeticity is determined as the minimal pressure of liquid or gas resulting in the appearance of leaks. Sometimes hermeticity is defined as the maximal thickness of the casting wall in which a leak will appear under a certain predetermined pressure.

Linear shrinkage is defined as the relative reduction of the casting's linear size in horizontal directions during solidification and subsequent cooling of the solid casting:

$$\varepsilon_n = \frac{l_o - l_i}{l_o} \cdot 100\%$$

In this equation l_o stands for the original size of casting; l_i is its size at a given moment of time during cooling.

In some cases before linear shrinkage begins, some initial expansion of the casting may take place. In such cases linear shrinkage should be evaluated according to the formula [293]:

$$\varepsilon_n = \frac{l_o + \Delta l_p - l_i}{l_o + \Delta l_p} \cdot 100\%$$

In this expression Δl_p stands for the value of the initial "pre-shrinkage" expansion.

Complete linear shrinkage (from the temperature of its onset and to room temperature) is defined using an indicator of linear displacements, which is constantly in contact with the movable part of the mold. Samples cast into such molds have rectangular shapes with the two head parts – one of them is immobile, while the other may move as a result of shrinkage and pre-shrinkage expansion [295].

In the case of hot cracking the most important parameter is linear shrinkage ε_{kp}, that is evaluated in the temperature range from its beginning and up to solidus temperature. The value of ε_{sol} could be determined on special apparatuses that record the temperature dependence of linear shrinkage curves [19]. In real castings with complex shapes shrinkage is always constrained. As a result, shrinkage stresses and strains (elasto-plastic) appear. They are the main cause of the formation of cracks in shaped castings. In aluminum alloys shrinkage cracks typically appear above the solidus temperature. This is why they are usually called "hot" or "solidification" cracks (contrary to "cold" cracks forming for different reasons in the solid state).

Tendency to the formation of hot cracks is called "hot cracking". This is undoubtedly the most important casting property for aluminum alloys. Elimination of hot cracks in aluminum castings represents the most complex problem for metal scientists and cast shop engineers. In order to characterize them quantitatively, different technological probes are used in practice [19]. For example, in Russia the most widely used probe is the so-called "ring probe". According to this method, molten metal is poured into a sand mold containing a steel rod. Thus, obtained ring samples have outer diameter of 107 mm and thickness of 5 mm (Figure 4.3). The internal diameter of the rings is defined by the diameter of the steel rod and can vary from 7 to 97 mm. Consequently, the ring width can vary from 50 to 5 mm (with the step of 2.5 mm). Hot cracking index (HCI) is defined as the maximal width of the ring, in mm, in which first crack(s) appear. The lower this value, the better a considered alloy is in terms of its resistance to hot cracking, and vice versa.

In laboratory studies two mold probes for hot cracking are often used – ring probe and pencil probe [19]. In the ring probe the outer diameter of the solidified samples is equal to 60 mm, while the inner diameter can vary from 30 to 50 mm. The HCI is defined in these cases as the maximal rod diameter in which cracks have appeared in the ring casting of the studied alloy, or as the total length of all cracks at a constant rod diameter.

In the case of pencil probe a special mold that could be opened and closed is used for casting of seven cylindrical samples with head parts (Figure 4.4). The

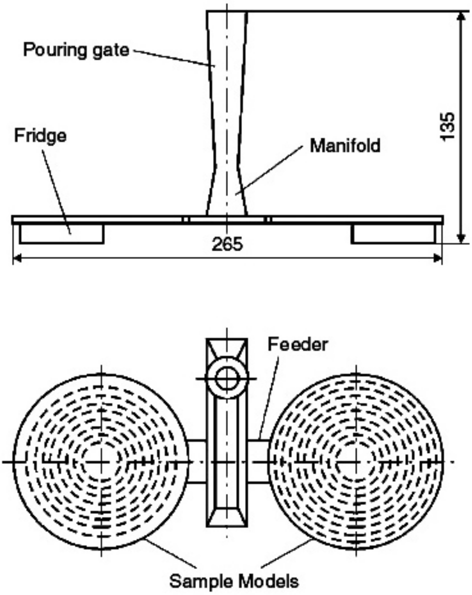
Pouring gate
Fridge
Manifold
135
265
Feeder
Sample Models

Figure 4.3 Schematic of the so-called "ring semi-mold" probe for assessing hot cracking tendency.

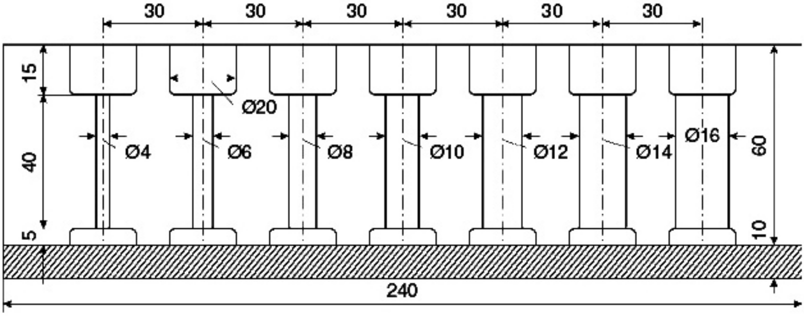
30
30
30
30
30
30
15
40
5
Ø20
Ø4
Ø6
Ø8
Ø10
Ø12
Ø14
Ø16
60
10
240

Figure 4.4 Schematic of the so-called "pencil" probe for hot cracking.

diameter of the head parts is always the same (20 mm), while the diameter of cylinders can vary from 4 to 16 mm with the step of 2 mm. The length of the middle part of the cylinders is equal to 40 mm; while their overall length is 60 mm. HCI in this case is defined as the maximal diameter of the cylindrical portion of the sample that still does not reveal any cracks. When the HCI becomes higher, hot cracking of a given aluminum alloy gets worse.

The last of the important casting properties is macrosegregation – the difference in chemical composition of casting in its different parts. According to Dobatkin [63] in casting aluminum alloys macrosegregation manifests itself in the form of two effects – zonal and local effects.

Zonal macrosegregation is characterized by the continuous variation of the alloy chemical composition along the cross-section of a casting or an ingot. At the same time, local macrosegregation manifests itself in the form of random concentration inhomogeneities. Zonal macrosegregation is typical of ingots obtained using semi-continuous casting technique, while in shaped castings it appears very rarely. In the latter case, most often local macrosegregation is encountered related to trapping of aluminum melt enriched with different alloying elements in cavities and shrinkage pores and cracks. Experimentally this type of macrosegregation can be assessed using data on microstructure and the results of chemical composition.

Metals science analysis of castability of aluminum alloys is based on the Bochvar theory of casting properties, which was further developed by Novikov. This theory, in turn, is based on the analysis of influence of chemical composition and microstructure upon castability in the whole solidification range and studies of non-equilibrium phase diagrams.

Before the pioneering works of Bochvar appeared, casting properties of alloys were always linked to the whole solidification range. This approach ignored profound differences of microstructure and properties of semi-solid material at different temperatures inside this range. In Ref. [296] an assumption was made that shrinkage of a casting is possible not at any temperature but only after the formation of a crystalline carcass in its whole volume. The principal property of this structure (as well as the principal difference between liquids and solids at normal conditions) is that *it can support shear stresses.* In the general case such stiff carcass is formed inside the solidification range (although sometimes it can happen just at the solidus temperature). The volume fraction of the solid phase that is necessary for the formation of a crystalline carcass depends, first of all, upon the shape(s) of crystals. In the course of dendritic solidification the temperature of its formation becomes higher as "branching" of dendrites increases. Correspondingly, the higher the temperature is, the greater the volume fraction of the liquid phase and the lower the volume fraction of the solid would be. The line on a phase diagram that connects the points corresponding to the formation of such crystalline carcass is at the same time the temperature of the onset of linear shrinkage (see Figure 4.5) [294].

Bochvar proposed to call the temperature range between this line and the non-equilibrium solidus of alloys "the effective solidification range". In this range alloys are in the solid–liquid state and possess the fundamental property of all solids – ability to retain their original shape(s), or to support shears. In the temperature range between the onset of linear shrinkage and the liquidus line alloys will be in the liquid–solid state and will possess the fundamental properties of liquids – to fill the shapes of forms into which they are poured [294].

The notions of "liquid–solid", "solid–liquid" states of matter and the effective solidification range were the key in Bochvar's theory of casting properties of alloys. To a great extent basic casting properties are related to the temperature range in which "solid–liquid" state exists, the concentration–temperature range

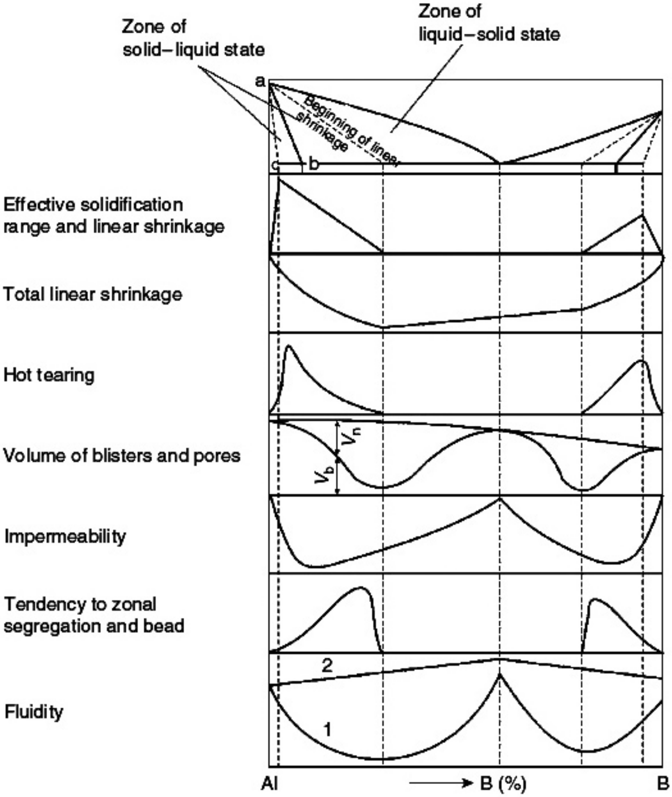

Figure 4.5 Dependence of alloy castability on chemical composition for alloys of the eutectic type.

of this effective solidification interval, and also by microstructure and mechanical properties of alloys in this condition.

Figure 4.5 represents the basic schematics demonstrating the connection between the basic casting properties of aluminum alloys (for a binary eutectic system) and their composition as related to the existence of effective solidification range.

Molten metal fluidity at constant overheating above the liquidus temperature at first decreases then starts growing as the concentration of alloying element becomes higher and approaches the eutectic point (curve 1 in Figure 4.5a).

Maximal molten fluidity will be observed for pure metal (in our case aluminum) and also for the eutectic, which solidify at constant temperatures. Minimal molten metal fluidity is characteristic of alloys with sufficiently broad solidification range.

This could be explained in the following way. The channel in the molten metal fluidity probe is filled in two stages: (1) from the moment of pouring molten metal in until the onset of solidification and (2) from the onset of solidification until complete stop of metal flow, when a sufficient amount of solid crystals is formed. At constant overheating above the liquidus temperature the second stage of the process is the key, and for this reason liquid fluidity is defined mostly by the solidification characteristics. For narrow solidification range (e.g., in alloys close in composition to eutectic point) solidification proceeds by an almost continuous front from the mold walls; the channel gets narrower, but molten metal continues to get through and comes to a complete halt at a later solidification stage and at a higher volume fraction of the solid phase.

In alloys solidifying in more or less broad temperature range large dendritic crystals with branches are formed, which rapidly close the cross-section of the channels at the early solidification stages.

If casting is conducted at the same temperature but for alloys with different concentrations, then, as the liquidus temperature goes down, alloys with higher concentrations of alloying element will remain in the liquid state longer, and their fluidity will be increasing (curve 2 in Figure 4.5).

It is quite clear that unlike most other casting properties, molten metal fluidity will be defined only by alloy behavior in the liquid and liquid–solid states. After transition into the solid–liquid state there will be no fluidity at all.

The value of the volume shrinkage during solidification is defined by the processes taking place in the liquid–solid and solid–liquid states. The overall volume and the ratio of shrinkage cavities to diffuse porosity, according to Bochvar, continuously changes as a function of alloy composition (Figure 4.5).

In eutectic alloys solidifying at constant temperature without temperature transition range from liquid into solid phase, only one large shrinkage cavity should be formed. In alloys solidifying in the temperature range there is always a transition zone present, in which by the end of solidification molten metal ends up in isolated unfed micro-volumes located in between the dendritic arms. Due to smaller specific volume of the solid phase as compared to liquid, such micro-volumes after solidification will inevitably transform into shrinkage pores. Such inter-dendritic or dendritic diffuse porosity is always present in shaped castings. The relative volume fraction of these pores is maximal for alloys with a broad liquid–solid solidification range (Figure 4.5).

It should be mentioned that the overall amount of scattered pores in aluminum castings also depends on gas content (mostly hydrogen) and its changes during solidification. At realistic hydrogen content in molten aluminum alloys ($>0.1\,\mathrm{cm}^3/100\,\mathrm{g}$ of liquid) it will always be present in shrinkage pores in aluminum alloys. Besides, gas may form its own pores, randomly distributed along the casting cross-section (unlike shrinkage pores, which always appear in the sites where solidification comes to full completion).

As it was mentioned above, the appearance of diffuse pores inevitably reduces the hermeticity of castings. Hermeticity depends upon the total volume of pores, their sizes, distribution and, very importantly, on whether the pores are open and interconnected via dendritic channels or isolated from each other. According to Bochvar hermeticity must be maximal for eutectic alloys and minimal for alloys with broad solidification range.

Unlike volume shrinkage, reduction of linear sizes appears only in the solid–liquid state. Above the temperatures of its onset thermal contraction of castings does not result in their decreased linear sizes. Indeed, in the liquid–solid state alloys behave like liquids, possess high fluidity, and the gap between the mold walls and the casting itself simply cannot be formed.

For this reason linear shrinkage commences at the moment of the formation of crystalline carcass. In eutectic alloys with increased content of alloying element the temperature corresponding to the onset of linear shrinkage gradually decreases to eutectic temperature. As a result, the effective solidification range, as could be seen from Figure 4.5, at first increases, then decreased to zero (when the line corresponding to the temperature of linear shrinkage crosses eutectic horizontal). The large effective solidification range (ΔT_{eff}) will correspond to that alloy the composition of which represents the concentration threshold for non-equilibrium eutectic appearance (see Figure 2.4).

The value of linear shrinkage during solidification (ε_{sol}) changes as a function of composition similar to Δt_{eff}. In particular, its maximal value is attained for the alloy corresponding to point K in Figure 2.24. ε_{cr} is an important casting property because it is this property that defines to a significant extent the expected hot cracking tendency for a given alloy.

Hot cracking is the most "important" casting property. Indeed, cracks represent the most dangerous defect of castings, and their formation should be absolutely excluded. Tendency to hot cracking is intimately related to the value of the effective solidification range: the higher the range, the worse hot cracking issue becomes for alloys of a given system. Figure 4.5 clearly demonstrates that the maximum of hot cracking is attained for that alloy the composition of which corresponds to the appearance of non-equilibrium eutectic. According to Bochvar, qualitative explanation of this phenomenon is in the growth of linear shrinkage with increased solidification range. It is the constrained nature of such shrinkage that may cause the formation of hot cracks.

Detailed studies of hot cracking were conducted by Novikov [19]. He demonstrated that in reality the maximum of the effective solidification range does not necessarily coincide with the maximum on the "hot cracking–composition" curve. According to Ref. [19], alloy's hot cracking tendency is defined by the three variables: width of the temperature range of brittleness in the effective solidification range; temperature dependence of linear shrinkage; and the achieved level of plastic deformation. Figure 4.6a represents the dependence of the relative elongation at temperatures above non-equilibrium solidus for alloy Al–1.5%Cu with different grain structures (equiaxed and columnar) as an example. It can be seen that for the equiaxed structure the width of brittleness temperature range is smaller (curve 1) and plasticity is somewhat higher than for the columnar structure (curve 1). The difference in the attained values of the relative elongation inside the brittleness range is insignificant just several tenths of a percent. However, it

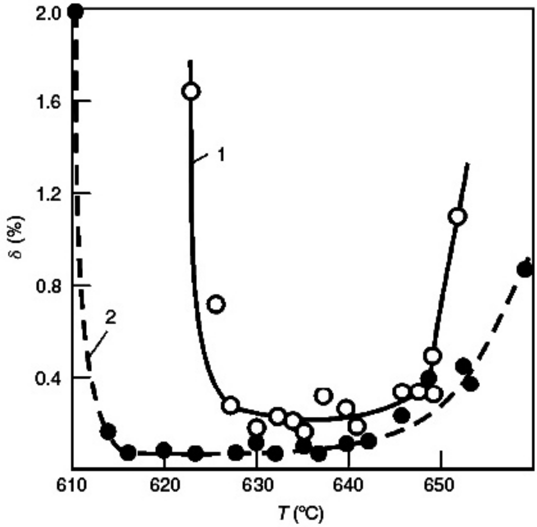

Figure 4.6 Temperature dependence of the relative elongation for alloy Al + 1.5%Cu: (1) equiaxial structure, and (2) columnar structure [19].

has significant influence because the value of the linear shrinkage ε is of the same order of magnitude. Figure 4.6b represents the data on linear shrinkage. The curves are all somewhat lower than those corresponding to the δ–T curve, but may cross it sometimes. It is the sign and value of the difference of δ and ε in the brittleness temperature range that defines the level of hot cracking.

In Ref. [293] it was proposed to employ as a value of hot cracking the so-called "plasticity measure" (PM): $PM = S/\Delta t_{\text{brittle}}$, where S is the area under the δ–T and ε–T curves inside the brittleness range, while $\Delta t_{\text{brittle}}$ is the value of this interval (Figure 4.7a). In the temperature range where $\delta < \varepsilon$, the area behind the curves is considered "negative"; if $\delta > \varepsilon$, it is considered "positive" (see Figure 4.7b, where $PM = (S_1 - S_2)/\Delta t_{\text{brittle}}$).

It should be stressed that the lower boundary of the brittleness temperature range does not always coincide with the temperature of non-equilibrium solidus. Such a coincidence is usually typical of those alloys in which a sufficient amount of the liquid phase is formed at these temperatures, for example alloy Al + 7%Cu and more. However, in alloy with only 1.5%Cu at the same non-equilibrium solidus temperature (548°C), the lower boundary of the brittleness range is above 600°C (Figure 4.6). This happens because in order to reduce the relative elongation to several tenths of a percent the appearance of substantial amounts of the liquid phase in intergranular locations is required. Only in such a situation will brittle intergranular fracture process go on.

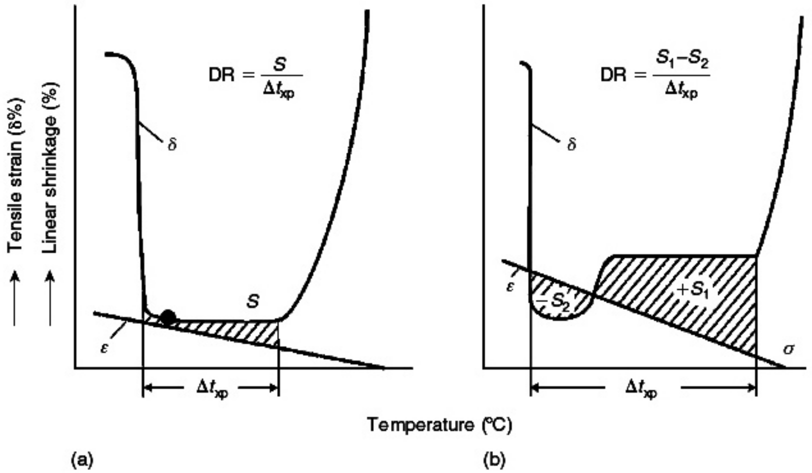

Figure 4.7 Schematic for assessment of alloy plasticity in the solid–liquid state [180].

Mechanical testing at temperatures above solidus is conducted upon heating of as-cast samples [19, 227]. In weakly alloyed materials (e.g., in alloy Al–1.5%Cu) at temperature of non-equilibrium solidus only relatively small amount of liquid phase will appear due to melting non-equilibrium eutectic (Al) + $CuAl_2$. A significant raise in temperature is required to increase the amount of the liquid phase in such alloy to make brittle fracture mechanism possible (Figure 4.7a, curve 1).

The upper boundary of the brittle fracture temperature range, that is the temperature of the onset of significant increase in alloy plastic flow as it approaches the boundary of the liquid–solid state, corresponds to the formation of continuous liquid interphases along which grains can slip with ease with respect to one another [19, 293].

From this discussion it follows that the effective solidification range is not the only criterion of hot cracking. Microstructure also exerts strong influence: shapes and sizes of grains; overall amount, distribution, and average size of eutectic inclusions; other parameters that define microstructure in solid–liquid state. Nevertheless, the effective solidification range still remains the most important and most universal "predictor" of hot cracking tendency for any aluminum alloy.

In conclusion, let us analyze briefly the level of casting properties of some standard aluminum alloys. The available results are generalized in table of Appendix 5.3. It can be clearly seen that the best castability is attained for copperless 3xx series alloys with high (>7%) content of silicon: alloys A413.2, 364.2, 356.0. Casting properties of Cu-bearing 3xx alloys are somewhat worse, especially for alloys with smaller amounts of silicon (C355, 363.1, 308.0). Finally, the worst castability is observed for aluminum alloys with broad effective solidification range

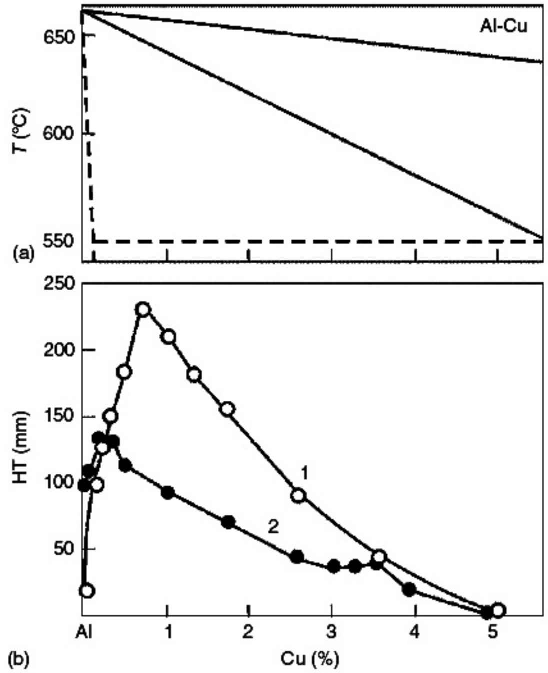

Figure 4.8 Dependence of hot cracking index on composition for alloys Al–Cu prepared out of aluminum with purity A96, (a); and A7, (b) (Probe K1, diameter 30 mm [19]).

on the basis of Al–Mg (535.0, 585.0), Al–Zn–Mg (707.0), and Al–Cu systems (249.0 + 0.8%Mn + 0.2%Ti, 249.0 + 0.6%Mn + 0.2%Ti + 0.2%Cd) – also see Section 5.

4.1.2 Concentration dependence of casting properties

Today there exists a significant amount of information on the dependence of casting properties (especially hot cracking) on the composition of different binary, ternary, and multicomponent Al-based alloys. Most of the experimentally obtained data are in agreement with the predictions of the Bochvar theory outlined above. Again, the data on hot cracking curves are the most complete. A review of research efforts completed before 1966 can be found in the monograph of Novikov [19]. Figures 4.8–4.19 represent the most important dependencies borrowed from Ref. [19]. Figures 4.19–4.22 provide diagrams "hot cracking–composition" constructed (mostly at Moscow Institute of Steel and Alloys) after 1966. The HCI in Figures 4.8–4.19 was determined using the ring

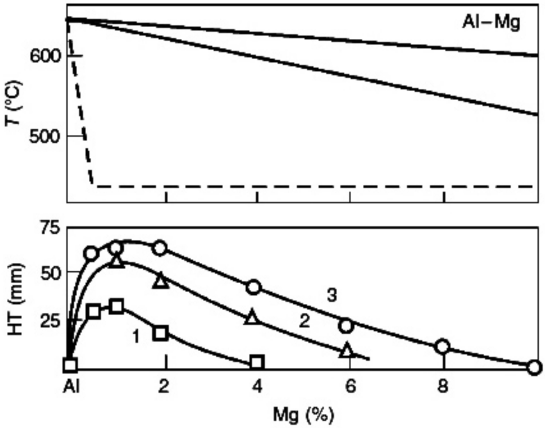

Figure 4.9 Dependence of hot cracking index on composition for alloys Al–Mg; 1, 2, and 3 – superheating above the liquidus temperature by 20° C, 60° C, and 100° C (probe K2, [19]).

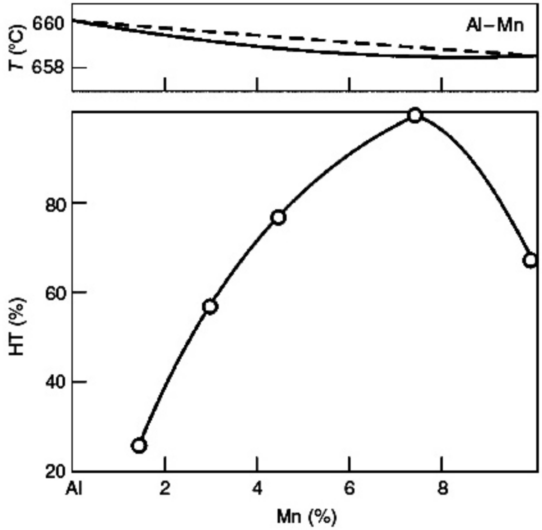

Figure 4.10 Dependence of hot cracking index on composition for alloys Al–Mn, K1 probe with diameter 30 mm.

mold probe; in Figures 4.20–4.21 – using the pencil probe; and in Figure 4.22 – using the ring probe.

Comparison of the presented results with the corresponding phase diagrams of binary and multicomponent systems (see Section 1.2) clearly demonstrates

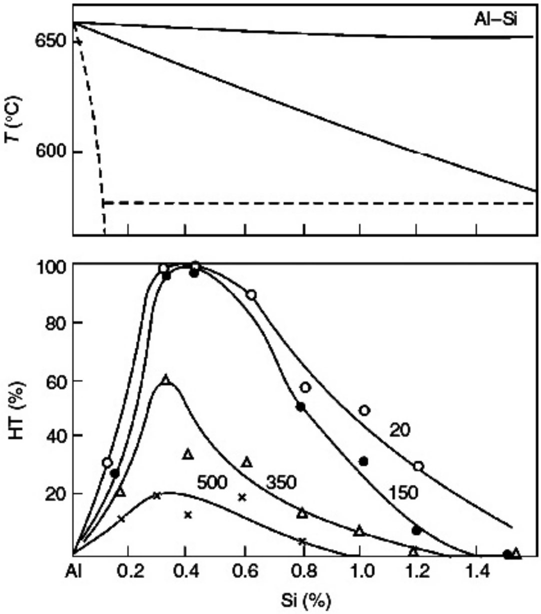

Figure 4.11 Dependence of hot cracking index on composition for alloys Al–Si, K3 probe; data near curves indicates mold temperature [19].

that, in accordance with schematic in Figure 4.5, the maximum of hot cracking corresponds to the concentration boundary of appearance of non-equilibrium eutectics, for which the effective solidification range is the highest. This effect is particularly pronounced for binary systems (Figures 4.8–4.12).

Examples of experimental dependencies of liquid fluidity on composition of binary alloys Al–Cu and Al–Mg are presented in Figure 4.23. In the case of constant superheating above the liquidus temperature (curve 1) there is a minimum in these curves, similar to Figure 4.5. However, the maximum of liquid fluidity for Al–Si alloys does not coincide with the eutectic point. Most probably, this is due to the fact that significant increase of the liquidus temperature (defining the casting temperature) with only minor increase of the silicon concentration does not "compensate" the negative influence of small amounts of primary silicon upon liquid fluidity of hyper-eutectic Al–Si alloys.

For casting alloys Al–Cu the dependencies of the volume fraction of scattered porosity on composition were constructed experimentally (Figure 4.24). They correlate well with the schematic presented in Figure 4.5: porosity changes as a curve with a maximum that lies in between the eutectic point and the concentration boundary of appearance of non-equilibrium eutectic. Similarly, the

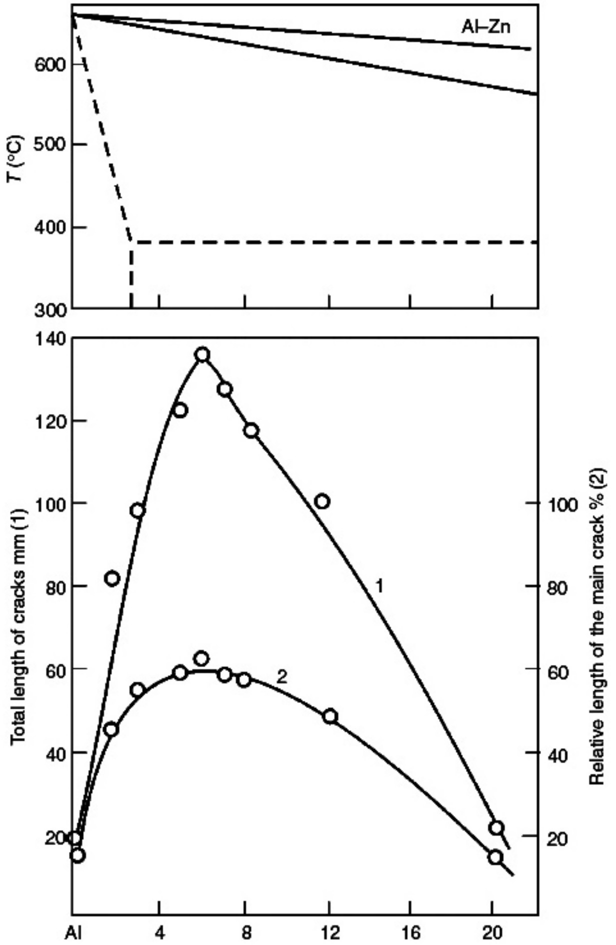

Figure 4.12 Dependence of hot cracking index on composition for alloys Al–Zn. K1 probe, diameter 38 mm [19].

concentration dependence of hermeticity also follows the pattern of Figure 4.5 (see Figure 4.25 for the Al–Si system).

Figure 4.5 and experimentally constructed concentration dependencies of casting properties indicate that good castability could be expected in all those cases when the effective solidification range is small, and the overall amount of

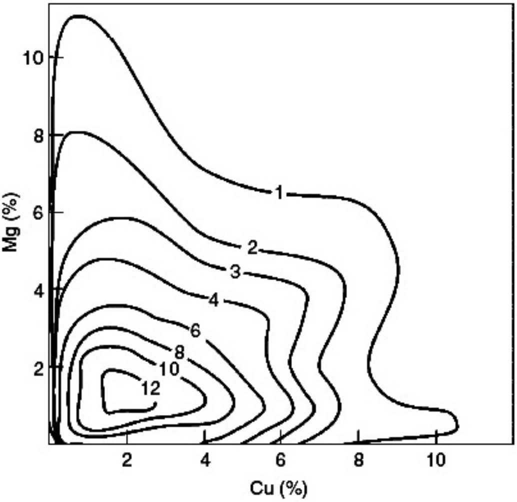

Figure 4.13 Dependence of hot cracking index on composition for alloys Al–Cu–Mg K2 probe [19].

eutectic components in microstructure is relatively large. This fact is fundamental for understanding the metals science of all casting aluminum alloys.

4.2 MECHANICAL PROPERTIES

Mechanical properties of aluminum alloys to a very significant extent are specific of each particular alloying system and alloy conditions in which they are determined (e.g., as-cast or heat-treated using different regimes). Such specifics are due to very significant differences of phase composition and microstructure of alloys belonging to different systems. However, aluminum alloy castings obey some general rules, which will be considered below. In greater details mechanical properties of specific aluminum alloys will be discussed in Chapters 5 and 6.

Qualitatively the dependence of mechanical properties of as-cast and heat-treated aluminum alloys on their composition and microstructure is quite well understood [61–63, 180]. We know, for example, that grain refinement and reduced dendrite cell sizes due to accelerated cooling (or powerful ultrasonic or electromagnetic treatment) of solidifying metal increases its plasticity and strength not only in as-cast condition, but also after subsequent heat treatments. For this reason, to a significant extent the mechanical properties of shaped castings

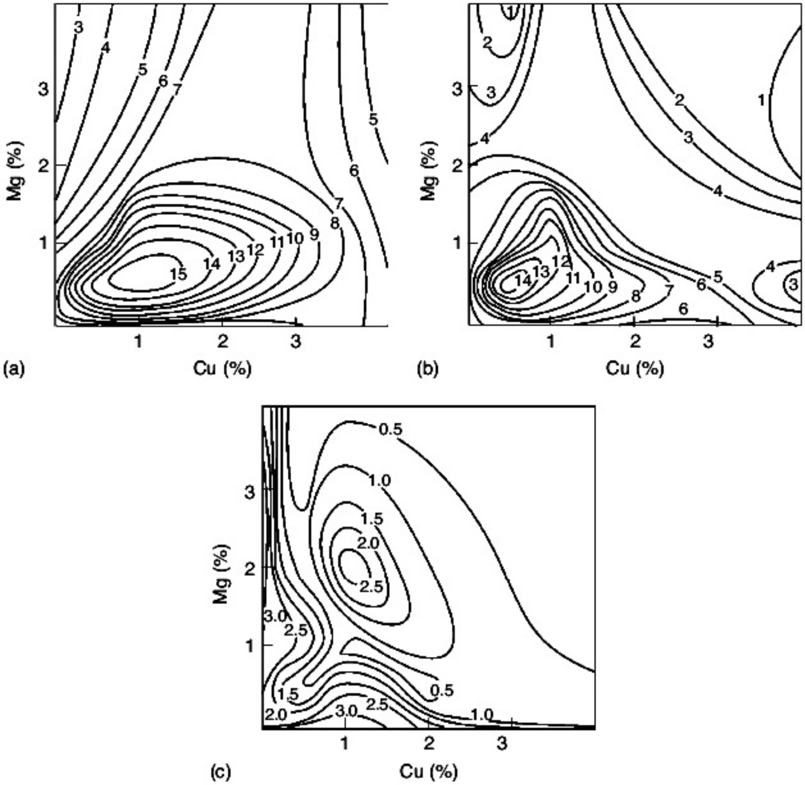

Figure 4.14 Dependence of hot cracking index on composition for alloys Al–Cu–Mg–Si containing (a) 0.5%Zn, (b) 1%Zn, and (c) 2%Zn; K2 probe, HCI in mm.

obtained by casting into metallic molds are generally higher than for casting into sand. If the width of the mold walls decreases, this will favorably affect the general level of mechanical properties. Moreover, the level of casting properties grows as the mold walls get thinner.

The influence of as-cast microstructure upon the properties of fabricated products is well established now. Moreover, it is used in practice to control and "engineer" these properties. In our work quantitative relations between different properties of aluminum castings in different conditions, and their as-cast microstructure, were established. Systematic studies were conducted to understand the hereditary influence of all important microstructure characteristics of ingots and castings upon properties and microstructure of fabricated products. These important issues are discussed in the present section; it

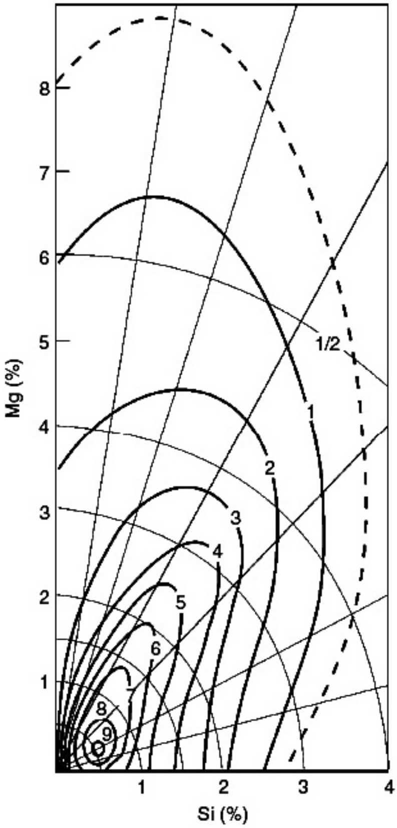

Figure 4.15 Dependence of hot cracking index on composition for alloys Al–Mg–Si (K2 probe) [19].

is also demonstrated how the obtained regularities could be used for optimization of ingot and casting heat treatments in industry, and for *a priori* calculations of mechanical properties of fabricated products using data on microstructure of the corresponding castings even before the completion of such experiments.

The basic mechanical properties analyzed below are those obtained under the conditions of uniaxial tension. These properties are usually specified for castings in their technical documentation. Consequently, let us consider first the data on tensile stress–strain curves at room temperature, as well as the physical meaning of these results as related to the samples of particular geometrical shapes obtained out of aluminum alloy castings.

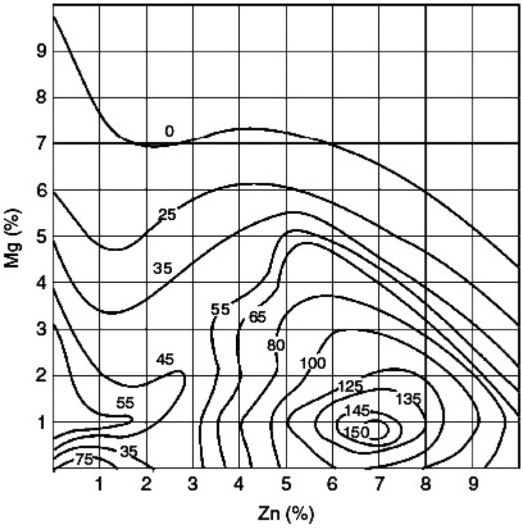

Figure 4.16 Dependence of hot cracking index on composition for alloys Al–Mg–Zn (K2 probe) [19].

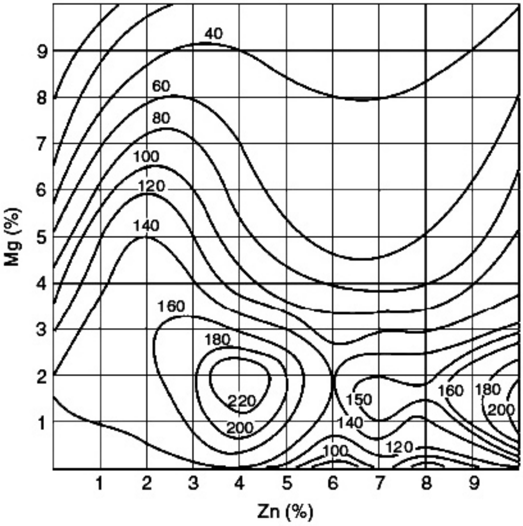

Figure 4.17 Dependence of hot cracking index on composition for alloys Al–Mg–Zn–0.5%Cu (K2 probe) [19].

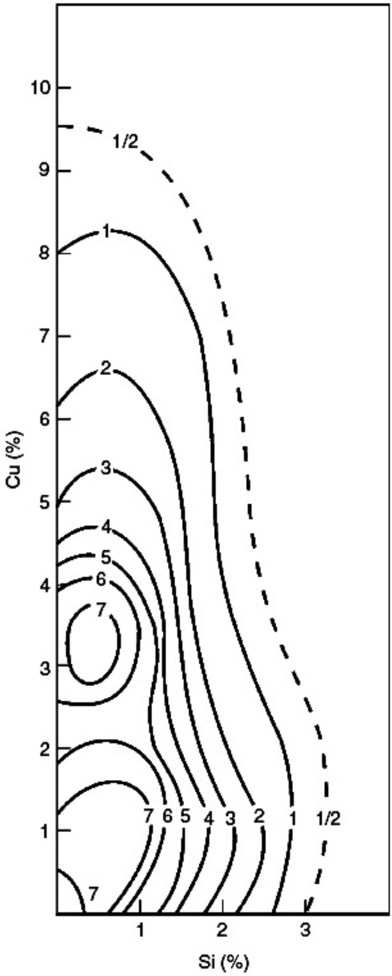

Figure 4.18 Dependence of hot cracking index on composition for alloys Al–Si–Cu (K2 probe) [19].

4.2.1 Geometry of tensile diagrams for as-cast and quenched aluminum alloys, and its connection to the structural transformations accompanying deformation

According to the existing ASTM standards for most technical requirements to, and mechanical properties of, aluminum alloys at room temperature the most widely

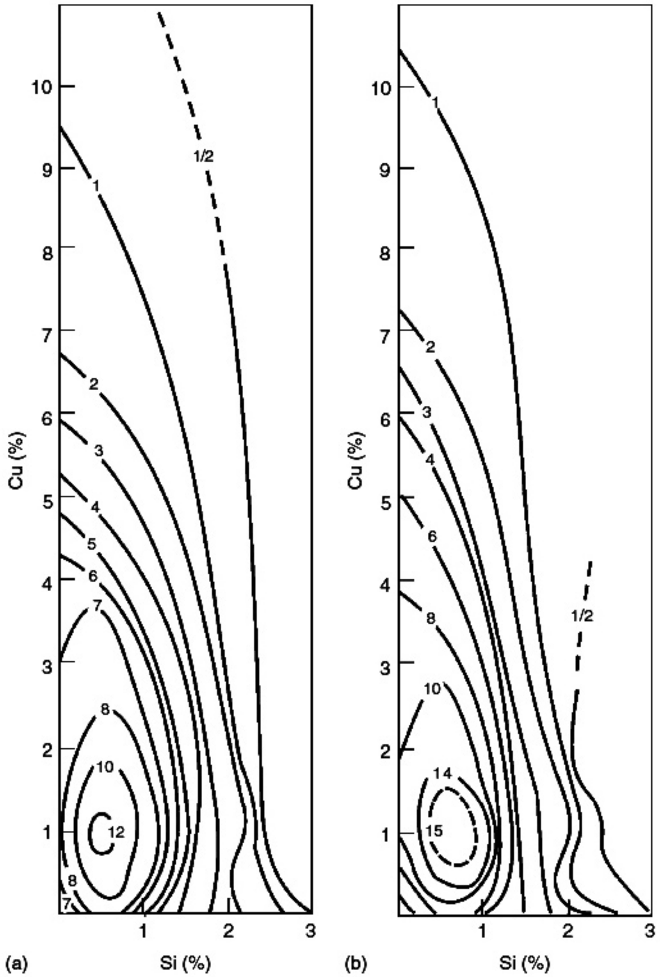

Figure 4.19 Dependence of hot cracking index for alloys Al–Si–Cu–Mg containing 0.2% Mg, (a), and (b) 0.5%Mg (probe K2).

used properties are yield strength, ultimate strength, and relative elongation during uniaxial tension, and also Brinell hardness. The physical and technical meaning of tensile properties may differ quite significantly for different materials due to the geometry of their deformation diagrams.

In order to understand the role of microstructural parameters upon mechanical properties of castings, numerous stress–strain curves were analyzed for binary alloys Al–Cu and Al–Mg, industrial alloys on the basis of these systems, and also

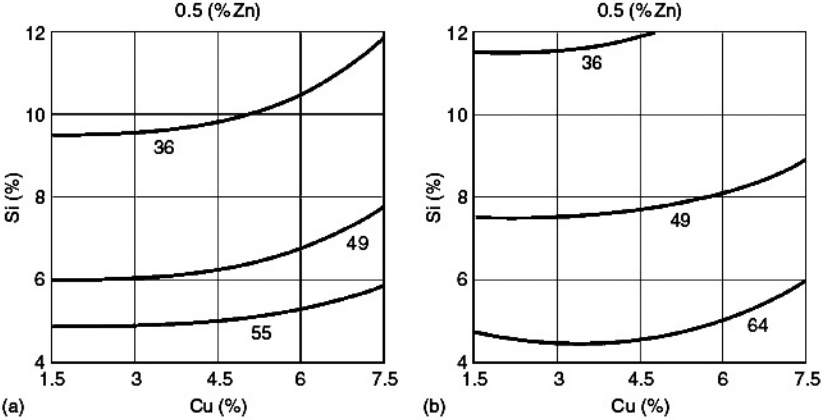

Figure 4.20 Iso-lines of hot cracking index for alloys of the Al–Si–Cu–Mg–Zn at magnesium concentrations 0.2% and 1.2% and 0.5% Zn: (a) 0.2%Mg and 0.5%Zn; (b) 1.2%Mg and 0.5%Zn.

the Al–Mg–Zn system and different 3xx series alloys. In all cases for testing apparatuses with different machine stiffness and applied strain rate ~1 mm/min, smooth tensile curves were obtained without any indications of plastic instabilities. Only in the case of castings made out of Al–Mg alloys (>3%Mg) the Portevin–LeChatelier effect was observed – serrated stress–strain curves due to the effect of dynamic strain aging [297–300]. Figure 4.26 illustrates several typical cases of such diagrams obtained for the samples cut out of castings with different levels of strength and elongation.

One should mention that the appearance of such plastic instabilities as Portevin–Le Chatelier serrations and bands, ludering, etc., always depends on the existence of peculiar features in alloy constitutive behavior (e.g., for PLC effect – negative strain-rate sensitivity) and the geometrical conditions of testing. For example, the PLC serrations, which could be clearly seen for some Al–Mg alloys in tensile testing, may almost completely disappear if pure shear deformation mode is applied, and become considerably less pronounced in bulge (biaxial) testing.[1]

---

[1] For a more detailed exposition of these experiments and modeling work, the interested reader is referred to the papers listed in this footnote: M.V. Glazov and C. Laird, Size Effects of Dislocation Patterning in Fatigued Metals, *Acta Metall. Mater.*, Vol. 43, No. 7, (1995) pp. 2849–2857; M.V. Glazov, L. Llanes and C. Laird, Self-Organized Dislocation Structures (SODS) in Fatigued Metals, *Phys. Stat. Solidi (A)*, Vol. 149 (1995) pp. 297–321; M.V. Glazov, D.R. Williams and C. Laird, Temporal dissipative structures in cyclically deformed metallic alloys, *Applied Physics A (Springer-Verlag)*, Vol. 64, (1997), pp. 373–381; M. Zaiser, M.V. Glazov, L.A. Lalli and O. Richmond, On the Relations Between Strain- and Strain-Rate Softening Phenomena in Some Metallic Materials: a Computational Study, *Comp. Mater. Sci.*, Vol. 15 (1999), pp. 35–49; M.V. Glazov, D.J. Lege, F. Barlat and O. Richmond, Computer Simulation of Annealing and Recovery Effects on Serrated Flow in Some Al-Mg Alloys, *Metall. Mater. Trans.*, Vol. 30A, (1999) pp. 387–397; M.V. Glazov, M.V. Braginsky, L.A. Lalli and O. Richmond, On the derivation and analysis of the "machine equation" in finite deformations, *Applied Physics A (Springer-Verlag)*, Vol. 67, No. 5, (1998) pp. 571–578; V. Bulatov, O. Richmond and M.V. Glazov, An Atomic Dislocation Mechanism of pressure-dependent plastic flow in pure aluminum, *Acta Materialia*, Vol. 47/12, (1999), pp. 3507–3514; S.N. Rashkeev, M.V. Glazov and O. Richmond, Irregularities and modulated dislocation patterns in plastically deformed metals: the Eckhaus

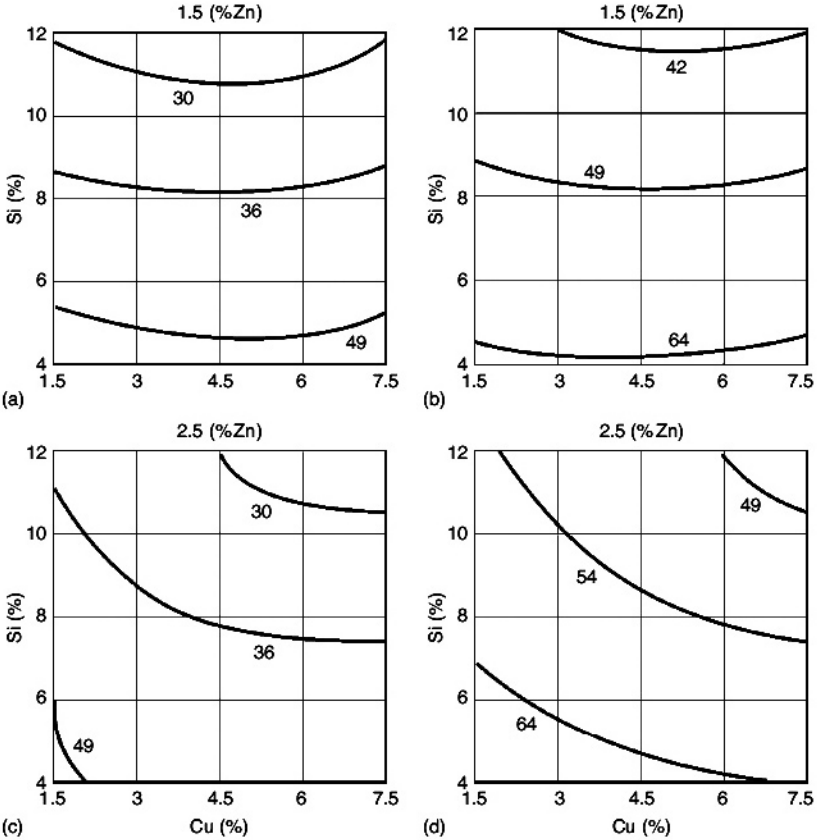

Figure 4.21 Iso-lines of hot cracking index for alloys Al–Si–Cu–Mg–Zn at magnesium concentrations 0.2% and 1.2% and different concentrations of Zn: (a) 0.2%Mg and 1.5%Zn; (b) 1.2%Mg and 1.5%Zn; (c) 0.2%Mg and 2.5%Zn; (d) 1.2%Mg and 2.5%Zn.

(Continued)

instability, *J. Mech. Behav. Mater., (London)*, Vol. 10, No. 1, (1999), pp. 7–30; S.N. Rashkeev, M.V. Glazov, O. Richmond and E.C. Aifantis, Modulated Dislocation Patterns in Plastically Deformed Metals, *Proc. of the Richmond Symposium – Integration of Material, Process and Product Design*, ed. by N. Zabaras, R. Becker, S. Ghosh and L. Lalli, Balkema Publishers, Rotterdam, (1999) pp. 19–26; S.N. Rashkeev, M.V. Glazov and F. Barlat, The eckhaus instability – a possible wavelength changing mechanism in the evolution of dislocation patterns, *Comp. Mater. Sci.*, Vol. 21, (2001) pp. 230–242; F. Barlat, M.V. Glazoff, J.C. Brem and D.J. Lege, A Simple model for dislocation behavior, strain and strain rate hardening evolution in deforming aluminum, *Int. J. Plasticity*, vol. 18, (2002) pp. 919–939; M.V. Glazoff, F. Barlat, and H. Weiland, Continuum physics of phase and defect microstructures: bridging the gap between physical metallurgy and plasticity of aluminum alloys *Int. J. Plast.*, Vol. 20, No. 3, (2004) pp. 363–402. This paper is used at MIT, Dept. of Materials Science and Engineering as "recommended reading" for graduate-level course Physical Metallurgy by Profs. Russell and Van Vliet, see link http://ocw.mit.edu/OcwWeb/Materials-Science-and-Engineering/3-40JSpring2004/Readings/

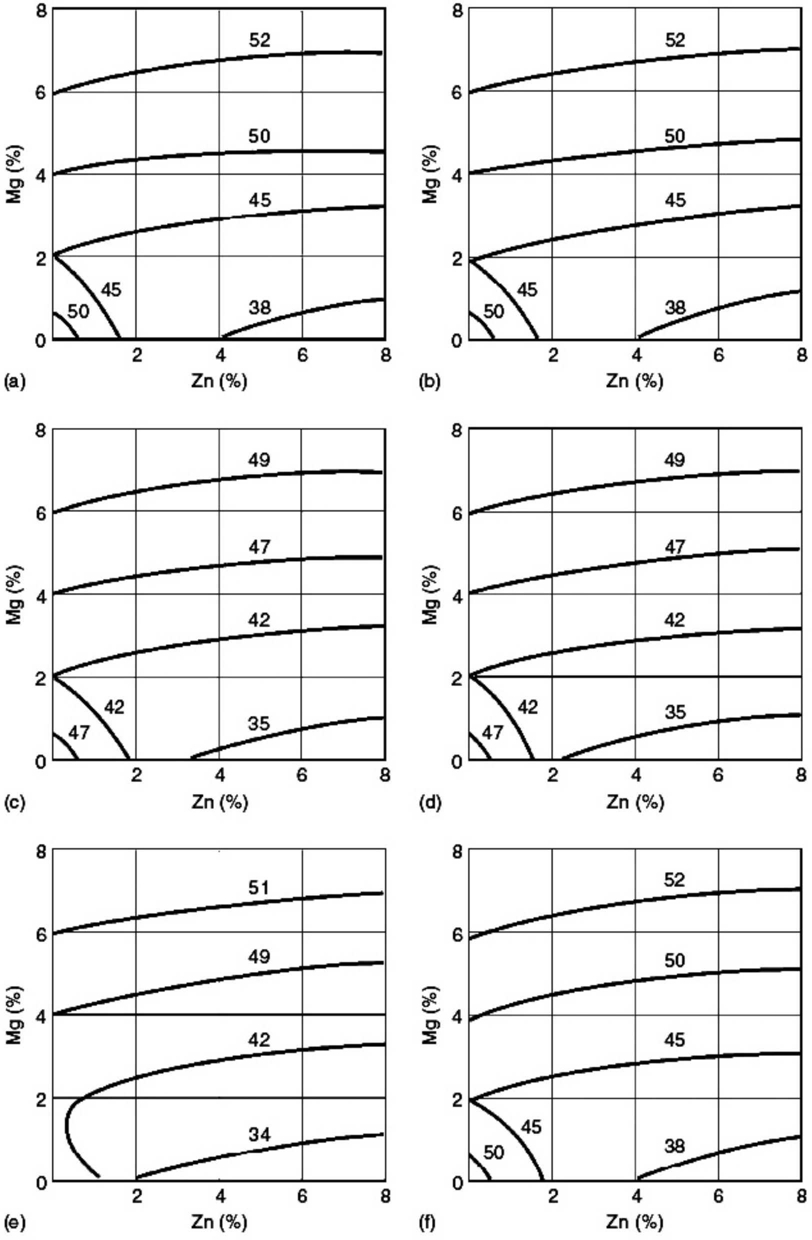

Figure 4.22 Iso-lines of hot cracking index for alloys Al–Mg–Zn–Cu–Fe–Si: (a) in the absence of Cu, Fe, and Si (<0.01%), (b) at 2%Cu and in the absence of Fe and Si, (c) at 4%Cu and in the absence of Fe and Si, (d) at 0.5%Fe and 0.5%Si and in the absence of Cu, (e) at 2%Cu0.5%Fe, and 0.5%Si, and (f) at 1%Fe1%Si, and in the absence of Cu.

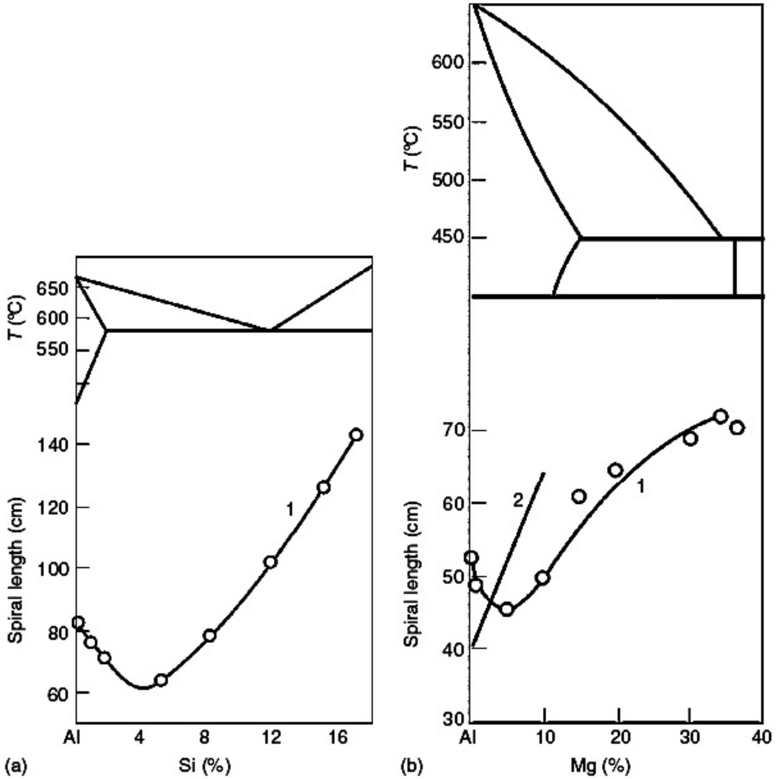

Figure 4.23 Dependence of molten metal fluidity upon composition in the systems Al–Si, (a); and Al–Mg, (b) [19]: 1 – constant superheating above liquidus temperature; 2 – constant casting temperature (700° C).

Moreover, dynamic transitions from strain softening instabilities (Luders bands) to strain-rate softening instabilities (PLC bands of different types) can be observed as a function of machine stiffness and temperature.[1] In particular, interpretation of the results of uniaxial tensile testing in true stress – true strain coordinates requires that these factors be taken into account explicitly.[1] A more detailed description of mechanical testing and its interpretation using the mechanics of finite deformations is presented in Appendix 6.[1]

The dependencies of mechanical properties on chemical composition and microstructure of studied cast and heat-treated aluminum alloys can change very significantly: yield strength ($\sigma_{0.2}$) – from 50 to 600 MPa, ultimate strength (σ_u) – from 100 to 650 MPa, relative elongation (δ) – from 0% to 30%. In most cases, especially for industrial alloys, deformation remains homogeneous up to fracture. However, in the case of some weakly alloyed and even commercial alloys in certain

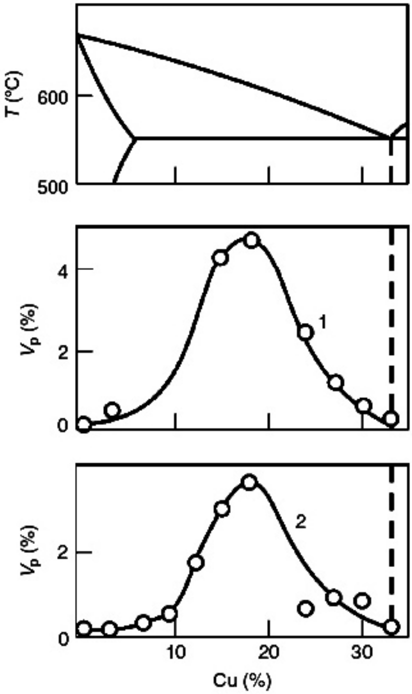

Figure 4.24 Dependence of the residual total volume of scattered pores (V_p) upon composition in the Al–Cu system: 1– sand casting; 2 – casting into metallic mold [19].

structural conditions (e.g., after quenching or annealing) deformation mode could become heterogeneous and accompanied by the processes of localization of plastic deformation (e.g., necking).

Analysis of the initial stages of the stress–strain curves indicated that the residual deformation for sufficiently ductile samples ($\delta > 2$–3%) could appear at relatively low stresses, which are several times smaller than the yield strength $\sigma_{0.2}$. Figure 4.27 illustrates the stress (σ)–residual strain (ε) curves for Al + 10%Mg alloy that was quenched after casting. The curves were obtained using the "Instron" testing machine with tension sensor for the calculated sample length. It can be seen that residual deformation could be measured at stresses <20 MPa at $\sigma_{0.2} = 90$ MPa. The coefficient of work hardening d_σ/d_ε, as it follows from Figure 4.27, rapidly decreases even during the earliest stages of plastic deformation (for alloy with 10%Mg – after ~0.1% elongation). As a result, the initial part of the stress–strain curve can be approximated by the following function:

$$\sigma = A\varepsilon^n$$

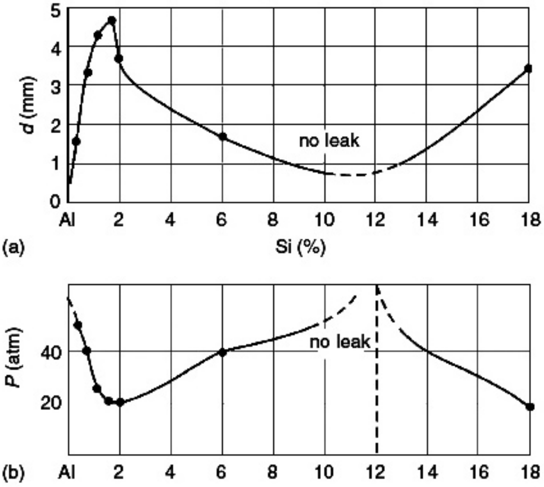

Figure 4.25 Dependence of hermeticity upon composition in the Al–Si system [19]: (a) d – thickness of casting corresponding to appearance of leak(s), and (b) p – water pressure corresponding to leak appearance in a casting with thickness 1.5–2 mm.

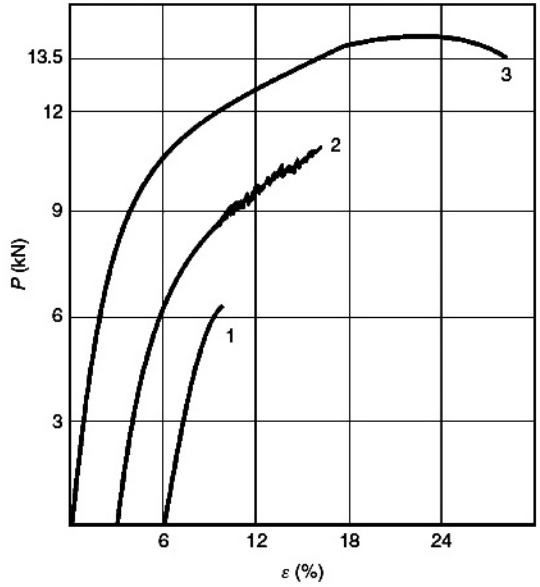

Figure 4.26 Typical tensile diagrams for aluminum alloys in as-cast and quenched states: 1 – casting alloy Al + 9%Mg; 2 – quenched alloy Al + 9%Mg; 3 – quenched alloy Al + 4.2%Cu.

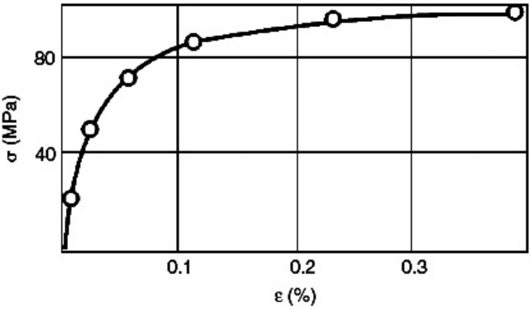

Figure 4.27 Tensile diagram for quenched alloy Al + 10%Mg in the coordinates stress σ–residual strain ε.

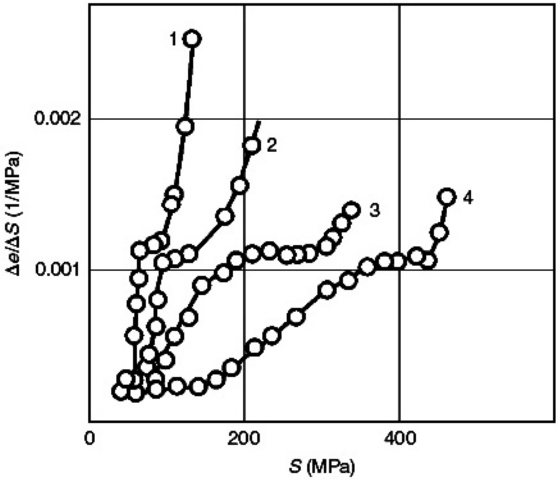

Figure 4.28 Dependence of the inverse value of the work hardening coefficient $\Delta e/\Delta S$ upon true stress S in quenched alloys of Al with 1.5%Mg (1); 3%Mg, (2, 3); and 9%Mg (4) with average grain size 0.35 (1); 0.28 (2); and 0.24 mm (3, 4).

The value of coefficient "*n*" is rather small and varies from 0.1 to 0.4 for different alloys.

The whole stress–strain tensile curve of polycrystalline FCC metals (including aluminum) consist of three or four stages of work hardening (see, e.g., Refs. [297–305]). As it was demonstrated in Refs. [303–305], these stages become particularly well defined if the true stress – true residual strain curves are used $S - (\Delta e/\Delta S)$, where S is the true (Cauchy) stress and e is the true strain (Figures 4.28 and 4.29). For a detailed derivation of the corresponding expressions that also take into account the machine's stiffness, the interested reader is referred to Appendix 6 (see also note[1]).

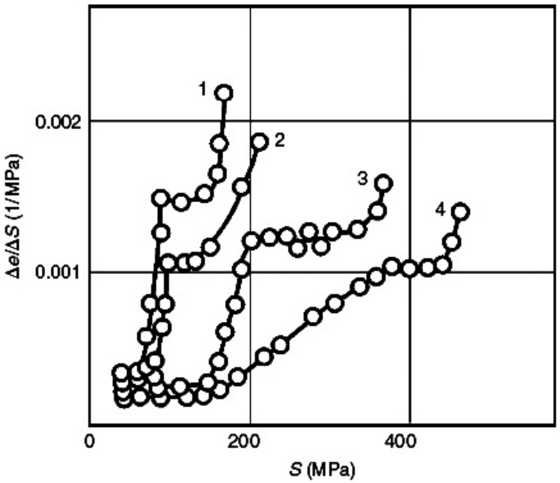

Figure 4.29 Dependence of the inverse value of the work hardening coefficient $\Delta e/\Delta S$ upon true stress S in quenched alloys of Al with 3%Mg (1, 2); and 9%Mg (3, 4) for average grain size 1.35 mm (1); 0.28 mm (2); and 0.24 mm (3, 4).

The multi-stage nature of work hardening was studied earlier for polycrystalline recrystallized copper [304, 306, 307]. As far as aluminum and its alloys are concerned, such studies are practically absent. For this reason, in collaboration with Kornaukhov, we conducted analyses of the work hardening curves for as-cast and quenched binary aluminum alloys containing 1.5–12.5%Mg, with parallel studies of the slip lines and dislocation microstructures at different deformation stages. Quenched single-phase alloys were studied in great detail. Samples were cut out of castings with diameter 40 mm solidified into metallic molds heated up to different temperatures. This procedure ensured that castings possessed different microstructures, in particular, grain size, after quenching. Testing was conducted with recording of the tensile data. The applied cross-head velocity in all cases was 1 mm/min at room temperature. In order to study the structure of slip lines at different stages of deformation optical microscopy was used. Surfaces were preliminary prepared using electro-polishing; dislocation microstructures were studied with transmission electron microscopy (TEM) using samples for foil preparation that were cut out in the direction perpendicular to the tensile axis.

It should be mentioned that transition between different types of plastic instabilities and dislocation structures in fatigue testing is markedly different from monotonic testing.[1] An effort to describe these dynamic transitions using the methods of self-organization theory and nonlinear, non-equilibrium thermodynamics was made by Glazov and Laird (*Acta Mater.*, v. 43, p. 2849, 1995) in relation to the so-called "ladder structure" of persistent slip bands in fatigued single crystals of aluminum.

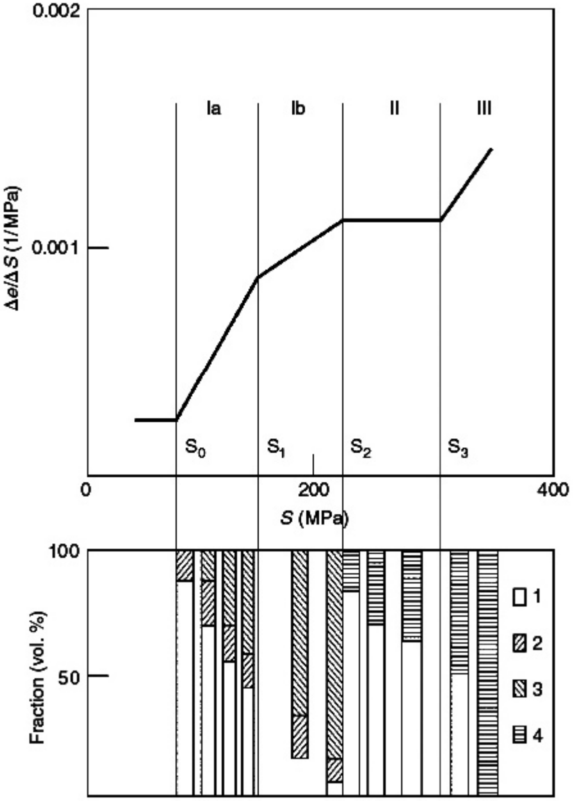

Figure 4.30 Four-stage diagram $\Delta e/\Delta S - S$ for quenched alloy Al + 6%Mg, compared to the relative fraction of the sample surface with different patterns of slip lines and bands: 1 slip lines and bands are absent; 2 – slip lines; 3 – slip bands located inside the grains; 4 – slip bands crossing grain boundaries.

The primary tension diagrams recorded in coordinates "applied force–absolute elongation" were subdivided by an arbitrary number of points into relatively straight segments. For each point the true stress, true strain, and the value of $\Delta e/\Delta S$ (inversely proportional to the coefficient of strain hardening) were determined. It is clear that for all alloys in the curves $(\Delta e/\Delta S) - S$ one can distinguish three or four stages with different tangents that are schematically presented in Figure 4.30. For some curves it was difficult to distinguish between the stages Ia and Ib, II, and III.

Figure 4.28 represents the results of testing of quenched samples with approximately similar average grain size (0.24–0.35 mm). It can be seen that as the degree of alloying increases the S_0, S_1, S_2, and S_3 stresses also increase (Figure 4.30), as well as the strain hardening coefficient $\Delta S/\Delta e$ on the third stage. The analysis of curves presented in Figure 4.28 indicates that the tangent on stage I decreases quite substantially as magnesium concentration in solid solution grows. This corresponds to smaller extent of work hardening during the initial stages of plastic deformation for alloys with higher concentration of alloying element. The observed changes in the behavior of the $(\Delta e/\Delta S) - S$ curves with increased alloying could be explained by increased resistance to plastic deformation at all stages due to higher atomic friction forces of the lattice and its increased resistance to dislocation propagation (Peierls stress) on the principal (111)<110> slip system.

Grain refinement in alloys with 3–9% Mg (Figure 4.29) results in smaller values of the tangents for stage I, and in increased stresses and higher strain hardening coefficient during stage III of plastic deformation.

If one proposes that the density of dislocations correlates to the average grain size [308], then higher level of work hardening indirectly signals that in alloys with the finest grain size the density of dislocations is higher at all deformation stages.

Metallographic inspection of the polished surface of the samples in the areas of homogeneous deformation revealed the following deformation patterns: slip lines in one or several systems, the propagation of which is arrested at grain boundaries (Figure 4.31a); strips formed as a result of dissociation of slip lines (Figure 4.31b); penetration of slip lines or their bundles from one grain into another (Figure 4.31c); steps (Figure 4.31d); fragmentation of steps due to cross-slip accompanied by the formation of the slip fall-offs (Figure 4.31e). The principal feature of the gradual surface topography changes accompanying plastic deformation is its increased heterogeneity that could be observed in separate grains and in each particular grain as well.

During the “elastic” deformation stage, that is in range I, the ratio $\Delta e/\Delta S$ is practically constant because the Hooke’s law is obeyed. Stage Ia begins when plastic deformation is initiated in a certain fraction of the sample volume (in the studied Al–6%Mg alloy slip lines occupied only 12% of the surface area at this stage). This was accompanied by the reduction in the strain hardening coefficient (increased $\Delta e/\Delta S$ with continuous onset of plastic flow in the whole volume of the sample since at this stage more and more of new dislocation sources and slip systems become operable). As the applied stress grows the overall fraction of the material volume involved in plastic deformation also grows for those primary slip systems where the density of dislocations is still not very high. For stage Ia this process defines the character of plastic deformation. Indeed, smaller value of $\Delta S/\Delta e$ (increased $\Delta e/\Delta S$) is defined by the fraction of material participating in the process of plastic deformation, while the extent of this process and the type of deformation structure depends upon the orientation and loading of each particular micro volume. The initiation of new dislocation sources still continues during stage Ib; however, their overall number is insignificant, and the reduction of the strain hardening coefficient slows down.

Stage II begins when slip lines fill the whole sample. Here, most probably, all source become operable, the volume of the sample gets “filled” with dislocations

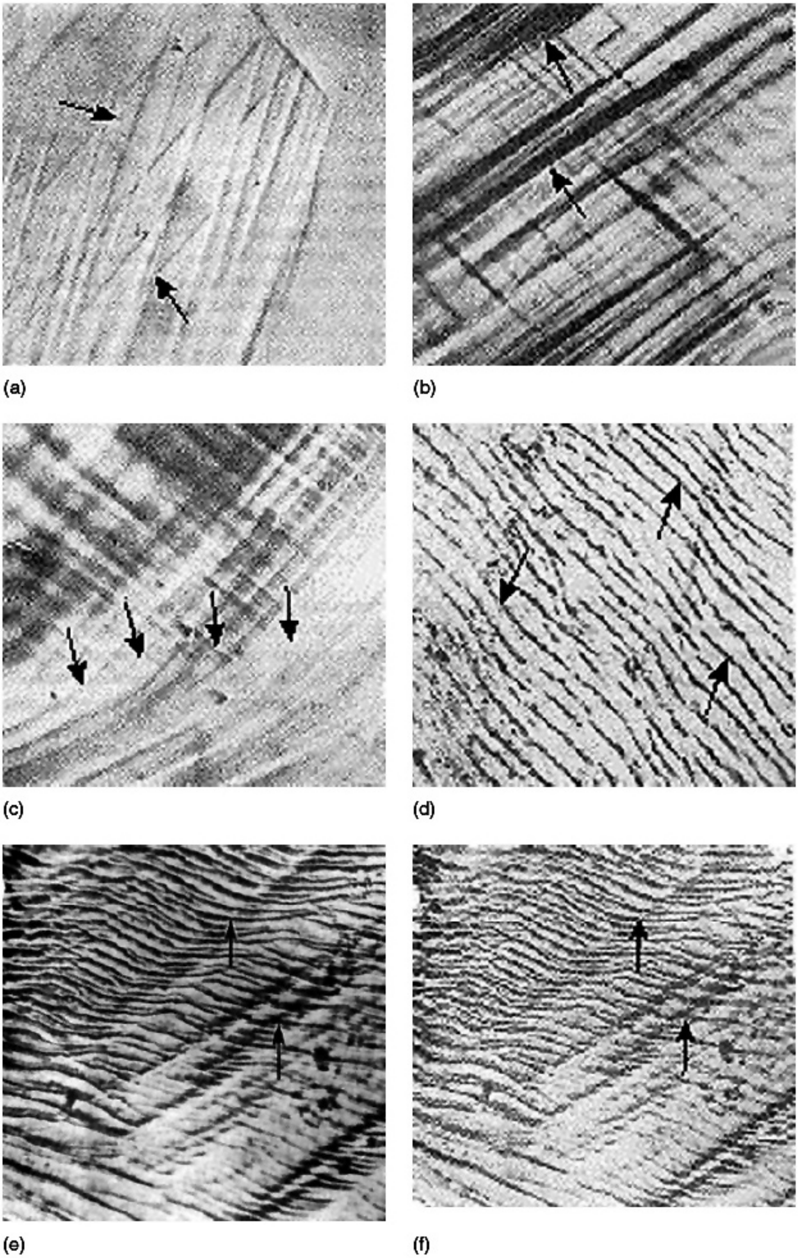

Figure 4.31 Slip lines corresponding to different stages of work hardening process in tensile testing of quenched alloy Al + 6%Mg; Arrows are used to indicate: (a, b) slip lines and bands; (c) position of grain boundary with slip lines crossing it; (d) steps; (e) slip fall-offs; (f) ledges. Optical microscopy, ×500.

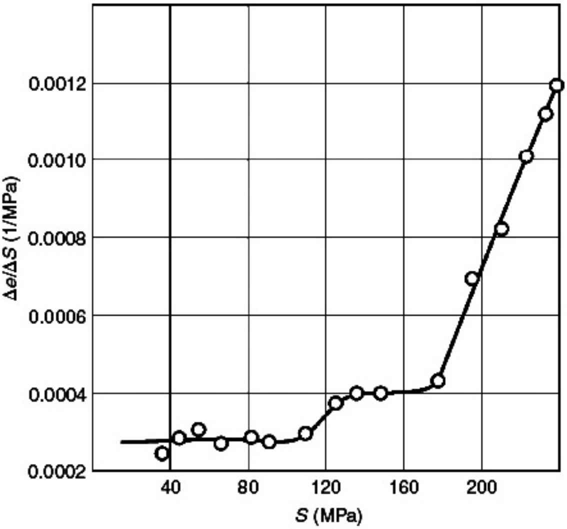

Figure 4.32 Diagrams $(\Delta e/\Delta S) - S$ for cast aluminum alloy Al + 6%Mg.

(S grows proportionally to elongation). Stage III begins at such stresses when for all grain boundaries slip lines in one grain initiate additional slip in adjacent grains (a gradual transition of slip lines across grain boundaries is observed). Due to the development of cross-slip the strain hardening coefficient decreases at this stage; deformation involves additional new slip systems.

TEM studies did not establish the direct link between the work hardening stages and the types of dislocation microstructures. As usual, with increased deformation the density of dislocations also grows; however, any qualitative changes in the types of dislocation substructures were not observed. This happens, of course, because of polycrystalline nature of all studied samples; for single crystals in monotonic and cyclical loading such correlations have been established quite reliably.

The analysis of the $(\Delta e/\Delta S) - S$ curves for as-cast aluminum samples also revealed the existence of three or four stages of their plastic deformation (Figure 4.32). The relation between the overall picture of the surface slip lines and the stages of work hardening for cast samples is in general retained. Some distinct features of this picture, compared to the quenched state, are related to the presence inside grains of cast alloys of dendritic cells that contain eutectic inclusions lined along the cell boundaries. However, due to small values of disorientation angles of dendritic cell boundaries, and also non-continuous deposits of eutectic inclusions along such boundaries, slip lines can easily traverse these boundaries (Figure 4.33).

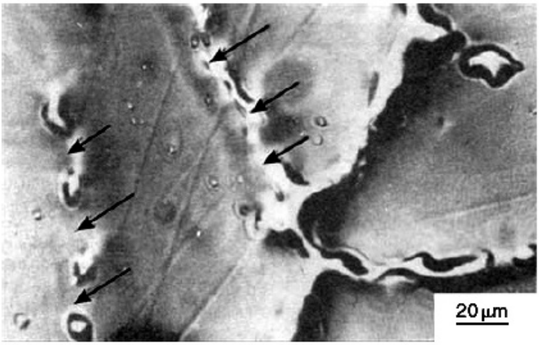

Figure 4.33 Transition of slip lines across the boundaries of dendritic cells (see arrows) on the surface of a cast sample of alloy Al + 9%Mg; light microscopy.

Based on the discussion above, one could make the following conclusions on the physical meaning of information (yield strength, ultimate strength) obtained in uniaxial tensile tests of castings in as-cast and quenched states, at different values of the final relative elongation. If $\delta \cong 0$, then yield strength cannot be determined at all, while the measured ultimate strength would correspond to brittle fracture. When $\delta > 0.2/0.5\%$ and macroscopically homogeneous deformation develops up to the point of fracture ($\delta < 10$–20%), then yield strength $\sigma_{0.2}$ characterizes resistance of plastic deformation in that moment in time only when a limited fraction of the sample volume is involved (10–15%, judging by the pictures of surface slip lines). Ultimate strength in this case defines resistance of different (for different samples) plastic deformation before fracture. Finally, if casting alloy is so ductile that necking precedes its fracture ($\delta > 10$–20%), then the physical sense of $\sigma_{0.2}$ does not change, while σ_B characterizes in this case resistance to the maximal homogeneous deformation.

All these considerations must be taken into account when analyzing data on mechanical properties of casting aluminum alloys.

4.2.2 Quantitative analysis of relations between tensile mechanical properties and structural characteristics of castings

Mechanical properties of castings must depend on a number of such characteristics of macro- and microstructure as shape and size of grains; the degree of refinement of microstructure (dendritic cell and constituent particles sizes), substructure, porosity, quantity, and size of primary intermetallic particles and non-metallic inclusions, the extent of zonal and dendritic microsegregation. Today, on a qualitative level, the role and influence of most of these microstructure parameters upon strength and plasticity of casting aluminum alloys are quite well understood. However, their relative "contributions" into certain alloy properties are studied insufficiently. This state of affairs could be explained by the complexity of extracting the role and influence of just one of these parameters upon a particular property because they are all intimately interconnected, and it is impossible to establish how a variation of just one parameter, with all other characteristics being constant, will affect properties.

Below an effort is made to establish the extent of influence of several important microstructure characteristics upon mechanical properties of castings (determined in tensile tests), and also to obtain a quantitative expression describing the dependence of such properties upon particular microstructure parameters [11, 309–314].

All experiments were conducted with as-cast and quenched binary aluminum alloy samples with 2–6% and 1.5–12.5%Mg, as well as with multicomponent industrial alloys on the basis of the Al–Cu and Al–Mg systems. Some 3xx series castings alloys solidified with different cooling rates in the 10^0–10^2 K/s range were also studied in this work. In as-cast condition all alloys of the Al–Cu and Al–Mg systems contained in their microstructure non-equilibrium eutectic, typically degenerate (Al_2Cu or Al_3Mg_2), which could be completely dissolved in the course of heating before quenching. In Al–Si alloys such heat-up resulted mostly in the dissolution of non-equilibrium excessive phases $CuAl_2$ and Mg_2Si.

In as-cast samples the following parameters were measured (using optical microscopy): average lineal grain size (D) and dendritic cell size (d); volume fraction (Q_V), thickness (m), and specific surface of hypo-eutectic inclusions (S), distance between such inclusions (l). The overall volume fraction of the pores (Q_p) or density, the degree of microsegregation (ΔC), and the concentration of alloying elements in (Al), (C_B^α), also were assessed quantitatively. In addition to the above-mentioned parameters, in as-cast alloys we estimated, using TEM, two important characteristics of substructure – the average lineal size of sub grains d' (in alloys of the Al–Mg system) and the overall density of dislocations, ρ.

In quenched samples (to be more precise, naturally aged, because testing was usually conducted in 5–6 days after quenching) the same structural characteristics were determined wherever possible. In industrial alloys with additions of transition metals, using TEM images, we measured such characteristics of aluminide dispersoids as size, number density of particles, and interparticle spacing. Naturally, for those samples where heat up before quenching resulted in complete dissolution of non-equilibrium eutectic, the values Q_V, m, S, and l were not estimated.

Mechanical properties ($\sigma_{0.2}$, σ_B, δ) were determined using tensile testing data at room temperature. To establish connections between mechanical properties and microstructural characteristics, the methods of correlation and regression analysis were used [232, 235, 315] in conjunction with computer processing of data.

4.2.2.1 The influence of grain size

The influence of grain size in the studied castings (mostly with diameter 50 mm) was conducted for only one factor – the average grain size (equiaxed microstructure). In as-cast Al–Cu alloys this parameter exerts weak influence

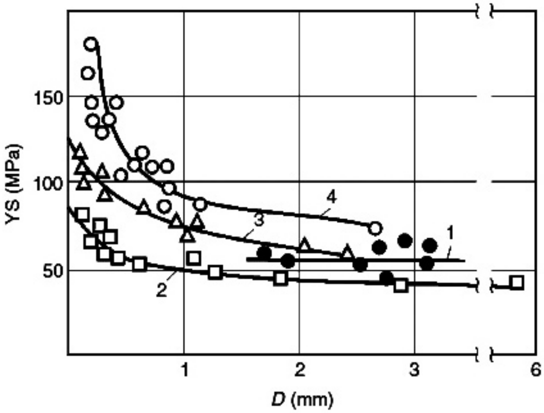

Figure 4.34 Dependence of $\sigma_{0.2}$ for casting alloys of Al with 4.2%Cu, (1), 3%Mg, (2), 6%Mg, (3), and 9%Mg, (4), upon grain size *D*.

upon mechanical properties, while in the case of Al–Mg alloys it affects properties quite substantially (Figure 4.34).

It was established that the coefficient of pair correlation that characterizes the linearity of interdependence of $\sigma_{0.2}$, σ_B, and *D*, for cast aluminum alloys with 3–9% magnesium is quite substantial (Table 4.1). However, the nature of dependence of mechanical properties on grain size is nonlinear, and for this reason the respective pair correlation coefficient is not a good indicator here. As can be seen from data presented in Figure 4.34 on the dependence of $\sigma_{0.2}$ of cast alloys Al–Mg on *D*, the yield strength declines sharply (almost twofold) when grain size increases to 1 mm, but after that any further microstructure coarsening affects properties very weakly.

As the contents of magnesium in alloy decreases, the influence of grain size upon mechanical properties becomes less pronounced. The curves $\sigma_{0.2}$–*D* constructed for different alloys are distinctly "divided" into groups corresponding to different materials (Figure 4.35).

It follows from Table 4.2 that the dependence of strength of cast Al–Mg alloys on grain size can be well described by the Hall–Petch relationship:

$$y = b_0 + b_1 D^{-1/2}$$

In this regression equation, y is a property of interest. In Al–Cu castings grain size was almost always greater than 1 mm, and it is for this reason that its influence upon mechanical properties was considerably less pronounced than for Al–Mg alloys in as-cast and in quenched states (Figures 4.34 and 4.35).

For quenched binary Al–Mg alloys (as well as for as-cast alloys) a nonlinear dependence of $\sigma_{0.2}$ and σ_B is typical that obeys the Hall–Petch equation

Table 4.1 Coefficients of pair correlation between mechanical properties and characteristics of microstructure of as-cast Al–Mg alloys

Content of Mg (%)	Property y	Correlation coefficient corresponding to microstructure characteristic						
		D	d	C_{Mg}^{α}	m	l	Q_p	Q_V
3, 6, 9	$\sigma_{0.2}$	−0.517*	−0.496*	0.735*	0.167	−0.662*	0.115	0.596
3		−0.801*	−0.659	−0.113	−0.485	−0.546	−0.254	–
6		−0.905*	−0.686	0.389	−0.724	−0.508	−0.766	−0.238
9		−0.700*	−0.560	0.131	−0.584	−0.454	−0.198	−0.014
3, 6, 9	σ_B	−0.547*	−0.697*	0.233	−0.478*	−0.444	−0.455	−0.044
3		−0.895*	−0.724	0.046	−0.628	−0.679	−0.387	–
6		−0.818*	−0.793*	0.350	−0.846*	−0.491	−0.824*	−0.348
9		−0.599	−0.648	0.276	−0.801*	−0.449	−0.510	−0.214
3, 6, 9	δ	−0.244	−0.360	−0.503*	−0.712*	−0.129	−0.632*	−0.626*
3		−0.858*	−0.822*	−0.016	−0.681	−0.669	−0.453	–
6		−0.710	−0.705	0.277	−0.723	−0.421	0.747	−0.263
9		−0.306	−0.428	0.401	−0.612	0.208	−0.452	−0.364

*Correlation coefficient corresponding to the probability of 0.999.

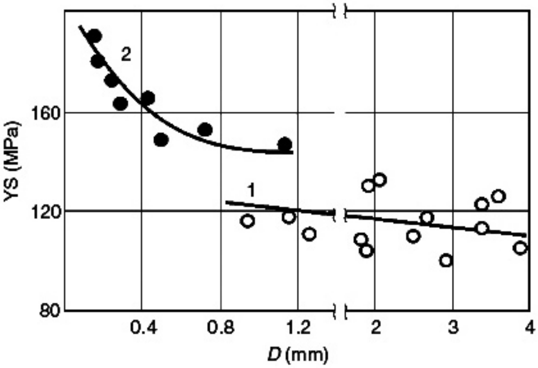

Figure 4.35 Dependence of $\sigma_{0.2}$ for quenched alloys of Al with 4.2%Cu, (1), and 9%Mg, (2) upon grain size *D*.

(Table 4.3). Similar results were obtained in experiments conducted in collaboration with Kornaukhov *et al.* [314] for industrial casting alloys 535.0 and 585.0 (Table 4.4). Moreover, in quenched state the influence of grain size upon properties of Al–Mg alloys can be revealed very clearly, because after quenching of these alloys other microstructural characteristics were more or less similar or uncorrelated to *D*. Consequently, one could state that in quenched castings made out of binary and industrial alloys of this system containing up to 10%Mg, grain refinement from 1–3 to 0.13–0.20 mm allows to increase yield strength by 20–50 MPa (or by 20–30%). Ultimate strength can be increased by 50–140 MPa (from 1.5 to 2 times) and relative elongation – by 5–10 times.

The relative elongation of Al–Mg alloys, similar to their strength, increases nonlinearly with decrease in the value of grain size. For its calculation one could also use the Hall–Petch type of equation, although in this case the error of calculations is much higher (see Table 4.2).

4.2.2.2 Influence of microstructure characteristics

These include parameters of microstructure that could be assessed using optical microscopy (d, Q_V, m, S, l), and also the volume fraction of the pores Q_p, the degree of alloying of (Al), C_B^α, and the extent of microsegregation ΔC.

Correlation statistical analysis of the relation between these mechanical properties and the characteristics of microstructure clearly demonstrated that the most important parameter was the average dendritic cell size *d*, which exerted very significant influence upon mechanical properties of all studied alloys in as-cast state (Tables 4.1 and 4.4). In addition to *d*, mechanical properties also depend upon such parameters as pore size, eutectic inclusions size, as well as the concentration of alloying element in aluminum solid solution C_B^α (either average or determined locally in the middle of dendritic cells) and the volume fraction of eutectic, Q_V.

Table 4.2 Equations ($y = b_0 + b_1 D^{-1/2}$) relating mechanical properties of alloys Al–Mg to grain size

Mg (%)	Property y	b_0	b_1	Range of y (MPa or %)	Λ[a] (MPa or %)	F ratio[b]
As-cast state						
3	$\sigma_{0.2}$	4.73	1.07	46–80	0.45	4.8
6		6.74	1.24	65–119	0.66	5.7
9		5.41	4.18	79–192	22	6.7
3, 6, 9	σ_B	7.1	6.28	75–350	37	3.3
3		9.18	4.85	75–239	15	8.0
6		8.36	5.28	93–297	27	6.2
9		0.915	10.2	86–230	43.5	3.5
3	δ	9.28	4.85	7.5–23.9	1.5	8.0
6		8.36	5.28	9.3–29.7	2.7	6.2
9		0.915	10.2	8.6–35	4.35	3.5
Quenched state						
3	$\sigma_{0.2}$	6.0	0.65	63–75	3.7	1.6
3	σ_B	12.0	4.4	141–196	9.2	17.6
6	$\sigma_{0.2}$	9.7	1.2	102–125	3.7	2.6
6	σ_B	20.6	4.0	249–297	18.5	8.6
9	$\sigma_{0.2}$	12.0	2.5	145–195	5.6	10.0
9	σ_B	21.2	7.45	289–425	17.6	10.1
6–10[c]	σ_B	35.9	28.0	164–388	61	2.3
6–10[c]	δ	43.8	26.1	14–344	4.9	4.1

[a] Residual mean quadratic error.

[b] Calculated as the ratio of dispersion of the average for a given forecast to the residual dispersion.

[c] Alloys of the 535.0 and 585.0 type.

Table 4.3 Equations ($y = b_0 + b_1 x^{-1/2}$) relating mechanical properties of cast industrial alloys of the Al–Mg system to grain and dendritic cell sizes

Y	b_0	b_1	X	Range of y (MPa or %)	Λ (MPa or %)
Alloys of the 535.0 and 585.0 type					
$\sigma_{0.2}$	5.41	4.18	D	140–176	18
Alloys of the 535.0 and 585.0 type					
σ_B	1.2	5.0	d	103–356	32
Alloys of the 535.0 and 585.0 type					
δ	−6.5	2.24	d	0–8.5	1.3
Alloys of the 535.0 and 585.0 type					
δ	−9.5	6.35	d	3.1–34.2	4.1

In Al–Cu castings, where $C_{\mathrm{Cu}}^{\alpha} \cong$ const., and the average grain size does not have any significant influence on properties, the average dendritic cell size in as-cast state determines the level of properties even after quenching. The change in the value of d from 20 to 300 μm reduces σ_B by a factor of 1.5–2; while δ falls by 70% and more. Similar changes of properties take place in as-cast state. Table 4.5 shows that both σ_B and δ of castings from Al–Cu alloys could be calculated using the d values with sufficiently high accuracy.

The value of C_B^{α} changes mostly when the alloy's chemical composition changes, in which case its influence is quite substantial. It is for this reason that the correlation coefficient between C_B^{α} and properties is so big (see Tables 4.1 and 4.4 for a number of aluminum alloys). In as-cast alloy of a given chemical composition C_B^{α} can be changed only by varying the volume fractions of excessive phases, containing the alloying element (copper or magnesium). As can be seen from Table 4.4, in alloys containing 4–6%Cu these variations are sufficient to exert significant influence upon alloy's strength. However, in most other cases these variations are not significant (fractions of a percent) and, correspondingly, the influence of C_B^{α} upon mechanical properties is considerably less pronounced. Similar conclusion can be made with respect to the influence of microsegregation ΔC upon mechanical properties.

The volume fraction of pores in Al–Cu castings (with the exception of several very slowly solidified samples) changed, as it was mentioned above, in a very narrow range. In aluminum–magnesium alloys this range was somewhat broader. It turned out that Q_{pores}, weakly correlated with d: reduction in the dendritic

Table 4.4 Coefficients of pair correlation between mechanical properties and characteristics of casting microstructure for alloys of the Al–Cu type

Contents of Cu (in %)	Property y	Correlation coefficient for a given microstructure parameter					
		d	C_{Cu}^{α}	ΔC	Q_V	S	m
2	$\sigma_{0.2}$	−0.308	0.280	−0.241	−0.577*	−0.479	−0.613
4.2		−0.236	0.845*	−0.469	−0.875*	−0.779*	−0.657
6		−0.228	0.911*	−0.807*	−0.923*	−0.795*	−0.426
2, 4.2, 6		−0.371*	0.922*	−0.632*	−0.194	−0.134	−0.041
2	σ_B	−0.566*	0.290*	−0.268	−0.598*	−0.416	−0.646*
4.2		−0.620*	0.683*	−0.406	−0.736*	−0.507	−0.836*
6		−0.640*	0.715*	−0.704*	−0.707*	−0.499	−0.786*
2, 4.2, 6		−0.618*	0.820*	−0.591	−0.172	−0.041	−0.226
2	δ	−0.790*	−0.051	−0.629	−0.034	0.198	−0.184
4.2		−0.850*	0.292	−0.452	−0.257	0.002	−0.740*
6		−0.622*	0.180	−0.222	−0.200	−0.039	−0.740*
2, 4.2, 6		−0.309	−0.372*	0.086	−0.393*	−0.292	−0.668*
2	HB	−0.181	0.543	−0.425	−0.671*	−0.508	−0.738*
4.2		−0.004	0.887*	−0.480	−0.954	−0.836*	−0.509
6		−0.171	0.922*	−0.775*	−0.952*	−0.839*	−0.435
2, 4.2, 6		−0.338*	0.907*	−0.610*	−0.184	−0.133	0.067

This table was comprised using data on Al–Cu alloys in as-cast and quenched states (after different time of heat treatment).

* Correlation coefficient corresponding to probability of 0.999.

cell size was accompanied by the increase in density. A closer connection was observed between d and pore sizes.

As a result, in alloy of a given composition the influences of microstructure parameters, to the first approximation, could be reduced to the influence of dendritic cell size upon mechanical properties. This parameter defines other important characteristics of microstructure (the average sizes of eutectic inclusions and pores). In addition to parameter d, it is also important to take into account the extent of alloying of the aluminum solid solution.

Table 4.5 Casting equations ($y = b_0 + b_1 d$) connecting mechanical properties of binary Al–Cu alloys with dendritic cell size (d)

Concentration of Cu (%)	Condition	Property y	b_0	b_1	Range of y (in MPa or in %)	Λ (in MPa or %)	F-ratio
2, 4.2, 6	As-cast	σ_B	19.5	−0.065	70–200	13	5.2
2	Quenched		16.5	−0.025	110–180	11	1.8
4.2	"		28.5	−0.08	110–280	7	5.6
6	"		36	−0.155	150–310	9	9.7
2	As-cast	δ	42	−0.16	7–33	2.1	8.1
2	Quenched		36.5	−0.12	11–27	2.3	6.8
4.2	As-cast		28	−0.17	1–23	1.1	8.6
4.2	Quenched		29.5	−0.14	6–25	1.7	7.1
6	As-cast		16	−0.1	0.5–12	1.8	3.9
6	Quenched		21	−0.16	0.5–17	2.7	3.7

For as-cast Al–Cu alloys the influences of grain size and the parameters of substructure (see below) are rather weak. However, reduction of cell size (due to increased molten metal cooling rate) from 190 to 30 μm, along with the corresponding refinement of eutectic colonies, results in the growth of ultimate strength by 130 MPa (i.e., by 1.5–2 times) and increase of relative elongation by 5–10 times (see Table 4.5). At the same time the yield strength of these alloys practically does not depend upon microstructure. After heat treatment the effect of microstructure influence observed in as-cast state is retained.

In Al–Si alloys (binary and multicomponent) the characteristics of microstructure are the most important for understanding their mechanical behavior. In the case of hypo-eutectic Al–Si alloys, the main influence upon strength and elongation is exerted by the morphology of silicon crystals in the eutectic. The more compact and disperse this eutectic is, the better level of tensile properties will be recorded in testing [11, 316]. This effect is well known in practice, when due to modification with sodium or strontium additions a more dispersed microstructure of eutectic colonies can be achieved.

In multicomponent industrial Al–Si alloys, in addition to the morphology of eutectic silicon particles, an important role belongs to the morphology of constituent particles, especially of the Fe-bearing ones. As in the case with eutectic silicon, increased level of dispersion of these particles attained due to

Table 4.6 Composition of excessive phases of solidification origin (constituent particles) present in microstructure of industrial 3xxx casting alloys

Phases	Concentrations of elements (mass %) (Al balance)							
	Si	Fe	Mn	Cu	Mg	Zn	Ni	Be
(Si)	~100	–	–	–	–	–	–	–
Al_5FeSi	12–15	24–28	<1	–	–	–	–	–
Al_8Fe_2Si	6–10	30–33	<1	–	–	–	–	–
$Al_{15}(Fe,Mn)_2Si$	8–13	0–31	1.5–29	–	–	–	–	–
Al_9FeNi	<4	4.5–14	–	–	–	–	18–28	–
$Al_8FeMg_3Si_6$	~33	~11	–	–	~14	–	–	–
Al_3Ni	–	–	–	–	–	–	~42	–
Al_6Cu_3Ni	–	–	–	47–51	–	–	12–12.5	–
$Al_3(Ni,Cu)_2$	–	–	–	22–31	–	–	24–34	–
$Al_4Be_5Fe_2$	<1	38–40	–	–	–	–	–	15–22
Al_8Fe_2BeSi	6–10	25–30	–	–	–	–	–	4–5
Al_2Cu	–	–	–	–	–	–	~52	–
Mg_2Si	37	–	–	–	63	–	–	–
$Al_5Cu_2Mg_8Si_6$	27–29	–	–	14–17	28–30	–	–	–

increased solidification rate and modifying effects, ensures increased characteristics of elongation in tensile testing.

In industrial casting alloys of the 3xx series several such phases can be present simultaneously, often 8–10 or even more. They all, to a different extent, affect mechanical properties of alloys. In Table 4.6, we provide the chemical composition of the most important phases in 3xx series casting alloys. As it can be seen, most of the alloying elements can enter several different phases with different morphology.

In terms of our ability to control their volume fractions and morphology, these phases could be divided into three groups:

1. Phases that could be dissolved in (Al) and coagulate during heating before quenching.
2. Silicon phase in eutectic, practically not changing its volume fraction during heating; however, it can be well spheroidized.

3. Phases that contain transition metals (Fe, Ni, Mn, Cr, etc.) that practically do not change its morphology in the course of any heat treatment.

In a given 3xx alloy its microstructure (in particular, the morphology of excessive phases of solidification origin) is defined, as usual, by the applied solidification rate. In Ref. [290] the equations of multiple linear regressions were obtained that related tensile mechanical properties with the following averaged microstructure characteristics of alloy AlSi7Cu4: total length of crossing eutectic crystals of silicon (K) by the sample plane; their shape coefficient, S – the ratio of particle width to length, the lineal size of the Fe-bearing particles (F); width of the particles of ternary eutectic $(\mathrm{Al}) + \mathrm{Si} + \mathrm{CuAl_2}$, ($T$); and the average size of dendritic cells of aluminum solid solution, d.

The obtained linear regression equations ($\sigma_{\mathrm{UTS}}, \sigma_{0.2}$ in MPa $\star\ 10^{-1}$; δ in %) were as follows:

$$\sigma_{\mathrm{B}} = 4.2 + 0.4K - 0.013F + 1.6T - 0.32d + 49.5S$$

$$\sigma_{0.2} = 8 + 0.265K - 0.175F + 0.64T - 0.077d + 21S$$

$$\delta = -2 + 0.004K - 0.019F + 0.96T - 0.11d + 8.6S$$

These linear equations can be considered as a qualitative illustration of the principle of additivity of influence of different microstructure parameters upon alloy's mechanical tensile properties.

When comparing the properties of chemically different Al–Si alloys that were solidified in approximately similar conditions, the difference in the levels of strength and plasticity (elongation) is again defined by the differences in microstructure. The strongest influence upon microstructure is exerted by the concentrations of silicon, magnesium, copper, and iron in a given alloy.

The role of silicon is well established [11]: as its concentration grows, the volume fraction of the (Al) + (Si) eutectic also grows. This is accompanied by improvement in castability and strength but reduction of elongation. The influence of copper and magnesium is related to several microstructural factors: the higher their content in 3xxx alloys, the higher the degree of alloying of aluminum solid solution will be. Also there will be more constituent particles of different phases ($\mathrm{Al_2Cu}$, Q, $\mathrm{Mg_2Si}$, etc.), and the eutectic microstructure becomes coarser. These alloying elements serve as the principal strengthening agents for 3xxx alloys, but at the same time exert negative influence upon alloy plasticity both in as-cast and heat-treated states. The degree of alloying of (Al), especially at small concentrations of copper (up to 1–2%) and magnesium (up to 0.2–0.3%) is, most probably, a more serious factor in comparison to the volume fractions of excessive phases of solidification origin.

4.2.2.3 The influence of substructure

As it was demonstrated in Chapter 2, the total dislocation density in aluminum alloy castings rather weakly depends upon alloy composition and conditions of its solidification. In as-cast condition the variations in dislocation density are of the order of $3 \times 10^8\ \mathrm{cm}^{-2}$ (industrial castings made of alloy

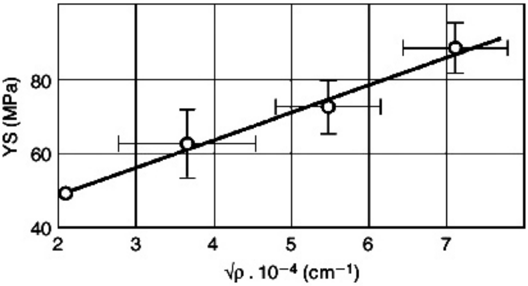

Figure 4.36 Dependence of conditional yield strength $\sigma_{0.2}$ of homogenized and weakly stretched alloy Al + 0.4% Cu upon dislocation density, ρ.

249.0 + 0.6%Mn + 0.2%Ti + 0.2%Cd cast into sand); 10^{10} cm^{-2} (rapidly solidified castings made of alloy Al + 10%Mg). In the quenched state these numbers are ~2 × 10^8–10^9 cm^{-2}. To establish the extent of influence of such dislocation density changes upon mechanical properties of castings is quite difficult because of the strong interference of such parameters as macro- and microstructure that change in parallel to dislocation density. To shed addition light upon this problem, additional special experiments were conducted.

Homogenized samples of alloy Al + 0.4%Cu and recrystallized after deformation samples of Al + 6%Mg and Al + 0.6%Cu with approximately the same grain size were all subjected to elongation by 1–5%. After that mechanical testing of these samples was conducted to obtain the values of yield strength and ultimate strength. Because of different degree of tensile deformation it was possible to create different dislocation densities in the samples that varied in the same limits as for castings. The formation of cell dislocation microstructure took place that was very close to that observed for cast Al–Cu alloys.

As a result, the dependencies of strength upon dislocation density ρ were obtained. One of these curves is shown in Figure 4.36. Yield strength, as always [317], linearly changes with $\sqrt{\rho}$. Its increase in the range of interest for dislocation density is quite substantial and is of the order of 80–100%. Ultimate tensile strength of all studied alloys (which characterizes resistance to a significant level of plastic deformation) and the final value of elongation practically did not depend upon dislocation density caused by weak preliminary work hardening.

Consequently, due to changes in dislocation density of alloys one could expect only insignificant changes in alloy resistance to small deformations, in particular, yield strength.

In the studied castings Al–Cu and Al–Mg of the same composition the difference in the overall dislocation density was insignificant (less than 3 × 10^9 cm^{-2}), and its influence even upon $\sigma_{0.2}$ could be safely ignored. After quenching, which reduces the density of dislocations and minimizes differences in alloy castings, the influence of dislocation density upon yield strength can be safely ignored. On the contrary, aging after casting without quenching must enhance the effect of such influence. This is well known from the practice of low-temperature thermomechanical treatment, for example, according to Ref. [166], plastic deformation of alloy 1201 sheet by 1–7% before artificial aging increases $\sigma_{0.2}$ by 27 MPa and σ_{UTS} by 35–55 MPa.

As it was demonstrated above, in cast aluminum–magnesium alloys the subgrain microstructure will be formed. The average subgrain size d′ decreases as the solidification rate becomes higher, and linearly depends upon the dendritic cell size d (see Figure 2.34). In binary alloys of aluminum with 3–9%Mg this relation is described by the following equation: $d' = 4 + 0.05d$. In turn, dendritic cell size for Al–Mg alloys is correlated to D. Consequently, the influence of grain and dendritic cell sizes upon mechanical properties of casting aluminum–magnesium alloys "includes", in a sense, the influence of the subgrain size as well. However, it is important to mention that in all studied samples the variation of d' takes place in relatively narrow limits from ~5 to ~10 μm when d changes by 400%. Such variation range for d' could change yield strength of Al–Mg alloys not more than 10–20 MPa (see Table 4.2). In as-quenched state the difference in subgrain size of Al–Mg castings is even smaller, and the influence of d' in this particular case could be safely ignored.

Mechanical properties of castings could be affected by the secondary precipitation of excessive phases. The possibility of their formation was considered in detail in Chapter 2. However, differences in the extent of decomposition of (Al), and in the morphology of decomposition products, with all other conditions being equal, do not seriously affect mechanical properties. This was established for alloys Al + 4%Mg + 3.5%Zn with different additions that caused very different changes in alloy strength after aging (see Table 2.13). Of course, differences in the number density and size of secondary precipitates that could be caused by different cooling rates of castings below the solidus temperature, must be quite substantial. However, in its pure form this effect is difficult to extract and quantify because changes in cooling rate results in the corresponding variations of all other microstructural parameters of castings.

Microstructure of quenched castings made of industrial aluminum alloys containing additions of transition metals contains dispersoids of the corresponding aluminides (first of all manganese) that are formed during isothermal heat treatment before quenching. The lineal sizes of manganese aluminides and interparticle spacing are usually of the order of 10^{-2}–10^{-1} μm and higher, so one should not expect that mechanical properties could be affected in any appreciable way. Indeed, as it follows from experiments with alloys 249.0 + 0.%8Mn + 0.2%Ti (on the basis of the Al–Cu system) and $AlMg_4Zn_{3.5}$, variations in temperature and time of the heat-up regimes before quenching, while significantly altering the morphology of Mn-bearing particles, practically does not affect the mechanical properties of quenched and aged castings (Table 4.7).

When a sufficiently large number of disperse Al_3Sc and Al_3Zr particles precipitate out of solid solution, the strengthening effect for aluminum alloys with additions of Sc and Zr becomes significant (see Chapter 6).

Table 4.7 The influence of heat-up regime before quenching upon mechanical properties of alloy AlMg$_4$Zn$_{3.5}$ before and after aging (110°C, 10 hours + 150°C, 16 hours)

τ (hours)	Quenched state			Aged state		
	$\sigma_{0.2}$ (MPa)	σ_{UTS} (MPa)	δ (%)	$\sigma_{0.2}$ (MPa)	σ_{UTS} (MPa)	δ (%)
Quenching temperature 525°C						
0.25	146	304	17.1	426	464	5.2
0.5	146	304	14.5	434	470	5.2
1.5	149	316	14.4	434	475	5.6
3	138	301	16.6	428	470	5.5
6	140	308	14.0	422	460	5.4
10	136	293	14.7	418	462	5.2
Quenching temperature 400°C						
1.5	138	280	16.6	352	389	3.6
5	151	311	17.7	383	419	4.5
10	152	315	15.9	405	444	4.5
16	147	307	14.4	413	458	4.9
24	154	319	12.6	414	454	5.3
36	151	296	10.4	417	463	5.2

Thus, tensile mechanical properties of as-cast and quenched aluminum alloys are mostly determined by the parameters of their macro- and microstructure. The fine aspects of aluminum solid solution microstructure in most cases are, most probably, of secondary importance for these properties.

Yield strength of castings before and after quenching is defined mostly by the average grain size and significantly changes when grains are refined to the sizes less than 1 mm. This can be clearly demonstrated for Al–Mg alloys (see Figures 4.34 and 4.35). However, if grain size varies in the range exceeding 1 mm, then yield strength in all studied alloys remains practically the same despite significant changes in microstructure. Apparently, relatively minor variations in the dislocation densities and small-angle boundaries do not affect the level of resistance to small deformations. The same is true with respect to pore size differences and different dispersoid particles (usually too coarse to have an impact upon dislocation glide in the very beginning of plastic deformation). As far as the weak influence

Table 4.8 Coefficients of regression ($b_0, b_1, \ldots, b_n$) in equations $y = b_0 + b_1x_1 + \cdots + b_nx_n$ relating mechanical properties of casting Al–Mg alloys to microstructural characteristics

Content Mg(%)	Property y	Regression coefficients								Λ (MPa or %)	F ratio
		$x_0 = i$	d (x_1)	D (x_2)	C^{α}_{Mg} (x_3)	m (x_4)	l (x_5)	Q_n (x_6)	Q_V (x_7)		
3, 6, 9	$\sigma_{0.2}$	5.44	–	−0.542	106	−5.17	−4.56	61.6	29.7	16.7	4.2
3		6.06	−0.6	−0.407	4360	–	−14.2	1100	–	11.9	6.9
6		5.99	–	−1.54	86.0	64.0	−0.621	−21.2	–	8.2	3.8
9		8.72	−111	−4.09	58.8	709	32.7	129	–	18.6	2.8
3, 6, 9	σ_B	2.0	−34.8	1.21	138	−917	−7.84	–	−44.8	41	2.7
3		25.1	45.2	−2.32	8385	–	−87.1	116	–	11.2	14.4
6		51.1	21.2	−2.50	−325	–	–	−214	−244	34	3.9
9		49.0	−223	–	881	−1820	108	–	288	40	4.2
3, 6, 9	δ	28.8	−38.8	−1.55	−110	−38.8	−136	–	−129	4.3	3.9
3		14.6	−101	−1.78	208	3400	–	340	–	3.1	3.9
6		4.57	−67.7	1.24	313	857	12.1	−510	–	6.6	1.7
9		−86.3	−108	3.66	1070	−1344	77.4	−223	370	3.0	2.7

of grain size is concerned, this is a well-known fact directly stemming from the Hall–Petch equation.

Ultimate strength and relative elongation of castings are to a significant extent defined by their microstructure. This could be explained by the connection existing between these properties (often characterizing resistance to fracture and material's ultimate ability to withstand deformation) and the number and size of the potential sources of crack initiation – inclusions of excessive phases and pores. If these sources are numerous and coarse, then smaller deformations will result in the nucleation and propagation of cracks.

Using aluminum–copper alloys as an example, one can see that even in quenched state, when non-equilibrium eutectic is completely (in alloys with 2 and 4.2%Cu) or almost completely (in alloy with 6%Cu) dissolved, a definitive connection exists between σ_{UTS} and δ, on the one side, and the average dendritic cell size in as-cast condition (see Table 4.5). This could be explained by the fact that d directly defines the size of shrinkage pores, which even after quenching remain larger in slowly solidified alloys with large values of d.

In hypo-eutectic Al–Si alloys and industrial alloys on the basis of the Al–Cu (249.0 + 0.8%Mn + 0.2%Ti, 249.0 + 0.6%Mn + 0.2%Ti + 0.2%Cd) and Al–Mg alloys (with increased concentration of impurities) the original dendritic cells after heat treatment practically do not change, because their grain boundaries are anchored by non-soluble Fe-and Mn-bearing constituents. For this reason the nature of hereditary influence of microstructure parameters in as-cast state is quite obvious.

Above, a connection existing between mechanical properties and microstructure was considered only for the cases of as-cast and quenched states. At the same time, many casting aluminum alloys, in particular on the basis of the Al–Cu, Al–Si–Mg, Al–Si–Cu–Mg, and other systems are subjected to artificial aging. Specifically designed experiments with these alloys demonstrated that the increase in strength with aging using the same regime is more or less similar provided the chemical composition of alloy remains the same, for different microstructures of castings in as-cast and quenched states.

For example, for Russian alloy VAL1 (Al + 6%Cu + 0.8%Mn + 0.15%Zr + 0.3%Ce) in quenched state $\sigma_{\mathrm{UTS}} = 32.9 - 0.149d$, while after aging $\sigma_{\mathrm{UTS}} = 37.4 - 0.144d$, that is only the value of the first coefficient changes. It characterizes the resistance to deformation inside dendritic cells. At the same time, the coefficient d remains practically constant. This happens because in castings with different original microstructure the distribution density of the products of aging is about the same in both cases (see Section 3).

4.2.3 Calculations of mechanical properties of castings using the totality of microstructural characteristics

Obviously, mechanical properties are defined by a number of microstructural parameters. For this reason, in principle, the most accurate calculations could be made using several most important microstructure parameters. Due to complexity of this microstructure in casting aluminum alloys the development of physics-based mathematical models is feasible only for a limited number of situations, as it will be demonstrated below. However, in order to obtain engineering equations giving a possibility to make such calculations with sufficient accuracy one could recommend the application of modern methods of statistical regression analysis.

Using experimental data on mechanical properties and different characteristics of microstructure for a number of alloys (partially described in the previous section), the following results were obtained: (1) equations relating properties of as-cast alloys to their as-cast microstructure; (2) universal equations of dependence of properties in different conditions (as-cast, quenched, after complete, and partial homogenization) upon microstructure before testing; (3) equations relating properties after heat treatment as a function of microstructure of as-cast alloys [309, 310, 312, 314, 318].

In Table 4.8, we provide the data on the coefficient of multiple linear regressions relating tensile properties of as-cast Al–Mg alloys to their microstructural characteristics. It is clear that these equations provide reasonable accuracy of prediction, although it is somewhat lower than the Hall–Petch equation (see Table 4.2). Most probably, this is due to strong nonlinear dependence of properties upon grain size.

For aluminum–copper alloys (studies were conducted for samples with $D > 1$ mm), when most microstructural parameters are linearly related to properties, the obtained regression equations were most accurate when several such parameters were used for calculations. Table 4.9 provides data for binary aluminum alloys with 2–6% of copper.

It was particularly interesting to develop predictive capability for mechanical properties of alloys in different tempers using just data on their original as-cast microstructure. The corresponding multiple regression equations are presented in Table 4.10. It can be seen that the accuracy of these equations is very high – mean quadratic error of calculations is just a bit higher than for a series of samples cut out of the same casting. It should be mentioned that all equations provided in Tables 4.8–4.10 were tested for data arrays not used for their derivation, a standard statistical practice. These "test" calculations demonstrated excellent "working properties" of the derived equations.

Figure 4.37 provides comparison of experimental results for strength of Al–Cu alloys to the predictions obtained using the following equation (see Table 4.9).

$$\sigma_B = 8 - 0.053d - 0.38Q_V + 0.096S - 0.3m + 0.225H_c + 0.097\Delta H$$

It can be seen that the results are in good agreement with experiment.

The most fundamental drawback of regression equations is in their very small scientific value – these equations do not give a possibility to assess the "true" contributions of different microstructure characteristics into mechanical properties. Such information in principle could be obtained using the methods of design of experiments and mathematical planning techniques [319]. However, in our case such prognostication techniques cannot be applied because all microstructural parameters are interrelated and cannot be set separately and independently.

Table 4.9 Coefficients of regression (b_0, $b_1, \ldots, b_n$) in equations $y = b_0 + b_1x_1 + \cdots + b_nx_n$ relating mechanical properties of Al–Cu castings on their microstructural characteristics

Content (Cu%)	Property y	Regression coefficients							Λ (MPa or %)	F ratio
		$x_0 = i$	x_1 (d)	x_2 (Q_V)	x_3 (S)	x_4 (m)	x_5 ($H_{\|\|}{}^a$)	x_6 (ΔH^b)		
2	$\sigma_{0.2}$	6.44	−0.00449	−0.0402	−0.0556	−0.173	0.0110	0.0149	8.8	1.4
6		14.5	−0.0145	−0.697	−0.00005	−0.048	0.0466	−0.0464	16.3	7.8
2, 4.2, 6		−0.668	−0.167	−0.266	0.0379	0.0812	0.167	0.0226	16.7	7.3
2, 4.2, 6		−1.61	–	–	–	–	0.169	–	17.7	6.4
2	σ_B	14.3	−0.0226	−5.70	0.339	−0.0836	0.0470	0.0489	15.8	9.7
6		32.7	−0.0798	−0.395	−0.668	−0.604	0.0472	0.0224	23.5	8.2
2, 4.2, 6		8.00	−0.0530	−0.380	0.0964	−0.301	0.225	0.0968	22.6	7.8
2, 4.2, 6		6.60	–	–	–	−0.432	0.212	–	32.5	3.8
2	δ	40.1	−0.111	−27.2	2.3	1.55	−0.0673	−0.108	3.93	4.1
6		24.0	−0.0520	0.135	−0.0969	−0.819	−0.0393	0.101	3.69	4.2
2, 4.2, 6		45.5	−0.0678	−0.659	−0.130	−0.551	−0.212	−0.0713	4.24	3.4
2, 4.2, 6		27.2	–	–	–	−0.671	−0.100	–	6.80	1.3

[a] H_c (10^{-1} MPa) – microhardness in the center of dendritic cells, proportional to C_c (and C^{α}_{Cu}).

[b] ΔH (10^{-1} Mpa) – difference of microhardness on the boundaries and in the center of dendritic cells, proportional to ΔC.

Table 4.10 Regression coefficients ($b_0, b_1, \ldots, b_n$) in equations $y = b_0 + b_1x_1 + \cdots + b_nx_n$ for dependence of mechanical properties of heat-treated Al–Cu alloys on microstructural parameters in as-cast state

Property y	Regression coefficients							Λ (MPa or %)	F ratio
	$x_0 = i$	x_1 (Q_V)	x_2 (S)	x_3 (m)	x_4 (d)	x_5 (H_c)	x_6 (ΔH)		
Al + (2/6)% Cu, temper T4[a]									
$\sigma_{0.2}$	3.48	−0.539	+0.171	1.22	−0.057	0.069	0.008	16.7	5.9
σ_u	18.4	−0.981	+0.280	0.962	−0.067	0.049	−0.126	27.5	4.5
δ	52.0	0.119	−0.186	−1.43	−0.051	−0.237	−0.213	4.24	3.5
HB	29.8	−12.8	11.98	15.0	−0.544	0.105	−0.063	95.8	5.2
VAL1, temper T4[b]									
σ_u	31.4	−0.758	+0.055	0.666	−0.133	–	–	12.8	5.8
δ	3.0	−1.60	−0.158	2.75	−0.153	–	–	2.09	3.1
VAL1, temper T6[c]									
$\sigma_{0.2}$	27.0	0.362	−0.048	−0.434	−0.040	–	–	10.8	1.0
σ_u	39.5	−0.600	0.027	0.914	−0.208	–	–	14.9	3.5
δ	−0.666	−1.08	0.118	1.86	−0.098	–	–	0.73	8.9

Work on alloy VAL1 was carried out in collaboration with Kolobnev, Aristova, and Altunina.

[a] Quenching $T = 540°C$, hold time 2–8 hours.

[b] Quenching $T = 540°C$, hold time 12 hours.

[c] Aging after quench at 175°C for 4 hours.

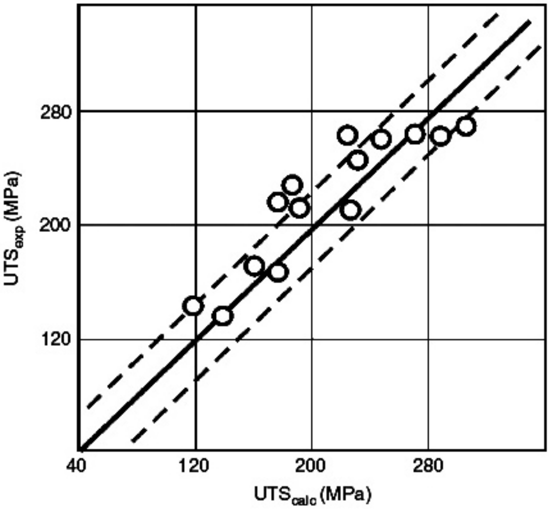

Figure 4.37 Comparison of calculated and experimental values of yield strength for alloys Al–Cu; Points correspond to control values; dashed line represents the boundaries of the corresponding probability range.

Physics-based models for metal properties as functions of the microstructure parameters are practically absent for casting aluminum alloys. However, in the previous section it was shown that in some particular cases, for example for as-cast and quenched alloys of the Al–Mg system, one could successfully apply the Hall–Petch model for single-phase microstructures $\sigma = \sigma_0 + K_y D^{-1/2}$. This model uses only one microstructure parameter – grain size. The model is applicable both to calculations of yield and ultimate strength for alloys with given chemical composition. If the magnesium concentration changes the values of σ_0, then K_y can also change substantially. This makes it difficult to obtain a single model for the description of different alloy concentrations. A notable exception from this rule is the model for $\sigma_{0.2}$ in as-cast state (see Table 4.2).

An effort was made to modify the Hall–Petch model by introducing into it a number of new parameters that would allow obtaining more universally applicable equations for calculation of different properties of castings from Al–Mg alloys with different composition. For that goal at first we studied the dependencies of σ_0 and K_y on magnesium concentration and the degree of residual information obtained at different levels of stress [312].

Experiments were conducted with binary alloys of aluminum with 1.5–12.5%Mg after quenching from 435°C (hold time 24 hours). As usual, each alloy was used to obtain a number of castings with different microstructure, in particular, with different grain size (0.13–2.8 mm). Using the tensile curves flow stresses σ_i were determined corresponding to 0.1%, 0.2%, 0.4%, 1.5%, and 10%

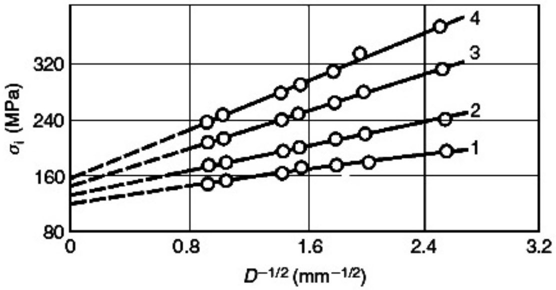

Figure 4.38 Dependence of conditional yield strength σ_I upon grain size D in alloy Al + 9%Mg at different degrees of residual deformation, %: 1–0.2%, 2–1%, 3–5%, and 4–10%.

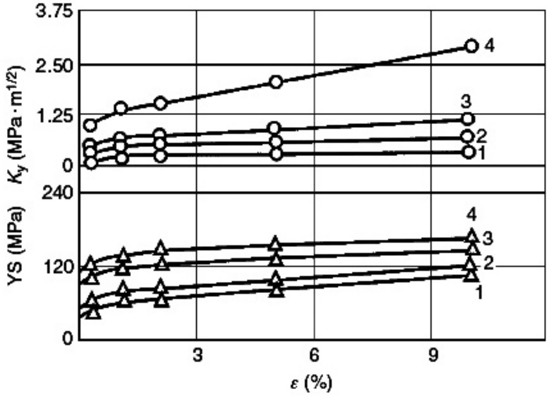

Figure 4.39 Dependence of σ_0 and K_c upon the degree of residual deformation ε in alloys of Al with 1.5%Mg (curve 1), 3%Mg (curve 2), 6%Mg (curve 3), and 9%Mg (curve 4).

residual deformation. Figure 4.38 presents the graphs in the $\sigma_i - D^{-1/2}$ coordinates that were used to estimate the parameter values σ_0 and K_y in the Hall–Petch equation. The dependencies of σ_0 and K_y on applied deformation and concentration of magnesium in aluminum solid solution C_{Mg}^{α} are presented in Figures 4.39 and 4.40.

As the applied strain grows (which was used to determine the flow stress), for all alloys the coefficients σ_0 and K_y also grow. The dK_y/de derivative grows with increased magnesium concentration. However, the value of $d\sigma_0/de$ weakly depends upon composition at $C_{Mg} = 9\%$ (Figure 4.39). When the concentration of magnesium in solid solution is increased up to 9%, the coefficients σ_0 and K_y grow at all degrees of residual deformation (Figure 4.40).

The physical interpretation of the coefficients σ_0 and K_y in the Hall–Petch equation is mostly based upon two models – the model of dislocation pile-up

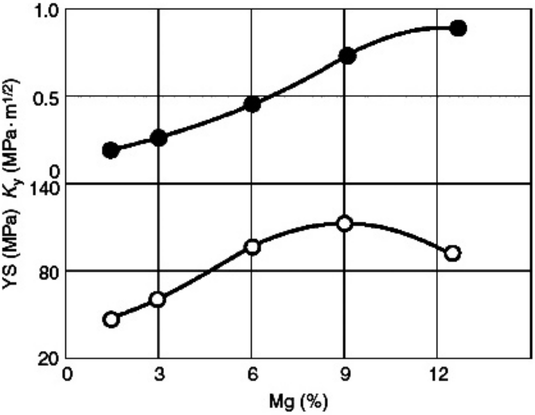

Figure 4.40 Dependence of σ_0 and K_c upon Mg concentration in (Al) for the degree of residual deformation equal to 0.2.

("forest dislocations") proposed in Refs. [320, 321] and the model of work hardening by Conrad *et al.* [308].

In both models the σ_0 parameter is considered as "friction stress" that characterizes resistance to dislocation motion inside the grains. For this reason σ_0 is very close to the value of yield strength or the flow stress of a single crystal. Hence growth of σ_0 as the degree of the (Al) alloying grows to 9%Mg, while the fall-off of σ_0 at $e = 0.1$–0.4% for alloys Al–12.5%Mg seems to be an anomaly (Figure 4.40). Growth of σ_0 with increased extent of deformation (Figure 4.39) is related to the continuous work hardening of the samples subjected to tensile testing. The value of $d\sigma_0/de$ must grow with alloying of (Al) because it is defined by the work hardening coefficient of a single crystal of the corresponding chemical composition. However, in binary alloys this growth becomes noticeable only for alloy containing 12%Mg (Figure 4.39).

The interpretation of K_y is more difficult and varies for the models of dislocation pile-up and work hardening. The obtained experimental data on the influence of magnesium concentration and the extent of residual deformation upon K_y could be easier explained if the second model is used. The required assumption is that for each alloy composition and flow stress (i.e., a certain applied strain) there exists a certain relation between the densities of dislocations for samples with different grain size [308].

Knowing the dependence of the Hall–Petch equation coefficients on concentration of magnesium in (Al) and the extent of residual deformation (Figures 4.39 and 4.40) it becomes possible to take into account the degree of alloying when deriving the equations connecting flow stress at different grain sizes for alloys of different chemical composition. This was done, for example, for yield strength of as-cast and quenched alloys 536.0 and 585.0, containing 6–10%Mg and different alloying additions and impurities [314].

As a result, σ_0 and K_y in the Hall–Petch equation can be replaced by their concentration functions (Figures 4.39 and 4.40) for all industrial Mg-bearing casting alloys, and it becomes possible to obtain a universal equation connecting their yield strength in as-cast and quenched state, to the average grain size and alloying of solid solution:

$$\sigma_{0.2} = 6.2 + 65\,C^{\alpha}_{\mathrm{Mg}} + 1/\sqrt{D}(38\,C^{\alpha}_{\mathrm{Mg}} - 1)$$

This equation ensures that the mean square error of calculations does not exceed ±15 MPa.

Taking into account the degree of (Al) alloying also increases accuracy of calculations of σ_{U} using the values of D for quenched castings out of industrial magnesium bearing casting alloys (see Table 4.3). The equation provided below ensures the mean quadratic error of calculations within the limits of ±33 MPa, instead of ±61 MPa when taking into account only grain size:

$$\sigma_{\mathrm{B}} = 2.3 - 163C^{\alpha}_{\mathrm{Mg}} + 1/\sqrt{D}(149C^{\alpha}_{\mathrm{Mg}} + 5.4)$$

The obtained relations between mechanical properties and different microstructural characteristics could find direct practical application when solving a number of important problems. For example, one could use microstructure data to assess the level of mechanical properties in any cross-section, including those positions where sample for mechanical testing simply cannot be cut out.

If it becomes possible to calculate the level of mechanical properties after heat treatment using just as-cast microstructure, this would allow revealing dangerous spots in castings where one should expect the minimal values of these properties, possibly not satisfying certain customer specifications. Furthermore, such equations help evaluate mechanical properties of castings on the early stage of their design. For that end, one could compute the cooling rate in different positions in castings (see e.g., Ref. [322]), then – microstructure parameters, and finally – mechanical properties.

4.2.4 The influence of casting microstructure upon fracture toughness and fatigue properties

In the last years the quality of castings is more and more often evaluated using characteristics of resistance to cracking (this is, first and foremost, fracture toughness K_{Ic}) and fatigue. These properties, as well as tensile properties, can vary in a broad range depending upon alloy's composition and microstructure.

Resistance of a given material to cracking characterizes its ability to arrest the propagation of cracks and their development. Fracture toughness, which is often evaluated as the critical stress concentration coefficient in plane strain conditions K_{Ic}, defines the level of stress at a certain distance from the crack front, at which its rapid unchecked propagation commences [323]. Fracture toughness testing is conducted using samples with a notch and a fatigue crack, which are loaded according to one of the several standard modes (e.g., in bending).

Fracture toughness K_{Ic} of casting aluminum alloys varies in the range from 7–8 to 50 MPa m$^{1/2}$ (Table A.5.1, Appendix 5.1, Table 4.11 and 5.12). As usual, the maximal values of fracture toughness are obtained for materials that display high plasticity under the conditions of static loading (with relative elongation more than 10–15%). Minimal values are typical for brittle samples (with elongation less than 1–2%). At intermediate levels of plasticity that is typical for most aluminum alloys, fracture toughness has a more complex relation to elongation, because it is also defined by the strength characteristics.

Numerous efforts to establish correlations between fracture toughness and a number of other mechanical properties of aluminum alloys ($\sigma_{0.2}$, σ_{UTS}, δ, and others) have not been successful as yet. The established rules are all of a very particular nature. For example, it is known [324] that for most wrought aluminum alloys, as well as for many steels and titanium alloys, fracture toughness decreases as the yield strength and ultimate strength grow. However, for industrial 3xx alloys and other casting alloys containing large volume fraction of excessive phases (and, correspondingly, possessing low ductility and elongation) this dependence is of quite opposite nature (Figure 4.41). In these alloys increased strength, at approximately the same level of elongation, actually enhances resistance to cracking.

Table 4.11 demonstrates this complex nature of dependence of fracture toughness upon other tensile properties for hypo-eutectic Al–Si alloys with 8%Si.

The lack of a clear connection between crack resistance and other mechanical properties, for which dependencies upon composition and microstructure have already been established, makes researchers conduct direct search for such regularities.

In aluminum, practically all alloying elements and impurities are dissolved via the mechanism of substitution, and the concentration of solid solutions weakly affects fracture toughness. For example, single-phase alloys solid solutions Al–Mg–Zn quenched after casting have a range of K_{Ic} from 28 to 33 MPa m$^{1/2}$, while concentration of zinc and magnesium varies from 3% to 7% each.

On the other hand, fracture toughness is very strongly affected by additions and impurities that cause the formation of excessive phases. As a rule, when concentration of such elements grows, fracture toughness becomes smaller. For this reason increased purity of aluminum with respect to low-soluble impurities (iron, nickel, silicon in non-3xx alloys) and decreased level of their alloying is the principal direction leading to increased crack resistance of aluminum alloys.

In most cases alloying affects resistance to cracking via microstructure modifications: changes in grain size and shapes, parameters of dislocation microstructure, volume fraction and sizes of constituent particles, etc.

Even more significant effect upon microstructure parameters can be obtained when the conditions of solidification and heat treatment are varied. Let us consider briefly the influence of different microstructure parameters upon fracture toughness.

Table 4.11 Fracture toughness and tensile mechanical properties of Al–Si alloys containing 8%Si in different tempers

Alloy	Condition (temper)		K_{Ic} (MPa m$^{1/2}$)	σ_B (MPa)	$\sigma_{0.2}$ (MPa)	δ (%)
$AlSi_8$	nm[a]	–	16	150	87	9
	bo	T4	18	160	64	22
	nm	–	17	110	70	4
	mo[a]	T4	18	130	63	10
	m[a]	–	24	170	83	20
	bo[a]	T4	27	170	63	25
	m	–	22	140	60	20
	bo	T4	24	150	60	27
$AlSi_8Mg_{0.3}$		–	18	190	155	4
	nm	T4	25	225	145	6
	bo	T6	30			
		T7	28			
$AlSi_8Cu_3$		–	21	220	185	4
	nm	T4	27	250	185	6
	bo	T6	31			
		T7	25			
$AlSi_8Cu_3Mg_{0.8}$		–	21	235	220	2
	nm	T4	25	340	240	6
	bo	T6	28			
$AlSi_8Cu_3$[b]		–	19	210	175	1
	nm	T4	25	310	250	2
	bo	T6	25	365	340	1.5
		T7	28	310	220	2.5

[a] nm: non-modified; m: modified; bo: cooling rate ~400 K/min; mo: cooling rate ~10 K/min.

[b] Composition of alloy $AlSi_8Cu_3$, in %: 8Si; 3Cu; 0.3Mo; 1Fe; 0.4Mn; 0.2Ni; 0.4Zn; 0.05Sn; and Pb.

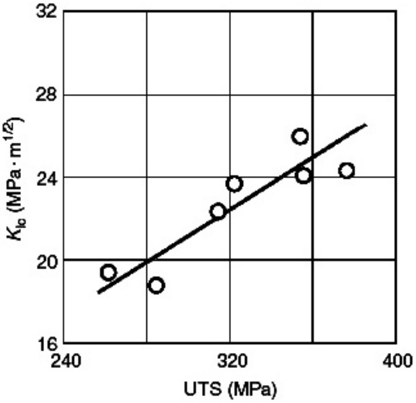

Figure 4.41 Dependence of fracture toughness K_{1c} upon yield strength $\sigma_{0.2}$ of casting aluminum alloys with a large volume fraction of eutectic.

According to existing experimental data, grain size is not uniquely connected to fracture toughness. In castings its influence in pure form is particularly difficult to reveal because the factors capable of changing grain size (e.g., solidification conditions) also affect other microstructural characteristics. In single-phase materials grain refinement must increase crack resistance. However, casting aluminum alloys always contain excessive phases, and in their presence the influence of grain size to a significant extent will be defined by the distribution of such particles on grain boundaries and inside the grains.

Dislocation structures existing inside grains in castings, as it was demonstrated in Chapters 2 and 3, do not change substantially enough to affect the level of material resistance to cracking. In the general case the influence of dislocation density upon fracture toughness will be defined by the absolute values of this density in compared materials, and also by immobilizing effects of dislocation pinning on the solute atmospheres (Cottrell effect) and constituents. As long as increased dislocation density, enhancing material hardening, does not result in significant reduction of its ability to deformation, fracture toughness will be growing. However, if the introduced dislocations are locked via different mechanisms and result in embrittlement of alloy material, then its ability to withstand cracking for obvious reasons will be going down.

Excessive phases exert a very strong influence upon fracture toughness of casting alloys. If their volume fraction in the matrix is increased, this always results in deterioration of crack resistance. Unlike other mechanical properties of polished samples, K_{Ic} depends very strongly not only upon disperse secondary particles forming in the course of decomposition of (Al), but rather, upon the presence or absence or the relatively coarse (of the micrometer size) particles of brittle intermetallic phases or particles of eutectic origin.

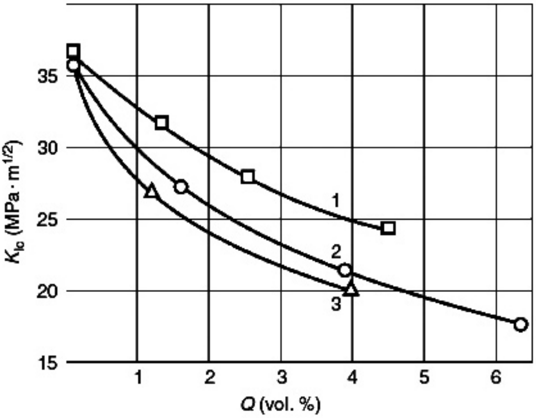

Figure 4.42 Dependence of fracture toughness K_{1c} for alloy Al + 7%Mg + 3%Zn upon volume fraction Q of excessive phases: 1 – $FeAL_3$, 2 – T (Al,Mg,Zn,Cu), and 3 – Mg_2Si.

Figure 4.42 illustrates how fracture toughness decreases when the volume fraction of excessive eutectic phases increases in quenched state (after casting) for alloy $AlMg_7Zn_3$. The extent of influence of different phases is defined mostly by particle morphology – the more compact and close to spherical these particles are, the smaller decrease in crack resistance. If, for example, the morphology of iron-bearing phases changes from needles of Al_3Fe to the ternary phase $Fe_2Al_4Be_5$ due to modification with beryllium, then fracture toughness of alloy $AlMg_7Zn_3$ can be almost completely restored to the level of alloy prepared out of pure aluminum (less than 0.01%Fe). This result is quite significant.

Disperse "secondary" products of the aging process also exert substantial influence upon resistance to cracking. In the course of aging fracture toughness of aluminum alloys typically goes down, especially when tempers of the T6 type are used (for maximal strength). This process is accompanied by the formation of metastable phase particles, partially coherent to the matrix. In this case the level of internal stresses attains the maximal value, ability of material to withstand deformation falls, and cracks nucleate and propagate easily. However, after overaging fracture toughness is significantly higher.

The influence of aluminum alloy casting microstructure upon their fatigue strength is not studied systematically. In a number of cases the general trend for this property is the same as for crack resistance.

As for many other materials, fatigue resistance increases in concert with strength and plasticity. There are several facts, however, that illustrate the "anomalous" influence of microstructure upon fatigue. For example, non-modified 3xx series alloys with coarse eutectic microstructure (large distances among silicon particle in the samples) possess lower resistance to high cycle fatigue than modified alloys [11].

Table 4.12 Chemical composition of the studied samples

Number of alloy	Alloy type	Concentration (mass %)									
		Si	Cu	Zn	Ni	Mn	Mg	Zr	Cr	Ti	Fe
1	AA354	9	1.8	<0.1	–	<0.1	0.5	–	–	<0.2	<0.2
2		<0.1	–	–	5	–	–	0.6	0.6	–	<0.1
3	AlZn6Ni4	<0.1	1	6	4	–	2	–	0.15	–	<0.1
4	AA206	<0.1	4.6	–	–	0.25	0.3	–	–	0.2	<0.1
5		<0.1	3	–	–	1.5	–	0.5	0.5	–	<0.1
6		<0.1	5	–	–	1.2	–	0.4	0.4	0.1	<0.1
7	249.0 + Mn + Ti + Cd	<0.1	5	–	–	0.7	0.2Cd	–	–	0.2	<0.1

In general, fatigue properties of aluminum castings are much lower than for wrought semi-fabricated products. This is due to the presence of different defects relating to casting process (pores, coarse intermetallic constituents). Table 5.10 presents the data on the limit of high cycle fatigue for aluminum alloys; usually it is not better than 70–90 MPa after 10^7 applied cycles.

Data on low cycle fatigue of casting aluminum alloys is scant and insufficient. The work [323] was one of the first attempts to study such properties in the temperature range from room temperature to 250°C for aluminum alloys of different systems with different types of microstructures. As can be seen from Table 4.12, seven alloys were studied: A354 (copper-bearing Al–Si alloy); A206 on the basis of the Al–Cu system; Russian high-strength casting alloy 249.0 + 0.6%Mn + 0.2%Ti + 0.2%Cd, also on the basis of the Al–Cu system; and four experimental compositions exhibiting high levels of static tensile mechanical properties and/or thermal stability.

Alloys 1–3 (Table 4.12) are of the hypo-eutectic type, with a large amount of eutectic, the remaining alloys # 4–7 possess microstructure mostly comprised of aluminum solid solution (Al) with a small amount of non-equilibrium eutectic in as-cast state, which could be dissolved in the course of heating before quench. All samples were machined out of heat-treated rods with diameter 22 mm and length 290 mm; the width of the sample working part was 8.5 mm and length 77.7 mm. Testing was conducted according to the scheme of cycling loading with the asymmetry coefficient of the cycle $R = 0.1$, applied frequency 10 Hz at temperatures 20°C, 150°C, and 250°C. The maximal applied stress at every cycle was constant and equal to 250 MPa. The main result obtained from each test was fatigue life – the total number of cycles to sample fracture at the applied $\sigma_{\max}$.

Table 4.13 The results of fatigue tests

Alloy number	Number of cycles to fracture					
	Sample number	$T_{\text{test}} = 20°\text{C}$	Sample number	$T_{\text{test}} = 150°\text{C}$	Sample number	$T_{\text{test}} = 250°\text{C}$
1	1–1	51 500	1–5	90 000	1–9	Fracture at $\sigma =$ 214/250 MPa
	1–2	28 440	1–6	103 000	1–10	
	1–3	59 300	1–7	45 800	1–11	
	1–4	73 500	1–8	68 000	1–12	
	1–1C	3 222 800	1–3C	176 000	1–5C	1300
	1–2C	153 700	1–4C	145 200		
	Average 53 185		Average 76 700			
2	2–1	8200	2–2	Fracture at $\sigma = 133$ MPa	2–3	Fracture at $\sigma = 140$ MPa
3	3–1	7800	3–3	25 400	3–5	Fracture at $\sigma = 140$ MPa
	3–2	5800	3–4	28 000		
4	4–1	45 800	4–5	51 300	4–7	Fracture at $\sigma = 240$ MPa
	4–2	47 400	4–6	47 600		
	4–3	47 600	4–7	46 800		
	4–4	35 600	4–8	29 200	4–8	Fracture at $\sigma = 246$ MPa
			4–9	20 500		
	Average 44 100		Average 39 080			
5	5–1	Fracture at $\sigma = 163$ MPa	5–2	Fracture at $\sigma = 133$ MPa	5–3	Fracture at $\sigma = 140$ MPa
6	6–1	29 500	6–2	3100	6–3	Fracture at $\sigma = 140$ MPa
7	7–1	4300	7–2	40 100	7–3	Fracture at 1st cycle

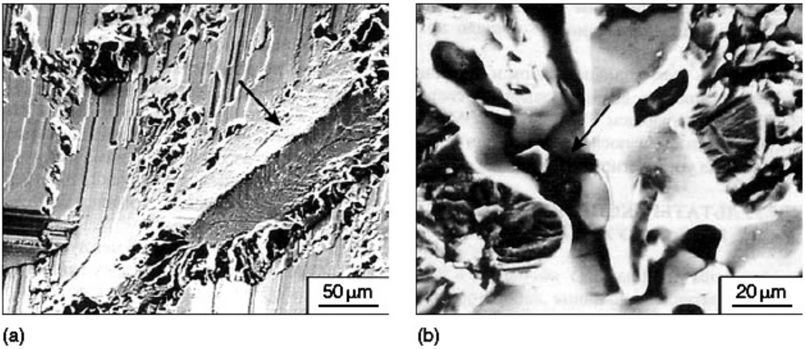

Figure 4.43 Fracture surfaces for alloy AA354 in direct vicinity of the point of fracture origination after fatigue testing at room temperature, SEM: (a) nucleation of crack near oxide inclusion, and (b) shrinkage pore (indicated by arrows), which served as crack initiation site.

Table 4.13 generalizes the results of these tests. It is clear that the highest fatigue life was established for two alloys AA354 and AA206 (1 and 4 in Table 4.12) with different types of microstructures. All other alloys were inferior in their fatigue performance.

The most detailed data was obtained for alloy AA354 (see Appendix 1). In addition to laboratory samples of this alloy, samples machined out of industrial castings were analyzed and tested (index "*C*" in Table 4.13). These industrial samples exhibited much better fatigue performance than their laboratory counterparts. Even at 250°C they sustained 1300 cycles before fracture at a relatively high value of $\sigma_{\max} = 250$ Mpa. Apparently, this is related to a higher purity of molten metal and lower porosity of industrial castings. Fractography analysis showed that fatigue cracks formed mostly near oxide patches (Figure 4.43a) and pores (Figure 4.43b). The overall number of such defects in industrial alloys was much smaller.

There is a clear connection between fatigue life of samples and the presence of oxide patches in industrial castings. When such defects were absent the number of sustained cycles was maximal, while the presence of large patches sometimes caused sharp (up to 10 times) reduction in fatigue life.

The extent of such influence of oxides upon fatigue life is even higher than of chemical composition and microstructure.

Nevertheless, microstructure of alloy AA354 does exert some influence upon resistance to low cycle fatigue. It was established that modifying significantly reduces fatigue life expectancy. Figure 4.44 represents microstructures of the studied industrial castings made of alloy AA354, which were obtained using modification of molten metal with strontium and without it. It is clear that the silicon crystallite size in modified eutectic is considerably smaller than without additions of strontium. Such disperse microstructure significantly improves the characteristics of strength and plasticity in static mechanical testing [66, 67]. The reduction of resistance to low cycle fatigue, at a first glance looks like an anomaly, as in

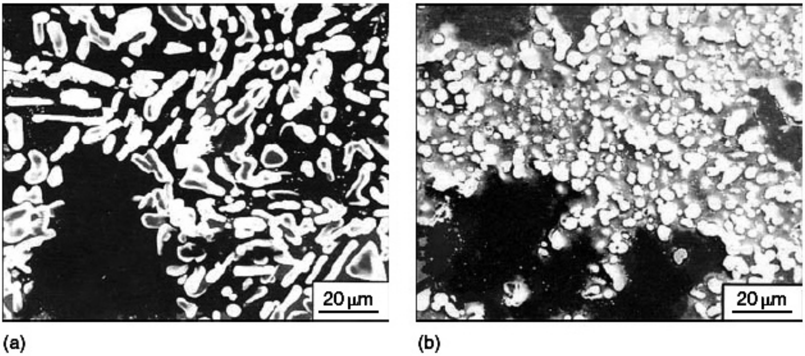

Figure 4.44 Microstructure of commercial casting made of alloy AA354 after quenching and aging in the T6 temper (SEM): (a) without modifiers, and (b) with additions of Sr.

the case of the already mentioned high cycle fatigue [11]. Assuming that modification does not introduce any changes except refinement of the eutectic, one could speculate that a possible reason for the observed effect was related to large width of "ductile" layers of aluminum solid solution between the crystals of brittle silicon in non-modified alloy. This, in turn, might reduce the rate of fatigue crack propagation and, correspondingly, improved fatigue life expectancy.

In the samples of other alloys crack nucleation was also noticed close to the surface and is often related to the presence of non-metallic inclusions (oxides) or casting porosity. This supports an assumption about the mechanism of fatigue-caused failure, according to which the principal factor is the size of defects and their number density, while microstructure plays only a secondary role.

It follows from Table 4.13 that two other alloys with large amount of the (Al) + $NiAl_3$ eutectic at room temperature have low cycle fatigue properties inferior to alloy AA354. In the case of experimental Al–Ni–Zr–Cr alloy #2 with high thermal stability (see Table 4.12) this could be easily explained: at room temperature it possesses relatively low strength $\sigma_{0.2} = 250$ MPa, $\sigma_{UTS} = 300$ MPa, while for alloy AA354 these characteristics are some 70–80 MPa higher. Consequently, at $\sigma_{max} = 250$ MPa alloy #2 has low fatigue life expectancy.

High-strength alloy #3 of the Al–Zn–Ni–Mg–Cu system is much stronger than AA354. At room temperature its yield strength and ultimate tensile strength are $\sigma_{0.2} = 480$ and $\sigma_{UTS} = 540$ MPa, respectively. However, its elongation is small ($\delta = 3/4\%$). Both high strength and low elongation could be explained by the properties of the matrix phase – aluminum solid solution with numerous products of its decomposition during aging. Probably, the development of fatigue cracks in such a matrix (less ductile and strained) is facilitated compared to alloy AA354. It is this fact that defines low fatigue life at low cycle loading for the casting alloy $AlZn_6Ni_4$. It should also be mentioned that the high cycle fatigue limit for alloy AA354 ($\sigma_{-1} = 130$ MPa) is somewhat lower than for $AlZn_6Ni_4$ ($\sigma_{-1} > 160$ MPa).

Out of alloys 4–7 (see Table 4.12) on the basis of the Al–Cu–Mn system alloy AA206 is studied in greatest detail. The results obtained for all other alloys should be considered as preliminary, because fatigue life was estimated for all of them using only one sample.

At room temperature fatigue life of alloy AA206 turned out to be somewhat lower than for AA354, which was cast in identical laboratory conditions – the difference in average values was ~20%. However, the results of static mechanical testing for AA206 are much better: $\sigma_{0.2} = 350/400$ MPa, $\sigma_{\mathrm{UTS}} = 440/460$ MPa at $\delta = 6\%$, while for alloy AA354 $\sigma_{0.2} = 280$ Mpa, $\sigma_{\mathrm{UTS}} \equiv 380$ MPa at the same level of elongation. This difference in properties could be explained by the peculiarities of alloys' microstructures. Firstly, alloy AA206 has a much broader solidification range and contains a significant number of shrinkage pores. Secondly, the level of plasticity of its matrix – decomposed (Al) – is probably lower than for AA354. Thirdly, the spheroidized particles of silicon forming after heat treatment can effectively retard the development of fatigue cracks in alloy AA354. In the case of AA206 such obstacles are simply absent.

Now let us consider fatigue life expectancy of the studied alloys at $T = 150$°C. For laboratory samples of AA354 it was appreciably higher than at room temperature. Similar effect was observed for alloys 3 ($AlZn_6Ni_4$) and 7 (AA249.0 + Mn + Ti + Cd). In all other cases, as could be seen from Table 4.13, an opposite picture was observed. It is interesting that for industrial alloys made of AA354, unlike for laboratory samples, some reduction of fatigue life also took place as compared to testing at room temperature.

This effect could be related to the different number of casting defects (pores and non-metallic inclusions) in laboratory and industrial castings. However, unequivocal explanation of the difference of the temperature influence upon fatigue properties for different alloys cannot be given at this time.

Table 4.13 demonstrates that the value of $\sigma_{\max} = 250$ MPa was too high for temperature 250°C: all samples made of laboratory castings were fractured already in the process of static loading at stresses lower than 250 MPa. Only one sample made of industrial casting of alloy AA354 could sustain the application of a small number of cycles (1300). It should also be noted that the maximal level of stress causing fracture at 250°C was documented for alloys on the basis of the Al–Cu–Mn system (#4 and #7, see Table 4.13). This agrees well with the data on the increased thermal stability of this alloy.

4.2.5 Some regularities in changes of mechanical properties with alloy chemical composition

The principal schematic of dependence of strength and elongation on composition of quenched and aged binary aluminum alloys of the eutectic type is shown in (Figure 4.45). In the domain of aluminum solid solution strength goes up, while the characteristics of plasticity go down. When the alloying element concentration exceeds the point of maximum solubility C_a, the characteristics of plasticity continue declining, while strength behavior becomes more

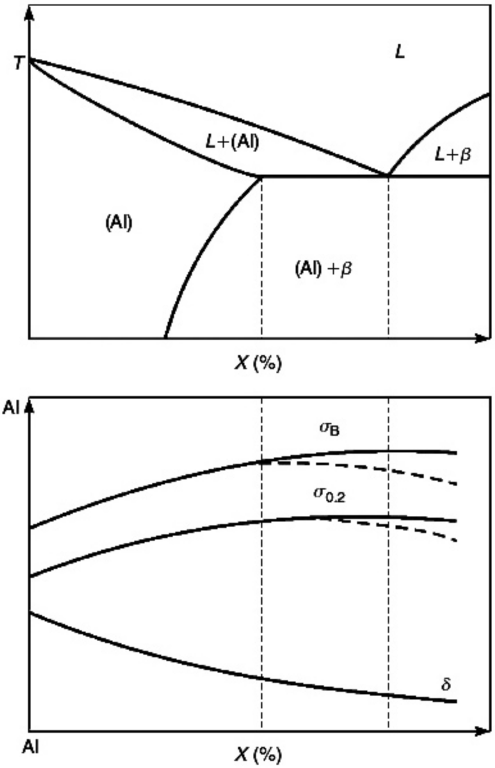

Figure 4.45 Schematic for dependence of tensile mechanical properties ($\sigma_{0.2}$, σ_B, and δ) on composition of quenched and aged alloys of the binary eutectic type.

complex: yield strength typically continues to go up; however, when elongation falls substantially, it can also start decreasing. The probability that ultimate tensile strength can decrease for alloys with large amounts of eutectic (especially at low solidification rates) is even higher (see dashed lines for concentration dependencies of σ_{UTS} and $\sigma_{0.2}$).

In the original as-cast state the dependencies of mechanical properties upon composition are even less predictable, but in most cases they are qualitatively analogous to the ones presented in Figure 4.45. As in a heat-treated state, the characteristics of strength grow with increased alloying, while plasticity goes down due to the increased concentration of alloying elements in (Al) and increased volume fraction of the brittle phases of eutectic origin.

Complex nature of these dependencies of mechanical properties upon composition even in binary alloys becomes more difficult to understand in the case of real industrial alloys containing impurities. Figures 4.46–4.59 represent concentration

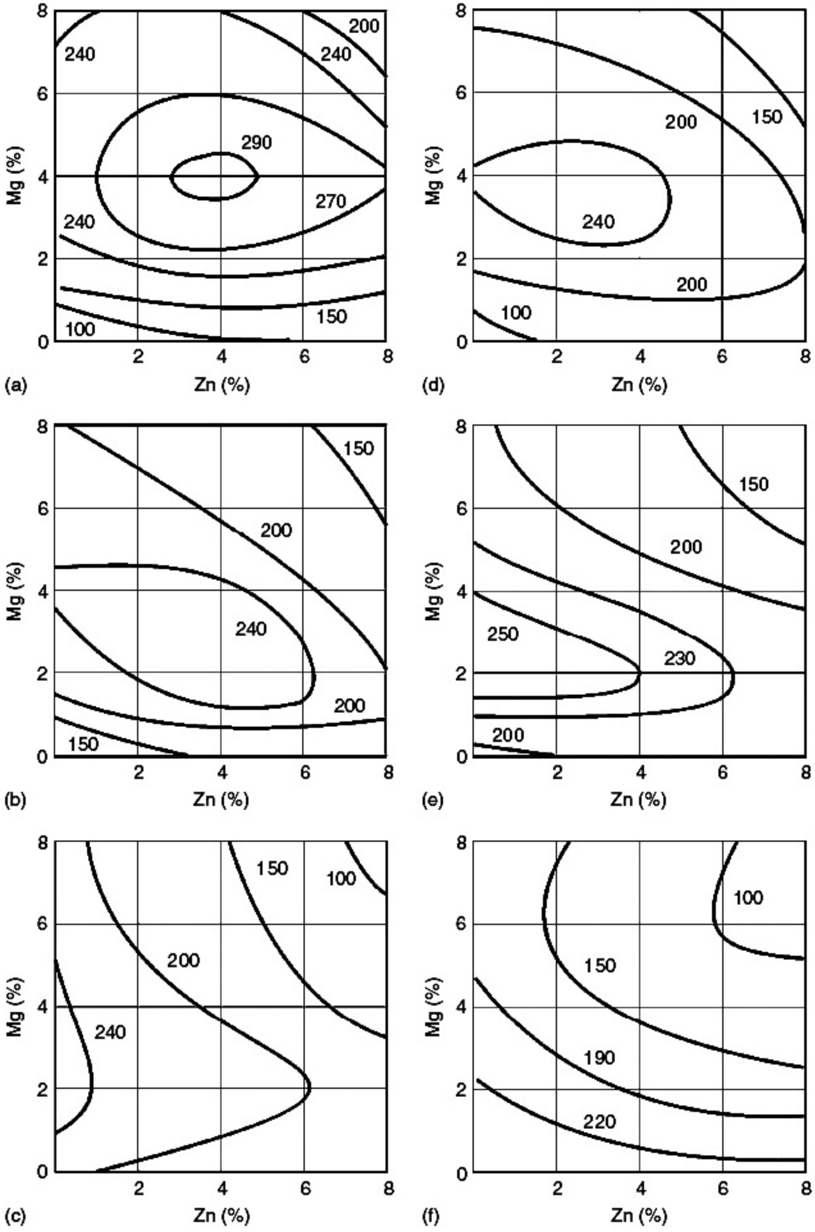

Figure 4.46 Iso-strength lines for σ_b as functions of composition for casting alloys Al–Zn–Mg–Cu–Fe–Si: (a) at 0%Cu, Fe, and Si; (b) at 2%Cu, 0%Fe and Si; (c) at 4%Cu, 0%Fe and Si; (d) at 0%Cu, 0.5%Fe and 0.5%Si; (e) at 2%Cu, 0.5%Fe and 0.5%Si; (f) at 4%Cu, 1%Fe and 1%Si (all alloys were cast out of Al99, which contains fraction of a thousandth of % of all impurities).

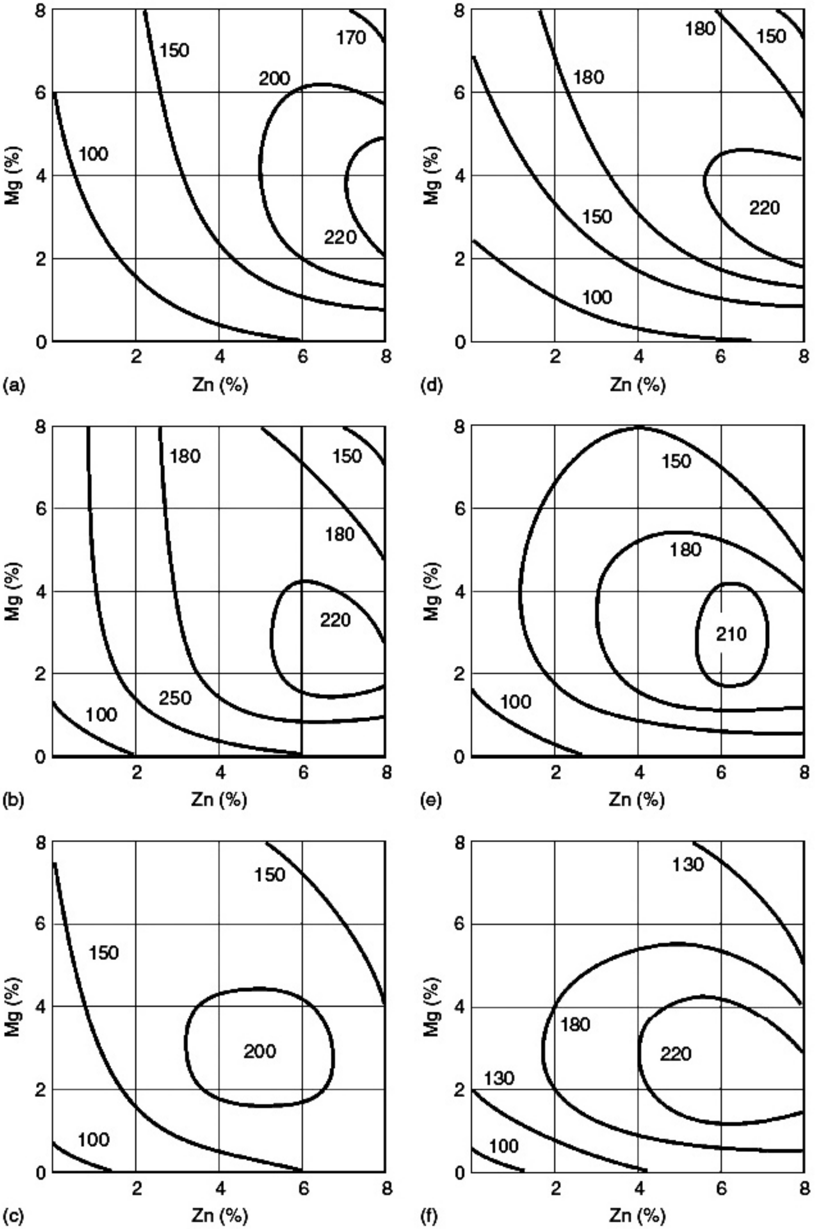

Figure 4.47 Iso-strength lines for $\sigma_{0.2}$ as functions of composition of casting alloys Al–Zn–Mg–Cu–Fe–Si: (a) at 0%Cu, Fe, and Si; (b) at 2%Cu, 0%Fe, and 0%Si; (c) at 4%Cu, 0%Fe, and 0%Si; (d) at 0%Cu, 0.5%Fe, and 0.5%Si; (e) at 2%Cu, 0.5%Fe, and 0.5%Si; and (f) at 2%Cu, 1%Fe, and 1%Si.

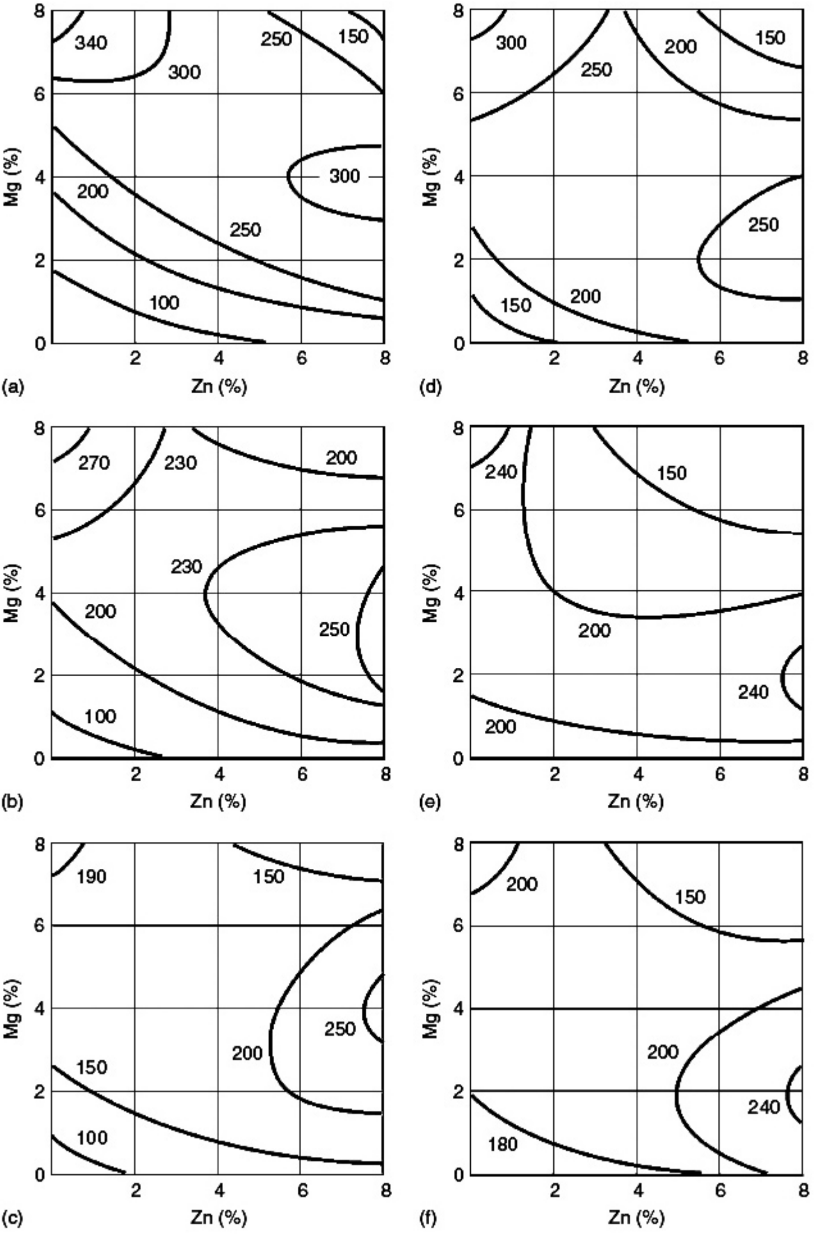

Figure 4.48 Iso-strength lines $\sigma_{0.2}$ as functions of composition for casting alloys Al–Zn–Mg–Cu–Fe–Si: (a) at 0%Cu, Fe, and Si; (b) at 0%Cu, 0.5%Fe and 0.5%Si; (c) at 0%Cu, 1%Fe and 1%Si; (d) at 2%Cu, 0%Fe, and Si; (e) at 2%Cu, 0.5%Fe, and 0.5%Si; (f) at 2%Cu, 1%Fe and 1%Si.

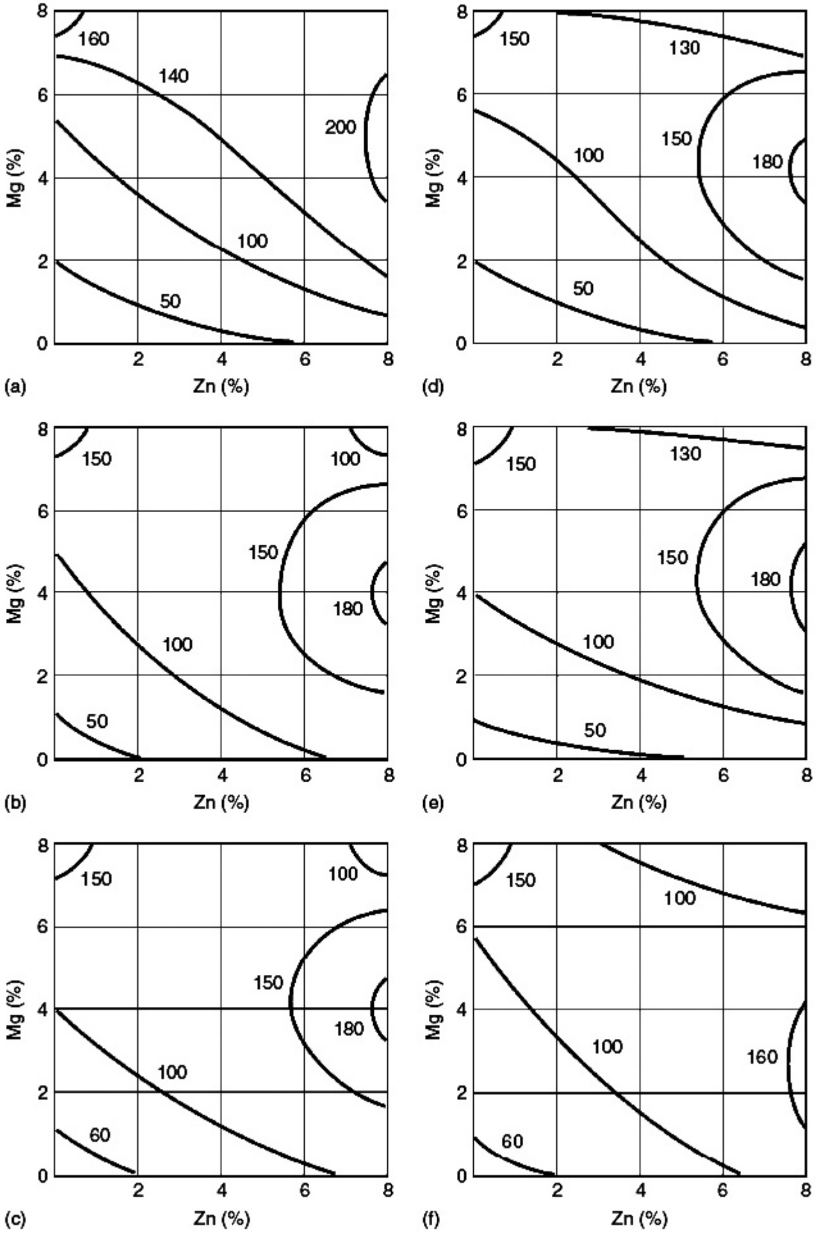

Figure 4.49 Iso-lines for $\sigma_{0.2}$ as functions of composition for quenched alloys Al–Zn–Mg–Cu–Fe–Si: (a) at 0%Cu, Fe, Si; (b) at 2%Cu, 0%Fe, and Si; (c) at 2%Cu, 1%Fe, and и 1%Si; (d) at 0%Cu, 0.5%Fe, and 0.5%Si; (e) at 0%Cu, 1%Fe, and 1%Si; and (f) at 4%Cu, 0.5%Fe, and 0.5%Si.

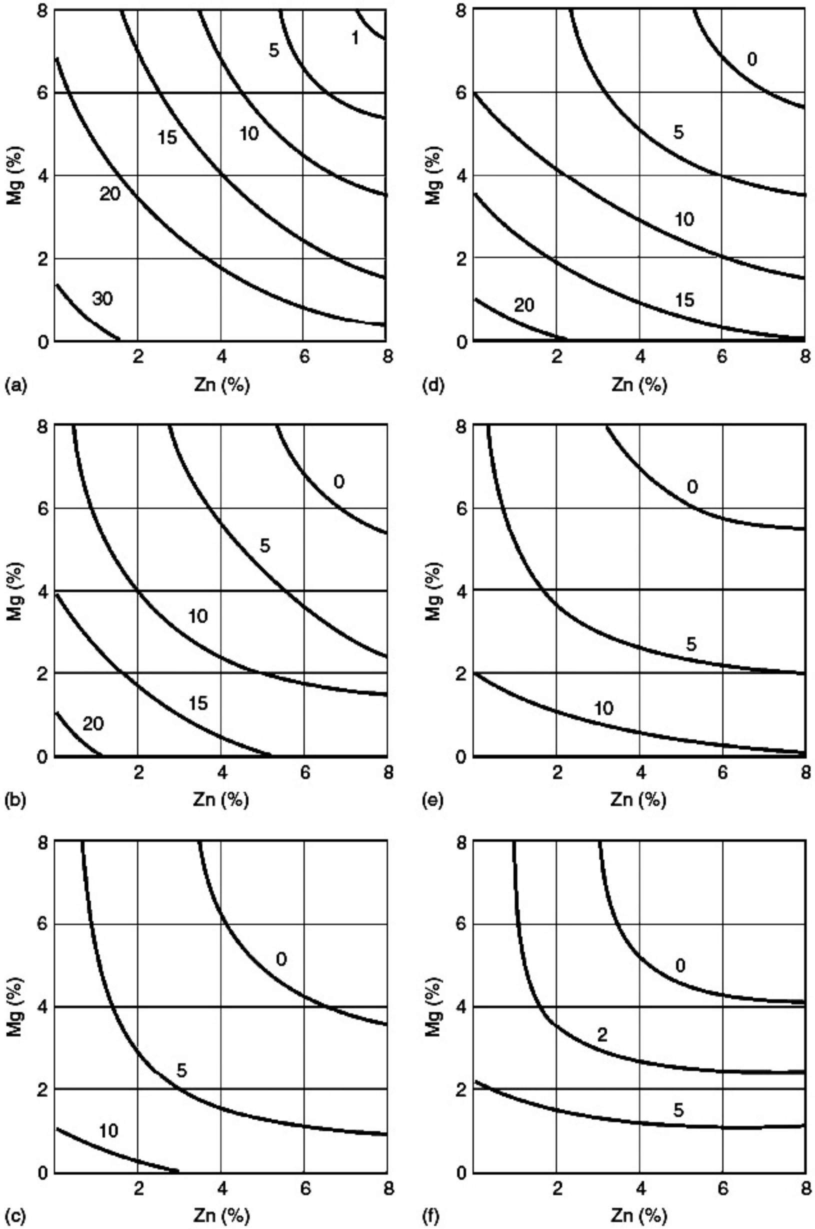

Figure 4.50 Lines of equal relative elongation for quenched alloys Al–Zn–Mg–Cu–Fe–Si: (a) at 0%Cu, Fe, and Si; (b) at 2%Cu, 0%Fe, and Si; (c) at 4%Cu, 0%Fe, and Si; (d) at 0%Cu, 0.5%Fe, and 0.5%Si; (e) at 2%Cu, 0.5%Fe, and 0.5%Si; and (f) at 4%Cu, 0.5%Fe, and 0.5%Si.

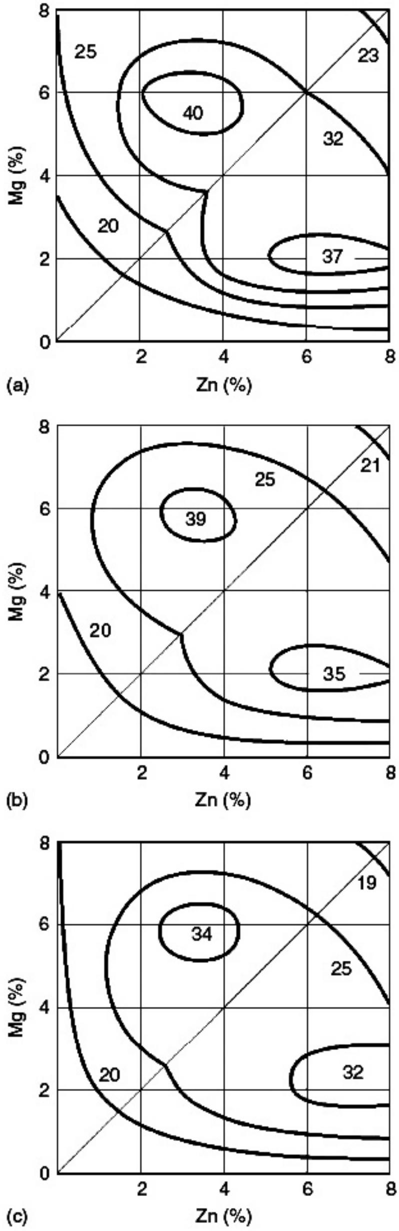

Figure 4.51 Iso-strength lines as functions of alloy composition for quenched and aged alloys Al–Zn–Mg–Fe–Si: (a) 0%Fe and Si; (b) at 0.5%Fe and 0.5Si; and (c) at 1%Fe and 1%Si.

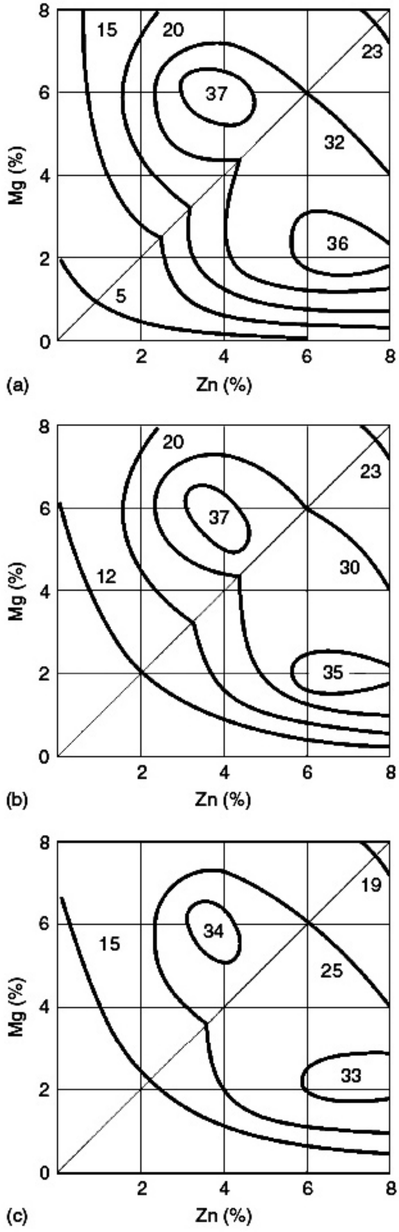

Figure 4.52 Iso-strength lines for $\sigma_{0.2}$ as functions of composition of quenched and aged alloys Al–Zn–Mg–Fe–Si: (a) aged at 0%Fe and Si; (b) at 0.5%Fe and 0.5%Si; and (c) at 1%Fe and 1%Si.

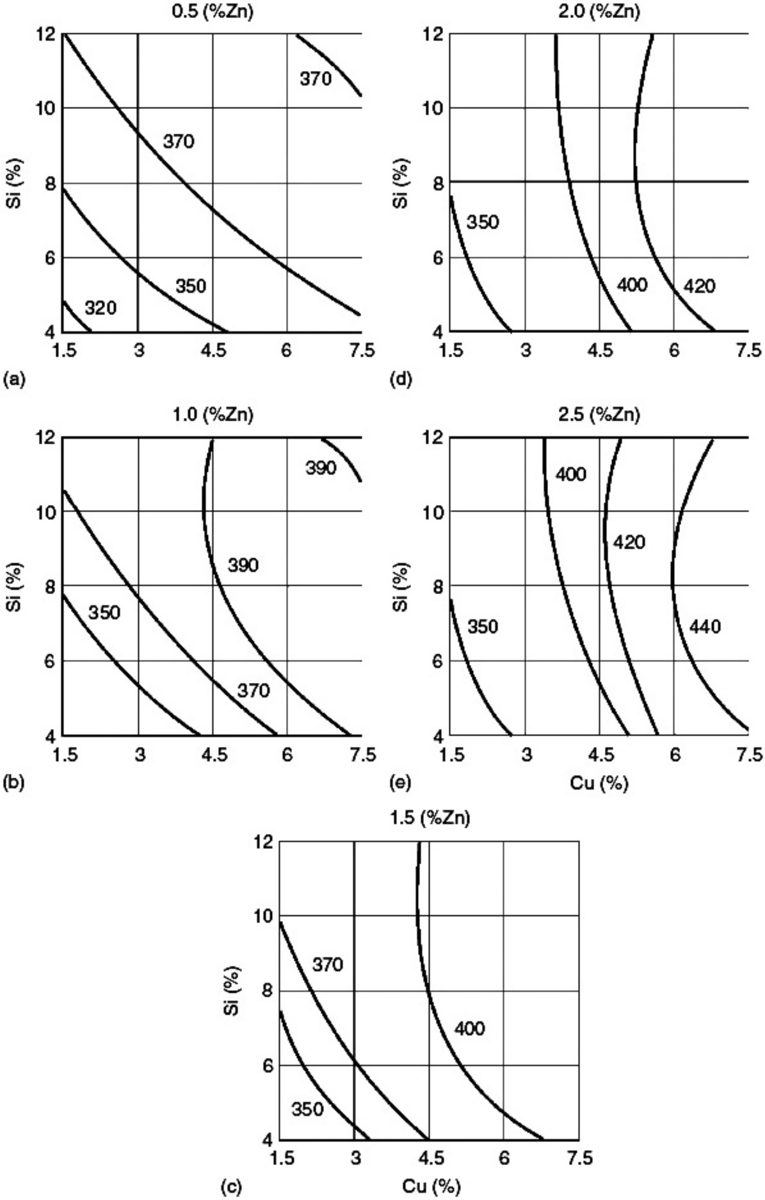

Figure 4.53 Iso-strength lines for σ_B as functions of composition of quenched and aged alloys Al–Si–Cu–Mg–Zn при 0.2%Mg и different contents Zn, %: (a) 0.5%; (b) 1%; (c) 1.5%; (d) 2%; and (e) 2.5%.

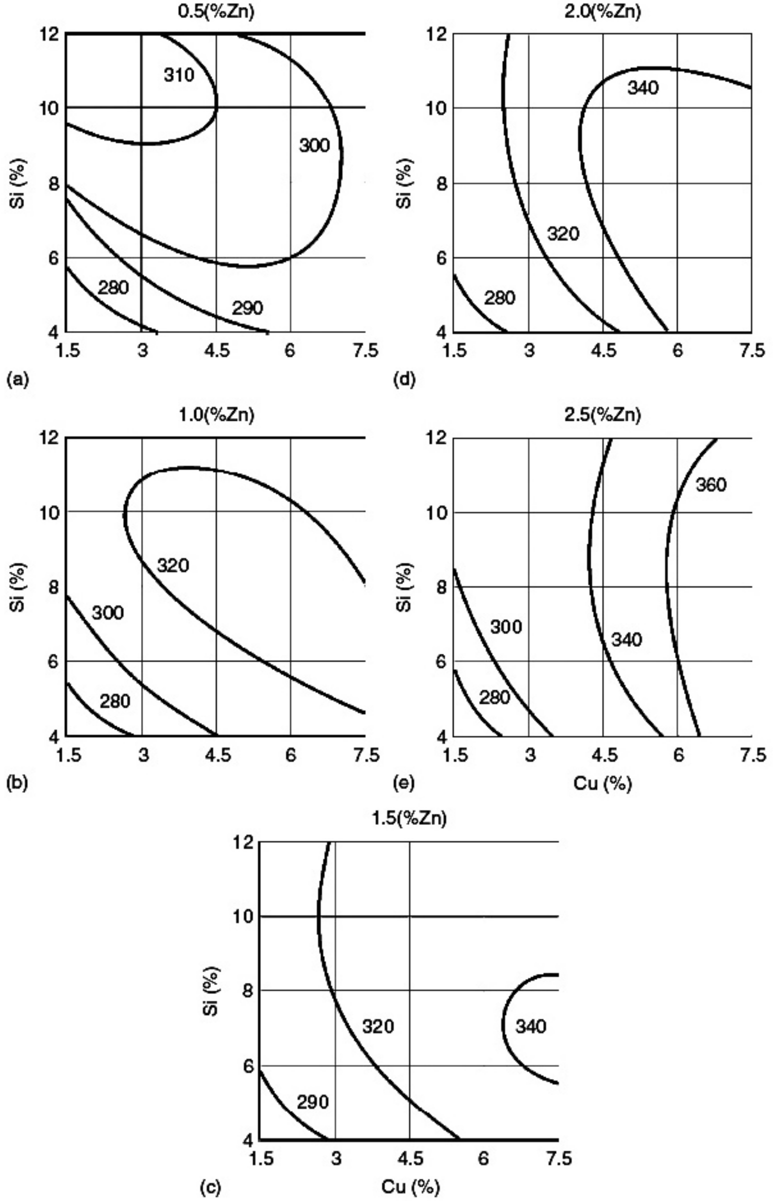

Figure 4.54 Iso-strength lines for σ_B as functions of composition for quenched and aged alloys Al–Si–Cu–Mg–Zn at 0.7%Mg and different contents of Zn, %: (a) 0.5%; (b) 1%; (c) 1.5%; (d) 2%; and (e) 2.5%.

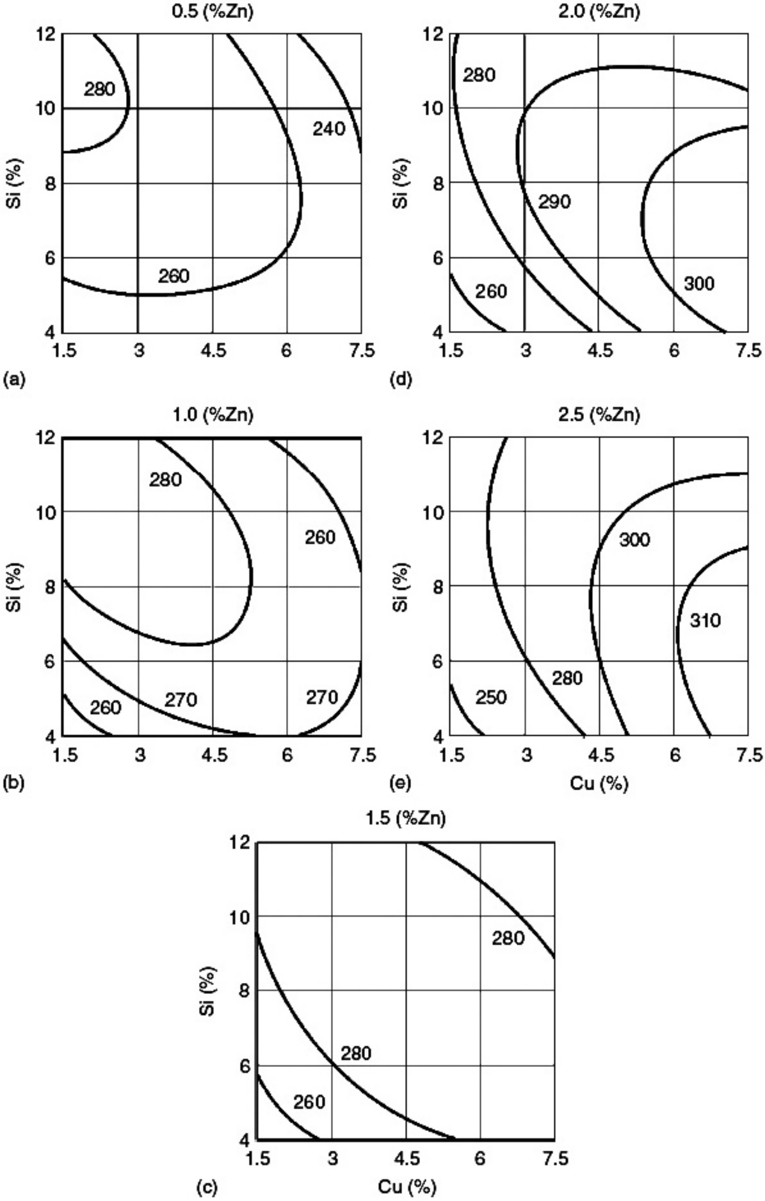

Figure 4.55 Iso-strength lines for σ_B as functions of composition for quenched and aged alloys Al–Si–Cu–Mg–Zn at 1.2%Mg and different contents of Zn, %: (a) 0.5%; (b) 1%; (c) 1.5%; (d) 2%; and (e) 2.5%.

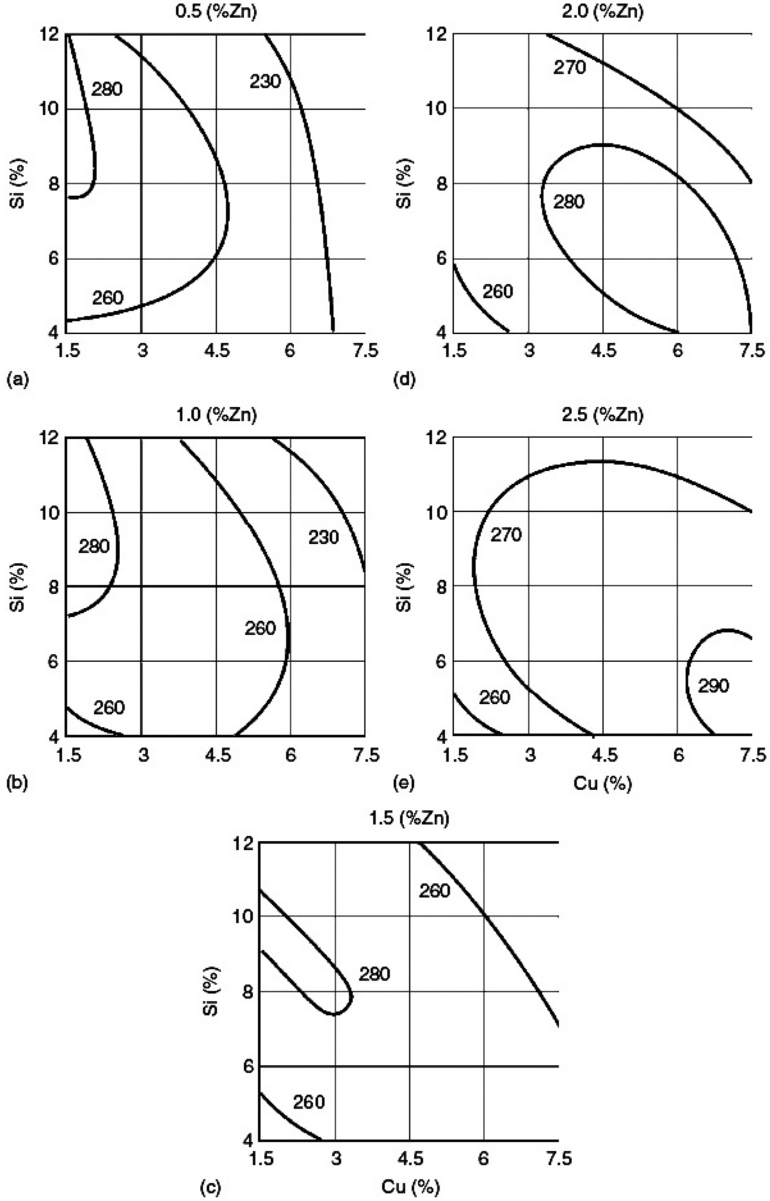

Figure 4.56 Iso-strength lines for σ_B as functions of composition of quenched and aged alloys Al–Si–Cu–Mg–Zn at 1.7%Mg and different contents of Zn, %: (a) 0.5%; (b) 1%; (c) 1.5%; (d) 2%; and (e) 2.5%.

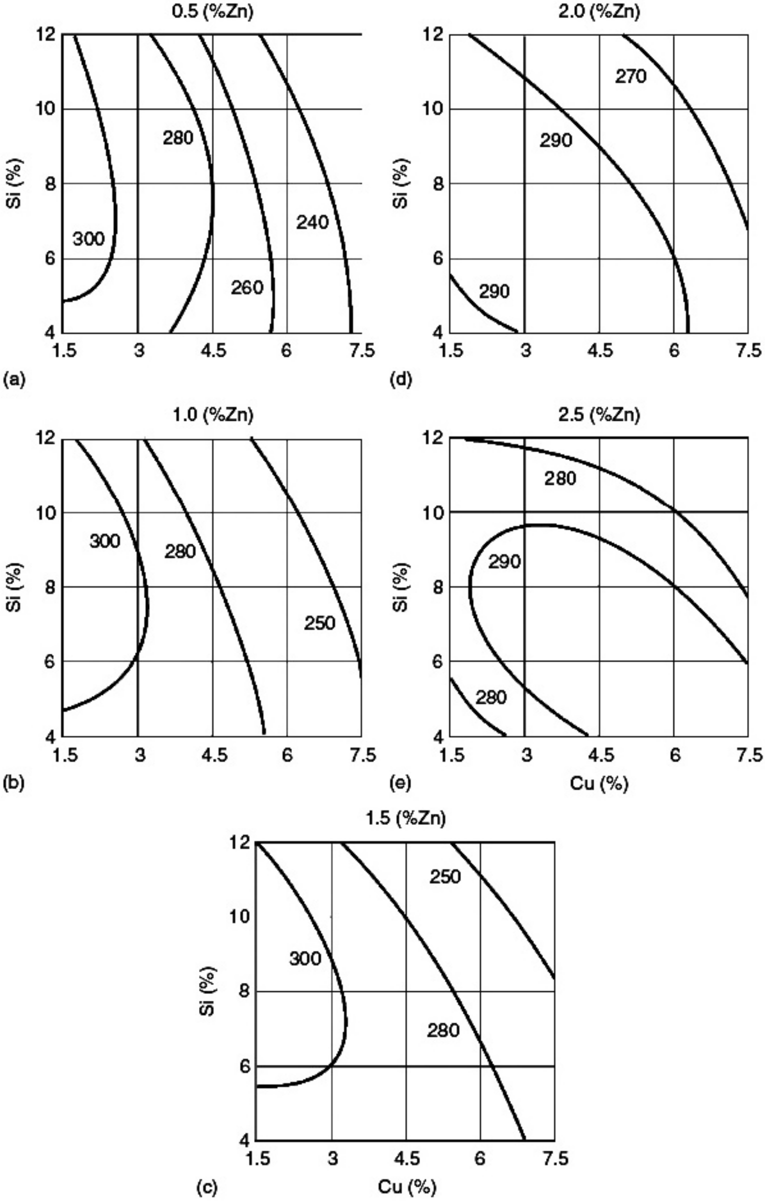

Figure 4.57 Iso-strength lines for σ_B as functions of composition for quenched and aged alloys Al–Si–Cu–Mg–Zn at 2.2%Mg and different Zn concentrations, %: (a) 0.5%; (b) 1%; (c) 1.5%; (d) 2%; and (e) 2.5%.

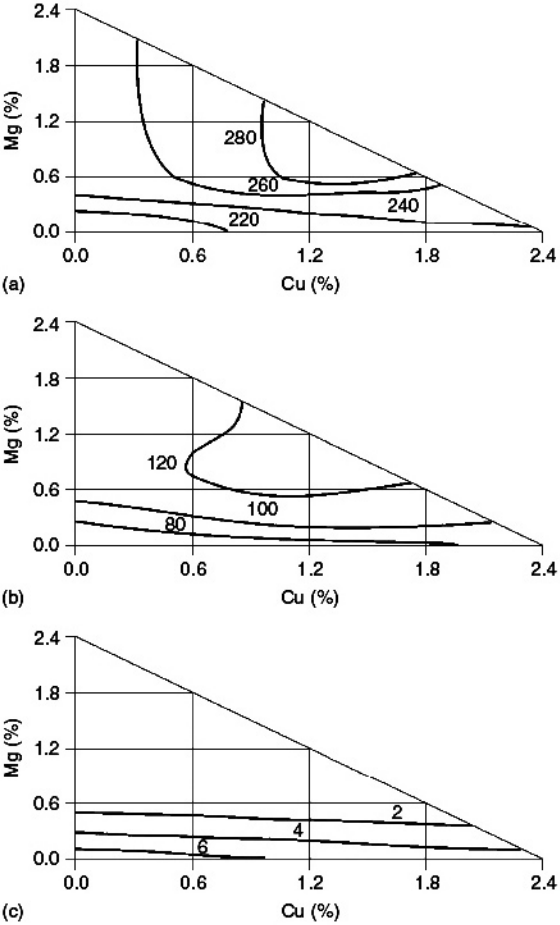

Figure 4.58 Iso-lines for ultimate strength σ_B, (a); for hardness H_B, (b); and for relative elongation, (c); as functions of alloy composition for alloys Al-7%Si–Cu–Mg, aged after casting for 6 hours at temperature 170°C.

dependencies of different tensile mechanical properties in as-cast and heat-treated states for high-strength alloys of the Al–Zn–Mg–(Cu) and Al–Si alloys obtained by the authors. These curves are represented in the form of iso-lines obtained using regression equations calibrated with experimental data on mechanical properties. The obtained equations could be used for improvements of composition for already existing alloys or development of novel aluminum casting alloys with required set of properties (see Chapter 6). Interpretation of these models in each

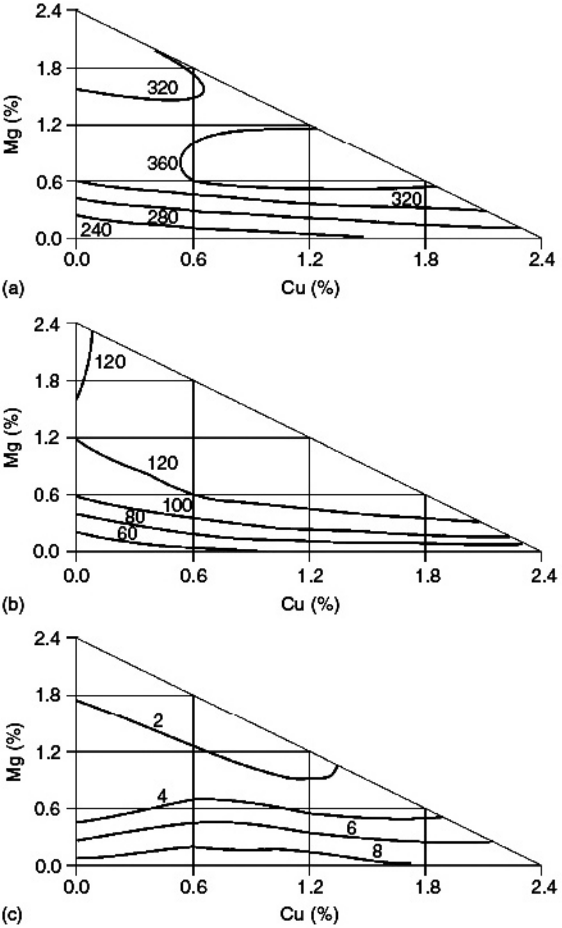

Figure 4.59 Iso-lines for: (a) ultimate tensile strength, UTS; (b) hardness H_B; and (c) relative elongation. All curves are presented as functions of alloy composition for alloys Al-7%Si–Cu–Mg after quenching (500°C, 6 hours) and aging (170°C, 6 hours)

particular case calls for detailed microstructural studies of the samples subjected to mechanical testing. This should be done both on micro- and macro-levels with subsequent application of the rules and regularities of the "microstructure – mechanical properties" type.

CHAPTER FIVE

INDUSTRIAL CASTING ALUMINUM ALLOYS

In this chapter we discuss microstructure and properties of the standard casting aluminum alloys described in the Teal Sheets of the Aluminum Association (AA) [1]. These alloys comprise the bulk of all commercial casting aluminum materials both for suppliers and end users of such products. A detailed list of the alloy chemical compositions is presented in Appendix 1. In this chapter we discuss the phase composition and basic properties of the AA casting alloys and also, in part, of some Russian casting alloys. In each section an alloy chemical composition is provided, as well typical mechanical properties of some alloys. The guaranteed values of yield strength, relative elongation, and hardness are given in Appendix 3.

In most Western countries, including Europe and the United States, a special three-digit system is accepted (plus one additional digit after the colon mark) [1, 2]. The first digit defines the basic alloying system: 4 – binary Al–Si alloys; 3 – Al–Si alloys with additions of other alloying elements; 2 – Al–Cu alloys; 5 – Al–Mg alloys.

It should also be noted that in addition to the adopted AA standards there exists quite a number of commercial alloys that find only limited use. Their designation can be quite complex sometimes. Several of such alloys are considered in Chapter 6.

5.1 AL–SI ALLOYS

5.1.1 General characterization of Al–Si Alloys

These alloys containing from 4% to 22%Si comprise more than 90% of all castings. This is related to their excellent castability, crack resistance and other good technological properties practically for all existing casting methods. More detailed information about the application of 4xx alloys can be found in reference texts [3–5, 7, 8].

The most important characteristics of Al–Si casting alloys that define their ease of use in industry are mechanical, corrosion, and casting properties. All of the latter are defined by the chemical composition and microstructure of these alloys. In turn, microstructure is defined by the conditions of melting, casting, and subsequent heat treatment. Below these issues will be discussed in logical, consequential fashion – the influence of chemical composition and microstructure

Casting Aluminum Alloys
ISBN-13: 978-0-08-045370-5
© 2007 Elsevier Ltd.
All rights reserved.

upon mechanical, corrosion resistance, and casting properties of the standard alloys described in Appendix 1.

By their very nature, 4xx and 3xx casting alloys are heterogeneous materials. The content of silicon in the (Al) matrix does not exceed 1.0–1.5%; most of the silicon enters into constituent particles, first and foremost, the silicon-based solid solution usually denoted as (Si). The basic alloying elements (in addition to silicon) in such alloys are copper and magnesium, seldom zinc and nickel. All of the principal alloying elements increase strength and hardness, but reduce somewhat alloy relative elongation.

In addition to the aluminum solid solution matrix and (Si), 4xx alloys often contain constituent particles (i.e., of the solidification origin) bearing iron, copper, magnesium, and manganese (less often – other elements such as nickel and even beryllium). Their influence upon alloy properties and microstructure will be discussed below.

The content of silicon varies from 4% to 22%. This whole range could be conditionally divided into three sub ranges: from 4% to 9%; from 10% to 13%; and from 14% to 22%. According to the binary Al–Si phase diagram (Figure 1.5) this corresponds to hypo-eutectic, eutectic, and hyper-eutectic alloys. According to the classification adopted in the present monograph, Al–Si alloys belong to materials of the second, third, and fourth groups (or X2, X3, and X4 in Figure 1.1). The lower Si limit (4%) is set by the need to attain a relatively narrow solidification gap and, consequently, good alloy castability (see Section 4.1). The upper limit is defined by the need to obtain at least the minimal level of plasticity because the silicon phase is quite brittle.

The concentration of magnesium, as a rule, falls within the range from 0.2% to 0.6%, and very rarely may exceed 1%. This directly follows from the Al–Si–Mg phase diagram (see Section 1.2.22). The lower limit is defined by the need to attain sufficient dispersoid hardening due to precipitation of secondary metastable phases β' and β'' (Mg_2Si). The upper limit must ensure the relatively small volume fraction of Mg-bearing eutectic phases (e.g., Mg_2Si) in order to attain a required level of plasticity. Among all alloying elements and impurities magnesium exerts the strongest influence upon mechanical properties of aged Al–Si alloys (per 1% added). For this reason the allowed concentration range is often very narrow (e.g., for Al–9Si premium castings, it is of the order of only 0.07%). The optimal concentration of magnesium depends not only upon other elements' concentrations, but also on the selected heat treatment scheme.

Copper allows achieving the highest level of strengthening of Al–Si alloys in as-cast condition. Its concentration could attain the level of 7–8%. This implies that in some casting alloys, for example, Al–5Si–7Cu the concentration of copper is higher than that of silicon. However, it is not practical to use more than 4–5%Cu, because its maximal solubility in (Al) is slightly higher than 4% (see Section 1.2.5). At the same time, Cu-bearing phases of eutectic origin exert strong negative influence upon alloy plasticity and other mechanical properties. After aging, copper dissolved in (Al) can precipitate in the form of secondary precipitates. In the case of the T6 heat treatment these will be, as a rule, metastable phases θ', θ'', and Q′. In the case of alloying of Al–Si with both Cu and Mg the optimal Cu concentration is of the order of 1–3%.

Zinc in the amount up to 12% (which corresponds to its maximal concentration in some commercial Al–Si–Zn alloys) can be practically completely dissolved in (Al). In small amounts it can also be dissolved in other phases; however, its strengthening effect in all cases is relatively weak. As an alloying element for casting alloys, zinc is not very perspective. However, if considered as impurity, such amounts allow a significant broadening of the range of Al–Si casting alloys manufactured from scrap.

Iron is usually an impurity in casting alloys and enters completely into one of the phases (either of eutectic origin or constituent particles). As a rule, it exerts negative influence upon mechanical properties. The extent of the influence of iron-bearing phases is defined by their morphology, size, and particle distributions. This, along with the requirements to the minimal values of mechanical properties, often defined a specification for Fe content in industrial Al–Si alloys. Such specifications could be very rigorous (<0.1%Fe for sand casting of complex shapes) or practically unrestricted (die casting – up to 2%Fe is allowed). The most harmful effect is exerted by the Al_5FeSi (β) needle-shaped particles, especially forming directly after solidification (primary crystals). For many phases of eutectic origin a more favorable "skeletal" morphology is observed (especially if alloyed with Mn), while in some other cases (for sufficiently rapid solidification) – finely dispersed morphology. An example is the Al_8Fe_2Si phase belonging to the Al–Si–Fe ternary system, which sometimes could be found in Al–Si alloys with small amounts of Si. It forms as a result of non-equilibrium solidification (see Section 2.3.1). The best morphology is globular, and it can be obtained if Be is added to casting alloys [3, 6, 12, 20–22]. In Al–Si casting alloys containing more than 0.5%Mg, even small amounts of iron (beginning with 0.1–0.15%) often results in the formation of the $Al_8FeMg_3Si_6$ quaternary phase [3, 6].

Manganese forms compound $Al_{15}(Fe,Mn)_3Si_2$ in the Al–Si–Fe–Mn system. This phase, as a part of eutectic microstructure, possesses skeletal morphology (Section 1.3.11). The presence of manganese allows avoiding the formation of needle-shaped inclusions of the Al_5FeSi phase. However, the overall amount of Mn + Fe should not exceed 1–1.5% (as a function of the silicon composition) because otherwise there is a sharp increase of the risk to obtain colonies of large primary $Al_{15}(Fe,Mn)_3Si_2$crystals [325]. It should be noted that in Al–Si alloys (unlike Al–Mg and Al–Cu alloys) the concentration of manganese in the aluminum matrix is relatively small, as it stems from the Al–Si–Mn phase diagram (see Figure 1.31b and Table 1.24). Typically the amount of manganese in 4xx and 3xx alloys does not exceed 0.5% (as alloying element or impurity; see Appendix 1).

Nickel binds iron into compound Al_9FeNi. Its eutectic inclusions can have different morphologies (skeletal, finely dispersed and compact, usually oval [6, 21]) as a function of alloy composition and solidification rate. Primary crystals of this intermetallic compound are very coarse and, consequently, undesirable in microstructure. In the case when materials of high purity are used nickel will form the Al_3Ni phase, as it stems from the phase diagram Al–Si–Ni (Section 1.2.26).

This phase is usually a part of eutectics (e.g., (Al) + (Si) + Al_3Ni). When Ni and Cu are both present in alloy composition, one could expect the formation of two compounds – Al_6Cu_3Ni and $Al_3(Ni,Cu)_2$, which results in depleting of the aluminum matrix of copper, even after quenching. When the concentration of nickel is at least 4% (if $C_{Fe} < 0.1\%$) then the formation of primary crystals of the Al–Ni phases is hardly possible. Nickel enters into chemical composition of many engine piston Al–Si alloys, sometimes in quite substantial amounts (up to 2–3%). This is explained by its positive influence upon the characteristics of thermal stability and thermal expansion coefficient.

Beryllium is the only alloying addition that allows obtaining globular inclusions of Fe-bearing constituents on a regular, consistent basis.

Such morphology is the best for mechanical properties and is typically observed in the case of the $Al_4Be_5Fe_2$. This phase is formed in many systems when the Be:Fe ratio is approximately 0.5–0.6 [6]. This requirement imposes limitations on the concentration of iron (not more than 1%) because it is unrealistic to use more than 0.5% of Be in alloys. In the Al–Si–Be–Fe system, in addition to this phase, a quaternary phase, Al_8Fe_2BeSi, can also be formed. Its typical morphology is skeletal, similar to that of the Al_8Fe_2Si and $Al_{15}(Fe,Mn)_3Si_2$ phases. Since complete binding of iron into the Al_8Fe_2BeSi phase is attained when Be:Fe ≈ 0.15–0.2, it becomes possible to prevent the formation of sharp Al_5FeSi needles even at 1.5–2%Fe using a relatively small amount of beryllium (0.2–0.3%). Since, according to the literature data, beryllium can form phases not only with iron, but also with nickel and manganese, the analysis of alloy phase composition in such situations could represent a very arduous task. Beryllium in the amount up to 0.4% enters into alloy compositions of some Russian industrial alloys (e.g., AK8l and AK8M3ch).

Thus, the aluminum matrix of the Al–Si casting alloys can contain only four elements (Si, Mg, Cu, Zn). All other chemical elements will enter into composition of different constituent particles. The most probable distribution of all the elements mentioned above between the aluminum matrix and constituent particles is presented in Table 5.1. For a more detailed analysis of the phase composition of multicomponent alloys it is recommended to use the corresponding phase diagrams (see Chapter 1), including non-equilibrium phase diagrams (see Section 2.3.1)

Often small additions of strontium and sodium are used in order to modify Al–Si eutectics; titanium and boron additions help refine grains of aluminum solid solution in hypo-eutectic Al–Si alloys; phosphorus – for refining the crystals of silicon in hyper-eutectic Al–Si alloys [3, 7]. These small additions practically do not exert any influence upon the Al–Si alloy phase composition, because their volume fraction is quite small.

In addition to iron, one should also mention two other low-melting impurities – lead and tin. Their maximum concentrations, as a rule, are limited to several hundredth of a percent (Appendix 1). They exert weak influence upon mechanical properties of alloys at room temperature but can cause hot cracking issues during casting and also reduce thermal stability.

Table 5.1 Distribution of alloying elements between aluminum matrix and excessive phases in Al–Si casting alloys

Phases	Alloying element							
	Si	Fe	Mn	Cu	Mg	Zn	Ni	Be
Aluminum matrix: (Al) and secondary phases								
(Al)	+	−	−	+	+	+	−	−
Al_2Cu	−	−	−	+	−	−	−	−
Mg_2Si	+	−	−	−	+	−	−	−
$Al_5Cu_2Mg_8Si_6$	+	−	−	+	+	−	−	−
(Si)	+	−	−	−	−	−	−	−
Al_2CuMg	−	−	−	+	+	−	−	−
Phases of solidification origin (constituent particles)								
(Si)*	+	−	−	−	−	−	−	−
Al_5FeSi*	+	+	−	−	−	−	−	−
Al_8Fe_2Si	+	+	−	−	−	−	−	−
$Al_{15}(Fe,Mn)_2Si$*	+	+	+	−	−	−	−	−
Al_9FeNi*	−	+	−	−	−	−	+	−
$Al_8FeMg_3Si_6^*$	+	+	−	−	+	−	−	−
Al_3Ni	−	−	−	−	−	−	+	−
Al_6Cu_3Ni	−	−	−	+	−	−	+	−
$Al_3(Ni,Cu)_2$	−	−	−	+	−	−	+	−
$Al_4Be_5Fe_2$	−	+	−	−	−	−	−	+
Al_8Fe_2BeSi	+	+	−	−	−	−	−	+
Al_2Cu	−	−	−	+	−	−	−	−
Mg_2Si	+	−	−	−	+	−	−	−
$Al_6Cu_2Mg_8Si_5$	+	−	−	+	+	−	−	−

* A possibility exists for the formation of primary crystals.

Table 5.2 Compositions of binary Al–Si alloys in castings.

Alloy	Si (%)	Fe (%)	Mn (%)	Ca (%)	Ti (%)	Cu (%)	Zn (%)	Al (%)
AK12 (Al–12Si)	10–13	0.5	0.4	0.08	0.13	0.02	0.06	Balance
AK12ch (Al–12Si)	10–13	0.35	0.08	0.08	0.08	0.02	0.06	Balance
AK12och (Al–12Si)	10–13	0.2	0.03	0.04	0.03	0.02	0.04	Balance

As a material for the preparation of multicomponent Al–Si alloys technically (commercial) pure aluminum is used in most cases (Table 1.3). Alternatively, one could use binary eutectic Al–Si master alloys (Table 5.2). They all differ in the allowable concentration of impurities, including iron – this defines purity of multicomponent alloys and the guaranteed level of mechanical properties.

The application of Al–Si master alloys makes alloy preparation much easier because pure silicon slowly dissolves in molten aluminum. However, as it follows from Table 5.2, even for the purest Russian alloys the allowed concentration of iron is ~0.2%, which could be unacceptably high for premium castings.

In the case of mass production, when a very high level of properties is not required, it is often possible to use Al–Si master alloys prepared out of scrap. Such Al–Si alloys (called "secondary") are much cheaper than primary Al–Si alloys not only because of the lower cost of master alloys, but also due to reduced energy expenditures during casting.

The most important properties for Al–Si casting alloys are (as for most other casting aluminum alloys): ultimate tensile strength (UTS), relative elongation (El), and Brinell hardness (HB) at room temperature. It is according to the level of these properties that the quality of end products must be evaluated in the plants. Castings, depending upon other technical requirements, could be subjected to other types of mechanical testing. The most widespread are fatigue tests, thermal stability, as well as fracture toughness and resistance to cracking. One should emphasize that Al–Si casting alloys are used mostly as construction materials. It is for this reason that mechanical properties are the most important quality indicators for them.

In Appendix 3 we present the data on the minimal guaranteed level of mechanical properties that must be met for standard Al–Si alloys obtained using different casting techniques. Typically mechanical properties are somewhat higher than the minimal required level.

Analysis of mechanical properties of Al–Si alloys (also see Section 4.2) makes it possible to establish several principal regularities for the influence of alloying element concentrations, casting technique and the used heat treatment scheme, upon alloy hardness, strength, and elongation. In particular, strengthening and embrittlement of alloys with increased concentration of alloying elements is due to their increased concentration in (Al), but even more importantly, due to the higher volume fraction of constituent particles (Table 5.1).

Increased concentration of impurities represents the basic difference between secondary and primary Al–Si casting alloys. Alloys cast out of scrap such as AK9 (Al–9Si), AK5M2 (Al–5Si–2Cu), AK5M7 (Al–5Si–7Cu), AK5M4 (Al–5Si–4Cu), AK8M3 (Al–8Si–3Cu), AK9M2 (Al–9Si–2Cu), and others (Appendix 1) are more contaminated than their respective analogs (compare, e.g., alloys: AK9 and AK9pch, AK7 and AK7pch, AK5M and AK5Mch). As a result, the guaranteed level of plasticity and elongation for secondary alloys is significantly worse than for the primary.

Thus, the principal alloy composition's influence upon mechanical properties is defined mostly by its phase composition and its changes. Within a single alloy specification variations in properties will be to a significant extent defined by changes in morphological properties of microstructure although, of course, changes of the phase composition during heat treatment also could exert a very significant influence upon different properties of castings.

The influence of selected solidification technique upon the achieved level of properties is mostly defined by the solidification rate and intimately related to it the degree of microstructure refinement. In the case of sand casting solidification rate is lower than in for mold casting or pressure casting.

As a result, dendritic cells of (Al) and crystals of excessive phases in castings solidified in metallic molds, are much smaller in size and more disperse (refined) than the crystals of silicon in eutectic colonies [3, 7]. Such finely dispersed microstructure certainly defines a higher level of most mechanical properties; in particular, strength and elongation at room temperature, when compared to castings obtained using the process of sand casting.

Similar results are obtained when the eutectics (Al) + (Si) are subjected to modification in high-silicon, especially copper-less, Al–Si alloys [3]. Increased refinement and branching of silicon crystals inside eutectic colonies results in a marked increase of all alloy tensile properties.

Even broader range of mechanical properties can be achieved with heat treatments. Appendix 4 provides information on a number of standard heat treatments for Al–Si casting alloys. It is clear that the most widespread heat treatments for such alloys are aging after casting (without quenching, T5 and O); aging after quenching (T6, T7); and also quenching without subsequent artificial aging (T4).

In the course of aging after casting (temper T5) the volume fractions and morphologies of constituent particles remain almost unchanged. However, the application of these heat treatments results in casting stress relief and decomposition of aluminum solid solution in those micro volumes, which were supersaturated as a result of non-equilibrium solidification (with respect to the maximum solubility at the temperature(s) of aging). This allows to reach a substantial level of strengthening (in comparison to as-cast state), which will be even higher if solidification was conducted at higher cooling rates (thus increasing supersaturation of aluminum solid solution) [325]. For this reason the T1 temper is most effective and is often used in the case of die casting, as well as other types of casting into thin-walled metallic molds.

The O temper is, in effect, a high-temperature aging process. It is accompanied by substantial coagulation of the secondary particles. As a result, strength characteristics could drop somewhat compared to as-cast state, while plasticity (elongation) grows. In order to conduct analysis of the phases in the decomposition products in the T5 and, particularly, in the O tempers, the Al–Si–Cu–Mg phase diagram should be used (see Section 1.3.7). One should consider not a given alloy composition, but rather, the composition corresponding to (Al) formed at given solidification conditions.

Quenching casting aluminum alloys (T4 temper) results in significant changes of their microstructure. In the course of high-temperature heating before quenching excess eutectic phases of non-equilibrium origin get dissolved (e.g., Al_2Cu and Mg_2Si), and the degree of the (Al) allowing grows. The morphology of constituent particles also changes, more or less significantly. Of the utmost importance are the changes taking place in the aluminum–silicon eutectic colonies. Isothermal heat treatment results in fragmentation and spheroidization of the silicon single crystals inside every colony and their subsequent coagulation (see Section 3.1.3). As a result, after quenching eutectic colonies are substituted by the numerous compact silicon crystals [3].

Such a profound microstructure change (as well as the reduction of the volume fraction of brittle excessive phases due to their dissolution) causes significant increase of plasticity in quenched castings compared to as-cast state (see Appendix 3).

Phase composition of Al–Si alloys in the T4 temper is most closely described by the equilibrium phase diagrams. Taking into account that commercial 3xx alloys may contain five components and more, it is useful to employ five-component phase diagrams in the domain of the Al–Si alloys (Section 1.4). However, one should keep in mind that iron-bearing phases usually do not undergo any changes during heat-up before quenching, even if they are non-equilibrium for a given alloy chemical composition.

High degree of alloying of the initial aluminum solid solution allows, by changing the temperature and time of aging after quenching (tempers T6 and T7 in Appendix 4), to realize a broad range of mechanical properties. In particular, the T6 temper is used to obtain high strength at the expense of reduced elongation. Overaging in the T7 temper ensures increased plasticity and dimensional stability of Al–Si castings, but the characteristics of strength are somewhat lowered. These differences in properties are defined by the morphology of aging products, which coarsen at elevated temperatures and increased heat treatment time.

In a number of cases altering the heat treatment scheme may result in the presence of different phases in decomposition products. For example, in copperless primary Al–Si alloys at low copper content the main products of aging are metastable modifications of the Mg_2Si phase (β' and β''). In Cu-bearing Al–Si alloys additional precipitates of metastable phases could also form – Al_2Cu (θ'' and θ'); Al2CuMg(S'); and less often stable θ-phase. Phase composition of overaged alloys can be analyzed using the Al–Si–Cu–Mg equilibrium phase diagram (Section 1.3.7). Such analysis is based on the composition of (Al) formed after quenching.

In addition to the three mechanical properties (UTS, El, and HB at room temperature), other important characteristics include fracture toughness, fatigue resistance, and thermal stability. In Appendix 5 data on fracture toughness (K_{Ic}), KCU toughness, durability limit (σ_{-1}) at room temperature, creep and temporal strength of Al–Si alloys at 300°C are provided.

Characteristics of crack resistance [21, 324], in particular, fracture toughness, of Al–Si alloys are not high compared to similar properties of wrought and casting aluminum alloys with microstructure of the solid solution type (i.e., with a relatively small volume fraction of coarse constituent particles). It is for this reason that the reduction of almost insoluble impurities in 4xx and 3xx alloys results in some improvement of the K_{Ic} and KCU values (see Appendix 5). Thus, one comes to the conclusion about correlation of these properties with the relative tensile elongation.

The overall level of durability in 4xx alloys is also relatively low and does not differ significantly for alloys of different types [5]. Obviously, durability must be linked both to strength and to plasticity. Its dependence on microstructural characteristics in a number of cases differs significantly from the corresponding dependencies of such properties in tensile tests. For example, in modified 4xx and 3xx alloys with the (Al) + (Si) eutectic tensile mechanical properties are significantly higher than for non-modified alloy. However, the durability limit varies in the opposite direction: it is higher for coarse eutectic colony microstructures.

Microstructure coarsening may positively affect alloy thermal stability [10]. Its level as a function of composition varies in a much broader range than other properties.

Creep resistance and temporal strength first and foremost are related to the concentration of copper: these properties improve as the Cu concentration grows [10]. Also favorable for thermal stability are the additions of nickel and magnesium at concentration higher than 1.3%. The reasons are related to the formation of additional crystals of intermetallic phases with favorable morphology, and in the case of copper – secondary precipitates.

Corrosion resistance is the second in importance (after mechanical properties) parameter characterizing reliability in service for Al–Si construction materials. Overall, corrosion resistance of this group of alloys could be assessed as average: they can be used in industrial atmospheres either with or without protection of the casting surfaces. The latter can typically be achieved with painting [3–7]. Al–Si alloys are not prone to corrosion under stress, and their corrosion rate in the air and in water depends upon their composition (the influence of temperature upon corrosion resistance of 3xx alloys is not completely understood even today).

Appendix 5 illustrates how corrosion resistance decreases when the degree of alloying increases. This is mostly related to the concentration of copper, which in 4xx alloys, as in many other aluminum alloys, is one most dangerous parameter for alloy corrosion performance. The highest corrosion strength against general corrosion is exhibited by copper-less Al–Si alloys with minimal concentrations of impurities (primary alloys Al–7Si; Al–9Si). The worst corrosion resistance is typical of secondary copper-bearing Al–Si alloys. Iron reduces corrosion resistance quite significantly, as well as non-metallic inclusions and shrinkage porosity in castings. Refinement of microstructure in general alleviates this problem due to smaller particle and pore sizes.

Castability is the most important technological property of Al–Si alloys. Its very high level (see Section 4.1) in comparison to other casting aluminum alloys allows them for many dozens of years to retain their leading position in industry as the principal material for aluminum alloy shape castings. All other standard alloys, as it was pointed out above, exhibit much worse casting properties. It is for this reason that their wide-spread application in industry is limited, in spite of advantages related to other, sometimes much better, properties. The best level of castability is demonstrated by copper-less Al–Si alloys with very narrow effective solidification gap. Castability attains the best value for the eutectic Al–Si alloy (Al–12Si).

Additions of copper broaden solidification range due to the depression of the solidus temperature (see phase diagram Al–Si–Cu in Section 1.2.15). This also causes some reduction in the levels of hot cracking resistance, molten metal fluidity, and hermeticity (due to increased porosity). The worst castability amongst Al–Si alloys is demonstrated by alloys of the Al–5Si–Cu type that contain additions of copper and magnesium in amounts resulting in the formation of small volume fraction of the low-melting eutectic $(Al) + (Si) + Al_2Cu + Al_5Cu_2Mg_8Si_6$ at 505–507°C.

5.1.2 Industrial 4xx and 3xx casting alloys without copper and zinc ("copper-less" alloys)

This group comprises aluminum alloys containing 6–11%Si and a small addition of magnesium (0.2–0.6%): such Russian alloys as AK12 (Al–12Si), AK7 (Al–7Si), AK9 (Al–9Si), AK8l (Al–8Si), AK10Su (Al–10Si–Sb) (see Table 5.3 along with their modifications and American alloys AA413.0, AA356.0, AA357.0), which are described in Appendix 1. Analysis of their phase composition in the T4 temper could be conducted using phase diagrams of the following systems: Al–Si–Fe (AK12), Al–Si–Fe–Mn (AK13), Al–Si–Mg (AK7pch), Al–Si–Fe–Mg (AK7ch), and Al–Si–Fe–Mg–Mn (AK9ch).

Phase composition of the aluminum matrix in the T6 and T7 tempers (and also T5) to a significant extent could be analyzed using the Al–Si–Mg phase diagram (Figure 1.28). If alloy composition contains more than 0.2–0.3%Cu, then it becomes necessary to consider the corresponding multicomponent phase diagrams (see Sections 1.3–1.4). Rigorously speaking, these alloy compositions at copper content close to the upper limit should be classified as copper-bearing Al–Si alloys. These materials are considered in Section 5.1.3

In order to properly analyze phase composition of as-cast alloys one should use non-equilibrium phase diagrams, in particular, Al–Si–Mg and Al–Si–Fe–Mg (Section 2.3). Typical mechanical properties of these materials are presented in Table 5.3; they could be significantly higher than the required minimal values (see Appendix 5).

Table 5.3 Solidification reactions under non-equilibrium conditions in a 413.1 alloy (11.4%Si, 0.46%Fe, and 0.18%Mn*) [After L. Bäckerud et al., Solidification Characteristics of Aluminum Alloys. Vol. 2: Foundry Alloys, Des Plaines: AFS/SkanAluminium, 1990]

Reaction	Temperatures (°C) at a cooling rate	
	0.3 (K/s)	5 (K/s)
$L \Rightarrow (Al)$	574–573	574
$L \Rightarrow (Al) + Al_5FeSi$	572	574–573
$L \Rightarrow (Al) + Al_{15}(FeMn)_3Si_2$		
$L \Rightarrow (Si)$		
$L \Rightarrow (Al) + (Si) + Al_5FeSi$	572–557	573–546
$L \Rightarrow (Al) + (Si) + Al_{15}(FeMn)_3Si_2$		
Solidus	557	546

*Also contains 1.1%Zn.

Eutectic Al–Si alloy Al–12Si contains only silicon as the alloying element; its principal structural component is the (Al) + (Si) eutectic. Due to significant Si concentration range (from 10% to 13%) this alloy's microstructure may contain small amounts of primary (Al) dendrites, and also primary (Si) crystals in the form of compact polyhedra (all these microstructures are very well studied and described, e.g., in Ref. [3]).

Casting alloys of the 4xx.0 series with low Mn content, irrespective of the concentrations of Fe and Si, fall into the temperature range below 576°C corresponding to the phase region $(Al) + Al_5FeSi + (Si)$. Although the total amount of the Al_5FeSi phase increases linearly with the Fe concentration, the phase "origin" can be different, that is the result of binary or ternary eutectic reactions (Tables 1.2 and 1.3), or primary solidification. The particles of this Fe-containing phase (both primary and eutectic) have plate-like morphology (needles in cross-sections as shown in Figure 5.1a, b), but their size depends on how the phase has been formed. The finest plates are characteristic of the ternary eutectic, and the largest particles represent primary crystals. If the amount of alloy impurities and etching techniques are varied, coloration could change to dark brown. These crystals can be most reliably identified by contrast when analyzing un-etched samples in scanning electron microscopy (SEM) (in the regime of back-scattered electrons). If particles of the silicon phase can hardly been seen on the background of aluminum matrix due to the close atomic numbers of Al and Si, the needles of the β-phase are much brighter. The O heat treatment does not change alloy microstructure compared to the one revealed via light microscopy.

Figure 5.2 shows polythermal cross-sections of the Al–Fe–Si phase diagram at different silicon concentrations. From the polythermal section at 7%Si

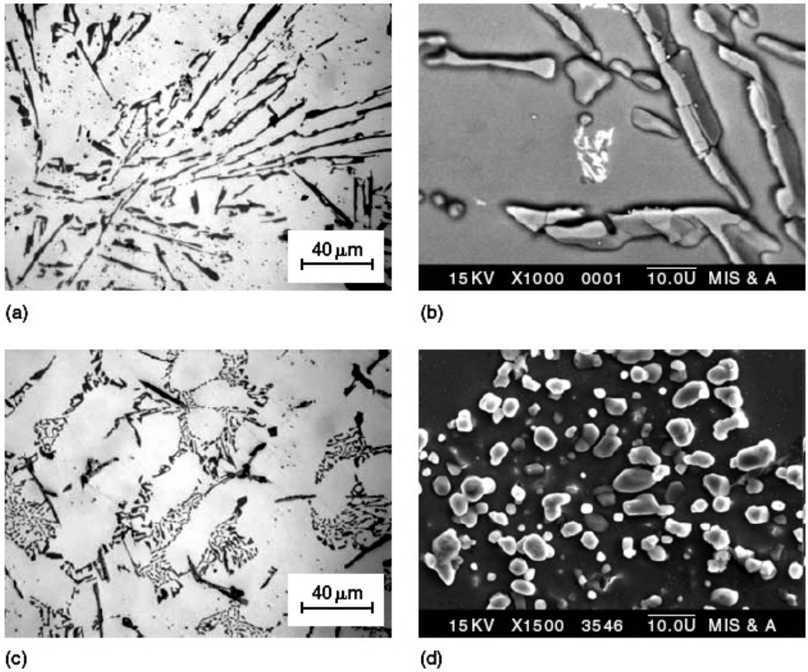

Figure 5.1 Microstructure of copperless Al–Si alloys: (a, b) AK12 (413.0), as cast, metallic mold; (c) AK7ch (356) as-cast; (d) AK8l (357), T6; (a, c) LM; (b, d) SEM.

(Figure 5.2b) it follows that at this Si concentration the primary Al_5FeSi phase is formed at iron concentrations above 1.6%Fe; and the binary eutectic, at >0.37%Fe. At 10%Si (Figure 5.2a), the primary crystals of the Al_5FeSi phase are formed at a lower concentration of iron (1%), but the boundary for the occurrence of the binary eutectic shifts towards higher iron concentrations (0.6%Fe) (Figure 5.1a). Obviously, no other Fe-containing phase appear at these Si concentrations under typical industrial solidification conditions. However, at 5%Si the Al_8Fe_2Si phase can appear as a result of non-equilibrium solidification (incomplete peritectic reaction $L + Al_8Fe_2Si \Rightarrow (Al) + Al_5FeSi$), if the concentration of Fe impurity exceeds 1.25% (Figure 5.2c). As a result, two Fe-containing phases can occur in the as-cast structure. As the Fe concentration and cooling rate increase, the amount of the Al_8Fe_2Si phase should go up.

Even small manganese additions to 4xx.0 series alloys (e.g., 444.0) (Appendix 1), lead to the formation of the $Al_{15}(FeMn)_3Si_2$ phase as follows from the isothermal section at 9%Si (Figure 5.3a). This phase has a more favorable skeletal morphology (Figure 5.1b) as compared with needle-like Al_5FeSi particles (Figure 5.1a, c); therefore the presence of manganese could be useful. However,

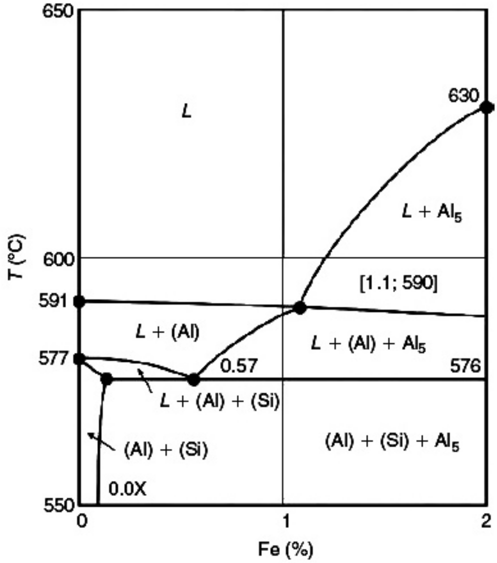

(a) Al–10%Si Al$_5$–Al$_5$FeSi

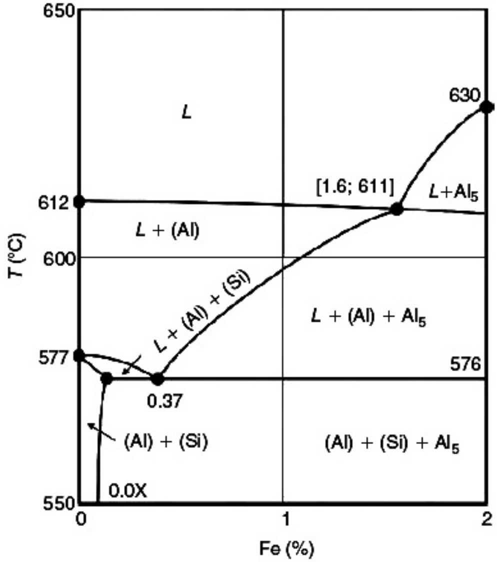

(b) Al–7%Si Al$_5$–Al$_5$FeSi

Figure 5.2 Polythermal sections of Al–Fe–Si phase diagram at (a) 10%Si, (b) 7% Si and (c) 5%Si.

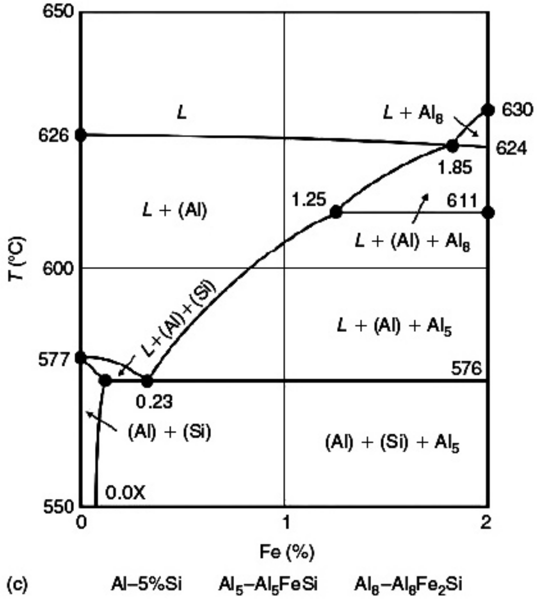

Figure 5.2 (Continued)

under real solidification conditions the complete binding of iron in the Mn-containing phase can be achieved only if the Al_5FeSi phase has not been formed before (i.e., during solidification). This becomes obvious from the analysis of peritectic reactions in this system (Table 1.33 and Figure 1.43). Indeed, during these reactions, the Al_5FeSi phase should vanish. But the peritectic reactions are usually incomplete and the Al_5FeSi phase remains in the structure as follows from the polythermal section at 9%Si and 0.15%Mn given in Figure 5.3b. If one assumes the total suppression of the peritectic reactions, then the complete binding of iron in the $Al_{15}(FeMn)_3Si_2$ phase is achieved at ~0.4% Fe but not at >1%Fe, as it follows from the equilibrium phase diagram. Typically, conglomerates of these phases are formed, together with silicon particles. This situation is unfavorable not only because of the presence of Al_5FeSi needles, but also because the Mn-containing phase grows on these needles instead of forming isolated dendritic inclusions. When this is taken into account, the Mn:Fe ratio required to prevent the formation of needlelike inclusions should be significantly higher than it follows from equilibrium phase diagram (~1:20 as it follows from the composition of the $Al_{15}(FeMn)_3Si_2$ phase – 31%Fe and 1.5%Mn). On the other hand, the increase of the total Fe and Mn concentration above 2.0–2.5% may result in the formation of primary $Al_{15}(FeMn)_3Si_2$ particles that have polygonal shapes and often occur as big clusters, which is evidently harmful for many properties, in particular for ductility and workability. At high concentrations of silicon (>8%)

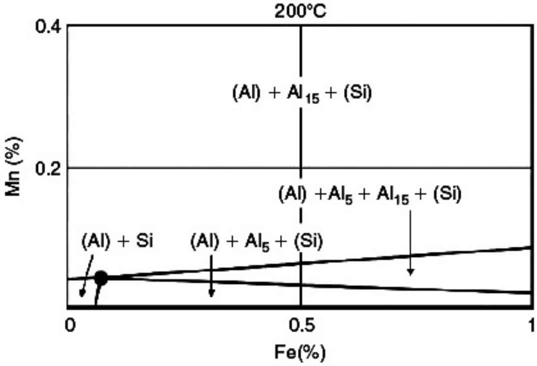

(a) Al–9%Si Al$_5$–Al$_5$FeSi Al$_{15}$–Al$_5$(FeMn)$_3$Si$_2$

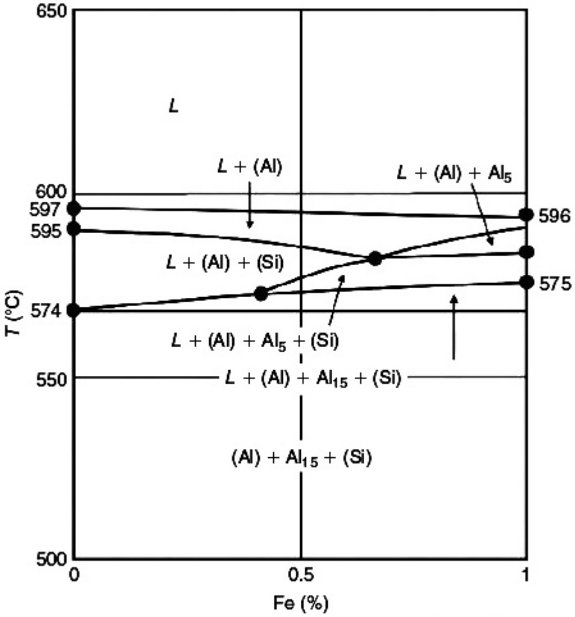

(b) Al–9%Si–0.15%Mn Al$_5$–Al$_5$FeSi Al$_{15}$–Al$_5$(FeMn)$_3$Si$_2$

Figure 5.3 (a) Isothermal and (b) polythermal sections of Al–Fe–Mn–Si phase diagram at 9%Si: (b)(i) 200°C and (ii) 0.15%Mn.

and iron (>1%), the use of manganese as a modifier of the Fe-containing phase appears to be inefficient.

Bäckerud *et al.* (see reference to Table 5.3) examined the solidification of a "eutectic" 413.0 alloy under non-equilibrium conditions and revealed the solidification reactions shown in Table 5.3. Primary (Al) grains and primary (Si) crystals can be simultaneously found in the structure, alongside eutectic particles of (Si), Al_5FeSi (needles), and $Al_{15}(FeMn)_3Si$ (skeletal particles).

Alloy *AK12* (Al–12Si, see Table 5.4) is manufactured out of primary metals. It has relatively low strength characteristics (see Table 5.5), but possesses excellent castability and good corrosion resistance. It is widely used in different areas such as hermetic castings, as well as fabricated products of very complex shapes working at temperatures not higher than 200°C.

Another eutectic Al–Si alloy is *AK13* (Al–13Si). Its principal difference from *AK12* is that it contains manganese and magnesium as alloying additions, not as impurities. This alloy is recommended for casting under pressure, presence of manganese allows to bind most of the iron in it into the $Al_{15}(Fe,Mn)_3Si_2$ phase, which increases the guaranteed level of mechanical properties compared to AK12.

Hypo-eutectic Al–Si alloys of the *AK9* (Al–9Si) type (also modifications *AK9s*, *AK9ch*, and *AK9pch*), alloyed with magnesium (0.17–0.4%) and manganese (0.2–0.5), contain from 8.5% to 11%Si. The principal microstructural components of these alloys in as-cast state are (Al) dendrites and (Al) + (Si) eutectic. Among the iron-bearing phases most probable is the presence of skeletal particles of the $Al_{15}(Fe,Mn)_3Si_2$ phase. Copper impurities form the $Al_6Cu_2Mg_8Si_5$ (Q) phase, the inclusions of which are characterized by sharp and irregular shaped edges. Magnesium silicide forms disperse inclusions that can be observed in light microscope with difficulty because of their small number density and sizes. Limits on the iron concentration in alloy AK9pch are more rigorous. As a result, needle-like plate cross-sections of the β-phase crystals can be found very rarely, and the overall number of the skeletal Mn-bearing particles is also very low.

During heat-up before quenching (necessary for the T4, T6, and T7 heat treatment regimes) either complete or partial fragmentation and spheroidization of the (Al) + (Si) eutectic particles takes place. Crystals of the Mg_2Si and Q phases dissolve completely in the matrix aluminum solid solution. Morphology of iron-bearing phases does not undergo significant changes. In alloy AK9pch obtained by casting into thin-walled metallic molds, silicon particles are globular and uniformly distributed in the (Al) matrix. This allows obtaining the highest level of mechanical properties. In the process of aging the formation of metastable modifications of Mg_2Si takes place. This results in significant increase of alloy's strength; however, elongation drops dramatically [325, 326]. Heat treatment according to the T5 regime does not cause microstructure changes that could be revealed with light microscopy. Some strengthening is related to the decomposition of supersaturated (Al), which formed in the process of casting.

Alloys AK9 and AK9s are obtained from secondary materials. They possess good mechanical and casting properties and satisfactory corrosion resistance. Due to its narrower composition range, alloy AK9s has a somewhat higher guaranteed value of the relative elongation. This alloy is used for casting large parts for which strength requirements are elevated (e.g., for engine carters). Main users of this alloy are automotive and agricultural industry.

Table 5.4 Chemical composition of copper-less Al–Si alloys (Russian nomenclature)

Alloy	Concentrations (%) (Al balance)						
	Si	Mg	Fe*	Mn	Cu	Zn	Other
AK12 (Al–12Si)	10–13	0.1	S: 0.7; M: 1; P: 1.5	0.5	0.6	0.3	–
AK13 (Al–13Si)	11–13,5	0.1–0.2	S: 0.9; M: 1; P: 1.5	0.1–0.5	0.1	0.15	–
AK9 (Al–9Si)	8–11	0.2–0.4	S: 0.9; M: 1.2; P: 1.3	0.2–0.5	1	0.5	–
AK9s (Al–9Si)	8–10.5	0.2–0.35	S: 0.7; M: 0.9; P: 1	0.2–0.5	0.5	0.3	–
AK9ch (Al–9Si)	8–10.5	0.17–0.3	S: 0.6; M: 0.9; P: 1	0.2–0.5	0.3	0.3	–
AK9pch (Al–12Si)	9–10.5	0.23–0.3	S: 0.3; M: 0.3; P: 0.3	0.2–0.35	0.1	0.3	–
AK8 (Al–8Si)	6.5–8.5	0.35–0.55	S: 0.6; M: 1; P: 1.5	0.1	0.3	0.3	Ti, Be
AK7 (Al–12Si)	6–8	0.2–0.5	S: 1.1; M: 1,2; P: 1.3	0.2–0.6	1.5	0.5	
AK7ch (Al–12Si)	6–8	0.2–0.4	S: 0.6; M: 1; P: 1.5	0.5	0.2	0.3	
AK7pch (Al–12Si)	7–8	0.25–0.4	S: 0.3; M: 0.4; P: 0.5	0.1		0.2	
AK10Su (Al–12Si–Sb)	0–11	0.1–0.5	P: 1.2	0.3–0.6	1.8	1.8	Sb

* S: sand casting; M: metallic mold; P: casting under pressure.

Table 5.5 Typical mechanical properties of some copper-less Al–Si alloys

Alloy	Condition*	UTS (MPa)	YS (Mpa)	δ (%)
AK12 (Al–12Si)	S (M), M	180	80	7
AK9ch (Al–12Si)	S (M), T5	260	200	4
AK7ch (Al–12Si)	M, T5	270	210	5
AK8l (Al–12Si)	S, T5	330	280	3

*M: mold casting; S: sand casting; (M): modified Al–Si eutectic.

Alloys AK9ch and AK9pch are prepared out of primary materials. They possess good castability and mechanical properties and also satisfactory corrosion resistance, which is higher than for alloy AK9. They also possess good hermeticity. Such alloys are used mostly for large cast parts, like engine carters, engine head gaskets, and other complex castings for automotive and agricultural industry. They could also be used in aerospace industry for casting parts with working temperature not higher than 200°C [3, 4, 8].

Hypo-eutectic Al–Si alloys of the *AK*7 (Al_7Si, AA356) type (in addition to the principal alloys there are also such modifications AK7ch and AK7pch) are alloyed with 0.2–0.4%Mg and contain from 6% to 8% of silicon. The principal microstructural components are dendrites of aluminum solid solution (Al) and the (Al) + (Si) eutectic. Because of iron impurities it usually contains significant amount of the plate-like crystals of the β-phase (Figure 5.1c). For this reason the eutectic in such alloys could be classified as ternary, $(Al) + (Si) + \beta$. Crystals of the β-phase that enter this ternary eutectic are characterized by the relatively short length (within one colony), which makes them less dangerous compared to particles formed according to the binary eutectic reaction $L \rightarrow (Al) + \beta$. As it follows from the polythermal cross-section shown in Figure 5.1, when the concentration of iron does not exceed 0.6%, the β-phase should be formed only according to the ternary eutectic reaction. On the other hand, when $C_{Fe} > 0.2\%$, alloys of the AK7 type fall into the $(Al) + (Si) + \beta + \pi$ phase domain. From this one comes to conclusion that the strengthening Mg_2Si phase is essentially non-equilibrium, because the formation of the fourth compound, the π-phase in solid state is highly improbable due to low value of the Fe diffusion coefficient in (Al).

Because alloys of the AK7 type do not contain manganese as alloying element, the skeletal particles of the $Al_{15}(Fe,Mn)_3Si_2$ are absent in most cases. The principal difference between AK7pch and other alloys of the AK7 type is in sharply lower amounts of the β-phase due to strict specification for allowable amounts of iron impurity. In alloy AK7 copper impurity forms the fourth phase, Q, that binds a portion of magnesium into it. Other impurities exert relatively insignificant influence upon the phase composition of such alloys. Heat treatment according to the T1 and T4–T7 schemes yields results similar to those obtained for the AK9 Al–Si alloy.

Alloy AK7 is manufactured out of secondary materials. It possesses satisfactory mechanical and casting properties, good corrosion resistance, which is higher than for AK9. It is used in industry for casting thin-walled parts of complex configurations that are supposed to carry or sustain moderate loads. Examples include different closures, engine body parts, heat exchangers, etc. Alloys AK7ch and AK7pch are manufactured out of primary materials. They are characterized by satisfactory mechanical and excellent casting properties, good corrosion resistance, and hermeticity. They are used for casting thin-walled articles of complex configuration in different areas, including aerospace industry.

Alloy *AK8l* (Al_8Si), as well as AK7pch and AK9pch, has strict limitations on the iron contents, but could contain somewhat larger amounts of magnesium (up to 0.55%) and additions of beryllium (0.15–0.4%). The principal microstructural components are dendrites of the aluminum solid solution (Al) and the (Al) + (Si) eutectic. According to the Al–Si–Fe–Be phase diagram (Section 1.3.1) iron is almost completely bound by the Fe- and Be- bearing phases of eutectic origin. Of those, the $Al_4Be_5Fe_2$ plays the key role in alloys of the AK8l type, the particles of which have globular shape(s). When the Fe:Be ratio is greater than 0.5, sometimes the quaternary compound (Al_8Fe_2BeSi) could form, which represents skeletal particles. Heat treatment according to the T5 and O schemes does not introduce any visible changes into the alloy microstructure. During heat-up and isothermal annealing before quenching, planar particles of eutectic silicon get fragmented and spheroidized (Figure 5.1d). Due to the changed morphology of the Si-phase it becomes more difficult to identify the globular particles of the $Al_4Be_5Fe_2$ phase in optical microscope [3, 7].

Alloy AK8l is manufactured out of primary materials. Due to increased amounts of magnesium this alloy in the T6 temper possesses the highest strength (UTS up to 350 Mpa) among all standard copper-less Al–Si alloys. It is used in aerospace and automotive (caterpillar) industries for casting loaded articles with complex configurations – parts of cockpit, frames, panels, details that require a high level of hermeticity, etc. Since all Be-bearing compounds are highly toxic, alloy AK8l finds only limited application. However, it should be mentioned that if the concentration of iron does not exceed 0.1%, it is not necessary to add beryllium into this alloy's composition.

Alloy *AK10Su* ($Al_{10}SiSb$) was developed primarily for casting under pressure; its principal difference from other Al–Si alloys is in addition of small amounts of Sb. It has a broad range of magnesium concentrations and allows the presence of up to 1.8% of copper and/or zinc, which makes its phase composition similar to that of Al–Si alloy AK9. Typical microstructures of copper-less Al–Si alloys are shown in Figure 5.1.

Commercial casting copper-less 3xx alloys (of the 356 type) usually contain only silicon and magnesium (Table 2.1), which reduces the analysis of phase composition to the ternary Al–Si–Mg phase diagram. In particular, the solubility values (Table 2.4) show that in the T4 state (after solution treatment at 530–550°C)

356.0-type alloys fall into the (Al) + (Si) phase region and, after artificial aging, into the (Al) + (Si) +Mg_2Si region. The binary (Al) + (Si) eutectic always forms in the temperature range 577–550°C (Table 2.3), after the primary crystallization of (Al). The ternary eutectic ((Al) + (Si) + Mg_2Si at 550°C), forms in commercial compositions only as a result of non-equilibrium solidification.

The presence of iron impurity in most of 3xx alloys (Appendix 1) requires that quaternary Al–Fe–Mg–Si phase diagram be used for the correct analysis of the phase composition. Within the compositional range of 356/357-type alloys, variation of silicon concentration does not affect the phase composition, which makes it convenient to use sections at a constant Si concentration. The isothermal sections plotted for equilibrium conditions (Figure 5.4) show that 356/357-type alloys can fall only into two four-phase regions, that is (Al) + (Si) + $Mg_2Si + \pi$ or (Al) + (Si)+ β (AlFeSi) + π. As a result, starting from 0.3% to 0.4%Fe, the iron impurity can completely bind magnesium into the π-phase, thus excluding the formation of Mg_2Si precipitates. However, this does not occur in reality, because at early stages of solidification iron mostly enters into the β(AlFeSi) phase that, due to the suppressed peritectic reaction $L + \beta\text{(AlFeSi)} \Rightarrow \text{(Al)} + \pi$ and low diffusion of Fe in (Al), is retained in the final structure. As a result, magnesium remains in the solid solution after quenching (Figure 5.4a) and can precipitate upon aging. The equilibrium phase composition at a temperature of aging shall be as it is shown in Figure 5.4b. Yet, due to the extremely low diffusion coefficient of iron in solid (Al) and the preferential precipitation of Mg_2Si (metastable modifications) upon decomposition of supersaturated solid solution, the Al–Fe–Mg–Si phase diagram cannot be directly used for the analysis of a non-equilibrium phase composition formed during aging. Rather, the composition of a supersaturated (in Si and Mg) solid solution should be placed on the relevant isothermal section of the Al–Mg–Si phase diagram (Section 1.2.22).

The polythermal sections at 7%Si and 0.2%Fe (Figure 5.5a), and 0.5%Fe (Figure 5.5b) can be used to follow the reactions during solidification and cooling in the solid state of a 356/357-type alloy at a typical concentration of iron. After primary solidification of (Al), the (Al) + (Si) eutectic is formed, and the remaining liquid reacts via the ternary eutectic reaction involving the Al_5FeSi phase. Under real casting conditions, the quaternary π compound and the Mg_2Si phase are found in as-cast alloys containing over 0.4%Mg (alloys of the 357.0 type). One may notice that the peritectic reaction (point P_1 in Table 1.32) with the formation of the quaternary π-phase occurs at higher magnesium content in the equilibrium phase diagram (0.75–0.77%Mg in Figure 5.5a, b). This discrepancy is an obvious result of non-equilibrium solidification. According to the equilibrium phase diagram, at low magnesium concentrations and at a typical Fe impurity level (356-type alloys), iron is bound mainly in the β(AlFeSi) phase. For example, the isopleth in Figure 5.5c shows that at 1%Mg (a concentration much higher than that in 357.0-type alloys) and at a relatively low iron concentration of less than 0.2%, the β(AlFeSi) phase is completely replaced by the quaternary compound that binds almost all iron.

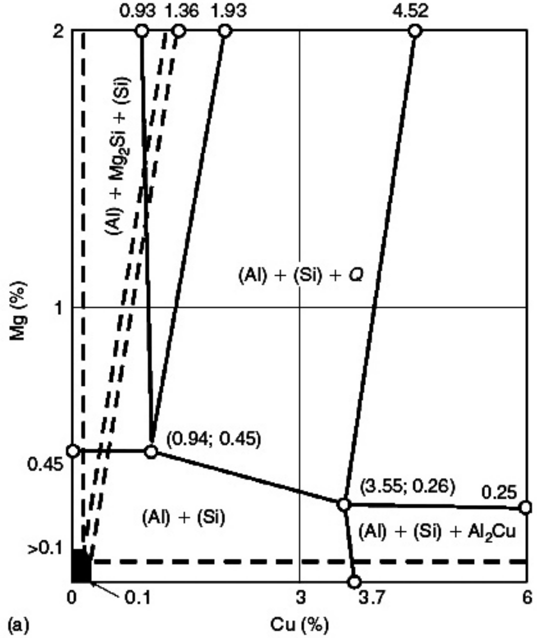

Figure 5.4 Isothermal sections of Al–Fe–Mg–Si phase diagram at 7%Si: (a) 540°C and (b) 200° C; β: Al_5FeSi; and π: $Al_8FeMg_3Si_6$.

Under real, non-equilibrium conditions, solidification is completed by the invariant eutectic reaction $L \Rightarrow (Al) + (Si) + Mg_2Si + Al_8FeMg_3Si_6$ at 554°C [6; also see Q.G. Wang. *J. Mater. Sci.*, 2001, Vol. 36, p. 739]. Due to the low concentrations of Fe and Mg, these eutectics usually degenerate into isolated inclusions of phases or their conglomerates. Bäckerud *et al.* report that the solidus of 356-type alloys can be as low as 505–519° C at a cooling rate of 5 K/s (Backerud *et al.*, see ref. in Table 5.3). Figure 5.6 shows the distribution of phase fields in the solid state after non-equilibrium solidification.

5.1.2.1 Fractography of copper-less Al–Si Alloys [3]

A general feature of all Al–Si alloys, including copper-less, is a large number of planar facets that are formed as a result of fracture of brittle silicon phase crystals (Figure 5.7). The degree of refinement of a given fractogram (i.e., average facet size) is directly related to the refinement of the original microstructure. In addition to facets there are also lighter ridges formed in the process of plastic deformation and fracture of (Al) matrix. The latter in copper-less Al–Si alloys has a sufficiently high level of plasticity, especially in as-cast state due to small degree of the aluminum solid solution alloying. In the presence of iron and manganese

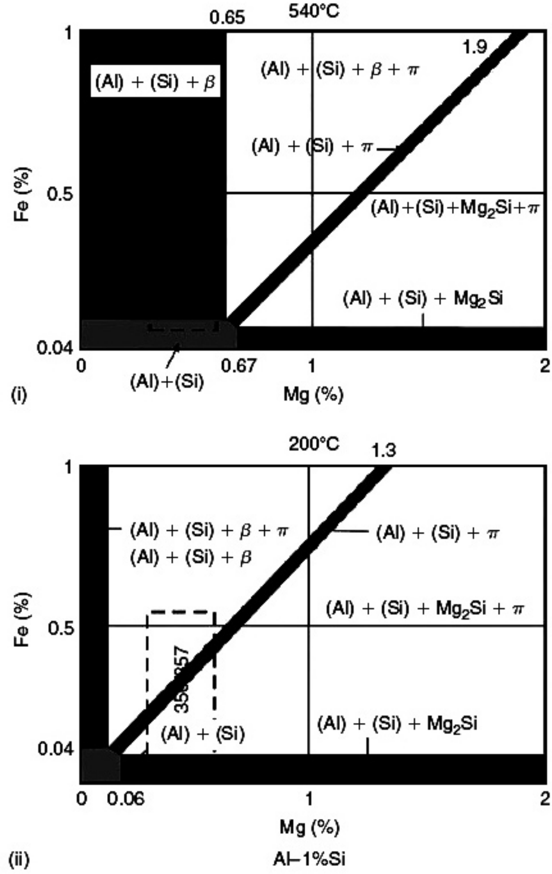
0.65
540°C
1.9
(Al) + (Si) + β
(Al) + (Si) + β + π
(Al) + (Si) + π
Fe (%)
0.5
(Al)+(Si)+Mg2Si+π
(Al) + (Si) + Mg2Si
1
0.04
0
0.67
1
2
(Al)+(Si)
Mg (%)
(i)
200°C
1.3
1
(Al) + (Si) + β + π
(Al) + (Si) + β
(Al) + (Si) + π
(Al) + (Si) + Mg2Si + π
Fe (%)
0.5
357
(Al) + (Si)
(Al) + (Si) + Mg2Si
0.04
0
0.06
1
2
Mg (%)
(ii)
Al–1%Si

Figure 5.4 (Continued)

one could observe the fracture traces for particles, which typically possess either needle-like or skeletal shapes. In as-cast non-modified Al–Si alloys many particles of the silicon phase have non-compact morphology and there is very little difference with particles of iron-bearing phases. In fracture surfaces (fracture diagrams) these minor differences become even less noticeable; for this reason particle morphology helps identify only sufficiently large elements of microstructure – primary crystals of Fe-bearing phases, non-metallic inclusions, pores, etc. These elements, as a rule, are distributed very non-uniformly, and just one fractogram is never enough to make a sound judgment about their quantities. A more reliable picture is obtained when many individual fields of view are analyzed at modest magnifications (X100–200 and even less than that).

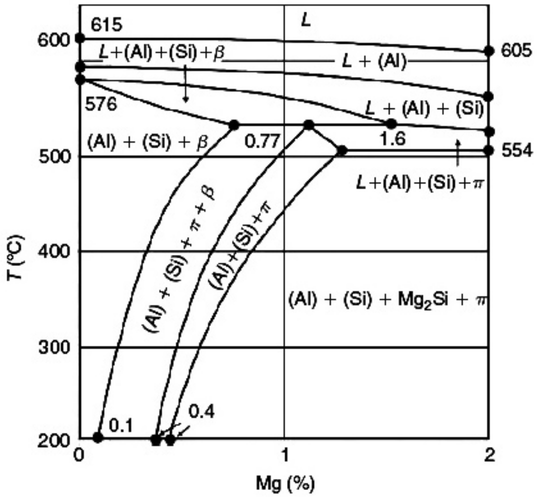

(a) Al–7%Si–0.2%Fe

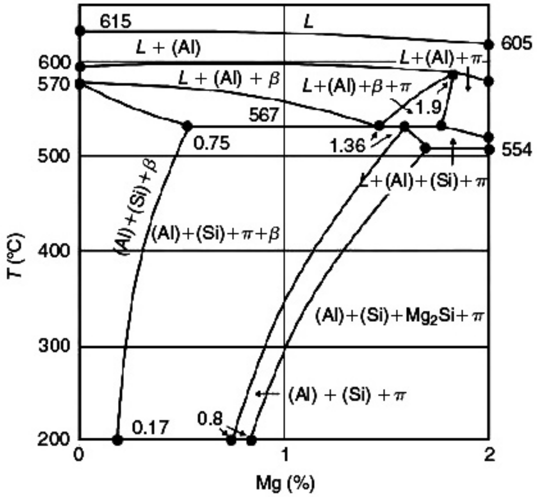

(b) Al–7%Si–0.5%Fe

Figure 5.5 Polythermal sections of Al–Fe–Mg–Si phase diagram at 7%Si: (a) 0.2%Fe; (b) 0.5%Fe; (c) 0.3%Mg; and (d) 1%Mg; β: Al_5FeSi and π: $Al_8FeMg_3Si_6$.

Fracture surfaces of heat treated samples contain pits as the principal structure element; these are formed when compact particles of the Si phase are fractured and subsequent growth of micropores takes place. The average size of pits is related to the size of Si particles and also to the plasticity of the (Al) matrix. The latter

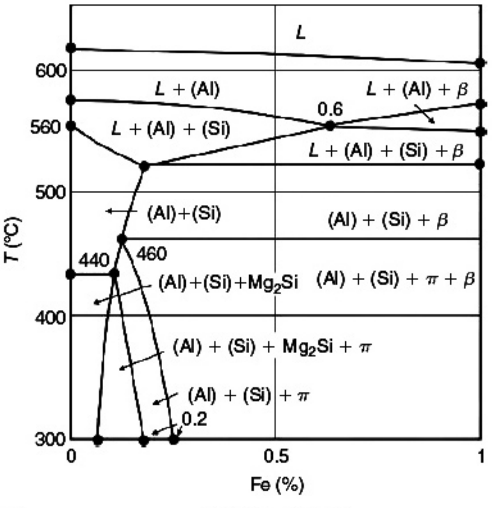
L
600
L + (Al)
L + (Al) + β
0.6
560
L + (Al) + (Si)
L + (Al) + (Si) + β
500
(Al)+(Si)
(Al) + (Si) + β
T (°C)
440
460
(Al)+(Si)+Mg_2Si
(Al) + (Si) + π + β
400
(Al) + (Si) + Mg_2Si + π
(Al) + (Si) + π
0.2
300
0
0.5
1
Fe (%)

(c) Al–7%Si–0.3%Mg

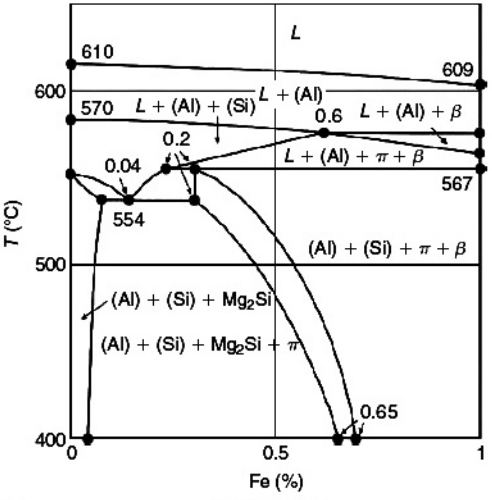
L
610
609
600
L + (Al)
570
L + (Al) + (Si)
0.6
L + (Al) + β
0.2
0.04
L + (Al) + π + β
567
554
T (°C)
(Al) + (Si) + π + β
500
(Al) + (Si) + Mg_2Si
(Al) + (Si) + Mg_2Si + π
0.65
400
0
0.5
1
Fe (%)

(d) Al–7%Si–1%Mg

Figure 5.5 (Continued)

defines the average pit depth as well, giving a possibility to make a judgment about the extent of the (Al) plasticity immediately before fracture.

This type of background actually makes it easier to distinguish the traces of Fe-bearing particle fracture, because they possess very characteristic morphology.

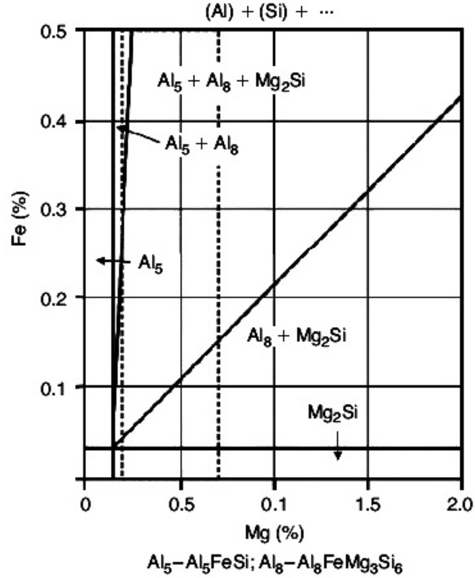

Figure 5.6 Non-equilibrium distribution of phase fields in Al–Fe–Mg–Si system at 7%Si in the as-cast state ($V_c \sim 10^{-1}$ K/s). All phase fields contain (Al) and (Si). Composition range of 356- and 357-type alloys is marked.

In the case of compact particles, like $Al_4Be_5Fe_2$ in casting alloy AK8l, they are more difficult to identify because, as a rule, they are located on the bottom of the pits, similar to the particles of silicon. In other words, fracture surfaces of alloy AK8l with globular particle morphology of Fe-bearing particles practically cannot be distinguished from fracture surfaces of high purity alloys AK7pch (C356.2) and AK9pch. In such cases the application of back-scattered electrons might be beneficial because it reveals iron particles having a somewhat lighter contrast. In the case of high concentrations of iron impurity (as it could be in alloys AK7 and AK9), the pit structure of fractured surface is hardly revealed because fracture mostly proceeds along non-compact particles, thus reducing the plastic deformation of the (Al) matrix.

5.1.3 Industrial Al–Si alloys with copper and zinc

In this section we will discuss Al–Si alloys containing copper (up to 8%) and zinc (up to 12%). The only exception will be engine piston Al–Si alloys, which are selected into a separate group.

The concentration of silicon (from 4% to 13%) allows classifying most of such alloys as hypo-eutectic. These are US alloys AA355.0, AA354.0, AA383.0, etc.,

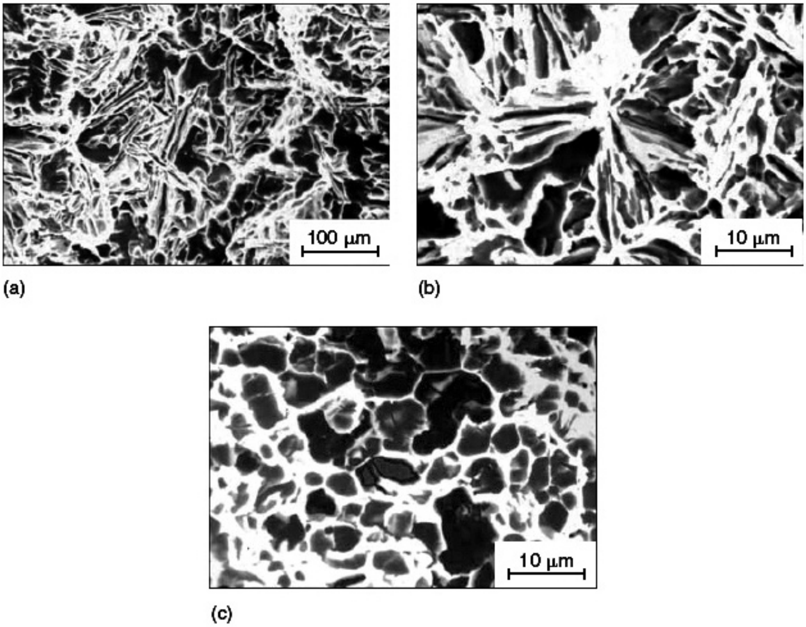

Figure 5.7 Typical fracture surfaces of copperless Al–Si alloys (mold casting), SEM: (a, b) AK9ch (F); (c) AK9ch (T6).

as well as their Russian analogs AK5M (Al–5Si–1Cu), AK5M2 (Al–5Si–2Cu), AK5M7 (Al–5Si–7Cu), AK8M3 (Al–8Si–3Cu), and AK9M2 (Al–9Si–2Cu) (see Appendix 1). Only alloy AK12M2 (Al–12Si–2Cu) possesses microstructure close to eutectic. The analysis of phase composition of most alloys in the T4 temper could be conducted using the Al–Si–Cu–Fe–Mg phase diagram (Section 1.4.1). Only high-purity alloys could be analyzed using quaternary phase diagram Al–Si–Cu–Mg (e.g., AK8M3ch). Even less often one could use the ternary Al–Si–Cu phase diagram, for obvious reasons. The phase composition of (Al) after aging (especially in the T7 temper) could be analyzed using the Al–Si–Cu and Al–Si–Cu–Mg phase diagrams. In the presence of manganese some information could be obtained from the corresponding multicomponent phase diagrams, which are not sufficiently studied even up to this point (see Section 1.4.2). In order to understand as-cast microstructures, one should use non-equilibrium phase diagrams (Section 2.3.1).

Al–Si alloys of this group differ from copper-less alloys by lower castability and corrosion resistance, but higher hardness in as-cast state. High purity alloys heat treated according to the T6 scheme exhibit the maximal values of strength (UTS up to 400 Mpa). This is realized in alloy AA354.0. Typical values of mechanical

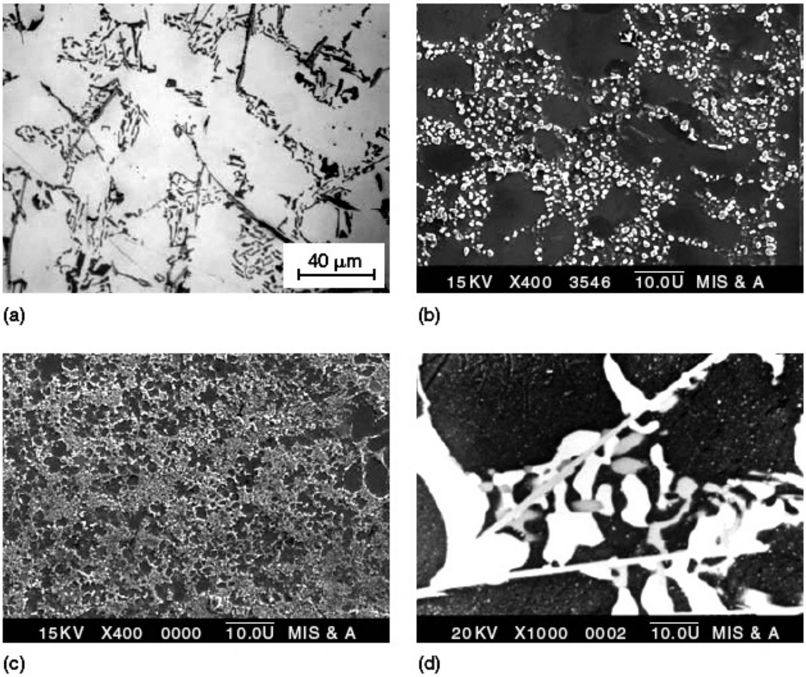
40 µm
15KV X400 3546 10.0U MIS & A
(a)
(b)
15KV X400 0000 10.0U MIS & A
20KV X1000 0002 10.0U MIS & A
(c)
(d)

Figure 5.8 Microstructures of 3xx.0 alloys with copper: (a) AK9M2 alloy (9%Si, 2%Cu, 1%Fe, 0.3%Mg), as-cast (metal mold), LM; (b) 354.0 alloy ($<$0.1%Fe), T6, SEM; (c) AK12M2 alloy (12%Si, 2%Cu, 0.8%Fe), die-casting, as-cast, SEM; (d) alloy containing 10%Si, 6%Cu, 0.5%Mg, and 0.15%Fe, sand casting ($V_c \sim 10^{-2}$ K/s), SEM.

properties of these materials are presented in Table 5.5; they can be significantly higher than the specified minimal values (see Appendix 3).

In alloys of the *AK5M* (Al–5Si–1Cu, analog 355) type the principal components of microstructure are (Al) dendrites and (Al) + (Si) eutectic, which in the presence of iron may contain the β-phase. Due to small concentration of silicon, the volume fraction of the primary (Al) crystals does not exceed 70–80 vol.%. Copper and magnesium in the process of solidification form phases Al_2Cu, $Al_5Cu_2Mg_8Si_6$, and Mg_2Si (as a rule, according to different eutectic reactions). These particles are mostly located along the grain boundaries, mostly in the form of veins or skeletal shapes (Figure 5.8a); quite often they can form complex conglomerates together with such phases as (Si). The volume fraction of these phases is usually not high, and after metallic mold casting these particles can only be revealed after detailed microanalysis.

Heat treatment according to the T5 scheme does not cause any microstructural changes that could be revealed with the methods of light microscopy. However, the formation of strengthening precipitates/dispersoids can take place during T5 heat treatment. Additionally, during heat-up before quenching a complete dissolution of copper and magnesium in (Al) takes place, as well as partial fragmentation of the silicon eutectic skeleton and its spheroidization. Iron-bearing phases do not sustain such changes.

Alloy AK5M is manufactured out of primary components. Its average level of mechanical and casting properties is worse than for alloys of the AK7 and AK9 type. It finds only limited application in industry, mostly in automotive and aerospace areas: engine cylinder heads, details of different apparatuses working at temperatures not higher than 250°C.

Alloy *AK5Mch* (analog 355.2) is a modification of AK5M. The principal difference between the two is in more rigorous control of iron content (0.4% vs 1% for casting into metallic molds), a narrower Mg concentration range, and small additions of titanium. This allows raising the guaranteed level of mechanical properties significantly, in particular, in the T6 temper, from 240 MPa to 300 MPa. The principal microstructural difference from the base alloy AK5M is in more strict control of iron content. Because of such control the volume fraction of Fe-bearing particles drops precipitously. This becomes particularly noticeable after quenching, when needle-like inclusions of Fe phases become especially visible against the background of globular silicon particles.

Alloy AK5Mch finds even more limited application in comparison to the base alloy, mostly in automotive and caterpillar industry. Its mechanical properties are slightly better than those of AK5M, though. The overall share of alloys AK5M, AK5Mch in the general tonnage of all aluminum casting alloys does not exceed 3%.

Alloy *AK5M2* (Al5Si2Cu) is characterized not only by the relatively forgiving control of impurities (iron up to 1.3%, zinc up to 1.5%), but also by broader range of the alloying element concentrations, especially copper (1.5–3.5%) and magnesium (0.2–0.8%). This makes it particularly attractive in terms of utilization of aluminum scrap. Alloy AK5M2 is one of the cheapest and most widespread casting alloys; it is mostly used in as-cast state (F temper). Similar to alloy AK5M, its principal microstructural components are dendrites of primary (Al) and aluminum silicon eutectic. To be more precise, there might be several eutectics comprising, in addition to (Si), phases containing Fe, Mn, Cu, Mg, and other chemical elements. Microstructure can change appreciably as a function of these elements' concentrations [327].

When the concentration of manganese is low, iron (the concentration of which is typically not less than 1%) mostly enters into the β-phase. On the contrary, if the concentration of manganese is closer to the upper limit, then needle-like inclusions of the β-phase are practically absent because all iron is tied up into the $Al_{15}(Fe,Mn)_3Si_2$ phase. Moreover, especially in the case of sand casting, primary crystals of this phase can precipitate directly from the liquid phase. The amounts of phases Al_2Cu, $Al_5Cu_2Mg_8Si_6$, and Mg_2Si are much higher than in alloy AK5M. Zinc, as a rule, completely enters the (Al) phase. During heat-up before quench, similar to alloy AK5M, particles of the silicon phase having more or less globular shapes are formed. However, as it follows from the cross-section of the Al–Si–Cu–Mg phase diagram at 9%Si and 500°C (Figure 5.10), not all magnesium and copper can get dissolved in (Al). Microstructure of heat treated castings often reveals Mg-bearing constituent particles ($Al_5Cu_2Mg_8Si_6$, Mg_2Si, and $Al_8FeMg_3Si_6$), because the magnesium concentration is usually close to the upper limit.

Alloy AK5M2 is produced out of secondary materials. It is characterized by satisfactory casting and corrosion properties. Its guaranteed level of mechanical properties is not high, although with proper optimization of chemical composition and good refining from non-metallic inclusions it could be not worse than for alloy AK5M. The share of alloy AK5M2 in the overall volume of industrial casting aluminum alloys is of the order of 15%. It is generally used for different articles carrying average loads: sewing machines, construction machines, etc.

The composition range for alloy *AK6M2* (Al6Si2Cu) substantially overlaps with Al–Si–Cu alloy AK5M2, but differs by a narrower concentration range for all alloying elements and more rigorous requirements for impurities content. Its microstructure, especially after heat treatment (T4, T6, and T7), is closer to microstructure of Al–Si alloy AK5M, differing only by a somewhat larger fraction of the particles of the silicon phase. Copper and magnesium almost completely dissolve in (Al) after quenching.

As a rule, alloy AK6M2 is manufactured out of primary materials. Its mechanical properties are satisfactory (see Table 5.6). It is mostly used for different articles carrying average loads, including automotive industry (e.g., cylinder heads).

In alloy *AK5M4* (Al5Si4Cu, analog AA308) the contents of copper is about the same as that of silicon. For this reason the volume fraction of Al_2Cu is higher than for other phases (with the exception of the silicon phase). A significant amount of copper (up to 1.5%) during casting enters the composition of (Al), which makes this Al–Si alloy harder in comparison to the alloys already discussed above. It has a broad concentration range for all alloying elements, rather mild limitations on the impurity concentrations and is mostly manufactured out of secondary materials. As a function of the Fe to Mn ratio, iron can enter the composition of one of the two phases: either β or $Al_{15}(Fe,Mn)_3Si_2$, having needle-like and skeletal morphologies, respectively. Magnesium is mostly present in the form of the $Al_6Cu_2Mg_8Si_5$ compound, and the formation of Mg_2Si particles in as-cast microstructure is highly unlikely.

The heat treatment scheme recommended for mold casting includes heat-up before quenching and causes break-up and spheroidization of the eutectic silicon plates. Crystals of Al_2Cu partially dissolve in the aluminum solid solution; the $Al_6Cu_2Mg_8Si_5$ phase disappears.

Strong increase of hardness during aging is caused by the formation of secondary particles of metastable compounds of the following phases: Al_2Cu, Mg_2Si, $Q(Al_6Cu_2Mg_8Si_5)$, and $S(Al_2CuMg)$. Concurrently, the relative elongation drops almost to zero, and the guaranteed level of strength even in the T6 temper is relatively low (200 MPa).

Alloy AK5M4 is manufactured out of secondary materials. It was developed as a thermally resistant alloy for brakes, pumps, etc. Having about the same properties

Table 5.6 Chemical composition of Cu- and Zn-bearing Al–Si alloys

Alloy	Concentrations (%) (Al balance)						
	Si	Cu	Mg	Fe[a]	Mn	Zn	Other elements
AK5M (Al5Si1Cu)	4.5–5.5	1–1.5	0.35–0.65	1	0.5	0.3	–
AK5Mch (Al5Si1Cu)	4.5–5.5	1–1.5	0.4–0.55	0.4	0.1	0.3	Ti
AK5M2 (Al5Si2Cu)	4–6	1.5–3.5	0.2–0.8	1.3	0.2–0.8	1.5	Ti
AK5M4 (Al5Si4Cu)	3.5–6	3–5	0.2–0.5	1.2	0.2–0.6	1.5	Ti
AK5M7 (Al5Si7Cu)	4.5–6.5	6–8	0.2–0.5	1.2	0.5	0.6	–
AK6M2(Al6Si2Cu)	5.5–6.5	1.8–2.3	0.3–0.45	0.6	0.1	0.06	Ti
AK8M (Al8Si1Cu)	7.5–9	1–1.5	0.3–0.5	0.8	0.3–0.5	0.3	Ti
AK8M3 (Al8Si3Cu)	7.5–10	2–4.5	0.45	1.4[b]	0.5	1.2	–
AK8M3ch (Al8Si3Cu)	7–8.5	2.5–3.5	0.2–0.45	0.4	–	0.5–1	Ti, B, Be
AK9M2 (Al9Si2Cu)	7.5–10	0.5–2	0.2–0.8	1	0.1–0.4	1.2	Ti
AK12M2 (Al12Si2Cu)	11–13	1.8–2.5	–	0.6–1	0.5	0.8	–
AK9Ts6 (Al9Si6Zn)	8–10	0.3–1.5	0.3–0.5	0.3–1	0.1–0.6	5–7	–
AK7Ts9 (Al7Si9Zn)	6–8	–	0.1–0.3	1.2	0.5	7–12	Ti

[a] M; [b] P.

Table 5.7 Typical mechanical properties of some copper-bearing Al–Si alloys

Alloy	Temper	UTS (MПa)	El (%)	HB
AK5M (Al5Si1Cu)	S, T5	220	180	1
AK8M3ch (Al8Si3Cu)	M, T5	400	340	4

M: casting into metallic mold; S: sand casting.

as alloy AK5M7, it contains less copper. As a result, its production volume is two times higher than of alloy AK5M7.

Alloy *AK5M7* (Al5Si7Cu) contains more copper than silicon. Formally speaking, it could be classified as an Al–Cu, as it is done by the AA (e.g., alloy AA238.0 contains 4% Si) [2]. However, in its phase composition and properties it is very similar to Al–Si alloy AK5M4. The difference between the two is in higher volume fraction of the Al_2Cu phase for the former, which is explained by its chemical composition. Because in alloy AK5M7 a significant fraction of the Al_2Cu inclusions is not dissolved in the process of heat-up before quenching, it is more brittle than AK5M4.

Alloy AK5M7 is manufactured out of secondary materials. It is used for caterpillar and automotive engine pistons. During the last several years thermally stable alloy AK5M7 is being replaced by AK5M4.

Alloy *AK8M* (Al8Si1Cu) contains copper and magnesium in a relatively narrow concentration range (1–1.5% and 0.35–0.55%, respectively); limitations on the allowable iron concentrations are also quite strict ($<$0.6%). Besides, it contains small additions of manganese and titanium. This Al–Si alloy is manufactured mostly out of primary materials. It is recommended for die casting and provides a comparatively high level of mechanical properties in the F temper (UTS $>$260 MPa, El $>$2%).

The principal microstructural components in as-cast state are dendrites of aluminum solid solution, (Al), and the (Al) + (Si) eutectic. Volume fractions of other phases are not high; as a rule, they possess compact morphology. Due to the presence of manganese, all iron is bounded into the skeletal inclusions of the $Al_{15}(Fe,Mn)_3Si_2$ phase. Due to the low copper concentration the volume fraction of the Al_2Cu phase does not exceed 1 vol.%. Magnesium enters the composition of such phases as $Al_5Cu_2Mg_8Si_6$ and Mg_2Si, the volume fractions of which are also low. In metallic mold castings (not to mention castings obtained under pressure) these particles can be hardly revealed with light microscopy. Other impurities do not exert any significant influence upon phase composition.

Aging after casting results in significant strengthening effect, and for this reason (especially for casting under pressure) the recommended temper is T5. Heat-up before quenching results in the formation of globular particles of the silicon phase; at the same time, magnesium and copper become completely dissolved in (Al).

Alloy AK8M possesses a good combination of mechanical and casting properties. It is used in different areas for manufacturing articles of complex shapes.

Alloy *AK8M3* (Al8Si3Cu), besides silicon and copper, does not contain any other alloying elements. However, a large amount of impurities is allowed: up to 1.3%Fe, and up to 0.45%Mg. This makes the AK8M3 alloy particularly suitable for manufacturing out of secondary materials or scrap. However, unlike the most widespread Al–Si alloy out of secondary materials, the AK5M2, the choice of materials for alloy AK8M3 is more limited, in particular, due to the relatively low magnesium concentration.

Alloy AK8M3 has heterogeneous microstructure. In addition to the primary (Al) crystals and eutectic silicon, it contains iron-bearing phases (mostly β), Al_2Cu, and $Al_4Cu_2Mg_8Si_5$. Due to high iron concentration in metallic mold cast alloy AK8M3 the overall amount of thin, extended plates of th β-phase is significant (Figure 5.8a) and they render a typical appearance of "dissected" aluminum matrix [3].

Heat-up before quenching results in the same changes of properties for other Al–Si alloys as well. However, because of higher allowed concentrations of alloying elements and impurities, the application of heat treatment is not recommended because the guaranteed level of mechanical properties is quite low, especially in the case of casting with low solidification rates. In this case a large volume fraction of the needle-like inclusions of the β-phase will define an almost zero plasticity, practically independent of any other changes. Alloy AK8M3 was developed mostly for casting under pressure that helps to form a disperse alloy microstructure. In this case the negative influence of the β-phase can be somewhat reduced. Additionally, the amount of copper entering the composition of (Al) grows. This alloy is used in automotive industry and in different kinds of electric machines for casting parts of complex shapes.

Although alloy AK8M3ch (Al8Si3Cu), as it follows from its name, represents a modification of the AK8M3 considered above, it differs significantly from it in microstructure and guaranteed level of properties [7, 9]. It is characterized not only by a narrower range of the copper and magnesium concentrations (like AA354 alloy), but also by additions of zinc and other three ancillary additions (Ti, Be, and B). Taking into account that the allowed impurities concentrations (including iron <0.4%) is also small, alloy AK8M3 can be manufactured only out of primary materials. It (like AA354 alloy) has the highest strength amongst all standard Al–Si alloys (in the T6 temper UTS >400 MPa, El >4%).

The principal microstructural components of the AK8M3 alloy are primary crystals of (Al) and the aluminum–silicon eutectic. Besides (Al), copper and magnesium also enter the composition of the Al_2Cu and $Al_4Cu_2Mg_8Si_5$ phases. Although iron is allowed only in the form of impurity, it can still be present in the following three phases: $Al_4Be_5Fe_2$, $AlBe_4Fe$ and $Al_{16}Fe_4Be_3Si_2$ [6]. If the ratio Be:Fe >0.5, then iron is completely bound into one of the ternary phases possessing globular morphology. At lower values of this ratio a quaternary compound, possibly of eutectic origin, is formed and can be identified via its skeletal morphology.

After the T6 heat treatment a microstructure is realized that is close to ideal for Al–Si alloys: globular particles of the silicon phase uniformly distributed in the aluminum matrix, which is dispersion hardened by intermetallic compound particles (Figure 5.8b).

Globular particles of the iron- and beryllium-bearing phases can be hardly observed against such a background using optical microscopy. If the iron concentration is controlled rigorously (not more than 0.1%), then addition of Be to the AK8M3ch alloy is not justified. This alloy is mostly used in automotive industry for manufacturing thin-walled, geometrically complex hermetic shapes.

Alloy *AK9M2* (Al9Si2Cu) is characterized by a broad range of alloying element concentrations and high concentrations of allowed impurities. For this reason, along with alloys AK5M2 and AK8M3 it is manufactured mostly out of secondary materials. Its microstructure is close to that for the latter alloy; the main difference is in smaller amount of the Al_2Cu phase and possible presence of the Mg_2Si phase and quaternary compound $Al_8FeMg_3Si_6$. However, overall microstructure is determined by the presence of eutectic silicon and needle-like β-phase particles. After heat-up before quenching, the application of the T6 temper results in complete or partial fragmentation and spheroidization of the Si phase. Additionally, all Cu- and Mg-bearing phases get dissolved. Alloy AK9M2 is characterized by good castability and average level of mechanical properties (in the F temper). It is mostly used in automotive industry.

In alloy *AK12M2* (Al12Si2Cu), unlike in other Al–Si alloys, iron is not impurity but an alloying element in the amounts up to 0.6–1.0%. According to the Al–Si–Fe phase diagram (Figure 1.2.26) when the concentration of Fe is that high, most of the β-phase enters the (Al)–(Si)–β eutectic (Figure 5.8c), which becomes the principal microstructural feature of this alloy. It is recommended for manufacturing of castings with complex shapes (casting under pressure is preferred), which ensures favorable (disperse) morphology of eutectic phases, as well as high enough concentration of copper in (Al). Such a microstructure allows obtaining relatively high level of mechanical properties in the T1 temper (UTS >260 MPa, El $>1\%$). If the content of silicon is closer to the upper limit, then microstructure may contain primary (Si) crystals. Alloy AK12M2 typically is not quenched, although this kind of heat treatment could increase its plasticity substantially. This alloy is manufactured mostly out of primary materials, although recently it was also manufactured out of scrap/secondary materials. It is used in automotive industry, including manufacturing of engine pistons.

Typical microstructures of copper-containing 3xx alloys are shown in Figure 5.8 and their phase composition features are described below.

Isothermal sections of the Al–Cu–Si phase diagram at 520°C and 200°C (Figure 5.9a) show that in alloys like 319.2 and 305.0 (Table 3.1) with a low concentration of iron impurity, copper shall be totally dissolved in (Al) during solution heat treatment, and precipitate as metastable modifications of Al_2Cu during aging. From the polythermal section at 6%Si in Figure 5.9b, it follows that after primary solidification of (Al) the binary (Al) + (Si) eutectic is formed,

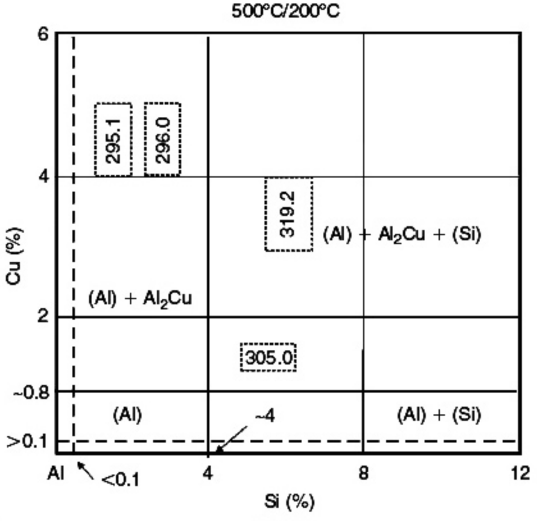
500°C/200°C
6
4
2
~0.8
>0.1
Al
<0.1
4
8
12
Cu (%)
Si (%)
295.1
296.0
319.2
305.0
(Al) + Al$_2$Cu + (Si)
(Al) + Al$_2$Cu
(Al)
~4
(Al) + (Si)

(a) Al–Si–Cu

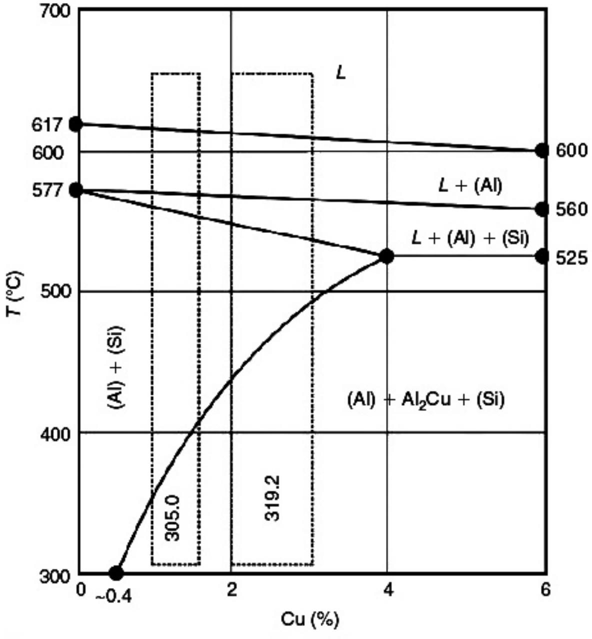
700
617
600
577
500
400
300
T (°C)
0
~0.4
2
4
6
Cu (%)
L
600
L + (Al)
560
L + (Al) + (Si)
525
(Al) + (Si)
(Al) + Al$_2$Cu + (Si)
305.0
319.2

(b) Al–6%Si

Figure 5.9 Isothermal (a) and polythermal (b, c) sections of Al–Cu–Si phase diagram: (a) 500°C (solid lines) and 200°C (dashed lines); (b) 6%Si; and (c) 10%Cu.

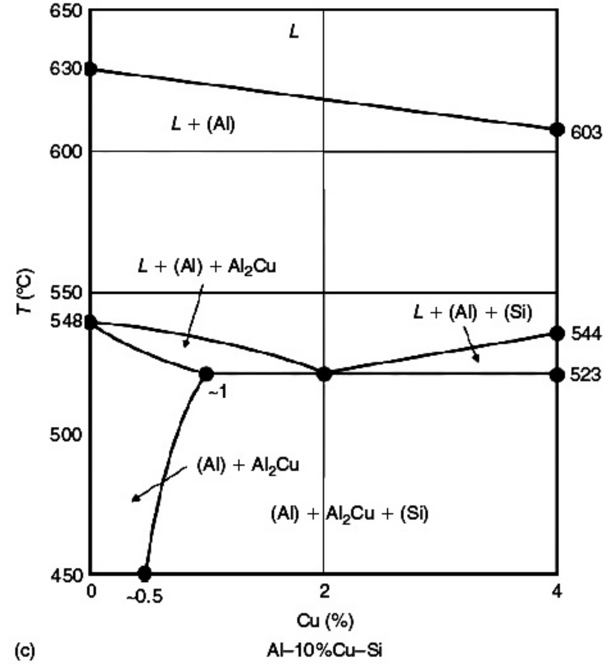

Figure 5.9 (Continued)

and the Al_2Cu phase can appear as a result of the ternary eutectic reaction at 525°C, which in 319.2 and 305.0 alloys is non-equilibrium.

The phase composition of 3xx.0-series alloys containing simultaneously magnesium and copper additions at a low concentration of iron impurity is reflected in isothermal sections of the Al–Si–Cu–Mg phase diagram shown in Figure 5.10. The phase boundaries Figure 5.10a are also valid at other concentrations of silicon, because in 3xx.0-series alloys this element is always present in excess. At sub-solidus temperatures these alloys, as a rule, fall into the phase region (Al)+(Si), that is all copper and magnesium are dissolved in (Al). At 200°C, various combinations of metastable modifications of the Mg_2Si, Al_2Cu, and Q phases can be formed depending on the ratio between Cu and Mg and the aging regime. These combinations determine the strengthening effect after aging.

It should be also noted that the phase composition of the products of aging could be (with caution) analyzed using isothermal cross-sections only if one knew the chemical composition of the supersaturated solid solution. This composition generally is very different from the composition of the entire alloy, due to the formation of excess phases and dispersoids and because of microsegregation. Note that real selection of metastable phases that precipitate during decomposition of

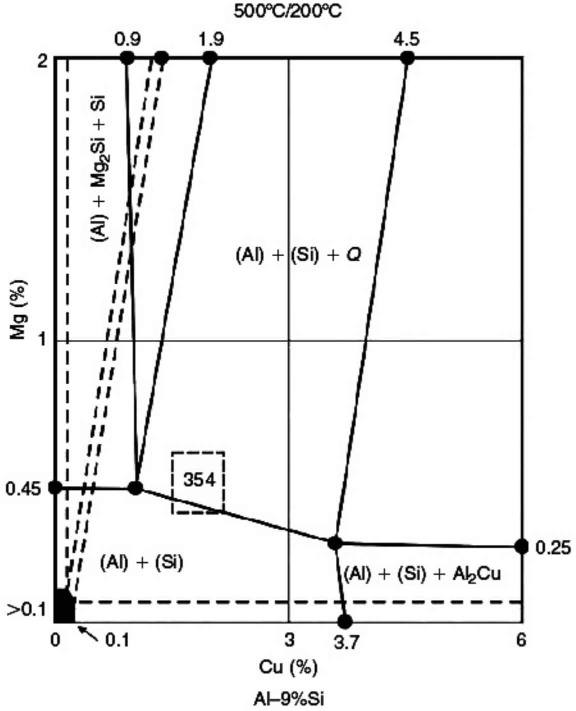

Figure 5.10 Isothermal sections of Al–Cu–Mg–Si phase diagram at 9%Si: 500°C (solid lines) and 200°C (dashed lines).

a supersaturated solid solution and participate in hardening of an alloy cannot be easily derived from the equilibrium phase diagram.

The polythermal sections at 10%Si (Figure 5.11) show that in 3xx.0-series alloys the Mg_2Si, Al_2Cu and Q phases are formed at lower temperatures than (Si), that is always after the (Al) + (Si) eutectic. In as-cast structure, the phases containing copper and magnesium appear either as components of complex eutectics involving (Al) and (Si), or as separate inclusions.

Figure 5.12a shows polythermal sections of the Al–Cu–Fe–Si phase diagram at 6%Si and 1%Fe. Obviously, iron impurity in 3xx.0-series alloys with low magnesium content can lead to the formation of only one phase – Al_5FeSi.

Alloys, in which silicon, magnesium, and iron are present simultaneously in amounts significantly affecting the phase composition, should be analyzed using the quinary Al–Cu–Fe–Mg–Si phase diagram (Figure 1.47). In 3xx.0-series alloys, the coupled effect of Cu, Mg, and Fe as applied to 333.0-type alloys (8–10%Si, 3–4%Cu, 0.05–0.5%Mg, up to 1.0%Fe, up to 1%Zn, up to 0.5%Mn)

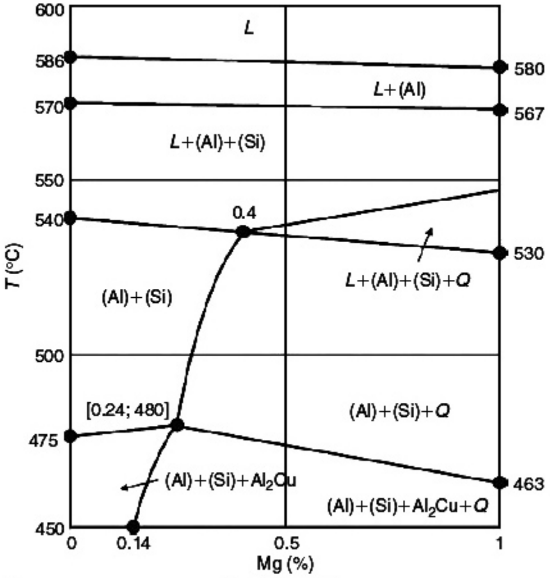

(a) Al–9%Si–3%Cu

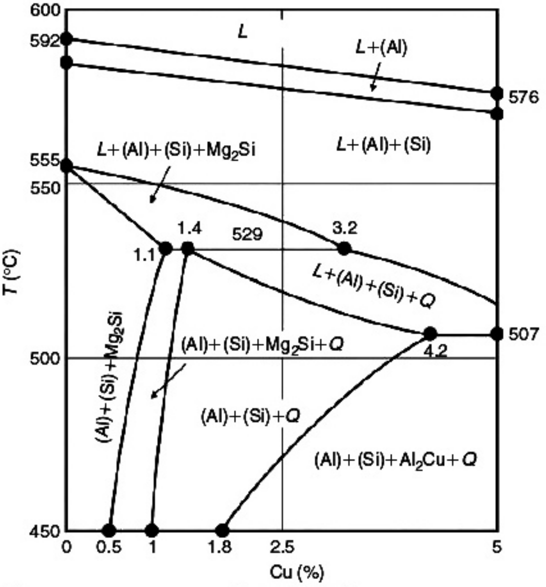

(b) Al–10%Si–1%Mg

Figure 5.11 Polythermal sections of Al–Cu–Mg–Si phase diagram at 10%Si: (a) 3%Cu; (b) 1%Mg.

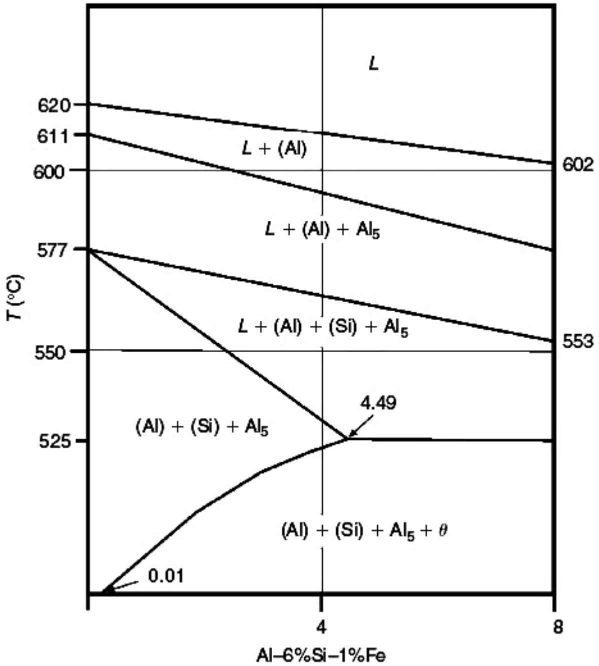

Figure 5.12 Polythermal section of Al–Cu–Fe–Si phase diagram at 6%Si and 1%Fe Al_5–Al_5FeSi.

can be followed by the isothermal sections at 10%Si (Figure 1.47c, d). The concentration of silicon (above 2–3%) has no effect on the position of the phase boundaries.

Polythermal section of the Al–Cu–Fe–Mg–Si phase diagram at 10%Si, 5%Cu, and 0.5%Mg in Figure 5.13 shows that, at comparatively low concentrations of iron (<0.5%), the (Al) + (Si) eutectic forms in 3xx.0-type alloys after primary solidification of (Al), and only after that the Al_5FeSi phase is formed. The presence of magnesium can lead to the formation of the $Al_8FeMg_3Si_6$ phase in the final stages of solidification. The as-cast structure of 3xx.0-type alloys can contain more that five phases as a result of non-equilibrium solidification. These phases form complex conglomerates of crystals as shown in Figure 5.8d, which are formed during multi-phase solidification reactions listed in Tables 1.38–1.40.

For example, Table 5.8 gives solidification reactions experimentally observed in a C355.2 alloy solidified under non-equilibrium conditions. The as-cast structure of this alloy contains seven excess phases. First five reactions in Table 5.8 agree well with the Al–Cu–Fe–Mg–Si phase diagram (Figure 1.47b), and the last two are different as they do not include the $Al_8FeMg_3Si_6$ phase. However, the

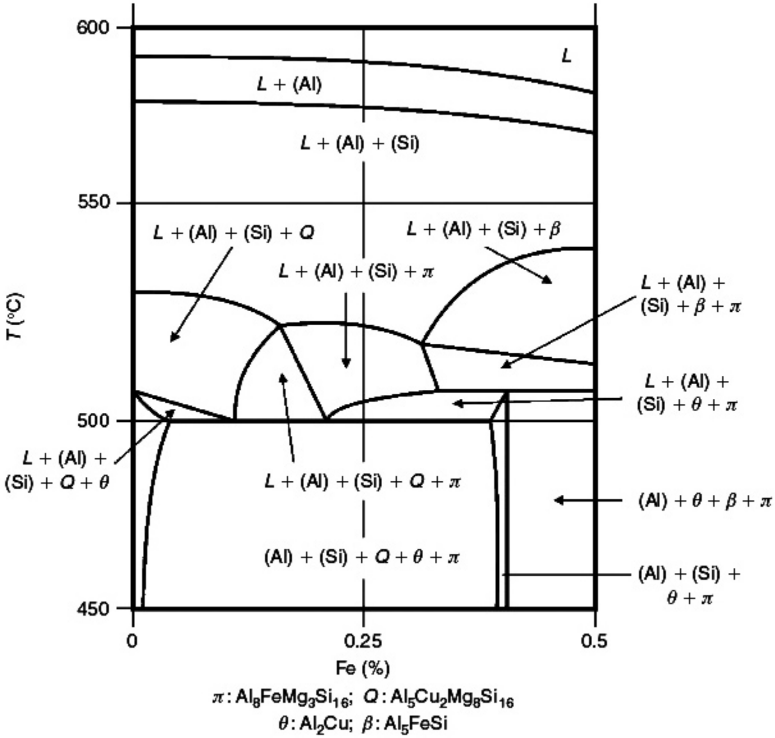

Figure 5.13 Polythermal section of Al–Cu–Fe–Mg–Si phase diagram at 10%Si, 5%Cu, and 0.5%Mg [54,55].

as-cast structure is so complex that the reliable experimental identification of all solidification reactions is doubtful.

In hyper-eutectic Al–Si alloys containing more than 11%Si (390.0 type), (Si) solidifies as a primary phase, and then (Al) is formed through eutectic reactions. The rest of solidification sequence is very much the same as in hypo-eutectic Al–Si alloys. Note that the quaternary π (AlFeMgSi) phase that has to form in these alloys according to the equilibrium phase diagram (Figure 1.47b) is not mentioned in Table 5.9. It is possible that during non-equilibrium solidification almost all iron is bound to the Al_5FeSi phase during the eutectic reaction $L \Rightarrow (Al) + (Si) + Al_5FeSi$, and there is not enough iron left for the formation of the quaternary phase. That assumption agrees well with the data in Table 5.9, where iron-containing phases do not form during lower-temperature reactions. On the other hand, the amount of the π-phase could be very small (with taking into account very low concentrations of iron in all multi-phase reactions, see Table 3.19), which makes the identification of this phase difficult.

Table 5.8 Solidification reactions under non-equilibrium conditions in a C355.2 alloy (5.05%Si, 1.04%Cu, 0.53%Mg, and 0.1%Fe)

Reaction	Temperatures (°C) at a cooling rate	
	0.3 (K/s)	5 (K/s)
$L \Rightarrow (\mathrm{Al})$	621–557	622–543
$L \Rightarrow (\mathrm{Al}) + (\mathrm{Si})$	557–551	543–537
$L \Rightarrow (\mathrm{Al}) + \mathrm{Al_5FeSi} + (\mathrm{Si})$	551–535	537–532
$L + \mathrm{Al_5FeSi} \Rightarrow (\mathrm{Al}) + (\mathrm{Si}) + \mathrm{Al_8FeMg_3Si_6}$		
$L \Rightarrow (\mathrm{Al}) + (\mathrm{Si}) + \mathrm{Al_8FeMg_3Si_6} + \mathrm{Mg_2Si}$	535–501	532–516
$L \Rightarrow (\mathrm{Al}) + (\mathrm{Si}) + \mathrm{Al_5FeSi} + \mathrm{Al_2Cu}$ $L \Rightarrow (\mathrm{Al}) + (\mathrm{Si}) + \mathrm{Al_5Cu_2Mg_8Si_6} + \mathrm{Al_2Cu}$	501–489	516–477
Solidus	489	477

Zn-bearing Al–Si alloys, for example *AK9Ts6* ($\mathrm{Al_9Si_6Zn}$) and *AK7Ts9* ($\mathrm{Al_7Si_9Zn}$) stand somewhat aside from the main group and have rather limited application; for this reason they are discussed here very briefly.

Although these materials are classified into a separate fifth group under Russian classification, their microstructure is very close to other Al–Si alloys because zinc does not form its own phases, while copper, magnesium, and iron can form only phases presented in Table 5.1. Zn-bearing Al–Si alloys are mostly manufactured out of secondary materials and possess good castability but limited mechanical properties. Their interesting feature is ability to self-quench after casting and strengthen as a result of further natural aging. The strengthening effect is noticeable but not very significant. Besides, at higher Zn concentrations the density of alloys will be growing. As a result, in the last time these alloys were applied infrequently, mostly in agricultural and electrical machine industry for casting parts of fuel pumps and other details carrying average loads.

5.1.3.1 Fractography of Cu-bearing Al–Si alloys with small amounts of silicon

In as-cast condition, as in all Al–Si alloys, a substantial portion of fracture surfaces is occupied by planar areas of brittle fracture of silicon and other phases [3] (Figure 5.14). At high iron concentrations needle- or plate-like areas may appear – a direct consequence of fracture of the β-phase. After heat treatment fracture surfaces of primary Al–Si alloys (with low Fe concentration) and with small amounts of copper are characterized by large number of pits. This becomes particularly

Table 5.9 Solidification reactions under non-equilibrium conditions in a B390.1 alloy (17.45%Si, 4.81%Cu, 0.56%Mg, 0.74%Fe, and 0.27%Mn), [Backerud et al., see reference to Table 5.3]

Reaction	Temperatures (°C) at a cooling rate	
	0.4 (K/s)	5 (K/s)
$L \Rightarrow (Si)$	634–617	622–562
$L \Rightarrow (Al)$, $L \Rightarrow (Al) + (Si)$	561	557
$L \Rightarrow (Al) + (Si) + Al_5FeSi$; $L \Rightarrow (Al) + (Si) + (AlMnFeSi)$	560–558	554–547
$L \Rightarrow (Al) + (Si) + Mg_2Si$	540–503	517–503
$L + Mg_2Si \Rightarrow (Al) + (Si) + Al_5Cu_2Mg_8Si_6 + Al_2Cu^*$ $L \Rightarrow (Al) + (Si) + Al_5Cu_2Mg_8Si_6 + Al_2Cu$	503–493	503–483
Solidus	493	483

* In our opinion, this reaction should include only one Cu-bearing phase, either Al_2Cu or $Al_5Cu_2Mg_8Si_6$.

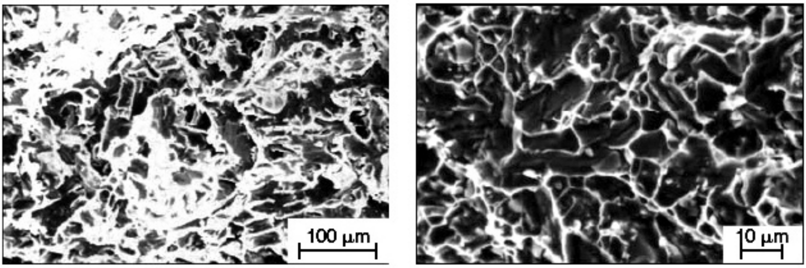

(a) (b)

Figure 5.14 Typical fracture surfaces of copper-bearing Al–Si alloys (AK5M2, mold casting): (a) F; (b) T6.

noticeable in the T4 temper. As a function of the used casting technique the average size of features comprising fracture surfaces may vary significantly, including porosity. The most coarse fracture surface is typical for alloys obtained by sand casting. Fracture surfaces of the high quality alloys of the AK8M3ch type in heat treated state are practically the same as for copper-less high-purity Al–Si alloys.

5.1.4 Engine piston Al–Si alloys

As a rule, these alloys contain large volume fraction of Si- or Ni-bearing phases, which ensures their high level of strength at elevated temperatures and low value of the thermal expansion coefficient. All standard alloys of this group contain nickel as an alloying element. These materials have complex heterogeneous microstructure, and a significant number of phases could be present (see Table 5.1).

In order to analyze phase composition of such alloys one needs, in the very least, quaternary phase diagrams, in particular, Al–Si–Ni–Fe (Figure 1.44). Although iron in engine piston alloys is an impurity, this element in concentrations as small as 0.3% (see Figure 1.25, phase diagram Al–Ni–Fe) can form more than 2 vol.% of the Al_9FeNi phase. It is this phase in the form of primary or eutectic crystals that is particularly typical for microstructure of engine piston Al–Si alloys. In addition to compounds with iron, nickel can enter the composition of Cu-bearing phases, as it follows from the Al–Cu–Ni phase (Figure 1.20). Rigorous analysis of microstructure of casting engine piston Al–Si alloys requires that the six-component phase diagram Al–Si–Ni–Cu–Mg–Fe be used, because all elements of this system are present in most industrial alloys and, most importantly, exert influence upon the alloy phase compositions. To assess possibilities of formation of certain phases in six-component alloys using only ternary and quaternary phase diagrams is difficult, and the results of such analysis could be only approximate even without considering the applied solidification rate.

Analysis of piston alloys is complicated by the formation of primary crystals of the silicon phase (Figure 5.15b) and often occurrence of "primary" Ni-containing phases. A simplified analysis of the phase composition of piston alloys can be performed using quinary phase diagrams in the range of Al–Si alloys, using some assumptions.

Evaluation of the equilibrium phase distribution in the solid state of quinary alloys with nickel (Figure 1.6) can be made based on the knowledge of all quaternary diagrams with silicon, that is Al–Fe–Ni–Si (Figure 1.44), Al–Cu–Ni–Si, Al–Mg–Ni–Si (Figure 1.46), Al–Cu–Mg–Si (Figure 1.39), Al–Cu–Fe–Si (Figure 1.37), and Al–Fe–Mg–Si (Figure 1.42).

Analysis of the phase composition of 393 type and FM piston alloys (Table 5.10) at a low concentration of iron impurity can be performed with the Al–Cu–Mg–Ni–Si diagram in the Si-rich region. According to the corresponding quaternary diagrams, the following phases can be in equilibrium with (Al) and (Si): Al_3Ni, $Al_3(CuNi)_2$, Al_7Cu_4Ni, Al_2Cu, Mg_2Si, and $Al_5Cu_2Mg_8Si_6$. All these phases can in various combinations be present in commercial piston alloys.

Scanning electron microscopy in the back-scattered electrons mode gives more possibilities in identifying other phases as the (Si) phase almost merges with the background. The identification of *M* and *Q* particles is most obvious, as the former appear as black and the latter as light-grey crystals, much lighter than the matrix. Figure 8a, b shows that the amount of black inclusions (*M*) decreases and the amount of light-grey particles (*Q*) increases with the increase in the copper concentration in FM120 to FM135 alloys. Note that, according to Figure 5.16, the *Q* and *M* phases are non-equilibrium in alloys FM120 and FM135, respectively.

The effect of alloying elements on the phase composition at a constant temperature is convenient to analyze using isothermal sections of a phase diagram.

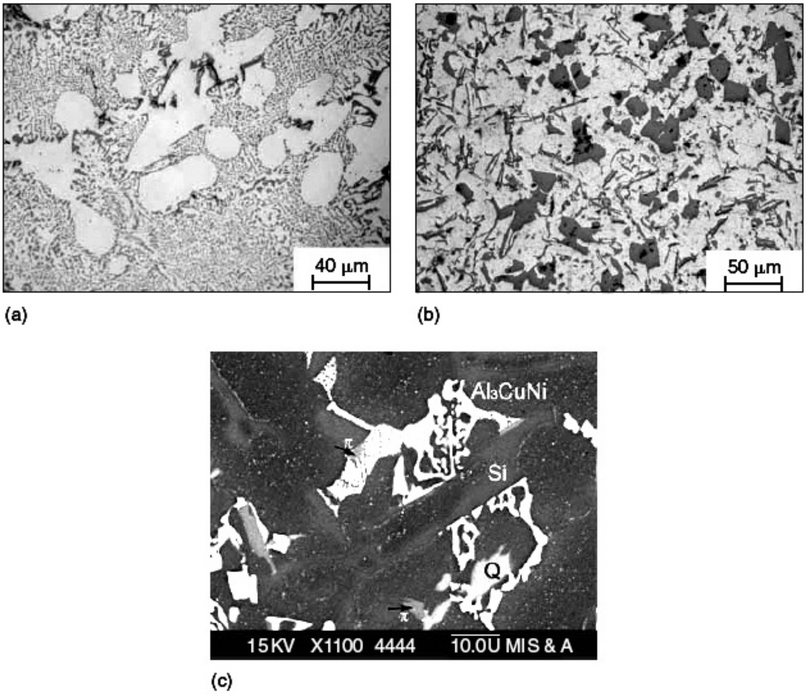

Figure 5.15 Microstructure of as-cast piston alloys: (a) AK12MMgN (AA 339); (b, c) FM135; (a, b) LM; (c) SEM.

Piston alloys are usually used in the stabilized state, that is annealed at 200–250°C (overaging after casting). Taking into account that the upper limit of operating temperatures is 300°C, the isothermal sections at this temperature and at about 13%Si (Figure 5.16) are most characteristic. Isothermal sections at lower and higher temperatures will look similar, only the change in the solid solubility of copper and magnesium should be taken into account.

It is noteworthy, however, to mention that the real phase composition at these temperatures can still be different from the equilibrium one, as the deviation from equilibrium during solidification cannot be eliminated by annealing at such a relatively low temperature.

The volume fraction of constituent phases can be calculated using the data on the phase composition and density and using a technique described elsewhere [2]. Figure 5.17 shows the effect of copper on the volume fraction of excess phases in alloys containing 13%Si, 1%Mg, and 1%Ni (AA339.1 type or FM135 from Table 5.10).

Table 5.10 Chemical composition of engine piston Al–Si alloys

Alloy	Concentrations (%) (Al balance)						
	Si	Ni	Cu	Mg	Fe*	Mn	Other
AK12MMgN	11–13	0.8–1.3	1.8–1.5	0.8–1.3	0.7	0.2	–
AK12M2MgN	11–13	0.8–1.3	1.5–3	0.8–1.3	0.8	0.2	Ti
AK21M2.5N2.5	20–22	2.2–2.8	2.2–3.0	0.2–0.5	0.9	0.2–0.4	Ti,Cr
KC740	16–18	1.1–1.7	1.8–2.4	0.7–1.2	0.5	0.6–1	–
KC741	19–22	1.1–1.7	1.8–2.4	0.7–1.2	0.5	0.6–1	–
AK18	17–19	0.8–1.3	0.8–1.5	0.8–1.3	0.5	0.2	–
GLS	11–13	1–1.3	1–1.3	0–1.3	0.5	0.15	–
AK10M2N	9.5–10.5	0.8–1.2	0.9–1.2	0.9–1.2	0.6	0.05	–

Alloy	Si (%)	Ni (%)	Cu (%)	Mg (%)	Fe (%)	Mn (%)
AK12MMgN	11–13	0.8–1.3	0.8–1.5	0.7–1.3	0.7	0.2
AK12M2MgN	11–13	0.8–1.3	1.5–3.0	0.7–1.3	0.8	0.3–0.6
AK18	17–19	0.8–1.3	0.8–1.5	0.8–1.3	0.5	0.2
AA393.0	21–23	2.0–2.5	0.7–1.1	0.7–1.3	1.3	0.1
AA336.0	11–13	2.0–3.0	0.5–1.5	0.7–1.3	1.2	0.35
AA339.1	11–13	0.5–1.5	1.5–3.0	0.6–1.5	0.9	0.5
FM 109	11.5–12.5	0.8–1.1	0.9–1.3	1.1–1.3	0.5	0.05–0.2
FM 113	11.5–12.5	0.8–1.2	3.0–3.3	0.9–1.2	0.35	0.15
FM 135	12.7–13.7	0.8–1.2	4.8–5.3	0.9–1.2	0.35	0.1
FM 120	12.0–13.5	0.7–1.3	0.8–1.5	0.9–1.3	0.65	0.05–0.3
FM 180	17.0–19.0	0.8–1.3	0.8–1.5	0.8–1.3	0.57	0.05–0.2
FM S2N	11.4–12.4	2.1–2.5	3.1–3.5	0.6–1.0	0.4	0.15
FM S2	11.0–12.0	2.3–2.8	3.3–3.8	0.6–0.9	0.5	0.15–0.25
FM B1	12.5–13.5	2.3–2.8	4.9–5.4	0.6–0.9	0.5	0.15–0.25
FM B2	12.2–12.6	2.7–3.0	3.9–4.3	0.6–0.9	0.5	0.15

*Russian alloys are given according to the alloy specifications rOCT 1583-93 and rOCT 30620-98, AA stands for the specification of the Aluminum Association (US), FM is the specification of the Federal-Mogul Corporation Powertrain Systems.

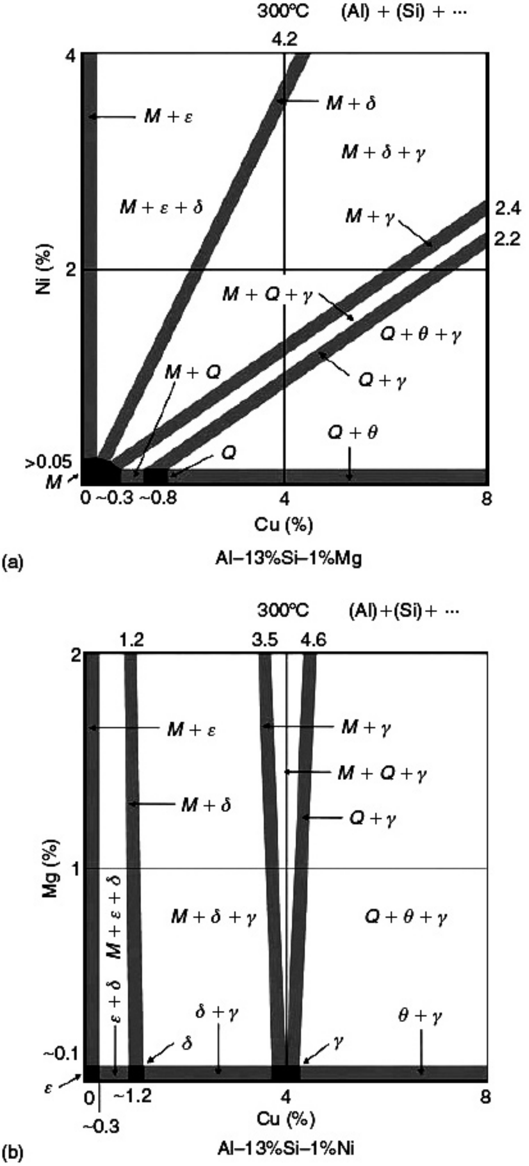

Figure 5.16 Isothermal cross-section of the Al–Cu–Mg–Ni–Si phase diagram at (a) 13%Si, 1%Mg, and 300°C and (b) 13%Si, 1%Ni, and 300°C.

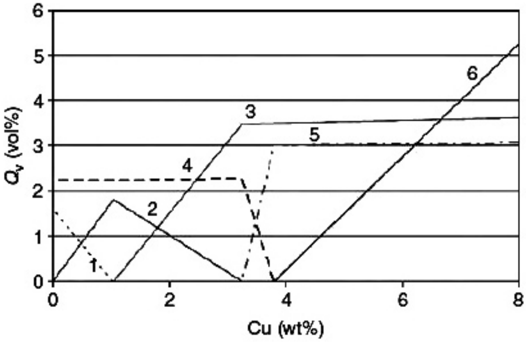

Figure 5.17 Volume fraction (Q_v) of phases vs Cu content at 13%Si, 1%Mg and 1%Ni (at room temperature): $1-\varepsilon$, $2-\delta$, $3-\gamma$, $4-M$, $5-Q$, $6-\theta$.

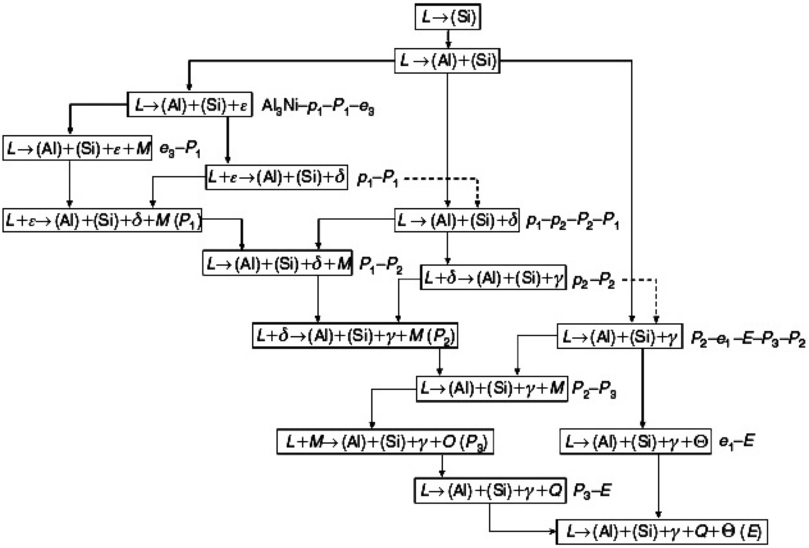
L→(Si)
L→(Al)+(Si)
L→(Al)+(Si)+ε
Al3Ni–p1–P1–e3
L→(Al)+(Si)+ε+M
e3–P1
L+ε→(Al)+(Si)+δ
p1–P1
L+ε→(Al)+(Si)+δ+M (P1)
L→(Al)+(Si)+δ
p1–p2–P2–P1
L→(Al)+(Si)+δ+M
P1–P2
L+δ→(Al)+(Si)+γ
p2–P2
L+δ→(Al)+(Si)+γ+M (P2)
L→(Al)+(Si)+γ
P2–e1–E–P3–P2
L→(Al)+(Si)+γ+M
P2–P3
L+M→(Al)+(Si)+γ+O (P3)
L→(Al)+(Si)+γ+Θ
e1–E
L→(Al)+(Si)+γ+Q
P3–E
L→(Al)+(Si)+γ+Q+Θ (E)

Figure 5.18 Reactions scheme for Al–Cu–Mg–Ni–Si system in the range of commercial piston alloys.

Figure 5.18 shows a flow diagram for solidification paths of piston alloys. Such diagrams are widely used for a more vivid representation of the solidification sequence in multicomponent alloys [10]. The (Si) phase is considered to form first, followed by the (Al) + (Si) eutectic. Further solidification reactions correspond to the polythermal projection shown in Figure 1(b). Taking the compositional range of piston alloys and the eutectic compositions into account, the formation

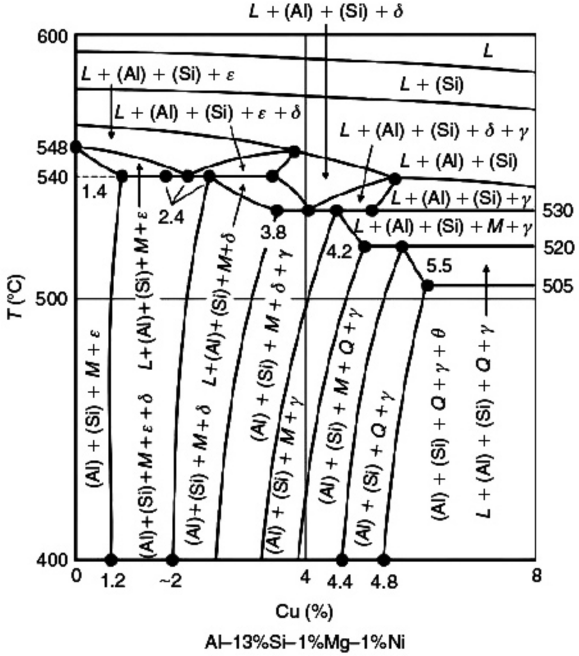

Figure 5.19 Polythermal section Al–Cu–Mg–Ni–Si phase diagram at 13%Si, 1%Mg and 1%Ni.

of ternary eutectics with *h*, *Q*, and *M* phases is unlikely. Under the conditions of non-equilibrium solidification, the total number of phases can be more than five, because the constitution of the polythermal projection suggests the presence of several peritectic reactions (apparently there should be more peritectic reactions than in the constituent quaternary systems).

An analysis of phase transformations during solidification and further cooling is easier to perform using polythermal sections (isopleths). The section at 13%Si, 1%Ni, and 1%Mg is shown in Figure 5.19.

If iron is present in an alloy to such an extent that it influences the phase composition (and that happens at a relatively low iron concentration, ≤0.5%), then the Al_9FeNi and $Al_8FeMg_3Si_6$ phases can appear in addition to the already considered phases. Alloys containing little copper can be analyzed using the Al–Fe–Mg–Ni–Si phase diagram. The more magnesium is in the alloy, the more probable the presence of the $Al_8FeMg_3Si_6$ compound becomes. A solution treatment should lead to complete or partial dissolution of Al_2Cu, Mg_2Si, and $Al_5Cu_2Mg_8Si_6$ in (Al), depending on the alloy composition. The remaining particles of these phases may acquire a globular shape. The Ni-containing phases do not change the morphology. After aging, the phase composition of the aluminum matrix can be analyzed using the Al–Cu–Mg–Si diagram, taking into account the composition of a supersaturated solid solution. If the alloys are heat treated without quenching, for the proper analysis one should know the composition of (Al) in the as-cast state. Alloys containing little magnesium can be analyzed using the Al–Cu–Fe–Ni–Si phase diagram. According to the constitutive quaternary diagrams, the following phases – Al_3Ni, $Al_3(CuNi)_2$, Al_7Cu_4Ni, Al_2Cu, Al_9FeNi, and Al_5FeSi – can be in equilibrium with (Al) and (Si). The most probable distribution of phase fields suggests that the phase composition of such alloys strongly depends on the iron concentration. If the concentration of iron is low, then, most probably, nickel will be bound to the phases $Al_3(CuNi)_2$ and Al_7Cu_4Ni. At higher iron content, when the ratio Fe:Ni ≈ 1 is achieved, the formation of the Al_9FeNi phase is most probable. Under conditions of non-equilibrium solidification and the nickel concentration at a lower nominal level, one can also expect the appearance of the Al_5FeSi phase, as it follows from the Al–Fe–Ni–Si phase diagram (Figure 1.44). During the solution heat treatment, which is rarely done with piston alloys, the Al_2Cu phase should totally dissolve in (Al). Other phases remain largely intact. During aging, the precipitation of Al_2Cu and its metastable modifications occurs.

Bäckerud *et al.* (see ref. in Table 5.3) examined the as-cast structure of a piston 339.1 alloy containing 11.9%Si, 0.99%Ni, 0.75%Fe, 0.95%Cu, 1.16%Mg, 0.2%Mn, and 0.33%Zn. The presence of Mn complicates the picture due to the formation of phases containing Mn and Fe. Table 5.11 shows that the

Table 5.11 Solidification reactions under non-equilibrium conditions in a 319.1 alloy containing 11.9%Si, 0.99%Ni, 0.75%Fe, 0.95%Cu*, 1.16%Mg, 0.2%Mn, and 0.33%Zn [Backerud et al., see reference to Table 5.3]

Reaction	Temperatures (°C) at a cooling rate	
	0.3 (K/s)	4 (K/s)
$L \Rightarrow (Si)$, $L \Rightarrow (Al)$, $L \Rightarrow (Al) + (Si)$	563–560	561–559
$L \Rightarrow (Al) + (Si) + Al_{15}(MnFe)_3Si_2$ $L \Rightarrow (Al) + (Si) + Al_5FeSi$	560–544	559–544
$L \Rightarrow (Al) + (Si) + Mg_2Si + Al_8FeMg_3Si_6$	544–538	544–534
$L \Rightarrow (Al) + Al_3Ni$ $L + Al_3Ni \Rightarrow (Al) + Al_3(CuNi)_2$	538–530	534–583
Complex reaction with Al_2Cu and other phases	530–499	
Solidus	499	483

*Lower than the nominal lower limit (see Table 7.2).

Mn-containing phase forms just after the formation of (Al) and (Si). During subsequent solidification, only reactions with participation of already considered in this section phases occur. The identification of all phase reported by Bäckerud *et al*. seems substantiated, except for the Al_3Ni the occurrence of which at the Fe:Ni ratio close to unity is not probable. Rather, one should expect the formation of Al_9FeNi. The structure of an AL30rus alloy (which is an analog of 319.1) contains considerable amount of Al_9FeNi crystals. In this alloy, the eutectic colonies (Al) + (Si) + Al_9FeNi are the main structure component as shown in Figure 5.15a. It should be noted that commercial piston alloys containing 11–13%Si and modified with phosphorus frequently contain considerable amount of primary silicon as a result of non-equilibrium solidification. On the other hand, the presence of Al_5FeSi needles in a 319.1 alloy seems logical from the analysis of the Al–Fe–Ni–Si phase diagram, as a result of suppressed peritectic reaction (P_2 in Table 1.32 and Figure 5.1b).

Alloys *AK12MMgN* (Al12Si1Cu1Mg1Ni) and *AK12M2MgN* (Al12Si2Cu1Mg1Ni) contain about 12%Si and approximately 1% of Ni and Mg; they differ only by copper concentration (2% and 1%, respectively). However, this does not influence alloys' microstructure and properties. In as-cast state the principal microstructural component is the aluminum–silicon eutectic (Figure 5.15a), inside which fragments of other phases could be seen, including Fe-bearing particles. Most of nickel enters the composition of the skeletal Al_9FeNi particles. Additionally, some primary crystals with irregular shapes might be present. Some nickel could be bound into the Cu-bearing phases ($Al_3(Ni,Cu)_2$ or Al_6Cu_3Ni), but their amounts are relatively small. Iron, in addition to Al_9FeNi, can be present in such compounds as $Al_8FeMg_3Si_6$ and $Al_{15}(FeMn)_3Si_2$. When its concentration exceeds 0.6–0.8% the formation of needle-like particles of the β-phase becomes quite likely. Due to high concentrations of magnesium, in alloys AK12M2MgN and AK12MMgN skeletal particles of Mg_2Si might be observed, as well as quaternary compound $Al_8FeMg_3Si_6$. Copper enters the composition of such phases as $Al_5Cu_2Mg_8Si_6$ and Al_2Cu, but the amount of the latter phase in alloy AK12MMgN is very low. Part of copper and magnesium get dissolved in (Al), which results in some strengthening effect – particularly noticeable after T1 heat treatment due to precipitation of metastable modifications of the Mg_2Si and $Al_6Cu_2Mg_8Si_5$ phases.

Alloy *AK21M2.5N2.5* (Al121Si2.5Cu2.5Ni) contains more than 20%Si. In other words, it is a typical hyper-eutectic alloy. In addition to the solidification of the (Si) phase, crystals of Al_9FeNi also could be formed. These primary crystals give a possibility to easily distinguish microstructure of AK21M2.5N2.5 from all other standard Al–Si alloys. All other elements of microstructure are approximately the same as for other engine piston Al–Si alloys: aluminum + silicon eutectic and particles of the $Al_5Cu_2Mg_8Si_6$ and Al_2Cu phases. The formation of magnesium silicide and β-phase is highly improbable. Alloy AK21M2.5N2.5 is characterized by high hardness, also at elevated temperatures. At the same time, due to its high volume fraction of excessive phases its plasticity is very low, and it has the lowest value of the thermal expansion coefficient among all standard casting aluminum

Table 5.12 Typical mechanical properties of some engine piston Al–Si alloys

Alloy	Temper	YS (MPa)	El (%)
AK12M2MgN	K,T1	200	0
AK21M2.5N2.5	K,T2	170	0

alloys. This alloy is manufactured out of primary and secondary materials; its casting is more labor-intensive in comparison to other Al–Si alloys: it is necessary to introduce a large amount of primary silicon at temperature around 800°C. It is used for manufacturing heavily loaded pistons with high requirements to their thermal stability and linear thermal expansion coefficient.

Fractography of these alloys is defined by their high heterogeneity. Indeed, in addition to the presence of significant amounts of the silicon phase, there are also large crystals of the Al_9FeNi intermetallic compound. As a result, fracture surfaces represent a number of facets of different sizes (Figure 5.8), which at small magnifications makes it difficult to establish the brittle character of fracture – there is a misleading impression of multiple light ridges typical for ductile fracture. At sufficiently high magnifications the cleavage steps on constituent particles become quite noticeable.

The T5 heat treatment practically does not change the nature of fracture surfaces, but reduces the overall share of plastic deformation. Based on the nature of fracture surfaces, it is difficult to distinguish alloys AK12M2MgN and AK12MMgN, especially at all other conditions being equal. On the other hand, it is very easy to identify the fracture surfaces of hypo-eutectic Al–Si alloy AK21M2.5N2.5, because large crystals of silicon having the shapes of polyhedra, can be easily fractured and leave the corresponding traces in the matrix [4].

5.2 ALLOYS ON THE BASIS OF THE AL–CU SYSTEM

Most industrial alloys on the basis of the Al–Cu system belong to the first structural group (see Section 1.1). Their primary microstructural component is the aluminum-based solid solution solidifying from the liquid phase and containing up to 5%Cu and fractions of a percent of ancillary additions and impurities. Volume and mass fractions of excessive phases of eutectic origin are not high, which ensures a high level of plasticity. Their ability to dispersion hardening results in higher strength (compared to Al–Si alloys). However, their both full and effective solidification ranges are much higher than for Al–Si alloys. As a result, castability of Al–Cu alloys is low, their casting into metallic molds may cause significant problems and for this reason they are manufactured using one-time molds.

In addition to this significant shortcoming, alloys on the basis of the Al–Cu system have another problem – low corrosion resistance.

The following alloying elements and impurities can be present in the Al–Cu alloys: manganese, magnesium, titanium, zirconium, chromium, iron, silicon, sometimes cadmium and silver. Their influence upon alloys' phase composition is discussed below.

Copper, in most cases, is distributed between (Al) and the Al_2Cu phase, but in the presence of other elements (Ni, Fe, and Mn) it could enter into the composition of different ternary phases (Table 5.13). Optimization of the copper concentration in the latter case is a difficult task that requires a systematic analysis of the corresponding multicomponent phase diagrams. The optimal Cu concentration in classical alloys of the AM5 type is ~5%, the temperature of heat-up for quenching is around 540° C, which directly follows from the binary phase diagram (Figure 1.3).

Manganese can be present in many Al–Cu alloys in the amounts up to 1%, and usually completely enters into the (Al) solid solution after solidification. In the course of heat up before quenching practically all manganese precipitates in the form of the $Al_{20}Cu_3Mn_2$ cigar-shaped dispersoids, which favorably affect strength at elevated temperatures. The presence of other elements (Ni, Fe, and Si) may result in the formation of different Mn-bearing phases of eutectic origin; this is typically undesirable, because results in the reduction of this element's concentration in the aluminum matrix.

Nickel in the presence of copper forms such compounds as Al_6Cu_3Ni or $Al_3(Ni,Cu)_2$. These are some of the most thermally stable, which exerts positive influence upon mechanical properties at elevated temperatures. This is true with respect to composition of such alloys as AA242.0 [2]. However, the formation of these compounds is accompanied by the reduction of the copper concentration in (Al) and, correspondingly, to lower strength at room temperature.

Magnesium is absent in all standard Russian Al–Cu alloys (as impurity it is allowed in concentrations not higher than 0.1%). However, it may enter the composition of such alloys as AA206.0, making them analogs of wrought aluminum alloys of the 2xxx series. Magnesium forms the Al_2CuMg phase, which in the course of non-equilibrium solidification precipitates as part of the ternary eutectic $(Al)+Al_2Cu+Al_2CuMg$ at 505–507°C, which makes the solidification range much broader. Casting properties, which are low without magnesium anyway, become particularly bad, significantly limiting the production of such alloys. The presence of silicon makes the formation of Mg_2Si and Al6Cu2Mg8Si5 possible, as it directly stems from the Al–Cu–Mg–Si phase diagram. The latter could be both of eutectic and secondary origin.

Iron, being able to form phases with manganese, nickel and copper itself, can exert substantial influence upon microstructure. This defines the need to analyze its influence inasmuch as it is the principal impurity in industrial Al–Cu alloys (along with Si). The presence of iron negatively affects mechanical properties, especially plasticity (elongation) fracture toughness, and, possibly, other properties. Castability is significantly less sensitive to the presence of this element.

Table 5.13 Distribution of alloying elements between the aluminum matrix and excessive phases in Al–Cu alloys

Phases	Alloying element								
	Cu	Mg	Mn	Fe	Si	Ni	Zr	Cr	Ti
Aluminum matrix: (Al) and secondary precipitates									
(Al)	+	+	+	–	+	–	+	+	+
Al_2Cu	+	–	–	–	–	–	–	–	–
Al_2CuMg	+	+	–	–	–	–	–	–	–
Mg_2Si	–	+	–	–	+	–	–	–	–
$Al_4Cu_2Mg_8Si_5$	+	+	–	–	+	–	–	–	–
(Si)	–	–	–	–	+	–	–	–	–
$Al_{20}Cu_3Mn_2$	+	–	+	–	–	–	–	–	–
$Al_{15}Mn_2Si_3$	+	–	–	–	+	–	–	–	–
Al_3Zr	–	–	–	–	–	–	+	–	–
Al_7Cr	–	–	–	–	–	–	–	+	–
Al_3Ti	–	–	–	–	–	–	–	–	+
Constituent phases (particles)									
Al_2Cu	+	–	–	–	–	–	–	–	–
Al_2CuMg	+	+	–	–	–	–	–	–	
(Si)	–	–	–	–	–	–	–		
Al_5FeSi	+	+	–	–	–	–	–		
Al_8Fe_2Si	+	+	–	–	–	–	–		
$Al_{15}(Fe,Mn)_2Si_3$	+	+	+	–	–	–	–		
Al_9FeNi	–	+	–	–	–	–	+		
Al_7Cu_2Fe	+	–	–	+	–	–	–	–	–
Al_6Cu_3Ni	–	–	–	+	–	–	+		
$Al_3(Ni,Cu)_2$	–	–	–	+	–	–	+		
Mg_2Si	+	–	–	–	+	–	–		
$Al_6Cu_2Mg_8Si_5$	+	–	–	+	+	–	–		

Table 5.14 Chemical composition of Russian Al–Cu alloys

Alloy	Concentrations (%) (Al balance)						
	Cu	Mn	Fe*	Si	Mg	Zn	Other
AM5	4.5–5.3	0.6–1	S: 0.2; M: 0.3	0.3	0.05	0.2	Ti
AM4(5Kd)	4.5–5.1	0.35–0.8	S: 0.15; M: 0.15	0.2	0.05	0.1	Ti, Cd

* S: sand casting; M: mold casting.

Iron impurity is usually rigorously controlled; for example, in alloy AA224.2 not more than 0.04%Fe is allowed [2].

Silicon enters the compositions of several casting Al–Cu alloys (e.g., AA295.0). This element does not form any phases with copper and possesses relatively high solubility in (Al). This allows improving castability somewhat at the expense of some low-temperature strength. However, silicon is bad for alloy thermal stability. Since the latter is one of the most attractive features of Al–Cu alloys, the maximal content of silicon is strictly controlled (e.g., not more than 0.02% in AA224.2).

Other alloying elements (typically used as ancillary additions) do not affect the phase composition of Al–Cu casting alloys. Titanium refines grains of (Al), cadmium and silver enhance the effect of dispersion hardening, chromium and zirconium, together with manganese, form dispersoids, thus positively affecting alloys' thermal stability [10].

The most probable distribution of all described elements between the matrix and constituent particles is illustrated by Table 5.13. It is clear from the table that many chemical elements can enter the composition of (Al); the overall number of eutectic phases is also quite high. In order to forecast the phase composition of multicomponent alloys it is useful to employ five-component phase diagrams, constructed in the Al–Cu area.

The optimal combination of mechanical properties is achieved for alloy "Al–5%Cu–1%Mn + ancillary additions (Ti, Zr, Cr, Ag, Cd)" with the minimal amounts of impurities, especially Fe, Si, and Mg (it will be further called "alloy of the AM5 type"). There are two Russian alloys of the Al–Cu type: *AM5* (Al5Cu) and *AM4.5Cd* (Al4.5CuCd) (Table 5.14). These alloys differ by the presence of ancillary cadmium additions in the latter. Their phases analysis can be successfully conducted using the ternary Al–Cu–Mn phase diagram, in particular, isothermal cross-sections at 200°C and 540°C (Figure 5.21).

Standard Al–Cu alloys are mostly used in those cases when articles with a high level of mechanical properties are required at room and elevated temperatures. Data provided in Table 5.15 and Appendix 3, clearly demonstrates the advantages of Al–Cu alloys over Al–Si in all the range of mechanical properties. Among all standard casting aluminum alloys Al–Cu as of today remain the strongest and most thermally stable. This is explained mostly by a very significant effect of dispersion hardening in the course of decomposition of (Al) due to the formation of the

Table 5.15 Properties of Al–Cu casting alloys

Сплав	Casting technique	Guaranteed level of properties, in (T6)			Typical properties, in (T6)	
		σ_B (MPa)	δ(%)	HB	σ_B (MPa)	δ(%)
AM5	S	333	4	90	360	4
	M	333	4	90	400	6
	P	–	–	–	420	8
AM4 (5Kd)	S	421	4	110	400	4
	M	490	4	120	440	5
	P	–	–	–	480	6
		K_{IC} (MPa × $m^{1/2}$)	KCU (J/m^2)	σ_{-1} (MPa)	σ_{100}^{300} (MPa)	$\sigma_{0.2/100}^{300}$ (MPa)
AM5	S	–	8	75	65	40
AM4 (5Kd)	S	27	10	80	80	50
	Hot fluidity[a] (mm)	Hot cracking[b] (mm)	Full linear shrinkage			
AM5	205	32	1			
AM4 (5Kd)	245	30	1.5			

[a] Rob probe; [b] VIAM ring probe (see Chapter 4).

GP-zones, coherent particles of θ'' and semi-coherent θ' ($CuAl_2$) phase, as well as by the relatively low diffusional mobility of the copper atoms (in comparison to Si, Mg, and Zn). Ancillary additions of transition metals (Mn, Ti, Cr, Zr, etc.) result in some further strengthening at room and especially at elevated temperatures. The mechanism is due to the formation of secondary aluminides during heat-up before quenching.

Additions of cadmium in Russian alloy AM4.5Kd and silver in alloy AA201.0 result in the significant increase of strength characteristics at temperatures close to room temperature T, as a result of the formation of the θ'-particles during aging.

Alloys of the AM5 type quenched from 545°C (hold time from 5 to 9 hours) into hot water and subject to artificial aging at 175°C during 3–5 hours (T6 temper). The principle of heat up before quenching is to achieve complete dissolution of the non-equilibrium phase Al_2Cu of eutectic origin (Figure 5.10). If the elements that could form low-melting (<545°C) eutectics are present (e.g., silicon and magnesium, Table 5.3), then heat-up for quenching is done in several steps. In the case of extended periods of work at elevated temperatures it is recommended to overage according to the T7 regime (250°C, 10 hours). Alloys of the AM5 type are used in as-quenched state without artificial aging (T4), which allows obtaining higher characteristics of plasticity and elongation accompanied by some reduction in strength. Rigorous limits are imposed upon the iron and silicon impurities (<0.2–0.3%); as a rule, these elements are present in the form of skeletal inclusions of the $Al_{15}(Fe,Mn)_2Si_3$ phase of eutectic origin. Typical microstructures of 2xx alloys are shown in Figure 5.20.

The easiest alloys for the analysis are those containing only copper and manganese. The isothermal sections at 540°C and 200°C appear to be the most characteristic and are shown in Figure 5.21a, b. The section at 540°C shows that 224.0-type alloys in T4 state contain only $Al_{20}Cu_2Mn_3$ as an excess phase. The section at 200°C demonstrates that in T7 state all alloys of this group are three-phase alloys.

During solidification, copper participates in eutectic reactions. The resultant eutectics are usually dispersed and appear as Al_2Cu veins at dendritic cell boundaries. Polythermal section at 0.5%Mn in Figure 5.21c demonstrates that these eutectics are non-equilibrium in 224.0-type alloys. Manganese, on the contrary, can be completely dissolved in (Al) during non-equilibrium solidification, even though its maximum equilibrium solubility in (Al) at room temperature does not exceed 0.05%. During high-temperature anneals, non-equilibrium Al_2Cu particles dissolve in (Al), while $Al_{20}Cu_2Mn_3$ dispersoids precipitate as a result of decomposition of the aluminum solid solution supersaturated in Mn (in accordance with Figure 5.21a). These dispersoids remain virtually unchanged during downstream processing and use. So, the as-quenched structure consists of the aluminum solid solution supersaturated with copper and (AlCuMn) dispersoids of sub-micron size. During subsequent aging, copper precipitates from the solid solution, forming hardening, metastable phases θ'' and θ' (Al_2Cu). Figure 5.22 demonstrates that additions of Mn decrease the amount of copper available for

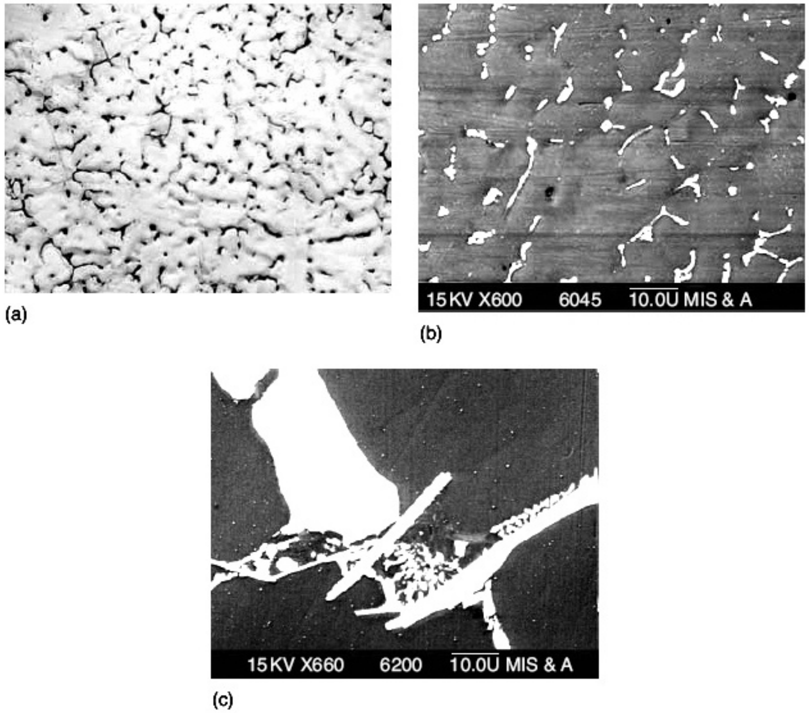

Figure 5.20 Typical microstructures of 2xx alloys: (a) as-cast (metal mold) AM5 alloy (Al–5% Cu–1%Mn, <0.1%Fe) alloy, LM; (b) Al–5%Cu–1%Mn–0.6%Fe alloy, T4, SEM, (c) Alloy containing 10%Cu, 2%Si, 0.5%Mg, and 0.5%Fe, sand casting, SEM.

hardening (because part of copper is bound in the $Al_{20}Cu_2Mn_3$ phase). For example, the volume fractions of $Al_{20}Cu_2Mn_3$ and Al_2Cu particles are 3 and 5 vol.%, respectively, in an annealed AM5 alloy of the average composition (5%Cu, 0.8%Mn).

The presence of iron impurity (>0.1%) in 224.0-type alloys usually results in the formation of Fe-containing phases. At low silicon concentration, the appearance of the Al_7Cu_2Fe phase is most likely. This phase is formed through eutectic reactions listed in Tables 5.7 and 5.8, and its maximum volume fraction is about 1.2 vol.% at a concentration of Fe of 0.3%.

The effect of manganese on the phase composition of a 224.0-type alloy (5%Cu, 0.2%Fe) is shown in Figure 5.22a, and the combined influence of iron and manganese can be traced in an isothermal section at 5%Cu in Figure 5.22b. At the temperature of homogenization (540°C), 224.0- and AM5-type alloys, irrespective of the Fe:Mn ratio, fall into the phase region $(Al) + Al_7FeCu_2 + Al_{20}Cu_2Mn_3$.

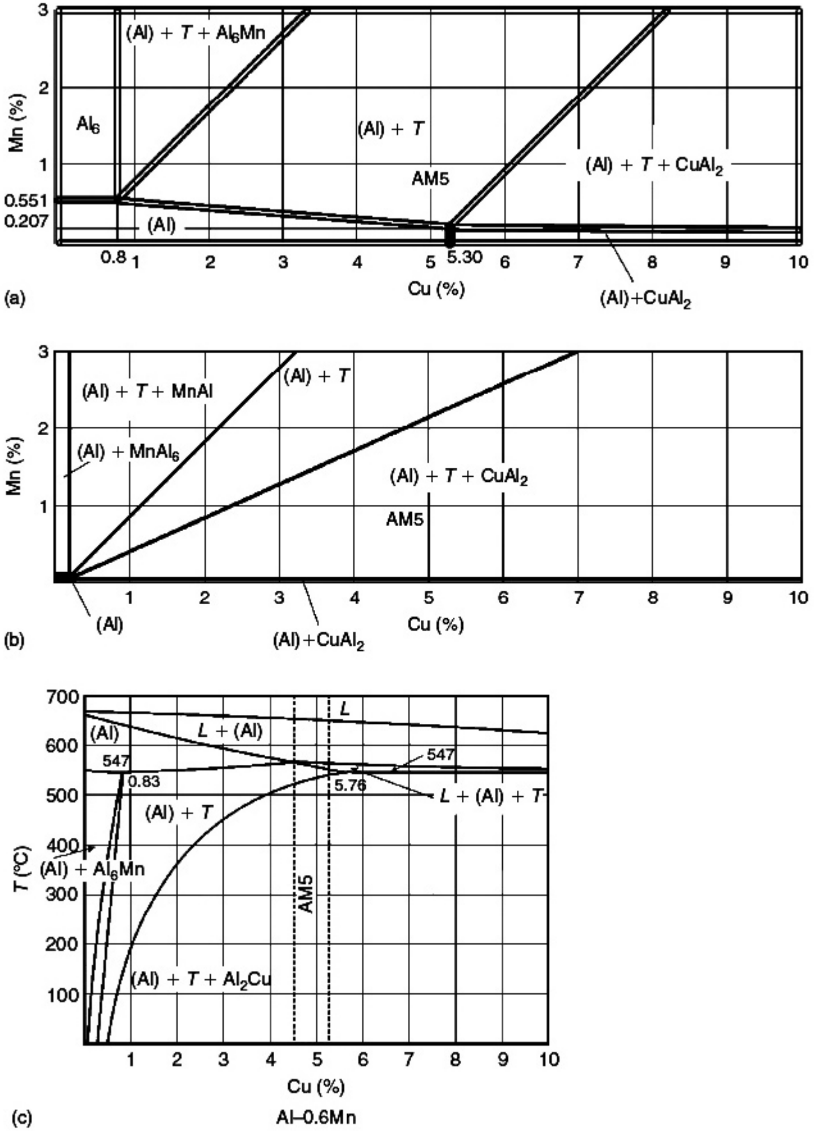

Figure 5.21 Isothermal (a, b) and polythermal (c) sections of Al–Cu–Mn phase diagram: (a) 540°C; (b) 200°C; and (c) 0.6% Mn with compositional ranges of AM5, 224.0, $T - Al_{20}Cu_2Mn_3$.

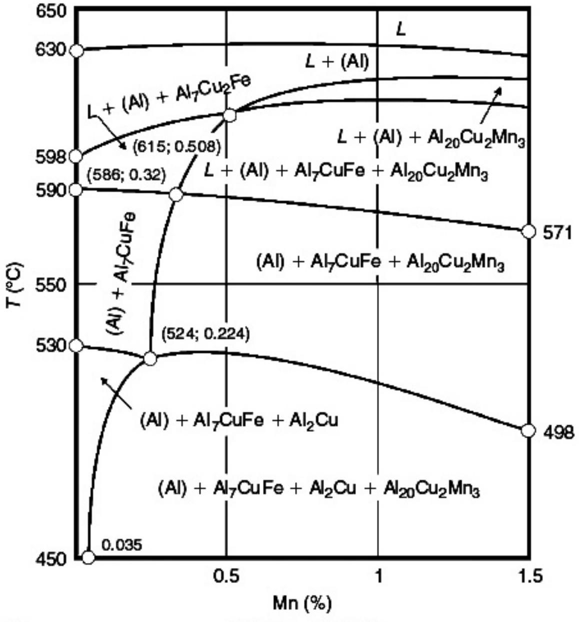

(a) Al–5% Cu–0.2% Fe

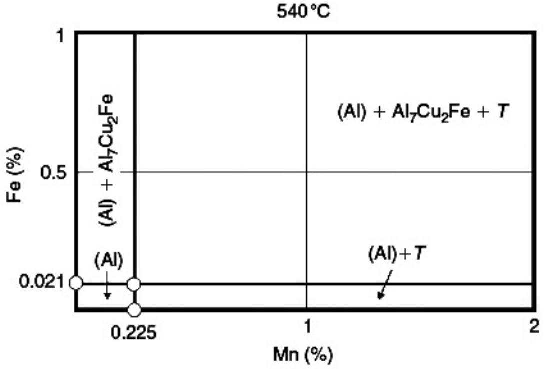

(b) Al–5%Cu

Figure 5.22 Polythermal (a) and isothermal (b) sections of Al–Cu–Mn–Fe phase diagram at 5%Cu: (a) 0.2%Fe and (b) 540°C.

The effect of silicon on the solidification sequence in 2xx.0-series alloys is considered by Belov et al. (see “Multicomponent Phase Diagrams: Applications for Commercial Aluminum Alloys”, Elsevier, 2005). The higher than usual concentration of Mn is necessary to show the peritectic reaction

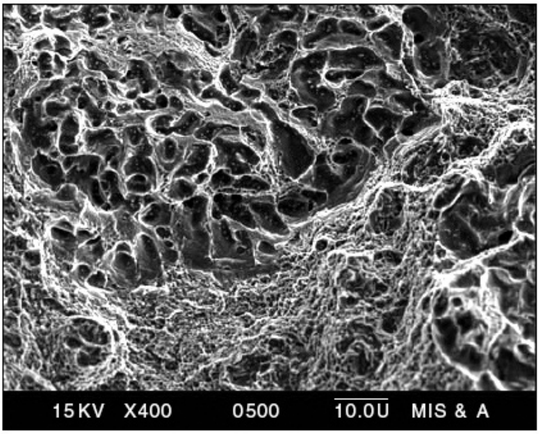

Figure 5.23 Typical fracture surface of alloy AM5 (T5 temper), SEM.

$L + Al_6Mn \Rightarrow (Al) + Al_{20}Cu_2Mn_3 + Al_{15}Mn_3Si_2$ and to assure the primary solidification of (Al). In alloys containing less than 2%Si, the $(Al) + Al_6Mn$ eutectic solidifies next to primary (Al) grains. However, the Al_6Mn phase is not retained in the solid state as it disappears during peritectic reactions. The same isopleth shows that $Al_{20}Ci_2Mn_3$ is present only in alloys with less than 1%Si. With taking into account that most of 1.5%Mn (almost all of it in low-silicon alloys) remains in aluminum solid solution during non-equilibrium solidification, this section can be used to determine the phase composition of dispersoids, for example an alloy with 5%Cu, 1.5%Mn, and 0.7%Si does not contain $Al_{20}Cu_2Mn_3$ precipitates.

In 2xx.0-series alloys, the coupled effect of Si, Mg, and Fe (neglecting Mn), can be traced by the phase distribution in solid state (Figure 1.48a). At a low concentration of silicon (and relatively high concentration of copper), these alloys fall into the five-phase region $(Al) + Al_2Cu + Mg_2Si + Al_7Cu_2Fe + Al_2Cu\,Mg$.

The principal applications of alloys of the AM5 type are in aerospace and military industries. Since the level of mechanical properties of these alloys is close to that of wrought semi-fabricated products, they can successfully compete with 2xxx series and other forgings obtained out of rod and plate for articles with complex geometrical configurations (e.g., space frames). Al–Cu casting alloys are used for manufacturing high quality details applied in aviation engineering and working at temperatures up to 300°C as well as for articles carrying heavy workloads and working at room and lower temperatures with a high level of vibrations. Alloys of the AM5 type possess, unlike Al–Si materials (see Section 5.1), a sufficiently high level of fracture toughness (Table 5.15).

One should note other Al–Cu alloys containing additions of nickel, silicon, and other elements and differing significantly from the AM5 type in their phase compositions. One of the most heat resistant alloys, Russian AL33 [10], contains

~1% of nickel, which can bind copper into ternary compounds. The concentration of copper in solid solution does not exceed 3%, and for this reason strength of AL33 at room temperature is lower than for AM5. However, high temperature strength of the first alloy is higher. This is probably because copper that is not tied up into the $Al_{20}Cu_3Mn_2$, relatively easily diffuses at elevated temperatures (>300°C) into (Al). As far as its influence upon thermal stability is concerned, it is surpassed by both dispersoids and constituent particles. The addition of nickel does not result in a significant improvement of castability because, similar to the AM5 alloys, solidification ends with the formation of a non-equilibrium eutectic Al_2Cu. Additions of 2%Ni can be found in some US alloys (e.g., AA242.0). American alloys of the 2xx series containing more than 2%Si, are closer in their chemical composition to copper-bearing Al–Si alloys (Section 5.1.3). For this reason we do not discuss these materials in the present section. Alloys containing smaller amounts of silicon, in particular developed in Russia during the last years (e.g.,VAL15) and alloys with cerium are discussed in Chapter 6.

5.3 AL–MG AND AL–MG–ZN ALLOYS

5.3.1 General characteristic of Al–Mg alloys

Casting alloys Al–Mg in terms of their microstructure should be classified into the first group (alloy T1 in Figure 1.1). Exception needs to be taken only for less widespread alloys with silicon additions, which contain relatively large volume fraction of eutectic phases (the latter should be classified as belonging to the second group). Distinctive features of these materials are high corrosion resistance, ductility and fracture toughness, good weldability. These alloys are non-heat treatable; however, at high concentrations of magnesium (more than 6%) due to solid solution strengthening in the quenched state they can attain $\sigma_b > 300$ MPa. Yield strength of these alloys is not high; even in the strongest alloy Al–10%Mg it does not exceed 200 MPa [10].

Al–Mg alloys (5xx series) are very sensitive to iron impurities, which grows with increased magnesium concentration. For the most complex castings limitations upon concentrations of Fe and Si are very strict; for example, in Russian alloy AMg61ch not more than 0.05% is allowed. This is because of the influence of iron not only upon mechanical properties, but also upon corrosion resistance. The latter is most probably related to the cathode Fe-bearing phases. Manganese, which enters the composition of many Al–Mg alloys, can partially neutralize the negative influence of iron upon corrosion resistance.

Alloys of the considered group (also containing alloy Al–4Zn–2Mg), in addition to magnesium, may contain (as alloying elements or impurities) such elements as manganese, silicon, iron, copper, zinc, titanium, zirconium, beryllium. The influence of these elements upon phase composition is considered below.

Magnesium in concentrations up to 5–6% can form during solidification a small amount of eutectic phase Al_8Mg_5. This implies that mostly it is present in the aluminum matrix. Since magnesium is an effective solid solution strengthening element, its concentration should be maintained at the upper limit if maximal strength is to be attained. As the concentration of magnesium grows, alloy castability must improve somewhat, while corrosion resistance, on the contrary, will decrease (especially stress corrosion cracking). During heat-up before quenching the Al_8Mg_5 phase will be completely dissolved in (Al), which results in increased strength and plasticity at the same time. Because of the peculiar features of Al_8Mg_5 phase, aging is not applicable to binary Al–Mg alloys; for this reason they are usually used in the T4 temper. In the course of natural (and especially artificial) aging, the formation of secondary particles of the Al_8Mg_5 takes place mostly along the boundaries of grains and subgrains. As the concentration of magnesium grows this process accelerates, which may result in the formation of continuous systems of vein-like deposits, mostly along the grain and sub-grain boundaries. Because of this industrial alloys usually contain not more than 11–12%Mg, that is much less than the limit solubility of Mg in (Al) (Figure 1.4).

Zinc can be present in some Al–Mg alloys (in addition to Al–Zn–4Mg, there are several other alloys that will be discussed in Chapter 6). As it follows from the Al–Mg–Zn phase diagram (Figure 1.29), it can in as-quenched state completely dissolve in (Al). During casting a certain fraction of Zn is expended for the formation of the eutectic $Al_2Mg_3Zn_3$ phase. Joint presence of magnesium and zinc in as-cast (Al) allows to achieve a significant increase in strength due to aging processes and precipitation of the T' phase (Al_2Mg_3Zn). It is desirable that the $Mg + Zn$ sum did not exceed 6–7%, this might result in increased corrosion cracking.

Manganese is often used in Al–Mg alloys in the amounts up to 1%. At low concentrations of Fe and Si this element can completely enter the composition of (Al), resulting in significant solid solution strengthening (in as-cast state). In the presence of iron and silicon one can expect, as a rule, the formation of the $Al_{15}(Fe,Mn)_2Si_3$ phase in the form of skeletal inclusions of eutectic origin.

Silicon, by binding magnesium into the Mg_2Si phase, reduces plasticity quite significantly but increases castability somewhat. This fact was used in the design of a limited number of commercial casting alloys (e.g., AMg5K), in which its content may reach 1.5–2%. In the presence of iron and manganese other phases could also be formed (e.g., Al_8Fe_2Si and $Al_{15}(FeMn)_3Si_2$). The concentration of silicon in (Al) is insignificant, which does not allow using aging to achieve strengthening effect due to the formation of the secondary β' and β'' (Mg_2Si) phase precipitates. In “classical” Al–Mg alloys (like AMg6l and AMg10) the maximum allowable concentration of the silicon impurity is rigorously limited.

Iron in Al–Mg alloys, in the absence of manganese and silicon, will form the Al_3Fe phase. Its needle-like inclusions dramatically reduce the level of mechanical properties. In the presence of these elements the formation of the $Al_{15}(FeMn)_3Si_2$ phase is most probable, which possesses more favorable skeletal morphology. In alloys for complex high quality castings the maximum iron impurity concentration is strictly limited (in alloy AMg6l not more than 0.05% of Fe is allowed). On the contrary, if the method of die casting is used, including high-magnesium alloys, then the amount of iron could be as high as 1%. Of course, if such materials are used for sand casting, one could expect the formation of coarse primary Al_3Fe crystals. Obviously, this will be accompanied by the deterioration of all alloy mechanical properties.

Copper, in most cases, is a harmful impurity, because during non-equilibrium solidification it can form the Al_6Mg_4Cu phase, reducing plasticity and corrosion properties. The concentration of copper in cast (Al) is not significant, but its negative influence upon plasticity is quite significant. As an alloying element copper (in the amounts up to 1%) could be present in composition of some casting alloys (e.g., AMg4K1).

The most probable distribution of all chemical elements discussed above between the aluminum matrix and constituent phases (particles) is illustrated in Table 5.16.

Al–Mg alloys are often alloyed with ancillary additions of Ti, Zr, and Be [10]. Zirconium and titanium are used as grain refiners of (Al), while beryllium prevents oxidation during casting and high-temperature heat treatment(s). These elements practically do not exert influence upon the phase composition of alloys.

As can be seen from the Al–Mg phase diagram (Figure 1.3), if the magnesium concentration is below 17%, the eutectic formation of Al_8Mg_5 should not be possible. However, in real life it takes place in practically all industrial casting alloys. This happens because the minimal magnesium concentration in such alloys is ~4.5%, while the boundary of appearance of the eutectic reaction (which degenerates into a single Al_8Mg_5 phase) in binary alloys extends from 0.5 to 4.5%Mg (depending upon solidification rate; see Section 2.2). The presence of additions and impurities in industrial alloys shifts this threshold toward even smaller magnesium concentrations.

During heat-up before quenching, which is the principal type of heat treatment of Al–Mg alloys for responsible applications, the eutectic Al_8Mg_5 phase is easily dissolved in (Al), increasing the Mg concentration in it. This ensures improvement of mechanical and corrosion properties of alloys. If other impurities and alloying elements are present that have low solubility in (Al), then microstructure of quenched Al–Mg alloys will contain such constituent particles as Mg_2Si, Al_3Fe, $Al_{15}(Fe,Mn)_3Si_2$, etc. (Table 5.12). These phases all exert negative influence upon characteristics of cast products. Inasmuch as these elements could be present in alloys in different relative amounts, to properly analyze their influence upon alloy phase composition one has to employ multicomponent phase diagrams (including five-component) in the domain of Al–Mg alloys (see Section 1.4).

Alloys *AMg6lch* (Al6Mg) and *AMg10ch* (Al10Mg) with minimal amounts of impurities and ancillary additions of Zr, Ti, and Be possess the best mechanical and corrosion properties. Their phase composition could be properly understood using a simple binary phase diagram, Al–Mg.

Table 5.16 Distribution of alloying elements and impurities between the aluminum matrix and excessive phases in Al–Mg and Al–Zn–Mg alloys

Phases	Mg	Zn	Mn	Fe	Si	Cu
Aluminum matrix: (Al) and secondary phases						
(Al)	+	+	+	−	−	+
Al_8Mg_5	+	−	−	−	−	−
$Al_2Mg_3Zn_3$ (Al_6Mg_4Cu)	+	+	−	−	−	+
Al_6Mn	−	−	+	−	−	−
$Al_{10}MgMn$	+	−	+	−	−	−
$Al_{15}Mn_2Si_3$	+	−	+	−	−	−
Phases of solidification origin (constituent particles)						
Al_3Fe	−	−	−	+	−	−
$Al_6(Fe,Mn)$	−	−	+	+	−	−
Al_8Fe_2Si	−	−	−	+	+	−
$Al_{15}(Fe,Mn)_2Si_3$	−	−	+	+	+	−
Mg_2Si	+	−	−	−	+	−
Al_8Mg_5	+	−	−	−	−	−
$Al_2Mg_3Zn_3(Al_6Mg_4Cu)$	+	+	−	−	−	+

Casting properties of Al–Mg alloys, especially hot cracking and molten metal fluidity, are appreciably higher than for 2xx-series alloys (Al–Cu). It is because of low tendency to hot cracking that they can be welded well using argon arc melting. However, due to their broad solidification range, they exhibit a tendency to the formation of porosity and high oxidation during melting. These shortcomings make it difficult to obtain good hermetic castings free from non-metallic (oxide) inclusions.

To improve castability of Al–Mg alloys, additions of up to 1.7%Si could be used. Such an addition results in the formation of the (Al) + Mg_2Si eutectic, improving structure of Al–Mg alloys in the solid–liquid state. However, crystals of Mg_2Si of eutectic origin possess unfavorable morphology and their presence reduces the level of mechanical properties, especially elongation and fracture toughness.

As it follows from the Al–Mg phase diagram (Figure 1.4), in alloys containing from 4.5% to 13%Mg after quenching from single-phase domain, the decomposition of supersaturated (Al) could take place. However, this decomposition does not cause any significant dispersion hardening, and for this reason aging of such alloys is not practiced, although quenched alloys with more than 7–8%Mg do exhibit an appreciable tendency to natural aging. After lengthy (several years) exposure to room temperature conditions, electron microscopy allows to reveal the presence of metastable particles of the β'- phase (see Section 3.2). This causes strengthening accompanied by the dramatic loss of plasticity. In real life work under applied loads will result in retarded fracture, which in corrosive environment will be supplemented by stress corrosion.

As it was already mentioned above, overall corrosion resistance of Al–Mg alloys is quite high. In as-quenched condition the rate of general corrosion is low in the air, in pure and sea water. If the concentration of Mg is lower than 6%, there is no tendency to stress corrosion and intergranular corrosion. However, the latter could be activated if temperature increases to 70–100°C and above. In this case (Al) decomposition will be accompanied by the formation of an almost contiguous layer of the β'- and β-phase (Al_8Mg_5) grain boundary precipitates, which cause the development of intergranular corrosion. It can be prevented using special heat treatments.

The working temperatures of Al–Mg castings must not usually exceed 100°C. High diffusion mobility of magnesium results in low thermal stability of Al–Mg alloys.

Alloys on the basis of the Al–Mg system are used in shipbuilding and other areas where articles must be working in moist atmosphere (e.g., internal hull sections, propellers). Al–Mg alloys are used for manufacturing responsible parts of gas apparatuses (instead of more expensive copper alloys) and also details for which high level of corrosion resistance and plasticity is required (e.g., in food processing industry – mixers, pipes, different sieves, etc.).

5.3.2 Industrial Al–Mg and Al–Mg–Zn alloys

Alloy *AMg6l* (Al6Mg) contains 6–7%Mg, concentrations of ancillary additions (Zr, Ti, Be) and impurities (including Fe and Si) do not exceed 0.2%. In as-cast state magnesium is distributed between (Al) and eutectic veins of the Al_8Mg_5 phase depending upon the applied solidification rate (see Section 2.2). Using unetched, mechanically polished samples it is difficult to observe and identify this phase with optical microscopy. Due to the presence of Fe and Si impurities the formation of such phases as Al_8Fe_2Si and Mg_2Si appears to be the most probable. Since their volume fractions cannot be large, they usually look like thin veins and are located along the dendrite cell boundaries along with the particles of the principal phase, Al_8Mg_5. Heat-up before quenching to dissolve the latter in (Al) is usually conducted at 430–440°C, that is below the non-equilibrium solidus temperature. Mechanical properties of the AMg6l alloy after quenching are substantially better when compared to the as-cast state.

Table 5.17 Composition of alloys belonging to the Al–Mg and Al–Zn–Mg systems

Alloy	Concentrations (%) (Al balance)						
	Mg	Mn	Si	Fe*	Cu	Zn	Other
AMg4K1.5M	4.5–5.2	0.6–0.9	1.3–1.7	M: 0.4	0.7–1	0.1	Ti,Be
AMg5K	4.5–5.5	0.1–0.4	0.8–1.3	S: 0.5; M: 0.4; P: 1.5	0.1	0.2	–
AMg5Mts	4.8–6.3	0.4–1	0.3	S: 0.3; M: 0.4; P: 0.5	0.3	–	–
AMg6l	6–7	0.1	0.2	S, M: 0.2	0.15	0.1	Zr,Ti,Be
AMg6lch	6–7	0.1	0.05	S, M: 0.05	0.05	0.05	Zr,Ti,Be
AMg10	9.5–10.5	0.1	0.2	S, M, P: 0.2	0.15	0.1	Zr,Ti,Be
AMg10ch	9.5–10.5	0.1	0.05	S, M, P: 0.05	0.05	0.005	Zr,Ti,Be
AMg11	10.5–13	–	0.8–1.3	S: 0.5; M: 1; P: 1.2	–	0.1	Ti,Be
AMg7	6–8	0.25–0.6	0.5–1	P: 0.9	0.1	0.2	–
ATs4Mg	1.5–2	0.2–0.5	0.3	S: 0.5	0.2	3.5–4.5	Ti

* S: sand casting; M: mold casting; P: casting under pressure.

Alloy *AMg6lch* (Al6Mg) represents a modification of the principal alloy of similar composition, but has much tougher restrictions on the presence of impurities (Fe and Si less than 0.05%); for this reason it has to be cast out of high purity primary materials. This alloy in the quenched state has single-phase microstructure and is the most corrosion resistant material among all aluminum casting alloys.

In as-cast state alloys of the AMg6l type are used for details carrying average static and small shock loads (similar to AK7ch). In as-quenched state (T4 temper) they can be used for somewhat higher levels of both loads. In particular, these alloys find applications in food industry [8].

Alloy *AMg10* (Al10Mg) differs from those discussed above by its higher magnesium concentration (about 10%), which makes it stronger, particularly in the T4 temper. It contains the same set of ancillary additions (Zr, Ti, Be) and similarly rigorous limitations on the impurity contents. Its as-cast microstructure is different from alloy AMg6l as it contains larger volume fraction of the Al_8Mg_5 "veins" (Figure 5.24). The latter exert negative influence both upon mechanical

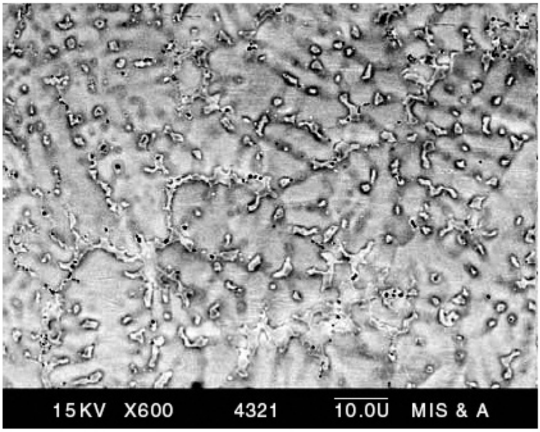

Figure 5.24 Microstructure of alloy AMg10ch in as-cast condition, SEM.

and corrosion properties. For this reason alloy AMg10 can be used only in the T4 temper. Alloy *AMg10ch* (Al10Mg) is a modification of the "parent" alloy but allows extremely low concentrations of the Fe and Si impurities (less than 0.05%). This ensures higher corrosion resistance and also improves fatigue characteristics. Alloys AMg10 and AMg10ch possess the highest strength (among Al–Mg alloys, UTS >350 MPa), as well as better castability than AMg6l (Table 5.18).

Alloys AMg10 and AMg10ch are recommended for work at high loads and at temperatures from −60° C to +60° C in different climatic conditions, including sea water (instead of copper alloys, wrought aluminum alloys, and stainless steels) [7].

Alloy *AMg5Mts* (Al5Mg1Mn) contains up to 1%Mn, that is in composition it is analogous to the wrought Al–Mg alloy AMg6. It is used for manufacturing shaped castings with different casting techniques (sand, metallic molds, die casting). It is used mostly in as-cast state because the additions of manganese enter (Al) during non-equilibrium solidification and result in significant solid solution hardening. Similar to alloy AMg6l, magnesium is distributed between (Al) and eutectic "veins" of the Al_8Mg_5 phase. The presence of iron and silicon impurities may result in the formation of such phases as $Al_{15}(Fe,Mn)_2Si_3$ and Mg_2Si. The appearance of other phases in as-cast microstructure is much less probable. Alloy AMg5Mts can be used for manufacturing piping for transportation of drinking water, in heaters, and marine equipment working at temperatures below 100°C [7].

Additions of manganese (0.2–0.6%) are also present in the chemical composition of alloy *AMg7* (Al7Mg), which is mostly used for die casting and ensures a satisfactory level of mechanical (UTS >250 MPa, El $>5\%$) and casting properties. This alloy also contains additions of silicon (0.5–1%), which is mostly tied

Table 5.18 Properties of alloys on the basis of the Al–Mg system

Alloy	Casting method	σ_B (MPa)	δ(%)	HB	KCU (J/m²)	σ_{-1}(MPa)
AMg5K	S	150	1	55		
	M	210	5	55		
AMg5Mts	S, M	290	9	60		
AMg6l	S	190	4	60	–	40
	M	220	6	60	5	
	S, M	230	6	60	15	
AMg6lch	S	200	5	60	–	
	M	240	10	60	9	
	S, M	250	10	60	20	
AMg10	S, M	320	12	75	15	60
AMg11	S, M	180	1	90	–	–
	S, M	230	1.5	90	10	35

	Corrosion properties			Casting properties		
	Average corrosion rate (g/m² hour)	UTS (rel. %)	El (rel.%)	MMFI (mm)	HCI (mm)	LSI (%)
AMg5K	0.004	6.5	33.3	320	12.5	
AMg5Mts	0.0019	6		300	22.5	1.3
AMg6l				264	15	1.1
AMg6lch				264	15	1.1
AMg10				270	12.5	1.2
AMg11				340	10	1.2

MMFI: molten metal fluidity index; HCI: hot cracking index; LSI: linear shrinkage index.

up into the magnesium silicide, thus enhancing castability but reducing plasticity of alloys. Iron impurity mostly enters the composition of skeletal inclusions of the $Al_{15}(Fe,Mn)_2Si_3$ phase. Castings obtained out of AMg7 are used without any heat treatment.

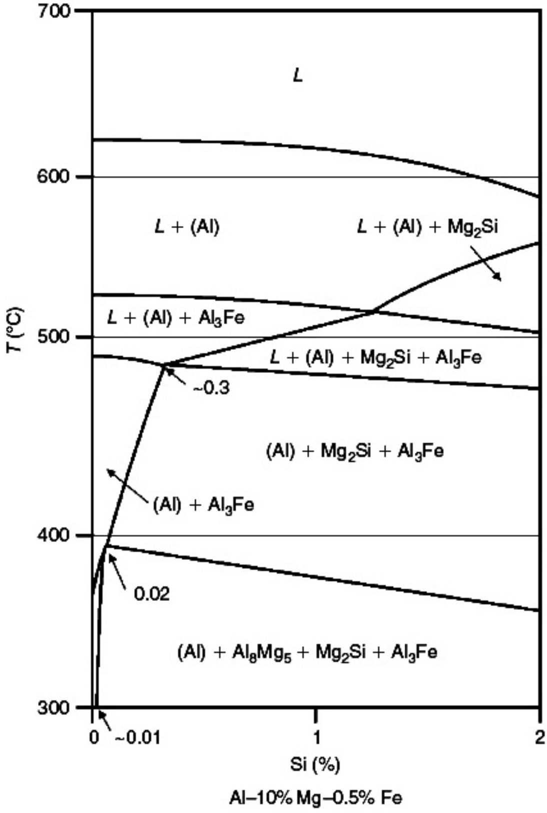

Figure 5.25 Polythermal section of Al–Fe–Mg–Si phase diagram at 10%Mg and 0.5%Fe.

Alloy *AMg11* (Al11Mg) contains the maximal amount of magnesium (up to 13%) amongst all standard aluminum alloys, both casting and wrought. Such a high concentration of the principal alloying element, together with additions of silicon (around 1%) allows obtaining for this alloy good molten metal fluidity, which is higher than that of alloy AMg10. It is mostly used for manufacturing shaped castings using different production techniques. Due to high concentrations of iron (up to 1%) and, consequently, larger volume fraction of the Fe- and Si-bearing phases, its mechanical properties are relatively low, even in the T4 temper. Microstructure of AMg11 typically contains needle-like inclusions of the Al_3Fe phase as well as the skeletal inclusion of Mg_2Si, as it follows from Al–Fe–Mg–Si phase diagram (Figure 1.42) and vertical cross-section at 10%Mg and 0.5%Fe (Figure 5.25).

Magnesium silicide is the principal phase in alloy *AMg5K1* (Al5Mg1Si), which has the lowest tendency to hot pre-solidification cracking among all Al–Mg alloys. This is related to the fact that there is no low-melting eutectic reaction resulting in the formation of Al_8Mg_5. This implies that the solidification range (and, possibly, effective solidification range) are narrower than for other Al–Mg alloys. Magnesium distributes between (Al) and Mg_2Si. The latter has well-developed skeletal morphology (so-called "Chinese script"). It is a very brittle phase, and its presence leads to low mechanical properties of alloys (UTS ~150 MPa, El ~1%). Since AMg5K contains additions of manganese, iron impurity is completely tied up into the $Al_{15}(Fe,Mn)_2Si_3$phase, which can be often found as part of the ternary eutectic $(Al) + Mg_2Si + Al_{15}(Fe,Mn)_2Si_3$. Castings produced out of the AMg5K alloy are used in ship building for parts carrying average workloads, working either in sea water or weakly basic environments at temperatures up to 200°C. This is higher than the limit temperatures for all other Al–Mg alloys [7].

Alloy *AMg4K1.5M* (Al4Mg1.5Si1Cu) differs from other Al–Mg alloys because it contains copper (around 1%). This allows obtaining some dispersion hardening effect after heat treatment using the T6 regime (Appendix 4), which, most probably, is related to the formation of the T' phase (Al_6Mg_4Cu). Indeed, this directly stems from the Al–Cu–Mg–Si phase diagram (Figure 1.39).

Alloy *ATs4Mg* (Al4Zn1Mg) is the only representative of the Al–Zn–Mg system. In composition it is close to the wrought aluminum alloy 7004. This alloy has relatively high level of mechanical properties even without heat-up for quenching. However, due to the low level of castability its application is hardly possible. In alloy ATs4Mg solidification ends according to the non-equilibrium eutectic reaction with participation of the $Al_2Mg_3Zn_3$ phase, but its amount is small and it can be revealed with significant difficulties using the technique of light microscopy. Impurities of iron and silicon are tied up into the particles of the Mg_2Si and $Al_{15}(Fe,Mn)_2Si_3$ that typically have skeletal morphology.

The phase composition of alloys of 5xx.0 without manganese can be analyzed using the Al–Fe–Mg–Si phase diagram (Figure 1.42). In the range of high-magnesium alloys (>5%Mg), this phase diagram has a relatively simple constitution, with most commercial alloys (except those containing 3–4%Mg) falling at room temperature into the phase region $(Al) + Al_3Fe + Al_8Mg_5 + Mg_2Si$. According to the equilibrium phase diagram, the Al_8Mg_5 phase is formed in casting 5xx.0-series alloys only in the solid state, by precipitation from the aluminum solid solution. However, under real casting conditions the majority of commercial casting alloys complete the solidification with the invariant eutectic reaction $L \Rightarrow (Al) + Al_3Fe + Al_8Mg_5 + Mg_2Si$ at 447°C. The non-equilibrium solidus can be as low as 428°C at a cooling rate of 6 K/s as measured by Bäckerud *et al.* for the 518.2 alloy.

As the concentrations of Fe and Si in the eutectic liquid are rather small, the Al_3Fe and Mg_2Si phases are formed in commercial alloys (except those that are high-purity with respect to Fe and Si) through bi- and monovariant reactions in a wide range of temperatures. Note, however, that there are some 5xx.0-series alloys that contain iron or silicon as alloying components, for example, up to 2.2%Si in a 512.2 alloy and up to 1%Fe in a 516.0 alloy. The solidification of such alloys can be traced using the polythermal section at 10%Mg and 0.5%Fe shown in Figure 5.25. After the solidification of primary (Al) grains, either $L \Rightarrow (Al) + Al_3Fe$ ($Si < 1\%$) or $L \Rightarrow (Al) + Mg_2Si$ ($Si > 1\%$) eutectics is formed. Under equilibrium conditions the alloys become solid after the formation of the ternary $L \Rightarrow (Al) + Al_3Fe + Mg_2Si$ eutectic. During non-equilibrium solidification, the remaining liquid disappears at 447–448°C following the invariant eutectic reaction $L \Rightarrow (Al) + Al_3Fe + Al_8Mg_5 + Mg_2Si$.

It should be noted that Mg_2Si particles (as distinct from Al_3Fe) can become globular upon high-temperature (>500°C) annealing, especially in cast products produced at high cooling rates. This structure modification is favorable for mechanical properties, especially ductility.

The equilibrium solidus of 5xx.0-series alloys is determined mainly by the concentration of magnesium (see Figure 2.3). Iron has minor effect, and silicon can even increase the solidus temperature. In alloys containing less than 5%Mg (e.g., 512.2) non-equilibrium solidification may produce the Al_8Fe_2Si phase as can be seen from Figure 2.4c.

NEW ALLOYS

The demands of rapidly evolving technology call for continuous research and development efforts aimed at invention of novel casting aluminum alloys. It often happens that the standard casting alloys, including high-quality materials, do not satisfy the rigorous requirements for applications in different areas of technology. This results in the efforts to use much more expensive manufacturing techniques such as rapid quenching from the melt (rapid solidification/power metallurgy, RS/PM), mechanical alloying, and seeding molten metal with ultra-disperse particles, etc. Very high costs of such materials limit substantially their widespread application. Consequently, the development of new casting alloys that could be cast using existing traditional equipment and yield high-quality shaped castings with higher level of properties than standard alloys, represents a challenging and actual problem. First of all, there is the need to increase alloy strength at room and elevated temperatures in conjunction with achieving higher corrosion resistance and good castability (including advanced techniques like die casting, casting into stiff molds, etc.). Recently there were several successful efforts going in this direction, and some of the developed new alloys find a limited industrial application. The authors believe that a very significant progress could be achieved in this field if advanced systems of alloying are chosen, and this issue is discussed in detail in this chapter.

6.1 ALLOYS WITH SMALL AMOUNTS OF EUTECTIC

As it was demonstrated in Sections 5.2 and 5.3, alloys containing small amounts of eutectic (e.g., on the basis of the Al–Cu, Al–Mg, and Al–Zn–Mg systems) have significant advantages – better mechanical properties. Based on this fact, an opinion was expressed that full utilization of the opportunity provided by these alloys could result in significantly broader applications. While efforts aimed at development of new casting alloys continued worldwide, in this text our goal is to review mostly the achievements in Russia since 1970–1980. This effort is justified because readers in the West usually did not have access to the body of work conducted in the former Soviet Union and in the Russian Federation.

Consequently, we describe below new high-strength alloys of the "solid solution" type (X_1 in Figure 1.1b) developed at Moscow Institute of Steel and

Casting Aluminum Alloys
ISBN-13: 978-0-08-045370-5

© 2007 Elsevier Ltd.
All rights reserved.

Alloys and some other organizations. These alloys could be classified into several groups:

1. Alloys on the basis of the Al–Mg–Zn system with approximately equal amounts of magnesium and zinc.
2. Alloys of the same system with the concentration ratio Mg:Zn $\approx$ 2.
3. Alloys on the basis of the Al–Zn–Mg–Cu system, close in their composition to wrought aluminum alloy AA7075.
4. Al–Cu alloys with ancillary additions of silicon ($<$1%).
5. Al–Mg alloys with ancillary additions of scandium.

All these materials are heat treatable and possess different levels of technological properties, thus allowing obtaining a number of advantages over standard casting aluminum alloys. It should be mentioned that the development of all alloys represented in Table 6.1 was preceded by the construction of dependencies of mechanical and casting properties upon chemical composition and parameters of heat treatment using the techniques of mathematical modeling (see Section 4.2.5). This gave the authors a possibility to justify the selection of future alloy compositions and heat treatments.

One of the first alloys developed using this design philosophy belonged to the Al–Mg–Zn system and was close in composition (3–6%Zn and 3–5%Mg) to the standard alloy ATs4Mg (or AL24), (Section 5.3). This similarity was properly underlined in the new alloy's mark: *AL24m* [328] and *AL24p* [329]. These alloys differed from their industrial analog by the elevated concentration of magnesium and transition metals (Mn, Cr, Ti, etc.) (see Table 6.1). Due to this modification, the effect of dispersion hardening in the course of quenching and subsequent aging was more pronounced. It had strength comparable to Al–Cu alloys (σ_B up to 450 MPa in the T6 temper); however, alloys AL24m and AL24p had higher corrosion resistance. Alloy AL24p possesses record-high mechanical properties in the T5 temper (UTS $>$ 340 MPa, El $>$ 6%), that is it can be used without high-temperature heating and quenching. However, their casting properties remained on a relatively low level, which is defined by the broad solidification range. Alloys AL24m and AL24p require that the iron and silicon impurities be strictly limited.

Systematic studies of the Al–Mg–Zn phase diagram in a broad concentration range allowed identifying a perspective concentration domain, which is seldom used for development of wrought aluminum alloys: 5–7%Mg and 2–3%Zn (Figure 6.1). These materials differ from Al–Mg alloys of the AMg6 type in their higher strength achieved after quenching and aging (T5, T6) due to the precipitation of a metastable phase, T' ($Al_2Mg_3Zn_3$). Among these, alloy *VAL11* (containing 6–7%Mg and 2–2.5%Zn) should be mentioned [9, 12], (Table 6.1). This alloy has the following values of mechanical properties in the T5 temper: UTS = 340 MPa, YS = 280 MPa, El = 6%, $K_{IC} = 37$ MPa·m$^{1/2}$. Alloy VAL11 possesses good corrosion resistance and satisfactory indexes of hot cracking and molten metal fluidity, which are higher than for alloy AL24p. One shortcoming of VAL11 is its strong dependence of mechanical properties on the concentrations

Table 6.1 Composition of high-strength and corrosion-resistant alloys on the basis of the Al–Mg–Zn–Cu system with low content of iron and silicon impurities

Alloy	Mg (%)	Zn (%)	Be (%)	Cu (%)	Mn (%)	Ti (%)	Zr (%)	Cr (%)
AL24m[a]	3–5	3–6	0.05–0.15	0.1–0.5Ce	0.3–0.9	0.1–0.4	0.1–0.4	0.1–0.3
AJI24p	3.5–4.5	3–4	0.01–0.1	–	0.3–0.7	0.1–0.3	0.01–0.1B	–
VAL11	6–7	2–2.5	0.07–0.15	–	0.1–0.2	0.1–0.3	0.1–0.3	0.1–0.2
VAL12	2–2.8	6.5–7.5	0.05–0.25	1–1.5	0.005–0.1B	0.1–0.3	0.05–0.25	–
VAL15	0.3–0.9Si	–	0.04–0.25Cd	4.5–5	0.5–0.9	0.15–0.35	0.05–0.25	–
01568	5–7	0.2–0.35Sc	0.04–0.1	–	–	0.03–0.1V	0.05–0.15	0.01–0.1Y

[a] $Mg + Zn < 8\%$.

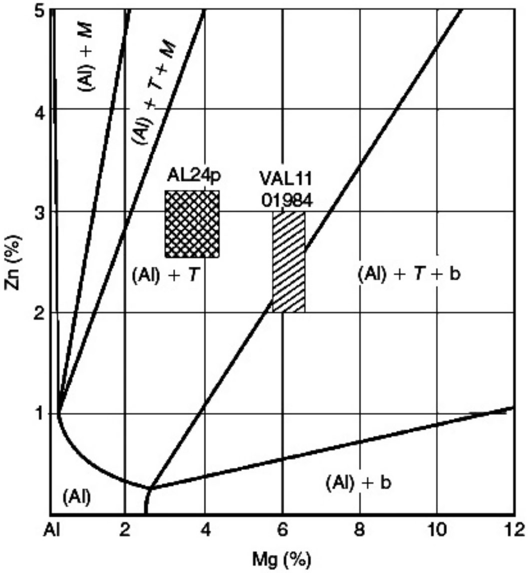

Figure 6.1 Isothermal cross-section of the Al–Mg–Zn phase diagram at 200°C.

of alloying elements (first of all, zinc), impurities (Fe and Si) and the selected aging scheme (this dependence is expressed much stronger than for Al–Si casting alloys). After aging according to the T6 scheme coarse grain boundary precipitates of the T phase can often be observed (Figure 6.2), which cause sharp drop in mechanical properties, especially El and K_{Ic} [334]. This is related to the change in the nature of alloy fracture mechanisms: from ductile intergranular (typical for the quenched state) (Figure 6.3a) to intragranular (Figure 6.3b). Alloy VAL11 should be cast out of pure primary components (similar to AMg6).

One of the most attractive systems for new casting alloy developers was the Al–Zn–Mg–Cu, which is the basic system for development of the strongest wrought alloys of the AA7075 type. Among several developments in this field, the new alloy *VAL12* (6.5–7.5%Z, 2–2.8%Mg, and 1–1.5%Cu) [9] has found some industrial application. The average value of (ultimate tensile strength URS) for this alloy in the T6 temper is 570 MPa. This is much higher than for the strongest casting alloys on the basis of the Al–Cu system (see Section 5.3). Strengthening after heat treatment is achieved due to disperse precipitates of the metastable T' ($Al_2Mg_3Zn_3$) and η' (Mg_2Zn) phases. Casting properties of this alloy are very low, which makes it difficult to obtain even relatively simple mold castings. The best results for VAL12 were obtained using the method of liquid stamping.

Alloy VAL12 and its modifications have high sensitivity to iron and silicon impurities; their maximal concentration should never exceed 0.1–0.2%. Otherwise its mechanical properties drop precipitously. For example, at 0.5%Fe

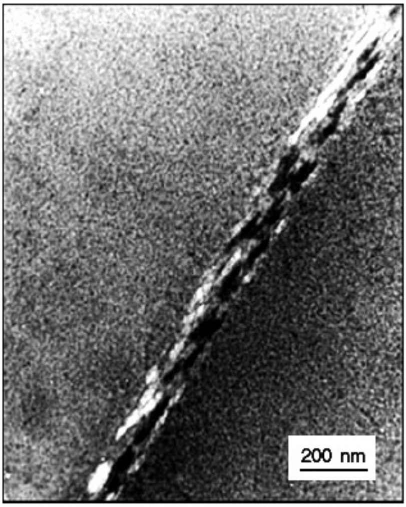

Figure 6.2 Grain boundary precipitates in alloy Al–6%Mg–3%Zn in the T7 temper, TEM.

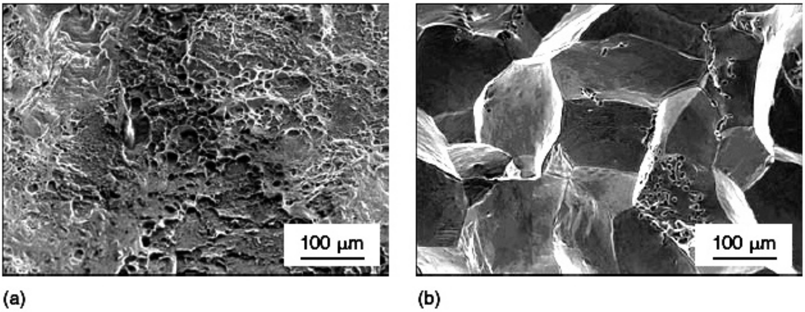

(a) (b)

Figure 6.3 Fracture surfaces of alloy Al–6%Mg–3%Zn, SEM: (a) T4, and (b) T6.

and 0.5%Si the following values were obtained: UTS < 400 MPa; El $< 0.5\%$; $K_{IC} < 20\,\mathrm{MPa{\cdot}m^{1/2}}$ [330].

Systematic efforts were made to raise the casting properties of Al–Cu alloys due to the introduction of silicon within the limits of its solubility in (Al) and the appropriate choice of ancillary additions. A number of new alloys were developed (e.g., *VAL15* (4.5–5%Cu and 0.3–0.9%Si) [331]), which, unfortunately, did not give any substantial advantages over the industrial alloys of the AM5 type. This happens because silicon, while enhancing castability, exerts strong negative influence upon thermal stability. Besides, even a small addition of silicon, as it follows from the Al–Cu–Si phase diagram (Figure 1.21), results in the strong depression of the solidus temperature.

One should also mention an experimental alloy *01568* (5–7%Mg and 0.2–0.35%Sc) on the basis of the Al–Mg–Sc system, which is close in properties to its wrought analog, the Russian 1570 alloy [23]. A unique combination of high strength (UTS > 360 MPa), plasticity (El > 16%), corrosion resistance, and excellent weldability make this alloy quite attractive for a number of applications in aerospace and military engineering. However, a very high price of scandium makes the application of such alloys unlikely in the foreseeable future.

Since all of the excellent properties of discussed alloys are ensured by very low content of iron and silicon impurities (<0.2%), a research effort was made to develop alloys allowing higher concentrations of these impurities (0.5% and higher of each). In particular, on the basis of the Al–Mg–Zn system alloys AMg4Ts3 (3–4.5%Mg and 3–4.5%Zn) and ATs4Mg2 (2–3%Zn and 1.6–2.5%Mg) were developed (out of secondary components) [333], which are close to the primary analogs in concentrations of magnesium and zinc (AL24m and Al24p), but could contain higher concentrations of Fe and Si. Strength of these secondary alloys, in particular, in the T6 temper, is sufficiently high (UTS = 430–450 MPa; YS = 350–380 MPa; HB = 135–140), but plasticity is low (El = 0.5–1%). The latter effect finds its explanation due to the unfavorable morphology of the Fe- and Si-bearing phases.

In order to increase elongation of alloys containing up to 0.5% Fe and Si, systematic studies were conducted on neutralizing the harmful influence of the Fe- and Si-bearing phases. It was established that in the case of the spherical shapes of the particles of these phases, their negative influence could be almost completely eliminated. For the most effective neutralization of iron it is recommended to introduce beryllium in the ratio Fe:Be ≈ 2, which directly stems from the Al–Be–Fe phase diagram (Section 1.2.1). In this case the iron impurity can be almost completely tied up into the globular inclusions of the $Al_4Be_5Fe_2$ phase.

Neutralization of the silicon impurity is achieved by high-temperature heat treatment (520–530°C) close to equilibrium solidus, which enhances fragmentation and spheroidization of the skeletal particles of Mg_2Si (see Section 3.1.3). As a result of chemical composition and heat treatment optimization microstructure is formed that consists of dispersoid hardened aluminum matrix and the globular inclusions of the $Fe_2Al_4Be_5$ and Mg_2Si phases (Figure 6.4). This type of microstructure ensures sufficiently ductile mechanism of fracture, in spite of the relatively high-volume fraction of brittle phases. Fractogram demonstrated in Figure 6.4b, illustrates the ductile nature of plastic deformation of the aluminum matrix, since the average pit size is significantly higher than that of the inclusions.

One of the first examples of realization of these principles (i.e., neutralization of harmful influence of the Fe and Si impurities (Table 6.2) was an experimental alloy possessing higher strength than VAL11: UTS = 430–450 MPa; YS = 350–380 MPa; HB = 135–140; El = 6–8%; $K_{IC} = 33–35\ \text{MPa} \cdot \text{m}^{1/2}$ [330, 334].

Alloy *01984* (5.5–6%Mg and 2.5–3%Zn) contains an ancillary addition of copper, resulting in significant strengthening effect while retaining high level of plasticity. It was successfully used for liquid stamping (forging) of castings of the average degree of complexity. However, similar to its analog (VAL11) it is

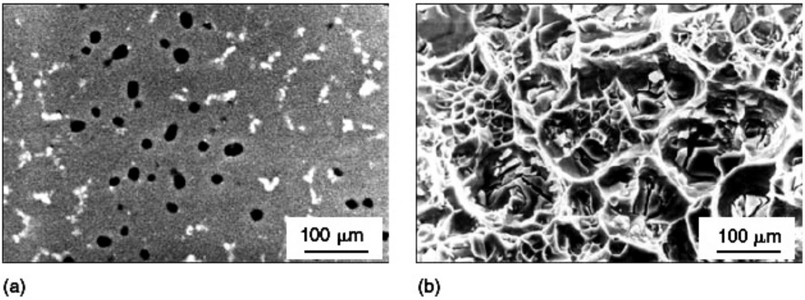

Figure 6.4 Microstructure (a); and fracture surface (b) of alloy c01984 containing 0.6%Fe, 0.5%Si, and 0.3%Be in the T6 temper (spheroidizing heat treatment), SEM.

highly sensitive to minor variations in chemical composition and aging treatment. Moreover, the effective neutralization of the Fe harmful influence requires that an optimal ratio of Fe:Be be maintained. This, obviously, is a very serious obstacle on the way to its industrial application. On the other hand, its high mechanical properties at high volume fractions of the Fe- and Si-bearing phases (Figure 6.4a), initiated further development of the microstructure optimization principles for high-strength eutectic alloys. These principles are considered in Section 6.2.

In particular, the established neutralization principles were applied for optimization of composition and heat treatment of the secondary casting alloy *AMg5K* (4.5–7%Mg, 0.6–1.5%Zn, and 0.6–1.5%Si) on the basis of the Al–Mg system [335]. This alloy was developed for manufacturing out of aluminum scrap of wrought alloys, first of all, of the 5xxx and 6xxx series. In the quenched state (T4 temper) alloy *AMg5K* possesses very reasonable level of properties: UTS > 240 MPa; $\sigma_{0.2} > 140$ MPa) at satisfactory level of plasticity (El > 2%).

Similar studies were conducted for alloys of the Al–Zn–Mg–Cu system. Out of the proposed experimental developments one should mention alloy 01976 (6–7%Zn, 1.6–2.4%Mg, and 1–1.5%Cu) [330, 336], the chemical composition of which is presented in Table 6.2. This alloy has lower (compared to VAL12) concentrations of zinc and magnesium in order to raise fracture toughness, and also ancillary additions of beryllium and calcium to neutralize harmful influence of Fe and Si impurities by binding these elements into particles with compact morphologies. Due to the optimization of composition and heat treatment, alloy 01976 possesses a good combination of mechanical properties (with somewhat lower strength). Even at concentrations of Fe and Si at 0.5% it has the following properties: UTS = 490–500 MPa; YS = 450–460 MPa; HB = 140–160; El = 6–10%; $K_{IC} = 24$–$26\ \mathrm{MPa} \cdot \mathrm{m}^{1/2}$. Microstructure of 01976 is close to that demonstrated in Figure 6.4a. Alloy was used successfully to manufacture different castings of simple shapes, mostly using the method of liquid stamping. Molten metal fluidity of this alloy is significantly better than for any Al–Cu alloys. However, 01976 has an even higher tendency to hot pre-solidification cracking than VAL12.

Table 6.2 Chemical composition of high-strength, corrosion-resistant alloys on the basis of the Al–Mg–Zn–Cu system with elevated levels of Fe and Si impurities

Alloy	Mg (%)	Zn (%)	Cu (%)	Fe (%)	Si (%)	Be (%)	Mn (%)	Ti (%)
AMg4Ts3[a]	3–4.5	3–4.5	0.3–1.5	0.85–1.5	<0.5	0.0001–0.1	0.3–0.8	0.01–0.2Zr
AMg4Ts2	2–3	1.6–2.5	1.7–2.7	0.6–1.5	<0.5	0.4–0.7Ni	0.3–0.7	0.01–0.2 0.1–0.3Zr
01984	5.5–6	2.5–3	0.25–0.35	<0.5	<0.5	0.01–0.25	0.01–0.02B	0.08–0.12
AMg5K	4.5–7	0.6–1.5	0.1–0.8	<1	0.6–1.5	<0.3Ni	0.2–0.6	<0.1Sn <0.15Pb
01976[b]	1.6–2.4[a]	6–7	1–1.5	<0.5	<0.5	0.15–0.25	–	0.1–0.2

[a] $Mg + Zn < 7.5\%$.

[b] If the Mg concentration does not exceed 2% to neutralize the harmful influence of silicon impurity it is necessary to introduce up to 0.5%Ca into the alloy composition.

Generalizing characterization of new alloys containing small amounts of eutectic, one should point at their drawbacks:

1. All alloys of the considered group have low casting properties and, consequently, could be used only for relatively simple castings. It needs to be emphasized that all potential resources for increasing castability *via* composition and heat treatment optimization are practically exhausted. In other words, alloys of the X_1 type (Figure 1.1) should be considered as not perspective for development of new casting alloys and casting of details and products of complex geometrical shapes.
2. In composition of all alloys (with the exception of secondary, Tables 6.1–6.2) the ancillary additions of beryllium are necessary in order to achieve improved properties. However, the application of beryllium is more and more limited in industry due to potential ecological problems and legal liabilities.
3. Neither of the described alloys exceeds the standard AM5 materials in thermal strength and resistance.

We discuss in detail in the next sections of this chapter how these important problems still could be solved.

6.2 GENERAL PRINCIPLES OF ALLOYING FOR EUTECTIC MATERIALS

Since new casting alloys of the "matrix" type (X_1 in Figure 1.1b) possess low castability prohibiting manufacturing of castings with complex shapes, additional research efforts were necessary in order to solve this difficult problem – to achieve a good combination of mechanical properties and castability.

The authors of this book proposed to use multicomponent eutectic alloys [337–342] that would satisfy the following requirements:

1. The amount of eutectic must be sufficient to ensure good level of castability, while the required level of mechanical properties could be attained *via* alloying of the aluminum matrix (in particular, it could be close in composition to alloys considered in Section 6.1).
2. The effective solidification range must be as narrow as possible.
3. Eutectic phases must have favorable morphology either immediately after solidification or after heat treatment (T4 or T6), similar to silicon particles in Al–Si alloys (Section 5.1).

These ideas can be illustrated using the generalized phase diagram Al–$K1$–$K2$ (Figure 6.5a) and the corresponding vertical section A_1–$K2$ (Figure 6.5b), where:

- $K1$ is the principal alloying element (Mg, Zn, Cu, Si) with significant solubility in (Al) that can form phase β_1.

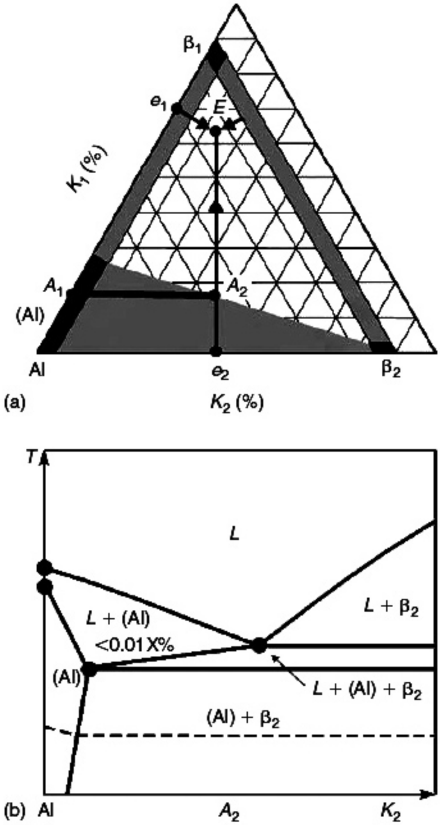

Figure 6.5 Schematics of phase diagrams Al–$K1$–$K2$ (a) and polythermal cross-section A_1–$K2$ (b).

- $K2$ is an eutectic forming element (Fe, Ni, Ce, etc.), which has low solubility in (Al) and forms phase β_2.
- A_1 is a chemical element containing $K1$ in the amounts up to solubility limit in (Al) at the temperature of quenching.

As it was already demonstrated in Section 4.2, alloy's strength is defined mostly by the microstructure of aluminum matrix, if it is understood as (Al) plus all strengthening dispersoids and/or precipitates (usually metastable), Table 1.4. Sufficiently high values of tensile strength and elongation are realized in commercial Al–Cu alloys (Section 5.2) and also in the new alloys belonging to the Al–Mg–Zn and Al–Zn–Mg–Cu systems (Section 6.1), with low concentrations of iron and silicon impurities. These are alloys of the X1 type (Figure 1.1), after heat

Table 6.3 Possible combinations of different types of (Al) solid solutions with eutectic phases

(Al) Matrix	Phase reaction, T_{NS} (°C)	Eutectic phases, β_2				
		(Si)	Mg_2Si	Al_3Ni	Al_9FeNi	Al_8Fe_2Si
Al–Si–Mg	$L \Rightarrow$ (Al) + (Si) + Mg_2Si, 555	+	+	+	+	+
Al–Cu–Si	$L \Rightarrow$ (Al) + (Si) + Al_2Cu, 525	+	–	–	–	+
Al–Cu–Si–Mg	$L \Rightarrow$ (Al) + (Si) + Al_2Cu + Q, 505	+	+	+	+	+
Al–Cu	$L \Rightarrow$ (Al) + Al_2Cu, 548	–	–	–	–	–
Al–Mg	$L \Rightarrow$ (Al) + Al_8Mg_5, 448	–	+	+	+	–
Al–Mg–Zn	$L \Rightarrow$ (Al) + Al_8Mg_5 + T, 447	–	+	+	+	–
Al–Zn–Mg–(Cu)	$L \Rightarrow$ (Al) + T + M, 475	–	+	+	+	+

treatment (quenching and aging) they have microstructure that consists almost completely of the (Al) matrix with the minimal amounts of constituent particles. Low casting properties of such alloys are related to their broad solidification range ($\Delta T = T_L - T_{NS}$). The latter, in turn, is defined by the relatively high position of the liquidus (T_L) and low temperatures of non-equilibrium solidus (T_{NS}). The values of T_{NS} are practically constant for each of the basic systems because they correspond to the temperature of solidification of the lowest-melting eutectic (Table 6.3). This eutectic, as a rule, is degenerated and could be observed in microstructure as a phase that contains all of the principal alloying elements (Figure 6.6). For example, for all alloys of the AM5 type that contain less than 5.7%Cu, the value of T_{NS} is 547°C, corresponding to the eutectic solidification $L \Rightarrow$ (Al) + Al_2Cu. In this case Cu stands for the "$K1$" element, while the β_1 – phase is represented by Al_2Cu. Concentration $K1$ is usually selected in such a way that during heat-up before quenching the β_1 phase can be dissolved completely in (Al).

In principle, by increasing the amount of eutectic (i.e., β_1 phase) one could increase somewhat casting properties of high-strength alloys of the matrix (solid-solution) type. However, practically speaking, the possibilities of this approach are limited because the $K1$ concentration is defined by its solubility limit in (Al) at the temperature of quenching. In particular, alloys of the AM5 type contain as much copper as feasible. In alloys on the basis of the Al–Zn–Mg type (e.g., ATs4Mg) one

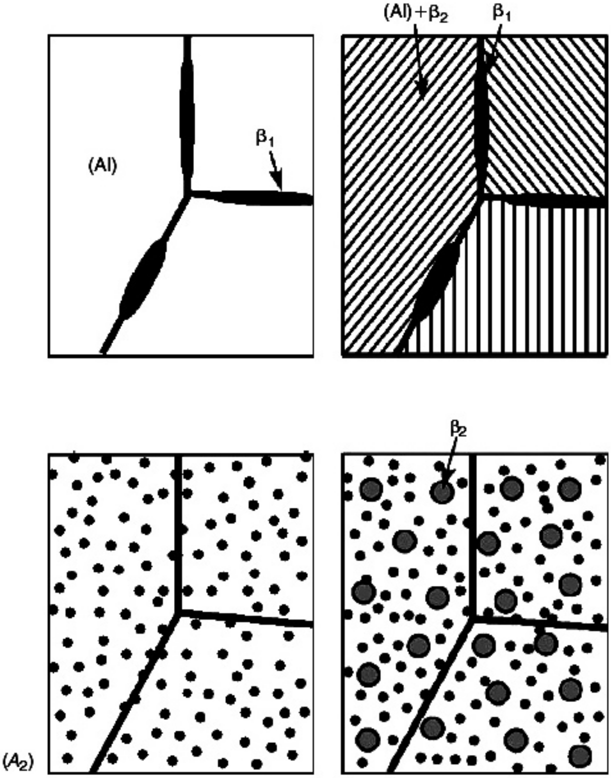

Figure 6.6 Schematics of microstructure of matrix – A_1 (a, c) and eutectic – A_2 (b, d). Types of alloys: a, b – as-cast state, and c, d – T6 temper.

could increase the solubility of magnesium and zinc according to the Al–Mg–Zn phase diagram (Figure 1.29) more than 100%. However, this is accompanied by significant deterioration of other properties (corrosion resistance).

The most reasonable way to increase alloy castability is to depress the liquidus temperature. This could be attained by the introduction of one or several components of the $K2$ type with low solubility in (Al), which would form the (Al) + β_2 eutectic. Taking into account the rules considered in Section 4.1, one could assume that castability will improve with the depression of liquidus temperature T_L. This implies that the castability maximum will be attained in alloy A_2, which is illustrated by the A_1–$K2$ cross-section (Figure 6.5b). On the other hand, as the concentration $K2$ grows, the volume fraction of the β_2 phase also increases, harming mechanical properties, especially elongation and fracture toughness. This is related to the fact that practically all excessive phases that could be found in aluminum alloys are brittle and get fractured first. This results in the formation of discontinuities serving as stress concentrators, especially in the case of needle-like morphology of particles. The negative influence of these inclusions – constituent particles can be significantly alleviated, if they possess globular shape and uniform distribution, that is to eliminate the largest stress concentrators. Such microstructure can be easily obtained in purely eutectic alloys since they are characterized by the presence of the most disperse particles, and in the process of annealing before quenching eutectic crystals of the β_2 phase can be fragmented into more compact particles (see Section 3.1.3).

Of all industrial casting alloys heat-treated Al–Si alloys (in the T6 temper) like AK8l and AK8M3ch possess microstructure close to optimal (Section 5.1). In these alloys β_2 is represented by the silicon phase, while the aluminum matrix consists of either Al–Si–Mg, Al–Si–Cu or Al–Cu–Si–Mg foundation. The former, according to the Al–Si–Mg phase diagram (Figure 1.28) corresponds, more or less, to some alloys of the 6xxx type (e.g., AA6081) used in aerospace industry, while the latter – to alloys similar to AA2014. One should mention that silicon could play the role of both $K1$ and $K2$ components; for this reason the overall concentration of this element needs to be subdivided into two parts.

Although the silicon phase allows achieving a high level of casting and average mechanical properties, in many cases it cannot be used in practical alloy design work. In particular, it is not well compatible with the aluminum matrix on the basis of the Al–Zn–Mg–Cu, necessary when maximal alloy strength is desirable (like in VAL12, see Section 6.1). Silicon phase could also be bad for alloy in those cases when special requirements need to be met in regards to the article surface. For example, it is bad when surfaces need to be treated with micro-arc (plasma electrolytic oxidation, PEO) oxidation technology [343].

In addition to the chemical elements considered above, aluminum alloys often contain Fe, Mn, Ni, Be, and some other additions. These elements have poor solubility in (Al) and usually form eutectic phases (see Chapter 1). Consequently, these phases can be considered as the "generic" β_2 phase. To reveal perspective alloy compositions it was necessary to analyze the corresponding phase diagrams, then to conduct experimental studies of some properties of both matrix and eutectic alloys [337, 338]. Possible combinations of the considered aluminum matrices and eutectic phases are presented in Table 6.3. The selected β_2 phases were sorted into the descending order in terms of the depression of the alloy T_L temperature: (Si), Mg_2Si, Al_3Ni , Al_9FeNi, and Al_8Fe_2Si.

As can be seen from Table 6.3, there is a sufficient number of combinations of the aluminum matrices and eutectic phases, which allows realizing the generalized diagram presented in Figure 6.5. The Al–Si–Mg is the most "universal" as it can be combined with all phases β_2 presented in Table 6.3. It should be mentioned that the general level of mechanical properties for alloys with different eutectic is about the same, while the hot cracking index correlates with the degree of liquidus depression temperature, T_L (Table 6.4). At a first glance, this result does not have any practical significance since the optimal composition with such a matrix is realized for Al–Si alloys of the 356/357 type. However, comparison of data

Table 6.4 Comparative characteristics of mechanical and casting properties of alloys in the basis of the Al–1%Si–0.6%Mg solid solution with different eutectic phases

Phase	Q_M (mass%)	Q_V (vol%)	T_L(°C)	ΔT(°C)	HB	σ_B (MPa)	δ (%)	HCI[a] (mm)
–	0	0	650	95	118	315	2.9	16
(Si)	11.0	11.0	577	22	123	370	4.3	<4
Mg_2Si	12.6	18.0	590	35	121	330	1.0	6
Al_3Ni	14.3	9.9	630	75	124	340	3.1	10
Al_9FeNi	10.6	8.4	640	85	123	335	2.5	12
Al_8Fe_2Si	8.9	7.3	635	80	121	325	2.5	12

[a] Hot cracking index measured using the so-called "pencil probe".

Table 6.5 Comparative characteristics of mechanical and casting properties of alloys on the basis of the Al–6%Zn–1.6%Mg–1%Cu solid solution with different eutectic phases

Eutectic phase	Q_M (mass%)	Q_V (vol%)	T_L (°C)	ΔT (°C)	HB	UTS (MPa)	YS (MPa)	El (%)	K_{Ic} (MPa $\times$ $m^{1/2}$)	HCI[a] (mm)
–	0	0	645	170	151	446	426	5.0	45.0	37.5
Mg_2Si	10.7	15.5	588	113	166	480	450	1.0	24.2	17.5
Al_3Ni	10.8	7.3	618	143	174	520	482	3.2	31.5	22.5
Al_9FeNi	8.1	6.2	632	157	166	505	465	1.9	27.5	27.5
Al_8Fe_2Si	5.0	3.8	630	155	164	490	462	1.4	25.4	27.5

[a] Hot cracking index using VIAM probe (lower is better, see Section 4.1).

obtained for matrix and eutectic alloys in the T6 temper indicates that the former possess lower plasticity compared to Al–Si, which is defined by pronounced intergranular fracture of this group of alloys. In alloys with the silicon phase fracture has well defined ductile nature, similar to that demonstrated in Figure 6.4b. Taking into account the role of globular particles in fracture mechanisms of alloy 01984 (see Section 6.1) one could make a conclusion that eutectic alloys may possess advantages over matrix casting alloys not only in castability, but also in mechanical properties.

Eutectic alloys on the basis of the Al–Zn–Mg–Cu high-strength matrix represent a significant interest; however, this matrix is incompatible with the silicon phase. It follows from Table 6.3 that eutectic alloys in which the (Al) matrix preserves the composition of the basic alloy, could be obtained with the participation of the following phases Mg_2Si, Al_3Ni, Al_9FeNi, and Al_8Fe_2Si. In Table 6.5

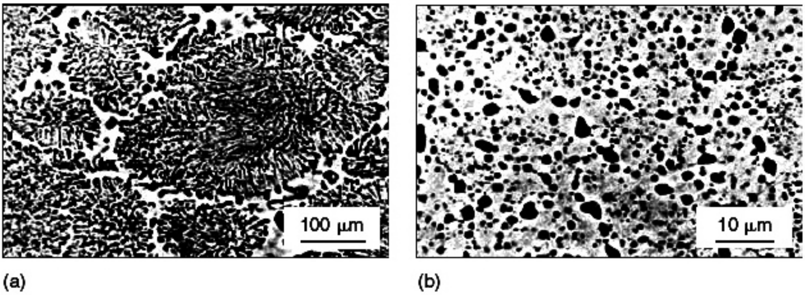

Figure 6.7 Microstructure of eutectic alloy Al–8%Mg–6%Zn–4%Si–1%Cu with Mg_2Si phase in as-cast (a) and heat treated (b) states.

we present some properties of the basic alloy Al–6%Zn–1.6%Mg–1%Cu and four eutectic alloys with this matrix. The common feature of all eutectic alloys is the relative refinement of their microstructure, together with high-volume fraction of the β_2 phase. Alloy with magnesium silicide is particularly interesting as its optimization results in a very unusual combination of component concentrations: 8%Mg, 6%Zn, 4%Si, and 1%Cu. With such a ratio of magnesium, zinc, and copper, in the absence of silicon, this alloy will be very brittle. The optimization of Mg and Si concentrations according to the point A_2 in Figure 6.5 results in the distribution of magnesium between the (Al) matrix (in the same amount as in the basic matrix alloy!) and the Mg_2Si phase. In as-cast condition this alloy has purely eutectic microstructure (Figure 6.7a). The (Al) + Mg_2Si eutectic colonies are refined and surrounded by the "veins" of non-equilibrium M phase, containing Al, Mg, Zn, and Cu. After homogenization at 450° C, the dissolution of the M phase in (Al) and partial fragmentation of the magnesium silicide crystals take place. Heat up to 520°C results in the formation of the uniformly distributed globular particles (Figure 6.7b) which ensures a relatively high level of mechanical properties after aging, even despite the fact that the volume fraction of Mg_2Si crystals exceeds 15 vol% (Table 6.5).

The data presented in Table 6.5 illustrate a strong correlation between hot cracking index and solidification range (ΔT). This indicates that in order to achieve maximal increase in castability it is necessary to design compositions with magnesium silicide.

Mechanical properties have different sensitivity to eutectic phases. If hardness, yield strength and, to a lesser extent, UTS are mostly defined by the degree of alloying of the aluminum matrix, plasticity, and fracture toughness depend very strongly on the degree of spheroidization and uniformity of distribution of eutectic inclusions, as well as on the properties of individual "generic" β_2 phase. The most globular morphology is characteristic of the Mg_2Si (Figure 6.7b) and Al_3Ni phases. Spheroidization of iron-bearing phases proceeds to a lesser extent, which, most probably could be related to low diffusivity of iron in aluminum. Alloys with the Al_9FeNi and Al_8Fe_2Si phases render only incremental improvements in castability. Consequently, the choice could be only between the Mg_2Si and Al_3Ni compounds. Practical application of high-strength alloys with Mg_2Si is not quite realistic, in spite of the significant improvement of castability and globular morphology of particles. This is because microstructure of such alloys is extremely sensitive to composition variations, which negatively influences the robustness, stability of alloy properties. At the same time, the combination of properties for alloy with nickel aluminide seems to be optimal. It is for this reason that it was selected as the foundation for development of a novel high-strength casting alloy AZ6N4 (see Section 6.3).

It should be noted that the phase composition of five-component systems (Al–Zn–Mg–Cu–Ni and Al–Zn–Mg–Cu–Si) very strongly depends upon the concentrations of components. In particular, nickel can form such compounds as Al_7Cu_4Ni and Al_3NiCu with copper (see Section 1.2.14), while at the same time most of alloy strengthening could be achieved due to the numerous metastable modifications of at least three phases (M, T, and S) from the Al–Zn–Mg–Cu system (see Section 1.3.8). For this reason more detailed and logically justified study of the influence of eutectic phases Al_3Ni and Mg_2Si upon alloy castability and strengthening, calls for a systematic consideration of the corresponding quaternary systems without copper (Al–Zn–Mg–Ni and Al–Zn–Mg–Si). The base composition was chosen to be Al–7%Zn–3%Mg that allows for the high effect of precipitation hardening due to the formation of the metastable T' ($Al_2Mg_3Zn_3$) phase [2, 7].

Preliminary evaluation of the Al–Zn–Mg alloys with nickel and silicon, shows that the addition of nickel results in the formation of only one phase (Al_3Ni). At the same time, the addition of Si may cause the formation of two phases (Mg_2Si and (Si)) [7]. In order to preserve magnesium in the solid solution, it was added to some alloys with Si in the weight ratio 1.73:1 that assures the binding of Si only into the Mg_2Si phase. Figure 6.8 illustrates the tentative distribution of phase fields in solid Al–Zn–Mg–Ni (a) and Al–Zn–Mg–Si (b) alloys.

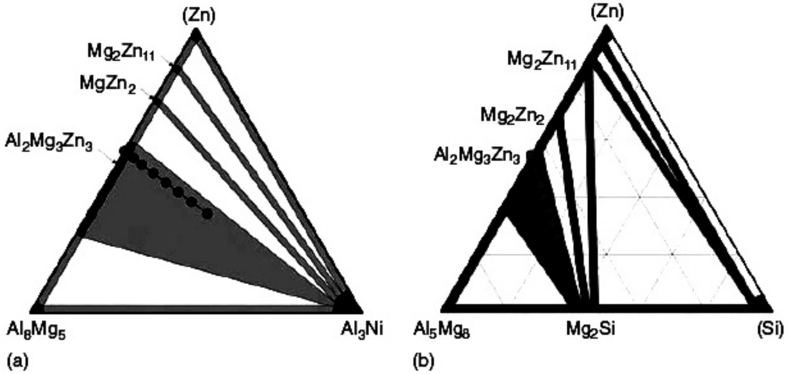

Figure 6.8 Distribution of phase fields in solid Al–Zn–Mg–Ni (a) and Al–Zn–Mg–Si (b) alloys with experimental alloys shown.

The analysis of alloy microstructure reveals the formation of non-equilibrium (Al) + *T* eutectics in all tested alloys. The addition of up to 4%Ni to the base alloy Al–7%Zn–3%Mg causes the formation of (Al) + Al_3Ni eutectics with a maximum volume fraction of the eutectics of 50 vol% (Figure 6.9a). At larger Ni concentrations, primary Al_3Ni crystals are formed. The addition of silicon to the base alloy results in similar consequences. However, an alloy with 4%Si (and 6.8% of additional magnesium) exhibits almost purely eutectic (Al) + Mg_2Si structure. At higher silicon concentrations, primary Mg_2Si particles are formed on the same scale with eutectic colonies (Figure 6.9b). Figure 6.9c, d shows that solution treatment results in the dissolution of the non-equilibrium *T* phase (first stage at 450°C) and spheroidization of Ni- and Si-containing particles (second stage at 500°C).

Polythermal sections given in Figure 6.10a, b are experimentally constructed using the results of microstructure examination and DSC and could be used for choosing the optimum alloy compositions and regimes of heat treatment. Thermodynamic calculations give good agreement with the experimental isopleths,

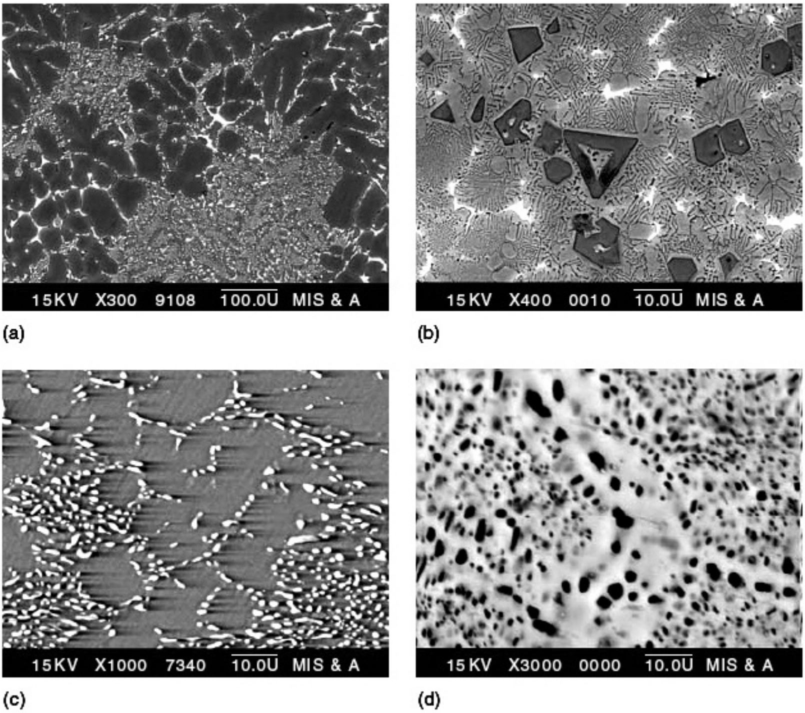
15KV X300 9108 100.0U MIS & A
(a)
15KV X400 0010 10.0U MIS & A
(b)
15KV X1000 7340 10.0U MIS & A
(c)
15KV X3000 0000 10.0U MIS & A
(d)

Figure 6.9 Microstructures of Al–7% Zn–3% Mg alloys with 4%Ni (a, c) and 5%Si (b, d) in as-cast (a, b) and annealed (c, d) condition.

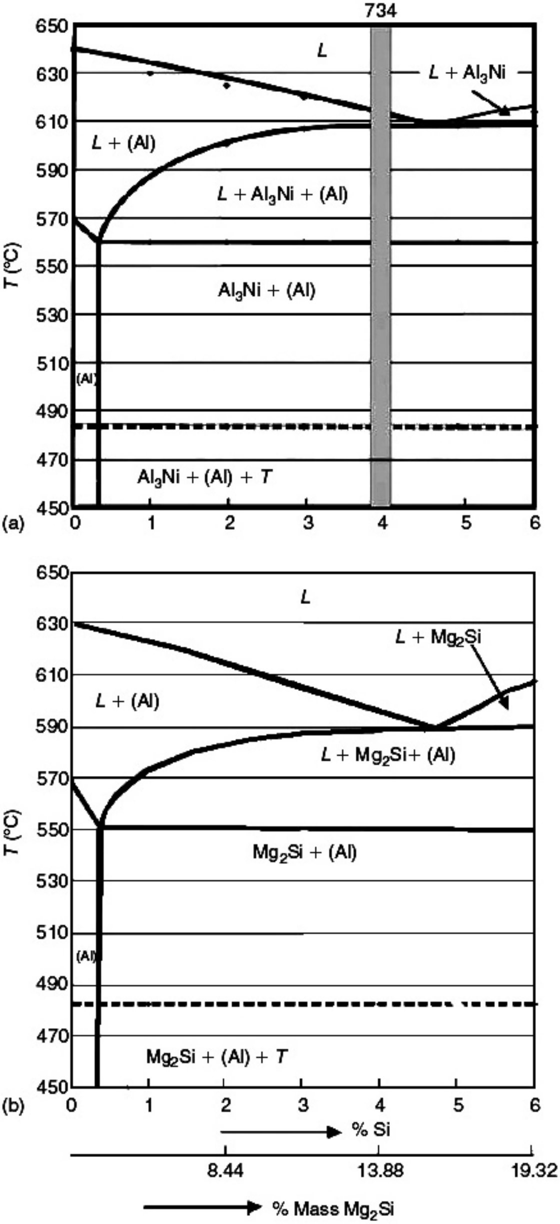

Figure 6.10 Polythermal sections of Al–7%Zn–3%Mg–Si (Mg_2Si) (a) and Al–7%Zn–3%Mg–Ni(b, c) alloys constructed experimentally (a, b) and by thermodynamic calculations (c).

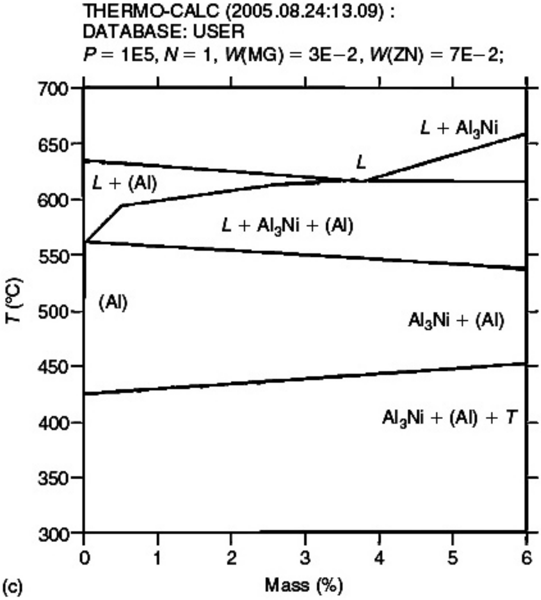

Figure 6.10 (Continued)

Table 6.6 Chemical composition, solidification range ($\Delta T = T_{\mathrm{L}}^{\mathrm{exp}} - T_{\mathrm{NES}}^{\mathrm{exp}}$) and HTS of experimental alloys

Alloy	Zn (%)	Mg (%)	Si (%)	Ni (%)	Fe (%)	ΔT (°C)	HTS (mm)
1 (base)	7.32	2.96	0.04	–	0.06	165	>16
2	7.6	3.32	0.08	4.34	0.07	139	14
3	8.04	9.11	3.65	0.1	0.07	106	12

except for the solvus of the T phase (Figure 6.10c). According to experimental data, solvus lines are in 380–420°C range.

The non-equilibrium solidus for most alloys is around 480–485° C. Therefore, their solidification range is determined by the liquidus temperature, T_{L}. Eutectic alloys have the narrowest solidification range and could hold promise for different foundry applications. The compositions of these alloys and the base alloy along with their solidification ranges and hot tearing susceptibilities are given in Table 6.6. One can see that the lower hot tearing susceptibility (HTS) corresponds to narrower solidification range.

Table 6.7 Thermal contraction data for the alloys given in Table 6.6[a]

Alloy	T_{NES} (°C)	T_{ES} (°C)	T_L (°C)	T_{TC} (°C)	ΔT_{eff} (°C)	ω (%)	ε (%)
1 (base)	465/482	–/563	630/632	550/–	85/68	0.1/–	0.18/0.135
2	465/483	–/525	604/613	519/–	54/36	0.093/–	0.16/0.095
3	475/482	–/529	581/583	480/–	5/–2	0.234/–	0.036/0.026

[a] Experimental values are in numerator and the calculated ones in denominator, for contraction/expansion parameters this means that the values are determined down to experimental or calculated non-equilibrium solidus, with the applied cooling rate of 6 K/s.

T_{NES}: temperatures of non-equilibrium

T_{ES}: equilibrium solidus

T_L: equilibrium liquidus

T_{TC}: thermal contraction onset

ΔT_{eff}: effective solidification range

ε: thermal contraction

ω: pre-shrinkage expansion.

The HTS can be more reliably correlated to the effective solidification range (between the temperature of thermal contraction onset, T_{TC}, and the non-equilibrium solidus, T_{NES}) and to the magnitude of thermal contraction in the solidification range. The results are given in Table 6.7. Thermal contraction begins in between equilibrium and non-equilibrium solidus temperatures at high-volume fractions of the solid, above 85%. The ranking of the effective solidification range and the thermal contraction accumulated in the solidification range agrees well with the ranking of HTS of alloys. The lowest thermal contraction (Alloy 3) is combined with the highest pre-shrinkage expansion that makes this alloy least vulnerable to hot tearing and shape distortions during solidification and most promising for precise shape casting applications.

Experimental alloy compositions have been tested using casting into well-known commercial shapes. The results confirm the positive effect of eutectic formation on reducing hot tearing. The base Al–Zn–Mg alloy cracks in sections that are more than 10 mm thick (Figure 6.11a), whereas the alloy with 4%Ni allows sand casting with sections less than 10 mm (Figure 6.11b).

The additions of nickel and compensated additions of silicon and magnesium to the base alloy should not decrease the amount of zinc and magnesium available in the solid solution after solution heat treatment for precipitation hardening. The hardening behavior was analyzed by aging alloys at 130° C. Figure 6.12 shows that alloys 2 and 3 (Table 6.6) demonstrate virtually the same hardening effect as the base alloy. Fine, uniformly distributed particles of the hardening T' phase were found in their microstructure. Globular morphology of eutectic constituents in the examined alloys (Figure 6.9c, d) makes these alloys similar by microstructure to heat-treated (T4 or T6) casting alloys of 3xx series. This gives hope that tensile properties of the examined alloys will be sufficiently high.

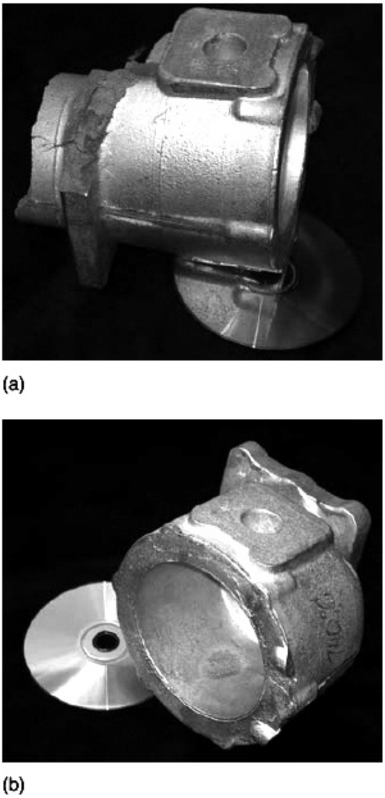

Figure 6.11 Shape castings from the base Al–7%Zn–3%Mg alloy (a) and the Al–7%Zn–3%Mg–4%Ni alloy (b).

It should be mentioned that the (Al) matrix of the Al–Cu system does not allow obtaining required microstructure with any of the five phases given in Table 6.3. This happens because the introduction of additions of Si and Ni in Al–Cu required for the formation of the corresponding phases, results in the unacceptably large changes in the (Al) composition. In turn, such a change does not allow preserving the properties of the basic (matrix) alloy of the AM5 type. In particular, silicon, which possesses comparatively higher solubility in (Al), forms a different matrix of the Al–Cu–Si system. This matrix has several characteristics making it inferior with respect to the original, silicon-less, one. Among these properties is high temperature strength (due to increased diffusion of Si in Al and reduction of the solidus temperature), as well as strength at room temperature (due to decreased solubility of Cu in Al). Alloys of the Al–Cu–Si system (e.g., AA296) even with small additions of silicon (up to 3%) are much closer in their mechanical properties

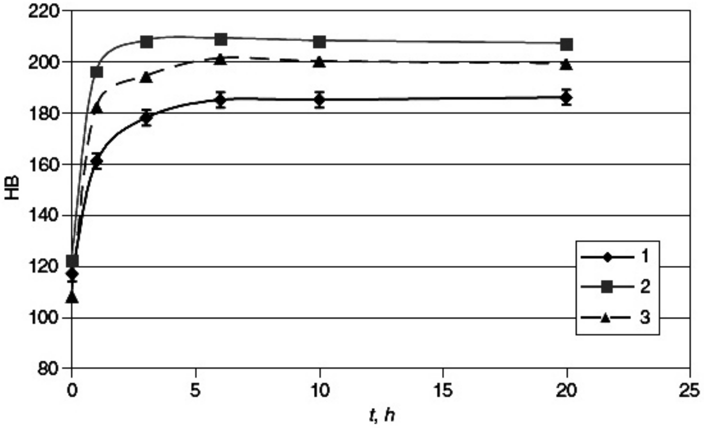

Figure 6.12 Hardening of the experimental alloys upon aging at 130°C.

to Al–Si alloys like AK5M7 (Al5Si7Cu) and AK5M4 (Al5Si4Cu), rather than to AM5 (Al5Cu, <0.2Si).

Some Al–Cu alloys (of the ÀL33 and AA242 types) contain additions of nickel, which helps somewhat to increase thermal stability. However, this is accompanied by the reduction of mechanical properties at room temperature, while castability remains the same [10]. This happens because nickel binds a significant amount of copper into non-soluble phases (Al_7Cu_4Ni or $Al_3(Cu,Ni)_2$) and, correspondingly, reduces its concentration in (Al), as it directly follows from the Al–Cu–Ni phase diagram (Figure 1.20). At the same time the remaining amount of copper is sufficient for solidification of non-equilibrium eutectic with the participation of the Al_2Cu phase. As a result, alloys of the ÀL33 possess a broad solidification range (see Section 4.1).

Addition of iron into Al–Cu alloys results in the formation of the Al_7Cu_2Fe phase during solidification. This is accompanied by the reduction of Cu concentration in (Al). Joint introduction of iron and nickel in approximately equal amounts allows retaining copper in the aluminum matrix. However, this does not result in a substantial improvement of alloy castability.

It directly follows from the discussion above that it is hardly possible to obtain eutectic compositions with aluminum matrix of the AM5 type and sufficiently narrow solidification range.

6.3 HIGH-STRENGTH ALLOY AZ6N4 AND ATS7MG3N4 (734)

High-strength weldable casting alloy AZ6N4 was developed by the authors using the basic composition; its properties are presented in Table 6.5. The term

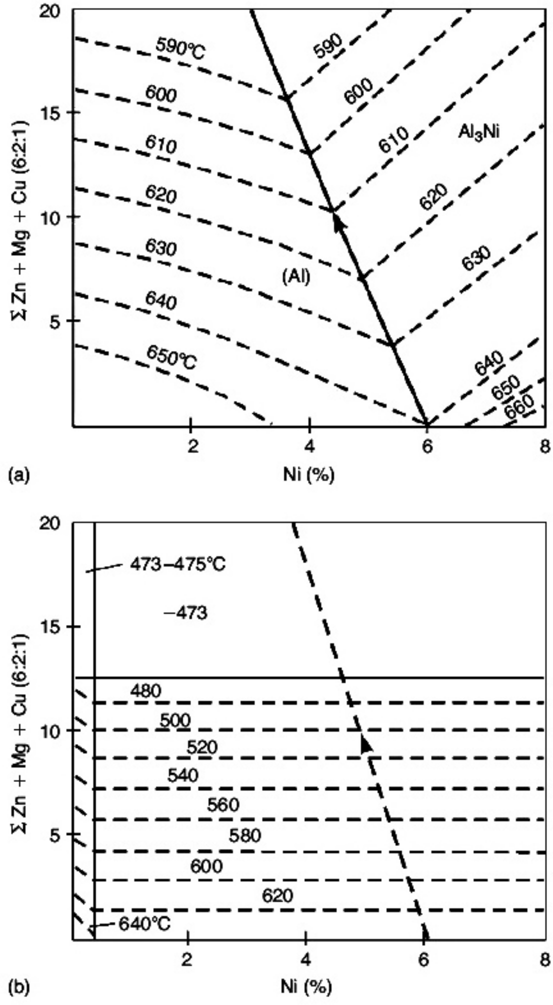

Figure 6.13 Liquidus (a) and solidus (b) of the phase diagram Al–Zn–Ni–Mg–Cu in the cross-section Al–Σ(Zn + Mg + Cu)–Ni; Zn:Mg:Cu = 6:2:1.

"nickalin" was proposed for it (as well as for other alloys on the basis of the (Al) + Al_3Ni) [344, 345]. In order to optimize the concentrations of the principal alloy components (i.e., nickel, zinc, magnesium, and copper) the authors have constructed the fragments of the Al–Zn–Ni–Mg–Cu phase diagram (Figures 6.13 and

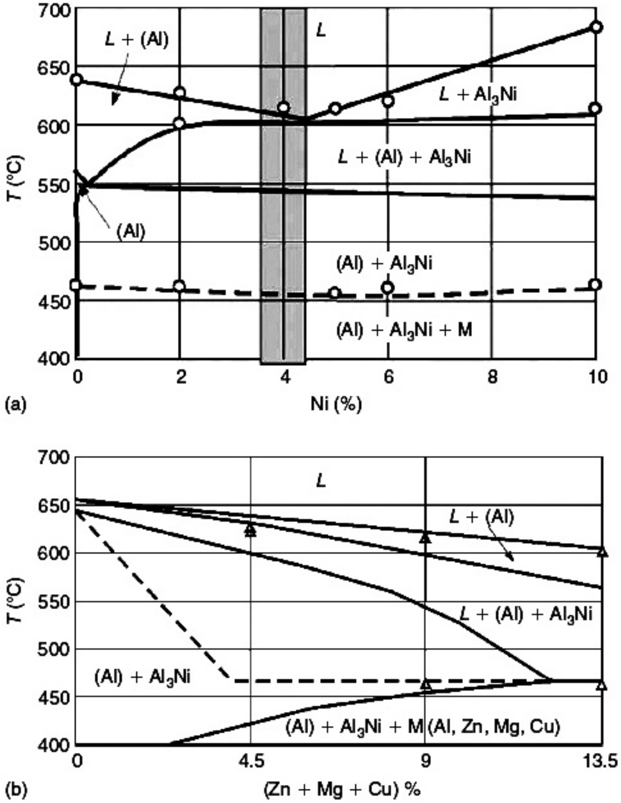

Figure 6.14 Polythermal cross-sections of the Al–Zn–Ni–Mg–Cu phase diagram: (a) 6%Zn, 2%Mg and 1%Cu; (b) 4%Ni and Zn:Mg:Cu = 6:2:1.

6.14), which helped to justify not only alloy composition range, but also its heat treatment. Below an analysis of the Al–Zn–Mg–Cu–Ni phase diagram is presented in its Al–Σ(Zn + Mg + Cu)–Ni cross-section, with the ratio Zn:Mg:Cu = 6:2:1 in the concentration domain up to 8%Ni and 18%Σ(Zn + Mg + Cu).

The liquidus surface of the constructed polythermal cross-section indicates (Figure 6.13a) that in the considered domain primary solidification is possible only for (Al) and Al_3Ni. After that, in a temperature range eutectic reaction $L \Rightarrow (Al) + Al_3Ni$ will proceed, which is clearly illustrated by the polythermal cross-section (Al–6%Zn–2%Mg–1%Cu)–Ni (Figure 6.14a). In non-equilibrium conditions solidification ends at 473–475°C following the eutectic reaction: $L \Rightarrow (Al) + Al_3Ni + M(Al, Zn, Mg, Cu)$. This phase reaction is close, both in its temperature and possibly composition, to the $L \Rightarrow (Al) + M(MgZn_2)$ reaction from the ternary Al–Zn–Mg system [14].

Thus, non-equilibrium solidus (T_{NS}) of alloys in the considered domain weakly depends upon the concentrations of alloying elements. Consequently, the solidification range ($\Delta T = T_L - T_{NS}$) mostly depends upon liquidus temperature (T_L). Polythermal cross-section provided in Figure 6.14a demonstrates that the narrowest solidification range (and the best castability) are achieved at ~4.5Ni% (i.e., in the eutectic point). The latter defines the optimal nickel concentration or, more precisely, the upper boundary of the range because primary Al_3Ni are unacceptable due to their coarse morphology. The main microstructural component in alloy Al–6%Zn–4.5%Ni–2%Mg–1%Cu in as-cast state are eutectic colonies $(Al) + Al_3Ni$. Along their boundaries the "veins" of the M(Al,Zn,Mg,Cu) phase (from non-equilibrium eutectic, Figure 6.15a) are deposited. It also follows from Figure 6.14a that the temperature of the first stage of heat treatment (T_1), must be below T_{NS} but above the solvus (T_{SS}). In this case one could achieve complete dissolution of the non-equilibrium M(Al,Zn,Mg,Cu) phases not accompanied by non-equilibrium melting. Due to the relatively low diffusivity of nickel in (Al), fragmentation and spheroidization of Al_3Ni crystals is possible only at temperatures not lower than 500°C (i.e., above T_{NS}). For this reason heat-up before quenching of such alloys includes two stages: in addition to homogenization at T_1 it is also necessary to conduct spheroidizing heat treatment at T_2, close to equilibrium solidus (Figure 6.14a). In this case, if the original as-cast microstructure was sufficiently refined, it becomes possible to attain the formation of globular particles of Al_3Ni (Figure 6.15b). Comparison of Figures 5.8b and 6.15b allows seeing similarity in microstructures of the 354 type alloys and "nickalin" AZ6N4 after heat treatment.

As the sum $\Sigma(Zn + Mg + Cu)$ grows, the optimal nickel concentration must be reduced according to the location of the binary eutectic figurative line (Figure 6.13a). Solidus (Figure 6.13b) and polythermal section at 4%Ni (Figure 6.14b) demonstrate that with increased $\Sigma(Zn + Mg + Cu)$ equilibrium solidus decreases. This makes it problematic to obtain globular particles of Al_3Ni with conventional mold casting. Indeed, annealing at temperatures even very close to solidus may require too lengthy treatment due to the insufficient degree of the eutectic refinement. If the concentrations of zinc, magnesium, and copper are reduced, then it becomes possible to conduct high-temperature heat treatments. However, their attractiveness is lower because strength of such alloys is also reduced.

Quenching and subsequent aging of high-strength nickel bearing alloys are conducted in a way similar to heat treatable Al–Si alloys. To achieve the best combination of strength, elongation, and corrosion resistance, it is recommended to use two-step aging processes, which ensure uniform distribution of strengthening particles. Typical microstructure of high-strength Ni-bearing alloy in the T6 temper obtained using TEM (transmission electron microscopy) is shown in Figure 6.15c. It should be mentioned that unlike in alloy VAL12, in Ni-bearing alloys large grain boundary particles practically cannot be found (Figure 6.2).

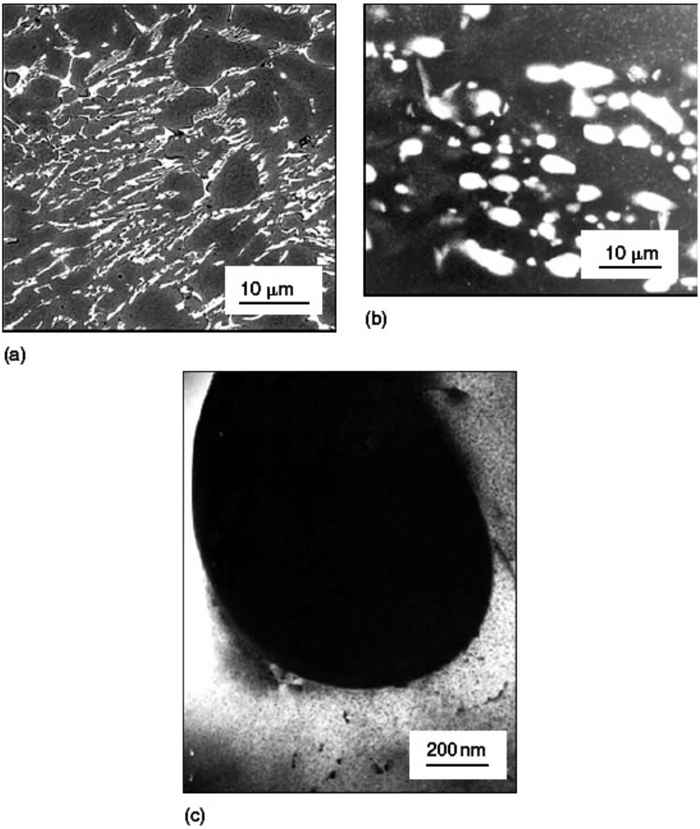

Figure 6.15 Microstructure (SEM – a, b) and fine structure (TEM – c) for alloy AZ6N4: (a) as-cast state, (b) T4, and (c) T6.

Most probably this is the reason of the high value of fatigue life of these alloys (Table 6.8). This effect could be explained by the positive influence of the uniformly distributed globular particles of Al_3Ni, as it was demonstrated in Ref. [346]. This conclusion is supported by the analysis of fracture surfaces, which reveal pits, but not intergranular fracture (Figure 6.16).

The construction of the composition-property curves and studies of the influence of ancillary additions allowed the authors to optimize the high-strength Ni-bearing alloy AZ6N4. Its strength is higher for Al–Si-type alloy AA354; moreover, it is better than the strongest known standard casting alloys of the AM5 type (Table 6.8). AZ6N4 is practically not worse VAL12 in strength, but significantly exceeds the latter in castability and fatigue life. This alloy was used for making

Table 6.8 Properties of Ni-bearing alloys AZ6N4, ATs7Mg3N4 (734) and other known high-strength casting aluminum alloys

Alloy	HB	UTS (MPa)	YS (MPa)	El (%)	σ^{a}_{-1}(MPa)	HCI[b](mm)
AA354	120	380	300	5	–	7.5
AM5	140	480	400	6	80	32.5
VAL12	175	550	500	3	90	35
AZ6N4	180	540	500	3	>160	22.5
ATs7Mg3N4	190	600	550	5	190	22.5

[a] After 10^7 cycles (mold casting).
[b] HCI: Hot cracking index using the VIAM probe.

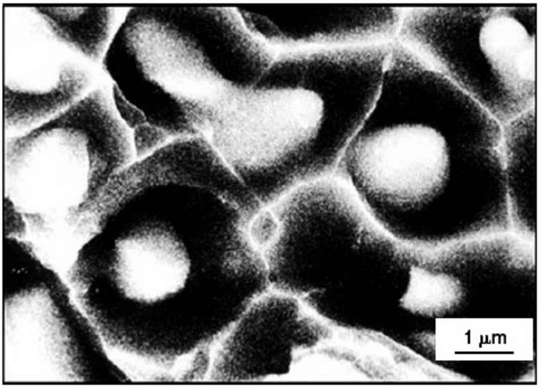

Figure 6.16 Fracture surface of alloy AZ6N4 after quenching and aging.

complex-shaped castings using different casting techniques into metallic mold. Figure 6.17 provides examples of castings obtained using forging and die casting. Ni-bearing alloy AZ6N4 was recommended for manufacturing responsible details instead of wrought alloy AA7075, which may provide significant savings due to reduction of sliver in metal cutting operations. It can be used for argon arc welding and makes it even more perspective because industrial wrought alloys on the basis of the Al–Zn–Mg–Cu system are very poorly weldable.

In the last years the authors conducted studies aimed at developing even stronger alloys than AZ6N4. In particular, alloy ATs7Mg3N4 on the base of Al–Zn–Mg–Ni system allowed obtaining record values for such properties as strength, elongation, and hot cracking index: $\sigma_B > 600$ MPa, $\sigma_{0.2} >$ MPa, $\delta > 5\%$,

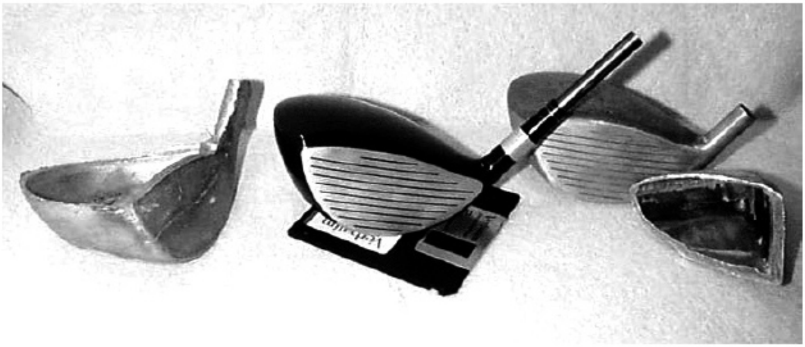

Figure 6.17 Castings made out of high strength alloy AZ6N4 prepared using the techniques of liquid stamping and die casting.

HCI < 14 mm (Table 6.8). This alloy design was based on the construction of the Al–Zn–Mg–Ni phase diagram in the aluminum corner (Figures 6.8a and 6.10a, c). In particular, polythermal cross-section Al–7%Zn–3%Mg–Ni (Figure 6.10a, c) clearly indicates that the introduction of up to 4%Ni results in the formation of the (Al) + Al_3Ni eutectic and narrowing of the solidification range. This improves casting properties, especially hot cracking (Table 6.7). To attain maximal strength in conjunction with good ductility in Cu-free alloy ATs7Mg3N4 after quenching and aging a special microstructure was realized consisting of the aluminum matrix strengthened by the secondary dispersoids of the T' phase ($Al_2Zn_3Mg_3$). In addition to that, microstructure contained uniformly distributed globular Ni-bearing particles. Coarse grain boundary precipitates were completely absent. For this reason the new alloy, unlike well-known high-strength casting alloys of the Al–Zn–Mg–Cu system, was not prone to intergranular fracture (Figure 6.2). In alloy ATs7Mg3N4 the decomposition of (Al) proceeds uniformly in the whole volume because interphase boundaries (Al)/Al_3Ni, similar to grain boundaries, enhance the formation of the secondary T-phase precipitates. Since the inclusions of globular Ni-bearing particles are uniformly distributed in the whole volume and mostly inside the grains they, to a larger extent, accelerate decomposition processes inside these grains. It is this interesting feature that allows achieving very high strength for this alloy. Due to improved casting properties alloy ATs7Mg3N4 is suitable for sand casting and manufacturing of shaped casting of average complexity (Figure 6.18).

Since alloys on the basis of the Al–Zn–Mg–Cu system (including Ni-bearing ones) possess poor corrosion resistance, research efforts were made to develop effective and economical solutions for alloy surface protection. Very promising results were obtained using the technique of microarc (or microplasmic) oxidation. Coatings obtained using this method protected metal surfaces reliably from corrosive environments, and also dramatically increased wear resistance [343] (see Figure 6.19).

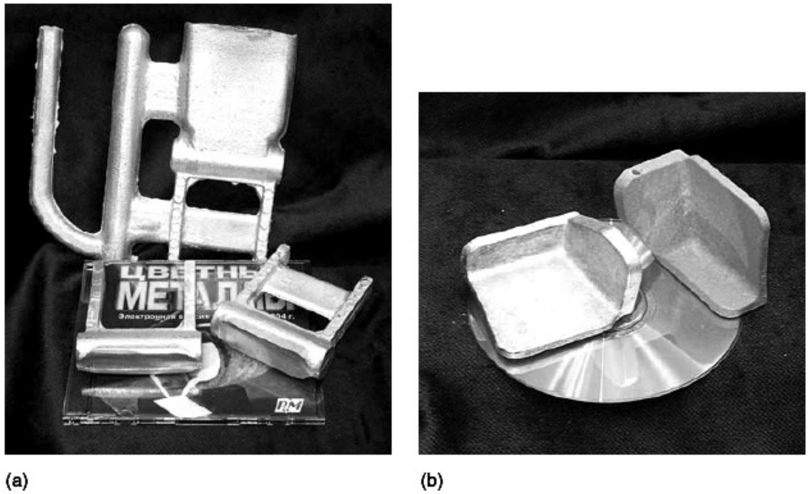

Figure 6.18 Mold casting of high-strength alloy 734.

6.4 ALLOYS DOPED WITH TRANSITION METALS FOR IMPROVED THERMAL STABILITY

In many cases construction materials must possess a high level of mechanical properties not only at room, but also at elevated temperature(s). This statement is fully applicable to casting aluminum alloys. Such property as the maximal level of working temperature is of special interest. For standard casting alloys of the AM5 type it does not exceed 250–300°C [7, 10]. Moreover, using traditional alloying approaches, it is very difficult to raise this level of working temperatures because diffusion of copper atoms in (Al) becomes activated. In addition, Al–Cu alloys possess poor castability; to improve it without significantly altering the aluminum matrix composition is hardly feasible (see Section 6.2).

The principles of design of high-strength aluminum alloys on the basis of eutectic compositions of the A_2 type (Figure 6.5) outlined in Section 6.2 can be used, in principle, for development of casting alloys with elevated thermal stability [348, 349]. However, in this case requirements to the aluminum matrix and eutectic-forming elements will be different because of the following reasons.

1. Elements $K1$ (Zn, Mg, Si) are rapid diffusers in aluminum at elevated temperatures and, consequently, cannot ensure the required level of alloy thermal stability.

2. Equilibrium solidus of the considered eutectic compositions A_2, as a rule, does not exceed 550°C and, consequently, the maximum working temperature cannot be higher than 300°C.
3. The values of non-equilibrium solidus temperature (T_{NS}) with elements of the $K2$ type are too low (Table 6.3) to ensure sufficiently narrow solidification range. This results in poor castability; the only exception from this rule is copper-less Al–Si alloys, but their thermal stability is low.

It is known that thermal stability of alloys can be increased by means of alloying with transition metals [10]. Positive results were obtained using rapid cooling (quenching) from the melt (granule and powder metallurgy – RS/PM), since in this case it was possible to realize microstructure that was distinctly different from microstructures formed in massive ingots at normal solidification rates [18].

In terms of their solubility in aluminum, transition metals (TM) could be divided into two groups: TM1 – having relatively high solubility (tenth of a percent and higher) and TM2 – with very low solubility in (Al), forming eutectic phases or constituent particles. As solidification rate grows (in the range of conventional casting technology), the solubility of TM1 in (Al) increases quite substantially, while the solubility of TM2 almost does not change. However, constituent particles get somewhat refined, and also the eutectic point shifts toward higher concentration of TM2. In the process of heat-up to 200–600°C, precipitation of secondary aluminides containing TM1 may take place. Improvement of thermal stability (in comparison to standard aluminum alloys) is achieved mostly due to higher volume fraction of disperse aluminides containing transition metals of both types (TM1 and TM2). Since the cost of RS/PM materials is quite high, it seems feasible to consider a possibility of development of novel thermally stable aluminum alloys via optimization of their composition and microstructure. It would be necessary to simultaneously use the following guidelines: (a) principles of alloying of rapidly quenched metals [18] and (b) principles of composition optimization of high-strength aluminum alloys considered in Section 6.2.

The joint application of these principles to casting aluminum alloys needs to simultaneously consider the following factors:

1. Aluminum matrix alloyed with TM1 that exert positive influence upon thermal stability and ensuring sufficiently high level of mechanical properties at room temperature.
2. Eutectic phase containing TM2, which will ensure a combination of good mechanical properties at room and elevated temperatures.
3. The narrowest possible solidification ranges to ensure the highest level of casting properties and refined microstructure of the second phase in eutectic.
4. The highest solidus temperature to ensure thermal stability.

To achieve the best economical solution, one should add to the described program a requirement of absence in alloy compositions of expensive materials; simplicity of heat treatment (in particular, absence of quenching); and a possibility of recycling alloy material without significant deterioration of properties.

Table 6.9 Characteristics of binary eutectics on the basis of aluminum with transition metals of the TM2 group

No	Eutectic composition (%)				Phase	Q_V (vol%)	T (°C)
	Ni	Fe	Ce	Al			
1	6	–	–	Balance	Al_3Ni	9.7	640
2	1.7	1.7	–	Balance	Al_9FeNi	8.1	649
3	–	–	12	Balance	Al_4Ce	14.3	640
4	–	2	2	Balance	$Al_{10}Fe_2Ce$	5.7	650
5	–	2	–	Balance	Al_6Fe[a]	6.4	–

[a] Metastable phase.

Most of these requirements, at least in principle, can be satisfied if one uses compositions of the Al–TM1–TM2 type, with the following conditions:

1. TM1 is one or several chemical elements that can enter in significant concentrations the composition of (Al) during solidification, and ensure strengthening after high-temperature aging due to the formation of secondary aluminides (dispersoids).
2. TM2 is one or several elements that form with aluminum diagrams of the eutectic type with high eutectic temperature.
3. TM1 and TM2 do not form phases among each other, at least, at required alloy concentrations.

The Al–Ni–Mn system could serve as an example of the Al-TM1-TM2 composition (e.g., please see polythermal cross-section in Figure 6.20).

The most perspective TM2 candidates are nickel, iron, and cerium (and other rare earth metals), which form refined eutectic (due to zero solidification range) with the participation of binary and ternary aluminides (Table 6.9). All eutectics presented in Table 6.9 have high melting temperature and are capable of fragmentation upon heating in spite of low solubility of TM2 in aluminum.

Microstructure of the (Al) + Al_3Ni eutectic in binary alloy is much more refined than in multicomponent AZ6N4 alloy with broad solidification range (Figure 6.10a), although both were obtained at the same values of V_c (around 10 K/s). This eutectic is remarkable because it ensures a more uniform microstructure in castings compared to aluminum–silicon. At a given solidification rate the Al_3Ni phase gets fragmented beginning at temperature ~430°C. Due to its original highly refined microstructure it becomes possible to obtain particles of sub-micrometer range. This makes casting microstructure very close to microstructure of granules made of aluminum alloys with transition metals TM2 [17]. The microstructure of the (Al) + Al_9FeNi eutectic is approximately the same,

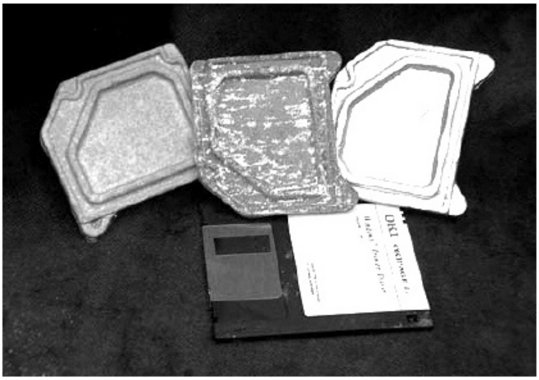

Figure 6.19 Shape casting made out of alloy ATs7Mg3N4 (Al–Cu–Mg–Zn–Ni), after heat treatment (right); the same alloy sample after corrosion testing (center); the same alloy with protective micro-arc coating after corrosion testing (left).

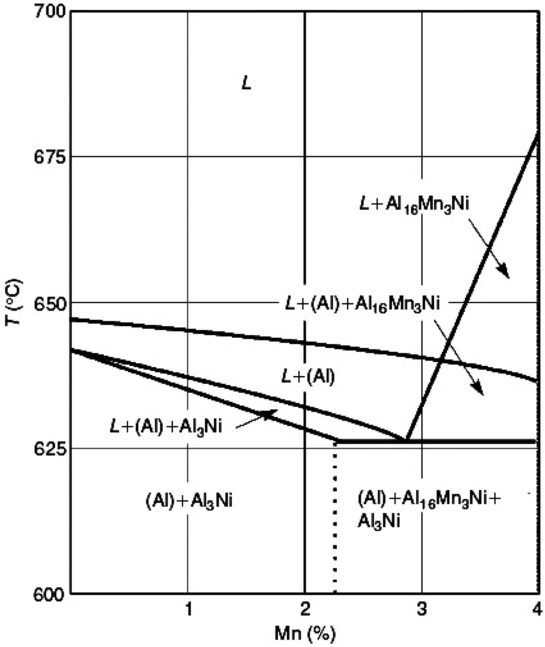

Figure 6.20 Polythermal cross-section Al-4%Ni–Mn for non-equilibrium conditions ($V_{\text{cooling}} \approx 10\,\text{K/s}$).

but slightly less refined; also it is less prone to fragmentation. In alloy with 12%Ce it is possible to attain the maximal volume fractionof the second phase (15 vol%); however, due to the very high concentration of expensive cerium practical application of alloys on the basis of this eutectic is hardly feasible. Alloy 4 containing much less cerium is of great interest; however, its microstructure is not as uniform as in alloys 1–3. It contains not more than 50% of the (Al) $+Al_{10}Fe_2Ce$ eutectic. Finally, the last eutectic is the cheapest but can be realized only at solidification rates not less than 8–10 K/s. In the case of slower solidification rate coarse needle-like inclusions of the Al_3Fe phase will be formed instead of metastable Al_6Fe phase in disperse eutectic.

The selection of elements capable of playing the role of TM1 was conducted on the basis of experimental studies done by the authors, taking into account available literature on rapidly quenched alloys.

The principal criterion was a given element's maximal solubility in (Al) and ability to raise the characteristics of thermal stability and strength. Scandium, titanium, chromium, vanadium, zirconium, molybdenum, manganese, and hafnium were selected as potential candidates. The influence of these elements upon microstructure and hardening was studied both using binary alloys Al–TM1, and alloys with additions of 2–6% of Ni. Given that many of these TM1 sharply raise the liquidus temperature, preparation of alloys and casting were conducted at 900°C.

The results of metallographic analysis of alloys with different TM1 concentrations allowed determining their concentrations corresponding to precipitation of primary aluminide crystals. In turn, this provided a possibility to estimate the values of maximal solubility ($C_{\max}$) of TM1 in (Al), while micro-XRD analysis helped refine the obtained values. Some characteristics of alloys containing 6% Ni and TM1 in the amounts close to $C_{\max}$ are presented in Table 6.10.

The values of volume and mass fractions (Q_V and Q_M) of the secondary aluminides were calculated using existing data on composition and density of aluminides and assuming complete precipitation of TM1 out of (Al). As can be seen fromTable 6.8, in castings it is possible to achieve much higher values of Cmax compared to the predictions using equilibrium phase diagrams (Appendix 2). Measurements of casting alloy hardness showed that all TM1 result in strengthening (some more, some less); the highest growth of HB was observed in the case of Mn and Cr additions.

To determine the influence of TM1 upon the (Al) ability to dispersion hardening, alloys were heat treated using multi-step scheme in the temperature range from 200°C to 600°C (with the step of 50°C) with 3-hour hold time at each step. This allowed obtaining the dependence of hardness (HB) on temperature of the last step [348, 349]. On the basis of the obtained data a conclusion was made that the most effective strengthening agents, as it should be expected, were scandium and zirconium. It should be mentioned that in the case of 0.6%Sc addition, strong hardening effect transform into softening at temperatures above 300°C. In order to achieve higher alloy thermal stability, it is preferable to use the addition of 0.8%Zr because the temperature of the onset of significant softening in this case

Table 6.10 Characteristics of experimental alloys containing 6%Ni and additions of transition metals (TM1)

TM1	C_{max}		T_s (°C)	Phase	Q_M (mass%)	Q_v (vol%)	HB^o	HB^{max}
	equil.	exp.						
Sc	0.3	0.6	655	$ScAl_3$ 35.7%Sc	1.7	1.5	68	115
Ti	0.28	1.0	665	$TiAl_3$ 37.2%Ti	0.7	0.6	68	68
V	0.4	0.5	661	VAl_{10} 15.8%V	2.5	2.2	70	70
Cr	0.8	0.8	661	$CrAl_7$ 21.6%Cr	3.7	3.2	76	76
Mn	1.8	2.0	657	$MnAl_6$ 25.3%Mn	7.1	5.8	91	91
Zr	0.28	0.8	660.3	$ZrAl_3$ 53%Zr	0.5	0.3	64	101
Mo	0.25	1.0	660.3	$MoAl_{12}$ 22.6%Mo	1.1	0.9	72	75
Hf	0.2	1.5	664	$HfAl_3$ 68.8%Hf	1.7	0.7	62	65

is higher than 400°C. Alloys with all other TM1 did not demonstrate a tendency to strengthening after heat treatment.

Studies of aging in binary Al–Zr alloys demonstrated that the effect of hardening increases with higher concentration of zirconium (up to 0.9%), and after that – changes insignificantly. Fine structure of alloy Al–0.8%Zr heat treated for maximum strength, reveal the presence of metastable Al_3Zr dispersoids with the average size 5–10 nm. The average dispersoid size remains about the same if zirconium is added into eutectic alloy Al–6%Ni.

Thus, it follows from the conducted experiments that the most perspective TM1 materials are manganese and zirconium. These metals are not very expensive, readily accessible, and allow realizing the optimal type of microstructure for casting alloy thermal stability.

The formation of supersaturated solid solution during solidfication of aluminum alloys containing transition metals is a function of two parameters: the initial temperature of the melt (T_m) and the cooling velocity (V_c) upon solidification and in the solid state. With increasing the cooling rate during solidification

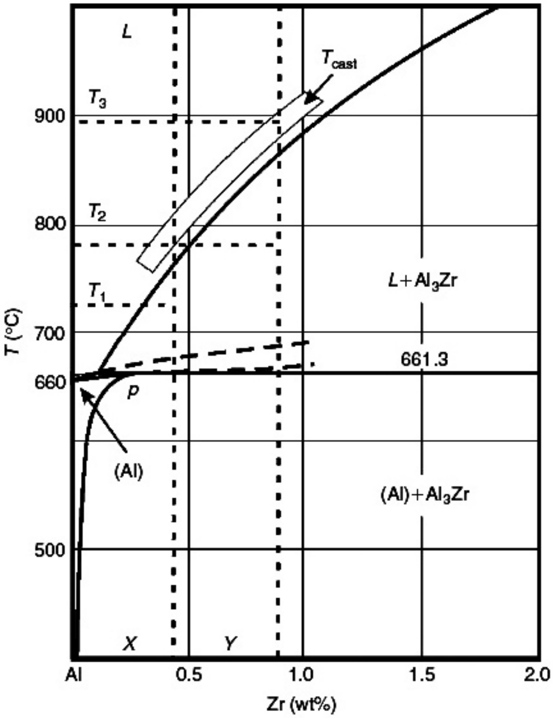

Figure 6.21 Simple schematic diagram showing equilibrium and non-equilibrium liquidus of Al–Zr alloys and illustrating the correct choice of casting temperatures and cooling rates during solidification for the complete introduction of Zr into supersaturated solid solution during solidification: T2 and V_{c1} represent the best choice for alloy X, T3 and V_{c2} – for alloy Y.

the concentration boundary at which primary crystals start to form, shifts toward larger concentrations of transition metal. This can be illustrated by a schematic non-equilibrium Al–Zr phase diagram as shown in Figure 6.21. Similar diagrams but for the formation of the metastable Al_3Zr phase and a supersaturated (Al) solid solution have been reported earlier. With increasing the cooling rate V_c the liquidus (T_L) and solidus lines for the solidification of aluminum solid solution are extended toward higher zirconium concentrations and the peritectic reaction does not occur under non-equilibrium solidification conditions. As a result, an anomalously supersaturated solid solution of Zr in (Al) can be formed. However, this phenomenon does not necessarily lead to the complete introduction of Zr into (Al) upon solidification. The additional condition for that is the absence of primary Al_3Zr crystals in the melt prior to the beginning of cooling. Obviously, the melt temperature and, therefore the casting temperature should be above the liquidus of the alloy. Otherwise, zirconium will be partially bound in primary

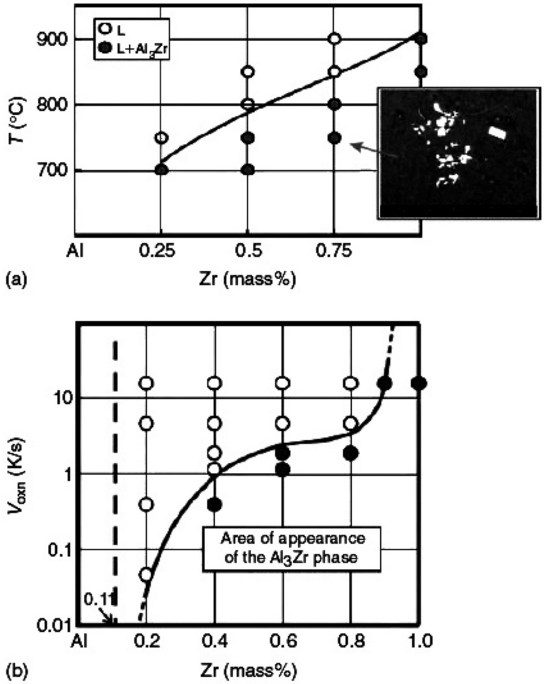

Figure 6.22 The influence of casting temperature (a) and cooling rate (b) upon solubility of zirconium in solid solution (binary system).

crystals and cannot enter the supersaturated solid solution at any cooling rate during solidification. For example, temperature T1 is too low for alloy X though cooling rate can be sufficient for the formation of a supersaturated solid solution. Proper casting temperature T2 for alloy X is absolutely unsuitable for alloy Y at any cooling rate. For alloy Y, temperature T3 should be chosen for the formation of a supersaturated solid solution containing all zirconium, providing that the cooling rate is sufficiently high. All these speculations demonstrate how important it is to know the liquidus temperature of alloys. Unfortunately, the liquidus surface in the Al–Sc–Zr system is not readily available from the literature. Therefore, we made our assessment based on our own experimental results. We also took into account the temperatures of invariant reactions from binary phase diagrams and experimental polythermal sections reported in the literature. The experimental liquidus isotherms of this system in the aluminum corner are given in Figure 6.22a. It demonstrates that the requirement $T_m > T_L$ must always be fulfilled (including rapid quenching conditions). Taking into account the necessary superheating of molten metals, one could modify this criterion in the following way: $T_m > T_L + 30$. Otherwise primary Al_3Zr crystals will be present in molten

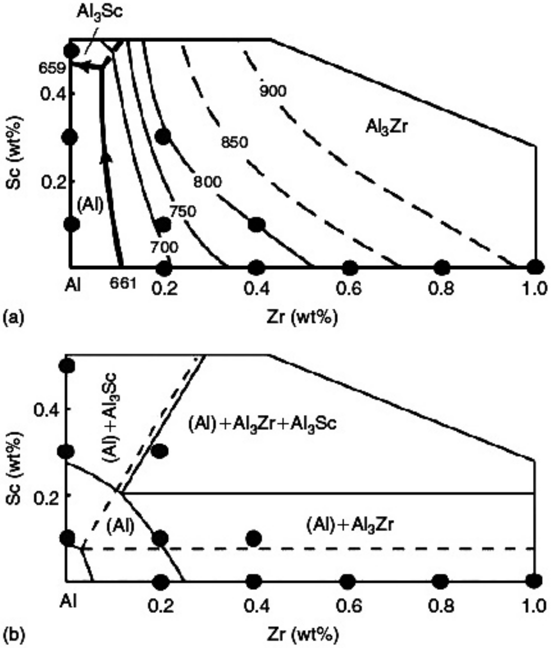

Figure 6.23 Liquidus isotherms (a) and isothermal cross-sections (b) at 640° (solid lines) and 450°C (dashed lines) of the Al–Sc–Zr phase diagram. Black dots show experimental alloys.

metal (i.e., before casting) and, obviously, in cast microstructure. Since the upper temperature limit in industrial conditions should not exceed 800–850°C, it is not feasible to consider Zr concentrations above 0.6%.

On the other hand, the cooling rate affects the formation of supersaturated solid solution of Zr in (Al). Figure 6.22b indicates that for thin-walled castings obtained in metallic molds ($V_c = 10$–$20\,\mathrm{K/s}$), the application of such Zr concentration should be possible. At lower concentrations even smaller cooling rates could be used with success.

In some cases chromium and scandium also could serve as TM1 elements. The former, according to Refs. [10, 18], allows to obtain the highest level of strength at temperatures above 350°C, while the latter could be used when high temperature of molten metal is unacceptable for some reason (which eliminates additions of zirconium as well).

When alloying with both scandium and zirconium is considered, it is useful to refer to the aluminum corner of the Al-Sc-Zr phase diagram shown in Figure 6.23. Figure 6.24 shows the dependence of hardness of some experimental Al–Zr alloys upon the temperature of the last step of annealing.

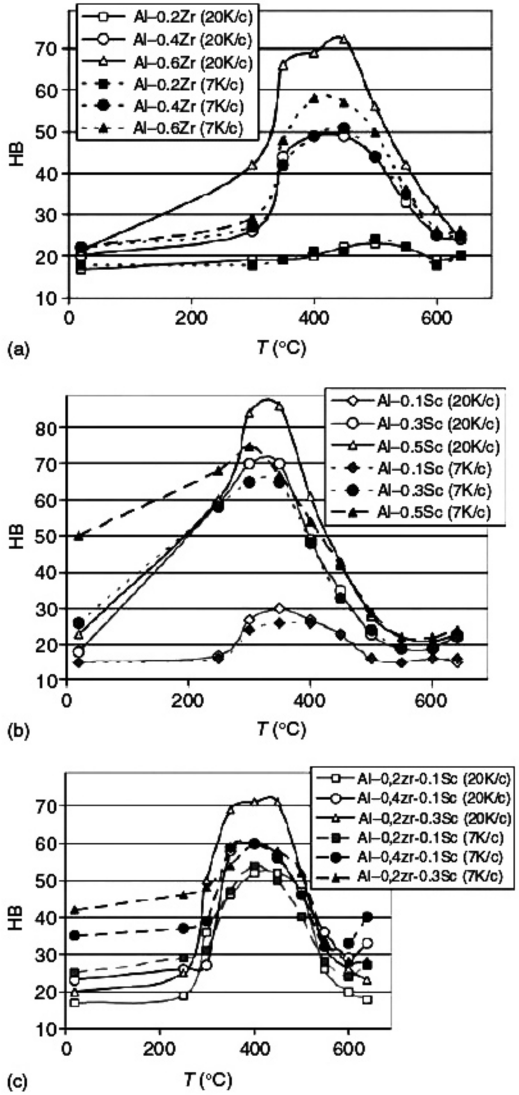

Figure 6.24 Dependence of hardness on the composition, cooling rate in the solid state, and the temperature of the last annealing step: (a) binary Al–Zr alloys, (b) binary Al–Sc alloys, and (c) ternary Al–Sc–Zr alloys.

There are three parameters to which we would like to pay attention to:

First, there is such important parameter as the temperature range of effective hardening. In the case of binary Al–Zr alloys, this temperature range is between 350°C and 450°C (Figure 6.24a). Binary Al–Sc alloys show a narrower temperature range of effective hardening, between 300°C and 350°C, almost no hardening can be observed above 450°C (Figure 6.24b); and ternary Al–Sc–Zr alloys gain the hardness in the temperature range between 350°C and 450°C (Figure 6.24c). The main difference between binary Al–Zr and ternary Al–Sc–Zr alloys is more rapid hardening of the latter in the range of 300–350°C. Recent publications reported the formation of complex $Al_3(ScZr)$ precipitates with the core enriched in scandium [2, 3]. This can explain the accelerated hardening in ternary alloys as compared to binary alloys. Scandium diffuses faster than zirconium in aluminum and forms clusters which then act as nucleation sites for the $Al_3(ScZr)$ phase.

Second parameter is the alloy composition. Hardening of binary Al–Zr alloys containing 0.2%Zr (i.e., maximum concentration in commercial aluminum alloys) is negligible, whereas 0.4%Zr produce a noticeable effect. Although a binary Al–0.1%Sc alloy shows some hardening, it can be considered rather weak. However, joint introduction of 0.2%Zr and 0.1%Sc gives much stronger effect than just arithmetic summation of individual contributions. The general tendency in all three groups of alloys is the higher the concentration of Sc and Zr, the larger the hardening effect.

The third important variable in these dependencies is the cooling rate at the completion of solidification (difference in solid and dashed lines in Figure 6.21). In binary Al–Zr alloys, slower cooling in the solid state does not affect the hardness of as-cast material and the hardening in the alloys containing 0.2–0.4%Zr. However, the hardening is less in the Al–0.6%Zr alloy cooled at V_{c1} (7 K/s) as compared to the same alloy but cooled at V_{c2} (20 K/s). The effect of the cooling rate is much more pronounced in Al–Sc alloys, being larger in more alloyed materials. The effect is two-fold. Firstly, the as-cast alloy is harder after being slowly cooled in the solid state; the difference can be as large as 2 times (approximately 30 HB) for the Al–0.5%Sc alloy. Secondly, the maximum hardness reached after annealing of a slowly cooled alloy is less than that for a faster cooled alloy (a difference of approximately 10–15 HB for the Al–0.5%Sc alloy). Similar effects are observed in ternary Al–Sc–Zr alloys, the hardness in the as-cast state being now the function of both the cooling rate and the concentration of the alloying elements.

The effect of alloy composition and cooling rate in the solid state on the hardening of experimental alloys is demonstrated in Figure 6.26 for three different states, that is, as-cast (Figure 6.26a, b), annealed to the maximum hardness (Figure 6.26c, d), and annealed with the last annealing stage at 500°C (Figure 6.26e, f). The last regime is practically important as 500°C is close to typical temperatures of solution treatment of most commercial aluminum alloys. The analysis of these dependences yields the following conclusions. The effect of alloying elements on the hardness in the as-cast state is very small at the higher cooling rate but becomes considerable at the lower cooling rate, the influence of scandium being

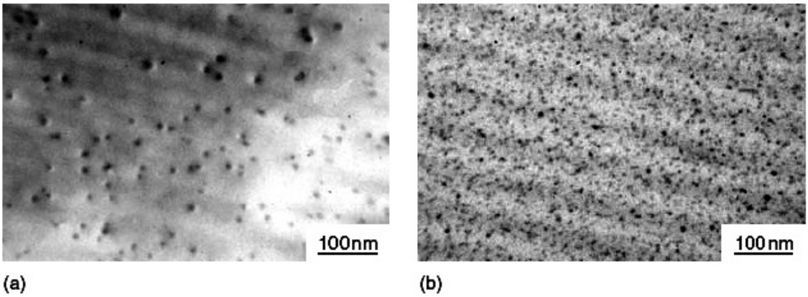

Figure 6.25 Microstructure of Al–0.2%Zr (in this alloy there are domains completely free of precipitates that are not shown here) and Al–0.6%Zr (b) alloys cooled at 20 K/s and annealed to maximal hardness (Fig. 6.24).

much more pronounced than that of zirconium (Figure 6.24a, b). After annealing to the maximum hardness (the annealing regimes are different for different alloys, see Figure 6.24), the effect of both alloying elements on the hardness is strong and comparable for both cooling rates (Figure 6.24c, d). On increasing the annealing temperature (last stage at 500°C), the effect of alloying elements on the hardness is similar at both cooling rates, but now the compositional range of harder alloys is located closer to the Al–Zr side of the concentration triangle.

The presented dependences give us some ground to speculate that the slower cooling rate may result in precipitation of hardening particles during cooling after the end of solidification, which causes the increased hardness in the as-cast state, and somewhat decreases the hardening effect after annealing to the maximum hardness. An examination of the internal structure of the examined alloys is, however, required to justify such a discussion.

Binary Al–Zr alloys annealed to the maximum hardness demonstrate rather inhomogeneous distribution and large spacing of Al_3Zr particles in the Al–0.2%Zr alloy as shown in Figure 6.25a, whereas the precipitation becomes much more homogeneous and numerous in the Al–(0.4–0.6)%Zr alloys (see Figure 6.25a, b). Note that the Al_3Zr phase is metastable (cubic L12) as has been confirmed by selected-area diffraction patterns, and its particles have a "coffee-bean" contrast attesting for their coherency with the matrix. These differences in the distribution and precipitation density of hardening particles explain the observed hardening behavior (see Figure 6.24a).

Addition of 0.1%Sc to the Al–0.2%Zr alloy makes its structure after annealing to the maximum hardness similar to that observed for the Al–0.4%Zr alloy: only now the precipitating phase is likely to be $Al_3(ScZr)$. Accordingly, a well-pronounced hardening effect is observed (see Figure 6.24c). The structure of annealed binary Al–Sc alloys is well studied elsewhere and has not been the subject of this work. Literature data show that the formation of the Al_3Sc phase during cooling after the end of solidification may result in the homogeneous or discontinuous precipitation. And Al_3Sc precipitates can retain the coherency at temperatures as high as 400°C [1] and during hundreds of hours at 350°C [13].

The Al–0.3%Sc–0.2%Zr alloy shows the most pronounced difference in the hardening behavior with respect to the cooling rate after the end of solidification as well as the highest peak hardness (see Figure 24c). The internal structure of this alloy was studied in detail. The structure of the alloy cooled after the end of solidification at V_{c1} exhibit all features of decomposition with rather inhomogeneous precipitation. As a result of this precipitation, the as-cast alloy is hardened. After cooling at V_{c2}, precipitation is much less pronounced. Accordingly the hardness of the alloy is lower but the alloy is more supersaturated in Sc and Zr. After annealing to the maximum hardness by regime S400, samples obtained at both cooling rates demonstrate intensive but rather inhomogeneous distribution of dispersoids as compared to the Al–0.1%Sc–0.2%Zr alloy. However, even this inhomogeneous precipitation results in considerable hardening. Logically, the hardening effect is higher in the alloy that has been more supersaturated before the beginning of precipitation (i.e., in the alloy cooled at V_{c2}).

In addition to the initial supersaturation of the solid solution, the distribution of precipitates and their volume fraction are important for hardening. The maximum hardness obtained on samples cooled at V_{c2} (20 K/s) can be correlated to the volume fraction of precipitates. As we showed the precipitation during cooling at this cooling rate was minimal. With taking into account that the equilibrium solubilities of Sc and Zr in (Al) at the given annealing temperatures are small, one can consider that both scandium and zirconium are completely bound in L12 dispersoids after annealing. Hardness and C-curves of several experimental alloys are illustrated by Figure 6.26 and Figure 6.27. The results obtained by the authors of the present work demonstrate that the maximum effect of hardening in aluminum alloys containing TM1 depends not only on the cooling rate during solidification, composition and annealing regime, but also on the casting temperature and the cooling rate after the end of solidification. The casting temperature should be chosen in such a way that the alloy is cast from above the liquidus of the highest melting compound, Al_3Zr in Al–Sc–Zr alloys. The cooling rate after the end of solidification should be sufficient to prevent the precipitation of dispersoids during cooling. Figure 6.27 illustrates the effect of composition and cooling rate in the solid state on the possibility of decomposition during cooling. The time–temperature–transformation (TTT) curves of low-alloyed materials are on the right-hand side of the cooling curves, which could not be justified for the following reasons: (1) it becomes increasingly difficult to completely introduce alloying elements in the solid solution; (2) high concentrations of Sc and Zr imply high melting and cast temperatures (see Figure 6.21 and Figure 6.23a), which in most cases makes such alloys unsuitable for commercial use; and (3) highly alloyed materials are prone to inhomogeneous distribution of precipitates, which decreases the efficiency of hardening.

Optimal concentrations of Mn and Zr and some technological parameters can be directly obtained from the analysis of non-equilibrium phase diagrams. In particular, the role of manganese in the formation of as-cast microstructure

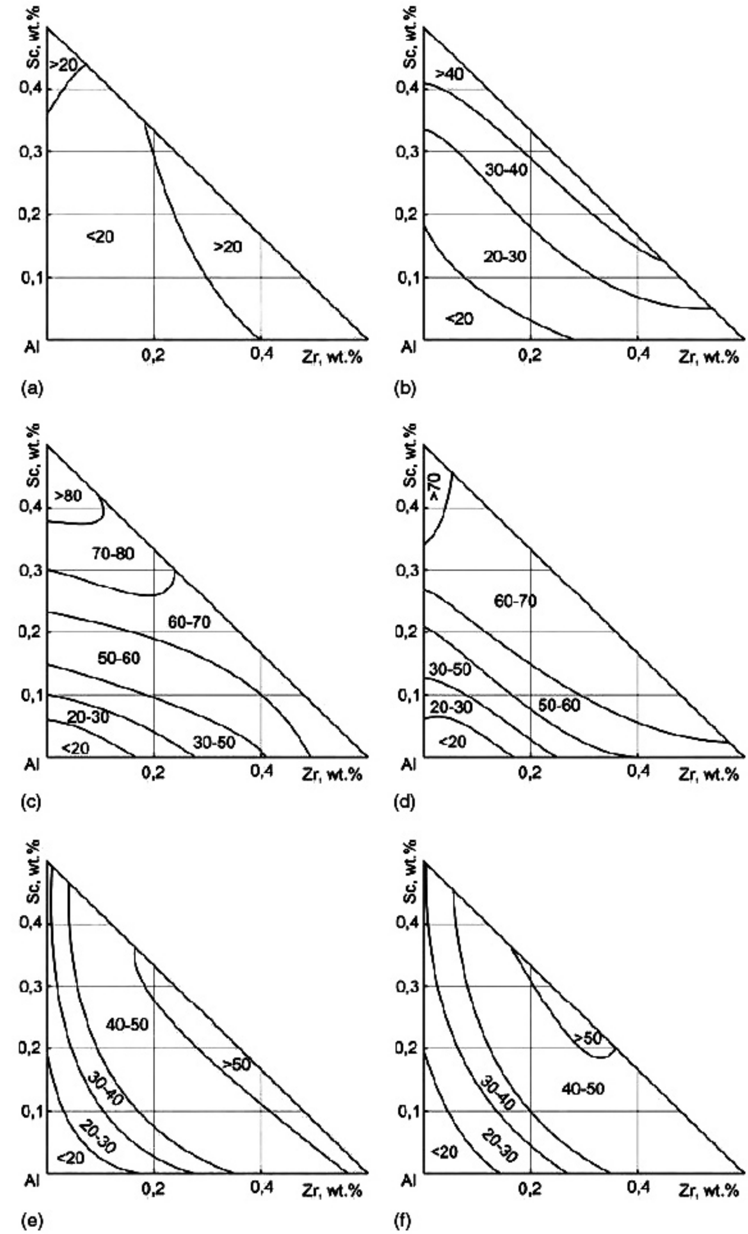

Figure 6.26 Effect of composition, cooling rate in the solid state, and the annealing regime on the hardness of experimental alloys: (a, c, e) cooling rate 20 K/s; (b, d, f) cooling rate 7 K/s; (a, b) as-cast condition; (c, d) maximum hardness; and (e, f) final step 500°C [355].

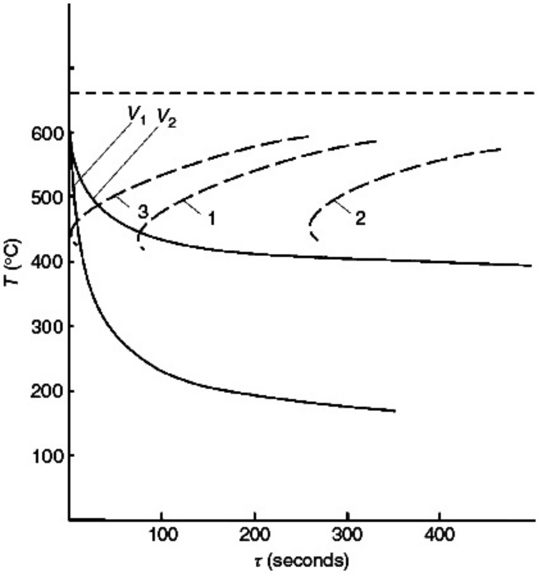

Figure 6.27 Schematic of C-curves (beginning of precipitation) explaining the effect of cooling velocity on alloy hardening.

could be traced if one uses the polythermal Al–4%Ni–Mn cross-section (Figure 6.20) constructed for V_c~10 K/s. It becomes clear from the analysis of this cross-section that at ~2.5%Mn (i.e., somewhat higher than at equilibrium conditions) it will completely enter the composition of (Al) upon solidification. Due to low diffusivity it will remain in (Al) even after cooling to room temperature, although its equilibrium solubility in (Al) is several hundredths of a percent.

During heating, beginning at 300–350°C, the formation of secondary (Al_6Mn) aluminides takes place, and manganese concentration falls down to equilibrium values. At 500°C still they remain pretty low. Strength is weakly affected by the decomposition of (Al), although the strengthening mechanism itself changes (from solid solution to dispersion). The additions of manganese to Al–Ni alloys practically do not affect either liquidus or solidus, which allows retaining narrow solidification range and excellent castability (see Section 4.1).

Unlike manganese, zirconium additions result in significant dispersion hardening effect due to the formation of secondary particles of metastable Al_3Zr (Figure 6.25). This influence is similar to the effect of scandium. Calculation of the Al_3Zr and Al_3Sc volume fractions demonstrates that the introduction of 0.2%Zr is approximately equivalent to 0.1%Sc. In other words, to achieve significant dispersion hardening with zirconium, it is

Table 6.11 Properties[a] of Al–Ni alloys Z1 and Z3 and other known thermally stable alloys

Alloy	HB	σ_B (MPa)	σ_{100}^{350} (MPa)	δ (%)	σ_{-1} (MPa)	HCI[b] (mm)
AK12MMgN (Al–12Si–1%Cu–1% Mg–1%Ni)	65	190	20	1	<50	6
AM5 (Al–5%Cu)	60	260	30	8	<80	>16
Z1 (Al–Ni–Mn–Zr)	80	270	40	5	110	4
Z3 (Al–Ni–Zr)	80	240	–	10	–	3

[a] Mechanical properties after 10 hour exposure at 400°C.

[b] HCI: hot cracking index using the pencil probe.

necessary to introduce not less than 0.5–0.6% of this chemical element. However, this may cause some difficulties related to the specific features of the Al–Zr phase diagram (Figure 6.21). Due to sharp increase of the liquidus temperature the temperature of molten metal must be higher than 800–850°C, because otherwise complete dissolution of Zr in liquid phase is impossible. Another interesting feature of the Al–Zr phase diagram is the broadening of primary solidification area (Al), upon accelerated molten metal cooling and solidification. In this case all zirconium which entered (Al), would be retained there until complete cooling. If V_c is less than 5 K/s, then it becomes possible to obtain in as-cast condition solid solution containing at least 0.5%Zr. If the applied cooling rate is not sufficiently high, then the formation of coarse primary crystals of Al_3Zr becomes possible, and this process is accompanied by the reduction of Zr concentration in (Al).

Decomposition of solid solution, accompanied by the precipitation of secondary particles of the Al_3Zr phase begins at 350–400°C. At higher temperatures the formation of the thermodynamically stable phase becomes possible, which is not as good a strengthening phase as the metastable one. Additions of zirconium (similar to manganese) allow retaining narrow solidification range and excellent castability of Al–Ni alloys.

Using the specifics of alloying process and casting technology discussed above, the authors have developed high thermal stability alloys Z1 and Z3 [345]. They exceed all known alloys of this group (e.g., AM5 and AK12MMgN) in practically all properties and could be used at temperatures up to 350–400° C (Table 6.11). Due to the narrow solidification range, they possess excellent castability and could be used to manufacture high-quality thin-walled castings of complex geometrical shapes (Figure 6.28).

Thermally stable alloys can be developed on the basis of other eutectics (e.g., Fe-bearing (Table 6.9)) which makes such alloys more economical. According to data in Ref. [350] the indices of thermal stability of alloys with the

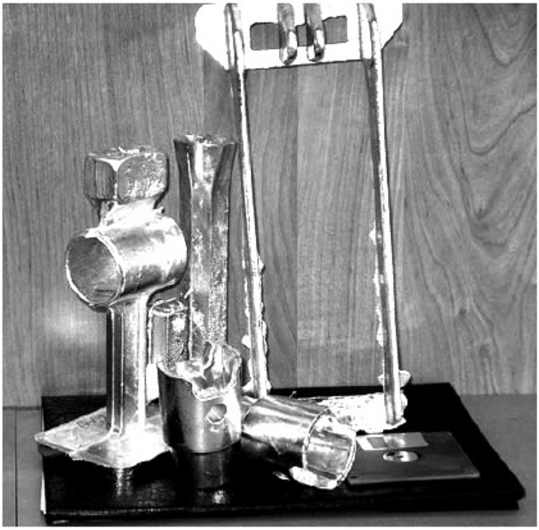

Figure 6.28 Casting made out of thermally stable Ni-bearing alloy AN4Mts2 (4205); mold casting.

Al_9FeNi and $Al_{10}Fe_2Ce$ phases at 400°C are higher than for alloys of the AL33 or ATsr1u type.

6.5 ALLOYS WITH SMALL AMOUNTS OF SILICON (<4%SI)

In many cases, especially in mass production, inexpensive alloys with average level of properties are required. Cost is defined by both alloy composition and selected casting technology. The former implies the maximal usage of secondary materials and the absence of expensive alloying additions, while the latter – simple and productive technological scheme. In particular, it would be great to have such alloys the composition of which for certain casting technologies would ensure in the F-temper or T1 (after low-temperature heat treatment) such a microstructure that typically corresponds to mechanical properties of alloys in the T4–T7 tempers.

In principle, such alloys could be developed using secondary materials of the Al–Mg–Zn system (AMg4Ts3, AMg4Ts2), which even in as-cast condition possess relatively high level of mechanical properties (Section 6.1). However, alloys of the Al–Mg–Zn system belong to the class of broad solidification range materials and possess low castability. This unfortunate circumstance limits their potential application in industry by casting into metallic molds with relative simple geometrical shape(s). Consequently, a new approach is required that would ensure that alloys possess required combination of casting and mechanical properties without application of high-temperature solution heat treatment and quench. Using the methods of composition optimization for alloys in the T4–T7 tempers (Section 6.2) and obvious limitations, thus formulated problem could be solved according to the following guidelines:

1. Aluminum matrix must be alloyed in such a way as to ensure the required level strength and some elongation.
2. Alloy eutectic must ensure a sufficient level of castability and hot cracking resistance, without any losses in elongation (due to favorable morphology of eutectic phases).
3. Desired microstructure must be attained without expensive additions (beryllium, cobalt, etc.) and/or technological processes (e.g., ultrasonic treatment of molten metal).

In this section we discuss a possibility of obtaining such a microstructure for Al–Si alloys containing small amounts of silicon. Such materials possess reasonable casting properties and could be manufactured out of secondary materials. In particular, in the case of high-purity alloys of the AA355 type alloyed with copper and having a close to optimal complex of properties (σ_B) does not exceed 200–220 MPa, while relative elongation is not higher than 3–5% (Section 5.1). At higher concentration of silicon (>5%) and iron impurity (>0.5%) mechanical properties will be even worse.

In addition to silicon, copper, and iron, many Al–Si alloys often contain additions of manganese, zinc, less often – other elements like nickel, beryllium, chromium, etc. (Table 5.1). The application of Ni, Cr, and Be is excluded from the context of the formulated goals, because it increases alloy cost. As a result, basic compositions for development of the new generation of alloys should be sought for in the Al–Si–Fe–Cu–Mg–Zn–Mn system.

Generalizing the data on cast alloy microstructure for materials of this system, one could characterize the following elements of microstructure that define the level of mechanical properties:

1. Primary crystals of (Al) alloyed with copper, silicon, and zinc.
2. Eutectic crystals of the (Si) phase.
3. Iron-bearing phases – Al_5FeSi (β), Al_8Fe_2Si (α), Al_3Fe (F), $Al_{15}(FeMn)_3Si_2$ (α_m), and others, of eutectic or primary origin.
4. Eutectic phases with copper, silicon, and magnesium – Al_2Cu, Mg_2Si, and $Al_5Cu_2Mg_8Si_6$.

As it was demonstrated in Section 5.1, the optimal microstructure of hypoeutectic Al–Si alloys should consist of the following elements: globular uniformly distributed particles of (Si) and, less often, other phases in the metallic matrix containing up to 3–4%Cu and up to 0.5–0.6%Mg. Such a microstructure could be obtained in heat treated Al–Si alloys of the AA356 or AA354 types in the T4 or T6 tempers prepared out of primary aluminum and containing additions of beryllium.

However, a typical as-cast structure of hypo-eutectic Al–Si alloys prepared out of secondary materials (similar to AK5M2) looks different: eutectic colonies of (Al) + (Si) and more complex Fe-, Cu-, and Mg-bearing eutectics are located along grain boundaries (inside each colony every phase represents a single crystal) [260]. If manganese or any other modifiers are not present, then needle-like crystals of the Al_5FeSi phase will be formed, which exert the strongest negative influence upon mechanical properties. Cast microstructure of this type corresponds to low mechanical properties, first of all, elongation. Taking into account that obtaining microstructure with globular particles in as-cast state is practically unattainable, the desired microstructure could be represented in the form of eutectic phases with relatively compact morphologies (e.g., oval or skeletal).

It is obvious that the desired microstructure could be realized in most cases only via selection of alloying elements and optimization of their concentrations. It is hardly possible to exert a strong influence upon microstructure by using casting techniques since substantial changes (compared to existing industrial technologies) could dramatically reduce all of the advantages related to the absence of the T4–T6 tempering.

The allowed concentration ranges for silicon and other elements of the selected system can be described as follows:

1. The contents of *silicon* must be within the limits from 2% to 4%, which is determined by the following reasons:

   - In comparison to standard Al–Si alloys (>4%Si) the volume fraction of eutectic (Al) + (Si) colonies will be reduced; this may result in the absence of continuous eutectic network around dendritic cells of (Al) and, correspondingly, positively affect elongation.
   - In the specified silicon concentration range, according to the Al–Si–Fe phase diagram (Figure 1.26) the contents of iron corresponding to the appearance of the first primary Fe-bearing crystals exceeds 1.5%. This serves as a criterion defining the usefulness of iron as an alloying element.
   - The lower limit for silicon concentration is defined by the need to achieve required level of casting properties, especially taking into account that in the Al–Si–Cu–Mg system the silicon phase enters the composition of all eutectics, which solidify the last (with participation of the Al_2Cu, Mg_2Si, and $Al_5Cu_2Mg_8Si_6$ phases).

2. The concentrations of *copper* and *magnesium* should be selected on the basis of the following considerations:

   - The lower boundary must ensure a sufficient degree of the (Al) alloying and, consequently, the required level of alloy strength.
   - The upper boundary must ensure a small volume fraction of the eutectic phases and their compact morphology to achieve a good elongation.
   - The amount of the low-temperature eutectic must be sufficient to ensure satisfactory castability.

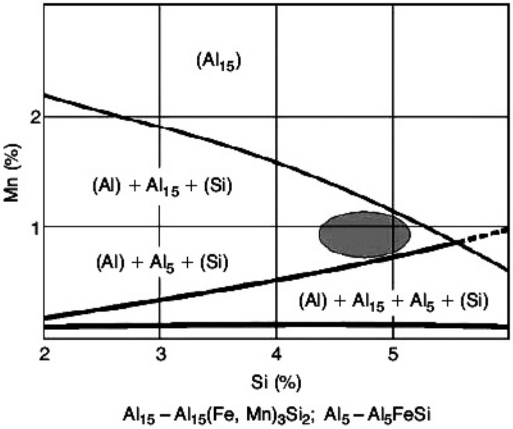

Figure 6.29 Distribution of phase domains in the aluminum corner of the Al–Si–Fe–Mn system at 1%Fe in as-cast state ($V_c \approx 10$ K/s).

3. *Zinc* in the amount up to 3% is almost completely dissolved in (Al) and does not have the composition of all other phases; this defines its allowable concentration as an impurity.
4. *Iron* (either as impurity or as alloying element) must completely enter one of the eutectic phases, for example, Al_8Fe_2Si (α) that ensures a more favorable morphology than the needles of Al_5FeSi (β). Since eutectic reactions with participation of iron commence at higher temperatures in comparison to the temperatures of all other eutectics, these phases will be located mostly in the central parts of dendritic cells and will not form a network of "veins" along grain boundaries. The upper limit with respect to iron (around 3%) is defined by the danger of formation of coarse primary Fe-bearing crystals reducing alloy mechanical properties (especially in the case of their large clusters or colonies).
5. *Manganese* forms the Al_{15}(FeMn)3Si2 phase in the Al–Si–Fe–Mn system, which, participating in eutectics (similar to Al_8Fe_2Si), possesses typical skeletal morphology. The presence of manganese gives a possibility to loosen the limitations with respect to silicon related to the need to avoid the formation of the β-phase needles. However, a danger arises that the formation of coarse primary crystals of $Al_{15}(FeMn)_3Si_2$ might take place simultaneously. This conclusion directly stems from the distribution of the phase domains constructed for as-cast state (Figure 6.29).

The most probable distribution of all alloying elements discussed above between the aluminum matrix and eutectic phases is about the same as for Al–Si alloys (Table 5.1).

Table 6.12 Composition, hardness, and tensile mechanical properties of some perspective alloys of the Al–Si–Fe–Cu–Mg–Mn system

No	Si (%)	Fe (%)	Mn (%)	Cu (%)	Mg (%)	HB	σ_B (MPa)	δ (%)
1	4	0.5	0.5	3	–	69	230	10
2	3.5	1	–	3	–	70	212	7
3	3.5	1	1	3	–	75	236	9
4	2.3	2.3	–	3	–	74	232	11
5	2.3	2.3	–	1	0.2	78	219	5

Taking into account the dependencies presented in Section 4.2.5, the most perspective alloys were selected for studies of mechanical and casting properties. Composition and properties of some of these alloys are presented in Table 6.12. Samples for testing were cut out of standard mold castings. Alloys contained different Fe-bearing phases: Al_8Fe_2Si in alloys 4–5; phase $Al_{15}(FeMn)_3Si_2$ in alloys 1, 3; and mostly phase Al_5FeSi in alloy 2. Alloys 1–4 contained 3%Cu, while the last one – 1%Cu + 0.2%Mg, which provided a possibility to assess the optimal alloying of the aluminum matrix. Results provided in Table 6.10 allow making a conclusion that alloys with 3%Cu and having favorable morphology of the Fe-bearing phases, must possess high relative elongation (around 10%) with satisfactory strength.

The influence of cooling rate during solidification upon microstructure and mechanical properties were studied using two alloys, the composition of which was chosen according to the results of experiments provided above: 1 – Al-2.3%Si-2.3%Fe-3%Cu and 2 – Al-3.8%Si-0.7%Fe-0.7%Mn-3%Cu (Table 6.13).

Microstructure of the first alloy (Figure 6.30a, b), in which all iron was tied up into the Al_8Fe_2Si phase, becomes coarser when V_c is reduced from 10 K/s to 1 K/s (i.e., the average size of dendritic cells, pores, and eutectic particles all become larger). At even lower solidification rate coarse primary crystals of the Al_3Fe phase will be formed, in complete agreement with the analysis of non-equilibrium solidification process in the Al–Si–Fe system.

Second alloy demonstrates only coarsening of microstructure with lower value of V_c (Figure 6.30c, d), without any changes in phase composition. Iron enters only the $Al_{15}(FeMn)_3Si_2$ phase, which has skeletal morphology, while needles could not be found. Microstructure of this alloy in the case of casting into standard metallic mold is close to ideal. Analysis of mechanical properties of these two alloys (Table 6.13) after mold casting and sand casting indicates that metallic mold casting gives much better level of properties (strength and elongation). This allows to conclude that coarse skeletal particles of $Al_{15}(FeMn)_3Si_2$ are as harmful as the

Table 6.13 Mechanical properties and parameters of microstructure of two perspective low-Si Al–Si alloys in as-cast state

N	CT[a]	V_c[b] (K/s²)	σ_B (MPa)	$\sigma_{0.2}$ (MPa)	δ (%)	KCU (J/cm²)	d[c] (μm)	HV_{Al}[d]	C_{Cu}[e]
1	K	3	218	106	11	0.6	47	79	1.5
	3	0.3	100	87	3	–	160	74	–
2	K	3	224	110	8	0.6	54	81	1.1
	3	0.3	114	108	5	–	150	77	–

[a] CT: casting technique.

[b] V_c cooling rate.

[c] Dendritic cell size for primary crystals of (Al).

[d] Microhardness (Al).

[e] Concentration of copper in (Al).

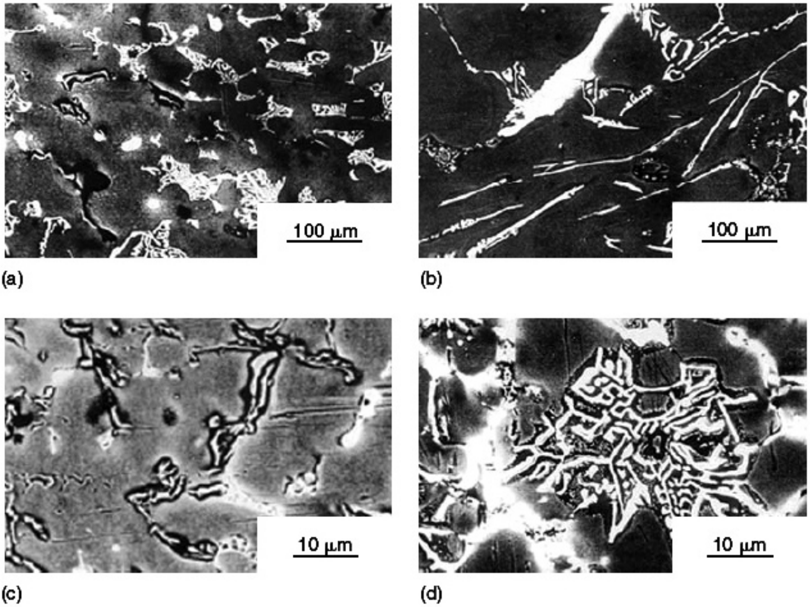

Figure 6.30 Microstructure of cast alloys Al–2.3%Si-2.3%Fe–3%Cu (a, b) and Al-3.8%Si-0.7%Fe–0.7%Mn–3%Cu (c, d) after mold casting (a, c); sand casting (b, d), SEM.

needles of Al_3Fe. A certain contribution into this effect, obviously, is made by porosity, which is much more pronounced in the case of sand casting.

Molten metal fluidity of the first alloy (with the Al_8Fe_2Si phase is about the same as for other Al–Si alloys of the AK5M type (320–350 mm using the rod probe); however, their hot cracking index is somewhat worse (15–20 mm against 10–12.5 mm using the VIAM probe). This alloy could be used for the production of castings of average complexity using the technique of die casting or liquid stamping. The second alloy (with the $Al_{15}(FeMn)_3Si_2$ phase) has a much better hot cracking index (12.5–15 mm), which gives hope for its more widespread application.

According to the results of thermal analysis, the temperatures of solidus (upon cooling) are about the same and are equal to ~513–517°C. This corresponds to the eutectic reaction $L \Rightarrow (Al) + (Si) + Al_2Cu$. The second alloy has a somewhat lower liquidus temperature (630–635°C against 640–645°C). Since the general solidification ranges of both alloys are quite close, higher casting properties of the second alloy are most probably connected to its narrower effective solidification range.

This page intentionally left blank

LITERATURE

Chapter 1

1. Registration Record of Aluminum Association Alloy Designations and Chemical Composition Limits for Aluminum Alloys in the Form of Castings and Ingot, 1989.
2. GOST 1583–93. *Splavy alyuminievye liteinye.* Izd-vo standartov, Moscow, 1993.
3. Gilbert Kaufman J. (ed.). *Properties of Aluminum Alloys: Tensile, Creep and Fatigue Data at High and Low Temperatures*, ASM International and The Aluminum Association, Washington, DC, Materials Park, Ohio, 1999.
4. Siluminy: Atlas struktur i fraktogramm / Sprav.izd. / Prigunova A.G., Belov N.A. i dr. /Pod red. Yu.N.Tarana i V.S.Zolotorevskogo. MISiS, Moscow, 1996, 175 pp.
5. Entony, U.N., Ashton, F.R., Boll, M.D. et al., *Aluminum. Properties and Physical Metallurgy*, edited by John E. Hatch, ASM, Metals Park, OH, 1984.
6. Belov, N.A., Aksenov, A.A. and Eskin, D.G. *Iron in Aluminum Alloys: Impurity and Alloying Element*. Taylor and Francis, London, 2002, 360 pp.
7. Promyshlennye alyuminievye splavy /Sprav.izd./ Alieva S.G., Al'tman M.B. i dr. Metallurgiya, Moscow, 1984, 528 pp.
8. Primenenie alyuminievyh splavov /Sprav.izd./ Al'tman M.B., Arbuzov Yu.P. i dr./. Metallurgiya, Moscow, 1985, 344 pp.
9. Stroganov, G.B. *Vysokoprochnye liteinye alyuminievye splavy*. Metallurgiya, Moscow, 1985, 216 p.
10. Kolobnev, I.F. *Zharoprochnost' liteinyh alyuminievyh splavov.* Metallurgiya, Moscow, 1973, 320 p.
11. Stroganov, G.B., Rotenberg, V.A. and Gershman, G.B. *Splavy alyuminiya s kremniem.* Metallurgiya, Moscow, 1977, 271 pp.
12. Postnikov, N.S. *Uprochnenie alyuminievyh splavov i otlivok.* Metallurgiya, Moscow, 1983, 118 pp.
13. Zaharov, A.M. *Promyshlennye splavy tsvetnyh metallov. Fazovyi sostav i strukturnye sostavlyayuschie.* Metallurgiya, Moscow, 1980, 256 pp.
14. Mondol'fo, L.F. *Aluminum Alloys – Structure and Properties*, Butterworth, Boston, 1976, 424 pp.
15. Drits, M.E., Bochvar, N.R. i dr./. *Diagrammy sostoyaniya sistem na osnove alyuminiya i magniya: Spravoch.izd.* Nauka, Moscow, 1977, 228 pp.
16. Belov, N.A., Zolotorevskii, V.S., Evseev, Yu.V. and Ivanov, V.A. Vliyanie litiya na strukturu i mehanicheskie svoistva siluminov, *Tehnologiya Legkih Splavov*, 1989, No. 7, pp. 8–11.
17. Metallicheskie primesi v alyuminievyh splavah/ A.V. Kurdyumov, S.V. Inkin, V.S. Chulkov, G.G. Shadrin. Metallurgiya, Moscow, 1988, 143 pp.
18. Dobatkin, V.I., Elagin, V.I. and Fedorov, V.M. *Bystrozakristallizovannye alyuminievye splavy*. VILS, Moscow, 1995, 341 pp.
19. Novikov, I.I. *Goryachelomkost' tsvetnyh metallov i splavov.* Nauka, Moscow, 1966, 299 pp.
20. Belov, N.A. and Kurdyumova, T.A. Diagramma sostoyaniya Al-Si-Fe-Be i vozmozhnosti neitralizatsii Fe-faz v siluminah, *Izv. AN SSSR, Metally*, 1989, No. 2, pp. 210–215.
21. Zolotorevskii, V.S., Belov, N.A. and Kurdyumova, T.A. Optimizatsiya struktury vtorichnyh siluminov s tsel'yu povysheniya ih plastichnosti i vyazkosti razrusheniya. *Izv. VUZOV, Tsvetnaya metallurgiya*, 1989, No. 1, pp. 76–88.
22. Murali, S., Raman, K.S. and Murthy, K.S.S. In: *Proc. ICAA5*, Grenoble, July 1996, *Mater. Sci. Forum*, Vol. 217–222, Transtec Publications, Zuerich, Part 1, pp. 207–212.

Casting Aluminum Alloys
ISBN-13: 978-0-08-045370-5

© 2007 Elsevier Ltd.
All rights reserved.

23. Toropova, L.S., Eskin, D.G., Kharakterova, M.L. and Dobatkina, T.V. *Advanced Aluminum Alloys Containing Scandium. Structure and Properties*, OPA, Amsterdam, 1998.
24. Elagin, V.I., Zaharov, V.V. and Rostova, T.D. Alyuminievye splavy, legirovannye skandiem. *Metallovedenie i termicheskaya obrabotka metallov*, 1992, No. 1, pp. 24–28.
25. Marquis, E.A. and Seidman, D.N. *Acta Mater.*, 2001, Vol. 49, pp. 1909–1919.
26. Pikunov, M.V. Plavka metallov, kristallizatsiya splavov, zatverdevanie otlivok. MISiS, Moscow, 1997, 376 pp.
27. Metallovedenie alyuminiya i ego splavov /Sprav.izd./ Belyaev A.I., Bochvar O.S. i dr. Metallurgiya, Moscow, 1983, 280 pp.
28. Ghosh, G. In: *Ternary Alloys*, edited by G. Petzow and G. Effenberg, VCH, Weinheim, Vol. 1, 1990, pp. 346–350.
29. Belov, N.A., Zolotorevskii, V.S. and Evseev Yu.V. Struktura, fazovyi sostav i mehanicheskie svoistva liteinogo splava Al-7%Mg-3%Zn s dobavkami Fe i Be, *Izv. VUZOV., Tsvetnaya metallurgiya*, 1985, No. 5, pp. 71–77.
30. Yunusov, I., Ganiev, I.N. and Shishkin, E.A. Diagramma sostoyaniya Al-Cu-Ce v oblasti, bogatoi alyuminiem. *Izv. AN SSSR, Metally*, 1991, No. 3, pp. 200–203.
31. Zarechnyuk, O.S., Myskin, M.G. and Ryabov, V.R. *Izv. AN SSSR, Metally*, 1969, No. 2, pp. 164–166.
32. Sokolovskaya, E.M., Kazakova, E.F. and Filippova, A.A. *Izv. AN SSSR, Metally*, 1988, No. 2, pp. 209–210.
33. Belov, N.A. and Lavrischev, Yu.V. *Izv. VUZOV., Tsvetnaya metallurgiya*, 2000, No. 6, pp. 37–43.
34. Grieb, B. In: *Ternary Alloys*, edited by G. Petzow and G. Effenberg, VCH, Weinheim, Vol. 4, 1991, pp. 59–63.
35. Zarechnyuk, O.S, Yanson, T.I. and Ryhal' R.M. Sistema Ce-Ni-Al v oblasti 0-0,333 at.% tseriya. *Izv. AN SSSR, Metally*, 1983, No. 4, pp. 192.
36. Belov, N.A. and Naumova, E.S. Perspektivy sozdaniya konstruktsionnyh liteinyh splavov evtekticheskogo tipa na osnove sistemy Al-Ce-Ni, *Metally*, 1996, No. 6, pp. 146–152.
37. Belov, N.A., Naumova, E.A. and Eskin, D.G. Casting alloys of the Al-Ce-Ni system: microstructural approach to alloy design. *Mater. Sci. Eng. A*, November 1999, Vol. 271, 1–2, pp. 134–142.
38. Saunders, N. and Rivlin, V.G. *Z. Metallkde.* 1987, Vol. 78, No. 11, pp. 795–801.
39. Legendre, B. and Harmelin, M. In: *Ternary Alloys*, edited by G. Petzow and G. Effenberg, Weinheim, Vol. 4, 1991, pp. 475–489.
40. Philips, H.W.L. *Annotated Equilibrium Phase Diagrams of Some Aluminum Alloy Systems*, Inst. Met. Monograph 25, London, 1959.
41. Prince, A. and Effenberg, G. In: *Ternary Alloys*, edited by G. Petzow and G. Effenberg, Verlagsgesellschaft, Weinhein, Vol. 4, 1991, pp. 547–566.
42. Chen, S.-L., Zuo, Y., Liang, H. and Chang, Y.A. *Metall. Mater. Trans.*, 1997, Vol. 28A, No. 2. 435 pp.
43. Ansara, I., Hoch, M., Saunders, N. and Schmid, E.E. In: *Ternary Alloys*, edited by G. Petzow and G. Effenberg, VCH, Weinheim, Vol. 5, 1992, pp. 241–249.
44. Ran, Q. In: *Ternary Alloys*, edited by G. Petzow and G. Effenberg, VCH, Weinheim, Vol. 5, 1992 pp. 250–264.
45. Denholm, W.T., Esdaile, J.D., Siviour, N.G. and Wilson, B.W. *Metall. Trans. A*, Vol. 15A, No. 7, 1984, pp. 1311–1317.
46. Budberg, P. and Prince, A. In: *Ternary Alloys*, edited by G. Petzow and G. Effenberg, VCH, Weinheim, Vol. 5, 1992, pp. 309–323.
47. Ghosh, G. In: *Ternary Alloys*, edited by G. Petzow and G. Effenberg, VCH, Weinheim, Vol. 5, 1992b, pp. 394–438.
48. Zaharov, A.M., Gul'din, I.T., Arnol'd, A.A. and Matsenko, Yu.A. *Izv. AN SSSR, Metally*, 1988, No. 3, pp. 178–181.
49. Barlock, J.G. and Mondolfo, L.F., *Z. Metallkde.*, 1975, Vol. 66, No. 10, pp. 605–611.
50. Yuong, Du, Julius Schuster, Frans Wetser, et al., *Metall. Trans. A*, 2004, Vol. 35A, pp. 1613–1628.

51. Zaharov, A.M., Gul'din, I.T., Arnol'd, A.A. and Matsenko, Yu.A. *Izv. AN SSSR, Metally*, 1988, No. 2, pp. 90–94.
52. Zaharov, A.M. *Diagrammy sostoyaniya chetvernyh sistem.* Metallurgiya, Moscow, 1964b, 240 pp.
53. Zaharov, A.M. *Mnogokomponentnye metallicheskie sistemy s promezhutochnymi fazami.* Metallurgiya, Moscow, 1985.
54. Belov, N.A. and Kol'tsov, A.V. Fazovaya diagramma sistemy Al–Cu–Fe–Mg–Si v oblasti Al–Cu splavov. *Izv. VUZOV., Tsvetnaya metallurgiya*, 2002, No. 2, pp. 37–48.
55. Belov, N.A., Gusev, A.Yu. and Eskin, D.G. Evaluation of five-component phase diagrams for the analysis of phase composition in Al-Si alloys. *Z. Metallkde.*, 1998, Vol. 89, No. 9, pp. 618–622.
56. Zaharov, A.M., Gul'din, I.T., Arnol'd, A.A. and Matsenko, Yu.A. v sb.: *Metallovedenie i Obrabotka Tsvetnyh Splavov*, Nauka, Moscow, 1992, pp. 6–17.
57. Fridlyander, I.N. *Vysokoprochnye deformiruemye alyuminievye splavy*. Oborongiz, Moscow, 1960, 291 pp.
58. Zaharov, A.M., Gul'din, I.T., Arnol'd, A.A. and Matsenko, Yu.A. *Izv. AN SSSR, Metally*, 1989, No. 4, pp. 214–218.
59. Davignon, G., Serneels, A., Verlinden, B. and Delaey, L. *Metall. Trans. A*, Vol. 27A, 1996, No. 11, pp. 3357–3361.
60. Belov, N.A. *Struktura i mehanicheskie svoistva evtekticheskih splavov sistemy Al-Si-Mg-Ni, Metally*, 1993, No. 5, pp. 133–138.
61. Kolobnev, I.F., Krymov, V.V. and Polyanskii, A.P. *Spravochnik liteischika: Tsvetnoe lit'e iz legkih splavov.* Mashinostroenie, Moscow, 1974, 415 pp.

Chapter 2

62. Bochvar, A.A. *Metallovedenie*. Metallurgizdat, Moscow, 1956, 495 pp.
63. Dobatkin, V.I. *Slitki alyuminievyh splavov*. Metallurgizdat, Sverdlovsk, 1960, 175 pp.
64. Saltykov, S.A. *Stereometricheskaya metallografiya.* Metallurgiya, Moscow, 1970, 375 pp.
65. Novikov, I.I. and Zolotorevskii, V.S. *Dendritnaya likvatsiya v splavah*. Nauka, Moscow, 1966, 156 pp.
66. Dobatkin, V.I. *Nepreryvnoe lit'e i liteinye svoistva splavov*. Oborongiz, Moscow, 1948, 153 pp.
67. Flemings, M.C. *Solidification Processing*. McGraw Hill Book Company, New York, 1974.
68. Metody ispytaniya, kontrolya i issledovaniya mashinostroitel'nyh materialov: Spravochnoe rukovodstvo. T.1: Fizicheskie metody issledovaniya metallov /Pod red. A.T. Tumanova. Mashinostroenie, Moscow, 1971, 552 pp.
69. Principles of Analytical Electron Microscopy, edited by David C. Joy, Alton D. Romig, Jr., and Joseph I. Goldstein, New York, Plenum Press, 1986.
70. Newbury, D.E., Joy, D.C., Echlin, P., Fiori, C.I. and Goldstein, J. *Advanced Scanning Electron Microscopy and X-ray Microanalysis.* Plenum Press, New York, 1986.
71. Birks, L.S. *Electron Probe Microanalysis.*, Interscience Publishers, N.-Y., London, 1963, 216 pp.
72. Lyuttsau, V.G. *Rentgenovskaya mikroskopiya: Dokt. dis.* MISiS, Moscow, 1972.
73. Vainblat, Yu.M. and Buharina, N.V. *V kn.: Elektronnomikroskopicheskie issledovaniya struktury zharoprochnyh splavov i stalei.* Metallurgiya, Moscow, 1969, pp. 98–104.
74. Vgessers, I. and Helbach, R. *J. Scient. Instrum.*, 1969, No. 9, 828 pp.
75. Hirsch, P.B., Howie, A., Nicholson, R.B., Pashley, D.W. and Whelan, M.J. *Electron Microscopy of Thin Crystals*. Butterworths, London, 1965.
76. Shtremel, M.A. and Belyakov, B.G. FMM, 1968, t. 25, vyp. 1, pp. 140–151.
77. Friedel, J. *Dislocations*. Pergamon Press, Oxford, London, 1964.
78. Utevskii, L.M. *Difraktsionnaya elektronnaya mikroskopiya v metallovedenii*. Metallurgiya, Moscow, 1973, 583 pp.
79. Kurdyumov, A.V. *Flyusovaya obrabotka i fil'trovanie alyuminievyh rasplavov.* Metallurgiya, Moscow, 1980, 196 pp.
80. Golikov, I.N. *Dendritnaya likvatsiya v stali*. Metallurgizdat, Moscow, 1958.

81. Golikov, I.N. and Maslenkov, S.B. *Dendritnaya likvatsiya v stalyah i splavah*. Metallurgiya, Moscow, 1977, 223 pp.
82. Pikunov, M.V., Belyaev, I.V. and Sidorov, E.V. *Kristallizatsiya splavov i zatverdevanie otlivok s orientirovannoi strukturoi*, Vladimir, 2002.
83. Novikov, I.I., Glazov, V.M., Zolotorevekii, V.S. *V kn.: Issledovanie splavov tsvetnyh metallov*. Vyp. 3. *Izd-vo AN SSSR*, Moscow, 1962, pp. 136–142.
84. Hasselblatt, M. *Z. Phys. Chemie*, 1913, Bd 13, No. 1, 139 pp.
85. Popov, A.A. *Fazovye prevrascheniya v metallicheskih splavah*. Metallurgizdat, Moscow, 1963, 311 pp.
86. Miroshnichenko, I.S. *Vliyanie skorosti ohlazhdeniya na kristallizatsiyu metallicheskih splavov: Dokt. dis.* DGU, Dnepropetrovsk, 1975.
87. Linle, K., Ranor, G.V., Hume-Rothery W. *J. Inst. Met.*, 1946, Vol. 73, pp. 83–89.
88. Dobatkina, V.I. *Plavka i lit'e alyuminievyh splavov: Spravochnoe rukovodstvo /Pod red.* Metallurgiya, Moscow, 1970, 416 pp.
89. Gol'der, Yu.G. *Izv. VUZOV., Tsvetnaya metallurgiya*, 1974, No. 4, pp. 140–143.
90. Falkenhagen, G., Hofman, W. *Z. f. Metallkunde*, 1952, Bd 43, No. 3, S.69.
91. Salli, I.V. and Miroshnichenko, I.S. *DAN SSSR*, 1960, T. 132, No. 6, pp. 1364–1367.
92. Varich, N.I. and Kolesnichenko, K.E. *Izv. VUZOV, Tsvetnaya metallurgiya*, 1960, No. 4, pp. 131–136.
93. Hofman, W. *Aluminium*, 1938, Bd. 20, 865 pp.
94. Miroshnichenko, I.S. Voprosy formirovaniya metastabil'noi struktury splavov. Neravnovesnaya kristallizatsiya. Sb. Statei pod red. DGU, Dnepropetrovsk, 1987.
95. Kuznetsov, G.M. i dr. *Izv. VUZOV. Tsvetnaya metallurgiya*, 1989, No. 6, pp. 91–94.
96. Bunk, W. and Dittrich, M. *Aluminium*, 1967, No. 7, S.435.
97. Pikunov, M.V. *Liteinoe proizvodstvo*, 1966, No. 10, pp. 25–26.
98. Novikov, I.I., Lyuttsau, V.G. and Zolotorevskii, V.S. *FMM*, 1963, T. 16, No. 2, pp. 241–250.
99. Rozin, K.M. *ZhFH*, 1978, No. 7, pp. 1652–1657.
100. Smith, V.G., Tiller, W.A. and Ritter, I.W. *Canad. J. Phys.*, 1955, Vol. 33, 723 pp.
101. Scheuer, E. *Z. f. Metal.*, 1931, Bd. 23, No. 8, 237 pp.
102. Gulyaev, B.B. *Liteinye protsessy*. Mashgiz, Moscow, 1960, 416 pp.
103. Zakharov, E.D. *V kn.: Deformiruemye alyuminievye splavy*. Oborongiz, Moscow, 1961, pp. 214–228.
104. Langsrud, Y. In: *Proc. Workshop Effect of Iron and Silicon in Aluminum and Its Alloys*, Balatonfured, Hungary, May, 1990, pp. 95–116.
105. Churbakova, T.N. *Issledovanie protsessa proizvodstva deformirovannyh alyuminievyh polufabrikatov iz splavov sistemy Al-Mg-Si c pozitsii sovremennogo metallovedeniya*. Budapesht, Doktorskaya dissertatsiya, 1986.
106. Kurdyumova, T.A., Zolotorevskii, V.S. and Belov, N.A. *Vliyanie sostava i struktury siluminov na harakteristiki ih treschinostoikosti* v sb.: *Metody povysheniya konstruktsionoi prochnosti metallicheskih materialov.* MDNTP, Moscow, 1988, pp. 139–143.
107. Belov, N.A. *Optimizatsiya sostava i struktury konstruktsionnyh liteinyh alyuminievyh splavov evtekticheskogo tipa, Dis. dokt. tehn. nauk.* MISiS, Moscow, 1994.
108. Movchan, B.A. *Mikroskopicheskaya neodnorodnost' v lityh splavah*. Gostehizdat, Kiev, 1962, 340 p.
109. Kohn, A. and Philibert, T. *Met. Treatment*, 1960, Vol. 27, 218 pp.
110. Doherty, R.D. and Freest, A. *Met. Trans.*, 1973, Vol. 4, No. 1, pp. 115–124.
111. Cole, G.S. *Met. Trans.*, 1971, Vol. 2, No. 2, pp. 357–370.
112. Barbanel' R.I., Bochvar, O.S. and Ehina E.V. *V kn.: Legkie splavy i metody ih obrabotki.* Nauka, Moscow, 1968, pp. 135–138.
113. Melford, D.A. and Grander, O.A. *JISI*, 1968, Vol. 206, No. 2, 128 pp.
114. Coates, F. *Trans. AIME*, 1968, 242, No. 5, pp. 800–809.
115. Miroshnichenko, I. S., *Struktura i svoistva bystroohlazhdennyh splavov Sb. Statei pod. red.* DGU, Dnepropetrovsk, 1988.
116. Miheeva, V.I. *Himicheskaya priroda vysokoprochnyh splavov alyuminiya s magniem i tsinkom*. Izd-vo AN SSSR, Moscow, 1947, 131 pp.

117. Diagrammy sostoyaniya sistem na osnove alyuminiya i magniya/Drits M.E., Bochvar, N.R. and Kadaner, E.S. Nauka, Moscow, 1977, 278 pp.
118. Kuznetsov, G.M. and Smagulov, D.U. *Izv. VUZOV., Tsvetnaya metallurgiya*, 1974, No. 5, pp. 117–122.
119. Kuznetsov, G.M., Zolotorevskii, V.S., Kurbatova, A.V. and Smagulov, D.U. Teoreticheskie i eksperimental'nye issledovaniya vnutrikristallitnoi likvatsii v splavah Al-Mg-Zn. *Izv. VUZOV. Tsvet. Met.* No. 1, 1979.
120. Kuznetsov, G.M. and Smagulov, D.U. *Izv. VUZOV., Tsvetnaya metallurgiya*, 1974, No. 4, pp. 136–139.
121. Pfann, W.G. *Zone Melting*, Krieger Publ. Co., Huntington, New York, 1978, 310 pp.
122. Istomin-Kastrovskii, V.V., Novikov, I.I. and Zolotorevskii, V.S. *FMM*, 1971, T. 32, No. 2, pp. 442–445.
123. Elagin, V.I. *Legirovanie deformiruemyh alyuminievyh splavov perehodnymi metallami*. Metallurgiya, Moscow, 1975. 247 pp.
124. Backerud, L. *Iernocontorets*, 1968, Vol. 152, No. 3, 109 pp.
125. Setyukov, O.A., Novikov, I.I., Semenov, A.E. and Zolotorevskii, V.S. *Izv. VUZOV., Tsvetnaya metallurgiya*, 1972, No. 4, pp. 117–120.
126. Setyukov, O.A., Semenov, A.E. and Zolotorevskii, V.S. Izv. VUZOV., *Tsvetnaya metallurgiya*, 1975, No. 2, pp. 118–121.
127. Sperry, P. *J. Met.*, 1955, Vol. 7, No. 1, Sec. II, 145 pp.
128. Trabasso, R.E., Tankins, E.5. and Vigione I. *Canadian Metallurg. Quarterly*, 1972, Vol. 11, No. 2, 43 pp.
129. Livanov, V.A. *V kn.: Trudy pervoi tehnologicheskoi konferentsii metallurgicheskih zavodov*. Oborongiz, Moscow, 1945, pp. 5–10.
130. Movchan, B.A. *Granitsy kristallitov v lityh metallah i splavah.* Tehnika, Kiev, 1970, No. 212, pp. 131.
131. Pikunov, M.V. *Liteinoe proizvodstvo*, 1966, No. 10, pp. 25–26.
132. Fridlyander, I.N. *Nauch. tr. VIAM*, 1949, VYP. 9, 65 pp.
133. Fridlyander, I.N. *V kn.: 3atverdevanie metallov.* Mashgiz, Moscow, 1958, pp. 275–298.
134. Spear, R.E. and Gagdneg, G.R. *Mod. Casting*, 1963, Vol. 43, No. 5, 209 pp.
135. Alexander, V. and Rhines, F. *J. Met.*, 1950, Vol. 188, No. 10, pp. 1267–1273.
136. Matija, N., Giessen, V.S. and Ggant, N.I. *J. Inst. Met.*, 1968, Vol. 96, 30 pp.
137. Voreen, O., Evensen, J.E. and Pedersen, T.B. *AFS Trans*, 1984, 459 pp.
138. Horwath, I.A. and Mondolfo, L.F. *Acta Met.*, 1962, Vol. 10, No. 11, 1037 pp.
139. Ibaraki Masao, A.O. *J. Jap. Inst. Met.*, 1968, Vol. 32, No. 7, 670 pp.
140. Ibaraki Masao Okomoto, T. and Kishitake, K. a. o. Memor. Inst. Scient. and Industr. Res., Osaka Univ., 1968, Vol. 25, pp. 101–115.
141. Lashko, N.F. and Lashko, S.V. *Nekotorye problemy svarivaemosti metallov.* Mashgiz, Moscow, 1963, 300 pp.
142. Kamenetskaya, D.S., Piletskaya, I.B. and Rahmanova, E.P. *FMM*, 1956, T. 11, vyp. 2, pp. 254–258.
143. Mal'tsev, M.V. *Modifitsirovanie struktury metallov i splavov*. Metallurgiya, Moscow, 1964, 214 pp.
144. Teleshov, V.V. and Zolotorevskii, V.S. *Izv. VUZOV., Tsvetnaya metallurgiya*, 1971, No. 4, pp. 120–123.
145. Kats, A.M., Pikunov, M.V. and Bahtiarov, R.A. *Tsvetnye metally*, 1968, No. 5, pp. 81–83.
146. Balandin, G.F. *Formirovanie kristallicheskogo stroeniya otlivok*. Mashinostroenie, Moscow, 1973, 287 pp.
147. Chalmers, B. Principles of Solidification, Wiley, New York, 1996.
148. Indenbaum, G.V. and Popov, D.N. *FMM*, 1962, T. 14, vyp. 2, pp. 205–211.
149. Indenbaum, G.V. and Fishman, Yu.M. *FMM*, 1964, T. 17, vyp. 3, pp. 419–427.
150. Ovsienko, D.E., Zasimchuk, I.K. and Meleshko, L.I. *V kn.: Rost i nesovershenstva metallicheskih kristallov*. Naukova Dumka, Kiev, 1966, pp. 220–230.
151. Sosnina, E.I. and Meleshko, L.I. *V kn.: Rost i nesovershenstva metallicheskih kristallov*. Naukova Dumka, Kiev, 1966, pp. 211–220.

152. Fogsten, J. *Doctoral dissertation*, Totainemi Technical University, Helsinki, 1969, 120 pp.
153. Oshima, R. and Fujita, E. *Trans. J. Inst. Met.*, 1969, Vol. 10, 57 pp.
154. Nagata, A. and Izumi, O. *J. Jap. Inst. Light Met.*, 1971, Vol. 21, No. 12, 817 pp.
155. Nagata, A. and Izuti, O. *J. Jap. Inst. Light Met.*, 1971, Vol. 21, No. 12, 826 pp.
156. Bochvar, A.A. *Izv. AN SSSR, OTN*, 1947, No. 10, pp. 1369–1372.
157. Bochvar, A.A. *V kn.: Tehnologiya tsvetnyh metallov*. Metallurgizdat, Moscow, 1947, pp. 5–8.
158. Zolotorevckii, V.S. and Novikov, I.I. Istomin-Kastrovekii, V.V. and Orelkina T.A. *V kn.: Splavy tsvetnyh metallov*. Nauka, Moscow, 1972, pp. 53–62.
159. Istomin-Kastrovskii, V.V., Vittenberg P.M., Mishin A.S. and Zolotorevskii, V.S. *Izv. VUZOV, Tsvetnaya metallurgiya*, 1975, No. 5, pp. 107–112.
160. Yakushin, B.F., Chernavskii, D.M., Orelkina, T.A. and Zolotorevskii, V.S. *Izv. VUZOV, Tsvetnaya metallurgii*, 1976, No. 2, pp. 141–145.
161. Zolotorevekii, V.S., Orelkina, T.A. and Istomin-Kastrovskii, V.V. *Izv. AN SSSR, Metally*, 1978, No. 3, pp. 158–65.
162. Gorelik, S.S. *Rekristallizatsiya metallov i splavov. 2-e izd.* Metallurgiya, Moscow, 1978.
163. Obinata, I., Oelschligel, O. and Takeuchi, V. *J. Inst. Met.*, 1967, Vol. 95, p. 158.
164. Nagata, A. et al. *Trans. Jap. Inst. Met.*, 1969, Vol. 10, 52 pp.
165. Obinata, I., Izumi, O. and Oelschlegel, O. a.o. *Trans. Jap. Inst. Met.*, 1969, Vol. 10, pp. 107–114.
166. Struktura i svoistva polufabrikatov iz alyuminievyh splavov: Spravochnik /Pod red. V.A.Livanova. Metallurgiya, Moscow, 1974, 432 pp.
167. Tiller, W.A. *The Science of Crystallization: Macroscopic Phenomena and Defect Generation*, Cambridge, Cambridge University Press, 1991.
168. Bochvar, A.A. and Raboty, D.K. *Chernova v oblasti metallovedeniya i ih znachenie v sovremennoi nauke.* IMET im. A.A.Baikova, Moscow, 1968. 19 pp.
169. Materials Science and Technology: A Comprehensive Treatment, ed. by Cahn, R.W., Haasen, P., and Kramer, E.J., 11 volumes, Wiley-VCH, New York, 2005, 15,000 pp.
170. Nagata, A. a.o. *J. Jap. Inst. Light Met.*, 1970, Vol. 20, 539 pp.
171. Theler, I.I., Bichsel N. *Z. f. Metal.* 1967, No. 3, p. 195.
172. Lindroos, V.K. and Miekkoja, N.M. *Phil. Mag.*, 1967, Vol. 16, No. 141, 593 pp.
173. 50 Years Progress in Crystal growth, ed. by Feigelson, R., Elsevier, Amsterdam, 2004.
174. Tiller, A. *Acta Met.*, 1962, Vol. 10, 681 pp.
175. Goss, A.J., Benson, K.E. and Pfann, W.G. *Acta Met.*, 1956, Vol. 4, 332 pp.
176. Evans, K.R. and Flanagan, W.F. *Phil. Mag.*, 1966, Vol. 7, 32 pp.
177. Zasimchuk, I.K. and Ovsienko, D.E. *FMM*, 1967, T. 24, vyp. 2, pp. 329–337.
178. Zasimchuk, I.K. and Ovsienko, D.E. *FMM*. 1967, T. 24, Byp. 3, pp. 430–435.
179. Ovsienko, D.E. *V kn.: Rost i nesovershenstva metallicheskih kristallov.* Naukova Dumka, Kiev, 1966, pp. 165–191.
180. Zolotorevskii, V.S. *Struktura i prochnost' lityh alyuminievyh splavov.* Metallurgiya, Moscow, 1981, 191 pp.
181. Billig, E. *Proc. Roy. Soc.*, 1956, Vol. 235, No. 1200, 37 pp.
182. Tiller, V.A. *V kn.: Teoriya i praktika vyraschivaniya kristallov: Per. s angl. /Pod red. D.E.Temkina i E.I.Givargizova.* Metallurgiya, Moscow, 1968, pp. 294–350.
183. Indenbom, V.L. *Kristallografiya*, 1967, No. 2, pp. 294–298.
184. Indenbom, V.L. *Izv. AN SSSR, Ser. fiz.*, 1973, T. 37, No. 11, pp. 2258–2267.
185. Seitz. F. *Phys. Rev.*, 1950, Vol. 50, 820 pp.
186. Schock, V.S. and Tiller, W.A. *Phil. Mag.*, 1960, Vol. 5, No. 49, 43 pp.
187. Howe, S. and Elbaum, S., *Phil. Mag.*, 1961, Vol. 6, No. 70, pp. 1215–1240.
188. Jackson, K.A. *Phil. Mag.*, 1962, Vol. 7, No. 81, 1615 pp.
189. Thomas, G. *Phil. Mag.*, 1959, Vol. 8, 1213 pp.
190. Kelly, A. and Nickolson, R.B. Precipitation Hardening, Pergamon Press, London, 1963.
191. Hirth, J.P. and Lothe, J. *Theory of Dislocations*, Second Edition. John Wiley, New York, 1982, 857 pp.

192. Henkin, M.L. and Lokshin, I.H. *Razmernaya stabil'nost' metallov i splavov v tochnom mashinostroenii i priborostroenii*. Mashinostroenie, Moscow, 1974, 255 pp.
193. Prohaszka, *Acta Met.*, 1963, Vol. 11, 125 pp.
194. Dobatkin, V.I., Gabidullin, R.M., Kolachev, B.A. and Makarov, G.S. *Gazy i okisly v alyuminievyh deformiruemyh splavah.* Metallurgiya, Moscow, 1976, 263 pp.
195. Hamilton, D.R. *Acta Met.*, 1964, Vol. 12. 1094 pp.
196. Bernshtein, M.L. *Struktura deformirovannyh metallov*. Metallurgiya, Moscow, 1977, 264 pp.
197. Pollard, W.A. *J. Inst. Met.*, 1965, Vol. 93, No. 6, pp. 339–346.
198. Pedrix, Ch., Perrin, F., and Motheillet, F., in: Creep and Recovery, ASM International, Metals Park, OH, 1957, pp. 255–283.
199. Fridlyander, I.N. *V kn.: Trudy pervoi tehnologicheskoi konferentsii metallurgicheskih zavodov*. Oborongiz, Moscow, 1945, pp. 134–139.
200. Dobatkin, V.I., Grishkovets, Ya.G. and Yakovlev, V.I. *V kn.: Metallovedenie splavov legkih metallov*. Nauka, Moscow, 1970, pp. 137–143.
201. Drits, M.E. *Doklady AN SSSR*, T. 257, No. 2, pp. 353–356.
202. Promyshlennye deformiruemye, spechennye i liteinye alyuminievye splavy: Spravochnoe rukovodstvo /Pod red. F.I.Kvasova i I.N.Fridlyandera. Metallurgiya, Moscow, 1972, 552 p.
203. Davydov, V.G., 3aharov, V.V., Zaharov, E.D. and Novikov, I.I. *Diagrammy izotermicheskogo raspada rastvora v alyuminievyh splavah*. Metallurgiya, Moscow, 1973. 152 pp.

Chapter 3

204. Novikov, I.I. *Teoriya termicheskoi obrabotki metallov*. Metallurgiya, Moscow, 1986, 480 pp.
205. Voronov, S.M. *Izbrannye trudy po legkim splavam*. Oborongiz, Moscow, 1957, pp. 515–545.
206. Vol, A.E. *Stroenie i svoistva dvoinyh metallicheskih sistem*. Fizmatgiz, Moscow, 1959, T. 1.
207. Gertsriken, S.D. and Dehtyar, I.Ya. *Diffuziya v metallah i splavah v tverdoi faze.* Fizmatgiz, Moscow, 1960.
208. Zeit, V. *Diffusion in Metals, Russian translation from German*, Foreign Literature, Moscow, 1958.
209. Aaron, N.V. *Metal Sci. J.*, 1968, Vol. 2, 192 pp.
210. Tanzilli, R.A. and Heckel, R.W. *Trans. AIME*, 1968, Vol. 242, 2313 pp.
211. Singh, S.N. and Flemings, M.S. *Trans. AIME*, 1969, Vol. 245, 1803 pp.
212. Whelan, M.I. *Metal Sci. J.*, 1969, Vol. 3, 95 pp.
213. Singh, S.N., Bardes, V.R. and Flemings, M.S. *Met. Trans.*, 1970, Vol. 1, No. 5, pp. 1383–1388.
214. Singh, S.N., Bardes, B.P. and Flemings, M.S. *Met. Trans.*, 1970, Vol. 1, 1383 pp.
215. Aaron, N.V. and Kotler, G.R. *Met. Trans.*, 1971, Vol. 2, 393 pp.
216. Bernhardt, W. *Neue Hutte*, 1971, Bd. 16, No. 12, 740 pp.
217. Zolotorevskii, V.S., Teleshov, V.V., Adler, Yu.P. and Kuk, E.V. *Izv. VUZOV, Tsvetnaya metallurgiya*, 1966, No. 6, pp. 116–120.
218. Zolotorevskii, V.S. and Teleshov, V.V. *MiTOM*, 1970, No. 7, pp. 44–49.
219. Zolotorevskii, V.S., Kuk, E.V. and Ravich, I.G. *Izv. VUZOZ., Tsvetnaya metallurgiya*, 1966, No. 5, pp. 129–134.
220. Csurbakova, T.N., Zolotorevskiy, V.Sz., Novikov, I.I. Kohaszat, 1968, Bd. 101, No. 7, pp. 284–287.
221. Csurbakova, T., Zolotorevskiy, V.Sz., Novikov, I.I. Kohaszat, 1970, Vol. 103, No. 4, pp. 174–178.
222. Kazeev, S.A. *Kinetika v prilozhenii k metallovedeniyu.* Oborongiz, Moscow, 1956.
223. Bochvar, A.M. and Kestner, O.E. *Vestnik metallopromyshlennosti*, 1928, No. 11, pp. 57–60.
224. Livanov, V.A., Golohmatova, G.N. and Pastuhova, G.A. *V kn.: Issledovanie splavov tsvetnyh metallov*. Izd-vo AN SSSR, Moscow, 1960, pp. 72–83.
225. Livanov, V.A. *Voprosy metallovedeniya i tehnologii proizvodstva polufabrikatov iz alyuminievyh i titanovyh splavov*. ONTI VIAM, Moscow, 1964.

226. Martin, J.W., Doherty, R.D. and Cantor, B. *Stability of Microstructure in Metallic Systems*, 2nd edition, Cambridge Solid State Series, Cambridge University Press, 442 pages, 1997.
227. Eskin, D.G., Suyitno, Katgerman L. *Prog. Mat. Sci.*, 2004, Vol. 49, No. 5, pp. 630–711.
228. Krymov, V.V. and Fedorova, V.K. *V kn.: Metallovedenie i obrabotka tsvetnyh metallov i splavov*. Metallurgizdat, Moscow, 1957, pp. 101–120.
229. Belousov, N.N. *Termicheskaya obrabotka otlivok iz alyuminievyh splavov*. LDNTP, Leningrad, 1960.
230. Kolobnev, I.F. *Termicheskaya obrabotka alyuminievyh splavov*. Metallurgiya, Moscow, 1966, 394 p.
231. Zolotorevskii, V.S. and Novikov, I.I. *Tehnologiya legkih splavov*, 1970, No. 3, pp. 3–5.
232. Hald, A. Mathematical Statistics with Technical Applications, John Wiley, New York, 1954.
233. Norman T. J. Bailey, Statistical Methods in Biology, 3rd edition, Cambridge University Press, Cambridge, 1995.
234. Nalimov, V.V. *Primenenie matematicheskoi statistiki pri analize veschestva*. Fizmatgiz, Moscow, 1960.
235. Teleshov, V.V. *Tehnologiya legkih splavov*, 1971, No. 5, pp. 9–12.
236. Novikov, I.I., Zolotorevskii, V.S., Kuk E.V. and Indenbaum, S.V. *Izv. AN SSSR, Metally*, 1969, No. 2, pp. 125–128.
237. Lavender, I.O. and Jones, F.W. *JISI*, 1949, Vol. 163, No. 1, pp. 14–17.
238. Ward, M. and Widdowson, R. *JISI*, 1965, Vol. 203, No. 5, pp. 486–492.
239. Kattamis, T.Z. and Flemings, M.S. *Trans. AIME*, 1965, Vol. 233, 999 pp.
240. Kalinowski, L. *Archiwum budowy maszyn*, 1968, Bd. 15, No. 1, 21 pp.
241. Weinberg, F. and Buhr, R.I. *JISI*, 1969, Vol. 207, 1114 pp.
242. Guy, A.G., Blake, R.G. and Hiroshi Oikawa. *Trans. AIME*, 1967, Vol. 239, No. 6, pp. 771–774.
243. Fuchs, E.G. Banyaszati es Kohaszati Lapok. *Qntode*, 1968, No. 2, 17 pp.
244. Fuks, E.G., Chur6akova, T.N. *Izv. VUZ. Tsvetnaya metallurgiya*, 1977, No. 2, pp. 107–114.
245. Zolotorevskii, V.S., Kurbatova, A.V. and Raitbarg, F.L. *Izv. AN SSSR, Metally*, 1974, No. 2, pp. 140–143.
246. Novik, F.S., Fomishkin, M.A. and Zolotorevskii, V.S. *Izv. AN SSSR, Metally*, 1968, No. 6, pp. 163–167.
247. Kurbatova, A.V. and Zolotorevskii, V.S. *Izv. VUZOV., Tsvetnaya metallurgiya*, 1975, No. 5, pp. 119–122.
248. Backerud, L. Z. f. *Metallkunde*, 1966, No. 4, pp. 260–265.
249. Verdier, I. *Rev. Met.*, 1972, Vol. 69, No. 2, p. 107.
250. Alyuminii: Per. s angl. /Pod red. A.T.Tumanova, F.I. Kvasova, I.N. Fridlyandera: Moscow, Metallurgiya, 1972, 663 pp.
251. Hansen, M. Constitution of Binary Alloys, McGraw Hill, 1958.
252. Aksenov i dr. Izvestiya RAN. *Metally*, 1992, No. 6, syu80–83.
253. Belov, N.A., Istomin-Kastrovskii, V.V. and Naumova, E.S. Issledovanie raspada anomal'no peresyschennyh tverdyh rastvorov v lityh splavah na osnove alyuminiya, legirovannyh tsirkoniem. *Izv. VUZOV, Tsvetnaya metallurgiya*, 1996, No. 4, pp. 45–50.
254. Bishop, M. and Fletcher, K.E. *Met. Rev.*, 1972, Vol. 17, 203 pp.
255. Kirkaldy, I.S. *Trans. ASM*, 1963, Vol. 56, 837 pp.
256. Kirkaldy, I.S. *Acta Met.*, 1965, Vol. 13, 907 pp.
257. Krishtal, M.A. *Mehanizm diffuzii v zheleznyh splavah*. Metallurgiya, Moscow, 1972, 400 pp.
258. Mondolfo, L.F. *Met. a. Mater.*, 1971, No. 6, 95 pp.
259. Marumo, T., Fujikawa, S. and Hirano, K. *J. Jap. Inst. Light Met.*, 1973, Vol. 23, No. 1, pp. 17–25.
260. Taran, Yu. N. and Mazur, V.I. *Struktura evtekticheskih splavov*. Metallurgiya, Moscow, 1978.
261. Dolzhenkov, I.N. and Dolzhenkov, I.I. *Sferoidizatsiya karbidov v stali*. Metallurgiya, Moscow, 1984, 142 pp.
262. Belov, N.A., Alabin, A.N. and Eskin, D.G. Improving the Properties of Cold Rolled Al–6%Ni sheets by alloying and heat treatment. *Scripta Mater.*, 2004, Vol. 50/1, pp. 89–94.

263. Belov, N.A., Zolotorevskii, V.S. and Luzgin, D.V. Vliyanie termoobrabotki na morfologiyu zhelezosoderzhaschih faz v alyuminievyh splavah. *Perspektivnye materialy*, 1997, No. 3, pp. 76–85.

264. Luzgin, D.V. Issledovanie struktury i svoistv liteinyh alyuminievyh splavov, legirovannyh zhelezom, Dis. kand. tehn. nauk, MISiS, Moscow, 1995.

265. Novikov, I.I. *Teoriya termicheskoi obrabotki metallov*. Metallurgiya, Moscow, 1986, 480 pp.

266. Livshits, B.G. *Metallografiya*, Metallurgiya, Moscow, 1990, 334 pp.

267. Ost, K.T. *V kn.: Teoriya i praktika vyraschivaniya kristallov: Per. s angl. /Pod red. D.E. Temkina i E. I. Givargizova*. Metallurgiya, Moscow, 1968, pp. 543–587.

268. Shorshorov, M.H., Erohin, A.A., Chernysheva, T.P. i dr. *Goryachie treschiny pri svarke zharoprochnyh splavov* Mashinostroenie, Moscow, 1973, 224 pp.

269. Zolotorevskii, V.S. and Istomin-Kastrovskii, V.V. *DAN SSSR*, 1975, T. 222, No. 2, pp. 326–328.

270. Novikov, I.I., Zolotorevskii, V.S., Levin, L.I. and Drits, A.M. *V kn.: Struktura i svoistva legkih splavov*. Nauka, Moscow, 1971, pp. 112–117.

271. Pribory i metody fizicheskogo metallovedeniya. T. 1: Per. s angl. /Pod red. F. Veinberga. Mir, Moscow, 1973, 427 pp.

272. Ryum, N. *Acta Met.*, 1969, Vol. 17, No. 3, pp. 269–278.

273. Nes, E. *Acta Met.*, 1972, Vol. 20, No. 4, pp. 499–506.

274. Thundal, V. and Sundberg, Ya. *J. Inst. Met.*, 1969, Vol. 97, No. 5, 160 pp.

275. Adenis, O. and Moulin, I. *Rev. Met.*, 1969, No. 2, 135 pp.

276. Ageeva, G.N., Zolotorevskii, V.S. and Tsaregorodtseva, A.I. *V kn.: Voprosy sudostroeniya: Ser.* Metallurgiya, vyp. 17. TsNII "Rumb", Leningrad, 1974, pp. 30–39.

277. Levin, L.I., Zolotorevskii, V.S., Zaharov, V.V. and Kurbatova, A.V. *Izv. VUZOV., Tsvetnaya metalpurgiya*, 1975, No. 5, pp. 129–133.

278. Levin, L.I., Zolotorevskii, V.S. and Zaharov, V.V. i dr. Tehnologiya legkih splavov, 1976, No. 7, pp. 3–7.

279. Belousov, N.N., Zolotorevskii, V.S. and Kashevnik, L.Ya. i dr. *Izv. VUZOV., Tsvetnaya metallurgiya*, 1977, No. 3, pp. 94–99.

280. Kolachev, B.A., Livanov, V.A. and Elagin, V.I. *Metallovedenie i termicheskaya obrabotka tsvetnyh metallov i splavov*. Metallurgiya, Moscow, 1972.

281. Naess, S.E. and Hoier R. *Z. f. Metallk.*, 1972, Vd. 63, No. 5, 248 pp.

282. Elagin, V.I., Zaharov, V.V. and Rostova, T.D. *Tsvetnye metally*, 1982, No. 12, pp. 96–99.

283. Boble, P.C., Erdman–Jesritzer, F. and Sholbel, W. *Aluminium (BRD)*, 1983, Bd. 59, No. 8, pp. 592–597.

284. Blake, N. and Hotkins, M.A. *J. Mater. Science*, 1985, No. 20, pp. 2861–2867.

285. Elagin, V.I., Zaharov, V.V. and Rostova, T.D. *Tehnologiya legkih splavov*, 1984, No. 4, pp 5–11.

286. Drits, M.E. i dr. Metallovedenie i termicheskaya obrabotka metallov, 1985, No. 4, pp. 48–50.

287. Drits M. E. i dr. *Doklady AN SSSR*, 1981, T. 257, No. 2, pp. 363–366.

288. Elagin, V.I., Zaharov, V.V. and Rostova, T.D. Metallovedenie i termicheskaya obrabotka metallov, 1983, No. 7, pp. 57–60.

289. Toropova, L.S. et al. *Advanced Aluminium Alloys Containing Scandium*. Gordon and Breach Science Publishers, Australia, 2002, 175 pp.

290. Elagin, V.I. i dr. *V kn.: Metallovedenie, lit'e i obrabotka legkih splavov*. Metallurgiya, Moscow, 1986, pp. 180–189.

291. Novikov, I.I., Semenov, A.E., Setyukov, O.V. and Zolotorevskii, V.S. *V kn.: Metallovedenie i tehnologiya legkih splavov*. Nauka, Moscow, 1976, pp. 39–45.

292. Buinov, N.N. and Zaharova, R.R. *Raspad metallicheskih peresyschennyh tverdyh rastvorov*. Metallurgiya, Moscow, 1964, 141 pp.

Chapter 4

293. Novikov, I.I., Zolotorevskii, V.S. and Lisovskaya, T.D.V. kn. Issledovanie splavov tsvetnyh metallov, vyp. 4, M.: AN SSSR, 1963, 130 pp.

294. Bochvar, A.A. and Novikov, I.I. Tehnologiya tsvetnyh metallov. Sb. Trudov MITsMiZ, No. 23. Metallurgizdat, Moscow, 1952, pp. 5–15.
295. Bochvar, A.A. and Sviderskaya, Z.A. *Izv. AN SSSR*, OTN, 1947, No. 3, 349 pp.
296. Bochvar, A.A. and Zhadaeva, O.S. Yubileinyi sbornik trudov NITsMIZ, 1940, No. 9, pp. 5–12.
297. McLean, D. *Mechanical Properties of Metals.* John Wiley & Sons, London, New York, 1962.
298. Murty, K.I., Mohamed, F.A. and Dorn, I.E. *Scripta Met.*, 1971, Vol. 5, No. 12, 1087 pp.
299. Startsev, V.I., Il’ichev, V.Ya. and Pustovalov, V.V. *Plastichnost’ i prochnost’ metallov i splavov pri nizkih temperaturah.* Metallurgiya, Moscow, 1975, 328 pp.
300. Kravchenko, V.E., Kolachev, B.A. and Gabidullin, R.M. *Izv. VUZOV, Tsvetnaya metallurgiya,* 1976, No. 5, pp. 105–110.
301. Jaoul, B. *J. Mech. Phys. Solids*, 1957, No. 5, 95 pp.
302. Honeycombe, R.W.K., *The Plastic Deformation of Metals*, 2nd edition, Edward Arnold, London, England, 1984.
303. Schwink, Ch. *Phys. Stat. sol.*, 1965, Vol. 8, 457 pp.
304. Krause, O. and Gottler, E. *Phys. Stat. sol.*, 1965, Vol. 9, 485 pp.
305. Zanke, G. *Z. Naturf.*, 1963, Bd 18a, No. 5, p. 795.
306. Popov, L.E., Sollertinskaya, E.S. and Tsypin, M.I. *FMM*, 1975, T. 39, vyp. 6, pp. 1303–1304.
307. Tsypin, M.I., Sollertinskaya, E.S. and Bradets, V.V. Metallovedenie i termicheskaya obrabotka tsvetnyh metallov i splavov: Nauch. tr./ Giprotsvetmetobrabotka, vyp. 58, Metallurgiya, Moscow, 1978, pp. 9-13.
308. Ultrafine-Grain Metals, ed. By H. Conrad et al., Syracuse University Press, Syracuse, NY, 1970.
309. Zolotorevskii, V.S. and Teleshov, V.V. *Izv. VUZOV, Tsvetnaya metallurgiya*, 1970, No. 1, pp. 121–126.
310. Zolotorevskii, V.S. and Teleshov, V.V. *Izv. AN SSSR, Metally*, 1971, No. 5, pp. 187–194.
311. Zolotorevskii, V.S. *V kn.: Problemy metallovedeniya tsvetnyh metallov.* Nauka, Moscow, 1978, pp. 128–137.
312. Altunina, L.A., Aristova, N.A. and Zolotorevskii, V.S. i dr. *MiTOM*, 1972, No. 8, pp. 9–14.
313. Kornauhov, A.S. and Zolotorevskii 8.S. *Izv. VUZOV, Tsvetnaya metallurgiya*, 1976, No. 4, pp. 157–160.
314. Kornauhov, A.S., Belousov, N.N., Zolotorevskii, V.S. and Kashevnik, L.Ya. *Izv. VUZOV, Tsvetnaya metallurgiya*, 1979, No. 1, pp. 122–127.
315. Draper, N.A. and Smith, H. *Applied Regression Analysis*, Wiley, New York, 1981.
316. Al’tman, M.B. *Nemetallicheskie vklyucheniya v alyuminievyh splavah.* Metallurgiya, Moscow, 1965, 322 pp.
317. Vainblat, Yu.M. and Hayurov, S.S. *FMM*, 1972, T. 33, pp. 866–871.
318. Zolotorevskii, V.S. and Kornauhov, A.S. *Izv. VUZOV, Tsvetnaya metallurgiya*, 1976, No. 1, pp. 113–118.
319. Nalimov, V.V. *Teoriya eksperimenta.* Nauka, Moscow, 1971, 207 pp.
320. Nall, E.O. *Proc. Phys. Soc.*, 1951, Vol. 64V. 747 pp.
321. Petch, N.I. *JISI*, 1953, Vol. 173, 25 pp.
322. Veinik, A.I. Teoriya zatverdevaniya otlivok. Mashgiz, 1960, 435 pp.
323. Zolotorevskii, V.S., Lainer, I.S. and Belov, N.A. Malotsiklovaya ustalost’ liteinyh alyuminievyh splavov *Izv. VUZOV, Tsvetnaya metallurgiya*, 2001, No. 4, pp. 43–48.
324. Belov, N.A., Zolotorevskii, V.S. and Gusev, A.Yu. Vyazkost’ razrusheniya standartnyh siluminov Metallovedenie i termicheskaya obrabotka metallov, 1992, No. 10, pp. 32–33.

Chapter 5

325. Belov, N.A. and Zolotorevskii, V.S. Optimizatsiya sostava malokremnistyh siluminov dlya povysheniya mehanicheskih svoistv v litom sostoyanii. *Izv. VUZOV, Tsvetnaya metallurgiya,* 2001, No. 5, pp. 67–76.

326. Belov, N.A. and Gusev, A.Yu. Optimizatsiya kolichestva magniya i medi v siluminah tipa AK7, Metallovedenie i termicheskaya obrabotka metallov, 1996, No. 3, pp. 10–13.
327. Belov, N.A., Zolotorevskii, V.S. and Evseev, Yu.V. Modifitsirovanie Fe-faz v silumine tipa AK5M2 dobavkami perehodnyh metallov. *Tsvetnye metally*, 1988, No. 1, pp. 68–70.

Chapter 6

328. Krasil'nikov, G.L. Razrabotka i issledovanie vysokoprochnogo liteinogo splava na osnove sistemy alyuminii-tsink-magnii, Dis. kand. tehn. nauk, MISiS, Moscow, 1978.
329. Kurillov, A.G. Razrabotka i issledovanie vysokoprochnyh splavov sistem Al-Mg-Zn i Al-Mg-Zn-Cu, MISiS, Dis. kand. tehn. nauk, Moscow, 1979.
330. Zolotorevskii, V.S., Ratner, A.D., Belov, N.A., Aksenov, A.A., Alekseev, V.F and Baev, V.A. Struktura novyh vysokoprochnyh liteinyh alyuminievyh splavov na osnove tehnicheskogo alyuminiya, v sb.: *Metallovedenie i obrabotka tsvetnyh splavov*. Nauka, Moscow, 1992, pp. 142–157.
331. Gotsev, I.S. Strukturno-fazovyi analiz sistemy Al-Cu-Si-Mn i razrabotka vysokoprochnogo i zharoprochnogo splava, *Avtoref. dis. kand. tehn. nauk*, VIAM, Moscow, 1989.
332. Levchenko, A.B. Razrabotka i issledovanie struktury i svoistv splava vtorichnogo syr'ya na osnove sistemy Al-Mg-Sc, Dis. kand. tehn. nauk, MISiS, Moscow, 1987.
333. Zavarzin, I.A. Issledovanie i razrabotka i vtorichnyh liteinyh splavov na baze sistemy Al-Mg-Zn-Cu, Dis. kand. tehn. nauk, MISiS, Moscow, 1981.
334. Belov, N.A. Zakonomernosti vliyaniya sostava i struktury na vyazkost' razrusheniya liteinyh splavov sistemy Al-Mg-Zn-Cu i razrabotka vysokoprochnogo splava na baze etoi sistemy s povyshennym soderzhaniem primesei, Dis. kand. tehn. nauk, MISiS, Moscow, 1985.
335. Mansurov, Yu.N. Razrabotka i issledovanie vtorichnyh liteinyh magnaliev, Dis. kand. tehn. nauk, MISiS, Moscow, 1986.
336. Aksenov, A.A. Razrabotka i issledovanie vysokoprochnyh i plastichnyh liteinyh splavov na osnove sistemy Al-Zn-Mg-Cu, Dis. kand. tehn. nauk, MISiS, Moscow, 1988.
337. Belov, N.A. Ispol'zovanie mnogokomponentnyh diagramm sostoyaniya dlya optimizatsiya struktury i sostava vysokoprochnyh liteinyh alyuminievyh splavov, *Izv. VUZOV, Tsvetnaya metallurgiya*, 1995, No. 1, pp. 48–57.
338. Belov, N.A. Optimizatsiya sostava i struktury konstruktsionnyh liteinyh alyuminievyh splavov evtekticheskogo tipa, Dis. dokt. tehn. nauk, MISiS, Moscow, 1994.
339. Zolotorevskii, V.S. and Belov, N.A. Novye liteinye alyuminievye splavy v kn.: Nauchnye shkoly Moskovskogo Gosudarstvennogo instituta stali i splavov (tehnologicheskogo universiteta)-75 let. Stanovlenie i razvitie, MISiS, Moscow, 1997, pp. 353–358.
340. Zolotorevskii, V.S. and Belov, N.A. Novye liteinye alyuminievye splavy dlya mashinostroeniya, Tehnologiya legkih splavov, 1997, No. 4, pp. 20–24.
341. Belov, N.A. and Zolotorevskii, V.S. Perspektivy sozdaniya novyh alyuminievyh splavov na osnove mnogofaznyh evtektik. *Perspektivnye materialy*, 1999, No. 3, pp. 5–12.
342. Zolotorevskii, V.S. and Belov, N.A. Novye liteinye alyuminievye splavy dlya mashinostroeniya, v sb.: Problemy razvitiya avtomobilestroeniya v Rossii, Izbrannye doklady II-IV mezhdunarodnyh nauchno-prakticheskih konferentsii (1996–1998)/ pod red. G.K.Mirzoeva, A.N.Moskalyuka, M.M.Krishtala – Tol'yatti, AO AVTOVAZ, 1999, pp. 145–149.
343. Belov, N.A., Zolotorevskij, V.S. and Shatrov, A.S. Selecting of aluminium casting alloys for plasmochemical ceramic coating. *Proc. 8th Int. Conf. on Al-Alloys and Their Physical and Mechanical Properties (ICAA8)*, 1–5.07.02 Materials Science Forum, Cambridge, UK, Vol. 396–402, Part 3, pp. 1709–1714.
344. Belov, N.A. and Zolotorevskii, V.S. Novye vysokoprochnye liteinye splavy na osnove alyuminievo-nikelevoi evtektiki (nikaliny), Nauchno-tehnologicheskoe obespechenie deyatel'nosti predpriyatii, institutov i firm: Materialy seminary. M.MGIU, 2003, pp. 584–593.

345. Belov, N.A. and Zolotorevskii, V.S. Liteinye splavy na osnove alyuminievo-nikelevoi evtektiki (nikaliny) kak vozmozhnaya al'ternativa siluminam. *Tsvetnye metally*, 2003, No. 2, pp. 99–105.
346. Belov, N.A. Vliyanie evtekticheskih faz na harakter razrusheniya vysokoprochnyh liteinyh alyuminievyh splavov, Metallovedenie i termicheskaya obrabotka metallov, 1995, No. 6, pp. 20–24.
347. Belov, N.A., Cheverikin, V.V., Zolotorevskii, V.S. and Istomin-Kastrovskii, V.V. Vliyanie nikelya na strukturu i mehanicheskie svoistva termicheski obrabotannyh otlivok splava Al-7%Zn-3%Mg. *Tsvetnye metally*, 2005, No. 5, pp. 71–76.
348. Belov, N.A. Principles of optimising the structure of creep-resisting casting aluminium alloys using transition metals. *J. Adv. Mater.*, 1994, Vol. 1, No. 4, pp. 321–329.
349. Belov, N.A. Aluminium casting alloys with high content of zirconium. *Proc. 5th Int. Conf. on Al-Alloys and Their Physical and Mechanical Properties (ICAA 5)*, 1–5.07.96 Materials Science Forum, Grenoble, France, 1996, Vol. 217–222, pp. 293–298.
350. Belov, N.A., Zolotorevskii, V.S. and Luzgin, D.V. Zharoprochnye liteinye alyuminievye splavy, legirovannye zhelezom. *Metally*, 1994, No. 3, pp. 70–76.

APPENDIX ONE

COMPOSITIONS OF STANDARD CASTING ALUMINUM ALLOYS

Tables A.1.1–A.1.3 provide data on standard compositions of Russian and US casting aluminum alloys (Aluminum Association). Concentrations of alloying elements are given for the lower and upper boundaries of the concentration range in mass percent (two digits); for impurities the maximally allowable level is denoted by one digit. Alloys are presented in the ascending order of the principal alloying element concentration growth (silicon for Table A.1.1, copper for Table A.1.2, and magnesium for Table A.1.3). Letters S, P, and M correspond to casting into sand, under pressure (die casting), and into metallic mold.

Casting Aluminum Alloys
ISBN-13: 978-0-08-045370-5

© 2007 Elsevier Ltd.
All rights reserved.

Table A.1.1 Systems AA4xx and AA3xx

No.	Country	Alloy	Si	Cu	Mg	Fe	Mn	Zn	Ni	Ti	Other
1	USA	435.2	3.3 3.9	0.05	0.05	0.4	0.05	0.1	–	–	–
2	USA	305.2	4.5 5.5	1 1.5		0.14 0.25	0.05	0.05	–	0.2	–
3	USA	A305.1	4.5 5.5	1 1.5	0.1	0.15	0.1	0.1	–	0.2	–
4	USA	A305.2	4.5 5.5	1 1.5	0.1	0.15	0.1	0.1	–	0.3	–
5	USA	A305.0	4.5 5.5	1 1.5	0.1	0.2	0.1	0.1	–	0.2	–
6	USA	305.0	4.5 5.5	1 1.5	0.1	0.6	0.5	0.35	–	0.25	Cr^a
7	Russia	AK5Mч	4.5 5.5	1 1.5	0.4 0.55	0.3	0.1	0.3	–	0.13	–
8	Russia	AK5M	4.5 5.5	1 1.5	0.35 0.6	S–0.6 P–1.5	0.5	0.3	–	–	–
9	USA	C355.0	4.5 5.5	1 1.5	0.4 0.6	0.2	0.1	0.1	–	0.2	–
10	USA	355.0	4.5 5.5	1 1.5	0.4 0.6	0.6	0.5	0.35	–	0.25	Cr^a

11	USA	A355.0	4.5 5.5	1 1.5	0.45 0.6	0.09	0.05	0.05	–	0.04 0.2	–
12	USA	C355.1	4.5 5.5	1 1.5	0.45 0.6	0.15	0.1	0.1	–	0.2	–
13	USA	355.1	4.5 5.5	1 1.5	0.45 0.6	0.5	0.5	0.35	–	0.25	Cr[a]
14	USA	A355.2	4.5 5.5	1 1.5	0.5 0.6	0.06	0.03	0.03	–	0.04 0.2	–
15	USA	C355.2	4.5 5.5	1 1.5	0.5 0.6	0.13	0.05	0.05	–	0.2	–
16	USA	355.2	4.5 5.5	1 1.5	0.5 0.6	0.14 0.25	0.05	0.05	–	0.2	–
17	Russia	AK5M4	3.5 6	3 5	0.2 0.5	S1 P1.4	0.2 0.6	0.6	0.5	0.13	–
18	Russia	AK5M2	4 6	1.5 3.5	0.2 8	S1 P1.3	0.2 0.8	0.5	0.5	0.13	–
19	USA	443.2	4.5 6	0.1	0.05	0.6	0.1	0.1	–	0.2	–
20	USA	C443.2	4.5 6	0.1	0.05	0.7 1.1	0.1	0.1	–	–	–
21	USA	B443.1	4.5 6	0.15	0.05	0.6	0.35	0.35	–	0.25	–

(*Continued*)

Table A.1.1 (Continued)

No.	Country	Alloy	Si	Cu	Mg	Fe	Mn	Zn	Ni	Ti	Other
22	USA	B443.0	4.5 6	0.15	0.05	0.8	0.35	0.35	–	0.25	–
23	USA	A443.1	4.5 6	0.3	0.05	0.6	0.5	0.5	–	0.25	Cr[a]
24	USA	A443.0	4.5 6	0.3	0.05	0.8	0.5	0.5	–	0.25	Cr[a]
25	USA	443.1	4.5 6	0.6	0.05	0.6	0.5	0.5	–	0.25	Cr[a]
26	USA	443.0	4.5 6	0.6	0.05	0.8	0.5	0.5	–	0.25	Cr[a]
27	USA	C443.1	4.5 6	0.6	0.1	1.1	0.35	0.4	0.5	–	Sn[b]
28	USA	C443.0	4.5 6	0.6	0.1	2	0.35	0.5	0.5	–	Sn[b]
29	USA	363.0	4.5 6	2.5 3.5	0.15 0.4	1.1	–	3 4.5	0.25	0.2	Sn[c]
30	USA	363.1	4.5 6	2.5 3.5	0.2 0.4	0.8	0.1	3 4.5	0.25	0.2	Sn[c]
31	USA	308.2	5 6	4 5	0.1	0.8	0.3	0.5	–	0.2	–

32	USA	308.1	5 6	4 5	0.1	0.8	0.5	1	–	0.25	–
33	USA	308.0	5 6	4 5	0.1	1	0.5	1	–	0.25	–
34	Russia	AK5M7	4.5 6.5	6 8	0.2 0.5	S-2.7	0.5	0.6	0.5	–	–
35	Russia	AK6M2	5.5 6.5	1.8 2.3	0.3 0.45	0.6	0.1	0.6	0.05	0.15	–
36	USA	319.2	5.5 6.5	3 4	0.1	0.6	0.1	0.1	0.1	0.2	–
37	USA	319.1	5.5 6.5	3 4	0.1	0.8	0.5	1	0.35	0.25	–
38	USA	A319.1	5.5 6.5	3 4	0.1	0.8	0.5	3	0.35	0.25	–
39	USA	319.0	5.5 6.5	3 4	0.1	1	0.5	1	0.35	0.25	–
40	USA	A319.0	5.5 6.5	3 4	0.1	1	0.5	3	0.35	–	Sn[b]
41	USA	B319.0	5.5 6.5	3 4	0.1 0.5	1.2	0.8	1	0.5	0.25	–
42	USA	B319.1	5.5 6.5	3 4	0.15 0.5	0.9	0.8	1	0.5	0.25	–

(*Continued*)

Table A.1.1 (Continued)

No.	Country	Alloy	Si	Cu	Mg	Fe	Mn	Zn	Ni	Ti	Other
43	USA	D357.0	6.5 7.5	–	0.55 0.6	0.2	0.1	–	–	0.1 0.2	–
44	USA	C356.2	6.5 7.5	0.03	0.3 0.45	0.04	0.03	0.03	–	0.04 2	–
45	USA	B356.2	6.5 7.5	0.03	0.3 0.45	0.06	0.03	0.03	–	0.04 2	
46	USA	B357.2	6.5 7.5	0.03	0.45 0.6	0.06	0.03	0.03	–	0.04 2	–
47	USA	C357.2	6.5 7.5	0.03	0.5 0.7	0.06	0.03	0.03	–	0.04 2	–
48	USA	A444.2	6.5 7.5	0.05	0.05	0.12	0.05	0.05	–	0.2	–
49	USA	C356.0	6.5 7.5	0.05	0.25 0.45	0.07	0.05	0.05	–	0.04 2	–
50	USA	B356.0	6.5 7.5	0.05	0.25 0.45	0.09	0.05	0.05	–	0.04 2	–
51	USA	B357.0	6.5 7.5	0.05	0.4 0.6	0.09	0.05	0.05	–	0.04 2	–

52	USA	357.1	6.5 7.5	0.05	0.45 0.6	0.12	0.03	0.05	–	0.2	–
53	USA	357.0	6.5 7.5	0.05	0.45 0.6	0.15	0.03	0.05	–	0.2	–
54	USA	C357.0	6.5 7.5	0.05	0.45 0.7	0.09	0.05	0.05	–	0.04 2	–
55	USA	445.2	6.5 7.5	0.1	–	0.6 1.3	0.1	0.1	–	–	–
56	USA	A444.1	6.5 7.5	0.1	0.05	0.15	0.1	0.1	–	0.2	–
57	USA	A444.0	6.5 7.5	0.1	0.05	0.2	0.1	0.1	–	0.2	–
58	USA	444.2	6.5 7.5	0.1	0.05	0.13 0.25	0.05	0.05	–	0.2	–
59	USA	F356.2	6.5 7.5	0.1	0.17 0.25	0.12	0.05	0.05	–	0.04 2	–
60	USA	A356.2	6.5 7.5	0.1	0.3 0.45	0.12	0.05	0.05	–	0.2	–
61	USA	356.2	6.5 7.5	0.1	0.3 0.45	0.13 0.25	0.05	0.05	–	0.2	–
62	USA	A357.2	6.5 7.5	0.1	0.45 0.7	0.12	0.05	0.05	–	0.04 2	–

(*Continued*)

Table A.1.1 (Continued)

No.	Country	Alloy	Si	Cu	Mg	Fe	Mn	Zn	Ni	Ti	Other
63	USA	F356.0	6.5 7.5	0.2	0.17 0.25	0.2	0.1	0.1	–	0.04 2	–
64	USA	A356.0	6.5 7.5	0.2	0.25 0.45	0.2	0.1	0.1	–	0.2	–
65	USA	A356.1	6.5 7.5	0.2	0.3 0.45	0.15	0.1	0.1	–	0.2	–
66	USA	A357.0	6.5 7.5	0.2	0.4 0.7	0.2	0.1	0.1	–	0.04 2	–
67	USA	444.0	6.5 7.5	0.25	0.1	0.6	0.35	0.35	–	0.25	–
68	USA	356.0	6.5 7.5	0.25	0.2 0.45	0.6	0.35	0.35	–	0.25	–
69	USA	356.1	6.5 7.5	0.25	0.25 0.45	0.5	0.35	0.35	–	0.25	–
70	USA	343.1	6.7 7.7	0.5 0.9	0.1	0.9	0.5	1.2 1.9	–	–	Cr–Sn[d]
71	USA	343.0	6.7 7.7	0.5 0.9	0.1	1.2	0.5	1.2 2	–	–	Cr–Sn[d]
72	USA	320.0	5 8	2 4	0.05 0.6	1.2	0.8	3	0.35	0.25	–

73	USA	320.1	5 8	2 4	0.1 0.6	0.9	0.8	3	0.35	0.25	–
74	Russia	AK7	6 8	–	0.2 5	0.1	0.2 0.6	0.5	0.3	–	–
75	Russia	AK7ч	6 8	0.2	0.2 0.4	0.6	0.5	0.3	–	–	–
76	Russia	AK7Ц9	6 8	0.6	0.1 0.3	0.7	0.5	7 12	–	–	–
77	Russia	AK7Pч	7 8	0.1	0.2 0.4	0.3	0.1	0.2	–	0.13	–
78	USA	324.0	7 8	0.4 0.6	0.4 0.7	1.2	0.5	1	0.3	0.2	–
79	USA	324.2	7 8	0.4 0.6	0.45 0.7	0.6	0.1	0.1	0.1	0.2	–
80	USA	324.1	7 8	0.4 0.6	0.45 0.7	0.9	0.5	1	0.3	0.2	–
81	Russia	AK8л	6.5 8.5	0.3	0.35 0.55	0.6	0.1	0.3	–	0.2	–
82	USA	AK8M3ч	7 8.5	2.5 3.5	0.2 0.45	0.4	–	0.5 1	–	0.13	Be[e]
83	USA	328.0	7.5 8.5	1 2	0.2 0.6	1	0.2 0.6	1.5	0.25	0.25	Cr[f]

(*Continued*)

Table A.1.1 (Continued)

No.	Country	Alloy	Si	Cu	Mg	Fe	Mn	Zn	Ni	Ti	Other
84	USA	328.1	7.5 8.5	1 2	0.25 0.6	0.8	0.2 0.6	1.5	0.25	0.25	Cr[f]
85	USA	358.2	7.6 8.6	0.1	0.45 0.6	0.2	0.1	0.1	–	0.12 0.2	Cr[g]
86	USA	358.0	7.6 8.6	0.2	0.4 0.6	0.3	0.2	0.2	–	0.1 0.2	Be[h]
87	Russia	AK8M	7.5 9	1 1.5	0.3 0.5	S0.7 M–0.9	0.3 0.5	0.3	–	0.2	–
88	USA	354.0	8.6 9.4	1.6 2	0.4 0.6	0.2	0.1	0.1	–	0.2	–
89	USA	354.1	8.6 9.4	1.6 2	0.45 0.6	0.15	0.1	0.1	–	0.2	–
90	USA	364.0	7.5 9.5	0.2	0.2 0.4	1.5	0.1	0.15	0.15	–	Cr 0.25–Sn 0.15
91	USA	364.2	7.5 9.5	0.2	0.25 0.4	0.7 1.1	0.1	0.15	0.15	–	Cr–Sn[i]
92	USA	380.2	7.5 9.5	3 4	0.1	0.7 1.1	0.1	0.1	0.1	–	Sn[j]
93	USA	B380.1	7.5 9.5	3 4	0.1	1	0.5	0.9	0.5	–	Sn[k]

94	USA	A380.1	7.5 9.5	3 4	0.1	1	0.5	2.9	0.5	–	Sn^{k}
95	USA	380.2	7.5 9.5	3 4	0.1	0.7 1.1	0.1	0.1	0.1	–	Sn^{j}
96	USA	380.0	7.5 9.5	3 4	0.1	2	0.5	3	0.5	–	Sn^{k}
97	USA	A380.0	7.5 9.5	3 4	0.1	1.3	0.5	3	0.5	–	Sn^{k}
98	USA	B380.0	7.5 9.5	3 4	0.1	1.3	0.5	1	0.5	–	Sn^{k}
99	USA	408.2	8.5 9.5	0.1	–	0.6 1.3	0.1	0.1	–	–	–
100	USA	359.2	8.5 9.5	0.1	0.55 0.7	0.12	0.1	0.1	–	0.2	–
101	USA	359.0	8.5 9.5	0.2	0.5 0.7	0.2	0.1	0.1	–	0.2	–
102	USA	A305.3	8.5 9.5	3 3.5	0.1	0.15	0.1	0.1	–	0.4	–
103	Russia	AK9M2	7.5 10	0.5 2	0.2 0.8	1	0.1 0.4	–	0.5	0.13	–
104	Russia	AK8M3	7.5 10	2 4.5	0.45	P-1.3	0.5	–	0.5	–	–

(*Continued*)

Table A.1.1 (Continued)

No.	Country	Alloy	Si	Cu	Mg	Fe	Mn	Zn	Ni	Ti	Other
105	Russia	AK9Ц6	8 10	0.3 1.5	0.3 0.5	0.3 1	0.1 0.6	5 7	0.3	–	(Sn+Pb)^{l}
106	USA	333.0	8 10	3 4	0.05 0.5	1	0.5	1	0.5	0.25	–
107	USA	A333.0	8 10	3 4	0.05 0.5	1	0.5	3	0.5	0.25	–
108	USA	333.1	8 10	3 4	0.1 0.5	0.8	0.5	1	0.5	0.25	–
109	USA	A333.1	8 10	3 4	0.1 0.5	0.8	0.5	3	0.5	0.25	–
110	USA	409.2	9 10	0.1	–	0.6 1.3	0.1	0.1	–	–	–
111	USA	A360.2	9 10	0.1	0.45 0.6	0.6	0.05	0.05	–	–	–
112	USA	360.2	9 10	0.1	0.45 0.6	0.7 1.1	0.1	0.1	0.1	–	Sn^{j}
113	USA	A360.0	9 10	0.6	0.4 0.6	1.3	0.35	0.5	0.5	–	Ni–Sn^{m}
114	USA	360.0	9 10	0.6	0.4 0.6	2	0.35	0.5	0.5	–	Sn^{b}

115	USA	A360.1	9 10	0.6	0.45 0.6	1	0.35	0.4	0.5	–	Sn[b]
116	Russia	AK9ч	8 10.5	0.3	0.17 0.3	S–0.6 P–1	0.2 0.5	0.3	0.1	–	–
117	USA	332.2	8.5 10.5	2 4	0.9 1.3	0.6	0.1	0.1	0.1	0.2	–
118	USA	332.0	8.5 10.5	2 4	0.5 1.5	1.2	0.5	1	0.5	0.25	–
119	USA	332.1	8.5 10.5	2 4	0.6 1.5	0.9	0.5	1	0.5	0.25	–
120	Russia	AK9Pч	9 10.5	0.1	0.23 0.3	0.3	0.2 0.35	0.3	–	0.12	–
121	USA	361.0	9.5 10.5	0.5	0.4 0.6	1.1	0.25	0.5	0.2 0.3	0.2	Cr–Sn[n]
122	USA	361.1	9.5 10.5	0.5	0.45 0.6	0.8	0.25	0.4	0.2 0.3	0.2	Cr–Sn[n]
123	Russia	AK9	8 11	1	0.2 0.4	P–1.3 S–0.9	0.2 0.5	0.5	0.3	–	–
124	Russia	AK10Cy	9 11		0.1 0.5	P–1.2	0.3 0.6		0.5	–	–
125	USA	383.2	9.5 11.5	2 3	0.1	0.6 1	0.1	0.1	0.1	–	Sn[j]

(Continued)

Table A.1.1 (Continued)

No.	Country	Alloy	Si	Cu	Mg	Fe	Mn	Zn	Ni	Ti	Other
126	USA	383.1	9.5 11.5	2 3	0.1	1	0.5	2.9	0.3	–	Sn^{b}
127	USA	383.0	9.5 11.5	2 3	0.1	1.3	0.5	0	0.3	–	Sn^{b}
128	USA	411.2	10 12	0.2	–	0.6 1.3	0.1	0.1	–	–	–
129	USA	384.2	10.5 12	3 4.5	0.1	0.6 1	0.1	0.1	0.1	–	Sn^{j}
130	USA	A384.1	10.5 12	3 4.5	0.1	1	0.5	0.9	0.5	–	Sn^{k}
131	USA	384.1	10.5 12	3 4.5	0.1	1	0.5	2.9	0.5	–	Sn^{k}
132	USA	A384.0	10.5 12	3 4.5	0.1	1.3	0.5	1	0.5	–	Sn^{k}
133	USA	384.0	10.5 12	3 4.5	0.1	1.3	0.5	3	0.5	–	Sn^{k}
134	USA	369.0	11 12	0.5	0.25 0.45	1.3	0.35	1	0.05	–	Cr–Sn^{o}
135	USA	369.1	11 12	0.5	0.3 0.45	1	0.35	0.9	0.05	–	Cr–Sn^{o}

136	USA	B413.1	11 13	0.05	0.1	0.4	0.1	0.1	0.05	0.25	–
137	USA	B413.0	11 13	0.05	0.1	0.5	0.1	0.1	0.05	0.25	–
138	USA	A413.2	11 13	0.05	0.1	0.6	0.1	0.05	0.05	–	Sn^b
139	USA	413.2	11 13	0.1	0.07	0.7 1.1	0.1	0.1	0.1	–	Sn^j
140	USA	A413.1	11 13	0.1	1	1	1	0.4	0.5	–	Sn^b
141	Russia	AK12(АЛ2)	11 13	0.6	0.2 0.15	P–1.5 S–0.7	0.5	0.3	–	–	–
142	USA	A413.0	11 13	1	0.1	1.3	0.35	0.5	0.5	–	Sn^b
143	USA	413.0	11 13	1	0.1	2	0.35	0.5	0.5	–	Sn^b
144	Russia	AK12MMгH	11 13	0.8 1.5	0.8 1.3	0.7	0.2	0.2	0.8 1.3	–	–
145	Russia	AK12M2	11 13	1.8 2.5	0.15	S–0.6 P–1	0.5	0.8	0.3	–	–
146	Russia	AK12M2MгH	11 13	1.5 3	0.8 1.3	0.8	0.3 0.6	0.5	0.8 1.3	0.13	–

(Continued)

Table A.1.1 (Continued)

No.	Country	Alloy	Si	Cu	Mg	Fe	Mn	Zn	Ni	Ti	Other
147	USA	385.1	11 13	2 4	0.3	1.1	0.5	2.9	0.5	–	Sn^q
148	USA	385.0	11 13	2 4	0.3	2	0.5	3	0.5	–	Sn^q
149	USA	A390.0	16 18	4 5	0.45 0.65	0.5	0.1	0.1	–	0.2	–
150	USA	390.0	16 18	4 5	0.45 0.65	1.3	0.1	0.1	–	0.2	–
151	USA	B390.0	16 18	4 5	0.45 0.65	1.3	0.5	1.5	0.1	0.2	–
152	USA	A390.1	16 18	4 5	0.5 0.65	0.4	0.1	0.1	–	0.2	–
153	USA	390.2	16 18	4 5	0.5 0.65	0.6 1	0.1	0.1	–	0.2	–
154	USA	B390.1	16 18	4 5	0.5 0.65	1	0.5	1.4	0.1	0.2	–
155	USA	392.0	18 20	0.4 0.8	0.8 1.2	1.5	0.2 0.6	0.5	0.5	0.2	Sn^q
156	USA	392.1	18 20	0.4 0.8	0.9 1.2	1.1	0.2 0.6	0.4	0.5	0.2	Sn^q

157	Russia	AK21M2.5H2.5	20 22	2.2 3	0.2 0.5	0.9	0.2 0.4	0.2	0.8 1.3	0.2	Cr[r]
158	USA	393.0	21 23	0.7 1.1	0.7 1.3	1.3	0.1	0.1	2 2.5	0.1 0.2	V[s]
159	USA	393.2	21 23	0.7 1.1	0.8 1.3	0.8	0.1	0.1	2 2.5	0.1 0.2	–
160	USA	393.1	21 23	0.7 1.1	0.8 1.3	1	0.1	0.1	2 2.5	0.1 0.2	–

[a] Cr 0.25
[b] Sn 0.15
[c] Sn 0.25
[d] Cr 0.1, Sn 0.5
[e] Be 0.12
[f] Cr 0.35
[g] Cr 0.05
[h] Be 0.2
[i] Cr 0.25–0.5; Sn 0.15
[j] Sn 0.1
[k] Sn 0.35
[l] (Sn+Pb) 0.3
[m] Ni 0.5, Sn 0.15
[n] Cr 0.2–0.3; Sn 0.1
[o] Cr 0.3–0.4; Sn 0.1
[p] Sn 0.05
[q] Sn 0.3
[r] Cr 0.3
[s] V 0.08–0.15

Table A.1.2 System Al–Cu (AA2xx)

No.	Country	Alloy	Cu	Mn	Mg	Si	Fe	Ni	Zn	Ti	Other
1	USA	242.2	3.5 4.5	0.1	1.3 1.8	0.6	0.6	1.7 2.3	0.1	0.2	–
2	USA	208.2	3.5 4.5	0.3	0.03	2.5 3.5	0.8	–	0.2	0.2	–
3	USA	242.0	3.5 4.5	0.35	1.2 1.8	0.7	1	1.7 2.3	0.35	0.25	Cr[a]
4	USA	242.1	3.5 4.5	0.35	1.3 1.8	0.7	0.8	1.7 2.3	0.35	0.25	Cr[a]
5	USA	243.1	3.5 4.5	0.15 0.45	1.9 2.3	0.35	0.3	1.9 2.3	0.05	0.06 0.2	Cr[b]
6	USA	243.0	3.5 4.5	0.15 0.45	1.7 2.3	0.35	<0.4	1.9 2.3	–	0.06 0.2	V[c]
7	USA	208.1	3.5 4.5	0.5	0.1	2.5 3.5	0.9	0.35	1	0.25	–
8	USA	208.0	3.5 4.5	0.5	0.1	2.5 3.5	1.2	0.35	1	0.25	–
9	USA	A242.2	3.7 4.5	0.1	1.3 1.7	0.35	0.6	1.8 2.3	0.1	0.07 0.2	Cr[d]
10	USA	A242.1	3.7 4.5	0.1	1.3 1.7	0.6	0.6	1.8 2.3	0.1	0.07 0.2	Cr[d]

11	USA	249.0	4.2 4.5	0.4	0.4	0.05	0.1	–	3	–	–
12	USA	204.2	4.2 4.9	0.05	0.2 0.35	0.15	0.1 0.2	0.03	0.05	0.15 0.25	Sn[e]
13	USA	A242.0	3.7 5	0.1	1.2 1.7	0.6	0.8	1.8 2.3	–	0.07 0.2	Cr[d]
14	USA	295.2	4 5	0.3	0.03	0.7 1.2	0.8	–	0.3	0.2	–
15	USA	296.2	4 5	0.3	0.35	2 3	0.8	–	0.3	0.2	–
16	USA	295.1	4 5	0.35	0.03	0.7 1.5	0.8	–	0.35	0.25	–
17	USA	295.0	4 5	0.35	0.03	0.7 1.5	1	–	0.35	0.25	–
18	USA	296.1	4 5	0.35	0.05	2 3	0.9	0.35	0.5	0.25	–
19	USA	296.0	4 5	0.35	0.05	2 3	1.2	0.35	0.5	0.25	–
20	USA	A201.0	4 5	0.2 0.4	0.15 0.35	0.05	0.1	–	–	0.15 0.35	Ag[f]
21	USA	A201.1	4 5	0.2 0.4	0.2 0.35	0.05	0.07	–	–	0.15 0.35	Ag[f]

(Continued)

A.1.2 (Continued)

No.	Country	Alloy	Cu	Mn	Mg	Si	Fe	Ni	Zn	Ti	Other
22	USA	A201.2	4 5	0.2 0.4	0.2 0.35	0.05	0.07	–	–	0.15 0.35	Ag[f]
23	USA	B201.0	4.5 5	0.2 0.5	0.25 0.35	0.05	0.05	–	–	0.15 0.35	Ag[g]
24	USA	204.0	4.2 5	0.1	0.15 0.35	0.2	0.35	0.05	–	0.15 0.3	Sn[e]
25	USA	A206.0	4.2 5	0.2 0.5	0.15 0.35	0.05	0.07	0.03	0.05	0.15 0.3	–
26	USA	206.0	4.2 5	0.2 0.5	0.15 0.35	0.1	0.15	0.05	0.1	0.15 0.3	Sn[e]
27	USA	A206.2	4.2 5	0.2 0.5	0.2 0.35	0.05	0.07	0.03	0.05	0.15 0.25	Sn[e]
28	USA	206.2	4.2 5	0.2 0.5	0.2 0.35	0.1	0.1	0.03	0.05	0.15 0.25	Sn[e]
29	Russia	AM4.5Kд	4.5 5.1	0.35 0.8	0.05	0.2	0.15	0.1	–	0.25	Zr[h]
30	USA	201.0	4 5.2	0.2 0.5	0.15 0.55	0.1	0.15	–	–	0.15 0.35	Ag[f]

31	USA	201.2	4 5.2	0.2 0.5	0.2 0.55	0.1	0.1	–	–	0.15 0.35	Ag^f
32	USA	203.2	4.8 5.2	0.2 0.3	0.1	0.2	0.35	1.3 1.7	–	0.15 0.25	Sb–Co–Zr^i
33	Russia	AM5	4.5 5.3	0.6 1	0.05	0.3	0.2(S) 0.3(M)	0.1	–	0.15 0.35	Zr^j
34	USA	203.0	4.5 5.5	0.2 0.3	0.1	0.3	0.5	1.3 1.7	–	0.15 0.25	Sb–Co–Zr^i
35	USA	224.2	4.5 5.5	0.2 0.5	–	0.02	0.04	–	–	0.25	V–Zr^k
36	USA	224.0	4.5 5.5	0.2 0.5	–	0.06	0.1	–	–	0.35	V–Zr^l
37	USA	213.0	6 8	0.6	0.1	1 3	1.2	0.35	2.5	0.25	–
38	USA	213.1	6 8	0.6	0.1	1 3	1	0.35	2.5	0.25	–
39	USA	240.1	7 9	0.3 0.7	5.6 6.5	0.5	0.4	0.3 0.7	0.1	0.2	–
40	USA	240.0	7 9	0.3 0.7	5.5 6.5	0.5	0.5	0.3 0.7	0.1	0.2	–
41	USA	222.0	9.2 10.7	0.15 0.35	0.15 0.35	2	1.5	0.5	0.8	0.25	–

(*Continued*)

Table A.1.2 (Continued)

No.	Country	Alloy	Cu	Mn	Mg	Si	Fe	Ni	Zn	Ti	Other
42	USA	222.1	9.2 10.7	0.5	0.2 0.35	2	12	0.5	0.8	0.25	–
43	USA	222.1	9.2 10.7	0.5	0.2 0.35	2	1.2	0.5	0.8	0.25	Zr–V[k]
44	USA	238.0	10 11	–	0.25	4	1.5	–	–	–	–

[a] Cr 0.25
[b] Cr 0.2–0.4
[c] V 0.06–0.2
[d] Cr 0.15–0.25
[e] Sn 0.05
[f] Ag 0.4–1
[g] Ag 0.5–1
[h] Zr 0.15
[i] Sb 0.2–0.3, Co 0.2–0.3, Zr 0.1–0.3
[j] Zr 0.2
[k] V 0.05–0.15, Zr 0.1–0.25
[l] V 0.1, Zr 0.2

Table A.1.3 System Al–Mg (AA5xx)

No.	Country	Alloy	Mg	Mn	Si	Fe	Cu	Zn	Ti	Be	Other
1	Russia	АЦ4Мг	1.5 2	0.2 0.5	–	0.5	–	3.5 4.5	0.1 0.2	–	–
2	USA	515.0	2.5 4	0.4 0.6	0.5 1	1.3	0.2	0.1	–	–	–
3	USA	515.2	2.7 4	0.4 0.6	0.5 1	0.6 1	0.1	0.05	–	–	–
4	USA	516.0	2.5 4.5	0.15 0.4	0.3 1.5	0.35 1	0.3	0.2	0.1 0.2	–	Ni[a]
5	USA	516.1	2.6 4.5	0.15 0.4	0.3 1.5	0.35 0.7	0.3	0.2	0.1 0.2	–	Ni[a]
6	USA	513.0	3.5 4.5	–	0.3	0.4	0.1	1.4 2.2	–	–	–
7	USA	514.0	3.5 4.5	–	0.35	0.5	0.15	0.15	–	–	–
8	USA	511.0	3.5 4.5	–	0.3 0.7	0.5	0.15	0.15	–	–	–
9	USA	512.0	3.5 4.5	–	1.4 2.2	0.6	0.35	0.35	–	–	–
10	USA	514.2	3.6 4.5	0.1	0.3	0.3	0.1	0.1	0.2	–	–

(Continued)

Table A.1.3 (Continued)

No.	Country	Alloy	Mg	Mn	Si	Fe	Cu	Zn	Ti	Be	Other
11	USA	513.2	3.6 4.5	0.1	0.3	0.3	0.1	1.4 2.2	0.2	–	–
12	USA	511.2	3.6 4.5	0.1	0.3 0.7	0.3	0.1	0.1	0.2	–	–
13	USA	512.2	3.6 4.5	0.1	1.4 2.2	0.3	0.1	0.1	0.2	–	–
14	USA	514.1	3.6 4.5	0.35	0.35	0.4	0.15	0.15	0.25	–	–
15	USA	511.1	3.6 4.5	0.35	0.3 0.7	0.4	0.15	0.15	0.25	–	–
16	Russia	АМг4К1	4.5 5.2	0.6 0.9	1.3 1.7	0.4	0.7 1	0.1	0.1 0.25	0.003	–
17	Russia	АМг5*к*	4.5 5.5	0.1 0.4	0.8 1.3	S-0.5 P-1.5	0.1	–	–	–	–
18	Russia	АМц5МЦ	4.8 6.3	0.4 1	0.3	0.3 0.5	0.3	–	0.05 0.15	–	–
19	Russia	АМг6лРч	6 7	0.1	0.05	0.05	0.05	0.05	0.05 0.15	0.05	Zr^b
20	Russia	АМг6л	6 7	0.1	0.2	0.2	0.15	0.1	0.05 0.15	0.05	Zr^b

21	USA	535.0	6.2 7.5	0.1 0.25	0.15	0.15	0.05	–	0.1 0.25	–	Cr[c]
22	USA	B535.0	6.5 7.5	0.05	0.15	0.15	0.1	–	0.1 0.25	–	–
23	USA	A535.0	6.5 7.5	0.1 0.25	0.2	0.2	0.1	–	–	–	–
24	USA	B535.2	6.6 7.5	0.05	0.1	0.12	0.05	–	0.1 0.25	–	–
25	USA	535.2	6.6 7.5	0.1 0.25	0.1	0.1	0.05	–	0.1 0.25	–	Be[d]
26	USA	A535.1	6.6 7.5	0.1 0.25	0.2	0.15	0.1	–	0.25	–	–
27	Russia	AMг7	6 8	0.25 0.6	0.5 1	0.9	0.1	0.2	–	–	–
28	USA	518.0	7.5 8.5	0.35	0.35	1.8	0.25	0.15	–	–	–
29	USA	518.2	7.6 8.5	0.1	0.25	0.7	0.1	–	–	–	Ni–Sn[e]
30	USA	518.1	7.6 8.5	0.35	0.35	1.1	0.25	0.15	–	–	Ni–Sn[f]
31	USA	585.0	10	0.15	0.25	0.3	0.25	0.15	0.25	–	–

(Continued)

Table A.1.3 (Continued)

No.	Country	Alloy	Mg	Mn	Si	Fe	Cu	Zn	Ti	Be	Other
32	Russia	АМг10	9.5 10.5	0.1	0.2	0.2	0.15	0.1	0.05 0.15	–	Zr[b]
33	USA	520.2	9.6 10.6	0.1	0.15	0.2	0.2	0.1	0.2	–	–
34	USA	520.0	9.5 10.6	0.18	0.25	0.3	0.25	–	–	0.005	–
35	Russia	АМг11	10.5 13	–	0.8 1.2	0.9	–	0.1	0.05 0.15	–	–
36	Russia	АЦ4Мг	1.5 2	0.2 0.5	–	0.5	–	3.5 4.5	0.1 0.2	–	–

[a] Ni 0.25–0.4, Sn 0.1, Pb 0.1max

[b] Zr 0.12

[c] Cr 0.005

[d] Be 0.003–0.007

[e] Ni 0.05, Sn 0.05

[f] Ni 0.15, Sn 0.15

APPENDIX TWO

PRINCIPAL CHARACTERISTICS OF BINARY PHASE DIAGRAMS CLOSER TO ALUMINUM SIDE*

Table A.2.1 Principal characteristics of binary phase diagrams closer to aluminum side

No.	Element	Reaction	C_a (mass%)	$C_{e,p}$ (mass%)	$T_{e,p}$ (°C)	Phase β
1	Ag	E	55.6	70	566	$AlAg_2$ (85–93%Ag)
2	As	E	<1?	<1?	~657	AlAs (73.5%As)
3	Au	E	0.35	5	642	Al_2Au (77.8–79%Au)
4	B	E	0.01	0.02	659.5	AlB_2 (44.5%B)
5	Ba	E	0.1	3.5	651–652	Al_4Ba (56%Ba)
6	Be	E	0.08	0.8	645	Be (>99%Be)
7	Bi	E (M)	<0.01	99.7	269	Bi (>99.7%Bi)
8	C	E	<0.01	<0.01	~660	Al_4C_3 (25.3%C)
9	Ca	E	~0.01	7.6	617	Al_4Ca (27%Ca)
10	Cd	E (M)	0.4	7.2	321	Cd (>99.9%Cd)
11	Ce	E	0.05	12	650	$CeAl_4$ (57%Ce)
12	Co	E	0.02	~1	657	Al_2Co_9 (32.7%Co)
13	Cr	P	0.8	0.4	661	$CrAl_7$ (22%Cr)
14	Cu	E	5.7	33.2	547	$CuAl_2$ (52%Cu)
15	Dy	E	0.05	35	637	Al_3Dy (69.8%Dy)
16	Er	E	0.05	~6	655	Al_3Er (67.3%Er)

(Continued)

Casting Aluminum Alloys
ISBN-13: 978-0-08-045370-5

© 2007 Elsevier Ltd.
All rights reserved.

Table A.2.1 (Continued)

No.	Element	Reaction	C_a (mass%)	$C_{e,p}$ (mass%)	$T_{e,p}$ (°C)	Phase β
17	Fe	E	0.05	1.8	655	$FeAl_3$ (40%Fe)
18	Ga	E	∼20	99	26.3	Ga (>99.95%Ga)
19	Gd	E (Рд)	0.2	25	652	Al_3Gd (68.9%Gd)
20	Ge	E	7.2	54	424	Ge (>99.5%Ge)
21	Hf	P	1.2	0.5	∼664	Al_3Hf (68.8%Hf)
22	In	E (M)	<0.01	99.95	155	In (>99.955In)
23	La	E	0.05	12	642	Al_4La (58.4%La)
24	Li	E	4.2	7.5	602	AlLi (17.8–25%Li)
25	Mg	E	17.4	35	450	Mg_5Al_8 (35%Mg)
26	Mn	E	1.8	1.9	658	$MnAl_6$ (25%Mn)
27	Mo	P	0.25	∼0.1	660.3	$Al_{12}Mo$ (22.6%Mo)
28	Na	E (M)	<0.002	∼100	97	Na (∼100%Na)
29	Nb	P	0.22	0.15	662	Al_3Nb (53.5%Nb)
30	Nd	E	0.05	30	637	$Al_{11}Nd_3$ (59.3%Nd)
31	Ni	E	0.04	6.0	640	$NiAl_3$ (42%Ni)
32	O	?	<0.001	?	∼660	Al_2O_3 (47.1%O)
33	P	?	<0.001	<0.015	∼660	AlP (53.5%P)
34	Pb	E (M)	<0.002	99.997	327	Pb (>99.997%Pb)
35	Pd	E	<0.002	23	605	Al_3Pd (56.9%Pd)
36	Pr	E	<0.1	∼12	654	Al_4Pr (56.6%Pr)
37	Pt	E	<0.1	7	657	$Al_{21}Pt_2$ (64.3%Pt)
38	Pu	E	∼0.06	13	652	Al_4Pu (69.2%Pu)
39	Re	E	∼0.01	∼2	∼597	$Al_{12}Re$ (36.4%Re)
40	S	E	<0.001	∼0.05	659	Al_2S_3 (63.2%S)
41	Sb	E	<0.1	∼1	658	AlSb (81.9%)

42	Sc	E	0.3	0.6	655	$ScAl_3$ (36%Sc)
43	Se	E	<0.001	<0.1	~657	Al_2Se (81.6%Se)
44	Si	E	1.65	12	577	(Si) (>99.5%Si)
45	Sm	E	<0.1	~15	633	Al_3Sm (64.9%)
46	Sn	E	~0.06	99.5	228	Sn (>99.6%Sn)
47	Sr	E	<0.01	<1	~659	Al_4Sr (44.8%Sr)
48	Ta	P	0.25	0.1	667	Al_3Ta (69.1%Ta)
49	Tb	E (Pd)	0.1	10	644	Al_3Tb (66.5%Tb)
50	Th	E	~0.8	~24	627	Al_3Th (74.2%Th)
51	Ti	P	1.3	0.12	661	$TiAl_3$ (37%Ti)
52	U	E	0.06	13	~647	Al_4U (68.8%U)
53	V	P	~0.1	~0.4	661	$Al_{10}V$ (15.8%V)
54	W	P	0.06	0.16	660	$Al_{12}W$ (36.2%W)
55	Y	E	0.17	9.5	637	Al_3Y (52.4%Y)
56	Zn	E	82	94.9	382	(Zn) (>99%Zn)
57	Zr	P	0.28	0.11	661	$ZrAl_3$ (53%Zr)

*Used notions for non-variant phase reactions: E, eutectic; P, peritectic; M, monotectic; Pd, peritectoid (see Figures 1.1 and 1.6).

This page intentionally left blank

APPENDIX THREE

GUARANTEED MECHANICAL PROPERTIES OF STANDARD RUSSIAN ALUMINUM ALLOYS

Table A.3.1 Guaranteed mechanical properties of standard Russian aluminum alloys

Alloy	Casting technique	Type of heat treatment	UTS (MPa)	Relative elongation (%)	Brinell hardness, HB
			Not less than		
AK12 (Aл2)	SM, MC, KM	–	147	4.0	50
	M	–	157	2.0	50
	P	–	157	1.0	50
	SM, MC, KM	T2	137	4.0	50
	M	T2	147	3.0	50
	P	T2	147	2.0	50
AK13 (AK13)	P	–	176	1.5	60
AK9 (AK9)	S, B, M, P, CSP	–	157	1.0	60
	M, P	T1	196	0.5	70
	SM, C	T6	235	1.0	80
	M	T6	245	1.0	90
AK9c (AK9c)	M, P	–	147	2.0	50

(*Continued*)

Casting Aluminum Alloys
ISBN-13: 978-0-08-045370-5

© 2007 Elsevier Ltd.
All rights reserved.

Table A.3.1 (Continued)

Alloy	Casting technique	Type of heat treatment	UTS (MPa)	Relative elongation (%)	Brinell hardness, HB
			Not less than		
	M	T1	196	1.5	70
	M	T6	235	3.5	70
АК9ч (Ал4)	S, B, M, P	–	147	2.0	50
	M, P, PP, KM, SM	T1	196	1.5	60
	SM, BM	T6	225	3.0	70
	M, CSP	T6	235	3.0	70
	S	T6	225	2.0	70
АК9Рч (Ал4-l)	S, B, M, P	–	157	3.0	50
	M, P, CSP	T1	196	2.0	70
	SM, BM	T6	245	3.5	70
	M, CSP	T6	265	4.0	70
АК8Р (Ал 34)	S	T5	294	2.0	85
	S	T4	255	4.0	70
	M	T5	333	4.0	90
	M	T4	274	6.0	80
	P	–	206	2.0	70
	P	T1	225	1.0	80
	P	T2	176	2.5	60
АК7 (АК7)	S	–	127	0.5	60
	M	–	157	1.0	60
	S	T5	176	0.5	75
	M	T5	196	0.5	75
	P	–	167	1.0	50

Table A.3.1 (Continued)

Alloy	Casting technique	Type of heat treatment	UTS (MPa)	Relative elongation (%)	Brinell hardness, HB
			Not less than		
	CSP	–	147	0.5	65
АК7ч (Ал19)	S, SC, M	–	157	2.0	50
	P	–	167	1.0	50
АК7ч (Ал19)	S, B, M, P	T2	137	2.0	45
	CSP	T4	186	4.0	50
	S, SC	T4	176	4.0	50
	M, CSP	T5	206	2.0	60
	S, SC	T5	196	2.0	60
	SM, MC	T5	196	2.0	60
	SM, MC	T6	225	1.0	70
	SM, MC	T7	196	2.0	60
	SM, MC	T8	157	3.0	55
	K	T6	235	1.0	70
	M	T7	196	2.0	60
	M	T8	157	3.0	55
АК7Рч (Ал9-1)	S, SC	T4	196	5.0	50
	M, KM	T4	225	5.0	50
	S, B	T5	235	4.0	60
	SM, CST	T5	235	4.0	60
	M, KM	T5	265	4.0	60
	CST, MC	T6	274	2.0	70
	M, MC	T6	294	3.0	70

(Continued)

Table A.3.1 (Continued)

Alloy	Casting technique	Type of heat treatment	UTS (MPa)	Relative elongation (%)	Brinell hardness, HB
			Not less than		
	P	–	196	1.0	50
	P	T2	167	2.0	45
	SC, MC	T7	206	2.5	60
	SC, MC	T8	167	3.5	55
AK10Cy (AK10Cy)	M	–	167	1.0	70
AK52 (AK5M2)	S	–	118	–	65
	M	–	157	0.5	65
	S	T5	196	–	75
	K	T5	206	0.5	75
	S	T8	147	1.0	65
	M	T8	176	2.0	65
	P	–	147	0.5	65
AK5M (Ал5)	S, B, M	T1	157	0.5	65
	S, B	T5	196	0.5	70
	M	T5	216	0.5	70
	S, B	T6	225	0.5	70
	S, B, M	T7	176	1.0	65
	M	T6	235	1.0	70
AK5Mч (Ал5-l)	S, B, M	T1	176	1.0	65
	S, B	T5	274	1.0	70
	M, MC	T5	294	1.5	70
	S, B, M	T7	206	1.5	65
AK6M2 (AK6M2)	M	T1	196	1.0	70
	M	–	230	2.0	78.4

Table A.3.1 (Continued)

Alloy	Casting technique	Type of heat treatment	UTS (MPa)	Relative elongation (%)	Brinell hardness, HB
			Not less than		
	M	T5	294	1.0	75
AK8M (Ал32)	S	T6	245	1.5	60
	M	T1	196	1.5	70
	M	T6	265	2.0	70
	P	–	255	2.0	70
	P	T2–1	255	1.7	70
	S	T5	235	2.0	60
	M	T5	255	2.0	70
	S	T7	225	2.0	60
	M	T7	245	2.0	60
	S	T1	176	0.5	60
	P	T1	284	1.0	90
	P	T2	235	2.0	60
AK5M4 (AK5M4)	S	–	118	–	60
	M	–	157	1.0	70
	M	T6	196	0.5	90
AK5M7 (AK5M7)	S	–	127	–	70
	M	–	157	–	70
	M	T1	167	–	90
	S	T1	147	–	80
	P	–	118	–	80
AK8M3 (AK8M3)	M	–	147	1.0	70
	M	T6	216	0.5	90

(*Continued*)

Table A.3.1 (Continued)

Alloy	Casting technique	Type of heat treatment	UTS (MPa)	Relative elongation (%)	Brinell hardness, HB
			Not less than		
AK8M3ч (BAл8)	M, CSP	T4	343	5.0	90
	K	T5	392	4.0	110
	P	–	294	2.0	75
	P	T5	343	2.0	90
	P	T2	215	1.5	60
	S	T5	345	1.0	90
	B	T5	345	2.0	90
	S	T7	270	1.0	80
	M	T7	295	2.5	85
AK9M2 (AK9M2)	M	–	186	1.5	70
	P	–	196	1.5	75
	M	T6	274	1.5	85
	M	T1	206	1.4	80
AK.12M2 (AKI2M2)	M	–	186	1.0	70
	P	T1	260	1.5	83.4
AKI2MMгH (Aл30)	M	T1	196	0.5	90
	M	T6	216	0.7	100
AKI2M2MгH (Aл25)	M	T1	186	–	90
AKI2M2.5H2.5	M	T2	157	–	90
(BKжлC-2	M	T1	186	–	100
AM5 (AлI9)	S, B, M	T4	294	8.0	70
	S, B, M	T5	333	4.0	90
	S	T7	314	2.0	80
AM4.5Kд (BAл 10)	S, B	T4	294	10.0	70

Table A.3.1 (Continued)

Alloy	Casting technique	Type of heat treatment	UTS (MPa)	Relative elongation (%)	Brinell hardness, HB
			Not less than		
	K	T4	314	12.0	80
	S, B	T5	392	7.0	90
	M	T5	431	8.0	100.0
	S, B	T6	421	4.0	110
	M	T6	490	4.0	120
	S	T7	323	5.0	90
АМгКl.5	M	T2	211	2.0	81
(АМг4К1.5М1)	M	T6	265	2.3	104
АМг5К (АлI3)	S, B, M	–	147	1.0	55
	P	–	167	0.5	55
АМг5Мц (Ал28)	S, B	–	196	4.0	55
	M	–	206	5.0	55
	P	–	206	3.5	55
АМг6л (АЛ23)	S, B	–	186	4.0	60
	M, P	–	216	6.0	60
	S, M, B	T4	225	6.0	60
АМг6лч (АЛ23-1)	S, B	–	196	5.0	60
	M, P	–	235	10.0	60
	S, M, B	T4	245	10.0	60
АМг10 (АЛ27)	S, M, P	T4	314	12.0	75
АМг10ч (АЛ27-1)	S, SC, M, P	T4	343	15.0	75
АМг11(АЛ22)	S, B, M	–	176	1.0	90
	S, B, M	T4	225	1.5	90

(*Continued*)

Table A.3.1 (Continued)

Alloy	Casting technique	Type of heat treatment	UTS (MPa)	Relative elongation (%)	Brinell hardness, HB
			Not less than		
	P	–	196	1.0	90
АМг7 (АЛ29)	P	–	206	3.0	60
АК7Ц9 (АЛ11)	S, B	–	196	2.0	80
	M	–	206	1.0	80
	P	–	176	1.0	60
	S, B, M	T2	216	2.0	80
АК9Ц6 (АК9Ц6р)	S	–	147	0.8	70
	M, P	–	167	0.8	80
АЦМг (АЛ24)	S, B	–	216	2.0	60
	S, B	T5	265	2.0	70

1. Notation: S – sand casting; MC – mold casting using cast models; M – mold casting; P – casting under pressure; CSP – casting with solidification under pressure (liquid stamping); SC – shell casting; AM – alloy was subjected to modifying.

2. Notation for different types of heat treatment: T1 – artificial aging without quench; T2 – annealing; T4 – quenching; T5 – quenching and short time (incomplete) aging (under-aging); T6 – quenching and complete artificial aging; T7 – quenching and stabilizing treatment; T8 – quenching and softening treatment.

3. Mechanical properties of alloys АК7Ц9 and АК9Ц6 are determined after not less than one day of aging.

4. Mechanical properties are presented for a given casting technique; could also be used for shell casting.

APPENDIX FOUR

RECOMMENDED HEAT TREATMENTS OF STANDARD RUSSIAN CASTING ALUMINUM ALLOYS

Casting Aluminum Alloys
ISBN-13: 978-0-08-045370-5

© 2007 Elsevier Ltd.
All rights reserved.

Table A.4.1 Recommended heat treatments of standard Russian casting aluminum alloys

		Quenching			Aging	
Alloy	Heat treatment	Heat-up temperature (°C)	Time of exposure (hours)	Cooling agent temperature (°C)	Heat-up temperature (°C)	Time of exposure (hours)
AK12	T2	–	–	–	300 ± 10	2–4
AK9	T1	–	–	–	175 ± 5	5–17
	T6	535 ± 5	2–6	Water (20–100)	175 ± 5	10–15
AK9ч	T1	–	–	–	175 ± 5	5–17
	T6	535 ± 5	2–6	Water (20–100)	175 ± 5	10–15
AK9Pч	T1	–	–	–	175 ± 5	5–17
	T6	535 ± 5	2–6	Water (20–100)	175 ± 5	10–15
AK8	T1	–	–	–	190 ± 5	3–4
	T2	–	–	–	300 ± 10	2–4
	T4	535 ± 5	10–16	Water (20–100)	–	–
	T5	535 ± 5	10–16	Water (20–100)	175 ± 5	6
AK7	T5	535 ± 5	2–7	Water (20–100)	150 ± 5	1–3
AK7ч	T2	–	–	–	300 ± 10	2–4
	T4	535 ± 5	2–6	Water (20–100)	–	–
	T5	535 ± 5	2–6	Water (20–100)	150 ± 5	1–3
AK7ч	T5	535 ± 5	2–6	Water (20–100)	*Two-step heating*	
					190 ± 10^a	0.5
					150 ± 5^b	2

	T6	535 ± 5	2–6	Water (20–100)	200 ± 5	2–5
	T7	535 ± 5	2–6	Water (80–100)	225 ± 10	3–5
	T8	535 ± 5	2–6	Water (80–100)	250 ± 10	3–5
AK7Pч	T2	–	–	–	250 ± 10	2–4
	T4	535 ± 5	2–12	Water (20–50)	–	–
	T5	535 ± 5	2–12	Water (20–50)	150 ± 5	3–10
	T6	535 ± 5	2–12	Water (20–50)	175 ± 5	3–10
	T7	535 ± 5	2–12	Water (80–100)	225 ± 10	3–5
	T8	535 ± 5	2–12	Water (80–100)	250 ± 10	3–5
AK5M2	T5	525 ± 5	3–5	Water (20–100)	175 ± 5	5–10
	T8	525 ± 5	3–5	Water (20–100)	250 ± 10	3–5
AK5M	T1	–	–	–	180 ± 5	5–10
	T5	525 ± 5	3–5	Water (20–100)	175 ± 5	5–10
	T5	*Two-step aging heat-up*				
	T5	515 ± 5[a]	3–5	–	–	–
		525 ± 5[b]	1–3	Water (20–100)	175 ± 5	5–10
	T6	525 ± 5	3–5	Water (20–100)	200 ± 5	3–5
	T7	525 ± 5	3–5	Water (20–100)	230 ± 10	3–5
		Two-step aging heat-up				
		515 ± 5[a]	3–5	–	–	–
		525 ± 5[b]	1–3	Water (20–100)	230 ± 10	3–5

(*Continued*)

Table A.4.1 (Continued)

Alloy	Heat treatment	Quenching			Aging	
		Heat-up temperature (°C)	Time of exposure (hours)	Cooling agent temperature (°C)	Heat-up temperature (°C)	Time of exposure (hours)
AK5Mч	T1	–	–	–	180 ± 5	5–10
	T5	525 ± 5	3–10	Water (20–100)	175 ± 5	5–10
	T5	*Two-step aging heat-up*				
		515 ± 5^a	3–7	–	–	–
		525 ± 5^b	2–5	Water (20–100)	175 ± 5	5–10
	T7	525 ± 5	3–10	Water (20–100)	230 ± 10	3–5
	T7	*Two-step aging heat-up*				
		515 ± 5^a	3–7	–	–	–
		525 ± 5^b	2–5	Water (20–100)	230 ± 10	3–5
AK6M2	T1	–	–	–	180 ± 5	5–10
	T5	525 ± 5	3–5	Water (20–100)	175 ± 5	5–10
AK8M	T1	–	–	–	200 ± 10	5–8
	T2	–	–	–	280 ± 10	5–8
	T5	*Two-step aging heat-up*				
		505 ± 5^a	4–6	–	–	–
		515 ± 5^b	4–8	Water (20–100)	150 ± 5	10–15
	T6	515 ± 5	2–8	Water (20–50)	170 ± 5	8–16
	T6	515 ± 5	2–8	Water (20–50)	*Two-step heat-up*	
					130 ± 5^a	2–3

					160 ± 5^b	4–6
	T6	*Two-step aging heat-up*				
		505 ± 5^a	4–6	–	–	–
		515 ± 5^b	4–8	Water (20–100)	170 ± 5	8–16
	T6	505 ± 5	4–6	–	–	–
	T6	515 ± 5	4–8	Water (20–100)	*Two-step heat-up*	
					130 ± 5^a	2–3
					160 ± 5^b	4–6
	T7	*Two-step aging heat-up*				
		505 ± 5^a	4–6	–	–	–
		515 ± 5^b	4–8	Water (80–100)	230 ± 5	3–5
AK5M4	T6	490 ± 10	5–7	Water (20–100)	170 ± 10	5–7
AK5M7	T1	–	–	–	180 ± 10	1–5
	T6	490 ± 10	5–7	Water (20–100)	185 ± 5	1–2
AK8 Mз	T6	500 ± 10	5–7	Water (20–100)	180 ± 10	5–10
AK8M3ч	T4	*Three-step aging heat-up*				
		490 ± 5^a	4–6	–	–	–
		500 ± 5^b	4–6	–	–	–
		510 ± 5^c	4–6	Water (20–100)	–	–
	T5	515 ± 5	4–6	Water (20–100)	160 ± 5	6–12

(Continued)

Table A.4.1 (Continued)

Alloy	Heat treatment	Quenching			Aging	
		Heat-up temperature (°C)	Time of exposure (hours)	Cooling agent temperature (°C)	Heat-up temperature (°C)	Time of exposure (hours)
AK9M2	T6	515 ± 5	5–7	Water (20–100)	200 ± 5	1–2
AKI2MMrH	T6	520 ± 5	4–6	Water (20–100)	180 ± 5	6–8
	T1	–	–	–	190 ± 10	6–12
	T6	520 ± 5	1.5–6	Water (20–70)	180 ± 5	12–16
					200 ± 5	and 6–8
					and 210 ± 10	
AKI2M2MrH	T1	–	–	–	–	10–12
AK5	T4	545	10–12	Water (20–100)		–
AM5	T4	*Two-step aging heat-up*				
		530 ± 5^a	5–9	–	–	–
		545 ± 5^b	5–9	Water (20–100)	175 ± 5	–
	T5	545 ± 5	10–12	Water (20–100)		3–6
		Two-step aging heat-up				
		530 ± 5^a	5–9	–	–	–
		545 ± 5^b	5–9	Water (20–100)	175 ± 5	3–6
	T7	545 ± 5	10–12	Water (80–100)	250 ± 10	3–10
	T7	*Two-step aging heat-up*				

		530 ± 5^a	5–9	–	–	
AM5	T7	545^b	5–9	Water (80–100)	250 ± 10	3–10
AM4.5Kд	T4	545	10–14	Water (20–100)		
		Two-step aging heat-up				
		535 ± 5^a	5–9	–	–	–
		545^b	5–9	Water (20–100)	–	–
	T5	545	10–14	Water (20–100)	155 ± 5	3–8
	T5	*Two-step aging heat-up*				
		535 ± 5^a	5–9		155 ± 5	3–8
		545^b	5–9	Water (20–100)	–	–
	T6	545	10–14	Water (80–100)	170 ± 5	6–10
	T6	*Two-step aging heat-up*				
		535 ± 5^a	5–9		–	–
		545^b	5–9	Water (20–100)	170 ± 5	6–10
	T7	545	10–14	Water (80–100)	250 ± 5	3–10
	T7	*Two-step aging heat-up*				
AM4.5Kл		535 ± 5^a	5–9			
		545^b	5–9	Water (80–100)	250 ± 5	3–10
AMг6	T4	430 ± 10	20	Water (100) or oil (20)	–	–

(*Continued*)

Table A.4.1 (Continued)

Alloy	Heat treatment	Quenching			Aging	
		Heat-up temperature (°C)	Time of exposure (hours)	Cooling agent temperature (°C)	Heat-up temperature (°C)	Time of exposure (hours)
АМг6лч	T4	430 ± 10	20	Water (100) or oil (20)	–	–
АМг10	T4	430 ± 10	20		–	–
АК7ц9	T2	300 ± 10	2–4	–	–	
Ац4Мг	T5	580 ± 5	4–6	Water (100)	120 ± 5	8–10
АМг11	T4	425 ± 5	15–20	Water (100) or oil (40–50)	175 ± 5	5–17
АК9с	T1	–	–	–	–	–
	T6	435 ± 5	2–6	Water (20–100)	175 ± 5	10–15

[a] Two-step heating before quenching for alloys AK5M, AM5, AK8M, and AM4.5KД is recommended only in those cases when massive fragments (higher than 40 mm) of cast parts are present; this is recommended in order to avoid non-equilibrium melting.
[b] To reduce residual stresses it is recommended to treat large complex castings with water at temperature 80–100°C.
[c] If higher strength (by ~10–15%) is required for casting made of alloyAK9ч. In the case of AK9Pч it is allowed to increased heat-up temperature before quenching to (545 ± 5)°C, accompanied by the mandatory reduction of iron concentration to 0.1–0.2% and manganese for alloy AJI4 down to 0.25–0.35%.

APPENDIX FIVE

DATA ON FRACTURE TOUGHNESS AND SHOCK TOUGHNESS, FATIGUE LIFE, CHARACTERISTICS OF THERMAL STABILITY, CORROSION RESISTANCE, AND CASTABILITY OF STANDARD AL–SI ALLOYS

Table A.5.1 Characteristics of crack resistance, fracture toughness, fatigue properties, and thermal stability

Alloy	Temper	K_{1c} (MPa $m^{1/2}$)	KCU (J/m^2)	σ^{a}_{-1} (MPa)	$\sigma^{300\,b}_{100}$ (MPa)	$\sigma^{300}_{0.2/100}$ (MPa)
AK12	T2	–	5	42	28/25	12
AK9	T5	–	2.4	75	–	–
AK9ч	T6	21	4	75	28/25	12.5
AK9Pч	T6	29	–	–	–	–
AK7	T5	–	3.7	70	–	–
AK7ч	T5	27	5(T4)	45(T4)	25	12
AK7Pч	T5	31	–	–	–	–
AK5M2	T5	–	2.6	65	–	–
AK5M	T5	22	3	65	35	24
AK5Mч	T5	26	–	–	–	–
AK5M4	T5	–	2.7	–	45	–
AK5M7	T6	–	2	50	–	–
AK8M3	T5	–	2.5	–	–	–

(Continued)

Casting Aluminum Alloys
ISBN-13: 978-0-08-045370-5

© 2007 Elsevier Ltd.
All rights reserved.

Table A.5.1 (Continued)

Alloy	Temper	K_{1c} (MPa m$^{1/2}$)	KCU (J/m^2)	σ^{a}_{-1} (MPa)	$\sigma^{300\,b}_{100}$ (MPa)	$\sigma^{300}_{0.2/100}$ (MPa)
AK8M3ч	T6	23	–	–	–	–
AK12M2	T1	–	25	–	–	–
AK12MMгH	T1	–	–	–	40	–
AK12M2MгH	T1	–	4	–	45	–
AK21M2.5H2.5	T1	–	1.2	–	–	–

[a] Limited fatigue strength σ_{-1} was determined for 2×10^7 or 2×10^8 applied cycles of loading with alternating bending. [b] Top – data for non-modified alloy σ^{300}_{100}; denominator – modified alloy.

Table A.5.2 Corrosion resistance of Al–Si alloys

Alloy	Corrosion rate (g/m^2 hour)		Loss in mechanical properties* (%)	
	In atmosphere	In water + 3% NaCl + 0.1% H_2O_2	$\Delta\sigma$	$\Delta\delta$
AK9ч	–	–	7.1 (w/o casting crust) 4.7(with casting crust)	54.6 41.4
AK9	0.002	0.21	–	–
AK7ч	–	–	6.3 (w/o casting crust) 6.2 (with casting crust)	23.5 42.1
AK5M	–	–	44.2 (w/o casting crust) 29.5 (with casting crust)	38.4 41.5
AK7	0.0008	0.2	–	–
AK5M2	0.14	0.24	–	–
AK5M4	0.015	0.25	–	–

*After corrosion during 3 months in aqueous solution of 3%NaCl + 0.1H_2O_2.

Table A.5.3 Casting properties of standard Al–Si alloys

Alloy	Molten fluidity (mm)[a]		Linear shrinkage (%)[b]	Hot cracking index (mm)[c]	Hermeticity		
	Rod	Spiral			HT[d]	P (N_2) (ΓPa)[e]	P (H_2O) (ΓPa)[e]
AK12	420	820	0.9–1.1	<5	T2	3	12. fracture
AK9	350	780	1.0–1.1	<5	–	–	–
AK9ч	360	800	1.0–11	<5	T6	3	20. fracture
AK7	340	760	1.0–1.2	<5	–	–	–
AK7ч	350	770	1.0–1.2	<5	T5	30	14. fracture
AK5M	340	750	1.1–1.2	7.5	T6	3	16. fracture
AK5M2	330	730	1.2–1.25	7.5	–	–	–
AK5M7	–	–	0.9–1.1	17.5	–	–	–
AK12M2MrH	425	–	1.15	5.0	T2	3	15. fracture
AK7Ц9	–	–	1.2–1.4	<5	T2	3	15. fracture

[a] Molten metal fluidity index (molten metal temperature 700°C).

[b] Total linear shrinkage.

[c] Hot cracking index (critical ring diameter using VIAM's probe).

[d] HT stands for Heat Treatment.

[e] Pressure of nitrogen and water vapor.

This page intentionally left blank

DERIVATION OF EQUATIONS DESCRIBING UNIAXIAL TENSILE TESTING IN FINITE DEFORMATIONS

In this Appendix equations are derived, following[1], to rigorously calculate true (Cauchy) stress and true strain for tests where cross-head displacement is measured for strain surrogate. Examples of tests which could benefit from this rigorous analysis include, for example, step-change strain rate sensitivity tests. It also shows an example where corrections for finite deformations are made for a uniaxial tension test which uses an extensometer to measure strain.

Typically the goal of testing is to probe the mechanical properties of the sample itself rather than the combined responses of the material element and the machine. In practice this corresponds to the case of a perfectly rigid machine (constant strain rate testing). In constant strain rate testing, displacements are controlled on the ends of the specimen, while at constant stress rate (soft machine) conditions tractions are subject to control. Obviously, in the real life some intermediate situation always develops, and modern servohydraulic machines can behave in a very soft or very stiff manner.[2] In this situation it is important to understand how the generalized stiffness of the "sample + machine" system, K, affects the results of mechanical testing. Knowledge of the effects of K on the strain to the onset of serrated flow or the point of instability in fracture work is especially valuable. Equally important, since plastic instabilities *develop at finite, rather than infinitesimally small deformations*, it is critical to assess how the introduction of different measures of stress and strain (see below) affects the results of mechanical testing and the measured behavior of a given material.

The results of computer simulations of propagative plastic instabilities[3] indicate that the nature of instability itself may change depending on the value of the generalized stiffness K, that is, at some critical value of K the Portevin–Le Chatelier serrations become impossible, and the Luders-type phenomena are observed instead. In modeling work[4] it was established that a continuous transition from PLC- to Luders-type instability takes place with the increase of the machine stiffness K (Figure A.6.1).

---

[1] Glazov M.V., Braginsky M.V., Lalli L.A. and Richmond O. On the derivation and analysis of the "Machine Equation" in finite deformations. *Appl. Phys. A (Springer–Verlag)*, 1998, Vol. 67, No. 5, pp. 571–578.

[2] The bulge test, for example, is run in engineering strain control to achieve constant true strain rate conditions. On the other hand, more sophisticated techniques must be used in order to vary the degree of stiffness depending on the specimen strain; this is important when determining the tearing modulus in fracture toughness experiments.

[3] See Glazoff M.V. *et al.*, *Metallurgical and Materials Transactions*, Vol. 30A, 1999, pp. 387–397.

[4] Zaiser M., Glazov M.V., Lalli L.A. and Richmond O. On the relations between strain- and strain-rate softening phenomena in some metallic materials: a computational study. *Comput. Mater. Sci.*, 1999, Vol. 15, pp. 35–49.

Casting Aluminum Alloys
ISBN-13: 978-0-08-045370-5

© 2007 Elsevier Ltd.
All rights reserved.

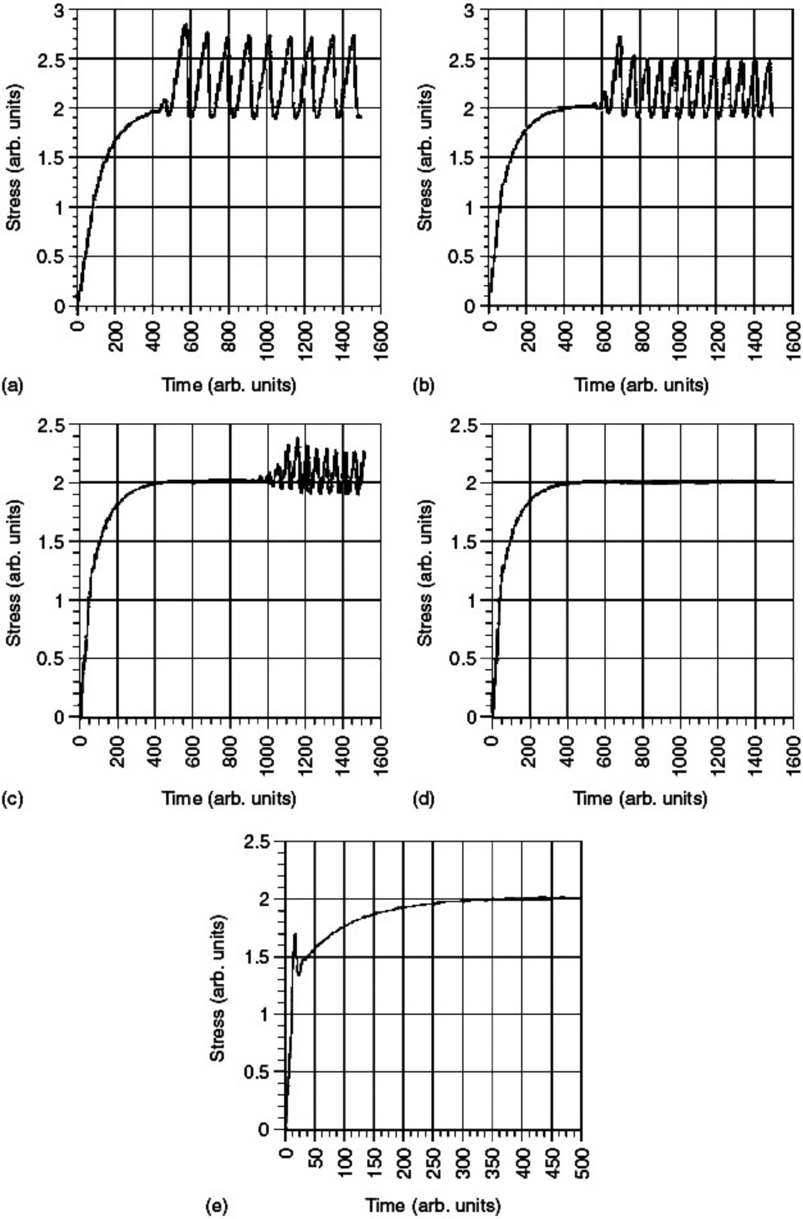

Figure A.6.1 Modeling of continuous transition from repeated yielding to the Luders phenomenon as a function of the increased generalized stiffness of the system "sample + machine".[3]

Obviously, this situation calls for a careful analysis of the so-called "machine equation" *for the case of finite deformations* which relates the mechanical properties of a sample (i.e., stress–strain curve) to the mechanical response registered by a testing machine and consequently serves as a scientific basis for interpreting the data of mechanical tests. As follows from the analysis below, in some cases even a reliable interpretation of mechanical testing data can be seriously distorted if the mechanical properties of the testing machine and geometrical characteristics of the sample are not taken into account. Consideration of the responses of the test material and the testing machine can help explain numerous previous experimental data concerning the influence of testing machine (e.g., "Instron" vs "Tinius Olsen" vs "Baldwin") on important mechanical properties of aluminum alloys such as the strain to the onset of serrated flow.

A.6.1 THE CASE OF INFINITESIMALLY SMALL DEFORMATIONS

Initially, it will be assumed that deformation of the sample is small and, thus, there is no need to introduce different measures of (finite) strain and stress. The following assumptions are implied: (1) the plastic deformation of the machine is negligible compared to the deformation of the sample (which is trivial – otherwise the machine will be useless after several tests); (2) the deformation of the sample is homogeneous (i.e., we neglect all effects of strain localization, propagating plastic instabilities of the Portevin–Le Chatelier and Luders type, etc.); and (3) the deformations of the sample and of the "machine" are small. Consider the following simple scheme given in Figure A.6.2.

The rectangle in this schematic denotes the sample, and the bold solid arrow-headed line is the "spring" characterizing the machine stiffness. Displacement of the right-hand side of the sample is zero, displacement of its left-hand side is denoted as u_s, while the total displacement of the system (sample + "spring") is denoted u_t (the measured displacement). The "spring" is characterized by its stiffness k, while the sample is characterized by its Young's modulus E. The stress–strain state is one-dimensional. Since the total displacement is a combination of the displacements of the sample and of the "spring", one can write:

$$u_t = u_s + \frac{P}{k} = u_s + \frac{\sigma A_0}{k} \tag{A.6.1}$$

with P denoting the force; A_0, the area of the sample cross-section; and σ, the normal stress in the sample. Assuming that the sample is deformed homogeneously and using displacements instead of deformations:

$$\dot{\sigma} = \frac{E}{l_0}[\dot{u}_s - (\dot{u}_s)^p] \tag{A.6.2}$$

where the superscript p denotes the plastic part, and l_0 denotes the length of the sample. We can also take a time derivative of equation (A.6.1) and substitute

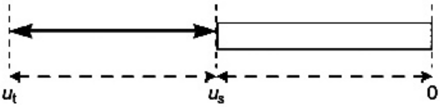

Figure A.6.2 On the derivation of the machine equation.[1]

equation (A.6.2) into it (neglecting upon differentiation the change of cross-sectional area in the course of deformation):

$$\dot{u}_t = \dot{u}_s + \frac{\dot{P}}{k} = \dot{u}_s + \frac{\dot{\sigma} A_0}{k} = \frac{EA_0 + kl_0}{kl_0}\dot{u}_s - \frac{EA_0}{kl_0}(\dot{u}_s)^P \tag{A.6.3}$$

From equation (A.6.3) it is obvious that

$$\dot{u}_s = \frac{kl_0}{EA_0 + kl_0}\dot{u}_t + \frac{EA_0}{EA_0 + kl_0}(\dot{u}_s)^P \tag{A.6.4}$$

After substitution of this result into equation (A.6.2):

$$\dot{\sigma} = \frac{kE}{EA_0 + kl_0}[\dot{u}_t - \dot{u}_s^P] \tag{A.6.5}$$

The coefficient $kE/(EA_0 + kl_0)$ is usually called "*the generalized stiffness*" of the "sample + machine" system, and equation (A.6.5) is traditionally called the "machine equation". In the case of an infinitely stiff machine ($k \to \infty$) the generalized stiffness of the sample + machine system simply becomes equal to the elastic (Young's) modulus of the sample divided by its total length. In this, and only in this case we can expect to measure "true" constitutive properties of the sample material which will not be "contaminated" by machine influence. However, in all other cases the geometrical characteristics of the sample, such as its cross-sectional area and length will affect the value of generalized stiffness. The same is true with respect to machine stiffness. Specifically, for very thin wires (which are characterized by a small value of cross-sectional area A_0) the measured mechanical response of the material sample will be stiffer compared to a thicker specimen.

In terms of deformation rates, equation (A.6.5) should be rewritten in the following form:

$$\dot{\sigma} = \frac{kEl_0}{EA_0 + kl_0}[\dot{e}_t^* - \dot{e}_s^P] = \frac{kE}{E\dfrac{A_0}{l_0} + k}[\dot{e}_t^* - \dot{e}_s^P] \tag{A.6.6}$$

where $\dot{e}_s^P$ is the plastic part of a deformation rate of the sample. It is important that $\dot{e}_t^*$ is not a deformation rate of any physical object, but just a time derivative of *the total displacement* divided by the instantaneous length of *the sample*. Where it is divided by the total length (sample + "spring") it would represent a total deformation rate, but for the whole system the assumption of homogeneous deformation is definitely not valid, and the length of the "spring" is not known.

A.6.2 THE CASE OF FINITE DEFORMATIONS

If total strain of the sample becomes sufficiently large (say, $\varepsilon > 0.1$), as it is inevitable in any work on fracture or plastic instabilities of metals, it becomes necessary to introduce finite strains and different measures of stress and strain. This implies that the initial (reference) configuration no longer instantaneously coincides with the current (deformed) configuration and, as a result, different "families" of stress and strain tensors can be determined with respect to these two configurations. As always, a Lagrangian tensor field can be defined in the initial (reference) configuration, while an Eulerian tensor field represents the current (deformed) configuration. A tensor field will be considered objective (i.e., not dependent on the observer) if it is unaffected by the superposed rigid body motion. It is also possible to introduce so-called "two-point" second order tensors which are defined with respect to both configurations. Examples include: a true (Cauchy) stress tensor σ (Eulerian objective), a nominal (or 1st Piola–Kirchoff) stress tensor (two-point objective), a 2nd Piola–Kirchoff stress tensor (Lagrangian objective, "symmetrized" 1st Piola–Kirchoff) and so on. The mechanical experiment under consideration still remains a simple uniaxial tension test with controlled cross-head velocity, and the process is supposed to be homogeneous and steady state. Consequently, the following basic assumptions will be made in the analysis: (1). Force and displacement/velocity of the machine head are measured; (2) Constitutive relationship connects true (Cauchy) stress and it's work-congugate deformation rate, which in this case is just the rate of the logarithmic Lagrangian strain (see below).

Consider a simple process of deformation – uniform extension with lateral contraction (also uniform due to symmetry). It will be assumed that plastic deformation of the machine is negligible compared to the plastic deformation of the sample itself. Since plasticity is essentially a rate problem, differentiation of equation (A.6.1) with respect to time gives:

$$\dot{u}_t = \dot{u}_s + \frac{\dot{P}}{k} \tag{A.6.7}$$

No assumptions are made concerning which quantity is controlled – it can be either velocity (in this case $\dot{u}_t = V$) or force rate. In the analysis of the constitutive relations, consider the following *deformation rate* tensor $\mathbf{D}$:

$$\mathbf{D} = \frac{1}{2}(\nabla\mathbf{v} + \mathbf{v}\nabla) \tag{A.6.8}$$

with $\nabla\mathbf{v}$ denoting the gradient of velocity in the *deformed* configuration. Deformation rate is sometimes called strain rate, but it is important to emphasize that there is no strain tensor for which its time derivative is equal to $\mathbf{D}$. In order to continue analysis it is necessary to consider a special process of deformation for which the principal directions of the Lagrangian strain do not vary with time, that is:

$$\mathbf{F}(t) = \mathbf{R}(t)\cdot\mathbf{U}(t)$$

$$\mathbf{U}(t) = \lambda_{\bar{i}}\mathbf{N}_i\mathbf{N}_i \tag{A.6.9}$$

The first of these equations represents the *polar decomposition* of the deformation gradient **F** into an orthogonal tensor **R** and symmmetric positive-definite tensor **U**, while the second equation represents an eigenvalue–eigenvector decomposition of **U** in which $\mathbf{N}_i$ are the principal directions and $\lambda_{\bar{i}}$ are the principal values of Lagrangian deformation. Horizontal bar in the subscript of $\lambda_{\bar{i}}$ in (9) is used to avoid confusion with the Einstein's summation convention which is used in the formula. In this case it can be proven that $\mathbf{D} = \mathbf{R}\cdot\dot{\mathbf{E}}\cdot\mathbf{R}^{\mathrm{T}}$, where $\mathbf{E} = \ln\mathbf{U}$ (logarithmic Lagrangian strain). In the mechanical experiment which is considered here we have a very simple process of deformation (i.e., uniform extension with lateral contraction). In this case it can be demonstrated that:

$$\mathbf{F}(t) = \mathbf{U}(t); \quad \mathbf{R}(t) = \mathbf{I}$$

$$\mathbf{D} = \mathbf{R}\cdot\dot{\mathbf{E}}\cdot\mathbf{R}^{\mathrm{T}} = \dot{\mathbf{E}} \tag{A.6.10}$$

This result automatically implies that for the deformation process under consideration, the deformation rate **D** is the rate of the natural, or logarithmic, strain. In uniaxial tension tests considered here the engineering strain is defined as $\varepsilon = \Delta L/L_0 = L/L_0 - 1 = \xi - 1$, whereas the natural (logarithmic) strain is equal to $\ln(L/L_0) = \ln(1+\varepsilon)$. For small strains ($\varepsilon$ is small) these two measures become identical . However, in the case of finite strains it is more convenient ("natural") to use the logarithmic strain because of its important property of additivity. Specifically, in a series of deformations $L_0 \rightarrow L_1 \rightarrow L_2 \rightarrow \cdots \rightarrow L_n$, the engineering strain is not additive, while for logarithmic strain, in terms of finite increments the strains are additive:

$$\varepsilon^n = \ln(L_1/L_0) + \ln(L_2/L_1) + \cdots + \ln(L_n/L_{n-1}) = \ln\prod_{i=1}^{n}(L_i/L_{i-1}) = \ln(L_n/L_0)$$

Consider now the total stretch ratio of the sample, ξ_s, as the elastic stretch superimposed onto the plastic stretch:

$$\xi_s = \xi_{\mathrm{el}}\cdot\xi_{\mathrm{pl}} = \frac{l_s}{l_{\mathrm{pl}}}\frac{l_{\mathrm{pl}}}{l_0} \tag{A.6.11}$$

For the logarithmic strains expressed in terms of stretch ratios, we get: $\varepsilon_s = \ln\xi_s = \ln\xi_{\mathrm{el}} + \ln\xi_{\mathrm{pl}} = \varepsilon_{\mathrm{el}} + \varepsilon_{\mathrm{pl}} = \frac{\sigma}{E} + \varepsilon_{\mathrm{pl}}$. Notice that $u_s = (\xi_s - 1)l_0$ and $\dot{u}_s = \dot{\xi}_s l_0$. Taking this into account, one can write down:

$$\dot{\sigma}/E = (\varepsilon_s - \varepsilon_{\mathrm{pl}})^{\cdot} = \dot{\varepsilon}_s - \dot{\varepsilon}_{\mathrm{pl}} \tag{A.6.12}$$

Consider now the time derivative of force having in mind that we need the connection of this derivative with the true (Cauchy) stress, since this is the measure of stress present in the constitutive relations. In general tensor form:

$$\begin{aligned} \mathbf{P} &= \mathbf{N}\cdot \mathbf{t}A_0 \\ \dot{\mathbf{P}} &= \mathbf{N}\cdot \dot{\mathbf{t}}A_0 \end{aligned} \tag{A.6.13}$$

where $\mathbf{N}$ denotes the unit normal to the cross-section, where the force is applied, while A_0 is the initial area of this cross-section and $\mathbf{t}$ is the nominal (1st Piola–Kirchoff) stress tensor. The nominal stress is connected with the true (Cauchy) stress by the following relation: $\mathbf{t} = J\mathbf{F}^{-1}\cdot\boldsymbol{\sigma}$, where $\mathrm{J} = \det(\mathbf{F})$ (i.e., the determinant of the deformation gradient). As a result, for the time derivative of the nominal stress we get:

$$\dot{\mathbf{t}} = \dot{J}\mathbf{F}^{-1}\cdot\boldsymbol{\sigma} + J(\dot{\mathbf{F}}^{-1})\boldsymbol{\sigma} + J\mathbf{F}^{-1}\cdot\boldsymbol{\sigma} \tag{A.6.14}$$

Using some simple tensor algebra we can rewrite equation (A.6.19) in the following form:

$$\dot{\mathbf{t}} = J\mathbf{F}^{-1}\cdot(\boldsymbol{\sigma} + D_{kk}\boldsymbol{\sigma} - \mathbf{L}\cdot\boldsymbol{\sigma}) \tag{A.6.15}$$

Taking into account that for our deformation process the vorticity tensor is identically equal to zero:

$$\mathbf{F} = \begin{bmatrix} \lambda_1 & 0 & 0 \\ 0 & \lambda_2 & 0 \\ 0 & 0 & \lambda_3 \end{bmatrix} \quad \mathbf{F}^{-1} = \begin{bmatrix} \lambda_1^{-1} & 0 & 0 \\ 0 & \lambda_2^{-1} & 0 \\ 0 & 0 & \lambda_3^{-1} \end{bmatrix}$$

$$\mathbf{D} = \mathbf{L} = \dot{\mathbf{F}}\cdot\mathbf{F}^{-1} = \begin{bmatrix} \dot{\lambda}_1\lambda_1^{-1} & 0 & 0 \\ 0 & \dot{\lambda}_2\lambda_2^{-1} & 0 \\ 0 & 0 & \dot{\lambda}_3\lambda_3^{-1} \end{bmatrix} \tag{A.6.16}$$

$$J = \lambda_1\lambda_2\lambda_3; \quad D_{kk} = \dot{\lambda}_1\lambda_1^{-1} + \dot{\lambda}_2\lambda_2^{-1} + \dot{\lambda}_3\lambda_3^{-1}$$

Finally we get:

$$\dot{\mathbf{t}} = \lambda_2\lambda_3\{\boldsymbol{\sigma} + (\dot{\lambda}_1\lambda_1^{-1} + \dot{\lambda}_2\lambda_2^{-1} + \dot{\lambda}_3\lambda_3^{-1})\boldsymbol{\sigma} - \dot{\lambda}_1\lambda_1^{-1}\boldsymbol{\sigma} \tag{A.6.17}$$

This is as far as the analysis can be extended without making additional constitutive assumptions on the connection between the three stretches. Obviously, many possibilities can be considered, and the simplest, although physically not very realistic, would be to assume that there are no lateral stretches, that is:

Case 1: $\lambda_2 = \lambda_3 = 0$. It is the simplest possible case. This assumption immediately leads to the identical equality of the nominal stress and the true Cauchy stress and their time derivatives (i.e. $\mathbf{t} = \boldsymbol{\sigma}$). This means that in terms of finite deformations, the equations remain the same as in the case of small deformations. Obviously, this case does not make much sense.

Case 2: The material is incompressible, that is, $J = 1$, $D_{kk} = 0$. In this case:

$$\dot{t} = \frac{1}{\lambda_1}(\dot{\sigma} - \dot{\lambda}_1 \lambda_1^{-1} \sigma) \tag{A.6.18}$$

Notice that in this particular case λ_1 corresponds to ξ_s. We get:

$$\dot{u}_t = \dot{\xi}_s l_0 + \frac{A_0(\dot{\sigma} - \dot{\xi}_s \xi_s^{-1} \sigma)}{K \xi_s} \tag{A.6.19}$$

This gives the connection between the total measured displacement/velocity and the deformation of the sample. For more details in this case the interested reader is referred to [Glaz4, Gla6].

Case 3: Plastic deformation is incompressible. This is more complicated than the previous case. It is still assumed that the mechanical experiment results in uniaxial extension accompanied by lateral contraction, but now it will be additionally assumed that this is true for both elastic and plastic deformation *independently* (before this assumption was made for the total deformation of the sample, which can be viewed as a superposition of elastic deformation over plastic deformation). Consider the multiplicative decomposition of the total deformation gradient of the material element into plastic and elastic deformation gradients: $\mathbf{F}_s = \mathbf{F}_{el} \cdot \mathbf{F}_{pl}$. Taking into account the stated assumptions on the deformation, it is easy to give the following representation for these deformation gradients:

$$\mathbf{F}_{el} = \begin{bmatrix} \xi_{el} & 0 & 0 \\ 0 & \xi_{el}^{-\nu} & 0 \\ 0 & 0 & \xi_{el}^{-\nu} \end{bmatrix} \tag{A.6.20}$$

where ν in formula (20) stands for the Poisson's ratio. Additional stretches can be easily found from the Hooke's law, assuming that it connects logarithmic strain with stress and also taking the symmetry considerations into account:

$$\frac{\sigma}{E} = \ln \xi_{el} - \frac{\nu\sigma}{E} = \ln \xi_2 = \ln \xi_3 \tag{A.6.21}$$

This results in $\ln \xi_2 = \ln \xi_3 = -\nu \ln \xi_{el}$ For the plastic deformation gradient, using the considerations of incompressibility and symmetry:

$$\mathbf{F}_{pl} = \begin{bmatrix} \xi_{pl} & 0 & 0 \\ 0 & \dfrac{1}{\sqrt{\xi_{pl}}} & 0 \\ 0 & 0 & \dfrac{1}{\sqrt{\xi_{pl}}} \end{bmatrix} \tag{A.6.22}$$

For the total deformation gradient:

$$\mathbf{F}_{\mathrm{s}} = \begin{bmatrix} \xi_{\mathrm{el}}\xi_{\mathrm{pl}} & 0 & 0 \\ 0 & \dfrac{\xi_{\mathrm{el}}^{-\nu}}{\sqrt{\xi_{\mathrm{pl}}}} & 0 \\ 0 & 0 & \dfrac{\xi_{\mathrm{el}}^{-\nu}}{\sqrt{\xi_{\mathrm{pl}}}} \end{bmatrix} \tag{A.6.23}$$

$$\mathbf{F}_{\mathrm{s}}^{-1} = \begin{bmatrix} \dfrac{1}{\xi_{\mathrm{el}}\xi_{\mathrm{pl}}} & 0 & 0 \\ 0 & \xi_{\mathrm{el}}^{\nu}\sqrt{\xi_{\mathrm{pl}}} & 0 \\ 0 & 0 & \xi_{\mathrm{el}}^{\nu}\sqrt{\xi_{\mathrm{pl}}} \end{bmatrix} \tag{A.6.24}$$

$$\mathbf{D} = \mathbf{L} = \dot{\mathbf{F}}_{\mathrm{s}} \cdot \mathbf{F}_{\mathrm{s}}^{-1} = \begin{bmatrix} \dfrac{\dot{\xi}_{\mathrm{el}}}{\xi_{\mathrm{el}}} + \dfrac{\dot{\xi}_{\mathrm{pl}}}{\xi_{\mathrm{pl}}} & 0 & 0 \\ 0 & -\nu\dfrac{\dot{\xi}_{\mathrm{el}}}{\xi_{\mathrm{el}}} - \dfrac{1}{2}\dfrac{\dot{\xi}_{\mathrm{pl}}}{\xi_{\mathrm{pl}}} & 0 \\ 0 & 0 & -\nu\dfrac{\dot{\xi}_{\mathrm{el}}}{\xi_{\mathrm{el}}} - \dfrac{1}{2}\dfrac{\dot{\xi}_{\mathrm{pl}}}{\xi_{\mathrm{pl}}} \end{bmatrix} \tag{A.6.25}$$

$$J = \xi_{\mathrm{el}}^{1-2\nu};\ D_{kk} = (1-2\nu)\frac{\dot{\xi}_{\mathrm{el}}}{\xi_{\mathrm{el}}} \tag{A.6.26}$$

Taking into account the fact that only one component of stress is non-zero, the following equation can be obtained:

$$\dot{t} = \xi_{\mathrm{pl}}\xi_{\mathrm{el}}^{-2\nu}\left[\dot{\sigma} - \left(\frac{\dot{\xi}_{\mathrm{pl}}}{\xi_{\mathrm{pl}}} + 2\nu\frac{\dot{\xi}_{\mathrm{el}}}{\xi_{\mathrm{el}}}\right)\sigma\right] \tag{A.6.27}$$

Substituting equation (A.6.30) into the rate form of the machine equation:

$$\dot{u}_{\mathrm{t}} = (\dot{\xi}_{\mathrm{el}}\dot{\xi}_{\mathrm{pl}} + \xi_{\mathrm{el}}\dot{\xi}_{\mathrm{pl}}) \cdot l_0 + \frac{A_0\xi_{\mathrm{pl}}\xi_{\mathrm{el}}^{-2\nu}\left[\dot{\sigma} - \left(\dfrac{\dot{\xi}_{\mathrm{pl}}}{\xi_{\mathrm{pl}}} + 2\nu\dfrac{\dot{\xi}_{\mathrm{el}}}{\xi_{\mathrm{el}}}\right)\sigma\right]}{K} \tag{A.6.28}$$

Elastic stretch and strain rate can be determined from equation (A.6.31) in the following form:

$$\xi_{\mathrm{el}} = \exp\left(\frac{\sigma}{E}\right);\ \dot{\varepsilon}_{\mathrm{el}} = \frac{\dot{\xi}_{\mathrm{el}}}{\xi_{\mathrm{el}}} = \frac{\dot{\sigma}}{E}$$

Substituting this equation into equation (A.6.28):

$$\dot{u}_{\mathrm{t}} = \left(\dot{\varepsilon}_{\mathrm{el}} + \dot{\varepsilon}_{\mathrm{pl}}\right)\xi_{\mathrm{el}}\xi_{\mathrm{pl}}l_0 + \frac{A_0\xi_{\mathrm{pl}}\xi_{\mathrm{el}}^{-2\nu}(E - 2\nu\sigma)}{K}\dot{\varepsilon}_{\mathrm{el}} - \frac{A_0\xi_{\mathrm{pl}}\xi_{\mathrm{el}}^{-2\nu}\sigma}{K}\dot{\varepsilon}_{\mathrm{pl}} \tag{A.6.29}$$

$$\dot{\varepsilon}_{\mathrm{el}} = \frac{K}{A_0 \xi_{\mathrm{pl}} \xi_{\mathrm{el}}^{-2\nu}(E - 2\nu\sigma) + K\xi_{\mathrm{el}}\xi_{\mathrm{pl}} l_0} \dot{u}_{\mathrm{t}} + \frac{A_0 \xi_{\mathrm{pl}} \xi_{\mathrm{el}}^{-2\nu}\sigma - K\xi_{\mathrm{el}}\xi_{\mathrm{pl}} l_0}{A_0 \xi_{\mathrm{pl}} \xi_{\mathrm{el}}^{-2\nu}(E - 2\nu\sigma) + K\xi_{\mathrm{el}}\xi_{\mathrm{pl}} l_0} \dot{\varepsilon}_{\mathrm{pl}} \tag{A.6.30}$$

After some tedious algebraic manipulations the final machine equation is obtained in the following form:

$$\begin{aligned} \frac{\dot{\sigma}}{E} = {} & \frac{K}{A_0 \xi_{\mathrm{s}} \exp\left(-\dfrac{(1+2\nu)\sigma}{E}\right)(E - 2\nu\sigma) + K\xi_{\mathrm{s}} l_0} \dot{u}_{\mathrm{t}} \\ & + \frac{A_0 \xi_{\mathrm{s}} \exp\left(-\dfrac{(1+2\nu)\sigma}{E}\right)\sigma - K\xi_{\mathrm{s}} l_0}{A_0 \xi_{\mathrm{s}} \exp\left(-\dfrac{(1+2\nu)\sigma}{E}\right)(E - 2\nu\sigma) + K\xi_{\mathrm{s}} l_0} \dot{\varepsilon}_{\mathrm{pl}} \end{aligned} \tag{A.6.31}$$

As before, this expression can be simplified somewhat if the fact that $E \gg \sigma$ is used, but this does not lead to any major changes.

Example: A simple example is presented below, which demonstrates how to make corrections for finite strains in an experimental set-up. Obviously, two cases should be considered.

1. *The case of direct control of cross-head displacement:* In this situation equation (A.6.31) is directly applicable for the analysis of the situation, and all of the analysis performed in the present report is correct and true.
2. *The case when direct measurements are performed using clip gages:* In this situation the analysis performed above becomes inapplicable. However, corrections for finite deformations still need to be performed, that is, strain needs to be measured in terms of natural (logarithmic) strain measures. With regard to stress measure, it is necessary to make a transition from the 1st Piola–Kirchoff stress (which is measured in the reference configuration, i.e., force is related to the initial cross-section area) to the true (Cauchy) stress, where force is divided by the instantaneous cross-section area of the sample. This is given by the equation: $\sigma = t \cdot \exp\left(\varepsilon_{\mathrm{pl}} + 2\nu\frac{\sigma}{E}\right)$, where σ stands for the true (Cauchy) stress and t is the 1st Piola–Kirchoff stress, ν is the Poisson's ratio and E is the Young's modulus [Gla4]. Strictly speaking, in order to estimate the value of σ using the data on experimentally measured 1st Piola–Kirchoff stress, it is necessary to solve a nonlinear algebraic equation. However, taking into account that for typical mechanical testing of aluminum alloys $\varepsilon_{\mathrm{pl}}$ is of the order of 0.1–0.2, it is possible to decompose the exponent into a Taylor series, retaining only the linear term of this decomposition, and to solve with respect to σ:

$$\sigma = t\frac{1 + \varepsilon_{\mathrm{pl}}}{1 - t \cdot (2\nu/E)}$$

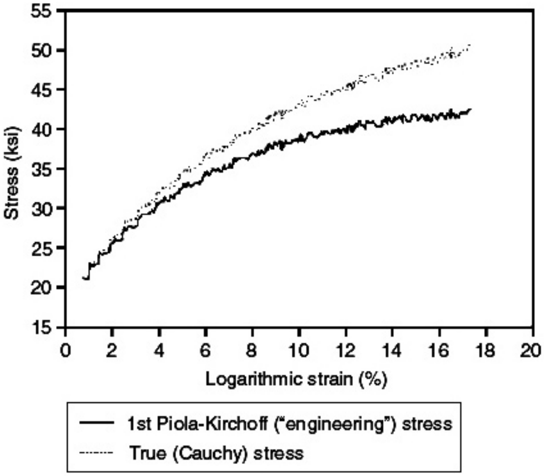

Figure A.6.3 The results of uniaxial tensile testing of aluminum alloy AA5182 with and without corrections for finite deformations.[1]

Finally, taking into account that for pure aluminum Poisson's ratio is equal to 0.34, and Young's modulus for alloy AA5182 is 1.03×10^7 psi, we can get the following final expression which can be used for these calculations:

$$\sigma = t \cdot (1 + \varepsilon_{\mathrm{pl}})(1 + 2\nu/E)$$

This expression was used in order to introduce corrections for finite deformations for experimental data on mechanical testing of 5182 can end stock. The results are presented in Figure A.6.3, with and without corrections for finite deformations. It is quite obvious that the difference is quite significant, especially in the area of large strains.

This page intentionally left blank

INDEX

activation energy of dissolution, 194
aging, 240–245
Ai–Si alloys
  casting properties of, 509
  characteristics of crack resistance, fracture toughness, fatigue properties, and thermal stability, 507–508
  corrosion resistance of, 508
Al alloys, 14, *see also specific* alloys
  alloying elements in, 2–6
  ancillary additions in, 6–9
  casting properties, *see* casting properties, of Al alloys
  impurities in, 9–11
Al–Be–Fe–Si phase diagram, 56–58
Al–Be–Fe system, 14–15, 16
Al–Be–Si system, 15–16
Al–Ce alloys, 14
Al–Ce–Cu system, 16
  non-variant reactions in, 18
  phase diagram, 17
Al–Ce–Fe system, 18
  non-variant reactions in, 20
  phase diagram, 19–20
Al–Ce–Ni system, 20–21
Al–Ce–Si system, 21–22
Al–Cr–Fe system, 22–23
Al–Cr–Mg system, 23–24
Al–Cr–Mn system, 24–26
Al–Cr–Si system, 26
  non-variant phase reactions in, 27
Al–Cu alloys, 425
Al–Cu–Fe–Mg system, 58
  non-variant phase reactions in, 60
  phase diagram, 59
Al–Cu–Fe–Ni system, 60–62
Al–Cu–Fe–Si system, 62–64
  non-variant reactions in, five-phase, 64
  phase diagram, 63
Al–Cu–Fe system, 26
  non-variant reactions in, 28
  phase diagram, 28
Al–Cu–Mg–Mn system, 64
  non-variant reactions in, 66
  phase diagram, 65
Al–Cu–Mg–Si system, 64–66
  non-variant reactions in, 68
  phase diagram, 67
Al–Cu–Mg system, 29–32
  non-variant reactions in, 31
  phase diagram, 30
Al–Cu–Mg–Zn system, 66–68
  non-variant reactions in, 71
  phase diagram, 70–71
Al–Cu–Mn system, 32–34
  non-variant phase reactions in, 33
  phase diagram, 32
Al–Cu–Ni system, 34–35
  non-variant phase reactions in, 35
  phase diagram, 34
Al–Cu–Si system, 36, 37
Al–Cu (2xx) alloys, 376–386
  alloying elements
    copper, 377, 381, 386
    iron, 377, 379, 381, 382
    magnesium, 377, 379
    manganese, 377, 379, 381, 382
    nickel, 377, 385–386
    silicon, 379, 381, 382, 384, 385–386
  castability in, 377, 379, 386
  mechanical properties, 379–386
  Russian alloy AM4.5Kd, 381, 385–386
Al–Cu–Zn system, 36–38
  non-variant reactions in, 38
  phase diagram, 38
Al–Fe–Cu–Mg–Si system, 82–84
  alloys rich in magnesium, 91
  alloys with high content of copper, 87–91
  alloys with high content of silicon, 85–87
  bivariant reactions in, 85
  monovariant reactions in, 86
  non-variant phase reactions of solidification in, 89
  non-variant reactions in, 86
  phase diagram, 84, 88

Al–Fe–Mg–Mn system, 68–69, 72
Al–Fe–Mg–Si system, 70–74
  non-variant five-phase reactions in, 74
  phase diagram, 73
Al–Fe–Mg system, 38–39
Al–Fe–Mn–Si system, 74–77
  chemical composition of intermediate phases in, 77
  non-variant five-phase reactions in, 76
  non-variant reactions in, 76
  phase diagram, 75
Al–Fe–Mn system, 39–40
Al–Fe–Ni–Si system, 77–79
  non-variant phase reactions in, 79
  phase diagram, 78
Al–Fe–Ni system, 41–42
  non-variant reactions in, 42
  phase diagram, 41
Al–Fe–Si system, 42–45
  phase diagram, 43
  solubility of Fe and Si in Al, 44
Allen–Cahn equations, 101
alloying elements
  functions, 2–6
  groups for aluminum alloy design, 1
alloying elements and constituent particles, in industrial casting alloys, 331, 332, *see also specific* alloys
alloys of the solid solution type, 107
alloy systems, basic, role of alloying elements in, 13–14
Al–Mg alloys, equations relating mechanical properties of, to grain size, 285, 286
Al–Mg alloys (5xx alloys), *see also* industrial Al–Mg and Al–Mg–Zn alloys
  alloying elements
    copper, 388
    iron, 388
    magnesium, 387
    manganese, 387
    silicon, 387
    zinc, 387
  castability in, 387, 389, 392
  casting properties of, 389–390
  characteristics, 386–390
  equilibrium solidus of, 396
Al–Mg–Mn–Si system, 79
  non-variant reactions in, 81
  phase diagram, 80
Al–Mg–Mn system, 45, 46
Al–Mg–Ni–Si system, 79–81
  phase diagram, 82
Al–Mg–Si system, 45–47
  joint solubility of Mg and Si in solid Al, 49
  non-variant phase reactions in, 48
  phase diagram, 47–48
Al–Mg–Zn alloys, characteristics of microsegregation in, 147
Al–Mg–Zn system, 47–49
  mutual solubility of Mg and Zn in solid aluminum, 52
  non-variant phase reactions in, 51
  phase diagram, 50
Al–Mn–Ni system, 49–50, 52
Al–Mn–Si system
  maximum solubility of Mn and Si in Al, 54
  non-variant four-phase reactions in, 54
  phase diagram, 53
Al–Ni alloys, 14
Al–Si alloys, 260, 290
  binary, 5–6
  casting, 2, 11, 12
Al–Si alloys, with low-Si, 442–447
  alloying elements distribution
    copper and magnesium, 443
    iron, 444
    manganese, 444
    and mechanical properties, 446
    silicon, 443
    zinc, 444
  microstructure of, 445–446
Al–Si alloys (4xx and 3xx alloys), 328, *see also* Al–Si alloys
  alloying elements
    beryllium, 330
    copper, 328–329, 335, 336
    iron, 329, 330, 332, 336, 346
    magnesium, 328, 335
    manganese, 329
    nickel, 329–330, 335, 368
    silicon, 328, 332, 337
    zinc, 329, 354
  castability, 336, 342, 344, 352, 359
  compositions, 332
  with copper and zinc, 351–367
    engine piston Al–Si alloys, *see* engine piston Al–Si alloys

    fractography of Cu-bearing Al–Si alloys with small amounts of silicon, 366–367
    phase composition of 3xx alloys, 361–366
    of Russian nomenclature, 352, 353–359
  copper-less Al–Si alloys (3xx and 4xx alloys), 336–351
    fractography of, 347–351, 352
    microstructure, 337–338
    phase composition, 336–342, 346
    of Russian nomenclature, 342–345
  corrosion resistance, 335–336
  distribution of alloying elements, 331
  mechanical properties, 332–336
Al–Si–Ni system, 54–55
Al– Zn–Mg–Cu system, 400, 424
  chemical composition of high-strength, corrosion-resistant alloys based on, 404
  eutectic alloys based, 410
Aluminum Association nomenclature alloys, 336, 386
ancillary additions, 6–9
$\mathrm{AT}s_7\mathrm{Mg}_3\mathrm{N}_4$ alloy, 423–425
AZ6N4 alloy, 418–423

beryllium, 9
binary Al alloys
  mechanical properties dependence and chemical composition, 311–326
binary alloys
  composition, and homogenization time, 201–205
  eutectic Al–Si master alloys, 332
  microsegregation elimination kinetics in, 201–206
  non-equilibrium eutectic (Q_{ME}) in a, 129–130
  volume fraction, 190–193
binary phase diagrams closer to aluminum side, 487–489
Bochvar theory, 252
β-phase inclusions, and dissolution, 186
Burgers vector, 113

cadmium, 9
Cahn–Hilliard equation, 100
castability, *see also* casting properties, of Al alloys
  in Al–Mg (5xx) alloys, 387, 389, 392
  improvement in eutectic alloys, 408, 412
  in industrial Al–Cu (2xx) alloys, 377, 379, 385
  in industrial Al–Si (4xx and 3xx) alloys, 336, 342, 344, 352, 359
casting Al alloys, *see also* new casting alloys; *specific* alloys
  aging after casting and quenching, 240–245
  castability dependence of, *see* casting properties, of Al alloys
  fracture toughness and fatigue properties of, 302–311
  grain microstructure of, 108
  high-strength weldable casting alloy, *see* AZ6N4 alloy
  homogenizing heat treatment for, *see* homogenization, processes in
  mechanical properties, dependence of, *see* mechanical properties, dependence of
  oxides and fatigue life of, 309
  standard, compositions of, 461–486
  with transition metals, *see* thermally stable alloys
casting Al alloys, substructure of
  decomposition of aluminum solid solution, 177–182
  dislocation microstructures
    influence of solidification conditions upon, 166–171
    mechanisms of formation, 171–177
  dislocation structures, types of, 162–166
Casting cooling rate and dissolution time, 200
casting hermeticity, 249, 254–255
casting properties, of Al alloys
  basic, 247–258
    hermeticity, casting, 249, 254–255
    hot cracking, 250–251, 255–257
    linear shrinkage, 249–250, 255
    liquid fluidity, 247, 254
    macrosegregation, 251–252
    molten metal fluidity, 247, 248, 253
    volume shrinkage, 254
  concentration dependence of, 258–262
casting properties, of Al–Mg alloys, 389–390
coagulation, in homogenization, *see* fragmentation and spheroidization processes

compositions, alloy
  of binary alloys and homogenization time, 201–206
  and subgrain growth during homogenization, 228–229
concentration
  of alloying elements and aging, 241
  of alloying elements and microsegregation
    binary alloys, 201–206
    multicomponent alloys, 206–213
  dependence on casting properties, 258–262
  gradient of excessive constituent particles, 186
  of silicon and microstructure of Al–Si alloys, 258–262, 290
  of transition metals and decomposition of Al solution, 230–240
copper and zinc bearing Al–Si alloys (of Russian nomenclature), 352
  AK6M2 (Al–6Si–2Cu), 355
  AK5M2 (Al–5Si–2Cu), 354, 355, 358, 359
  AK5M4 (Al–5Si–4Cu), 355, 357
  AK5M (Al–5Si–1Cu), 353–354, 355
  AK5M7 (Al–5Si–7Cu), 357
  AK8M3 (Al–8Si–3Cu), 358–359
  AK8M (Al–8Si–1Cu), 357–358
  AK9M2 (Al-9Si–2Cu), 359
  chemical composition of, 356
copper-less Al–Si alloys (of Russian nomenclature), 342–345
  AK7 (Al–7Si), 343, 344–345, 354
  AK8 (Al–8Si), 343, 345
  AK9 (Al–9Si), 342, 343, 344, 345, 354
  AK12 (Al–12Si), 332, 338, 342, 343, 344
  AK13 (Al–13Si), 342, 343
  AK10Su, 343, 345
corrosion resistance, Al–Si alloys (4xx and 3xx alloys), 335–336

decomposition of aluminum solid solutions, before quenching, 230–240
deformation diagrams, for as-cast and quenched aluminum alloys, 266–280
degree of alloying, tensile mechanical properties and, 286
dendritic solidification
  3D phase-field modeling of, 103
  of pure metals, 102–103
density, 111
  in alloys with subgrain microstructure, 113–114
  of dislocations, *see* dislocation density of alloys
dislocation density of alloys, 112–113
  and fracture toughness, 305
  tensile mechanical properties, and, 290–291
dislocation microstructures, 166
  alloys on the basis of Al–Cu system, 169–171
  alloys on the basis of Al–Mg system, 167–169
  and homogenization, 222–230
  influence of solidification conditions upon, 166–171
  mechanisms of formation in cast aluminum alloys, 171–177
dispersoids, 229, 231, 233–234, 238–239, 243
dissolution, during homogenization, *see also* dissolution kinetics
  activation energy of, 194
  of β-phase inclusions, 186
  kinetics and experimental studies, 190–194
  of non-equilibrium constituent particles, 184–190
  time, 193
    casting cooling rate and, 200
    and effect of refinement of as-cast microstructure on, 195–200
    equations relating, of excessive phases dissolved particles thickness, 197, 198–199
    of non-equilibrium eutectic dissolution, 188–189
dissolution kinetics
  experimental studies, 190–194
  and homogenization temperature dependence, 193–194
  microstructure characteristics of, 193, 195–196
  solidification rate and, 195

effective solidification range, 252–253
engine piston Al–Si alloys, 367–376, *see also* Al–Si alloys (4xx and 3xx alloys)
  chemical composition, 370
  fractography of, 376
  phase composition, 368–369, 373–376

of Russian nomenclature
  AK12M2MgN (Al12Si2Cu1Mg1Ni), 375, 376
  AK12MMgN (Al12Si1Cu1Mg1Ni), 375, 376
  AK21M2.5N2.5 (Al121Si2.5Cu2.5Ni), 375–376
equilibrium thermodynamics, 97
  of concentrationally non-uniform systems, 98–101
Eulerian tensor field, 515
eutectic alloys, 2
  multicomponent, 405–420
    alloy castability improvement, 408, 412
    mechanical properties, 411
    microstructure analysis, 411–413, 417–418
    phase composition in, 412–415
    silicon phase in, 409
  phase-field models of solidification of, 104–106

fatigue properties, of casting Al alloys, 302–311
five-component phase diagrams, 81–93
  Al–Fe–Cu–Mg–Si system, 85–91
  five-component systems with manganese, 91–93
fractography
  of copper-bearing Al–Si alloys with small amounts of silicon, 366–367
  copper-less Al–Si alloys (3xx and 4xx alloys), 347–351, 352
  of engine piston Al–Si alloys, 376
fracture toughness of casting Al alloys, 302–311
fragmentation and spheroidization processes, 213–222
friction stress parameter, 301

Ginzburg–Landau equation, 101
grain microstructure of cast aluminum alloy, 108
grain refinement, during homogenization, 229
grain size and homogenization, 222–230
grain size effect
  and fracture toughness, 305
  tensile mechanical properties, and, 281–282, 284, 285

Hall–Petch relationship, 282
heat treatment(s), for casting Al alloys
  homogenizing, 184, *see also* homogenization, processes in
  types, 183
hermeticity, casting, 249, 254–255
high-strength alloys of solid solution type, 397–398
high-temperature homogenization, 193, *see also* homogenization
  alloying element concentrations and, 211
  porosity and, 240
homogenization
  grain refinement in, 230
  grain size and dislocation microstructures, changes during, 222–230
  high-temperature, *see* high-temperature homogenization
  particle morphologies, change during, *see* fragmentation and spheroidization processes
  processes in
    decomposition of aluminum solid solution containing transition metals, 230–240
    dissolution of non-equilibrium constituent particles, 184–200
    fragmentation and spheroidization processes, 213–222
    grain size and dislocation microstructures, changes in, 222–230
    microsegregation elimination during, 200–213
    porosity development, 240
  solidification rate and, *see* solidification rate, during homogenization
  time
    and composition of binary alloys, 201–206
    and volume fraction, 190–193, 238–239
hot cracking, 250, 251, 255–257
  index (HCI), 250, 251
  probes, 250–251
hot tearing susceptibility (HTS), 415, 416
hypo-eutectic alloys, 2

impurities, 9–11
industrial alloys, 2, 3, 4, *see also specific* alloys

industrial Al–Mg and Al–Mg–Zn alloys, 390–396, *see also* Al–Mg alloys (5xx alloys)
  AMg7 (Al7Mg), 392, 393
  AMg11 (Al11Mg), 394
  AMg10 (Al10Mg) alloy, 391–392
  AMg5K1 (Al5Mg1Si), 395
  AMg4K1.5M (Al4Mg1.5Si1Cu), 395
  AMg6l alloy, 390
  AMg6lch (Al6Mg) alloy, 391
  AMg5Mts (Al5Mg1Mn), 392
  ATs4Mg (Al4Zn1Mg), 395
industrial casting Al alloys, *see specific* alloys

Kirkendall effect, 240

Lagrangian tensor field, 515
lead, 330, *see also* Al–Si alloys
linear shrinkage, 249–250, 255
liquid fluidity, 247, 254
lithium, 2
local macrosegregation, 252

machine equation, 514
macrosegregation, 251–252
macrostructure, 95
magnesium, 282
magnesium silicide, 161
manganese, 7, 151–154
mechanical properties
  of Al–Cu alloys, role of alloying elements and constituent particles in, 379–386
  of Al–Si alloys, 335–336
    heat treatment scheme and, 333–334
    and role of alloying elements and constituent particles in, 328–332
  of engine piston Al–Si alloys, *see* engine piston Al–Si alloys
mechanical properties, dependence of, 262–266
  calculation using microstructural parameters, 295–302
  on chemical composition, regularities in changes of, 311–326
  on microstructure
    fracture toughness and fatigue properties, 302–311
    geometry of deformation diagrams for as-cast and quenched aluminum alloys, 266–280
    tensile mechanical properties and, *see* tensile mechanical properties
micress (microstructure simulation software), 107
microsegregation
  in binary aluminum alloys, 119–125
  concentration threshold for appearance of non-equilibrium constituent particles (phases), 125–128
  elimination kinetics, 200
    binary alloys, 201–206
    multicomponent alloys, 206–213
  in three-component and industrial aluminum alloys
    key alloying elements, 145–151
    manganese, 151–154
  in two-component aluminum alloys, 115–119
microstructure, 95, 100, *see also specific entries*
  characteristics
    calculation of mechanical properties of castings using, 295–302
    tensile mechanical properties and, 284, 286–290
  and hot cracking, 257
  mechanical properties dependence on
    fracture toughness and fatigue properties, 302–311
    geometry of deformation diagrams for as-cast and quenched aluminum alloys, 266–280
    tensile mechanical properties and, *see* tensile mechanical properties
microstructure and homogenization
  characteristics of dissolution kinetics, 195–196
  fragmentation and spheroidization processes effect on, 213–222
  microsegregation elimination and, 200
    binary alloys, 201–206
    multicomponent alloys, 206–213
  refinement of as-cast microstructure, and dissolution kinetics, 195–200
molten metal fluidity, 247, 248, 253–254
multicomponent alloys, *see also* eutectic alloys, multicomponent

  grain size change in, 229
  microsegregation elimination kinetics in, 206–213

new casting alloys
  alloys with small amounts of eutectic, 397–405
    01568 alloy, 402
    01976 alloy, 403
    01984 alloy, 402–403
    AL24p alloy, 398
    Al– Zn–Mg–Cu system for, 400, 404
    AMg5K alloy, 403
    drawbacks, 405
    VAL11 alloy, 398, 399, 400
    VAL12 alloy, 399, 400
  Al–Si alloys, with low-Si, 441–447
  ATs7Mg3N4 alloy, 418–424
  AZ6N4 alloy, 418–424
  eutectic alloys, 405–418
  with small amounts of silicon, 441–447
  thermally stable alloys, with transition metals, 425–441
nickalin, *see* AZ6N4 alloy
non-equilibrium eutectic (Q_{ME}) in a binary alloy, 129–130
non-equilibrium solidification, 111
non-equilibrium solidification of binary alloys, 114
  microsegregation
    in binary aluminum alloys, 119–125
    concentration threshold for appearance of non-equilibrium constituent particles (phases), 125–128
    in two-component aluminum alloys, 115–119
  solidification
    constituent particles of secondary (excessive) phases, 128–132
    suppression of peritectic reactions, 132–134
non-equilibrium solidification of multi-component alloys
  microsegregation in three-component and industrial aluminum alloys
    key alloying elements, 145–151
    manganese, 151–154
  phase diagrams
    Al–Cu–Fe–Si system, 139–140
    Al–Fe–Mg–Si system, 140–143
    Al–Fe–Ni–Si system, 143–145
    Al–Fe–Si system, 134–138

order parameters, 100
oxides and fatigue life of cast Al alloys, 309

peritectic reactions, 132–134
phase composition
  of copper-less Al–Si alloys and in heat treatments, 336–342
  engine piston Al–Si alloys, 368–369, 371–375
  of 2xx series alloys, role of alloying elements and constituents particle, 381–386
  of 3xx series alloys, 361–366
  of 5xx series alloys, role of alloying elements and constituents particle, 386–390
phase diagrams
  Al–Cu–Fe–Si system, 139–140
  Al–Fe–Mg–Si system, 140–143
  Al–Fe–Ni–Si system, 143–145
  Al–Fe–Si system, 134–139
phase-field methodology, 101
  dendritic solidification of pure metals, 102–103
  phase-field models of solidification, 102
    of eutectic alloys, 104–106
  solidification microstructure calculations, 106–107
phase-field theory, 96
Piola–Kirchoff stress, 520, 521
porosity development, and homogenization, 240

quantitative characteristics of alloy structure and methods of its evaluation, 107–114

refinement of as-cast microstructure, 192, 195–200
regression equations, drawbacks of, 296
Russian aluminum alloys, 336, *see also* engine piston Al–Si alloys
  AM4.5Kd, 381, 386
  with copper and zinc, 351–366
  copper-less Al–Si alloys (3xx and 4xx alloys), 342–345
  mechanical properties, 491–498

Russian casting aluminum alloys, 181
  heat treatments of, 500–506
  precipitation and microstructure of, 178

secondary precipitation of excessive phases, 292
shrinkage voids, 247, 248–249
silver, 2
solidification, 254
  constituent particles of secondary (excessive) phases, 128–132
  dendritic, *see* dendritic solidification
  microstructure of calculations, 106–107
  phase-field models to, 102
    of eutectic alloys, 104–106
  suppression of peritectic reactions, 132–134
  volume shrinkage during, 254
solidification rate, during homogenization, 244
  and dissolution kinetics, 195
  and grain size distribution, 225–226
solid solution strengthening, 2–3
  copper addition and, 5
  zinc addition and, 5
spheroidization processes, *see* fragmentation and spheroidization processes
substructure of casting aluminum alloys
  decomposition of aluminum solid solution, 177–182
  dislocation microstructures
    influence of solidification conditions upon, 166–171
    mechanisms of formation, 171–177
  dislocation structures, types of, 162–166
  tensile mechanical properties and, 290–295

tensile mechanical properties, 280–281
  dislocation density of alloys and, 290–291
  grain size, 281–282, 284, 285
  microstructure characteristics, 284, 286–290
  of pores, 286–287
  secondary precipitation of excessive phases, 292
  subgrain microstructure and, 292
  substructure, 290–295
thermally stable alloys, with transition metals, 425–441
  Al–TM1–TM2 type composition, 426–427
  microstructure analysis, 427–429, 436, 437
ThermoCalc, 29, 106
Tiller's theory, 173
tin, 330
transition elements
  and aging of castings after casting and quenching, 240–245
  and decomposition of Al solid solutions, 230–240
transition metals
  in aluminum alloys, 7–9
  in thermally stable alloys, 425–441

uniaxial tensile testing in finite deformations, derivations of equations, 511–513
  finite deformations, 515–521
  infinitesimally small deformations, 513–514

volume fraction, 129, 130
  of excessive eutectic phases and fracture toughness, 306
  and homogenization time, 190–194
  of non-equilibrium phases in commercial alloys, 131
  of pores
    tensile mechanical properties and, 286–287
  of solidification, 252
volume shrinkage during solidification, 254

work hardening, 272, 277

zonal macrosegregation, 252